Summer 8-23-2024

Contributions to the Understanding of Turbulent Boundary Layers Over Curved Walls

Nicholas Zhu
Embry-Riddle Aeronautical University, ZHUN@my.erau.edu

CONTRIBUTIONS TO THE UNDERSTANDING OF TURBULENT BOUNDARY LAYERS OVER CURVED WALLS

By

Nicholas Xu Zhu

A Dissertation Submitted to the Faculty of Embry-Riddle Aeronautical University

In Partial Fulfillment of the Requirements for the Degree of

Doctor of Philosophy in Aerospace Engineering

August 2024

Embry-Riddle Aeronautical University

Daytona Beach, Florida

CONTRIBUTIONS TO THE UNDERSTANDING OF TURBULENT

BOUNDARY LAYERS OVER CURVED WALLS

By

Nicholas Xu Zhu

This Dissertation was prepared under the direction of the candidate's Dissertation Committee Chair, Dr. J. Gordon Leishman, Department of Aerospace Engineering, and has been approved by the members of the Dissertation Committee. It was submitted to the Office of the Senior Vice President for Academic Affairs and Provost, and was accepted in the partial fulfillment of the requirements for the Degree of Doctor of Philosophy in Aerospace Engineering

DISSERTATION COMMITTEE

J. Gordon Leishman Digitally signed by J. Gordon Leishman Date: 2024.08.28 12:48:18 -04'00'

Chair, Dr. J. Gordon Leishman

Ebenezer Gnanamanickam Digitally signed by Ebenezer Gnanamanickam Date: 2024.08.28 12:13:05 -04'00'

Co-Chair, Dr. Ebenezer P. Gnanamanickam

Richard J. Prazenica Digitally signed by Richard J. Prazenica Date: 2024.08.28 11:08:14 -04'00'

Member, Dr. Richard Prazenica

Sandra Boetcher Digitally signed by Sandra Boetcher Date: 2024.08.27 11:21:29 -04'00'

Member, Dr. Sandra Boetcher

MINNITI.ROBERT.JOSEPH.III.1230328265 Digitally signed by MINNITI.ROBERT.JOSEPH.III.1230328265 Date: 2024.08.26 19:22:35 -04'00'

Member, Dr. Robert Minniti III

Sirish Namilae Digitally signed by Sirish Namilae Date: 2024.08.28 14:43:49 -04'00'

Graduate Program Coordinator,
Dr. Sirish Namilae

08/28/2024

Date

Dean of the College of Engineering,
Dr. James W. Gregory

Date

Senior Vice President for Academic Affairs and Provost,
Dr. Kelly M. Austin

Date

To curiosity.

ACKNOWLEDGMENTS

When I drove down to Daytona five years ago, I was uncertain about the commitment I had made. Fast-forwarding, graduate school at Embry-Riddle has been a remarkable, life-changing experience, thanks to the amazing group of people I met along the way. Their mentorship and friendship have helped me grow immensely as an engineer and a person.

I want to start by expressing my gratitude to my two advisors. Prof. J. Gordon Leishman and Prof. Ebenezer Gnanamanickam have been exceptional mentors throughout this journey. Their insightful guidance, unwavering support, and positive encouragement have been crucial in completing this dissertation. I also extend my heartfelt thanks to Dr. Leishman for inviting me to study at Embry-Riddle in the spring of 2019—these past few years have been unforgettable, and I wouldn't trade them for anything.

I must thank Dr. Zheng Zhang for his invaluable insights on various topics and for always helping me overcome the challenges I encountered along the way. I am also thankful to Mr. Joel Mills and Mr. William Russo for their help in constructing the wind tunnel model and manufacturing the PIV calibration plates. They expertly machined essential components and patiently taught me how to use several tools in the workshop.

Of course, I have to thank my committee members for their technical insights. Prof. Richard Prazenica, Prof. Sandra Boetcher, and Dr. Robert Minniti have challenged me to think critically about certain issues I would have otherwise overlooked. Their feedback has been crucial to refining my dissertation.

Thank you to the Aerospace Department and the University for supporting my work through the GAANN fellowship, and giving me months of wind tunnel time. I want to thank Prof. Tasos Lyrintzis for supporting my conference travels. I must also acknowledge Ms. Cynethia Goodwyn for always being so helpful despite being very busy. Thank you also to Ms. Vilma Steel, Ms. Darlene McCoy, and Dr. Pamela Daniels for their hard work.

I also must acknowledge the Department of Defense SMART scholarship. Thank you, Dr. Minniti, Dr. Jason Anderson, and Ms. Charlotte George at Carderock for helping me

become part of this fantastic program. I look forward to working with you all.

I want to mention a few people at the University of Maryland who let me try my hand at experimental aerodynamics. To Dr. Andrew Lind, Prof. Anya Jones, and Prof. Jewel Barlow, thank you for the opportunity to work in your labs.

I could not have completed this journey without the support of my friends and family both in Florida and back home in Maryland. Thanks for sticking by my side.

ABSTRACT

A wind tunnel campaign was conducted to investigate the DARPA Suboff boundary layer. To emphasize the axisymmetric boundary layer, the generic submarine model's sail, appendages, and propeller were omitted. The study focused on the afterbody from 70–95% of the model length to examine the concurrent pressure gradient and wall curvature effects, which are commonplace in engineering. Three particle image velocimetry (PIV) configurations were employed to measure the boundary layer in detail: one spanned the entire afterbody, another had narrow strips sampled at 16 kHz, and the third used two simultaneous orthogonal measurement planes. Considerable effort was made to reduce the laser reflection, allowing seed particles to be measured less than 20 µm above the opaque wall. PIV measurements were acquired at Reynolds numbers up to $Re_\tau \approx 2{,}700$ or $Re_L \approx 8{\times}10^6$ based on model length, which is substantial for an axisymmetric body. The primary aims were to 1. Elucidate how the statistics and structure of a near-canonical boundary layer were modified along the Suboff afterbody and 2. Determine whether these alterations stemmed from pressure gradient, lateral curvature, or longitudinal curvature depending on their relative spatial patterns. The pressure gradient significantly affected the wall-tangent turbulence intensity, whereas the wall-normal intensity experienced the effects of longitudinal and lateral curvature. A scale decomposition demonstrated that large scales were more influenced by the non-equilibrium flow conditions than the small scales. Further investigation of the large scales relied on two-point statistical methods. Linear stochastic estimation showed that hairpin vortex packets had a significant role, irrespective of the pressure gradient and wall curvature. Consequently, the correlation contours based on the wall-tangent velocity were forward leaning. The near-wall structures were elongated/compressed with minor rotation, whereas structures at the boundary layer edge were rotated with minimal distortion. The resulting length scales were collapsed across all wall-parallel and -normal positions by a pressure gradient parameter, when shifted by roughly one boundary layer thickness to account for the delayed response of the structures. The wall-normal correlation contour's usual column shape was unaffected

near the boundary layer edge, whereas the near-wall structure developed, with downstream distance, a peak frequency and a forward-leaning appearance indicative of hairpin packet influence. The peculiar behavior in the cross-correlation of wall-tangent and wall-normal velocities was interpreted as longitudinal streamline curvature effects on the turbulent bulges and valleys, as indicated by a conditional average analysis. This finding motivated a study of the turbulent/non-turbulent interface. A modified interface detection criterion was necessary to account for wall-normal velocity and streamline curvature. The computed interface indicated that the boundary layer was intermittently turbulent in the outer 40–70% depending on the pressure gradient. Across these interfaces were velocity "jumps" that became more significant with adverse pressure gradients. Additionally, the large-scale motions underlying the interface bulges were gradually enlarged downstream.

TABLE OF CONTENTS

LIST OF FIGURES

LIST OF TABLES

NOMENCLATURE

a	Geometry radius
a^+	Geometry radius with viscous scaling
A_1, B_2	Constants for generalized log law
C	Log law constant
C_f	Friction coefficient
C_p	Pressure coefficient
$C_{p,0}$	Pressure coefficient without downstream strut
D	Model maximum diameter, mm
dp/dx	Pressure gradient, $\mathrm{Pa\,m^{-1}}$
f	Frequency, s^{-1}
f_c	Nyquist frequency, s^{-1}
f_s	Sampling frequency, s^{-1}
G	Wake function
H	Shape factor
k_i	Local kinetic energy
k_x	Streamwise wavenumber, $\mathrm{m^{-1}}$
l	Final interrogation window size, µm
l_ν	Viscous length scale, µm
l^+	Final interrogation window in wall unit
L	Model length, ft
L_a	Major axis of elliptical structure, mm
L_b	Minor axis of elliptical structure, mm
L_s	Length scale along streamline, mm
M	Lens magnification
n_t	Number of snapshots
n_s	Number of spatial locations times velocity components

p_x^+	Viscous scaled pressure gradient parameter
Q	Covariance matrix, $\mathrm{m^2\,s^{-2}}$
r	Radial position, mm
R	Hull maximum radius, mm
R_{ij}	Two-point correlation between two quantities
t^+	Viscous time scale
T_s	Sampling duration, s
u, v, w	Wall-parallel, spanwise, and wall-normal velocity fluctuations, $\mathrm{m\,s^{-1}}$
$\tilde{u}, \tilde{w}$	Wall-parallel and wall-normal velocity, $\mathrm{m\,s^{-1}}$
$\tilde{u}_{m,n}, \tilde{w}_{m,n}$	Wall-tangent and normal velocity at grid points defined by m and n, $\mathrm{m\,s^{-1}}$
$\overline{u^2}, \overline{w^2}, \overline{uw}$	Reynolds stresses, $\mathrm{m^2\,s^{-2}}$
$\overline{u_i^2}, \overline{w_i^2}, \overline{u_i w_i}$	Reynolds stresses conditioned about TNTI, $\mathrm{m^2\,s^{-2}}$
u_x, u_r, u_θ	Axial, radial, azimuthal velocity fluctuations, $\mathrm{m\,s^{-1}}$
$u_{x,0}$	Axial velocity without downstream strut, $\mathrm{m\,s^{-1}}$
u_η	Kolmogorov velocity scale, $\mathrm{m\,s^{-1}}$
u_τ	Friction velocity, $\mathrm{m\,s^{-1}}$
U, V, W	Wall-parallel, spanwise, wall-normal mean velocities, $\mathrm{m\,s^{-1}}$
U^+	Wall-parallel velocity scaled by friction velocity
U_c	Convection velocity , $\mathrm{m\,s^{-1}}$
U_e	Edge velocity, $\mathrm{m\,s^{-1}}$
U_i, W_i	Wall-tangent and wall-normal velocity conditioned on the interface, $\mathrm{m\,s^{-1}}$
U_r	Reduced order velocity vector matrix, $\mathrm{m\,s^{-1}}$
U_x, U_r, U_θ	Axial, radial, azimuthal mean velocities, $\mathrm{m\,s^{-1}}$
U_∞	Free-stream velocity , $\mathrm{m\,s^{-1}}$
$U\|_{z_i}, W\|_{z_i}$	Wall-tangent and -normal mean velocities conditioned on TNTI, $\mathrm{m\,s^{-1}}$
x_T, y_T, z_T	Streamwise, spanwise, and wall-normal directions in tunnel frame, mm
z	Wall-normal position, mm

z^+	Wall-normal position normalized by viscous length scale
z_i	Wall-normal interface position, mm
Z_i	Average wall-normal interface position, mm
α	Local structure inclination angle, deg
α_g	Global structure inclination angle, deg
α_w	Wall angle, deg
β_c	Clauser pressure gradient parameter
γ	Intermittency
δ	Boundary layer thickness, mm
δ^*	Displacement thickness, mm
δ_0	True boundary layer thickness, mm
δ_{99}	Boundary layer thickness where velocity is 99% of edge velocity
ϵ	Dissipation, $\mathrm{m^2\,s^{-3}}$
η	Kolmogorov length scale, µm
θ	Momentum thickness, mm
κ	von Kármán constant
λ_c	Cutoff wavelength, mm
λ_{ci}	Swirling strength, $\mathrm{s^{-1}}$
λ_T	Taylor microscale, µm
λ_x	Streamwise wavelength, mm
Λ	Eigvenvalues of covariance matrix
$\Lambda_{\max}$	Max wavelength, m
ν	Kinematic viscosity, $\mathrm{m^2\,s^{-1}}$
Π	Wake strength parameter
ρ	Density, $\mathrm{kg\,m^{-3}}$
σ_i	Standard deviation of interface location, mm
Σ	Singular values in the POD

Σ_r	A subset of the singular values from the POD
τ_w	Wall shear stress, Pa
τ_η	Kolmogorov time scale, µs
Φ	Spatial modes of proper orthogonal decomposition, $\mathrm{m\,s^{-1}}$
Ψ	Eigenvectors of covariance matrix
$\overline{\omega_i^2}$	Vorticity fluctuation conditioned about TNTI, $\mathrm{s^{-2}}$
Ω_i	Vorticity conditionally-averaged about the interface, $\mathrm{rad\,s^{-1}}$

ACRONYM

APG	Adverse pressure gradient
CCD	Charge-coupled device
CCM	Clauser chart method
CMOS	Complementary metal oxide semiconductor
DARPA	Defense Advanced Research Projects Agency
DHV	Downstream hairpin vortex
DNS	Direct numerical simulation
DVR	Dynamic velocity range
ESL	Embedded shear layer
FOV	Field of view
FPG	Favorable pressure gradient
LPT	Lagrangian particle tracking
LSE	Linear stochastic estimation
MCCM	Modified Clauser chart method
MDF	Medium density fiber
Nd:YAG	Neodymium-doped yttrium aluminum garnet
Nd:YLF	Neodymium-doped yttrium lithium fluoride
OFI	Oil-film interferometry
PIV	Particle image velocimetry
PHV	Primary hairpin vortex
POD	Proper orthogonal decomposition
SHV	Secondary hairpin vortex
SVD	Singular value decomposition
THV	Tertiary hairpin vortex
TKE	Turbulent kinetic energy
TNTI	Turbulent/non-turbulent interface

Q2, Q4	Quadrant 2 and 4 events
QSV	Quasi-streamwise vortices
UMZ	Uniform momentum zones
VITA	Variable interval time average
VLSM	Very-large-scale motion
WSS	Wall-shear stress
ZPG	Zero pressure gradient
ZS	Zagarola-Smits

1 Introduction

A boundary layer is formed with fluid motion relative to a surface. The boundary layer is a (usually) thin layer of retarded fluid formed as a result of the so-called no-slip boundary condition at the wall, where the fluid flow velocity must be zero relative to the surface. Because of this condition, the velocity grows gradually with distance away from the wall and eventually matches the irrotational outer flow. This region of increasing fluid velocity is known as the boundary layer.

When the boundary layer first forms along a surface, it is typically laminar. The flow travels in parallel laminas or thin layers in a laminar boundary layer. As it develops downstream, these laminas become unstable, and mixing occurs. Under this mixing state, the boundary layer is known as being turbulent.

In the engineering world, turbulent boundary layers are ever-present on various vehicles. In Fig. 1.1, airplanes, rotorcraft, cars, marine vehicles, etc., all have turbulent boundary layers developing along their fuselage, hull, and wings. One reason why boundary layers are essential is that they are tied closely to the aerodynamic drag (and other forces and moments) and correspondingly the energy expended to overcome it [9, 21]. Another reason is that pusher propellers on aerial and marine vehicles ingest the upstream boundary layer. In these situations, the boundary layer turbulence determines the propeller aero/hydrodynamic performances and the acoustic radiation [46, 47].

One challenge in understanding and modeling these engineering boundary layers is that they develop along surfaces with longitudinal and transverse curvatures. These surface curvatures can induce significant pressure gradients and potentially other effects that are not fully understood. Because the development of a canonical, i.e., zero-pressure gradient (ZPG), smooth-wall, flat-plate boundary layer, is well-studied [48–51], the community in recent years has begun to strive for a deeper understanding of pressure gradient and wall curvature effects [52–55].

With this goal in mind, the present work investigates the boundary layer formed along

Figure 1.1 Aerial and marine vehicles where boundary layers with pressure gradients and surface curvatures play a crucial role in the aero/hydrodynamic forces and moments

the tail of a representative model submarine. This boundary layer is the propeller inflow and, therefore, substantially influences the hydrodynamic loads and radiated noise. The challenge in understanding and predicting this flow stems from the tapering of the hull geometry. This tapering induces an initially favorable and subsequently adverse pressure gradient history, and possibly other effects related to the surface curvature.

Understanding how the pressure gradients and the wall curvatures affect the boundary layer's cascade of scales, particularly the coherent large scales, is the principal objective of this research. Figure 1.2 displays snapshots from streamwise and cross-stream planes (not measured simultaneously) of the wall-parallel u and wall-normal w velocities normalized by the (left-to-right) free stream. The instantaneous flow velocities in these figures reveal an intricate range of length scales. On the one hand, the largest scales are distinctly visible in the streamwise and spanwise planes as hills and valleys, zones of uniform momentum, etc.; on the other, the smallest scales are so fine that even state-of-the-art measurement techniques cannot easily resolve.

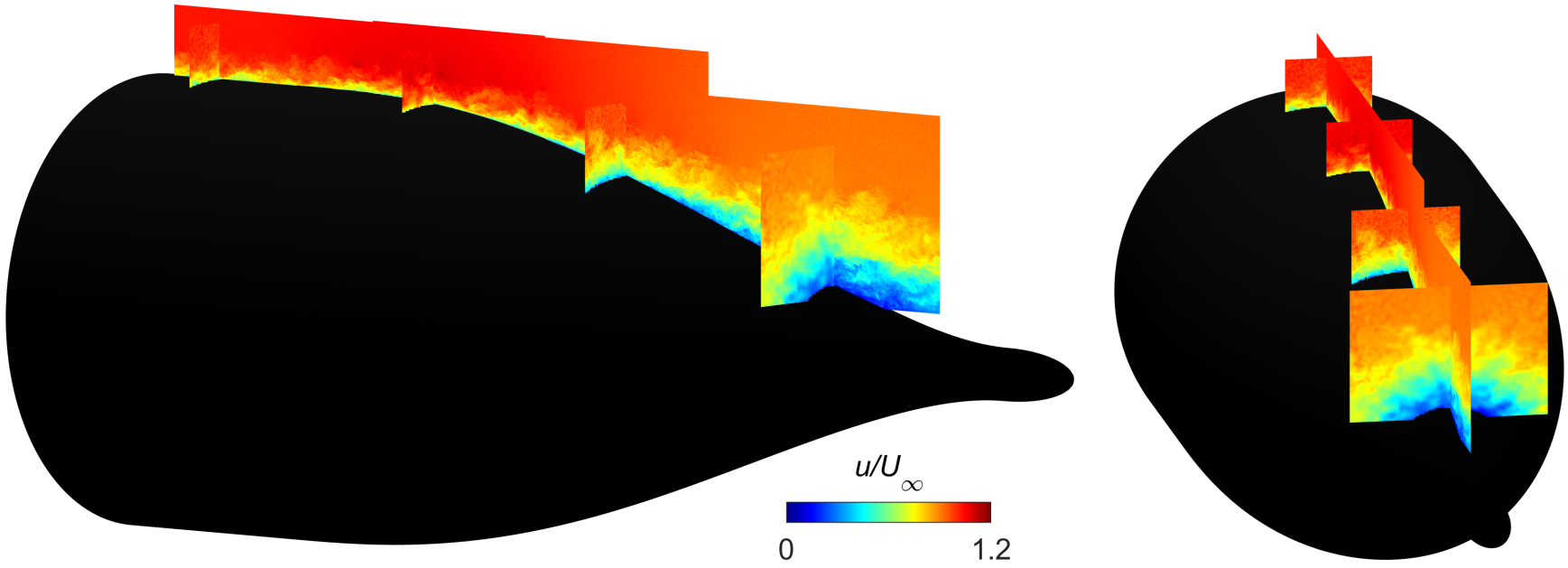

(a) *(b)*

Figure 1.2 Continued on next page.

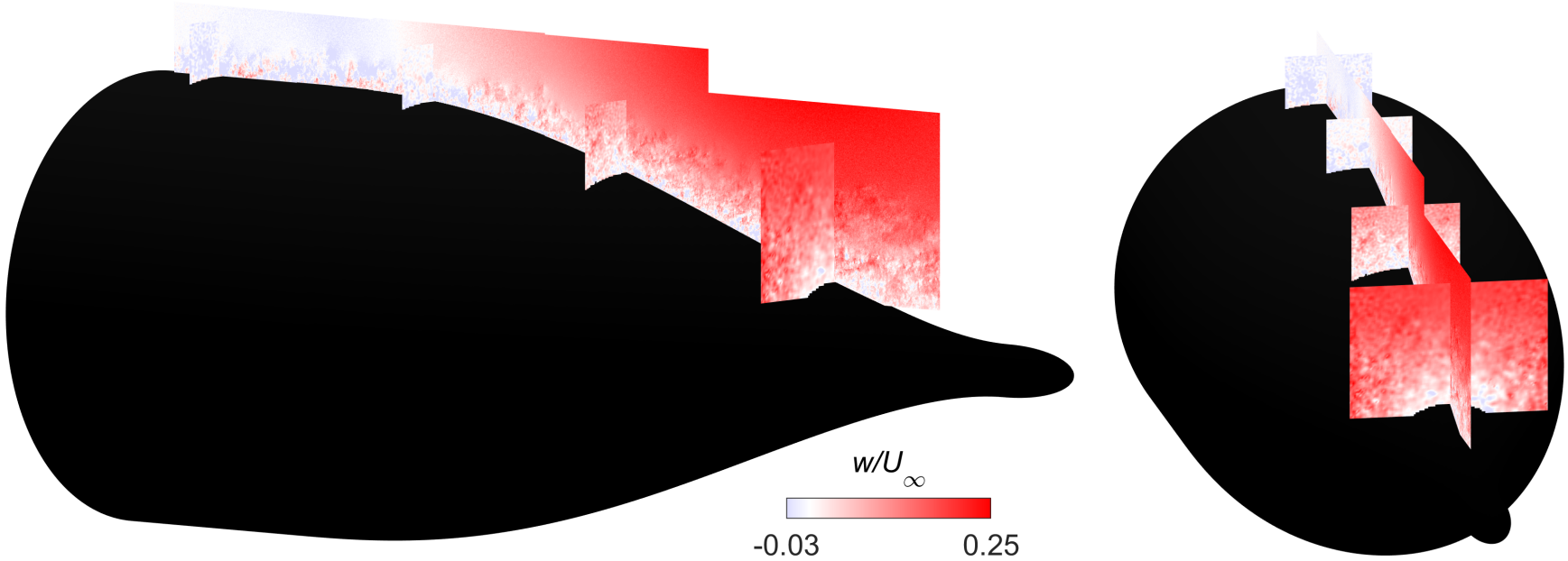

Figure 1.2 Streamwise and crosswise snapshots of the boundary layer's *(a,b)* wall-tangent u and *(c,d)* wall-normal w velocities. Snapshots are not time-correlated.

The purpose of this chapter is to motivate the remainder of this writing. A literature review is first provided with a discussion of the existing shortcomings in understanding in Section 1.1. The three objectives of this research are then enumerated in Section 1.2, guiding the research effort to better understand pressure gradient and wall curvature effects in turbulent boundary layers. Lastly, Section 1.3 overviews the organization of this document.

1.1 Literature Survey

The axisymmetric boundary layer investigated in this work was formed along a submarine hull. The emphasis was placed on the tail region of the submarine body, where the model's tapering geometry strongly decelerated the boundary layer. This boundary layer is interesting from a fundamental perspective because the flow physics underlying surface curvature and pressure gradient effects are relatively unknown. From a practical standpoint, understanding and predicting the characteristics of this boundary layer has clear engineering applications, not only to marine vehicles but also to aircraft, rotorcraft, cars, etc. Of course, there is a tremendous body of literature dedicated to the study of boundary layers, with many detailed reviews of the then-state-of-the-art [48, 49, 56] and a more recent one by Devenport and Lowe [51].

Prior works relevant to the current research can be sorted into three approaches:

1. Developing analytical and empirical models to describe the flow statistics [57–59] or the coherent structures' kinematics [60–64].

2. Documenting in measurements or simulations the changes in flow statistics with non-dimensional groupings such as Reynolds number, Clauser's pressure gradient parameter, acceleration parameter, etc. [3, 13, 65, 66], and finding suitable variables that minimize (or ideally eliminate) the streamwise development of turbulence statistics [5, 67, 68].

3. Identifying underlying coherent structures through qualitative or quantitative flow visualization [15, 19, 24, 69] and direct-numerical simulation [18, 70–72].

In practice, these different approaches are complementary. For example, understanding the coherent structures could provide candidate eddies for modeling efforts [64]. Conversely, the choice of a candidate eddy in a kinematic model that successfully replicates the measured boundary layer characteristics reinforces the importance of that coherent structure. As another example, the observed flow structures can offer insights into the appropriate scaling of the flow statistics [71, 73]. Also, changes in the flow statistics could reveal how the large and small scale structures are modified with growing Reynolds number or pressure gradient [3, 65, 74]. Therefore, workers utilize some complementary mixture of these approaches to form compelling arguments.

This literature survey is organized to mirror the results presented in this dissertation. First, Section 1.1.1 provides background on single-point flow statistics. Then, in Section 1.1.2, the boundary layer structure is discussed in detail as it is a significant focus of this dissertation. Following this structural perspective, prior works on the turbulent/non-turbulent interface are overviewed in Sections 1.1.4. Pressure gradient effects are discussed for each of these topics. Finally, Section 1.1.3 considers studies of axisymmetric boundary layers with significant lateral curvature.

1.1.1 Boundary Layer Statistics

A turbulent flow can be decomposed into mean and fluctuating components following the work of Osborne Reynolds. The mean velocity distribution is first reviewed in Section 1.1.1.1, followed by the Reynolds stress profiles in Section 1.1.1.2. This overview establishes a baseline understanding of how turbulence is quantified and understood.

1.1.1.1 Time-Mean Velocity

A fundamental question in studying pressure gradient effects is how the turbulence statistics are modified. In this regard, the canonical boundary layer is typically decomposed into four parts as illustrated in Fig. 1.3: the viscous sublayer, the buffer layer, the logarithmic region, and the wake region. Note the logarithmic scaling. The classical perspective is that the viscous sublayer and buffer layer are governed solely by viscous quantities, although re-

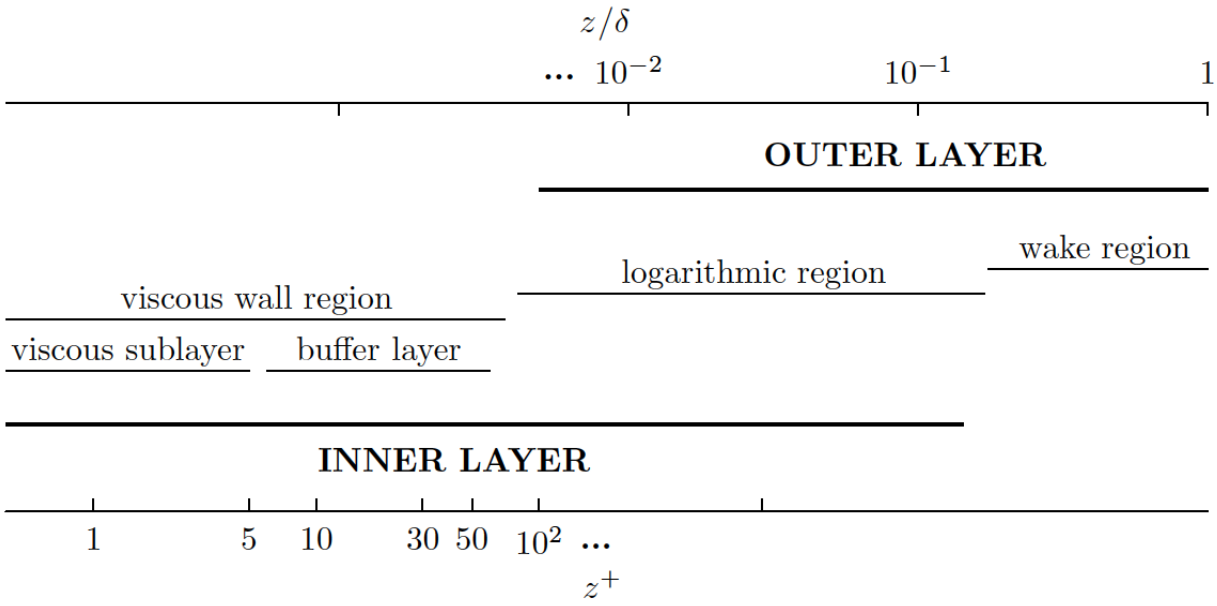

Figure 1.3 Classification based on wall-normal distance z of different regions in the boundary layer. Taken from Squire [1] and Pope [2].

cent works have suggested outer scale influences [62, 75, 76]. The logarithmic region where both inner and outer scaling must hold is also known as the overlap region or the inertial sublayer. The name "logarithmic" was derived from the mathematical form of the time-mean statistics. The wake region, which makes up 70% of the boundary layer thickness, is known for being intermittently turbulent. These boundary layer regions are well described by the law of the wall combined with the law of the wake [2].

Prandtl [57] posited scaling arguments for the boundary layer's mean streamwise velocity near the wall. He argued on a dimensional basis for the relationship,

$$\frac{U}{u_\tau} = f\left(\frac{z u_\tau}{\nu}\right). \tag{1.1}$$

In other words, the mean velocity U depends on the non-dimensional grouping of wall-normal distance z, friction velocity u_τ, and kinematic viscosity ν. In the $z^+ < 5$ viscous sublayer, the law of the wall [77] is

$$U^+ = z^+, \tag{1.2}$$

where the superscript "+" denotes viscous scaling with friction velocity u_τ and viscous length scale $l_\nu = u_\tau/\nu$. In the buffer region, between $5 < z^+ < 70$ [2, 78], the van Driest approximation well represents the velocity; see Pope [2] for details.

The log region approximately spans between $z^+ > 70$ and $z/\delta < 0.15$ [79]. One approach to deriving the logarithmic form is by asymptotic matching with the defect scaling law of von Kármán,

$$\frac{U_\infty - U}{u_\tau} = h\left(\frac{z}{\delta}\right), \tag{1.3}$$

where U_∞ is the free stream, and δ is the boundary layer thickness. Assuming that in the overlap region Eqs. 1.1 and 1.3 both hold, then by asymptotic matching [80], the slope of the inner and outer regions must be equal to some constant in the overlap region,

$$z^+\frac{\partial f}{\partial z^+} = -\frac{z}{\delta}\frac{\partial h}{\partial (z/\delta)} = \frac{1}{\kappa}, \tag{1.4}$$

with κ being the empirical von Kármán constant. This requirement leads to the log law of

$$U^+ = \frac{1}{\kappa}\ln(z^+) + C. \tag{1.5}$$

From experimental data, a good fit is given by $\kappa = 0.41$ and $C = 5.0$ [81]. Recently, Chauhan et al. [82] proposed $\kappa = 0.384$ and $C = 4.1$ for high Reynolds number flows. For additional background on the log law, see the explanations provided by Squire [1], Zimmerman [83], and the references therein.

Above the overlap region is the wake region or defect layer, extending beyond approximately $z/\delta > 0.3$. In the canonical boundary layer, the mean streamwise velocity in this region is aptly described by Cole's law of the wake [81], which when combined with the log law has the form,

$$U^+ = \frac{1}{\kappa}\ln(z^+) + C + \frac{\Pi}{\kappa}G\left(\frac{z}{\delta}\right). \tag{1.6}$$

In this equation, Π is the wake strength parameter, and G is the wake function [2]. The

term "wake" comes from the function G having a similar velocity profile as a plane wake, but there is no further similarity on a detailed level. In an instantaneous flow sense, much of the wake region alternates intermittently between being turbulent and non-turbulent (free stream) [30, 33, 84]. Schubauer [84] considered that the deviation from the log law in the wake region was related to this intermittency, and Krug et al. [85], building on the quiescent cores in pipe flow discovered by Kwon et al. [86], showed for boundary layer and internal flows that the wake region was recovered as a sum of the turbulent flow and the free stream weighted by the intermittency at each wall-normal position [83].

Clauser [87] was among the first to study turbulent boundary layers with adverse pressure gradients. He established a non-dimensional parameter, $(\delta^*/\tau_w)(dp/dx)$, to describe the balance between the wall shear stress τ_w, and the pressure force per unit length and width of $\delta^*(dp/dx)$, where δ^* is an effective boundary layer thickness. This dimensionless quantity is today known as the Clauser (or the Rotta-Clauser) pressure gradient parameter, commonly given the symbol β_c. Clauser investigated flows with constant β_c, which was argued to be a sufficient criterion for equilibrium. The author's analysis relied on the integral-momentum relations, providing insights into the mean flow and friction coefficient. This seminal work demonstrated the need for understanding pressure gradient effects, which can significantly modify the characteristics of the boundary layer. Much progress has been made since the work of Clauser [87], both in zero and non-zero pressure gradient flows.

The present understanding is that pressure gradients can affect the mean flow in both the inner and outer regions. In the viscous sublayer, Taylor's series expansion about the wall [58] shows that

$$U^+(z^+) = z^+ + 1/2 p_x^+ z^{+2} + \mathcal{O}(z^{+4}). \tag{1.7}$$

Here, z is the wall-normal coordinate, and $p_x^+ = \nu/(\rho u_\tau^3)\mathrm{d}p/\mathrm{d}x$. The superscript '+' denotes normalization with inner scales. The pressure gradient term is from the streamwise momentum equation simplified with an order of magnitude analysis into $-(1/\rho)\mathrm{d}p/\mathrm{d}x + \nu\partial U^2/\partial^2 z = 0$. This term is often neglected because $\mathrm{d}p/\mathrm{d}x$ is small. However, this assumption must be

reevaluated for pressure gradient flows as in Nickels [58], who provided a composite law for boundary layers with $-0.02 < p_x^+ < 0.06$. Note that $\beta_c = p_x^+(\delta^* u_\tau/\nu)$. The importance of accounting for the pressure gradient can be understood by rearranging Eq. 1.7 into $U^+(z^+) = z^+(1+1/2p_x^+ z^+)$. Taking the maximum pressure gradient encountered in this study of $p_x^+ \approx 0.02$, relative to a ZPG flow ($U^+ = z^+$), one can expect a 1% deviation at $z^+ = 1$ and a 5% deviation at $z^+ = 5$. These deviations are significant if near-wall measurements are used to infer the wall shear stress.

In the logarithmic law, the time-mean velocity in Eq. 1.6 requires the universal constants κ, C, and the wall shear stress τ_w. Workers have proposed that the constants κ and C should be modified to suit pressure gradient flows. Nickels [58] formulated a parametric model for the time-averaged velocity in pressure gradient boundary layers. He argued for a varying Kármán constant, κ, based on the idea that the appropriate velocity scale at the viscous sublayer edge changes as the sublayer thins or thickens in response to pressure gradients. Based on this model, κ should increase with FPG and decrease with APG, causing the log region to shift upward and downward relative to a ZPG flow. Similarly, Dixit and Ramesh [88] proposed changes to κ and C based on the local pressure gradient, which they coined the modified Clauser chart method (MCCM).

In the experiments by Harun [9], the wall shear stress deduced from oil-film interferometry (OFI) was used to show that the log region shifted downward with APG, consistent with the expectations of Nickels [58]. Recently, Knopp et al. [89] also assessed the log law with independent wall-shear stress measurements obtained from Lagrangian-particle tracking (LPT) [90] and OFI, arriving at a similar conclusion as previous workers. Without direct measurements of τ_w, the Clauser chart method is commonly used and assumes an overlap region (with slope $1/\kappa$) insensitive to Reynolds number and pressure gradient. For experiments where log region data is challenging to obtain, Kumar and Mahesh [91] and Volino and Schultz [92] have shown alternative methods of obtaining the wall shear stress [93]. The current work did not assess these variations, and the established universal constants and the

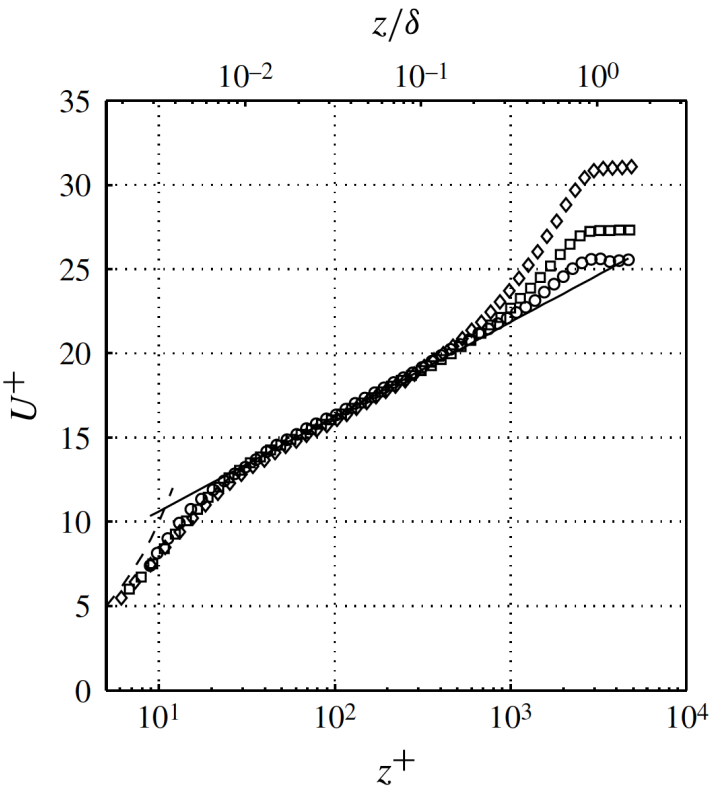

Figure 1.4 Time-mean streamwise velocity under zero (□), favorable $\beta_c = -0.42$ (○), and adverse $\beta_c = 1.74$ (◇) pressure gradients. $Re_\tau = 3{,}000$ for all boundary layers. The dashed line is $U^+ = z^+$, and the solid line is the log law. Figure from Harun et al. [3].

Clauser chart method were used to convey the statistical trends.

There were clear differences in the wake region of the mean streamwise velocity when encountering pressure gradients, as shown in early works [94, 95] and recent works of Harun et al. [3] and Monty et al. [6]. Harun et al. [3] measured boundary layers at $Re_\tau \approx 3{,}000$. Figure 1.4 shows that the wake region increased (decreased) its wake strength Π value with the mild APG (FPG). This trend was also affirmed in Vila et al. [52] for a boundary layer with spatially varying pressure gradients, although the wake region also depends on the flow history. In other words, the wake region of the boundary layer requires some distance to adjust to the evolving pressure gradient environment. Nonetheless, a growing wake region and an eroding log layer could point to modified entrainment activity [85].

1.1.1.2 Reynolds Stress

A typical distribution of the variance in streamwise velocity fluctuations $\overline{u^2}$ is shown in Fig. 1.6. The near-wall peak in the buffer layer at the wall-normal location $z^+ = 15$ has been related to streaks of quasi-streamwise vortices [96]. The outer peak, which is visible only at sufficiently high Reynolds numbers, is related to the large scales (e.g., superstructures [97]) in the logarithmic layer. At heights beyond the outer peak, the distribution of $\overline{u^2}$ also abides by a logarithmic form [98],

$$\overline{u^2}/u_\tau^2 = B_1 - A_1 \log(z/\delta). \tag{1.8}$$

$A_1 = 1.26$ is the Townsend-Perry constant, and B_1 is related to the wake and depends on the flow geometry. This log law was generalized by Meneveau and Marusic [59], who showed that at high Reynolds numbers, the inertial layer also exhibits a logarithmic trend in the higher even-order moments of its fluctuations.

Nagano et al. [4] investigated an increasingly adverse pressure gradient boundary layer. The flow properties of this APG boundary layer were documented using hot wires at four streamwise stations, and compared to a ZPG boundary layer at a similar Reynolds number. In the decelerating APG flow, the momentum thickness Reynolds number $Re_\theta = \theta U_e/\nu$ (U_e is edge velocity and ν is kinematic viscosity) increased from 1,290 to 3,350, with $Re_\tau = u_\tau \delta/\nu \approx 500$. Here, u_τ is the friction velocity, and δ is the boundary layer thickness. The strength of the APG was between $p_x^+ = 0$–0.029, or in terms of the Rotta-Clauser parameter $\beta_c = (\delta^*/\tau_w)(dp/dx) = 0$–$5.32$. The variable dp/dx is the streamwise pressure gradient, ρ is the density, τ_w is the wall shear stress, and δ^* is the displacement thickness.

The turbulence intensities of the three velocities are shown in Fig. 1.5. The solid line denotes the ZPG, and the symbols highlight the effects of the pressure gradient. Figure 1.5(a) shows that the streamwise turbulence intensity $\sqrt{\overline{u^2}}/U_\infty$ decreased predominantly in the logarithmic region, while in the inner and outer regions, the values remained invariant with the APG. A similar trend was observed for the spanwise velocity fluctuation $\sqrt{\overline{v^2}}/U_\infty$. However, the intensity of the wall-normal velocity fluctuation $\sqrt{\overline{w^2}}/U_\infty$ remained constant with the

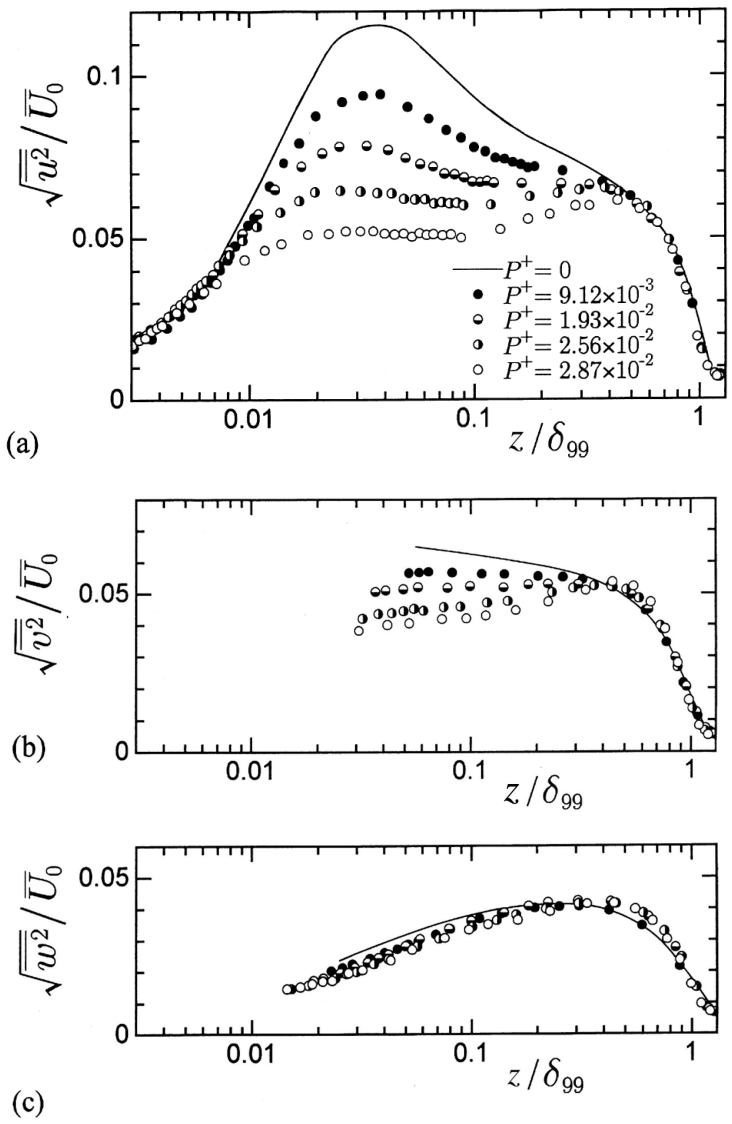

Figure 1.5 Root mean squared fluctuations of the *(a)* streamwise *(b)* wall-normal, and *(c)* spanwise velocities [4] relative to the free-stream velocity $U_\infty = \overline{U}_0$.

APG. This planar boundary layer will be a valuable comparison for the current axisymmetric boundary layer.

Harun et al. [3] and Monty et al. [6] examined the effects of pressure gradient on velocity fluctuation intensities by isolating the effects of Reynolds number and pressure gradient parameter. This analysis was done by fixing the Re_τ and varying the Clauser parameter β_c. As shown in Fig. 1.6(a), under an inner scaling, small variations were observed in the near-wall region, but an outer peak emerged in the log region as the APG grew stronger.

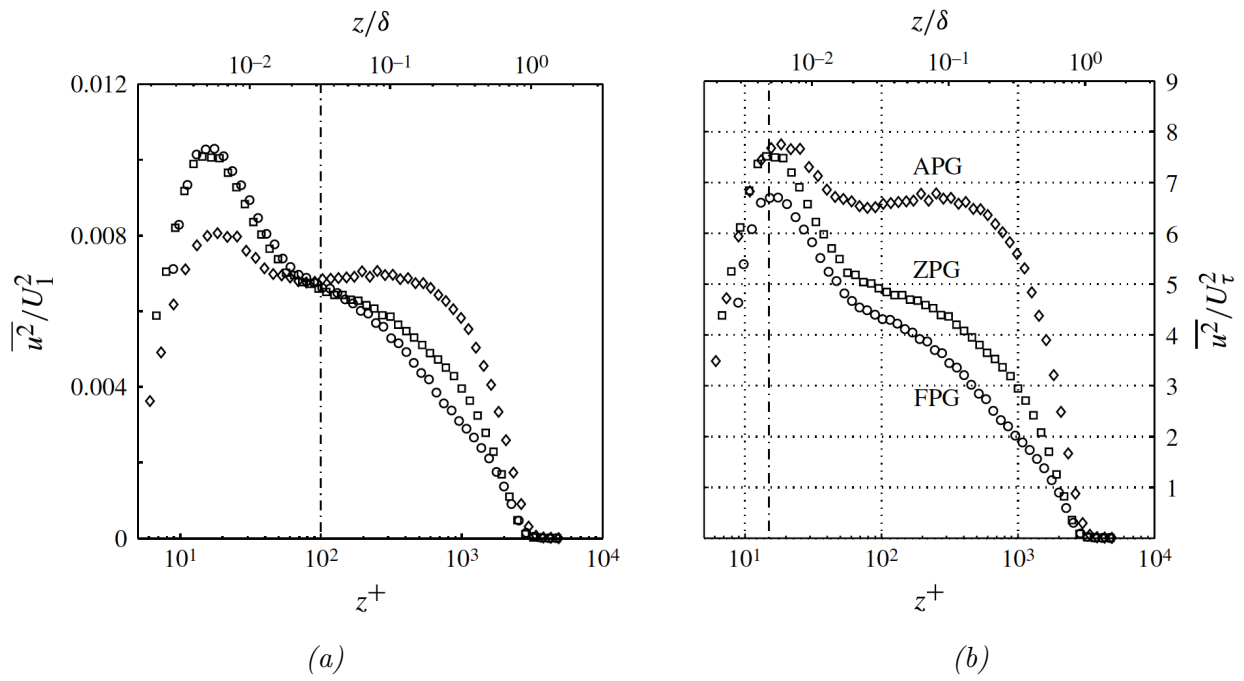

Figure 1.6 Variance of measured velocity normalized by *(a)* the edge velocity U_1 and *(b)* the friction velocity U_τ. Figures from Harun et al. [3].

Using the edge velocity as the reference in Fig. 1.6(b), the inner region decreased in the APG flow, and the outer peak was energized by the APG as before, although to a lesser extent.

Vila et al. [52] experimentally investigated the effects of a spatially evolving pressure history β_c across a Reynolds number range of $Re_\tau \approx$ 1,000–4,000. The ceiling height was gradually increased downstream to yield an initially favorable and subsequently adverse pressure gradient of up to $\beta_c = 2.4$. These authors reached similar conclusions as Harun et al. [3], finding that changing β_c with a fixed Re_τ affected the peak magnitude of the inner-scaled RMS. In contrast, varying the Re_τ while fixing β_c shifted the results to greater viscous-scaled wall distances. However, one distinction from Harun et al. [3] was the pressure gradient history effects. For an increasing β_c, the flow field expectedly behaved similarly to an equilibrium flow with a lower β_c, leading these workers to suggest an integrated history of β_c as a measure of the pressure gradient as opposed to the local value.

Using hot-wire anemometry, the decelerating, axisymmetric boundary layer of a body of revolution was studied by Balantrapu et al. [5]. This work advocated for an embedded

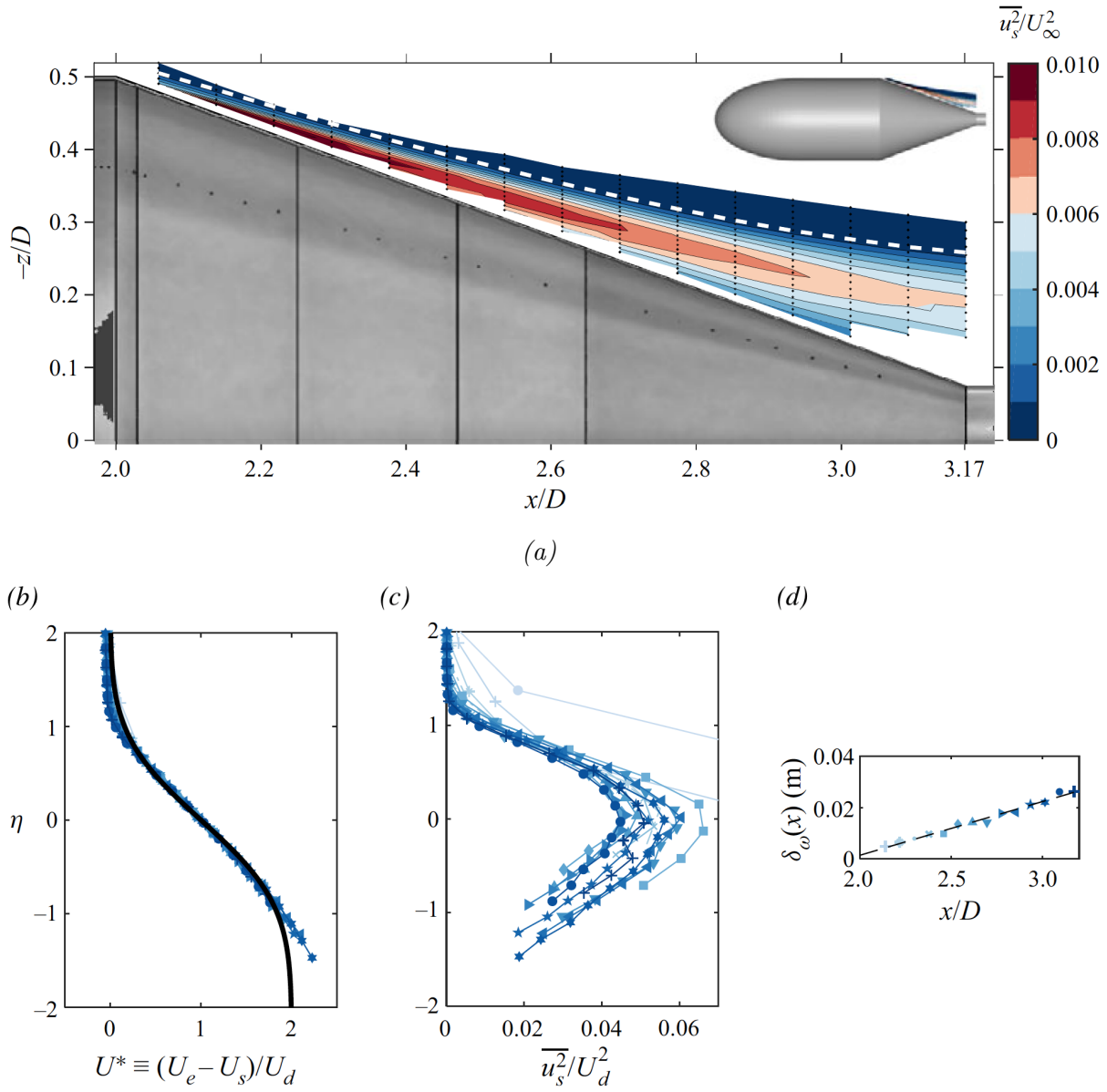

Figure 1.7 (a) Turbulence intensity as measured by hot-wire anemometry at various streamwise and radial stations. *(b)* Mean velocity and *(c)* turbulence intensity presented with an embedded shear layer scaling centered about the mean velocity profile inflection point. *(d)* Vorticity thickness used to normalize quantities. Figures are from Balantrapu et al. [5].

shear layer scaling (ESL) proposed by Schatzman and Thomas [99]. Figure 1.7(a) shows the measured velocity variance contour. Similar to the work of Nagano et al. [4] in Fig. 1.5, as the flow encountered the APG along the ramp, the energy decreased in the inner region, forming an energetic peak in the outer region whose location coincided with the inflection

point in the mean velocity profile. This coincidence, also observed in other APG flows [73], has led the community to postulate that this outer peak is fueled by an embedded shear layer, engendered by an inviscid instability from the mean velocity profile inflection.

Figures 1.7(b–d) show this ESL scaling of the mean velocity and the root-mean-square (RMS). Subfigure (b) shows the defect mean velocity profile centered about the inflection point and normalized by the vorticity thickness. Subfigure (c) shows the turbulence intensity normalized by the defect velocity, and subfigure (d) shows the vorticity thickness growing with streamwise distance at a rate comparable to a typical shear layer. These workers argued that the collapse in variance was good because, for non-equilibrium boundary layers, the criteria for collapse should be relaxed to the same order of magnitude as Maciel et al. [68] suggested. Evidence of ESL structures recently appeared in Silva and Wolf [73], who used spectral proper orthogonal decomposition [100] to elucidate roller-type structures.

Because turbulence is a multi-scale phenomenon, inspecting the large and small scales separately is insightful. In this manner, the behavior of the distinct scales and their mutual interactions can be better understood. A cutoff streamwise wavelength of $\lambda_x = \delta$ is common. Scale decomposition has been used in ZPG flows to describe the modulation of the near wall by large scales [76, 79].

Monty et al. [6] studied the effect of pressure gradient on the large and small scales. Careful attention was given to matching the Reynolds number because APG and growing Reynolds number both energize the large scales in the outer region. The flow was decomposed into large and small scales based on a cutoff wavelength of $\lambda_c = \delta$. Figure 1.8 shows the outcome of this decomposition for ZPG (thinnest line) and various APG flows (thicker lines), all at a matched $Re_\tau = 1900$. The large scales were significantly energized in the outer region, while less effect was seen in the near wall region for both the large and small scales. Also, the peak in large scales was observed to shift outward in wall units. These workers concluded that APG significantly energized the large scales, much more than increasing the Reynolds number would.

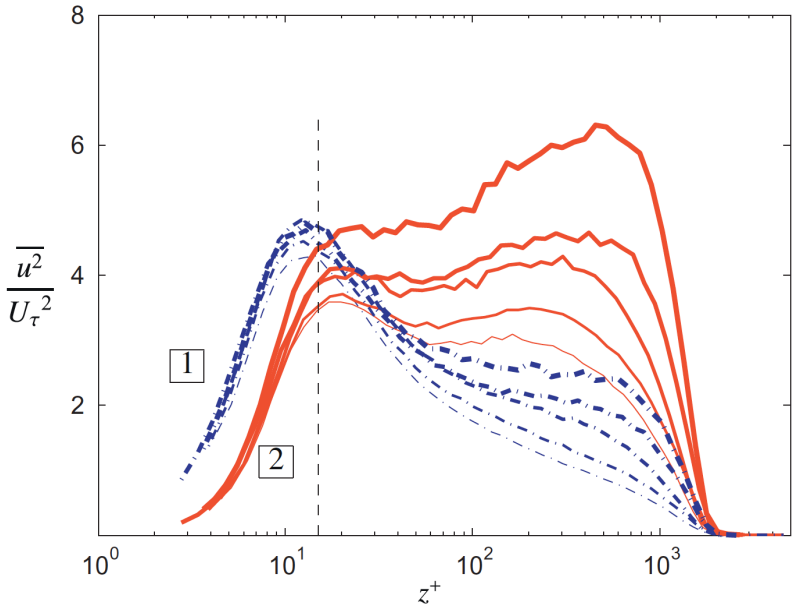

Figure 1.8 Turbulence intensity for ZPG and APG boundary layers at $Re_\tau = 1900$ decomposed into small ($\lambda < \delta$, broken lines) and large ($\lambda > \delta$, solid lines) scales. The thinnest line is ZPG, and thickness grows with APG strength. Figure taken from Monty et al. [6].

While finding the appropriate length and time scales [67, 68, 101] could offer insights into the flow physics or provide opportunities for modeling, this topic was not the focus of this dissertation. Consequently, the mean and variance of the data are provided under conventional scalings, and the observed trends are discussed in Section 3.2. The primary focus of this work, as discussed in the following section, was to understand the variations in the boundary layer structure.

1.1.2 Boundary Layer Structure

The study of flow structures aims to expose the coherence in turbulence and how they underpin the measured single-point turbulence statistics. Examination of the flow structure is motivated by the observation that turbulence is anisotropic and comprises well-organized, coherent motions. The definition of a coherent structure offered by Robinson [48], and the one used in this work, is

A three-dimensional region of the flow over which at least one fundamental flow

variable (velocity component, density, temperature, etc.) exhibits significant correlation with itself or with another variable over a range of space and/or time significantly larger than the smallest local scales of the flow.

The coherent structures that underlie canonical boundary layers are well known. Near-wall streaks, initially visualized by Kline et al. [96], reside in the sublayer and the buffer layer. The dynamics of these streaks are responsible for the peak in turbulence production near the wall. The hairpin vortex is a populous coherent structure found throughout the layer. Initially proposed by Theodorsen [69], hairpins were first visualized and described quantitatively by Head and Bandyopadhyay [15]. More recently, with the advent of direct numerical simulation and PIV, the organization of hairpin vortices is now much better understood [102]. They have also been visualized in the outer region [19] at low to moderate Reynolds numbers, helping explain the formation of turbulent bulges and superstructures [97].

The survey below emphasizes the outer region because the near-wall measurements were limited in this work. To this end, the coherent motion found in canonical, i.e., zero-pressure gradient, smooth-wall, flat-plate boundary layer, is reviewed, followed by a discussion on how pressure gradients affect the structural organizations. In particular, the review first examines the energy spectrum to understand how the dominant wavelengths are affected. Subsequently, the average signatures of eddies are discussed through the two-point correlation. These correlations primarily result from hairpin vortex packets, the final topic reviewed in this section.

1.1.2.1 Energy Spectrum

The energy spectrum is a direct reflection of the turbulence cascade, an idea set forth by the likes of Kolmogorov and Richardson [103]:

> ...Big whirls have little whirls that feed on their velocity,
> and little whirls have lesser whirls, and so on to viscosity.

Their pioneering works, to this day, continue to underpin the community's comprehension

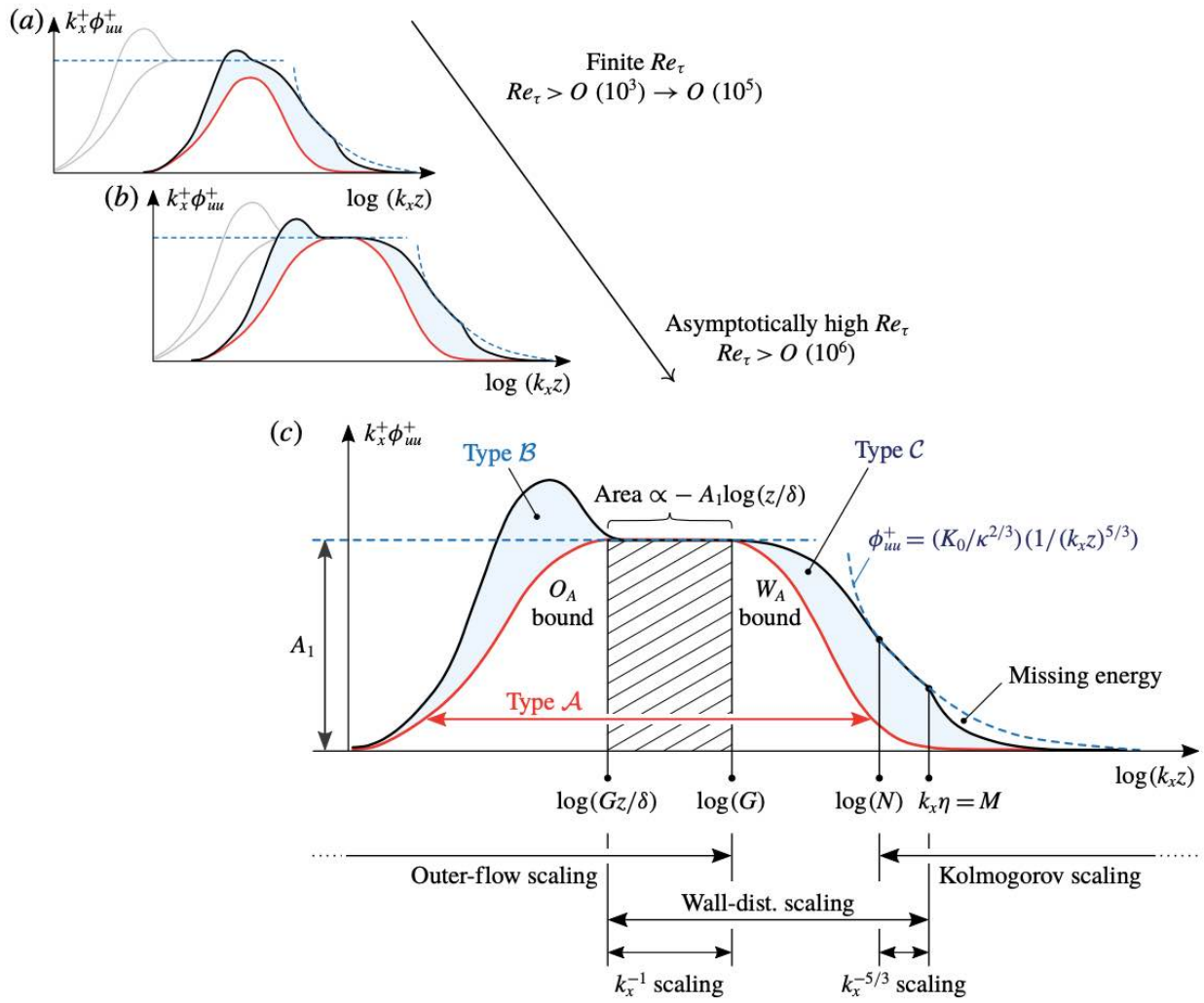

Figure 1.9 Idealized premultiplied spectrum with increasing Reynolds number. Figure from Baars and Marusic [7].

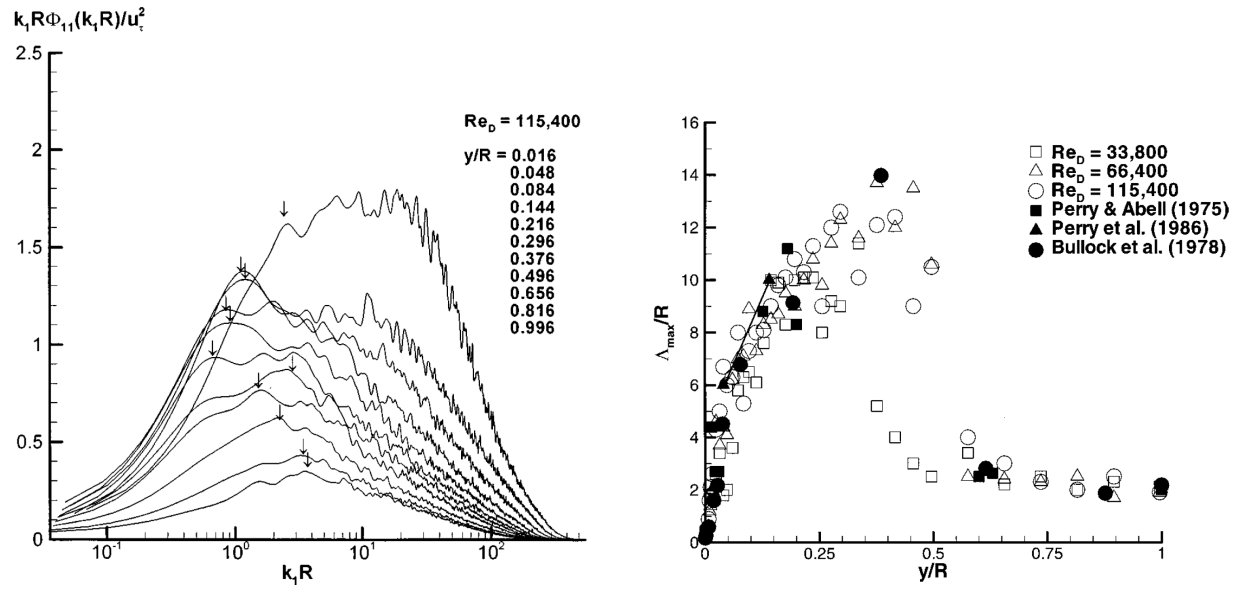

Figure 1.10 (a) Spectra of axial velocity fluctuations in pipe flow taken from various radial positions. Arrows point to the low-wavenumber energy peaks at $k_{\max}$. **(b)** Summary of wavelength $\Lambda_{\max} = 2\pi/k_{\max}$. Figures from Kim and Adrian [8].

of how energy is distributed across eddies of various scales. The current understanding of energy distribution is summarized in Fig. 1.9 from Baars and Marusic [7].

This figure decomposes an idealized premultiplied spectrum for asymptotically high Re_τ turbulence into parts A, B, and C [61, 104, 105]. Part A comprises the contribution of attached eddies [60] that would dominate at very high Re. In this region, ϕ follows k_x^{-1} [106, 107] (or equivalently f^{-1} because $k_x = 2\pi f/U_c$) as Perry and Chong [108] and numerous others have shown experimentally up to $Re_\tau \sim \mathcal{O}(10^5)$. Region B contains contributions from very large-scale motion (VLSM) [8] and superstructures [11]. Part C comprises small eddies of the Kolmogorov scale and follows $k_x^{-5/3}$. Note that the k_x^{-1} scaling in the overlap region between the large and small scales is only visible at higher Reynolds numbers. The spectra in the current work will appear like the one in Fig. 1.9(a).

Careful study of the spectra can yield an understanding of the turbulent structures. Kim and Adrian [8] provided the initial evidence for very-large-scale motions (VLSM) in pipe flows (Re_τ = 1,058–3,175) that extend up to 12–14 times the radius, an order of magnitude greater

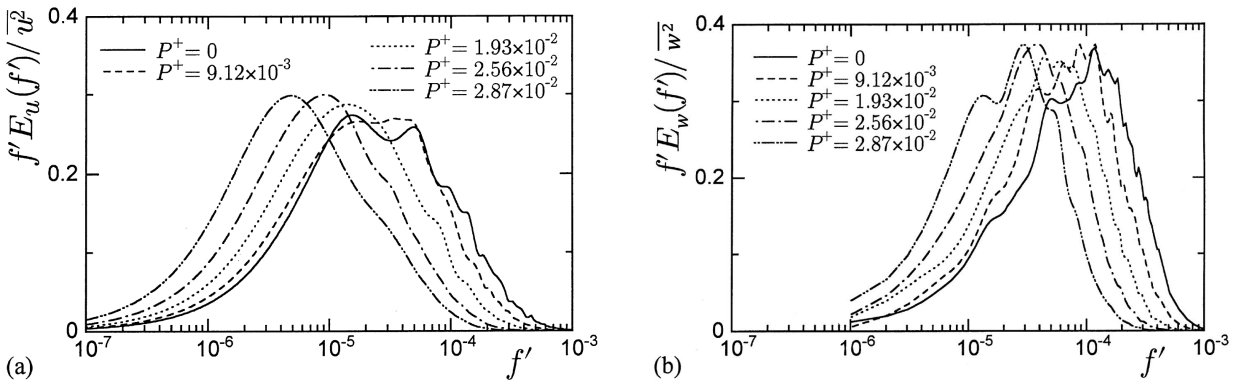

Figure 1.11 Spectra of *(a)* streamwise and *(b)* wall-normal velocity fluctuations for various pressure gradients. Figure from Nagano et al. [4]. The frequency $f' = f\nu/U_\infty^2$.

than the previously identified large-scale motions. These extended regions of coherence were deduced by inspecting the premultiplied spectra[1] of the axial velocity fluctuation, as shown in Fig. 1.10(a), where arrows highlight the low-wavenumber energy peak across various radial stations. The wavenumbers of these peaks were converted into wavelengths $\Lambda_{\max} = 2\pi/k$ and are displayed in Fig. 1.10(b). This figure shows the existence of wavelengths up to 14 pipe radii at roughly $y/R = 0.4$. Similar lengthy structures have been reported in boundary layers [97].

Nagano et al. [4] computed the spectra of an increasingly adverse pressure gradient boundary layer measured at various streamwise stations. Figure 1.11 shows the premultiplied spectra for the (a) streamwise and (b) wall-normal velocity fluctuations in the log region. As the adverse pressure gradient became more intense, the frequency of the premultiplied spectrum peak decreased. These workers interpreted the time scales elongated by the APG to imply that the turbulent motions became more gentle and less active. This interpretation, however, was likely a result of the decreased convection velocity in the APG region, which the dimensionless frequency $f' = f\nu/U_\infty^2$ did not account for. Using the edge velocity as the reference velocity may lead to better insights.

[1]Using a logarithmic abscissa shows the inner region trends but requires a premultiplication by the wavenumber or frequency to maintain the amount of energy under the curve between any two frequencies. $\Phi\,\mathrm{d}k = \Phi\,\frac{\mathrm{d}k}{\mathrm{d}(\log k)}\,\mathrm{d}(\log k) = k\Phi\,\mathrm{d}(\log k)$ by noting $\mathrm{d}(\log k) = 1/k\,\mathrm{d}k$.

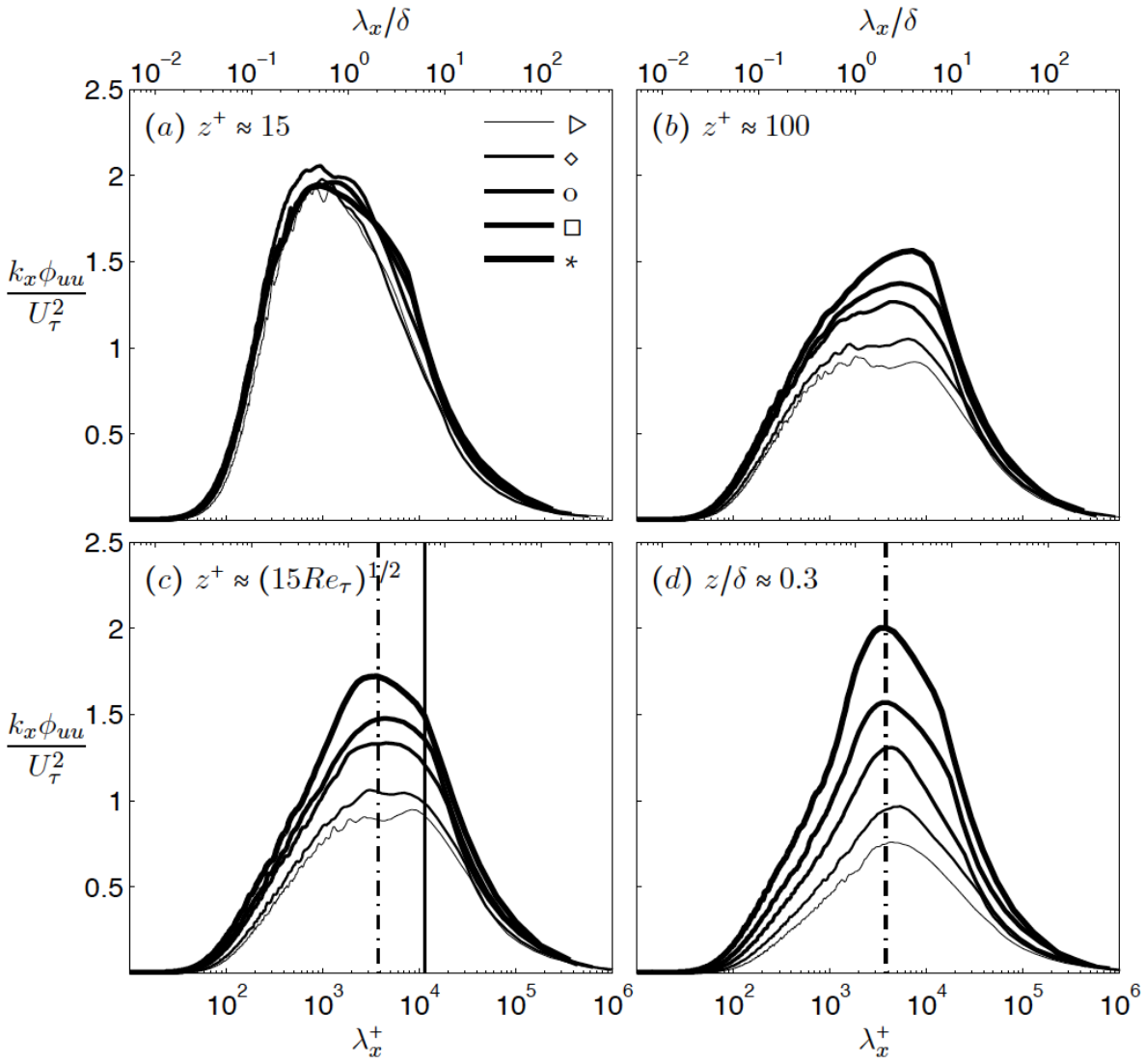

Figure 1.12 Figure and caption from Harun [9]. Pre-multiplied energy spectra of streamwise velocity fluctuation $k_x\phi_{uu}/U_\tau^2$ at constant $Re_\tau \approx 1900$ at selected heights from the wall. β_c increases with line in increasing line thickness. Symbols: ($\triangleright$) ZPG, ($\diamond$) $\beta_c = 0.91$, (o) $\beta_c = 1.67$, ($\square$) $\beta_c = 2.81$, ($\star$) $\beta_c = 4.54$. Solid line denotes $\lambda_x/\delta = 6$ and dashed-dotted line denote $\lambda_x/\delta = 2$.

Harun [9] studied equilibrium pressure gradient boundary layers with constant β_c. Specifically, the effect of β_c was investigated by fixing the Reynolds number Re_τ. Figure 1.12 shows the premultiplied spectra at four wall-normal locations taken from Harun [9]. In each subfigure, the thicker lines indicate stronger APG. In Fig. 1.12(a), the pressure gradient had little effect on the the near wall $z^+ = 15$. At $z^+ = 100$, Fig. 1.12(b) shows that while the ZPG and

low β_c exhibited a plateau, indicating a balance between small and large scales, the APG flows biased toward the large scales, developing a peak at $\lambda_x = 3\delta$. This shift toward large scales in the log region agrees with the findings of Nagano et al. [4].

Interestingly, at $z^+ = \sqrt{15Re_\tau}$, which is the log region center, Fig. 1.12(c) shows that the APG caused the flow to be most energetic at $\lambda_x = 3\delta$, even more so than the $\lambda_x = 6\delta$ commonly observed in canonical ZPG boundary layers. Lastly, in Fig. 1.12(d) at $z/\delta = 0.3$, the boundary layer was consistently most energetic at $\lambda_x = 2\delta$. The crucial takeaway from these spectra is that the emergence of structures with $\lambda_x = 3\delta$, which became more dominant than the well-known $\lambda_x = 6\delta$ structures in ZPG flow [97].

Volino [13] investigated a non-equilibrium pressure gradient boundary layer in a water tunnel between $Re_\tau = 500$–1,000. The pressure gradients were between $\beta_c = -1$ to 6. Laser Doppler velocimetry measurements were used to compute spectra of the streamwise and wall-normal velocities along with their co-spectra. Three scalings were examined: an outer scaling $k\delta$, an inner scaling $k\nu/u_\tau$, and a mixed scaling $k(\delta\nu/u_\tau)^{1/2}$.

The inner scaling was best for the wall-normal fluctuation w, and the mixed scaling was best for the streamwise u and the shear stress $\overline{uw}$. However, independent of the scaling, the peak location of the spectra was observed to shift slightly toward lower and higher wavenumbers in response to favorable and adverse pressure gradients, respectively. This shift in wavenumber agreed with the trends observed by Harun et al. [3] by recalling that the wavenumber k and the wavelength λ have an inverse relationship of $\lambda = 2\pi/k$. The author observed that the inner region responded more quickly to the pressure gradient than the outer region. He reasoned that close to the wall, the turbulence is dictated by the mean shear and responds more directly to changes in velocity. In contrast, the outer region lags in response as it must respond to the near wall changes. This understanding is consistent with Patel et al. [109], who believed that the pressure gradient effects occur predominantly near the wall.

Balantrapu et al. [5] measured the boundary layer of an axisymmetric body using hot-

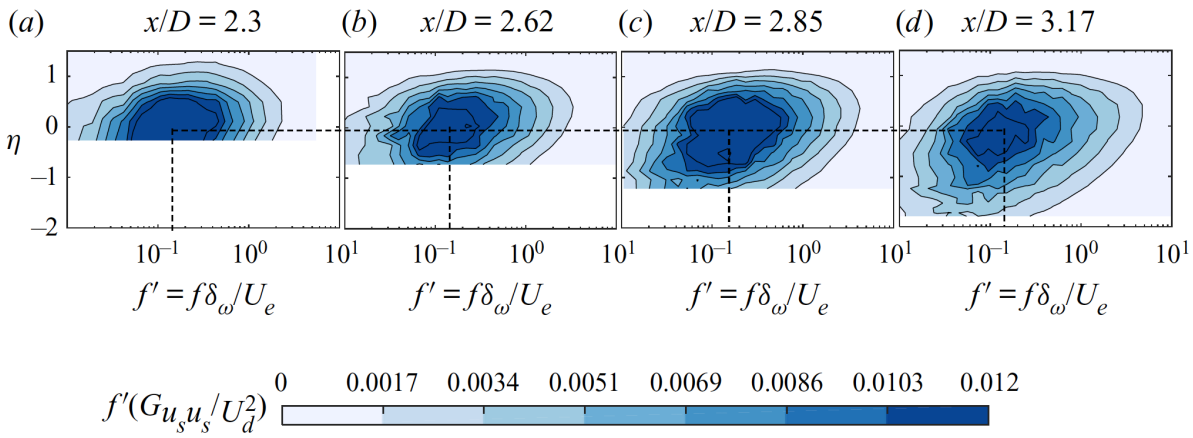

Figure 1.13 Two-dimensional premultiplied spectra of streamwise velocity at different streamwise stations in the decelerating region of a body of revolution. Embedded shear layer scaling shows good collapse of frequency content. Figure from Balantrapu et al. [5].

wire anemometry. Figure 1.13 shows the premultiplied spectra across radial stations. In this figure, the radial position and frequency were made dimensionless by the ESL scaling. Under this scaling, the dimensionless frequency was consistently 0.18 across all four streamwise stations. This similarity in spectra provided further support for the ESL scaling.

Romero et al. [74] compared the spectra of zero and adverse pressure gradient flows. The work aimed to assess the efficacy of a velocity scale that combined inner and outer scaling, $u^2_{\text{hyb}} = u^2_\tau + (dp/dx)z/\rho$. This scaling was proposed to address the rising outer peak [3]. Some success was found under this hybrid scaling, although additional work is necessary. The spectra were also used to highlight flow history effects by comparing two flows with matched β_c but different flow histories. Juxtaposing their spectra revealed differences despite the locally matched conditions, with each flow exhibiting some of its upstream characteristics.

Numerous scalings have been proposed to collapse the spectra. A review of pressure gradient flow spectra suggested that:

1. The embedded shear layer scaling appears promising, as it collapses the spectra across streamwise stations with varying β_c.

2. Adverse and favorable pressure gradients decrease and increase the wavelength, al-

though the variations in convection velocity should be considered.

3. The near-wall region adjusts faster to pressure gradients than regions further from the wall.

Based on these findings, the spectra sampled at four streamwise locations across the Suboff afterbody will be discussed.

1.1.2.2 Two-Point Correlation

The "footprint" of eddies convecting beyond a measurement point can be extracted using two-point correlations. Because no two coherent structures are identical, the two-point correlation shows an average (or typical) eddy. By computing how a variable is correlated with itself or another variable at other spatial locations, the two-point correlation analysis provides the typical region of influence, or shape and size, of the eddies passing through that point. For this reason, this method has been instrumental in helping understand the boundary layer structure in early [110] as well as recent works [10].

Early studies of boundary layer structure relied on two-point spatial and temporal correlations measured using stationary and traversing probes [110, 111]. The estimated correlations were used to understand and describe various aspects of boundary layers, such as the entrainment process [110], near-wall bursts [111], etc. The principal realization was that there are large-scale structures spanning nearly the entire thickness of the boundary layer and multiple boundary layer thicknesses in the streamwise direction, which Townsend [112] and Grant [113] inferred from the long tails of u velocity auto-correlations.

With direct numerical simulations (DNS), the three velocity components and the pressure are known at each grid point. Sillero et al. [10] performed DNS up to $Re_\tau = \delta^+ = \delta/l_\nu = 2{,}000$ for a canonical boundary layer. The friction Reynolds number Re_τ, also referred to as the Kármán number, represents the ratio of the boundary layer thickness to the viscous length scale. The two-point spatial correlation contours of streamwise R_{uu}, wall-normal R_{ww}, and spanwise R_{vv} are shown in Fig. 1.14 with respect to reference at a wall-normal position of

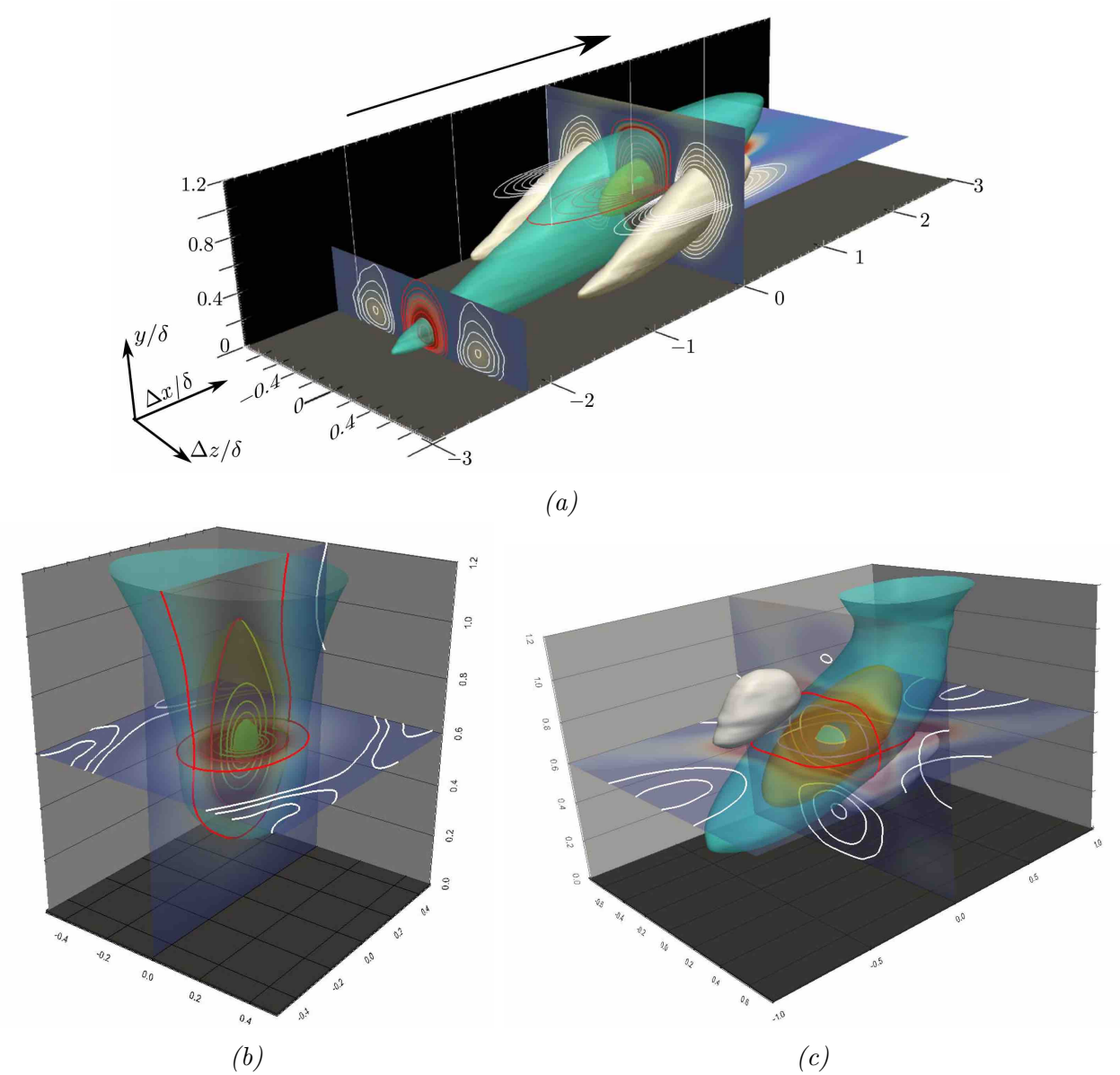

Figure 1.14 Three-dimensional correlation of *(a)* streamwise velocity R_{uu}, **(b)** wall-normal velocity R_{ww} and *(c)* spanwise velocity R_{vv}. Flow is from left to right. Figures from Sillero et al. [10].

$z/\delta = 0.6$.

The turquoise iso-surfaces are positive, and the white ones correlate negatively. The red and white lines indicate positive and negative correlations in the planes that intersect the iso-surfaces. For the streamwise velocity R_{uu} in Fig. 1.14(a), there was an elongated, forwarding-leaning structure flanked on each side by a negative lobe. The center and side lobes extended to the wall, indicating that the outer region influenced the near-wall structures. This type of structure has been interpreted as the low-speed region induced underneath hairpin packets [19]. The wall-normal R_{ww} shows a vertical cylindrical structure, whereas the spanwise R_{vv} reveals a forward-leaning region bounded by four anti-correlated lobes. It should be noted that

$$\iint R_{uu}\,\mathrm{d}y\,\mathrm{d}z = \iint R_{ww}\,\mathrm{d}x\,\mathrm{d}y = \iint R_{vv}\,\mathrm{d}x\,\mathrm{d}z = 0 \tag{1.9}$$

This statement applies to a steady, incompressible boundary layer, and can be derived based on mass conservation, as shown in Taylor [114] and Townsend [60]. This equation implies that the two-point correlations of u velocity sum to zero in the spanwise planes. Cross-correlations between different velocity components provide further insight into the boundary layer structure.

Hutchins et al. [11] used stereoscopic PIV to investigate a canonical boundary layer at $Re_\tau = 1010$. The cross-stream measurement planes were inclined relative to the floor. Linear stochastic estimation (LSE) [25] was performed to examine the cross-plane structure associated with high and low streamwise momentum. Note that LSE, which approximates the conditional average, essentially reduces to calculating a two-point correlation of u with v and w (R_{uv} and R_{uw}). Figures 1.15(a) and (b) show quivers that indicate the average in-plane flow fields in the two inclined cross-planes conditioned on a low-speed event ($u < 4u_\tau$). The conditional flow fields yielded roller structures that resembled hairpin vortices [49], as idealized in Fig. 1.15(c). Similar structures have been revealed in pipe flow DNS [72]. The effect of pressure gradient on these rollers was shown by Lee [14]. Adverse pressure gradient caused the rollers to grow taller as elaborated upon in Section 1.1.2.3.

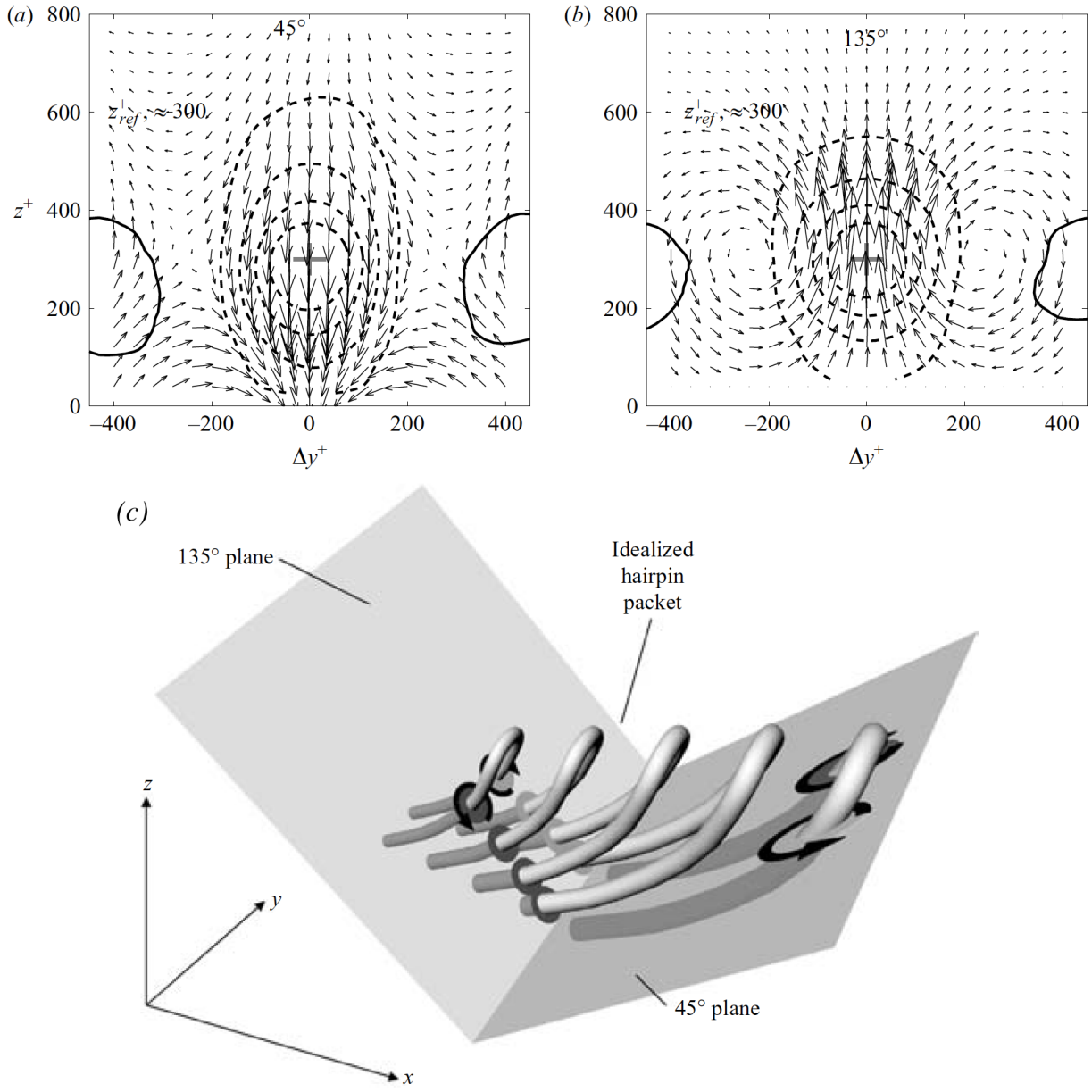

Figure 1.15 Linear stochastic estimation of spanwise and wall-normal velocities based on a low-speed u event in *(a)* 45° *(b)* 135° planes. (c) An idealized model of how hairpin packets intersect the two inclined planes. Images from Hutchins et al. [11].

Several workers have documented the effects of pressure gradient on the two-point correlation contours. Krogstad and Skåre [115] provided a structural perspective of APG boundary layers. These workers employed hot-wire anemometer rakes oriented in the wall-normal and spanwise directions to measure the flow velocities in ZPG and APG ($\beta_c = 20$) boundary layers with $Re_\tau \approx 4{,}000$. Assuming the large scales convect with the time-mean velocity, Taylor's hypothesis was invoked to transform the time-series data into the spatial domain. It was observed that two-point correlation contours R_{uu} based on the wall-parallel u were compressed in the streamwise and stretched in the spanwise directions by the APG. The wall-normal velocity correlation R_{ww} was invariant with the APG in the streamwise–wall-normal plane. The spanwise velocity R_{vv} correlation contour in the streamwise-spanwise plane, which had a square shape for a ZPG flow [10], was stretched and compressed in the streamwise and spanwise directions, respectively. The results in this work should be taken with caution because recent works [5, 116] have shown the convection velocity to be pressure gradient dependent and, in general, unequal to the mean velocity.

Equilibrium pressure gradient (i.e., constant β_c) boundary layers were investigated using DNS by Kitsios et al. [12]. Two-point correlations were computed at a wall-normal position equal to the displacement thickness, coinciding with the maximum variance. Figure 1.16(a)–(c) display the contours related to the streamwise u, wall-normal w, and spanwise v velocities, respectively. The green, blue, and red colors correspond to ZPG, mild APG ($\beta_c = 1$), and strong APG ($\beta_c = 39$) cases, respectively. The solid contours have values of 0.2 to 0.8 at increments of 0.2, and the dashed contours have a value of -0.1. Examining these figures, the correlated regions were significantly reduced by the adverse pressure gradient when normalized by the displacement thickness, particularly for the streamwise velocity. For the strong APG case, R_{uu} in Fig. 1.16(a) was less correlated with the wall region, perhaps indicating smaller influence on the near wall region. Additionally, R_{vv} in Fig. 1.16(c) revealed that, under a strong APG, the negative lobe became more significant underneath the positive region. These changes in flow structure should be further explored.

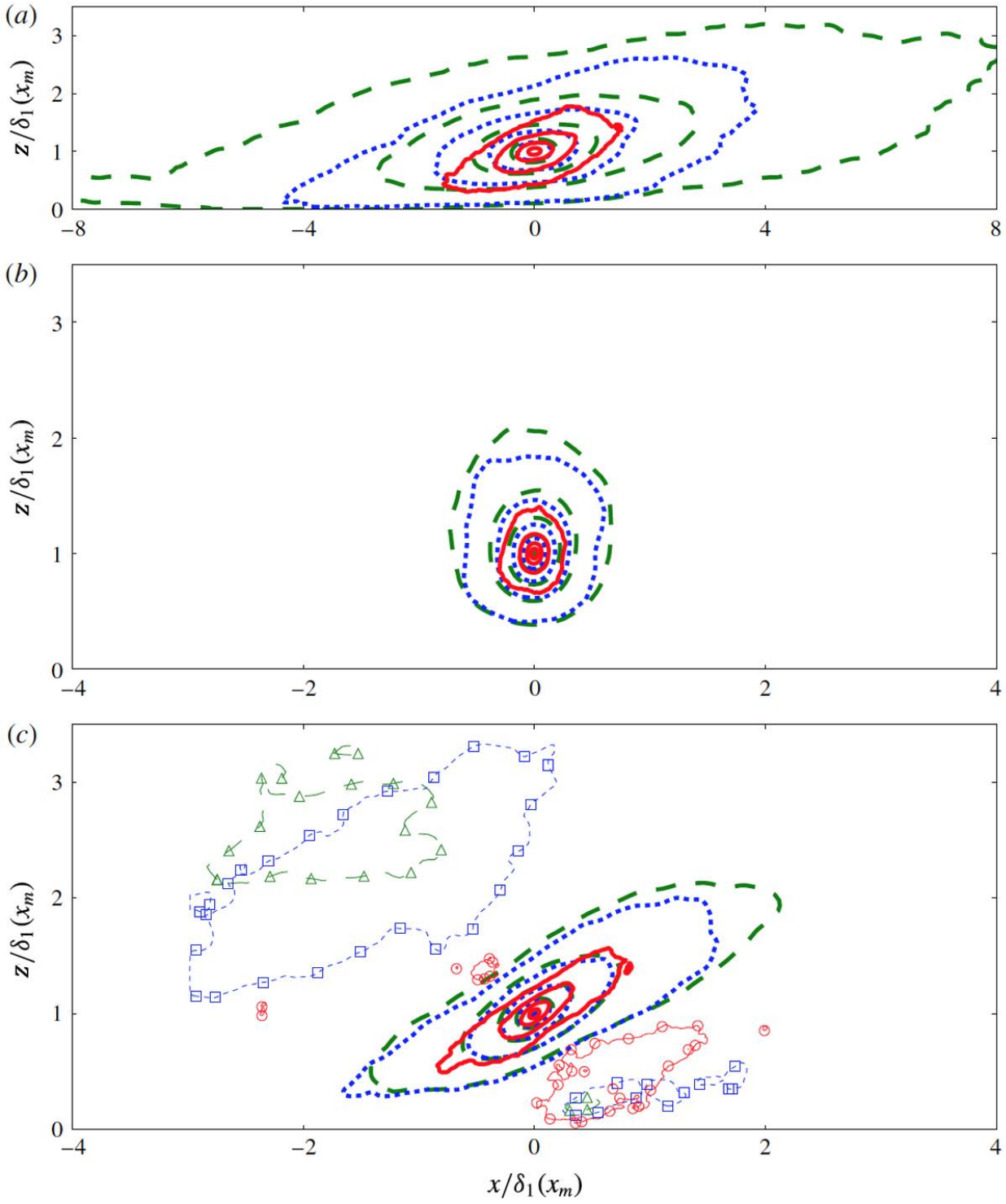

Figure 1.16 Two-point correlations of *(a)* streamwise, *(b)* wall-normal, and *(c)* spanwise velocities referenced to the velocity at the displacement thickness, δ_1. The solid contours have values of 0.2 to 0.8 at increments of 0.2, and the dashed contours have a value of -0.1. Green, blue, and red correspond to ZPG, mild APG ($\beta_c = 1$), and strong APG ($\beta_c = 39$) cases. Figure from Kitsios et al. [12].

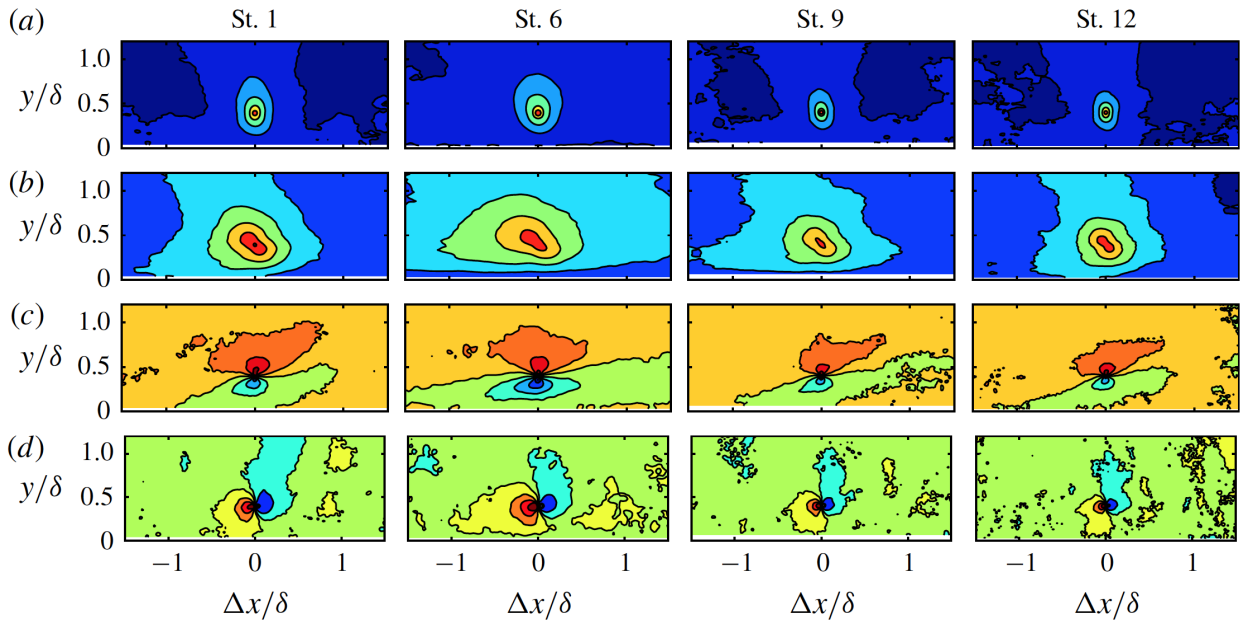

Figure 1.17 The four rows correspond to the two-point correlation of *(a)* the wall-normal velocity, *(b)* the streamwise–wall-normal, *(c)* the swirling strength with the streamwise velocity, and *(d)* the swirling strength and the wall-normal velocity. Each column corresponds to a different streamwise station in the non-equilibrium flow. Station 1 is ZPG, Station 6 is the end of the FPG, Station 9 is in the ZPG recovery, and Station 12 is in the APG. Figure from Volino [13].

Volino [13] examined the structure of a non-equilibrium boundary layer with $Re_\tau \sim \mathcal{O}(1{,}000)$. The non-equilibrium condition was created by adjusting the ceiling to induce an FPG region, a ZPG recovery, and an APG region. He showed that the two-point correlation of the streamwise velocity increased and decreased with FPG and APG relative to the ZPG baseline, respectively. Conversely, the inclination angle of the structures was reduced and increased by the FPG and APG regions. These findings were consistent with prior works [115].

Figure 1.17 shows other two-point correlations between various measured quantities in the streamwise–wall-normal plane. From left to right, these columns correspond to ZPG, FPG, ZPG recovery, and APG regions in the non-equilibrium flow. In Fig. 1.17(a), the wall-normal R_{ww} was overall invariant with the pressure gradient. Figure 1.17(b) correlated streamwise velocity u with the wall-normal velocity w at all spatial locations. These R_{uw} structures

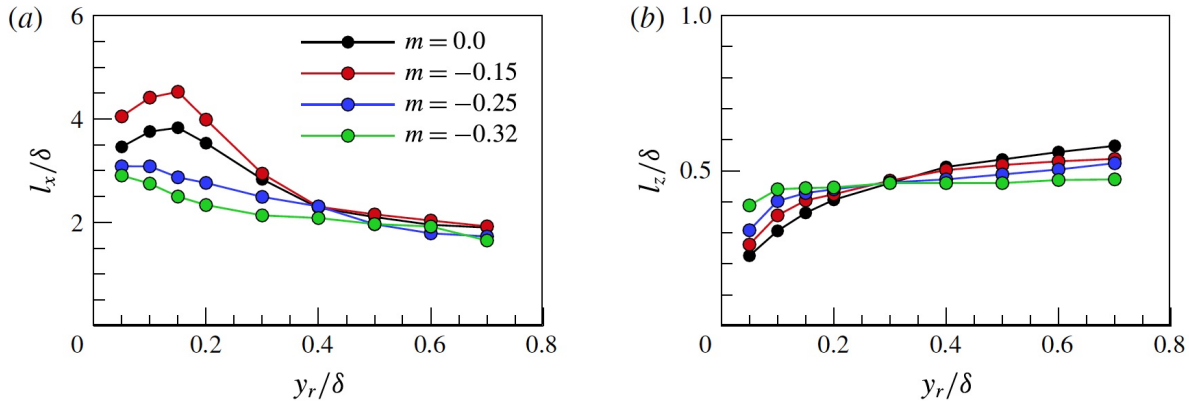

Figure 1.18 Variation of the *(a)* streamwise and *(b)* spanwise length scales based on two-point spatial correlation R_{uu} with pressure gradient. The free stream was prescribed as $U_\infty(x) = U_0(1 - x/x_0)^m$, so lesser values of m indicate greater β_c. x, y, and z are the streamwise, wall-normal, and spanwise directions. Values computed based on a $R_{uu} = 0.05$ cutoff. Figure from Lee [14].

were backward leaning and were stretched and compressed by the FPG and the APG. In Fig. 1.17(c) and (d), correlations between the swirling strength and the flow velocities revealed the hairpin heads. Observing the correlation between the swirling strength and the wall-normal velocity in Fig. 1.17(d), there was a greater region of correlation upstream of the reference, pointing to the enhanced Q2 ejection (uplifting of low streamwise momentum fluid) events taking place in the boundary layer. Similarly, the Q4 sweep (downdraft of high streamwise momentum fluid) was strengthened by the APG.

Lee [14] provided quantitative measures of the streamwise length scale based on R_{uu} in pressure gradient boundary layers, as shown in Fig. 1.18. A zero pressure gradient boundary layer and three with APG of $\beta_c = 0.73$, 2.2, and 9.0 were simulated by prescribing power-law free streams. A more negative exponent m of the free stream indicated a more intense APG. These simulations were performed with similar Reynolds numbers of $Re_\tau = 300$–400. As shown in Fig. 1.18(a), based on a cutoff of $R_{uu} = 0.05$, the ZPG flow's streamwise length scale normalized by the boundary layer thickness l_x/δ increased through the log layer, peaked at $z/\delta \approx 0.15$, and decreased to 2δ at the boundary layer edge.

Contrary to expectation, the mild APG case with $m = -0.15$ had structures longer than

the ZPG case. Subsequent stronger pressure gradient cases decayed monotonically through the layer thickness. All of the pressure gradient cases had similar outer region length scales, suggesting that the pressure gradients had the most pronounced effects on R_{uu} in the inner region. The spanwise length scale is detailed in Fig. 1.18(b), the more intense the APG cases also had the more uniform l_z. In the $m = -0.32$ case, l_z was essentially invariant through the boundary layer thickness, which was different from the ZPG case, where the spanwise length scale grows gradually moving away from the wall [117]. These results will help understand the effects of transverse curvature in the current axisymmetric boundary layer.

Subtle differences in the two-point correlation contour can point to changes in the structural composition of the boundary layer. Prior work has shown that adverse pressure gradients:

1. Reduce the streamwise extent of the forward-leaning, elongated streamwise R_{uu}, and increase its inclination angle.

2. Has little effect on the column structure of wall-normal R_{ww}

3. Affects the streamwise length sales in the lower half of the boundary layer.

4. Makes the spanwise length scale more uniform across the boundary layer thickness by increasing the near-wall length scale and decreasing the outer region length scale.

5. Enlarge the size of the roller structure created by R_{uw} and R_{uv}, the correlation of streamwise velocity u with the wall-normal velocity w and spanwise velocity v.

Two-point spatial correlations were computed in detail for the Suboff boundary layer to understand how the boundary layer structure changed with the rapid onset of pressure gradient and wall curvature.

Although the two-point correlation offers a sense of the boundary layer structure, it represents the composite footprint of all the eddies advecting past that point. The question

that follows is what form of individual eddies (if one exists) sums to the unique shape of the two-point correlation. This question is discussed in the following section.

1.1.2.3 Hairpin Vortex Paradiagm

This research emphasizes the large scales in the boundary layer outer region. This focus is motivated by the understanding that ingesting these large scales leads to the so-called haystacking, or sharp peaks, near the blade passage frequencies in the propeller's far-field noise spectra. In the outer region, the hairpin vortex is widely accepted as the coherent structure that populates much of the log region and even penetrates the wake regions of the boundary layer [102]. Therefore, the hairpin vortex organization was studied, and a survey of prior works is provided below.

Numerous investigators have described vortex loops, horseshoe, or hairpin vortices as a significant constituent of turbulent boundary layers. Since Theodorsen [69] introduced the concept of a hairpin, this flow structure has also been unified with other aspects of turbulent boundary layers such as uniform momentum zones [16, 118] and superstructures [97]. These studies and many others have provided a firm grasp of the canonical, i.e., zero-pressure-gradient, smooth-wall, planar boundary layer structure. However, relatively little is known about the combined effect of pressure gradients and surface curvatures, which are relevant to engineering vehicles.

A compelling case was made for the existence of hairpin vortices in the work of Head and Bandyopadhyay [15]. These authors used light sheets illuminating smoke particles to visualize the boundary layer structure. From the cine recordings of these particles, they observed that the dominant motion of the outer region at low Reynolds numbers was vortex loops or horseshoe vortices. They revealed forests of elongated hairpin vortices at higher Reynolds numbers ($Re_\theta > 2000$). These observations were idealized in Fig. 1.19 (flow is from right to left), where it is shown that the individual hairpins inclined forward at 45° to form an interface of 20°.

These flow structures were hypothesized to originate from the wall. To investigate, smoke

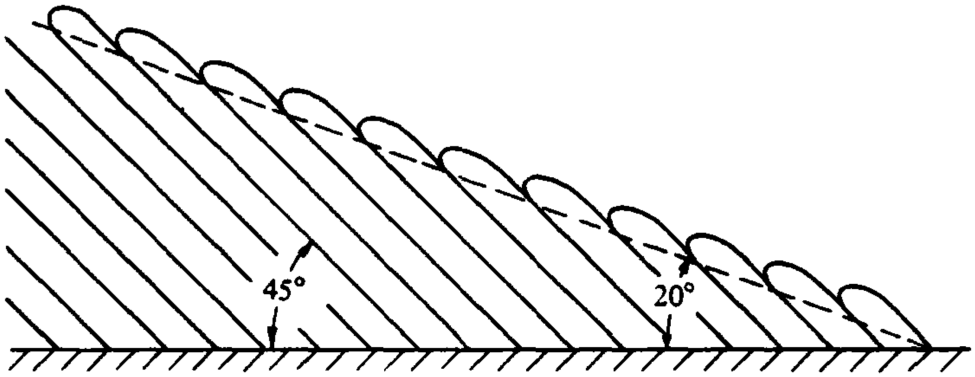

Figure 1.19 An idealization based on smoke visualization of the boundary layer structure, comprising hairpin vortices each inclined at 45° forming an interface of 20°. Flow is from right to left. Figure is from Head and Bandyopadhyay [15].

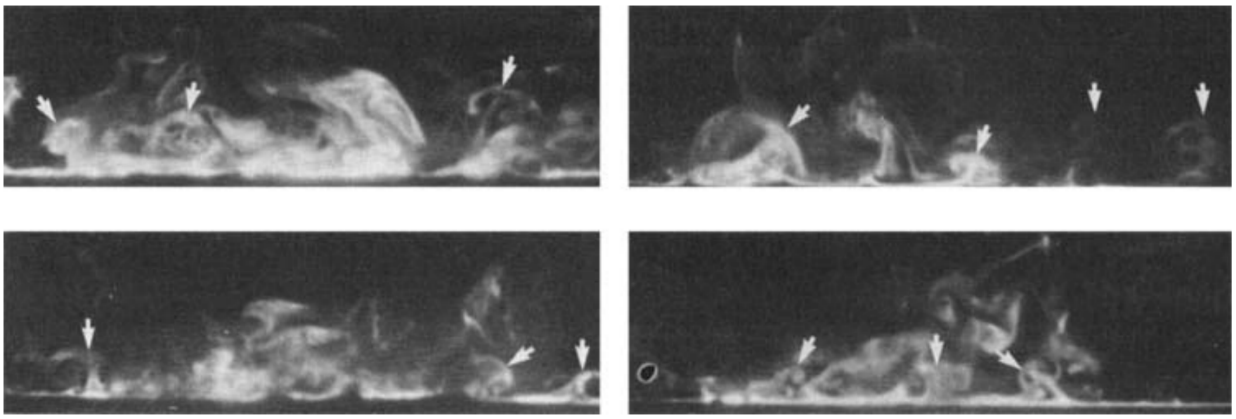

Figure 1.20 Spanwise plane shows a cross-section of vortical streaks. Figure is from Head and Bandyopadhyay [15].

was injected tangential to the surface, and transverse (to the free stream) light sheets were used to illuminate the smoke. The outcome shown in Fig. 1.20 was a few of many instances that revealed vortex pairs, suggesting that the longitudinal vortex motions near the wall may be the origin of hairpins or horseshoe vortices.

Significant advancement in understanding was obtained through particle image velocimetry (PIV). Meinhart and Adrian [16] used PIV to measure across a streamwise–wall-normal plane the velocity vectors of a canonical boundary layer ($Re_\theta = 6850$). These workers noticed zones of approximately uniform streamwise velocity as shown in Fig. 1.21. In this figure, the different zones were separated by regions of concentrated vorticity, which were interpreted as

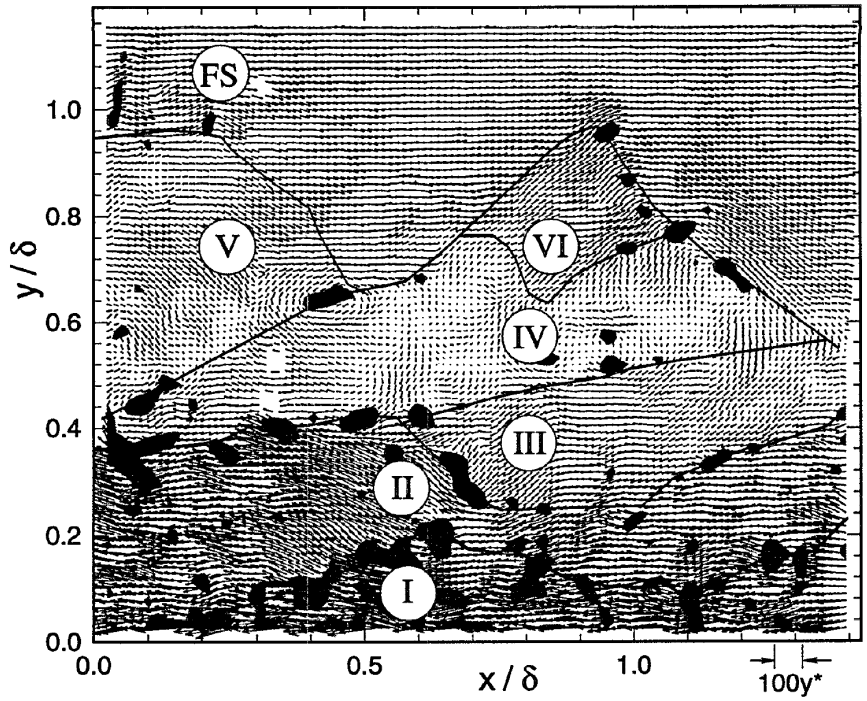

Figure 1.21 Instantaneous velocity field of a canonical boundary layer at $Re_\theta = 6850$ viewed in a convecting frame of $0.9U_\infty$. The dark regions show locations, where vorticity is nondimensionalized by fiction velocity and the wall unit, is less than -0.03. The lines denote boundaries of uniform momentum zones. Image taken from Meinhart and Adrian [16].

the heads of hairpin vortices in the near-wall region. A physical model was proposed where a group of aligned hairpins could cooperatively induce a significant streamwise extent of uniform low-speed fluid flow. However, the reason behind hairpin alignment was subsequently investigated in Zhou et al. [70].

The concept of autoregeneration was introduced by Zhou et al. [70] and further investigated in Zhou et al. [18]. Autoregeneration is the idea that a hairpin vortex with sufficient strength can generate other hairpin vortices upstream and downstream. To demonstrate this idea, a conditionally-averaged hairpin was inserted as an initial condition into the DNS of a turbulent channel flow ($Re_\tau = 180$) [17]. Figures 1.22(a) and 1.22(b) are the perspective view and side view of the resulting hairpin organization at $t^+ = 297$ visualized using the iso-surface of the swirling strength λ_{ci}. In these figures, there are four vortices, where the secondary (SHV), tertiary (THV), and downstream hairpin vortices (DHV) all originated

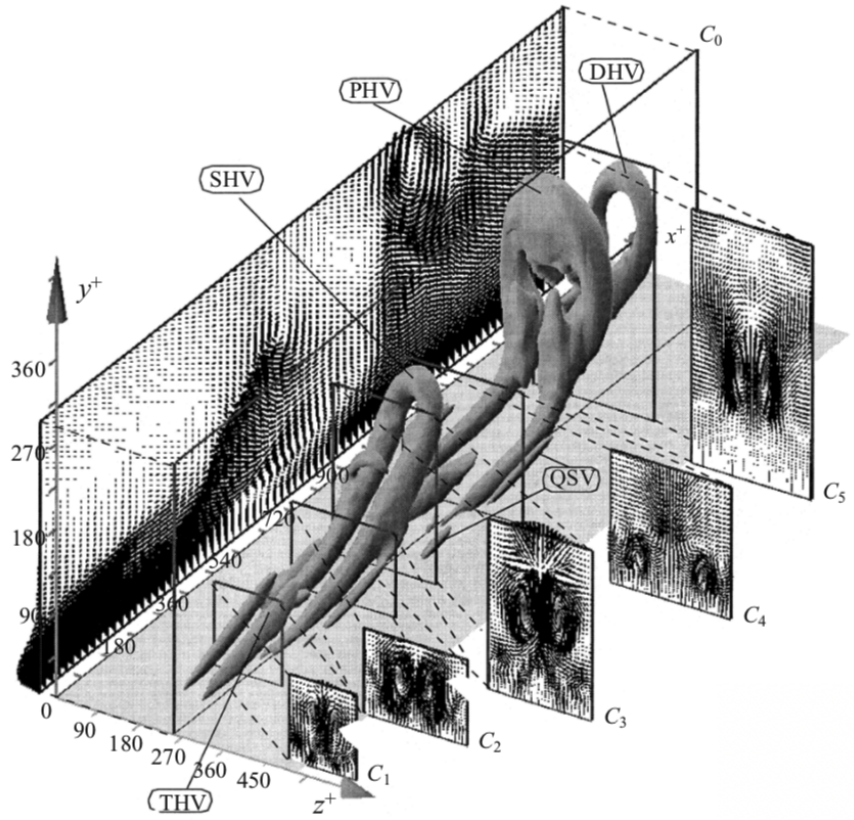

(a) Perspective view.

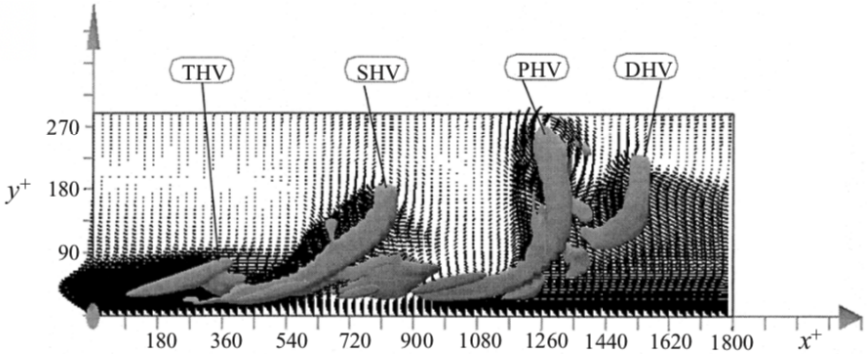

(b) Side view.

Figure 1.22 A conditionally-averaged hairpin was used as an initial condition in a fully developed channel flow DNS ($Re_\tau = 180$) [17]. The outcome of the hairpin autogeneration process shows secondary (SHV), tertiary (THV), and downstream (DHV) hairpins spawned from the original primary hairpin vortex (PHV), some of which are flanked by quasi-streamwise vortices (QSV). Images from Zhou et al. [18].

from the primary hairpin vortex (PHV). The mechanism by which these hairpins develop was explained based on the effects of the self-induced velocity and the channel flow mean shear on the head and legs of a hairpin vortex tube. Ultimately, the resulting velocity field

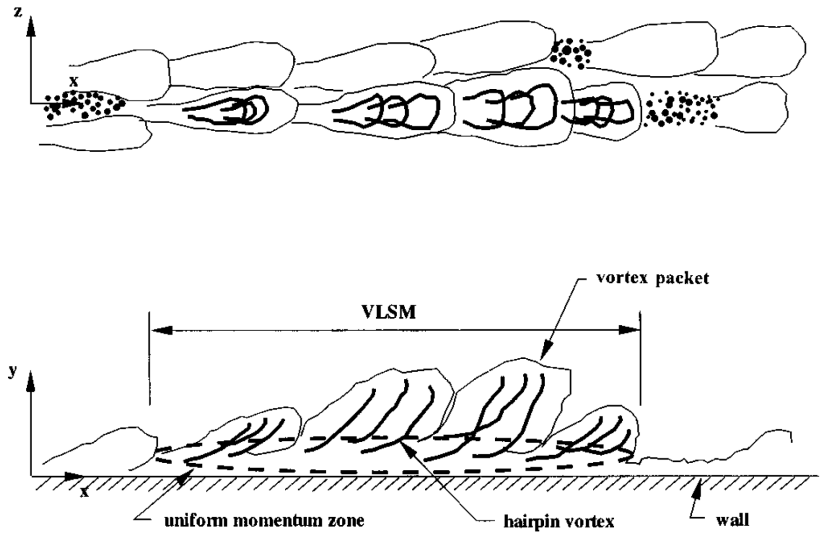

Figure 1.23 Conceptual model of aligned hairpin packets inducing a large region of low-momentum zone. Image taken from Kim and Adrian [8].

of the DNS data showed good qualitative agreement with a PIV dataset, highlighting the low-momentum zone induced by the hairpin packet formed by the autoregeneration mechanism. Also, by introducing a slightly asymmetric initial condition, single-leg cane hairpin vortices appeared in the autogeneration process.

The idea of hairpin packets inducing a large region of low streamwise momentum was further investigated in Kim and Adrian [8]. These workers examined the wavenumber spectra at various radii in a pipe flow, observing energy in wavelengths up to $14R$ (R is the pipe radius) at wall-normal distances of $y/R = 0.25$–0.4. The spectra suggested a flow motion with a length scale of an order of magnitude greater than the turbulent bulges (2–3δ) referred to as large-scale motions. A physical model based on the hairpin vortices was proposed to explain the energy observed in the low wavenumber regime. As illustrated in Fig. 1.23, the conjecture was that when hairpin packets align, they induce a significant region of low-speed fluid, which the authors coined "very" large-scale motion (VLSM). These VLSM are expected to be found in channel flows and boundary layers as well [119].

Previous works have mostly emphasized the near-wall region, while little is known about the structure in the outer layer. Therefore, Adrian et al. [19] investigated the outer region

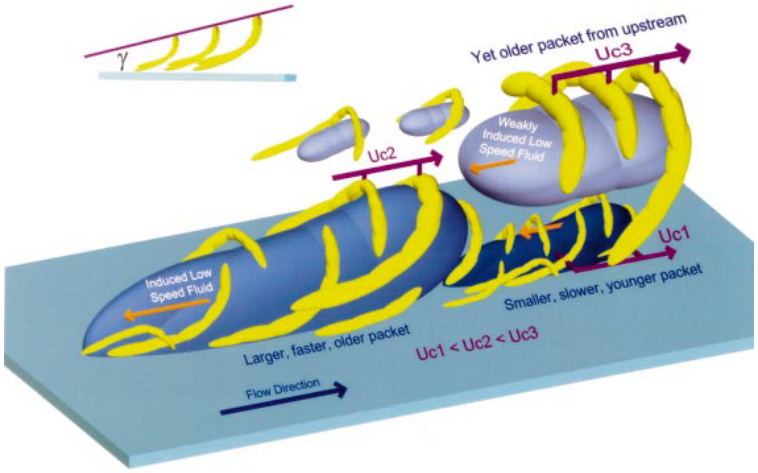

Figure 1.24 Idealized model of nested hairpin packets. Image from Adrian et al. [19].

of a zero-pressure gradient turbulent boundary layer at three Reynolds numbers of $Re_\theta = 930, 2370$, and 6850. PIV was performed across a streamwise–wall-normal plane. Galileon decomposition [102] of the PIV snapshots with various convection velocities showed that vortices populated the outer regions of these boundary layers. The significance of these vortices is that they likely represented the heads [48] of hairpin (or cane) vortices, which previous investigators have primarily found in the near-wall region. These vortices suggested that hairpins are present throughout the boundary layer, with older packets overtaking younger ones, as shown in Fig. 1.24. The authors state that these nested hairpin packets with different convection velocities likely create multiple uniform streamwise momentum zones (UMZ).

Building on the work by Adrian et al. [19], Christensen and Adrian [20] demonstrated the statistical significance of hairpin vortices in the outer region ($y^+ \geq 100$) of a channel flow. In addition to their notable instantaneous swirling strength, hairpin packets have a clear time-averaged footprint, as demonstrated by linear stochastic estimation (LSE). As shown in Fig. 1.25, the hairpins in each packet were positioned along an incline, which was, on average, at 12–13°, extending well into the outer region.

Beyond their existence, the evolution and mutual interaction of hairpin vortices are also

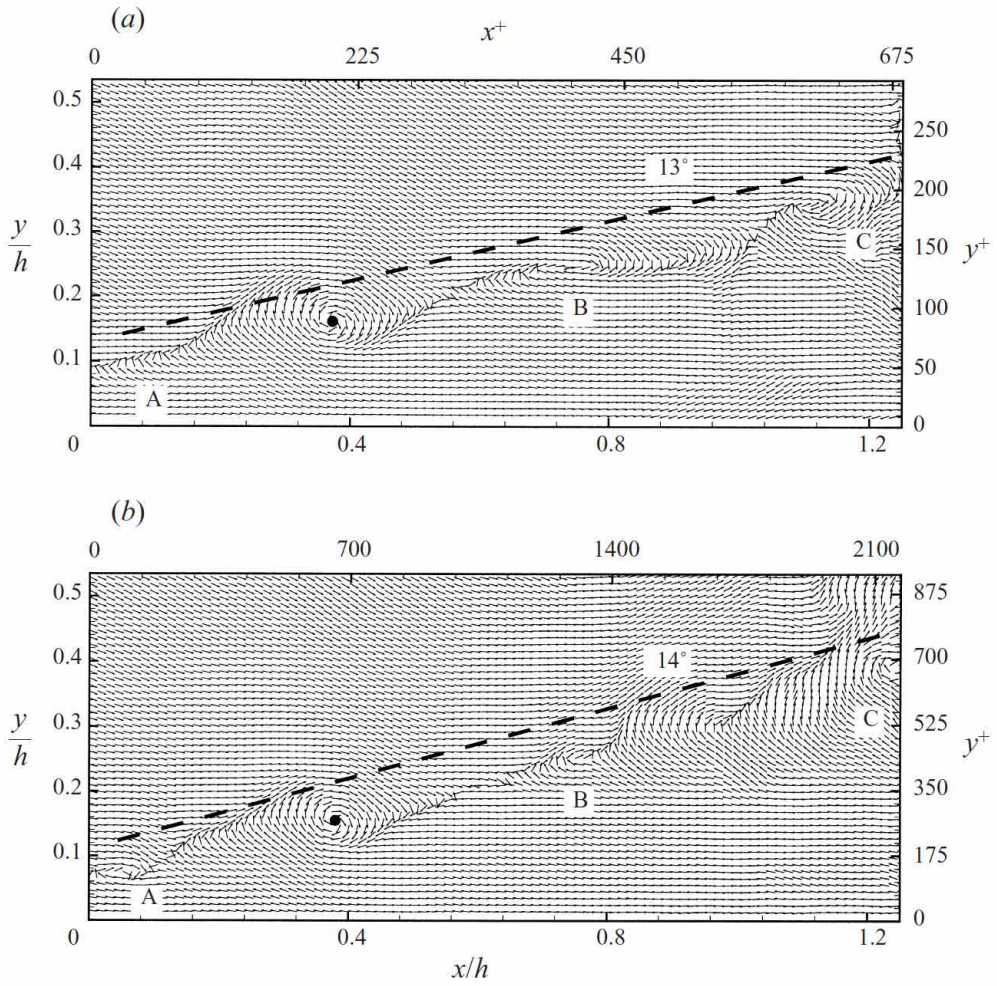

Figure 1.25 Linear stochastic estimation of u and w conditioned on the swirling strength showed hairpins aligned at roughly 13–14° at two Reynolds numbers of *(a)* $Re_\tau = 547$ and *(b)* $Re_\tau = 1734$. Figure from Christensen and Adrian [20].

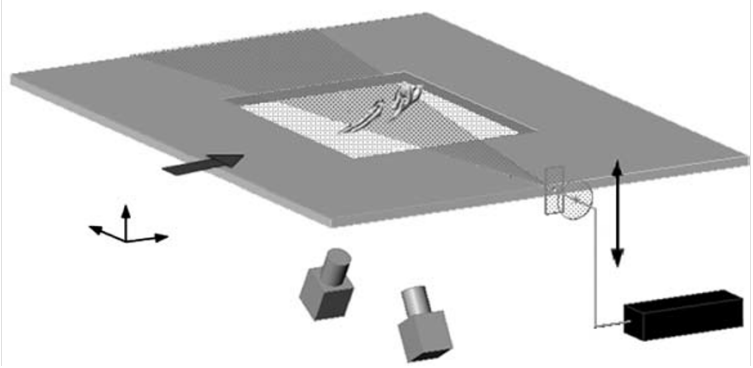

(a) Streamwise-spanwise stereoscopic PIV plane.

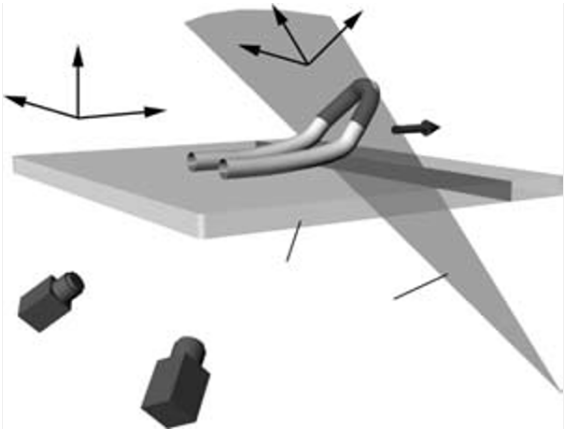

(b) Stereoscopic PIV plane inclined at 135°.

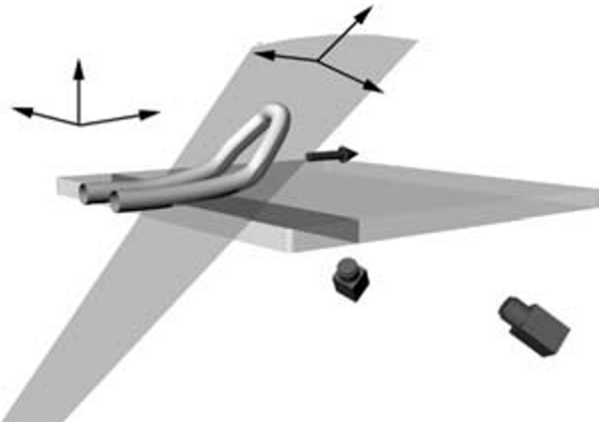

(c) Stereoscopic PIV plane inclined at 45°.

Figure 1.26 Stereoscopic PIV measurements performed by Ganapathisubramani et al. [21, 22] to understand hairpins vortices. Figure from Ganapathisubramani et al. [22]

interesting. Tomkins and Adrian [117] used a streamwise-spanwise PIV plane at different heights in the buffer and log regions to understand the spanwise structure. In the log layer, instantaneous flow fields revealed elongated regions of momentum deficit bounded by elliptic vortices interpreted as hairpin legs. Additionally, it was proposed that scale growth occurs on an eddy-by-eddy basis through vortex reconnection mechanisms. The spanwise width of the conditional structure was found to increase linearly with distance from the wall.

A series of streamwise-spanwise stereoscopic PIV measurements ($Re_\tau = 1060$) were made by Ganapathisubramani et al. [22], as shown in Fig. 1.26. The work investigated the signature of the hairpin vortices that Christensen and Adrian [20] and Adrian et al. [19] have highlighted in their streamwise–wall-normal plane PIV. In the log region, pairs of counter-rotating vortices, interpreted as the legs of hairpins, were observed to typically span 2δ in

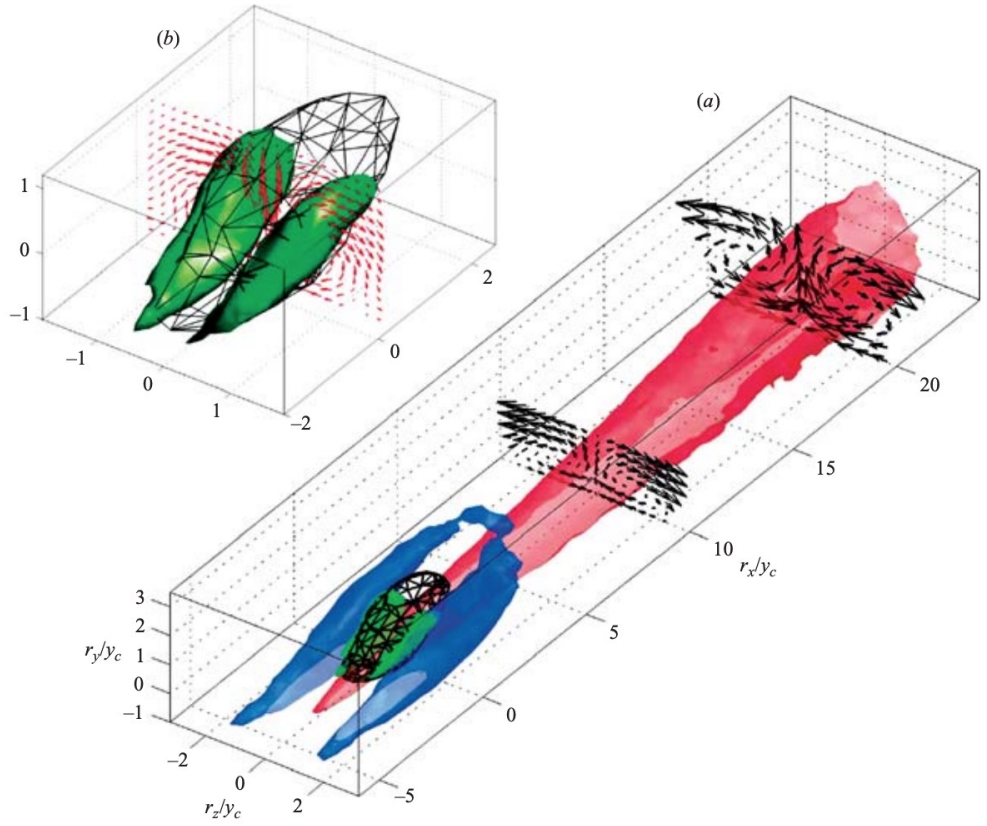

Figure 1.27 Isosurface of a DNS conditional flow field. Image from Del Alamo et al. [23].

the streamwise direction and carried (potentially more than) 25% of the Reynolds stress. However, the authors did not detect vortex packets or low-speed streaks beyond the log layer, suggesting that hairpins were no longer as coherently aligned. The findings in this work were further substantiated with additional PIV measurements and interpretations of two-point correlation contours in Ganapathisubramani et al. [21].

A dual-plane PIV setup was designed by Hambleton et al. [120] to simultaneously interrogate a streamwise-spanwise and a streamwise–wall-normal plane. An instantaneous snapshot showed streamwise streaks bounded by vortices in a manner consistent with the hairpin vortex paradigm. Linear stochastic estimation was used to definitively show in an averaged sense the hairpin heads and legs in the log region of both measurement planes.

Channel DNS was performed by Del Alamo et al. [23] up to $Re_\tau = 1900$. Figure 1.27 shows conditional structures in the log region reminiscent of hairpins. The red and blue

contours in this figure represent low- and high-speed regions, respectively. The quivers show the conditionally averaged v and w, revealing roller structures akin to hairpin legs. The authors related these extended low-speed zones to passive wakes, similar to the wake behind the jet in a cross-flow.

Lee and Sung [121] performed DNS of a spatially-evolving turbulent boundary layer spanning $Re_\theta = 500$–2560. Their analysis of the streamwise and spanwise integral scale corroborated the viewpoint of Ganapathisubramani et al. [22], that vortex packets dominated the log layer. Still, in the outer region, it was more common to find individual hairpins. Because of the abundance of hairpins in the log region, hairpin packets sometimes aligned to cooperatively induce significant extents (6δ) of low- and high-momentum zones, referred to as VLSM. Consequently, the streamwise length scale was greatest in the log region and decreased otherwise. In contrast, the spanwise length scale grew proportionately to the wall-normal distance. Regarding the origin of the long streamwise length scales, the authors, in support of Adrian et al. [19], suggested that VLSM forms when older, faster-moving packets merge with younger, slower packets, although other processes may exist.

Nickels [58] used time-resolved stereoscopic PIV measurements in a water tunnel to construct a flow volume by invoking Taylor's hypothesis. Average flow fields were conditioned on spanwise swirls at different heights, each revealing a hairpin structure below, which was a low-speed region, as shown in Fig. 1.28. Further from the wall, the hairpins were more inclined relative to the wall. This series of conditional flow fields was strong evidence of how hairpin packets cooperatively induce a region of low-speed fluid flow beneath them. This was the first experiment to provide three-dimensional hairpin structures.

Hutchins and Marusic [97] examined the structures in the logarithmic region of a canonical boundary layer. They used a spanwise array of 10 hot-wire probes to examine "superstructures" that energize this wall-normal region of the boundary layer. Note these superstructures are similar to the very-large-scale motion (VLSM) coined by Kim and Adrian [8] in pipe flows. The superstructures extended up to 20δ in length, which has been hid-

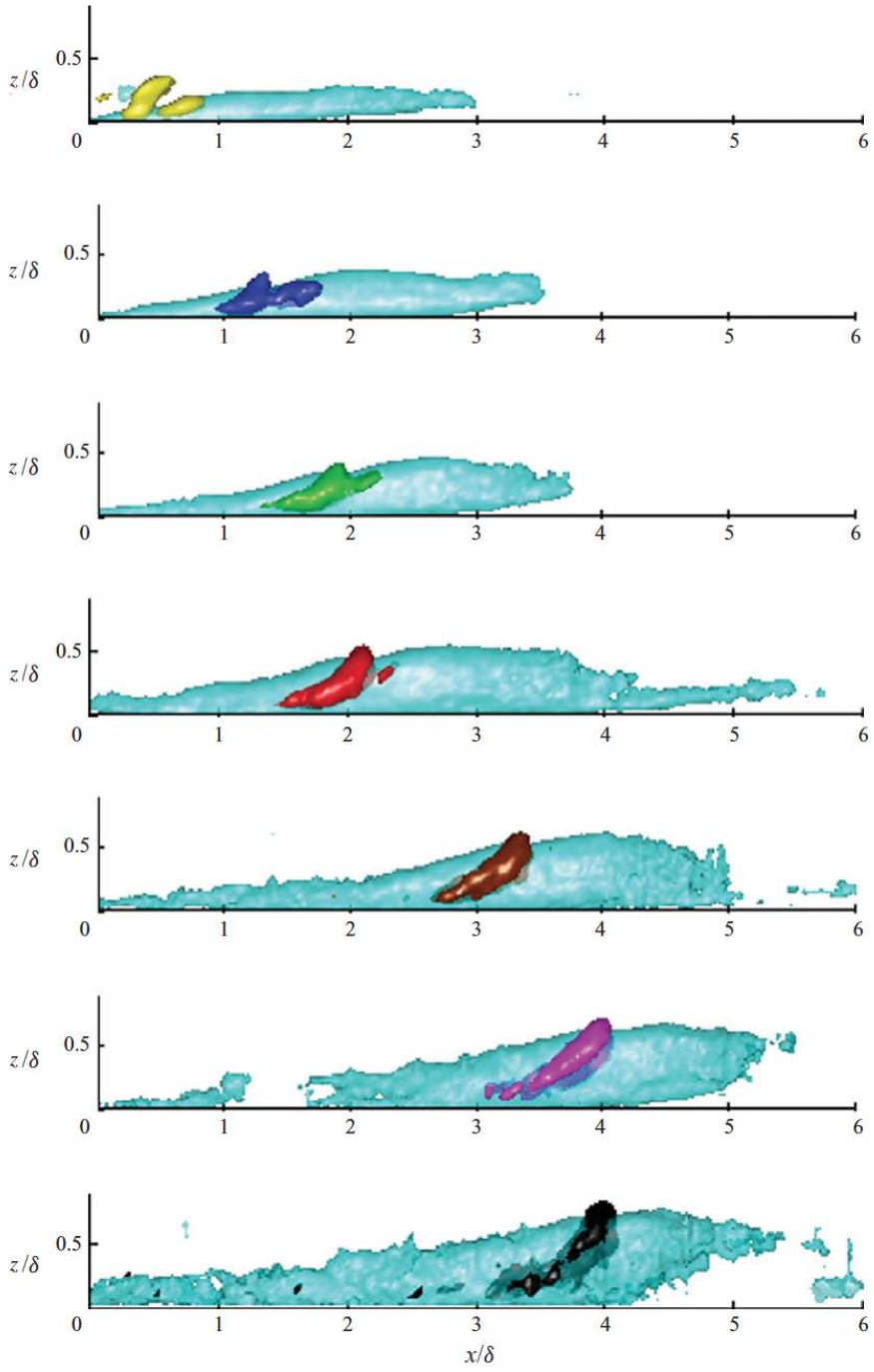

Figure 1.28 Conditionally averaged flow field based on swirl strength. Image from Dennis and Nickels [24].

den from the two-point correlation or spectral analysis because it tended to meander in the spanwise direction. By comparing measurements from various Reynolds numbers, including an atmospheric surface layer ($Re_\tau \approx 660000$), it was deduced that superstructures are a

persistent feature of turbulent boundary layers that scale with boundary layer thickness. Further, the authors highlighted how the superstructures imprinted on the near-wall cycle around $z^+ = 15$. Monty et al. [119] shared similar findings for pipe and channel flows.

Lee and Sung [122] studied the flow structures in the DNS of mildly adverse pressure gradient boundary layers ($\beta_c = 0.73$ and 1.68). Two APG equilibrium boundary layers with power law free streams [67] were investigated. In the outer region, the results were interpreted under the hairpin vortex paradigm. Linear stochastic estimation was used to quantify the typical organization of the hairpin vortices, which were now arranged along an 18° path instead of the 13° in ZPG boundary layers. Further, hairpin-like structures with a λ shape were predominantly responsible for Reynolds shear stress production in the outer region. The APG strengthened the swirling strength of these λ structures.

More recently, by prescribing power-law free streams, Lee [14] simulated three boundary layers with APG of $\beta_c = 0.73, 2.2$, and 9.0. These simulations had matching $Re_\tau = 300$–400. Linear stochastic estimation based on a spanwise swirl was used to elicit hairpin heads in a streamwise–wall-normal plane, as shown in Fig. 1.29. The four figures from top to bottom correspond to $\beta_c = 0, 0.73, 2.2$ and 9.0. Examining these figures, the hairpin heads were organized along a 13° incline with zero pressure gradient. The increased APG not only elevated this inclination but also appeared to weaken the streamwise hairpin alignment significantly and prevent the formation of superstructures (or VLSM). This reduction in hairpin alignment was consistent with the decrease in the streamwise length scale.

The spanwise plane was also studied by Lee [14]. The LSE was conditioned on a Q4 event at $z/\delta = 0.15$; the results are shown in Fig. 1.30. Again, the four subfigures correspond to boundary layers with $\beta_c = 0, 0.73, 2.2$ and 9.0. The general trend was consistent with the ZPG flow of Hutchins et al. [11], showing "roll modes" interpreted as hairpin legs. Here, the APG appeared to enhance the wall-normal and spanwise extent of the correlated region, with the most intense APG case extending nearly the entire boundary layer thickness. This upward extension of the roll mode was argued to be consistent with the finding of Bradshaw

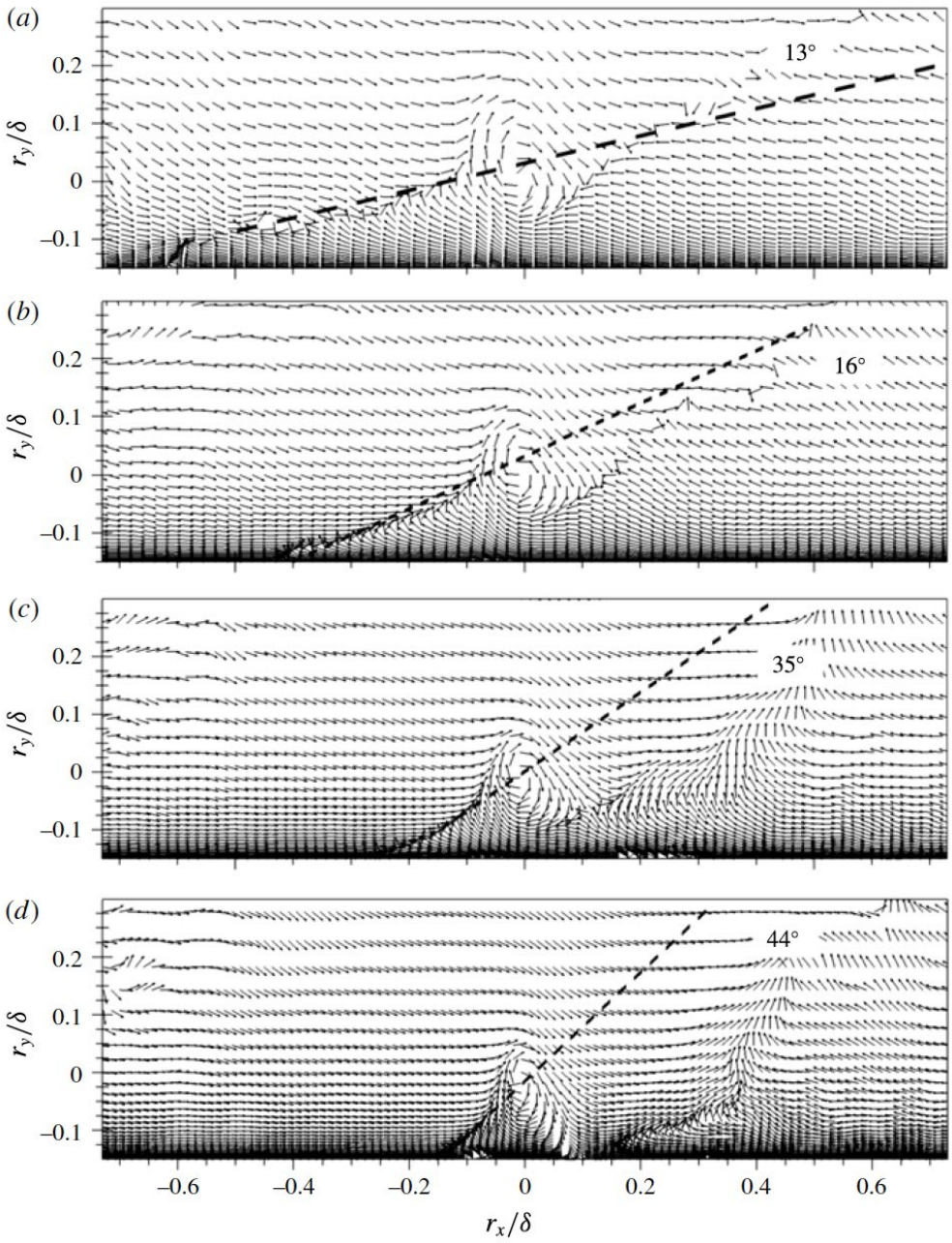

Figure 1.29 Linear stochastic estimation [25] of conditional velocity field based on spanwise swirl at $z/\delta = 0.15$. $(a–d)$ correspond to $\beta_c = 0, 0.73, 2.2$, and 9.0, respectively. Figure from Lee [14].

[123], who observed a rise in energetic, low-frequency content in the outer region of an APG flow. These simulations were performed at low Reynolds numbers, so the findings must be verified at higher Re_τ.

The hairpin vortex has gained widespread acceptance as the principal building block in

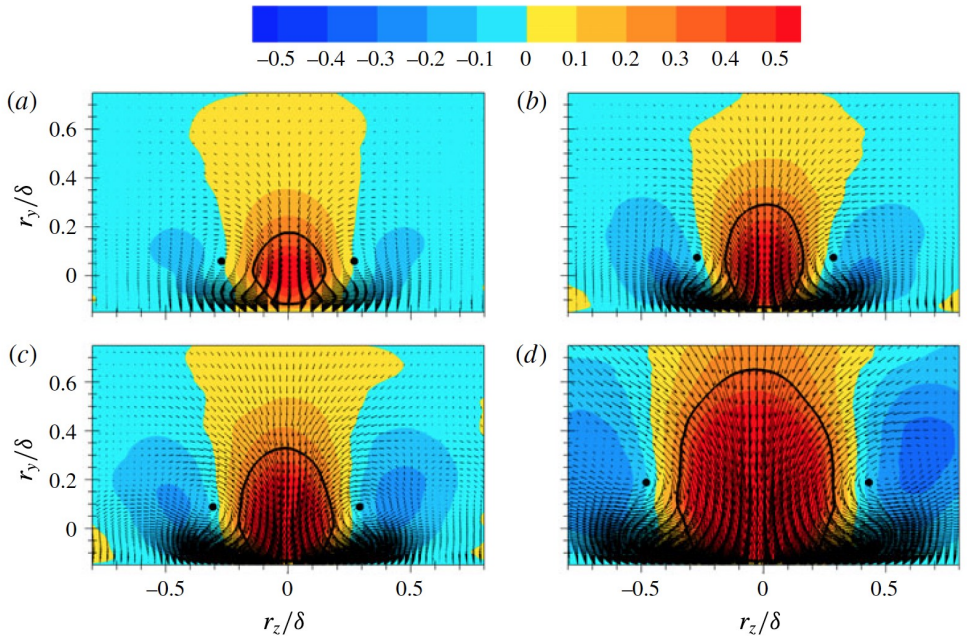

Figure 1.30 Linear stochastic estimation [25] of conditional velocity field based on Q4 event at $z/\delta = 0.15$. $(a–d)$ correspond to $\beta_c = 0, 0.73, 2.2$, and 9.0, respectively. Figure from Lee [14].

turbulent boundary layers [49]. Hairpins align to cooperatively induce significant regions of low and high momentum. Adverse (favorable) pressure gradients increase (decrease) the inclination angle along which hairpin packets are organized, similar to the effect on R_{uu}. Overall, there is relatively little information on hairpin vortex organization in non-equilibrium pressure gradient boundary layers. Based on the current research, no prior work has yet to detail the hairpin organization in decelerating, axisymmetric boundary layers. One of the goals of this work, therefore, is to investigate whether hairpins continue to play a significant role, and how they are affected by pressure gradient and transverse curvature.

1.1.3 Axisymmetric Boundary Layer

Numerous workers have studied axisymmetric bodies. However, the objectives of these studies vary from measuring the forces and moments, understanding the flow separation at angles of attack [124], to models for trajectory prediction [125, 126]. This discussion is limited to experiments and simulations focusing on the boundary layer characteristic.

Although axisymmetric boundary layers often encounter pressure gradients, it is worth-

while first to survey the community's knowledge of zero-pressure gradient cases. The cylindrical boundary layer is complicated by an additional length scale, the cylinder radius a. With this additional length scale, three flow regimes have been defined based on δ/a and $a^+ = au_\tau/\nu$ as discussed by numerous workers [127, 128] and conveniently summarized in Piquet and Patel [129]:

1. When δ/a and a^+ are both large, the boundary layer forms along slender cylinders, resulting in an almost entirely wake-like flow in the outer region, where the lateral curvature has significant influnence. Studies that fall into this category are Luxton et al. [127] with $9 \leq a^+ \leq 47$ and $26 \leq \delta/a \leq 42$, Willmarth et al. [130] with $a^+ \approx 33$ and $2 < \delta/a < 42$, and others.

2. When a^+ is large and δ/a is small, the cylindrical boundary layer behaves quite similarly to a flat plate. Boundary layers under this category include those of Afzal and Narasimha [131] with $0.6 < \delta/a < 2$, Wietrzak and Lueptow [128] with $a^+ = 30$ and $\delta/a = 5.7$, etc.

3. When δ/a is large, and a^+ is small, the flow can be considered an axisymmetric wake with vorticity being produced at its center by a singularity. Only a few studies have been conducted under these conditions.

As discussed in Section 3.1, the flow field under investigation falls into the second category, with $a^+ \sim \mathcal{O}(10^4)$ and $0.15 < \delta/a < 2$. Consequently, the present axisymmetric boundary layer is similar to a planar one, but transverse curvature effects were likely felt in the outer region, particularly as δ/a grew with streamwise distance.

The flow statistics can be impacted by lateral curvature. The mean streamwise velocity profile is known to be more "full," or in other words, the velocity defect is smaller in the outer region. This also implies that the velocity gradients are more significant near the wall, leading to a higher friction coefficient C_f. However, as discussed later, the near-wall dynamics are expected to remain similar. For large a^+ and δ/a of order unity, the logarithmic region

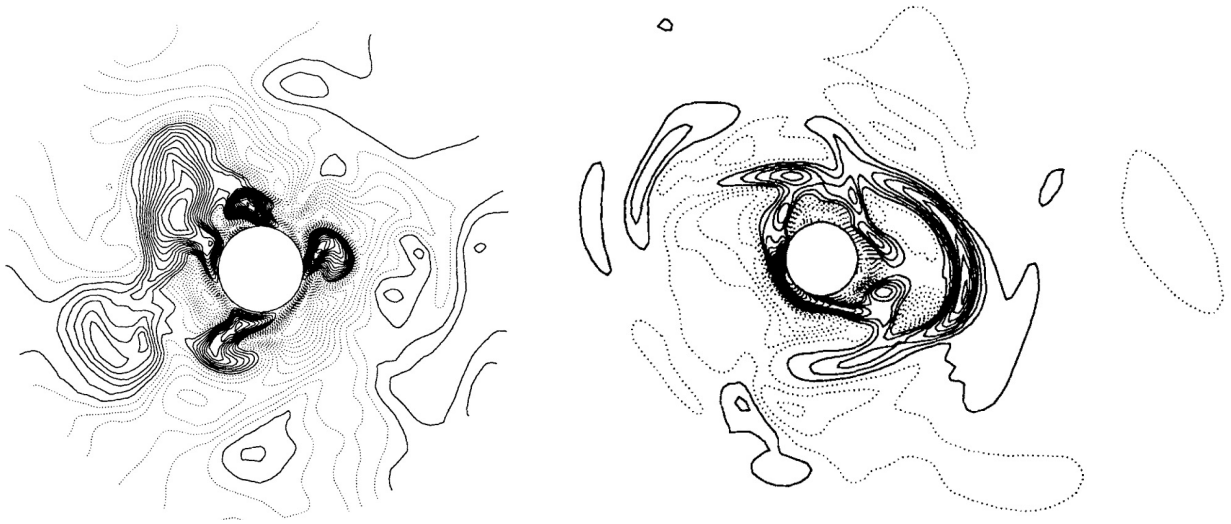

(a) *(b)*

Figure 1.31 Iso-contour of *(a)* axial velocity *(b)* axial vorticity from a direct numerical simulation. Figure from Neves et al. [26].

would still be present [131]; however, the slope of the log law $1/\kappa$ in Eq. 1.6 may be modified [26, 129] and the offset constant C has a weak dependence on $1/a^+$ [127]. The outer region exhibits a wake-like behavior and is well captured by a defect relation. The Reynolds stresses are known to decrease in the outer region, perhaps as a result of azimuthal spreading [132].

In the near-wall region, the burst-sweep dynamics should not be modified in the Suboff boundary layer given the small lateral curvature ($\delta/a < 2$) and large $a^+ \sim \mathcal{O}(10^4)$. Wietrzak and Lueptow [128] investigated an axisymmetric boundary layer with $\delta/a = 5.7$ by measuring the wall shear stress and the velocity simultaneously using hot wires. The RMS and histogram of wall-shear stress (WSS) fluctuation agreed with the zero pressure gradient case to within the uncertainty bounds, suggesting that the near wall burst-sweep dynamics were not modified by the lateral curvature. This point was reiterated by Piquet and Patel [129], who explained that the near wall peak remains at $z^+ = 13$–16 with a value around $3.2u_\tau$. In fact, Piquet and Patel [129] asserted that significant deviation from the linear sublayer profile would require $a^+ \sim \mathcal{O}(1)$.

Wietrzak and Lueptow [128] traversed a velocity probe in the wall-normal and azimuthal

directions relative to a wall shear stress (WSS) sensor and inferred the large-scale structures based on space-time correlations. The variable interval time average (VITA) was used to identify positive events (above the long time average) in the WSS and velocity, showing a phase lag in the shear stress probe relative to the velocity probe. This delay indicated forward-leaning structures that arrived at the velocity probe before the shear probe inclined at 18°, somewhat higher than recent planar cases [20].

Wietrzak and Lueptow [128] also shifted the velocity probe in the azimuthal direction (by $55\nu/u_\tau$, the half-width of a low-speed streak) and performed the cross-correlation with time delay. This measurement suggested large scales yawed at 9° relative to the longitudinal axis. These workers postulated that large structures in the outer region swept along the cylinder wall and passed to the other side, thereby creating the yawed structures. This hypothesis was based on previous flow visualization [133] and that the yawed structures scaled with outer quantities. When $\delta/a \gg 1$, large-scale structures can pass from one side of the flow to the other, similar to an axisymmetric wake almost as if the cylinder were invisible [133], as illustrated by the iso-contours from the DNS of Neves et al. [26] shown in Fig. 1.31. Perhaps this yawed structure is related to the spanwise R_{vv} in planar boundary layers [134, 135], the helical mode in pipes [62, 72].

In summary, the large scales likely remained forward-leaning for the regime of large a^+ and minor to moderate δ/a encountered on the Suboff. Still, they were distinct in their yawed structures and ability to move about more freely, even to the opposite side of the cylinder. Further, it remains to be seen how the varying cross-section of the tapering hull, i.e., $\mathrm{d}a/\mathrm{d}x$, plays a role.

However, the size of the large scales may be reduced relative to the planar case. The spectra of the WSS showed less energy at low frequencies relative to the planar case, consistent with Willmarth and Yang [136] and Snarski [137]. More energy distributed in the higher frequencies (because the RMS levels were comparable), combined with the finding of Willmarth and Yang [136] that the convection velocity was independent of lateral curvature,

suggested that dominant wall-pressure inducing eddies were of a smaller dimension because $f\lambda = U_c$, where f is the frequency, λ is the wavelength, and U_c is the convection speed.

While the physics of cylindrical boundary layers is interesting, one of the motives for studying axisymmetric boundary layers is their relevance to the hydrodynamics and hydroacoustics of underwater vehicles. In particular, flow models used for planar boundary layers require modifications that incorporate lateral and longitudinal wall curvature effects. For potential flow calculations, a rapidly thickening boundary layer resulting from APG requires the analyst to simultaneously (i.e., iteratively) predict the boundary layer growth and outer potential flow. For Reynolds-averaged numerical models, the mixing length and eddy viscosity can vary significantly in the presence of wall curvature-induced pressure gradients [109]. Under an extreme APG, flow separation may occur and is notoriously difficult to predict accurately. For this reason, various concurrent experimental and numerical efforts have sought to advance modeling capabilities and develop a deeper fundamental understanding.

Patel et al. [109] investigated the boundary layer of a 6:1 prolated spheroid, whose tail was modified to avoid flow separation. The work focused on the thick axisymmetric boundary layer formed over the latter half of the model, by measuring the mean and turbulence statistics using hot-wire anemometry. The authors argued that the longitudinal pressure gradient is felt mostly near the wall, whereas the lateral curvature mainly impacts the outer region. Further, they cautioned that the rapid thickening of the boundary layer leads to wall-normal variations in static pressure, an order-of-magnitude increase in wall-normal velocity, and dramatic decreases in Reynolds stresses, particularly in the outer region. Consequently, a successful numerical routine must account for the pressure gradient and the transverse curvature.

Huang et al. [138] made measurements to validate a numerical routine that predicts the boundary layer integral quantities along the stern of a body of revolution. Their measurement showed that the eddy viscosity, mixing length, and correlation length scale were proportional to the square root of the annulus area defined by the model surface and the

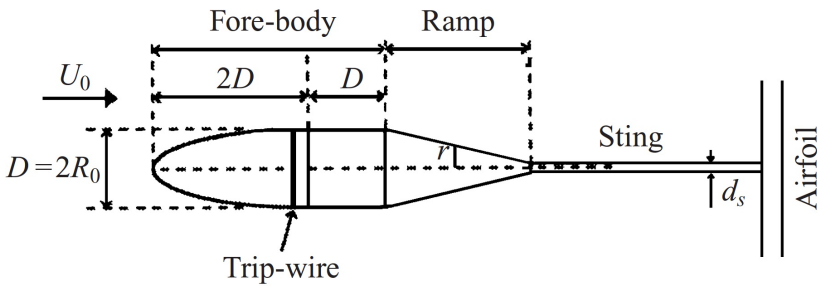

Figure 1.32 Stratford ramp setup from Hammache et al. [27].

boundary layer edge. This observation was incorporated into an iterative viscous-inviscid numerical algorithm to predict the mean velocity and various integral quantities across the entire stern boundary layer. While these time-mean quantities are useful, the underlying turbulent fluctuations are equally important and require a deeper understanding, particularly for higher-fidelity simulations.

The DARPA Suboff was introduced in Groves et al. [139] as a generic submarine to facilitate collaboration. Measurements of the Suboff were made in the Anechoic Flow Facility at Carderock as reported in Huang and Liu [44]. These measurements were primarily used to assess and improve numerical modeling capabilities, particularly regarding turbulence closure. These simulations captured the various vortical structures generated by the sail and appendages. The Suboff bare hull was the geometry investigated in this work.

The axisymmetric Stratford ramp was investigated by Hammache et al. [27] using digital PIV. The Stratford body shown in Fig. 1.32 has a ramp angle that continuously keeps the flow on the verge of separation. These workers investigated the sensitivity of this APG flow by studying two additional geometries with slightly more radical or conservative ramp angles. The radical ramp showed unsteady intermittent flow separations, whereas the conservative ramp had a thinner boundary layer. The Stratford body was also yawed relative to the free stream, with the flow separating on the leeward face. The focus of the current work differs in that a greater emphasis was placed on the boundary layer structure.

Jiménez et al. [140] investigated the wake of a body of revolution after the boundary

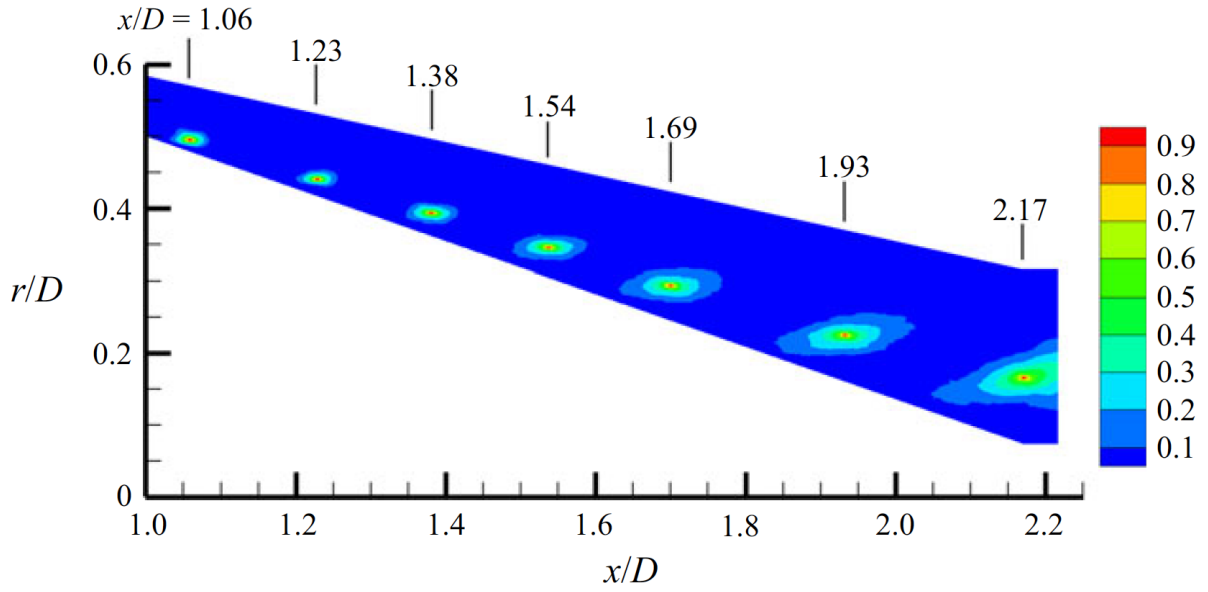

Figure 1.33 Two-point correlation of axial velocity fluctuation for advance ratio $J = 1.44$ along a mean streamline over the tail cone of a Stratford body. Figure from Zhou et al. [28].

layers have merged. The model investigated was the Suboff without its appendages, and the sail was extended to the floor and used as the model support. An extensive range of Reynolds numbers was investigated from 1.1×10^6 up to 67×10^6, and hot-wire measurements were made at various downstream locations. However, no information was given on the Suboff boundary layer itself.

In recent years, Virginia Tech and Notre Dame researchers have studied the Stratford body, including yawed cases [141]. Balantrapu et al. [5] measured a decelerating axisymmetric boundary layer using hot-wire anemometry and PIV ($Re_L = 1.9 \times 10^6$). The work aimed to understand the turbulent flow structures along the model tail, a region of significant adverse pressure gradient and lateral curvature. The work showed a good collapse of the flow statistics when normalized with an embedded shear layer (ESL) scaling. A subsequent publication [54] showed that the convection velocity of the large scales inferred from flush-mounted surface microphones agreed with the mean velocity at the inflection point observed in Balantrapu et al. [5], supporting the existence of ESL motions.

Complementary work was performed by Zhou et al. [28], who used large-eddy simulation

(LES) to carefully understand the various noise sources from a rotor ingesting an axisymmetric boundary layer. They affirmed that spectral oscillation results from constructive and destructive interference of consecutive rotor blades bisecting the same coherent structure, which are highlighted in Fig. 1.33 using two-point correlation. Hickling et al. [142] performed the corresponding experiments, elucidating the flow physics with PIV and beamforming [143]. These studies made strides toward a better understanding of axisymmetric boundary layers and the interplay with a propeller. The current research also focused on exposing the flow structure, although with a more extensive PIV campaign.

The Defense Science and Technology Organisation of Australia has been investigating a generic submarine model designed by Joubert [144, 145]. Recently, Manovski et al. [146] performed PIV with a high focal length lens, which was necessary to maintain an appropriate spatial resolution. The study validated the mean and RMS profiles of the boundary layer measured using PIV at various stations along the body against previous hot-wire anemometry and pitot tube data. They cited the effect of spatial averaging as a limiting factor, and proposed using Lagrangian particle tracking (LPT) techniques [147] to obtain higher spatial resolution. These researchers have also shown promising preliminary results of particle tracks [148] within a measurement volume of $\mathcal{O}(1000\ \mathrm{cm}^3)$ sampled at rates up to 20 kHz. These datasets would reveal the intricate characteristics of the axisymmetric boundary layer, and provide a valuable comparison with the Suboff investigated in this study.

Kumar and Mahesh [45] performed LES around the Suboff bare hull (without appendages or sail) at a length-based Reynolds number of $Re_L = 1.1 \times 10^6$. The study's computational grid was designed to capture the near-wall flow structures and the downstream wake up to fifteen diameters downstream of the body. The authors showed that in agreement with previous measurements [109, 149, 150], higher skin-friction drag and more significant decay of turbulence away from the wall relative to planar boundary layers. From the same research group, Morse and Mahesh [151] used LES to model the flow along the Suboff using a different coordinate system, also showing good comparison with measurements.

Another LES was carried out by Posa and Balaras [152, 153]. Unique to this study was the immersed-boundary method, allowing high Reynolds number simulations up to $Re_L = 12 \times 10^6$. These investigators studied the effects of the sail and appendages on the boundary layer and wake development, and how the time-mean quantities, e.g., velocity, turbulent kinetic energy (TKE), etc., were affected by Reynolds number. Although the simulation provided a host of coherent structures, emphasis was placed on the vortical structures, such as those trailing from the appendages. Few insights were given on the coherent structures that constitute the boundary layer.

Numerous experiments and simulations have focused on evaluating or enhancing the predictive accuracy of medium and high-fidelity numerical simulations. However, the current work delves into the intricate physics of this distinctive boundary layer in great detail. This in-depth analysis was enabled by various configurations of PIV, providing both datasets with significant spatial dynamic range as well as excellent spatial and temporal resolution. These measurements critically examined the unique boundary layer formed along the Suboff tail.

1.1.4 Turbulent Non-Turbulent Interface

Turbulence is often bounded by irrotational flow at its free boundaries. Traversing the flow from the turbulent to the non-turbulent side would reveal sharp changes in velocity, vorticity, and passive contaminants (e.g., temperature, smoke, colored dye) [154]. These abrupt changes occur across a thin layer, which, at any time, segregates the rotational turbulent flow from the irrotational free stream. This boundary is generally known as the turbulent/non-turbulent interface (TNTI). Because the mass flow rates of turbulent jets, wakes, and boundary layers continually increase with distance, the bounding solenoidal field must be gradually converted into rotational turbulence through entrainment promoted by the TNTI.

When the bulges and valleys in a turbulent boundary layer, similar to ones seen in Fig. 1.35, convect past a stationary probe, such as a hot-wire anemometer [29] or a photo-sensitive device [31], the signal alternates intermittently between periods of quiescence and intense fluctuations, as shown in Fig. 1.36. The fraction of time when the fluid is turbulent

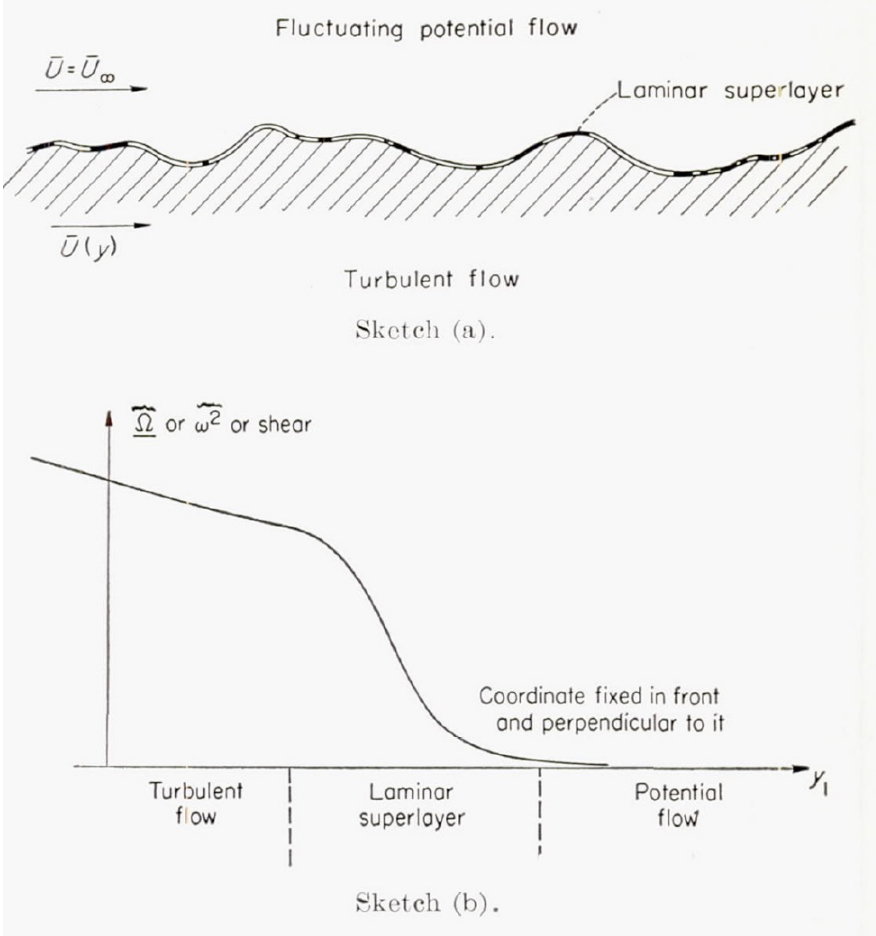

Figure 1.34 Corrsin and Kistler [29] proposed a viscous superlayer across which vorticity diffuses into the irrotational free stream.

was coined by Townsend [155] as the intermittency. The intermittency γ equals one near the wall ($z/\delta < 0.3$) and decreases gradually to zero at the boundary layer edge δ, as shown by the red line in Fig. 1.37b. The intermittency distribution is well-represented by the error function [31],

$$\gamma = \frac{1}{\sigma\sqrt{2\pi}} \int_z^\infty \exp\left[-\frac{(z - Z_i)^2}{2\sigma_i^2}\right] dz, \tag{1.10}$$

where Z_i is the average interface position, and σ_i is the variance of the interface position z_i. The wall-normal position of the interface z_i can be treated as a stochastic variable. Figure 1.37(a) shows the interface position z_i as nearly Gaussian [30, 31], with a mean of $Z_i/\delta_0 = 0.67$. Note that δ_0 is the true boundary layer thickness as would be obtained through a composite fit [82] and is roughly 20% greater than δ_{99} denoted using the dashed line.

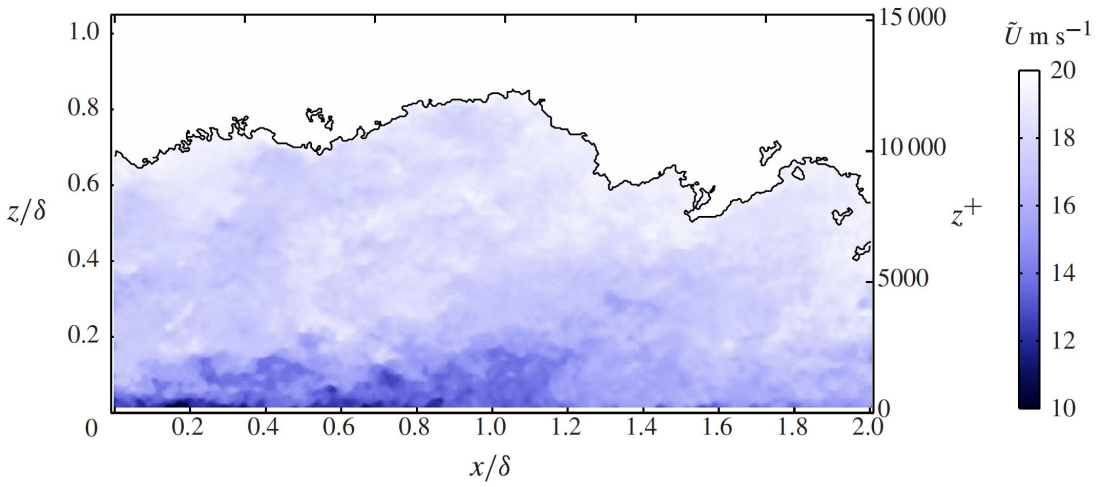

Figure 1.35 Instantaneous velocity snapshot with the corrugated black line denoting the turbulent/non-turbulent interface. $Re_\tau = 14500$. Figure from Chauhan et al. [30].

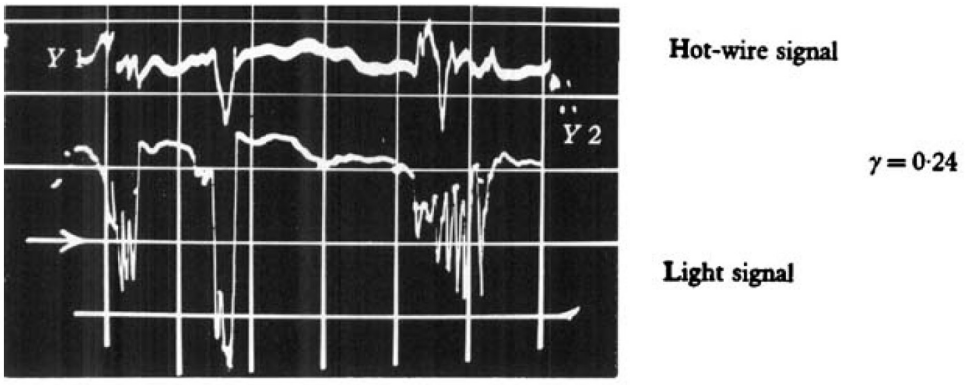

Figure 1.36 Examples of time history collected from a fixed probe. Figures from Fiedler and Head [31].

The current consensus is that the TNTI comprises two layers, a viscous/laminar superlayer [29] and a turbulent sublayer as described by Taveira and da Silva [156]. A laminar superlayer, proposed by Corrsin and Kistler [29] and illustrated in Fig. 1.34(a), was hypothesized to exist because vorticity must be transmitted to the irrotational region through diffusion, because there are no "macroscopic Reynolds type shear forces [29]," i.e., there are no turbulent eddies to carry the vorticity into the potential flow. Therefore, on a dimensional basis, the entrainment process must be governed by the Kolmogorov length scale $\eta = (\nu/\epsilon)^{1/4}$, time scale $\tau_\eta = (\nu/\epsilon)^{1/2}$, and velocity scale $u_\eta = (\epsilon\nu)^{1/4}$ [157–161]. The dissipate

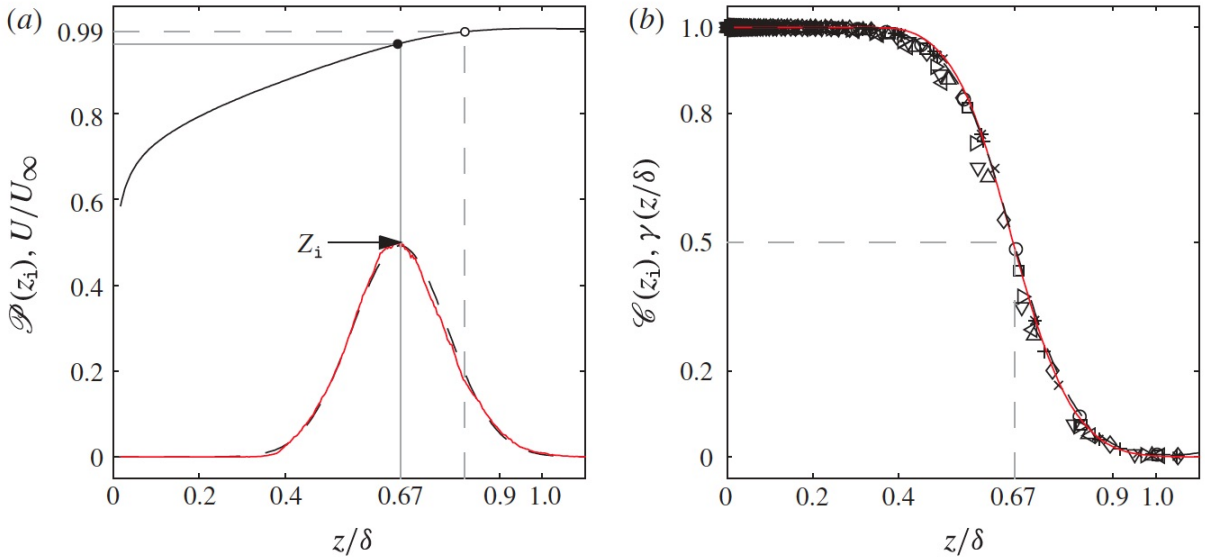

Figure 1.37 (a) Probability density function (PDF) of the interface position z_i; vertical dashed line correspond to δ_{99}. *(b)* The intermittency distribution γ for a canonical turbulent boundary layer. Figures from Chauhan et al. [32].

rate is ϵ and the viscosity is ν.

However, contrary to this hypothesis, most prior works on flows with mean shear have reported a finite TNTI with a thickness on the order of the Taylor microscale λ_T [33, 154, 160, 162–164]. This apparent contradiction was perhaps resolved by Taveira and da Silva [156] who performed kinetic energy budgets on a DNS that resolved the Kolmogorov scale. These workers discovered that the maximum kinetic energy activity was concentrated in a narrow region (a few Kolmogorov lengths) roughly one Taylor microscale above the TNTI. Therefore, most measurements and simulations, including the ones in the present work, do not have the spatial resolution to resolve the laminar superlayer. The present analysis will, therefore, focus on pressure gradient and wall curvature effects on the small- and large-scale motions of the entire TNTI.

Evidence of large-scale motion (of order δ) in the entrainment process can be seen in Fig. 1.35, where the potential region is separated from the rotational boundary layer by the wrinkled black line. This black line showcases the large-scale bulges and valleys, superposed on which are smaller-scale wrinkles.

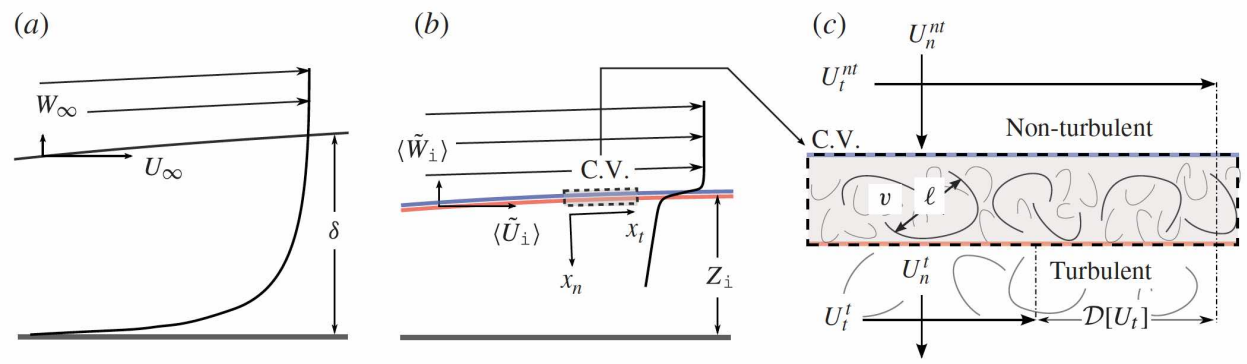

Figure 1.38 (a) Schematic of mean boundary layer with U_∞ and W_∞ as the free-stream velocities. δ is the boundary layer thickness. *(b)* Schematic of mean boundary layer profile conditioned on interface height Z_i now with conditionally averaged velocities. *(c)* Zooming into the TNTI superlayer, there are abrupt changes in the streamwise and wall-normal conditional mean velocities. Figures from Chauhan et al. [33].

One way to understand the TNTI small scales is to examine the conditionally averaged interface. In contrast to the unconditional mean velocity profile in Fig. 1.38(a), Fig. 1.38(b) shows a conditionally averaged profile where each instance is centered about the TNTI. Figure 1.38(c) zooms into the finite thickness of the TNTI, showing that the eddies should have dimensions on the order of the interface thickness. To this end, a conditional average about the interface is shown in Fig. 1.39(a), where $\mathcal{D}[\langle \tilde{U} \rangle]$ is the jump in streamwise velocity across the TNTI, and $(d\langle \tilde{U} \rangle / dz)_{\max}$ as the maximum rate of change of streamwise velocity in the interface denoted by the shaded region. Therefore, the width of the TNTI and the dimension of the turbulent eddies therein are on the order of the vorticity thickness [33, 163, 165],

$$\delta_\omega = \frac{\mathcal{D}[\langle \tilde{U} \rangle]}{\max d\langle \tilde{U} \rangle / dz}. \tag{1.11}$$

In addition to the velocity jump, the vorticity and Reynolds stresses also undergo rapid changes through the TNTI. Examining Fig. 1.40 [30], the three subfigures from left to right correspond to normalized spanwise vorticity, Reynolds shear stress, and normal stresses, including the RMS of fluctuating spanwise vorticity. As a result of the sizeable streamwise velocity increase across the interface, there is a peak in spanwise vorticity in the TNTI.

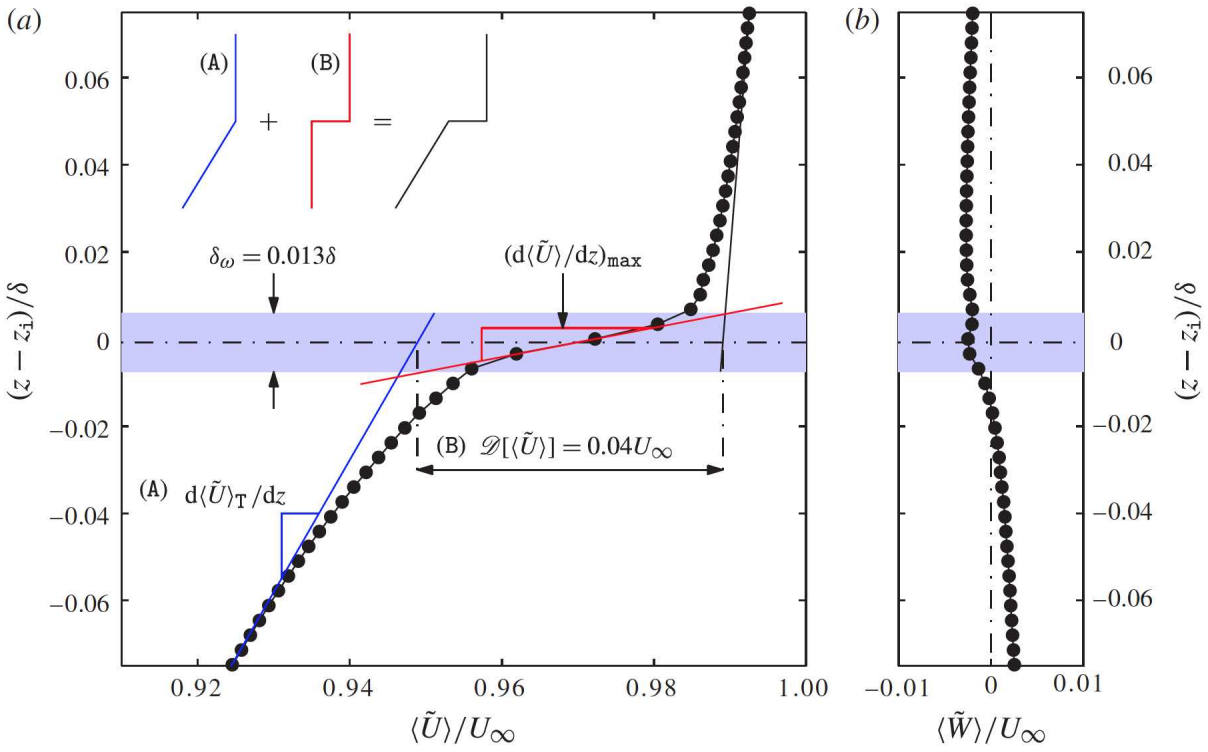

Figure 1.39 (a) Streamwise and *(b)* wall-normal velocity conditionally averaged on the interface position. The shaded region indicates the vorticity thickness and corresponds to the TNTI. Figures are from Chauhan et al. [30].

The Reynolds shear stress approached zero at the TNTI, implying that the u and w velocity fluctuations were no longer correlated. Note that this decorrelation does not mean an absence of velocity fluctuation beyond the TNTI, as shown in subfigure (c). The non-zero values in Fig. 1.40(c) were not experimental noise as the potential flow is also unsteady from interacting with the turbulence below.

Beyond identifying the large and small scales, the deeper question is how they each contribute to the entrainment process. Numerous workers have striven to understand the contributions of different scales through fractal analyses [166–168], kinetic energy budget [156, 162], or other means [30, 33]. One theory was that large scales "engulf" significant parcels of potential flow in the way that "amoeba ingests food" [169]. However, it does not have much experimental or numerical support [170]. In fact, Mathew and Basu [161] and Westerweel et al. [160] showed for wakes and jets with mean shear, and Holzner et al.

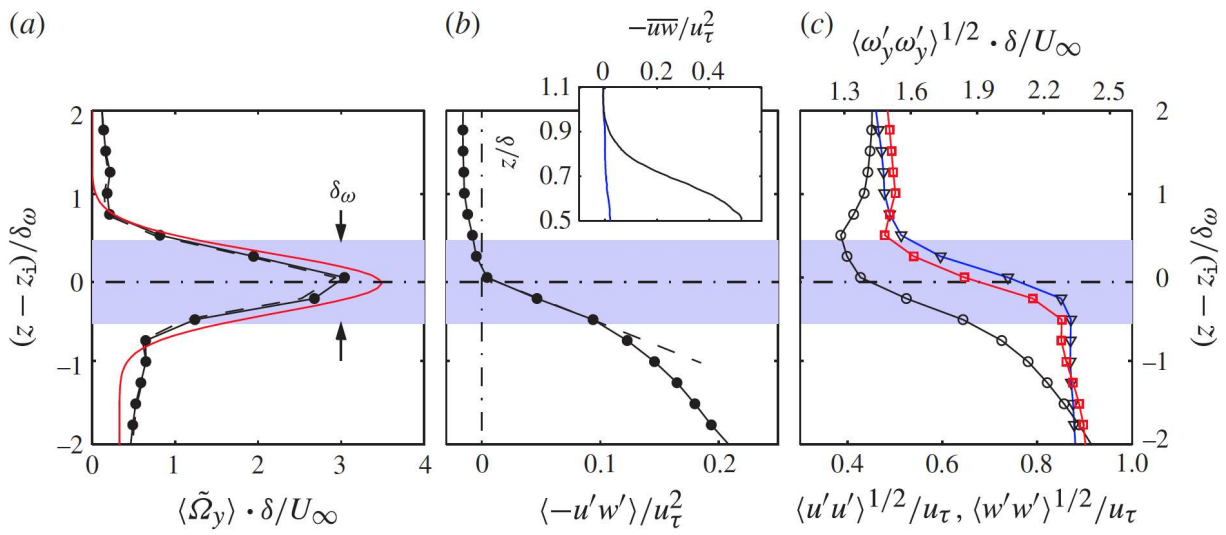

Figure 1.40 Conditionally-averaged statistics with respect to the interface z_i. *(a)* Circular markers shows normalized mean spanwise vorticity $\langle\Omega_y\rangle\delta/u_\tau$, and black dashed line is $\mathrm{d}\langle\tilde{U}\rangle/\mathrm{d}z$. *(b)* Reynolds shear stress with the dashed line showing locally linear behavior. *(c)* RMS of the spanwise vorticity (∇), streamwise fluctuation ($\circ$), and wall-normal fluctuation ($\square$).

[158, 159] for shear-free turbulence, that the outward growth of the turbulent region is driven by small-scale "nibbling." Studies at higher Reynolds numbers with greater separation between the large and small scales [30, 157] have reaffirmed these findings, and further suggested that energy-containing motions enhance the entrainment by increasing the area over which nibbling occurs [30, 167]. In a canonical boundary layer, the length of the TNTI is roughly three times the streamwise domain [30], resulting from large scales that distort the interface and, on occasion, cause it to fold over itself.

Understanding the entrainment on a detailed level usually requires time-resolved measurements to distinguish the interface velocity and the entrainment velocity [36]. Alternatively, one can gain a sense of the small and large scales by examining the interface geometry. Chauhan et al. [30] studied the auto-correlation of the interface-normal velocity and the wall-normal position of the interface to understand the small and large scales [171]. The small scale was roughly on the order of the vorticity thickness, and the large scale was roughly 1.7δ, consistent with the community's understanding of entrainment dynamics. A similar study

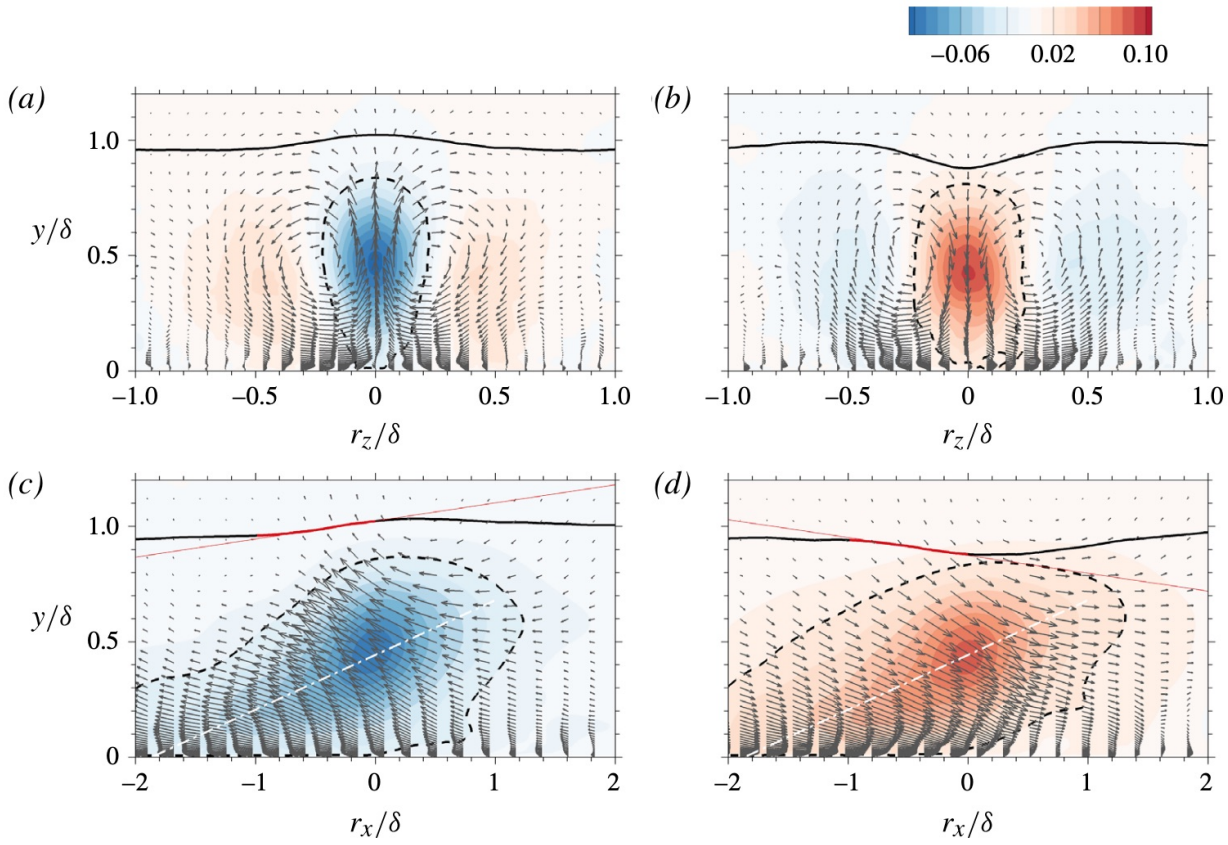

Figure 1.41 Conditionally averaged flow based on *(a,c)* low- and *(b,d)* high-speed events at $z/\delta = 0.5$ for a canonical boundary layer with $Re_\tau = 1000$. *(a,b)* show the cross-plane and *(c,d)* show the streamwise plane. Figures from Lee et al. [34].

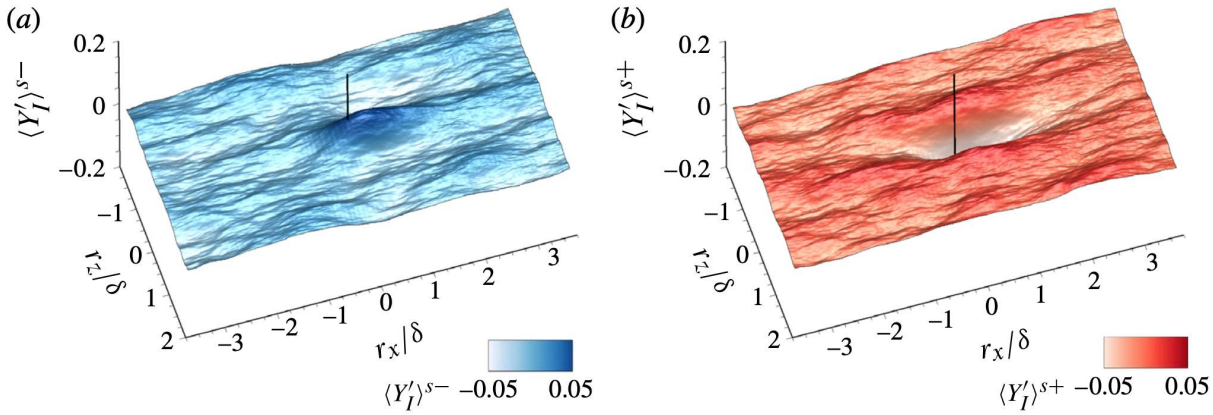

Figure 1.42 Average turbulent/non-turbulent interface conditioned on *(a)* low- and *(b)* high-speed large-scale motions. Figures from Lee et al. [34].

was conducted for the Suboff to examine the effects of pressure gradient and wall curvature.

A recent high-fidelity simulation has offered 3D perspectives of the entrainment pro-

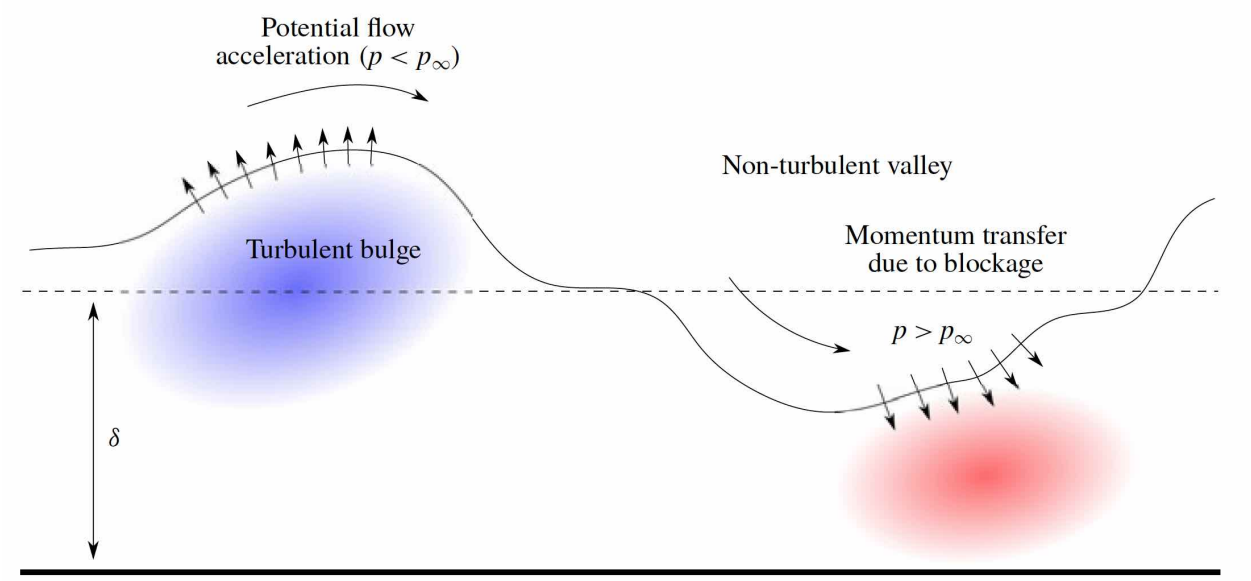

Figure 1.43 Overview of turbulent/non-turbulent interface kinematics in a ZPG boundary layer showing sweep and ejection following the Reynolds decomposition. Image from Reuther and Kähler [35].

cess. Figure 1.41 shows the conditional low- and high-speed events in spanwise and streamwise planes, taken from Lee et al. [34]. $Re_\tau = 1000$. Examining the streamwise planes in Figs. 1.41(c) and (d), the large-scale motions extended from the boundary layer edge to the wall, creating a bulge or an indent in the boundary layer edge. Observing the spanwise planes in Figs. 1.41(a) and (b), roller structures uplift or indent the upper boundary depending on their rotation. Figure 1.42 offers a three-dimensional perspective of the TNTI conditioned upon (a) high- and (b) low-speed events. High-speed events led to bumps in the interface, and low-speed events were associated with valleys.

Figure 1.43 from Reuther and Kähler [35] shows schematically how the Reynolds decomposition reveals bulges and valleys in the velocity fluctuations. The fluid accelerating around the bulge has low pressure and encourages bulge growth. This scenario could be interpreted as a momentum transfer from the higher-velocity free stream to the turbulence below. The Reynolds decomposition, however, may not be best for interpreting the entrainment mechanism. Other decompositions based on boundary layer height [172] or separation of turbulent and non-turbulent flows [35] may offer better insights. Without more detailed measurements

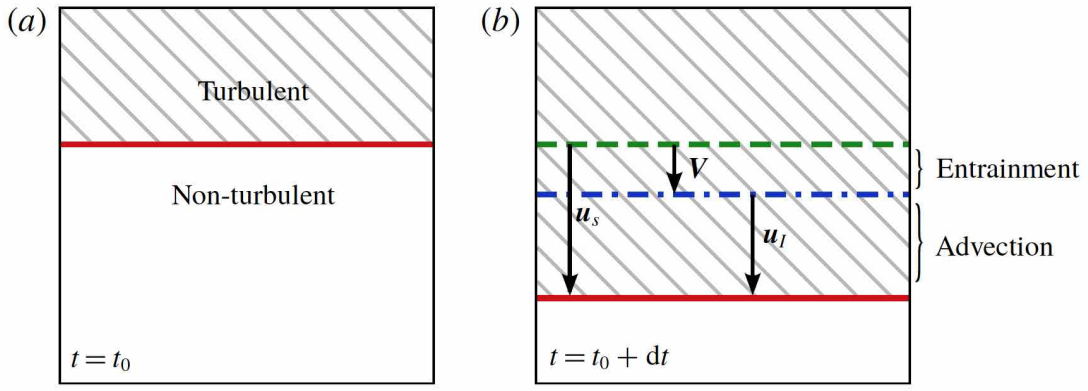

Figure 1.44 (a) Given a turbulent/non-turbulent interface, *(b)* the entrainment velocity V is the difference between the interface surface velocity u_s and the measured velocity u_I. Image from Mistry et al. [36].

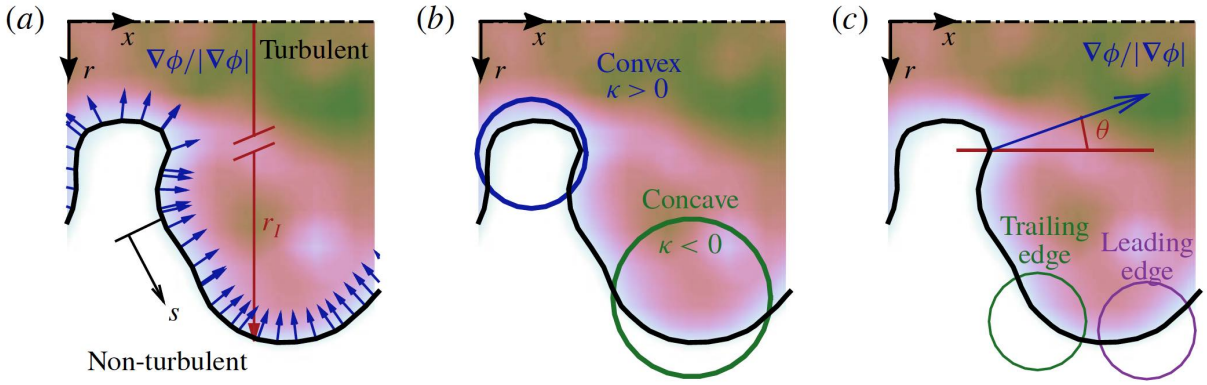

Figure 1.45 Conditional averaging for studying entrainment should focus on the interface's normal velocity, as well as the concavity and slope of the interface. Image from Mistry et al. [36].

of the interface movement, it is challenging to understand the entrainment flow kinematics.

A detailed study of entrainment kinematics was performed by Mistry et al. [36] using both time-resolved and spatially-resolved measurements. Spatial resolution was important because viscous scales dictate the thin TNTI. The time resolution was necessary to deduce the entrainment velocity, which Fig. 1.44 shows as the difference between the interface surface velocity and the measured velocity. A detrainment occurs when the measured velocity exceeds the interface velocity, whereby a turbulent fluid becomes irrotational. Figure 1.45 shows that entrainment kinematics should be studied considering the interface concavity and slope.

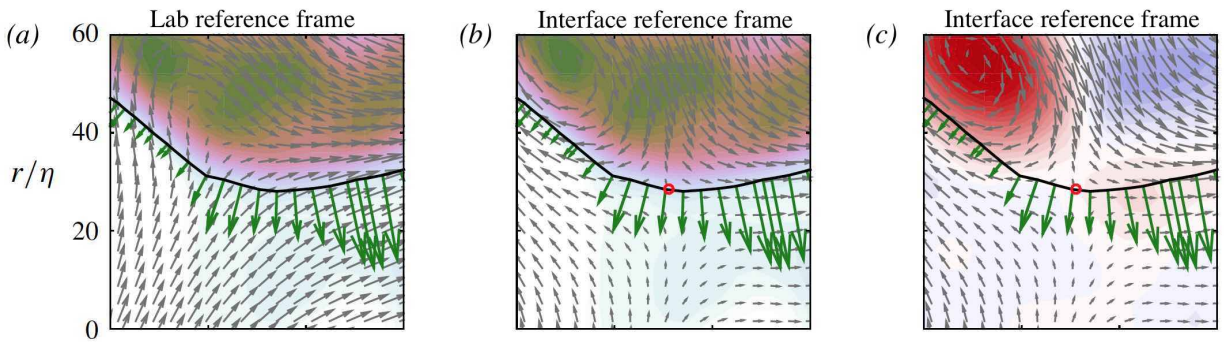

Figure 1.46 A reference frame moving with the interface is more suited to understanding the entrainment kinematics. Image from Mistry et al. [36].

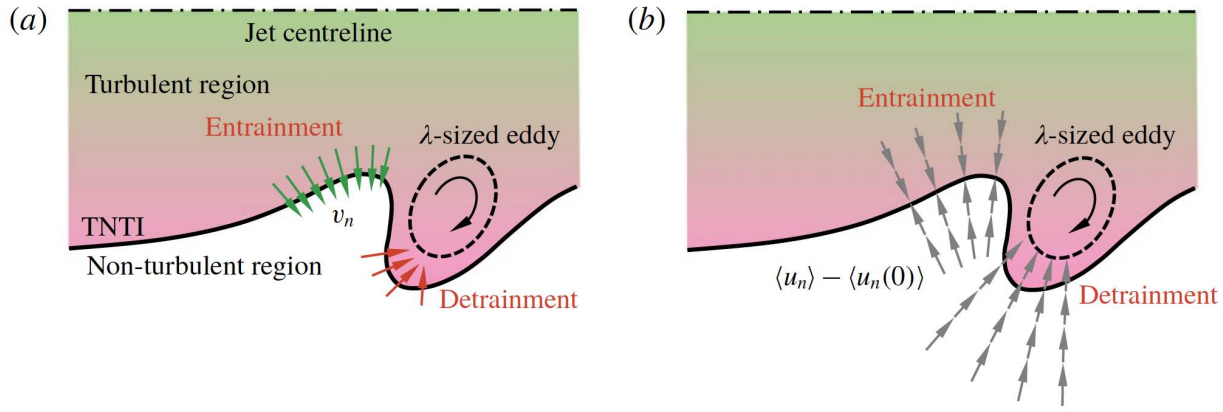

Figure 1.47 Convex and concave wrinkles corresponding to entrainment and detainment are driven by eddies on the Taylor microscale. Image from Mistry et al. [36].

A Lagrangian reference frame, i.e., one moving with the interface, is perhaps most suited to understanding the entrainment kinematics. Figure 1.46 shows a detrainment in the lab (a) and the interface (b, c) reference frames. Inspecting these figures, the interface frame shows the counterflow around the saddlepoint denoted by the red circle suggested to enhance the transport of rotational and irrotational fluid. Mistry et al. [36] also proposed an entrainment model shown in Fig. 1.47 where eddies on the Taylor microscale underlie the convex and concave wrinkles corresponding to entrainment and detrainment.

The effects of pressure gradient and wall curvature on the TNTI were considered by Fiedler and Head [31]. These workers found that the average interface location moved outward, and the width of the intermittent zone decreased for adverse pressure gradients. The

converse was true of favorable pressure gradients. The full depth of the boundary layer was intermittently turbulent under sufficiently strong FPG. The characteristic intermittency parameters are well related to the shape factor H.

Yang et al. [173] studied the TNTI in an APG turbulent boundary layer with $\beta_c = 1.43$. The authors concluded that the additional entrainment was achieved by increased interface length (i.e., surface area for nibbling) and enhanced viscous contributions to entrainment velocity. However, the reported effects of APG on the mean and variance of the interface position conflicted with the account of Fiedler and Head [31]. So, there are disagreements even on the statistics that require clarification.

Relatively fewer studies have investigated pressure gradient effects on the TNTI, with contradicting reports on even the intermittency and probability density of the interface location. For this reason, the detailed measurements in this work give insight into the statistics and structure of this unique TNTI.

1.2 Dissertation Objectives

Following a survey of prior works on planar and axisymmetric boundary layers, it was apparent that the behavior of boundary layers under the combined effect of pressure gradient and wall curvature requires further attention. A better comprehension of the underlying flow physics could enable engineering designs that improve the performance of aerial and marine vehicles. The specific research questions of this writing are as follows.

1. How do the pressure gradient and wall curvature alter the boundary layer characteristics compared to the canonical, i.e., smooth-wall, zero-pressure gradient, planar boundary layer? The present work performed detailed PIV measurements to report the flow properties comprehensively.

2. Are the observed deviations from the canonical state a consequence of the pressure gradient or the lateral/longitudinal wall curvature? The current understanding is that pressure gradient and wall curvature predominantly affect the inner and outer regions,

respectively.

3. How rapidly do the pressure gradient and wall curvature effects take place? Boundary layers, particularly the large scales, require time and distance to adjust to the changing environments [51].

This dissertation by no means completely answers these questions. Instead, this work intends to make inroads towards a better understanding and clarify future research directions.

1.3 Dissertation Organization

The current chapter surveyed prior boundary layer works. The review documented the fundamental understanding gained from studies of canonical, i.e., zero pressure gradient, smooth-wall, and planar boundary layers, from the standpoint of statistics and structure. It further assessed the general effects of pressure gradients and lateral curvature on boundary layer behavior. The chapter concludes by identifying gaps in the current knowledge and presenting the research questions this writing aims to address.

Chapter 2 describes the experimental approach. The chapter overviews the wind tunnel, the Suboff model, and the acquisition and processing of pressure and PIV data. Surface static pressure measurements were made to document the pressure gradients. Three PIV configurations interrogated the flow, including streamwise and cross-stream planes with varying spatial and temporal resolutions. Uncertainty levels are also reported.

Chapter 3 analyzes the turbulent boundary layer. The time-averaged velocity and Reynolds stresses will be discussed first. Then, two-point correlations were computed to elucidate the flow structure—it was discovered that the length scale varied as a function of the pressure gradient. Further, interesting flow structures were observed in the outer region and explained as turbulent entrainment. To this end, the conditional statistics and the turbulent/non-turbulent interface geometry were investigated. A central focus in each section was ascertaining whether deviations from the canonical state could be attributed to pressure gradient or wall curvature effects.

Chapter 4 concludes this dissertation by summarizing the findings. While a better understanding of pressure gradient and wall curvature effects has been obtained, numerous outstanding questions require further study. For this reason, future research directions were proposed for the Suboff geometry and, more generally, non-equilibrium boundary layers.

2 Experiments

This chapter details the experiment and the measurement approach. The account includes information about the wind tunnel, the wind tunnel model, and the static pressure and PIV measurements that were performed. The accuracy and uncertainty levels of the measurements are also reported.

2.1 Wind Tunnel

The study was performed at the Embry-Riddle low-speed wind tunnel, which was commissioned in 2018. Figure 2.1(a) shows a view of the tunnel circuit. The wind tunnel test section, shown in Fig. 2.1(b), is 4 ft (1.2 m) tall, 6 ft (1.8 m) wide, and 12 ft (3.7 m) long. The wind tunnel is unique in that 65% of the test section walls are made of optical-grade glass, permitting various configurations of cameras and lasers. The test section was twice the model's length, offering good wake development before the diffuser section.

The free-stream turbulence intensity in the test section was measured during the wind tunnel commissioning to be less than 0.1% at the flow speed of 150 $\mathrm{ft\,s^{-1}}$ (45.7 $\mathrm{m\,s^{-1}}$) and less than 0.25% for flow speeds up to 350 $\mathrm{ft\,s^{-1}}$ (107 $\mathrm{m\,s^{-1}}$). The spatial flow uniformity across the test section was less than 0.1% of the free stream, as measured using hot-wire anemometry and a turbulence sphere, and the angularity of the flow was less than $\pm 0.2\%$. Tapered corner fillets minimized the creation of a longitudinal pressure gradient in the test section because of the effects of boundary layer growth on the tunnel walls. The longitudinal pressure gradients in the test section were measured to be practically negligible [174].

The wind tunnel also had other valuable capabilities. A heat exchanger managed the air temperature, maintaining a uniform density and viscosity flow. Mufflers reduced the noise level from the breather slots and minimized acoustical flow disturbances that might have affected the turbulence levels in the free stream and on the model. A dedicated vent purged PIV seeding from the tunnel circuit, providing control over the seeding density during PIV tests. These wind tunnel capabilities all contributed to making high-quality flow measurements with good productive efficiency.

(a)

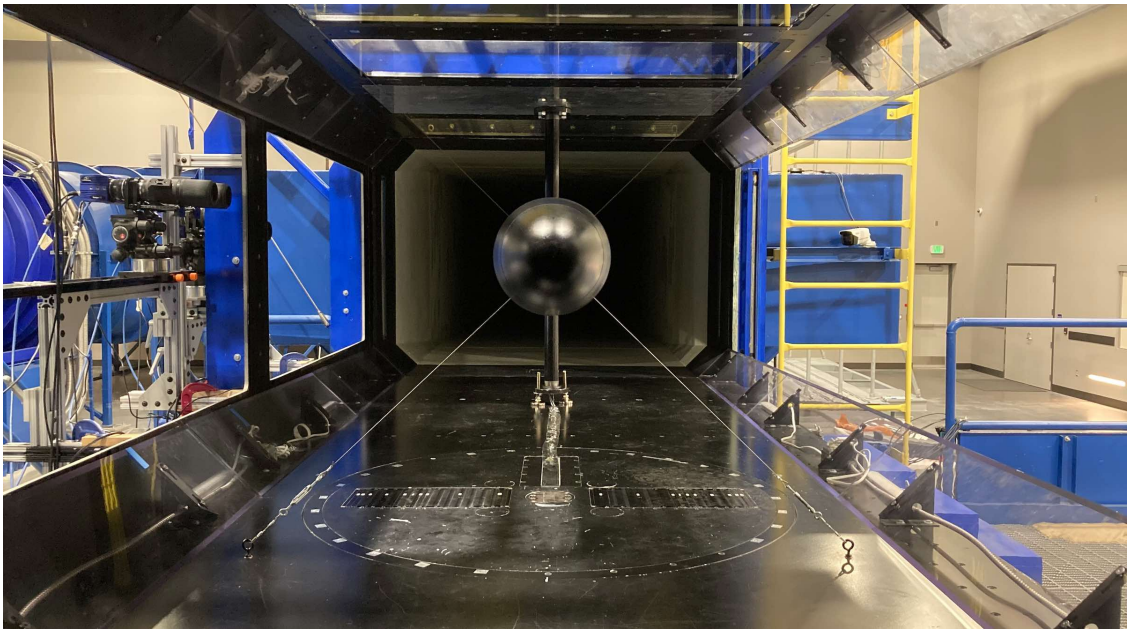

(b)

Figure 2.1 (a) View of the Embry-Riddle low-speed wind tunnel facility and *(b)* and looking down the test section.

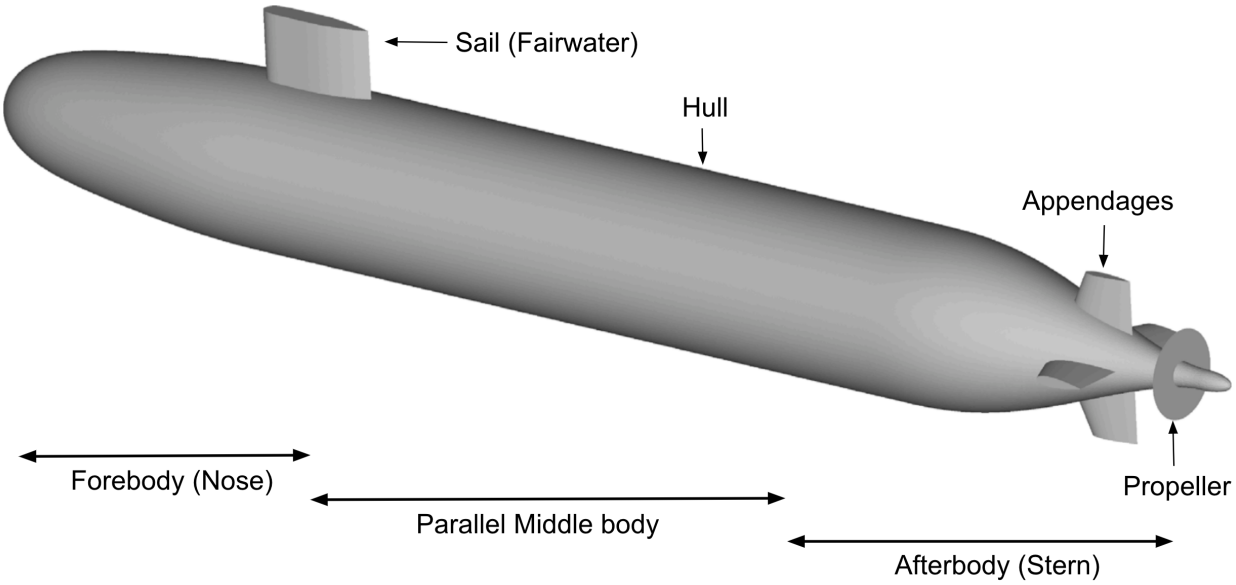

Figure 2.2 Submarine terminology. Original image from Zhou et al. [37].

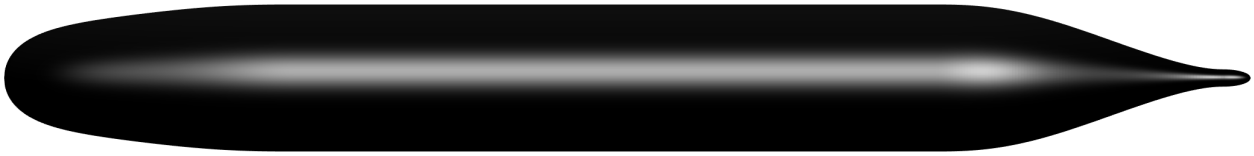

Figure 2.3 Side view of the DARPA Suboff hull.

2.2 Suboff Model

The Suboff [139] was the generic body of revolution investigated in this work. This model was proposed by the Defense Advanced Research Projects Agency (DARPA) as part of its "Submarine Offensive" initiative. An annotated diagram of the Suboff in Fig. 2.2 splits the hull into three segments: the forebody, the middle body, and the afterbody. The sail (or fairwater) sits above the hull and houses various antennas and the periscope. The appendages offer directional control, and the propeller, represented by a disk, provides thrust. For this study, the model's appendage, sail, and propeller were omitted, leaving the axisymmetric hull as shown in Fig. 2.3. The bare hull configuration permitted a detailed study of the afterbody's axisymmetric boundary layer.

A 1/55 scale model was constructed (with ± 0.015" tolerance, or $0.0034R$; R is the radius) and installed in the wind tunnel as shown in Fig. 2.4. Figure 2.5 is a schematic showing the

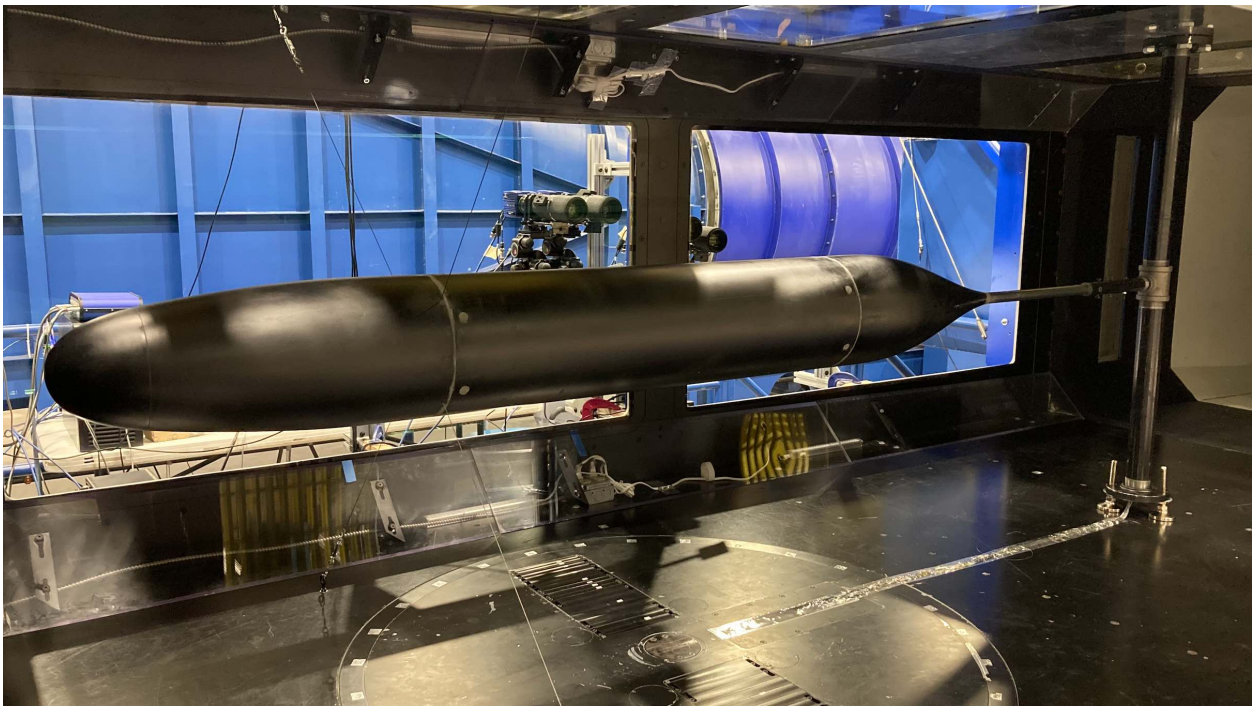

Figure 2.4 Suboff installed in the wind tunnel test section using a sting and four guy wires [5].

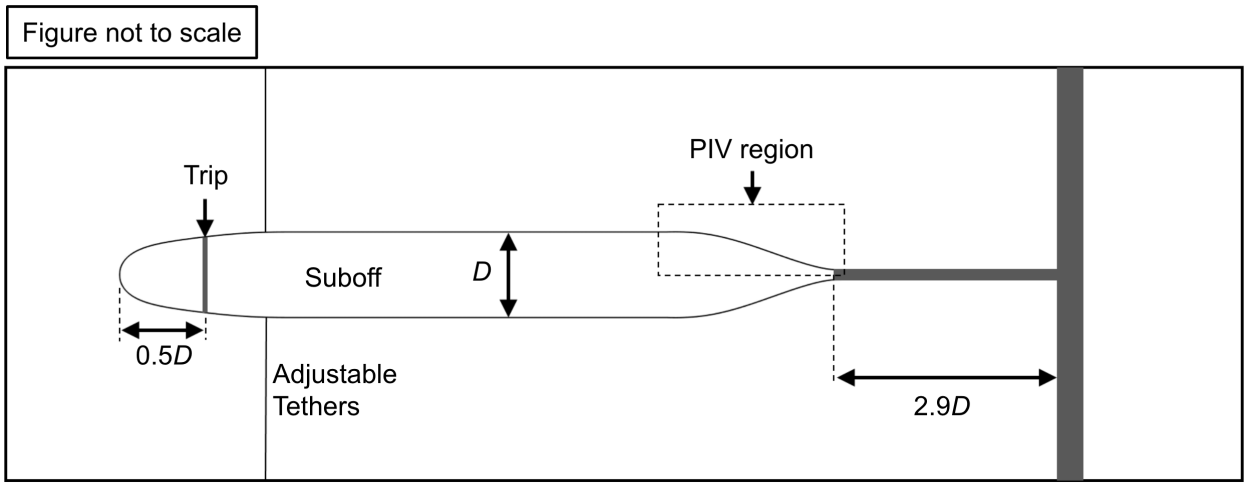

Figure 2.5 Schematic of the Suboff installed in the test section.

model installed in the test section, where the flow travels from left to right. The model was supported and aligned by a sting and four 1.2 mm wires near the nose (following the work of Hickling et al. [142]) to minimize boundary layer perturbations. The four wires used turnbuckles to align the model with the free stream, ensuring an axisymmetric flow.

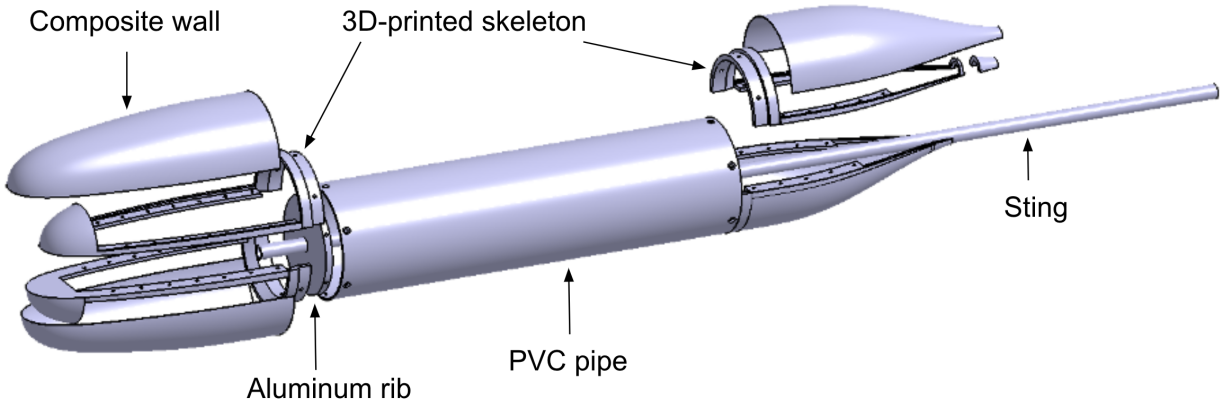

Figure 2.6 Exploded view of the pertinent components within the constructed Suboff model.

An axisymmetric boundary layer requires similar transition points at all circumferential stations. Therefore, a boundary layer trip was installed at $x/L = 0.06$ or $x/D = 0.5$, as discussed in Section 2.2.1.2. The distance between the floor-to-ceiling strut and the model was set using 2D potential flow at 2.9 hull diameters D; see Section 2.2.2.2 for details. Static pressure ports were installed along the entire length of this model, whereas the particle image velocimetry (PIV) honed in on the afterbody. Regarding PIV, a novel procedure was devised to attenuate laser surface reflections, allowing seed particles to be visualized < 20 µm above the wall. Appendix B provides additional details on this method.

2.2.1 Model Construction

As shown in Fig. 2.6, the model was divided into three segments—the forebody, the midbody, and the afterbody. The midbody was made of an extruded polyvinyl chloride (PVC) pipe, and the two ends were made following a composite vacuum bag approach. These segments were joined by aluminum ribs and a hollow shaft that extended through both ribs. To this end, Section 2.2.1.1 overviews the composite layup, and Section 2.2.1.2 discusses the boundary layer trip.

Figure 2.7 Mold for the forebody (left) and afterbody (right).

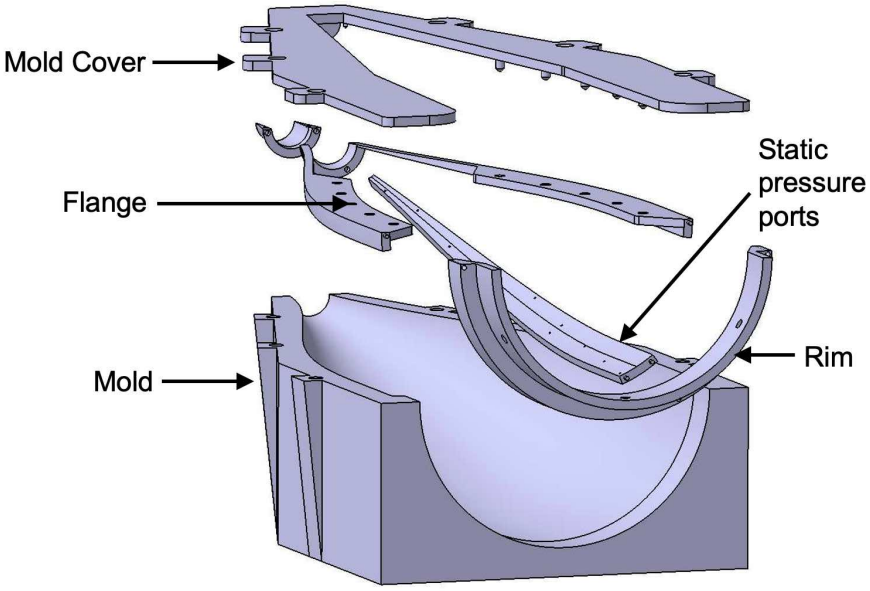

Figure 2.8 Exploded view of how the 3D-printed skeleton was inserted into the mold.

2.2.1.1 Composite Layup

A fused-deposition modeling (FDM) 3D printer was used to create the mold for the composite layup. The layer lines in the 3D print were covered by iteratively applying high-build filler primer and sanding with 220-grit sandpaper. The porous filler primer was sealed with polyurethane before the composite layup. The molds are shown in Fig. 2.7.

The vacuum bag composite layup used a 3D-printed skeleton, carbon fiber weaves, and honeycomb sheets. Figure 2.9 shows the materials used and the assembled product. First, the mold was treated with three layers of turtle wax and two coats of Fibreglast release. Once the mold release had thoroughly dried, Fibreglast epoxy (resin + hardener) was applied

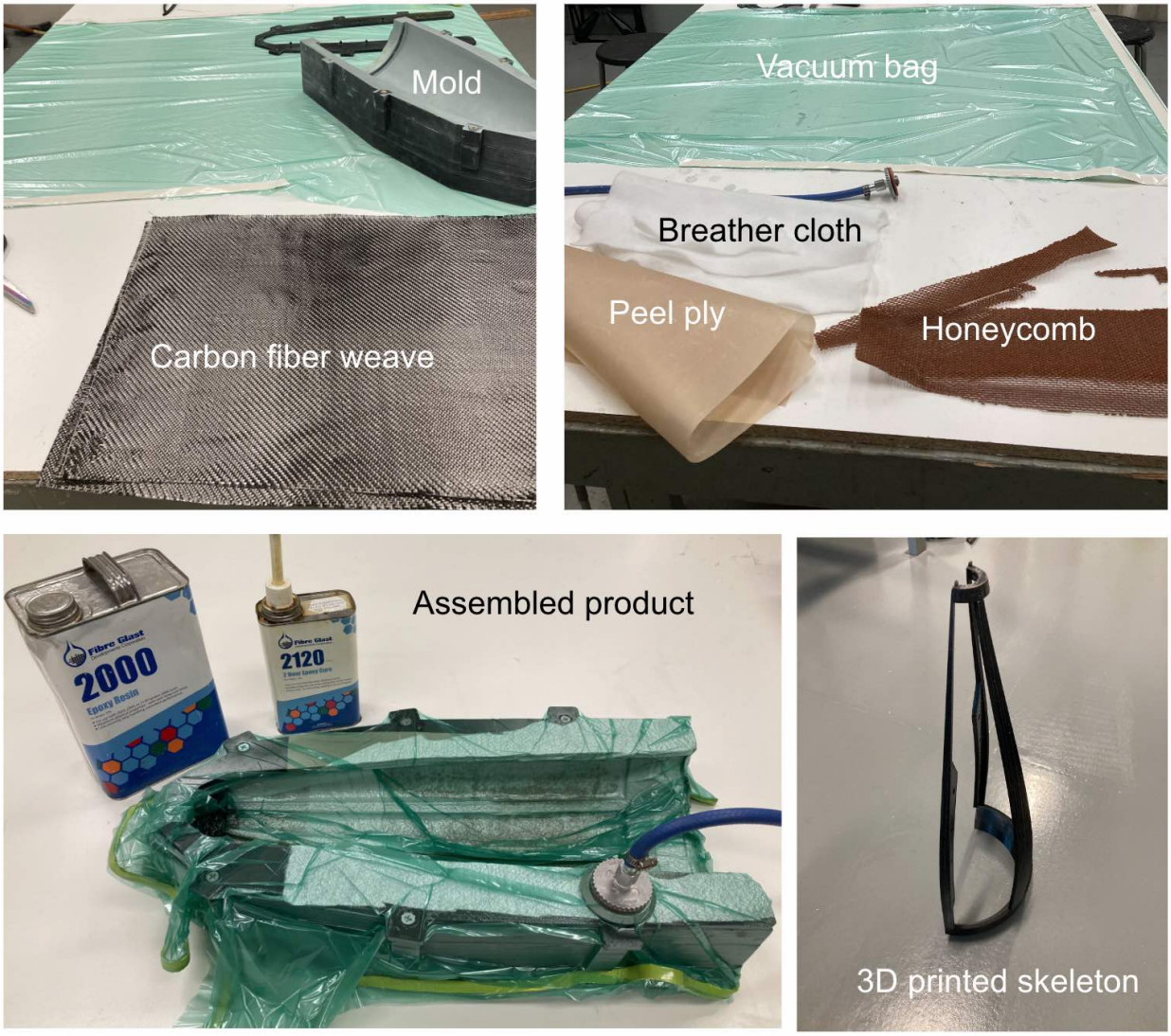

Figure 2.9 Overview of components and process in model construction.

Figure 2.10 Laser cut templates used to refine model geometry.

generously to the mold surface, so that the vacuum bagging would permeate the carbon fiber. Two layers of carbon fiber were placed in the mold. Then, as shown in Figure 2.8, the 3D-printed components were laid on top, and the whole assembly was squeezed into place by the mold cover. The 3D-printed skeleton was important because it incorporated flanges to join the two halves of the afterbody, a lip to fasten the afterbody and the midbody, and openings perpendicular to the surface for the pressure taps. The relative locations of the 3D-printed components were determined using pins. Subsequently, the peel ply was laid down, followed by the breather cloth. This assembly was placed into a sealed bag, which was then placed under a negative gauge pressure, forcing the carbon fiber into the shape of the mold. The negative pressure was applied for a few hours, and the composite was left to cure. After the outer shell, a 1/8" honeycomb and an inner wall of (two layers of) carbon fiber were laid by following the same procedure as above. This sandwich type of structure provided excellent structural rigidity.

However, the carbon fiber model was only as accurate as the 3D print, which has a tolerance of ±0.04" (1 mm) (depending on the user) for an FDM printer. This tolerance is somewhat high for typical wind tunnel models. For comparison, the tolerance of a machine shop model is around ±0.005" (0.1 mm), depending on the size of the model. Therefore, an

automotive body filler (Bondo) was used to seal the gap between the two halves, cover other imperfections, and lower the tolerance to ±0.015" (0.38 mm). The model's accuracy was confirmed with laser cutouts of the model geometry shown in Fig. 2.10 and feeler gauges.

The surface finish of a wind tunnel model is crucial. First, the Bondo was finished to 220 grit. Then, minor imperfections were removed with a few coats of filler primer. Next, two layers of matte black paint were applied to the model surface. Finally, the model was polished with progressively finer sandpaper up to 1000 grit. Typically, this surface finish would be sufficient. However, the challenge of measuring boundary layers on an opaque surface is that the laser reflection at the model saturates the camera pixels, which can no longer identify tracer particles. Although black is the least reflective color, PIV could still not resolve 1–2 mm off of the wall with reasonable certainty, when using the large-FOV PIV setup. This distance was significant because the outer edge of the log layer was as small as 3 mm. Therefore, additional measures were necessary to resolve the interesting flow phenomenon in the inner layer of the boundary layer. To this end, a combination of techniques was used to attenuate the laser reflection as overviewed in Section 2.4.5 and detailed in Appendix B.

2.2.1.2 Boundary Layer Trip

A boundary layer trip was necessary to mimic the natural transition of the full-scale Suboff and to ensure an axisymmetric flow field [175]. For ZPG boundary layers, several studies have investigated in detail the effects of tripping. Schlatter and Örlü [176] numerically investigated the effect of trip height using direct numerical simulations (DNS). They concluded that for a ZPG boundary layer, tripping should take place at $Re_\theta < 300$, and the effects of the trip will be negligible after $Re_\theta > 2{,}000$. Marusic et al. [177] experimentally found that it requires $\mathcal{O}(2000)$ trip heights before the boundary layer loses its memory of the trip in the outer region. However, it is challenging to directly translate these findings to the present axisymmetric boundary layer.

As for axisymmetric bodies, Erm et al. [175] investigated the boundary layer sensitivity to various trip wire sizes on the DST generic submarine model [144, 145] by measuring the

friction coefficient C_f, providing some guidelines on the appropriate trip wire size. Jiménez et al. [140] placed a 0.51 mm trip wire, 0.75 diameter downstream from the nose. Balantrapu et al. [5] used the Thwaites correlation method to estimate the laminar boundary layer thickness, and inserted a square trip to be 35% of the estimated thickness [178]. Based on guidelines from Erm et al. [175], Manovski et al. [146] used CAD-cut trip dots 0.29 mm in height and 1.27 mm in diameter, spaced 2.54 mm from one another to promote boundary layer transition at $x/L = 0.05$ on the DST generic submarine.

For the current Suboff, following the method summarized by Balantrapu et al. [5] and detailed in Schetz and Bowersox [178], a rectangular trip was installed at $0.5D$ [150] from the leading edge or equivalently at $x/L = 0.06$. The trip was 0.28 mm tall and 1.5 mm wide (in the streamwise direction). Based on estimates from the Rott-Crabtree method, the axisymmetric counterpart to Thwaites method [178], this trip was 20% and 40% of the boundary layer thickness at $U_\infty = 50$ and 200 $\mathrm{ft\,s^{-1}}$, the two flow speeds used in the present study. These trip heights were comparable to that of Balantrapu et al. [5], understanding that it was unreasonable to change trip dimensions between different flow speeds. This trip height was also comparable in dimensions to the tripping devices chosen by Erm et al. [175] and Manovski et al. [146], whose generic submarine was similarly sized to the one in the present study. As shown later, the resulting boundary layer thickness at the model's stern was roughly equal to the propeller radius, as is typical for a submarine.

The trip was manufactured by adhering double-sided Scotch tape to 400-grit sandpaper. The thickness of the trip was verified with a digital caliper. These sandpapers were then laser cut into precisely 1.5 mm wide strips. The trip location was determined using laser-cut templates and a self-leveling measurement laser diode.

2.2.2 Model Installation

There are a few considerations when installing the wind tunnel model. The first consideration was whether the test section walls would induce additional longitudinal pressure gradient on the Suboff boundary layer. The second was how far downstream the support

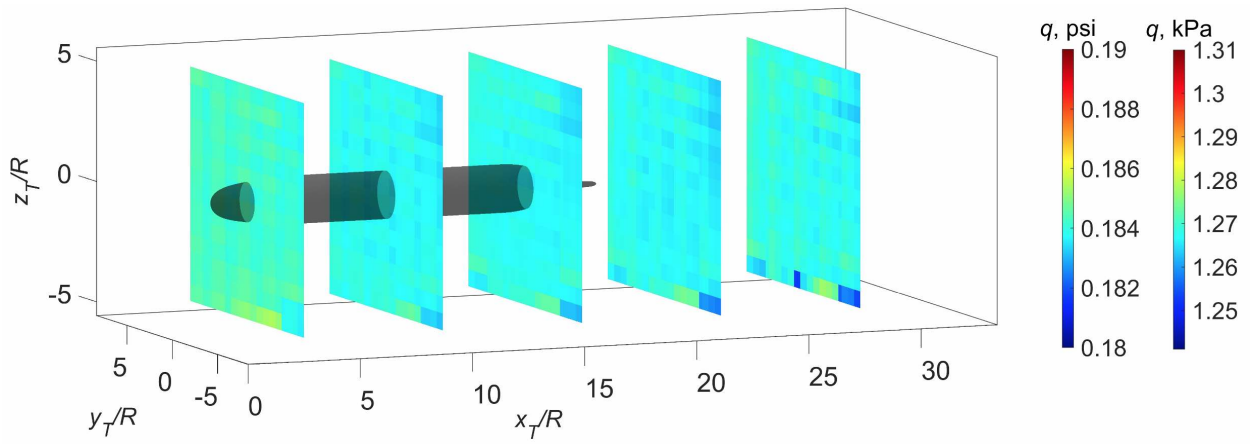

Figure 2.11 Distribution of dynamic pressure q measured in the test section. Data was acquired during the wind tunnel commissioning tests.

strut should be to reduce the upstream disturbance to negligible levels. The third concern was whether the model was aligned with the free stream, which was crucial for an axisymmetric boundary layer.

2.2.2.1 Tunnel Blockage

It must be recognized that in any wind tunnel, the test section walls may impact the measurements. For example, the proximity of the walls can affect the streamline curvature, which is primarily a function of the solid blockage of the model. Furthermore, any longitudinal pressure gradient in the test section because of boundary layer growth on the walls can affect the measurements, as discussed in Ch. 12 of Leishman [179]. Therefore, careful consideration of blockage and longitudinal pressure gradients is necessary.

The solid blockage of the Suboff model in the wind tunnel was 1.7%. This value was calculated by dividing the frontal projected area by the test section's cross-sectional area, excluding the corner fillets. The dynamic pressure q was measured at a free-stream velocity of $U_\infty = 150\ \mathrm{ft\,s^{-1}}$ during the tunnel commissioning. This probe was mounted on a 2D traverse at five streamwise locations in the test section, as shown in Fig. 2.11. The nose of the Suboff was 8 inches downstream of the tunnel entrance. However, the tunnel calibration showed that uniform flow was achieved well before this location.

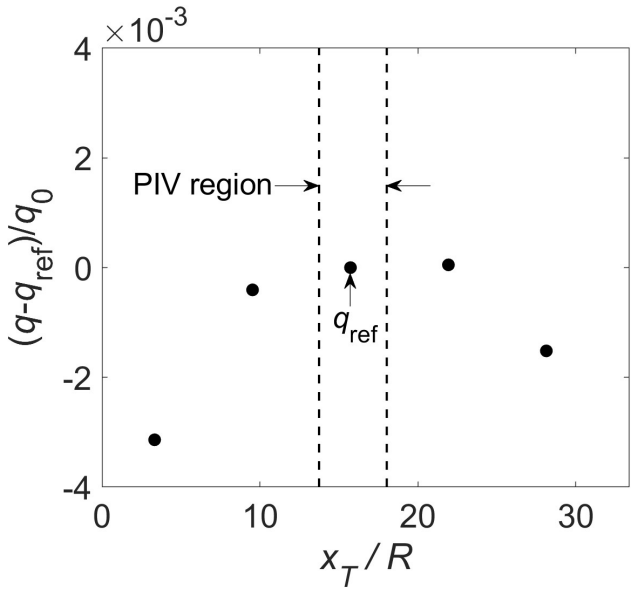

Figure 2.12 Deviation in dynamic pressure from the reference normalized by the mean dynamic pressure across five points. Measurements acquired at $U_\infty = 150$ ft s^{-1}.

At each streamwise station, the dynamic pressure q was computed as the average of all the points enclosed within the maximum Suboff radius shown in Fig. 2.11. Figure 2.12 shows the deviation from the reference dynamic pressure, q_{ref} in the PIV region, as a fraction of the dynamic pressure q_0 averaged across all five points. The deviations were less than 0.3% and even smaller near the region where the PIV measurements were taken.

The static pressure gradient dp/dx in the PIV region was computed to be $\mathcal{O}(1)$ Pa m^{-1}. In contrast, the maximum dp/dx experienced along the Suboff was $\mathcal{O}$(1000–10,000) Pa m^{-1}, as shown in Fig. 3.3(c). Therefore, it was concluded that any pressure gradient in the empty test section had negligible effects on the Suboff boundary layer development.

2.2.2.2 Support Strut Interference

Potential flow calculations were used to understand the upstream disturbance that the downstream supporting strut may cause. To this end, 2D sources and sinks were used to represent the closed Suboff body. Then, the support cylinder was represented by a doublet and shifted to different positions downstream of the trailing edge. To create the Suboff geometry, the potential flow required that:

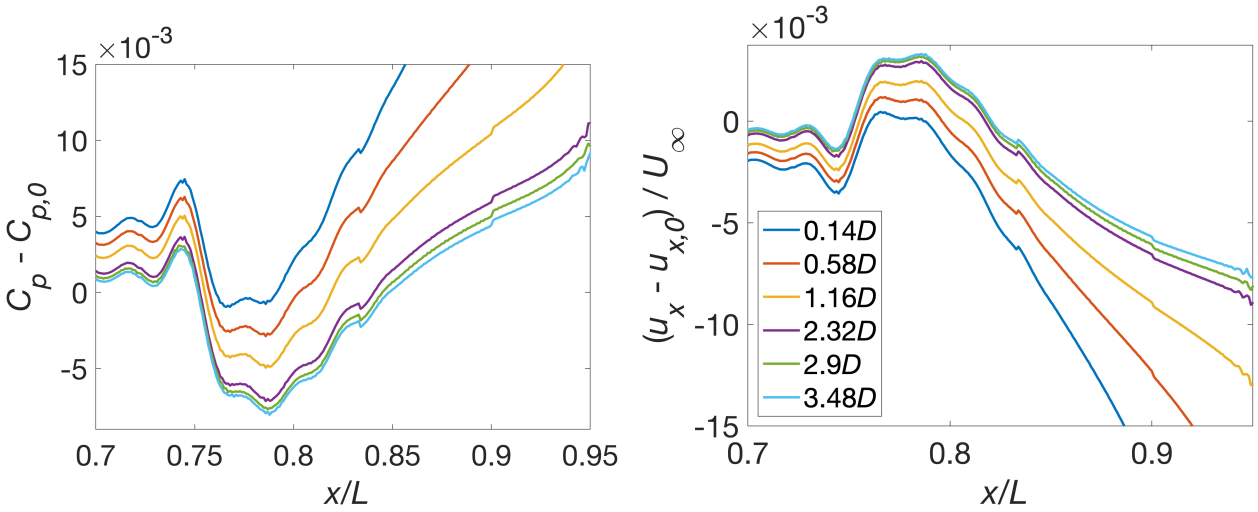

(a) Pressure Coefficient C_p *(b)* Axial velocity u_x

Figure 2.13 Deviation from baseline case without cylinder denoted with subscript "0" is approximately 1% when separation is greater than $2.9D$

1. The source and sink strengths sum to zero to ensure a closed Suboff body.
2. The flow tangency boundary condition is enforced at the model surface.
3. The leading and trailing edges of the body are stagnation points.

With these criteria, the coefficients representing the strengths of the individual sources were computed. The effect of the cylinder was documented by the deviation from the flow without the cylinder, denoted by subscript "0". Figure 2.13 shows that, at a separation distance of $2.9D$, the dimensionless deviations in pressure $C_p - C_{p,0}$ and axial velocity $(u_x - u_{x,0})/U_\infty$ reduced to 0.01. This deviation was deemed acceptably low, as any additional increase in offset distance yielded diminishing returns.

2.2.2.3 Model Alignment

The model was aligned with the test section with the aid of a digital inclinometer ($\pm 0.1°$ reading) and a self-leveling laser diode. Four turnbuckles (3/16" thread, 2" take up) were used to precisely orient the model into the free stream, but were placed far from the body to minimally perturb the flow. It is important to not under or over-tighten the turnbuckles to avoid excessive vibration from wire slack or risk of failure because of over-tension. The

turnbuckles were hand-tightened, and the excited notes of the plucked steel wires were used to qualitatively check that the loads were evenly distributed. Because of the minute free-stream angularity, further turnbuckle adjustments were not necessary after this initial alignment, as measured by the circumferential array of pressure ports discussed in Sections 2.3 and 3.1.

2.3 Surface Static Pressure

Surface static pressure measurements were acquired with the Scanivalve MPS4264 transducer, which has a range of 1 Psi (27" of H_2O) and a 24-bit A/D resolution. The uncertainty of the module was ± 4 Pa. The reference pressure was a dedicated instrument static pressure at the inlet, distinct from the pneumatic average of four static pressures (one on each wall at the inlet) used to set the test section flow speed. The dynamic pressure was computed based on the free-stream velocity and free-stream density. This density was computed using the equation of state, with the free-stream temperature and atmospheric pressure.

The static pressure was measured at 23 streamwise locations. These ports were staggered in the circumferential direction to reduce downstream flow disturbances and interference. Six circumferential pressure ports were placed at $x/L = 0.62$ to ensure an axisymmetric boundary layer. The static pressure was sampled at $f_s = 200$ Hz for 30 seconds at each flow speed. As discussed in Section 3.1, the streamwise pressure coefficient distribution C_p agreed well with the potential flow calculations and other published measurements. The circumferential pressure values agreed with each other to within the accuracy possible using the pressure transducer module.

2.4 Particle Image Velocimetry

Three particle image velocimetry (PIV) configurations were employed to understand this unique boundary layer. One configuration imaged nearly the entire afterbody ($x/L =$ 0.70–0.95). Another setup offered insights into the details of the frequency content of the flow. A third configuration focused on exposing the three-dimensionality of the boundary layer. The principal challenge common to all three PIV configurations was the laser surface reflection that saturated the camera pixels targeting the region 1–2 mm above the wall. Given

the current boundary layer thickness of only 2 cm in parts of the measurement domain, the wall-normal region covered by the laser was considerable. To this end, significant effort was devoted to mitigating surface reflections, and good success was achieved. The following sections detail the PIV setups, the flow vector calculations, data post-processing, and estimates of the associated uncertainties.

2.4.1 Large-FOV PIV

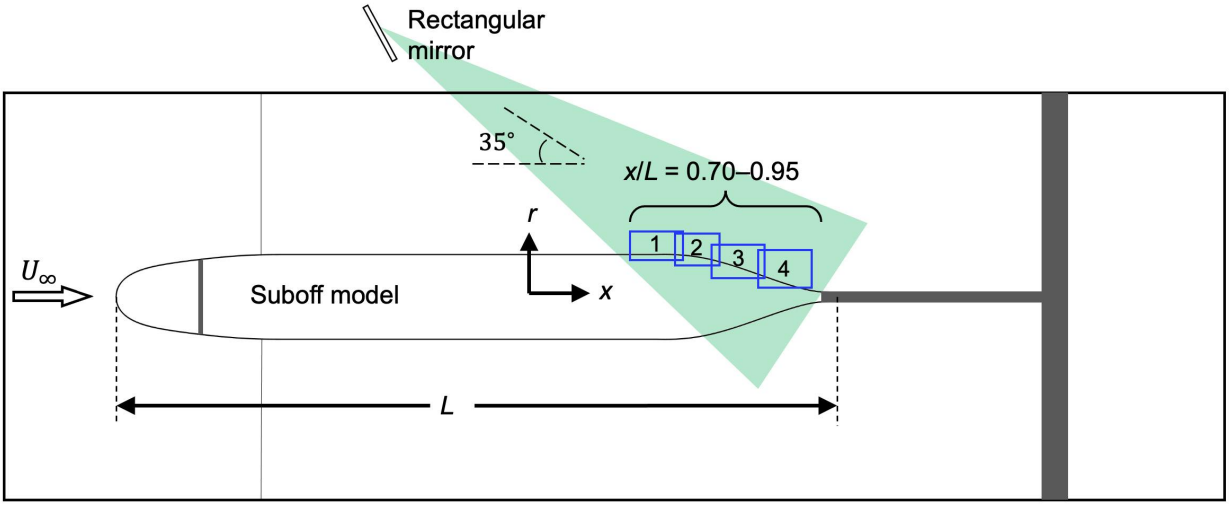

Figure 2.14 Experimental setup for the large FOV imaged by four side-by-side cameras.

Four 29-megapixel (4400×6600 px^2) CCD cameras were arranged side by side to capture a sizeable spatial domain as illustrated in Fig. 2.14 (not to scale). This setup imaged the afterbody between x/L =0.7–0.95, where the boundary layer experienced the combined effects of surface curvature and pressure gradient. Each camera was fitted with a 50 mm extension tube, and a 200 mm microlens to achieve a resolution of 22 µm px^{-1}. Bandpass filters were used to eliminate the Stoke-shifted laser surface reflection, as described in Appendix B.

The measurement domain was illuminated by a 532 nm, 380 mJ/pulse, Nd:YAG laser. This laser beam was steered through a collimator and a 20 mm cylindrical lens. The resulting laser sheet was then reflected into the test section with a rectangular mirror oriented at approximately 60° relative to the wind tunnel floor, as illustrated in Fig. 2.14. This optical arrangement of reducing the laser incident angle relative to the surface was a crucial part of

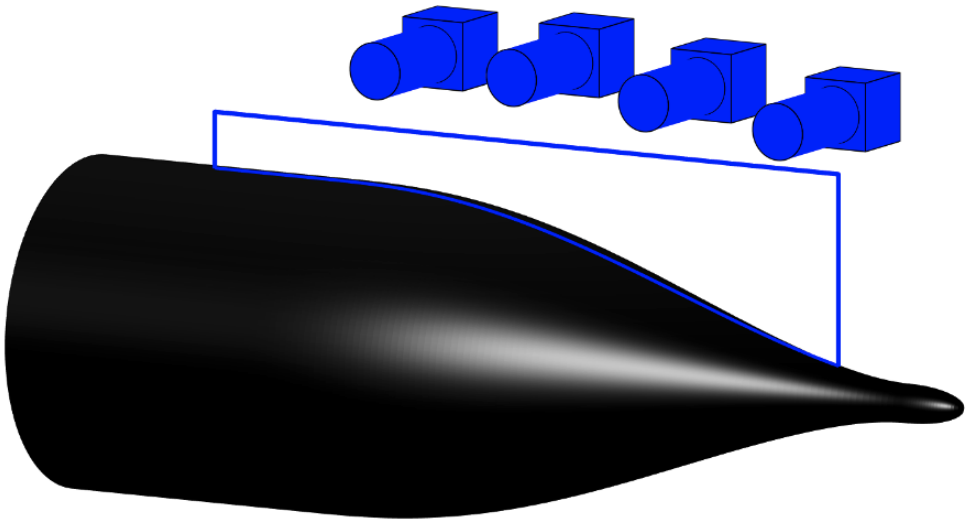

Figure 2.15 Four high-resolution cameras were arranged side by side to image the entire afterbody of the Suboff model

the setup that enabled measurements closer to the wall. The resulting laser sheet thickness was measured to be 1 mm on the model surface. The tracer particles illuminated by the lasers were quoted by the manufacturer as 0.2–0.3 µm in diameter. Global seeding was used, with the seed being ejected into the tunnel circuit and allowed to mix thoroughly to be homogeneous.

Measurements were made at two flow speeds of $U_\infty = 50\ \mathrm{ft\,s^{-1}}$ and $200\ \mathrm{ft\,s^{-1}}$. At each flow speed, roughly 3,000 image pairs were acquired at an average frequency of 0.2 Hz in a streaming fashion. These statistically independent snapshots provided good convergence in single- and two-point statistics [20]. The straddling times were 30 µs and 6 µs for the two flow speeds, leading to a free-stream particle displacement of roughly 15 px.

The raw images were processed in DaVis 10.2. The images were pre-processed with background subtraction, 3×3 smoothing to combat pixel locking [180], followed by perspective correction before the multi-step vector calculation. Outlier detection [181] was used to remove spurious vectors. The final interrogation window was $16\times16\ \mathrm{px^2}$ with 50% overlap. An adaptive weighting [182] was used with the final interrogation window to follow the changing flow gradients, which are typically maximum in the wall-normal direction for a boundary

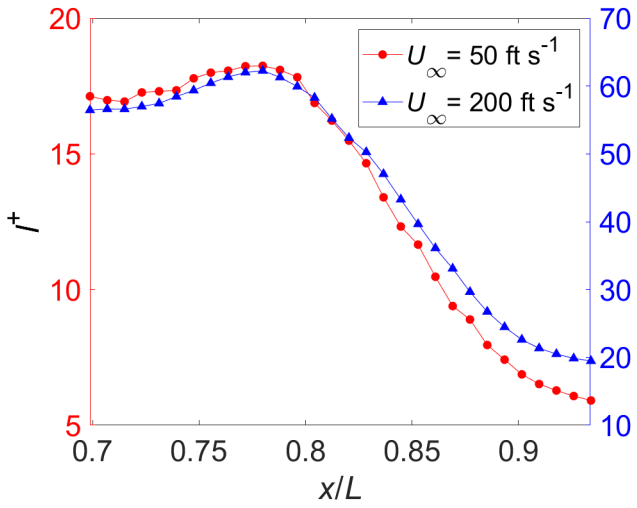

Figure 2.16 Size of final interrogation window in wall units $l^+ = l/l_\nu$ for both flow speeds. l is the final interrogation window size. The left and right ordinates correspond to $U_\infty = 50$ and 200 ft s^{-1}.

layer.

The spatial resolutions of the final window in wall units are summarized in Fig. 2.16. The left and right ordinates correspond to $U_\infty = 50$ ft s^{-1} and 200 ft s^{-1}. The final window of the streamwise plane was 17 and 56 wall units ($l_\nu = \nu/u_\tau$) at the most upstream location for the two flow speeds; the window was 6 and 20 wall units at the most downstream location. (Wall units are computed in Section 3.2.3.) This varying spatial resolution followed the trend of the wall shear stress, which depended on the pressure gradient. The PIV spatial measurement resolution at the lower Re was comparable to the recommended hot-wire resolution of roughly 20 µm [183, 184].

Although it was unclear whether guidelines from studies of canonical boundary layers apply in non-equilibrium scenarios [185], the reduced resolution at the higher Reynolds number implied that the smallest scales were not as well-resolved, and care should be taken when comparing the statistics with mismatched resolutions. This shortcoming was not considered a setback because the focus of this work was predominantly on the outer region large-scale structures [28], which should experience little attenuation, with spatial resolutions of 20–60l_ν [184].

At $U_\infty = 50$ ft s^{-1} and 200 ft s^{-1}, 2,373 and 2,914 snapshots were considered high enough quality, and so were retained for analysis. These results are summarized in Section 2.4.8. The measurement uncertainties are discussed in Section 2.4.7.

2.4.2 Time-Dependent PIV

The power spectrum is central to a complete understanding of the boundary layer [3, 5, 8]. For this reason, the flow was sampled at 16 kHz across four different streamwise locations, $x/L = 0.65$, 0.78, 0.85, and 0.92. These locations correspond roughly to the ZPG, end of FPG, increasing APG, and decreasing APG. Figures 2.17(a) and 2.17(b) show the two setups used to measure the flow field, where the second configuration used a mirror in the tunnel to redirect the laser sheet upstream, minimizing the angle between the surface and the laser sheet, and therefore the laser intensity on the model surface.

This mirror assembly was bolted to the ceiling, and compression was applied with leveling feet on the floor, a stiff and well-damped construction that eliminated laser sheet vibration even at 200 ft s^{-1}. The mirror-strut assembly is shown in Fig. 2.20. The distance between the strut and the most downstream point of the model was $1.8D$; D is the hull diameter. The blockage effect of this assembly was assessed by recording the static pressure distribution at both flow speeds. Comparisons in Fig. 3.4 showed that the mirror assembly had little effect on the flow field.

As shown in Fig. 2.18, the setup comprised two cameras of different magnifications. The (green) high-magnification camera zoomed in on a portion of the (blue) low-magnification camera measurement domain. The low-magnification camera (magnification $M = 0.25$) was fitted with a Scheimpflug adapter, a 50 mm bellow-type extension tube, a 200 mm Nikon microlens (f/4), and a 527 ± 5 nm band-limited filter. The high-mag camera ($M = 0.73$) was fitted with a Scheimpflug adapter, a 90 mm extension tube, a two-time teleconverter (2×TC), a 200 mm Nikon microlens (f/4, effectively f/8 with 2×TC), and finally a 527±5 nm filter. The Scheimpflug essentially acted as an additional spacer, as the oblique angle of the

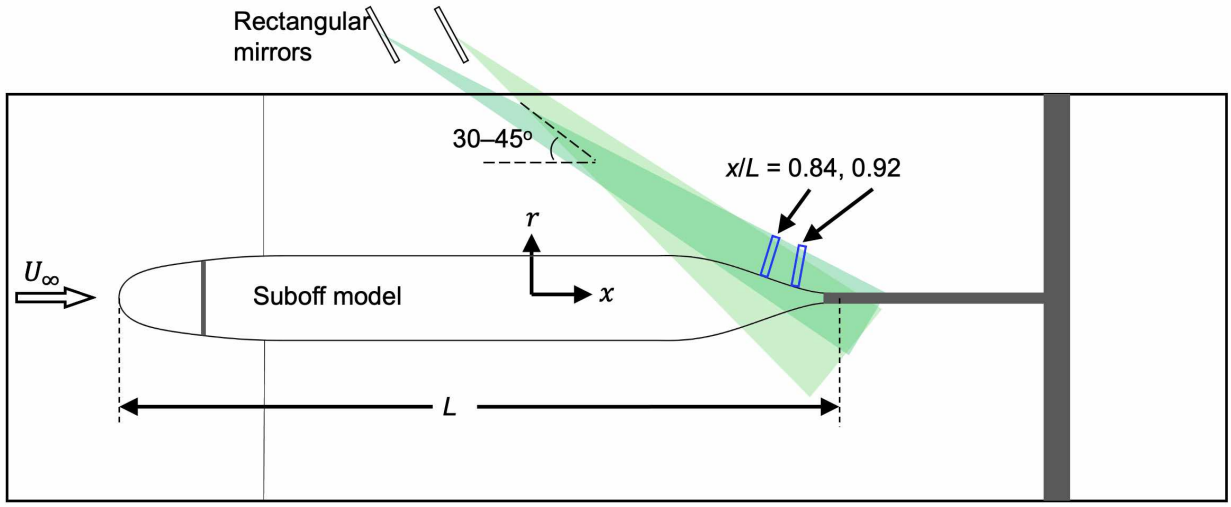

(a) Configuration 1.

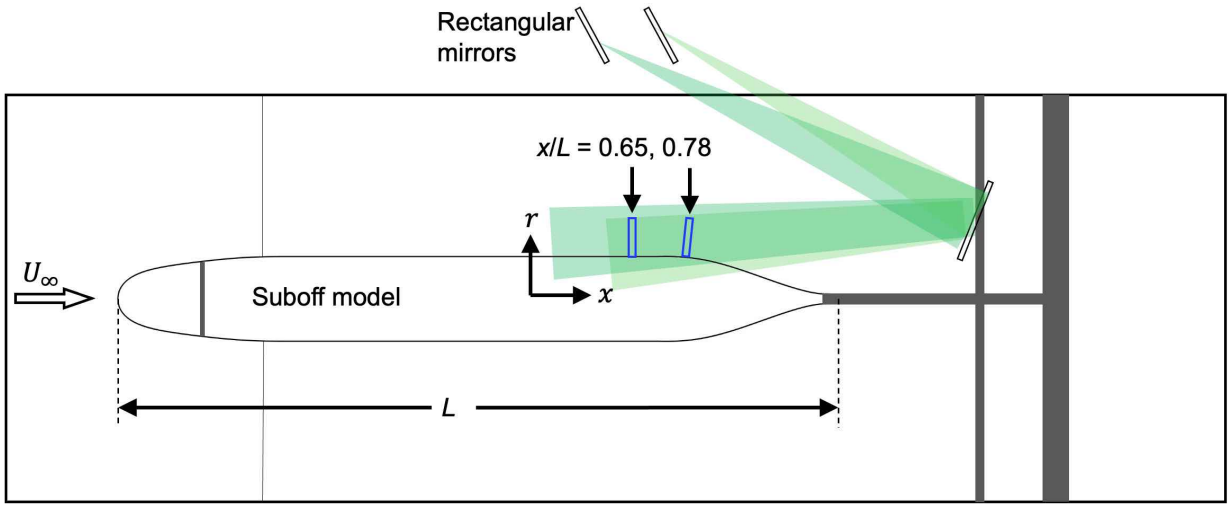

(b) Configuration 2 with a mirror installed in the test section.

Figure 2.17 Two configurations used during high sampling rate PIV.

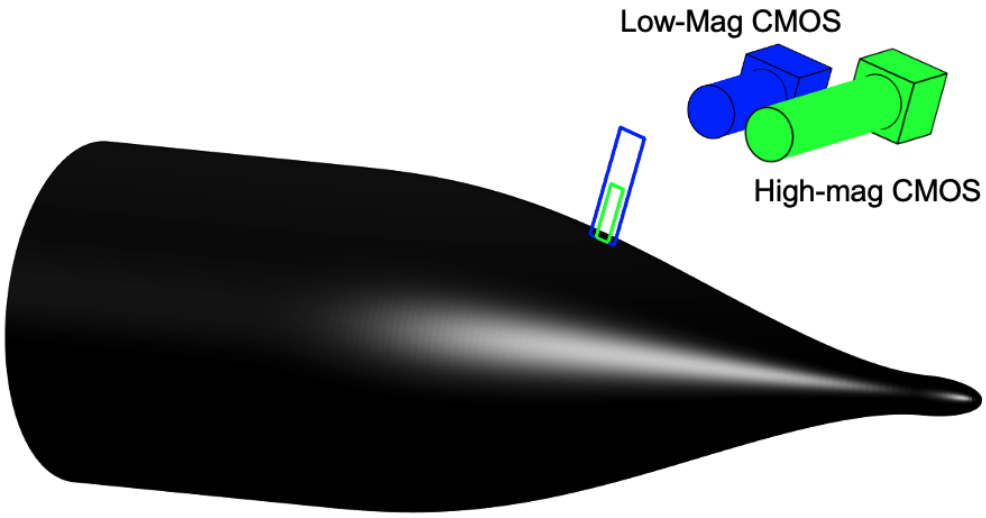

Figure 2.18 Cameras imaging wall-normal FOVs. The high-mag camera is shown in green and the low-mag in blue.

cameras was less than 10°, and because the FOV was relatively narrow. Indeed, a thin strip of roughly 125 px × 1000 px was necessary to obtain the desired sampling rate. The pixel resolutions of the cameras were 45 and 14 $\mu m\,px^{-1}$, respectively.

This measurement used two dual-head, 30 mJ/pulse (at 1 kHz), Nd:YLF lasers. Each laser pulse had a maximum frequency of 10 kHz. These two lasers were interlaced to obtain the desired sampling rate of 16 kHz. The timing diagram in Fig. 2.19 shows the lasers operated alternately. Frame straddling, i.e., correlating the second frame of the one image pair with the first frame of the following image pair, was not used because the flow speed was too high relative to the sample rate. (Although it could be feasible near the wall where the velocities are lower.) Each 1 mm thick laser sheet was formed by passing the beam through mirrors, a collimator, and a cylindrical lens (with 50 mm and 100 mm focal lengths). The two laser sheets were offset by no more than 1 px, as seen in the laser reflection imaged by the high-magnification camera.

The challenge in this setup was balancing the light intensity above the FOV and the light intensity striking the surface. This task was more challenging than simply reducing the laser surface reflection because the high laser repetition led to rapid heat build-up in the carbon

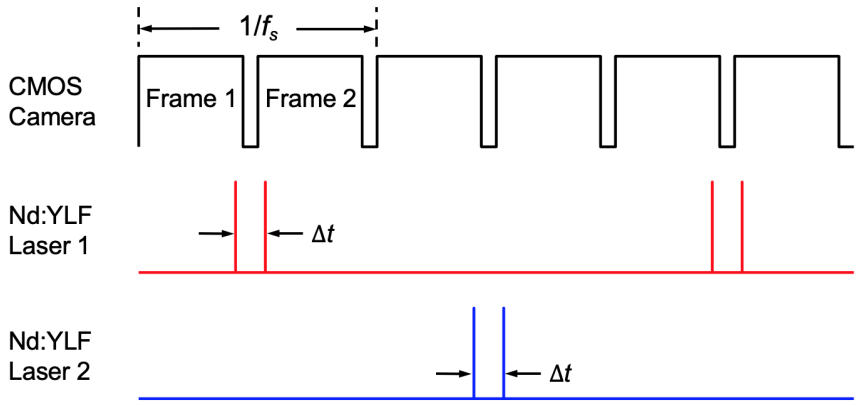

Figure 2.19 Synchronization of camera and lasers.

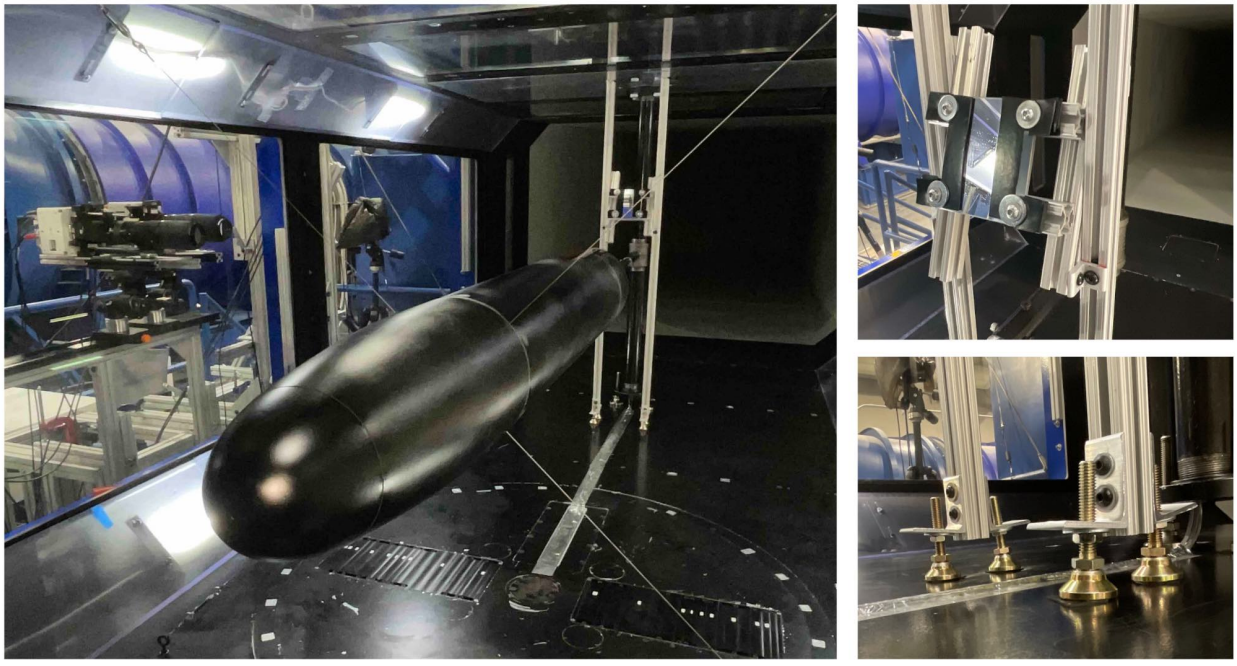

Figure 2.20 A mirror assembly was bolted to the ceiling and compression was applied with leveling feet on the floor.

fiber wall. Temperatures exceeding 200°C (400°F) as measured by an infrared thermometer scorched the smooth surface and created roughness. The solution was again to introduce the laser sheets at shallow angles, as shown in Fig. 2.17, and to apply a protective ceramic clear coat that required a few days to harden before use. This approach reduced the heat build-up and the light scattered toward the camera. The disadvantage of this laser configuration was some light intensity loss because of the increased distance between the laser source and the

region of interest (ROI), leading to greater laser sheet divergence, more light scattered by seed particles, and some losses because of additional mirrors. The reduced light intensity was also attributed to the significant drop-off in the laser pulse intensity as the repetition frequency was increased beyond 1 kHz. Further losses were incurred by the high camera magnification of $M = 0.73$. Nonetheless, using a mirror behind the model was determined to be the best way to reduce the laser reflection and illuminate the FOV.

Data was acquired at flow speeds of $U_\infty = 50$ ft s^{-1} and 200 ft s^{-1} across four streamwise stations of $x/L = 0.65$, 0,78, 0,85, and 0.92. At each station and flow speed, three datasets were acquired at a rate of $f_s = 16$ kHz for $T_s = 10$ s, and one dataset was measured at a rate of $f_s = 3$ kHz for $T_s = 60$ s. These sampling durations provided more than 10,000 eddy turnovers (δ/U_∞). This data was time-resolved for $x/L \geq 0.85$ at the lower Re according to the criterion of $f_c > u_\tau^2/(3\nu)$ [184] but was not otherwise. The straddling times between image pairs were $\Delta t = 15$ µs and $\Delta t = 4$ µs for free-streams of $U_\infty = 50$ ft s^{-1} and 200 ft s^{-1}, respectively, leading to maximum pixel displacements of 6 px and 17 px in the low- and high-magnification cameras. The camera fields of view in this setup were normal to the local wall, a natural reference frame for studying the boundary layer.

The measurements were processed in Davis 10.2 using an approach identical to the one described in Section 2.4.1. Background subtraction and 3×3 smoothing were performed before the multi-pass vector calculations with adaptive weighting. The final window was 32×32 px^2 with 50% overlap for both cameras. In wall units, the high-magnification camera's final interrogation window was, respectively, 22 and $74l_\nu$ for the two flow speeds at the most upstream location, and 7.4 and $25l_\nu$ at the most downstream x/L station. The low-magnification camera's resolution was roughly one-third that of the high-magnification camera.

2.4.3 Dual-Plane PIV

An orthogonal dual-plane PIV method [186] was implemented to obtain a three-dimensional perspective of this boundary layer. Figure 2.21 shows the experimental setup to comprise a streamwise plane (shown in blue) parallel to the free stream and a spanwise plane (red) per-

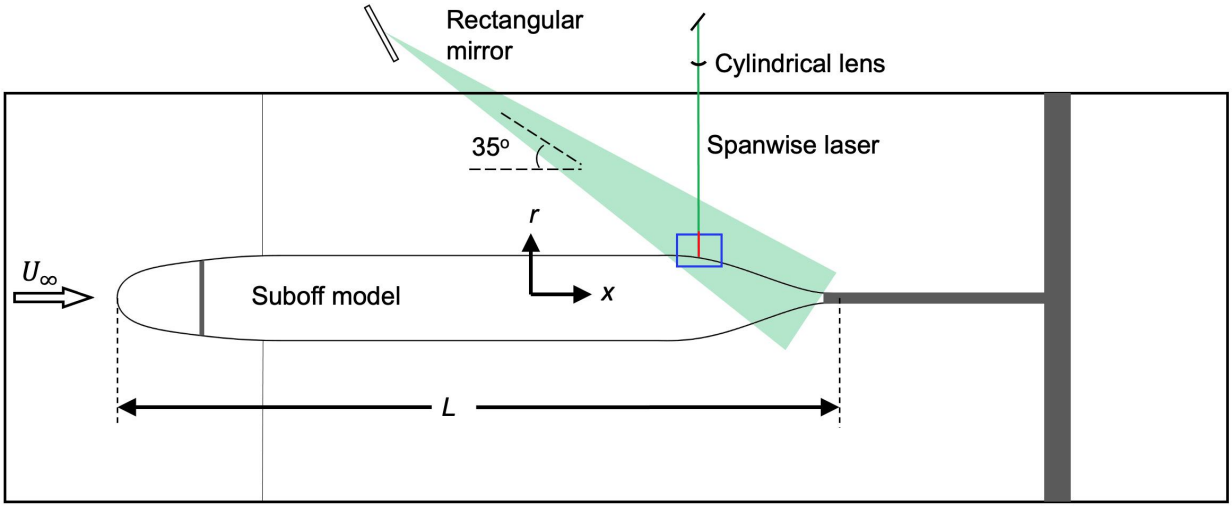

Figure 2.21 Test section set up for the dual-plane PIV comprising two mutually orthogonal planes.

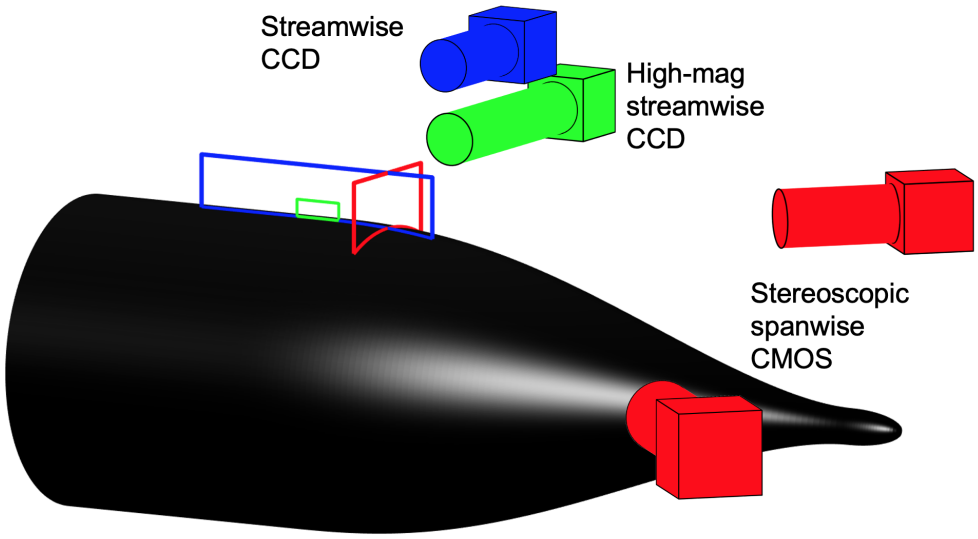

Figure 2.22 Cameras and corresponding fields of view for the dual-plane PIV measurements.

Figure 2.23 Streamwise cameras in the dual-plane PIV setup.

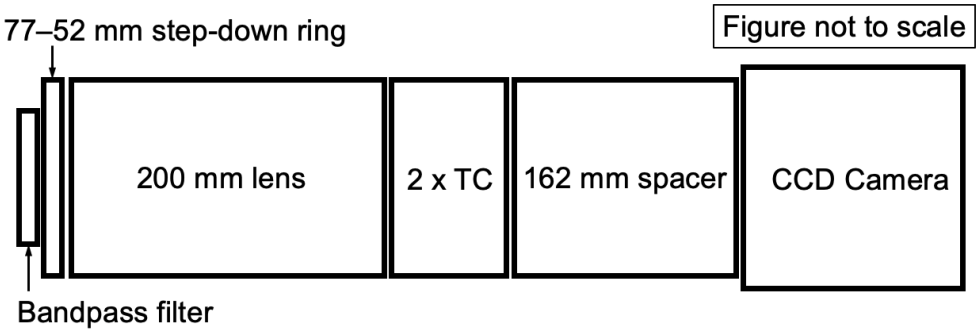

Figure 2.24 Various components of the high-magnification camera.

pendicular to the free stream. To reduce surface reflection, the streamwise laser was directed downstream at roughly 35°. The spanwise plane was oriented vertically, parallel to the radial r axis. The details of this approach are as follows.

Figure 2.22 shows the four camera configurations employed in this dual-plane PIV setup. Two four-megapixel CMOS cameras (shown in red in Fig. 2.22) were positioned in a stereoscopic arrangement ($\sim 45°$) to measure all three velocity components in the spanwise plane. Each camera was fitted with a 200 mm microlens (f/4), a Scheimpflug adapter, a 62–52 mm step-down ring, and a 52 mm diameter bandpass filter. One of the cameras, placed further away from the measurement plane, additionally used a 20 mm spacer to obtain the same magnification. Because of the oblique positions of the cameras, a Scheimpflug adapter was necessary to tilt the camera's plane of focus. The bandpass filter (527±5 nm) removed any laser reflection shifted to longer wavelengths by the rhodamine coating as discussed in Appendix B. The camera resolution was approximately 66 µm px^{-1} because the emphasis was on the spanwise geometry of the large scales. The pixel pitch of the CMOS camera was 10 µm, giving a magnification of $M = 0.15$.

Two cameras with different magnifications were used to interrogate the streamwise plane, as shown in Fig. 2.23, allowing the measurement of both the smallest and largest scales. The normal-magnification streamwise camera (blue in Fig. 2.22) used a 50 mm spacer, a 200 mm lens, and similarly a band-pass filter (532±5 nm). This camera had a pixel solution of 22 µm px^{-1}. The pixel pitch was 5.5 µm, leading to a magnification of $M = 0.25$.

The high-magnification streamwise plane camera is described schematically in Fig. 2.24. In this figure, From left to right, the light passed through a filter (532±5 nm), a 200 mm (f/2.8) microlens, a 2× teleconverter (TC), and 162 mm of spacer before arriving at the camera sensor. This arrangement of optics led to a magnification of $M = 1$ and a pixel resolution of 5.7 µm px^{-1}. This resolution was sufficient to interrogate the viscous sublayer at least in the lower Re case (l_ν = 20–60 µm). Particle tracking velocimetry would enable measurements closer to the wall.

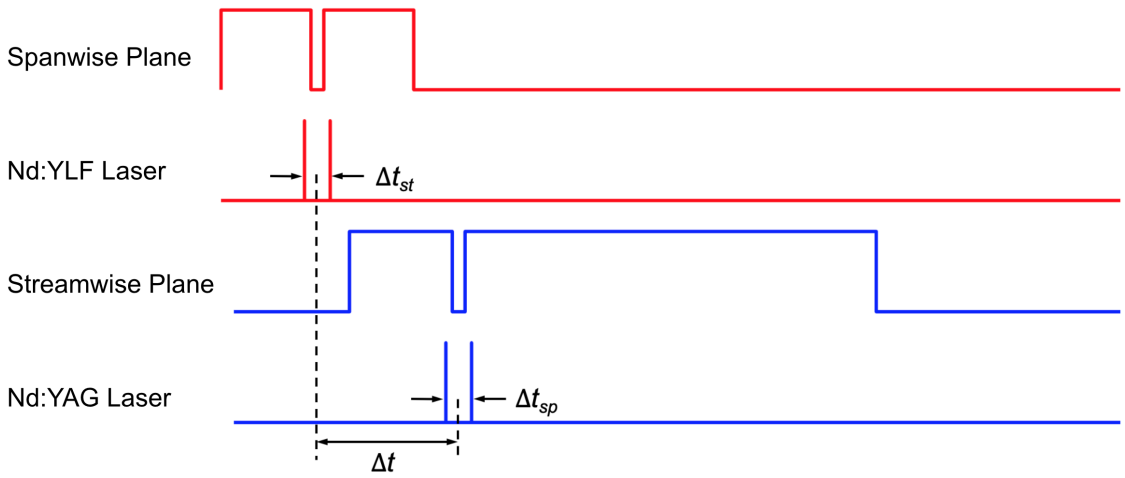

Figure 2.25 Timing diagram of the dual-plane PIV setup. Timing offset was used between the spanwise plane (shown in red) and the streamwise plane (blue) to eliminate optical interference.

Two types of lasers were used in this dual-plane setup, as shown in Fig. 2.21. The spanwise plane was illuminated with a 527 nm, 30 mJ/pulse (at 1 kHz), Nd:YLF laser. This laser was directed through a collimator and formed into a sheet by a 50 mm cylindrical lens. The spanwise laser sheet was measured to be 2–3 mm on the model surface. The increased laser sheet thickness better captured the out-of-plane displacement. The streamwise plane used the 380 mJ/pulse Evergreen Nd:YAG laser. This laser was formed into a 1 mm sheet by a cylindrical lens with a 50 mm focal length. The full power of the YAG laser was not used, as a further increase in laser intensity only increased the surface reflection without improving the vector quality.

One challenge in using a dual-plane PIV approach is the cross-talk between the two systems, namely that the camera exposure captures the particles illuminated in both planes. Historically, this issue is addressed in one of two ways. The first is to use two laser sheets of opposite polarization with polarizing filters fitted on the camera lens [187–192]. The second is to use two lasers of different wavelengths with short- and long-pass filters [193]. The current method of distinguishing between the two planes relies on a timing offset [118].

To this end, the high-speed CMOS cameras (with low minimum camera exposure time)

measured the spanwise plane first, followed by the two CCD cameras that sampled the streamwise plane. A similar timing offset scheme was used previously by Zhu et al. [194], and the current one was slightly modified as shown in Fig. 2.25. In this figure, the spanwise and streamwise planes are denoted using the red and blue colors, respectively; the high-magnification streamwise plane employed the same timing as the normal-magnification (blue) streamwise plane. The spanwise plane cameras were exposed first, followed by the streamwise plane cameras. Note that there was an overlap between the camera exposures of the two systems to minimize the timing offset Δt. This offset Δt was varied between different spanwise planes, depending on the minimum exposure time of the CMOS cameras, which changed with camera resolution, i.e., how many pixels were used.

A total of 3,000 image pairs were acquired at each of the four streamwise stations using a free-stream velocity of $U_\infty = 50$ ft s^{-1}. The streamwise locations of the spanwise planes were $x/L = 0.71$, 0.785, 0.85, and 0.92. The respective streamwise planes were roughly centered about these spanwise planes. The straddling time of the streamwise plane was 25 µs, and that of the spanwise plane was 30 µs. Because the spanwise plane had a lower pixel resolution, a larger straddling time was required to maintain good pixel displacement and low measurement uncertainty.

The acquired images were processed following the procedure described in Section 2.4.1. Background subtraction, 3×3 smoothing, and perspective correction were performed before the vector calculation. The final interrogation window was 16×16 px^2 with an adaptive window. The spanwise planes also used a final window of 16×16 px^2 with 50% overlap, except spanwise Plane 4, which used 24×24 px^2.

The streamwise normal-magnification camera had the same resolution as those used in the large-FOV setup in Section 2.4.1. The streamwise high-magnification camera was zoomed in four times as much as its regular magnification counterpart. The resolution of the spanwise planes was lower compared to the streamwise plane. In wall units, the spatial resolutions were $60l_\nu$ and $29l_\nu$ at the most upstream and downstream spanwise planes for $U_\infty = 50$ ft s^{-1}.

With a free-stream of $U_\infty = 200$ ft s^{-1}, the resolutions were decreased to $170l_\nu$ and $90l_\nu$. These measurement planes offered valuable insights into the spanwise signature of the large scales.

Unfortunately, the spanwise plane data in the dual-plane setup suffered from some image calibration issues and were considered unusable. The initial motivation was to customize calibration plates that conform to the model curvature. The problem, however, was the inconsistent offset distance between the two levels. Because of time constraints, the spanwise plane measurements were repeated at both $U_\infty = 50$ ft s^{-1} and 200 ft s^{-1} without the streamwise plane. The spanwise plane measurement setup and the data processing followed the abovementioned procedure. The streamwise planes at the two magnification levels were still usable.

2.4.4 Calibration

A calibration plate was fabricated to span the entire Suboff afterbody. This custom plate was necessary because the standard rectangular plate cannot follow the model geometry, implying that some near-wall points may not have the proper calibration. To this end, a medium-density fiber (MDF) board was first milled to have the model's negative. Then, the MDF was sealed with polyurethane and spray-painted white in thin, uniform layers. When the paint dried, shallow holes were laser rastered to be precisely 2 mm in diameter and spaced 6 mm apart. The resulting array of dark dots gave good contrast against the white board.

The calibration plate was mounted on the model, as shown in Fig. 2.26. The plate was centered about the model by precise laser cutouts. Further, the spring-loaded wingnuts on the back provided fine adjustments and stability, as shown in Fig. 2.26(b). Calibration plates were also attempted for the spanwise planes by milling out two different levels and following the same procedure. However, these calibration plates were not quite precise enough. In the future, more precise two-level calibration plates will be necessary.

(a)

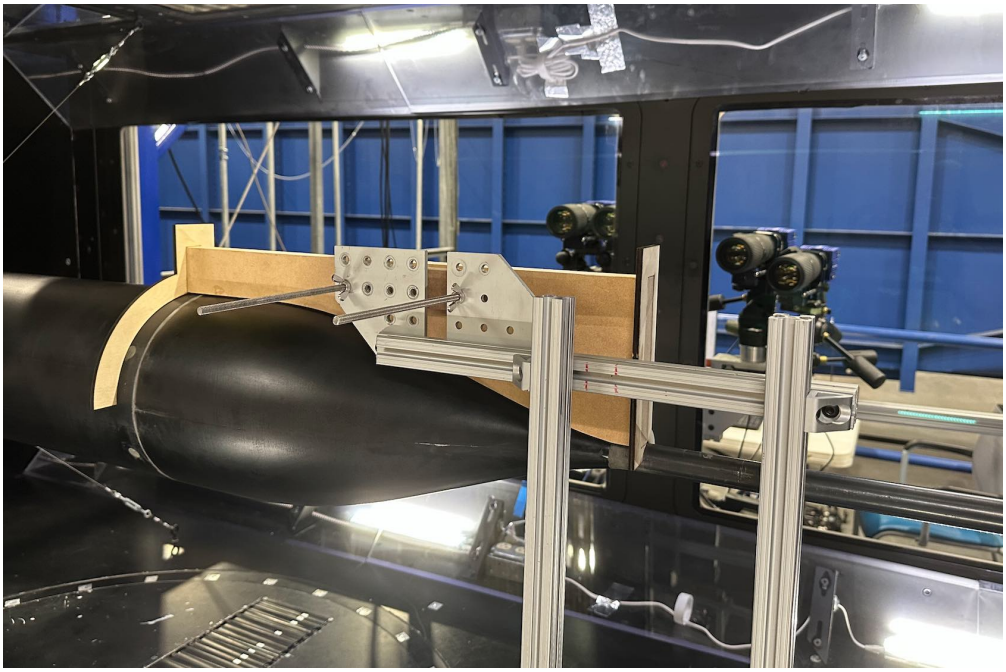

(b)

Figure 2.26 (a) Front and *(b)* back views of the manufactured calibration plate.

Figure 2.27 Close-up of the model surface treated with an in-house rhodamine solution and ceramic clear coats.

2.4.5 Surface Treatment for Near-Wall PIV

The major challenge that hinders near-wall PIV measurements is laser surface reflections. However, measuring close to the wall is critical as it is where many interesting activities occur for wall-bounded flows. The common solution is to use a glass floor and introduce the laser from below the glass. This approach was infeasible for a model with complex surface curvature. Significant effort was devoted to addressing this challenge, and some success was achieved, as summarized below. A detailed account can be found in Appendix B.

To lower the laser reflection intensity, the model surface was treated with an in-house rhodamine WT (Milliken Keyacid Rhodamine WT) mixture and a ceramic clear coat (Rust-Oleum High Heat Protective Enamel). Rhodamine WT is a fluorescent dye that absorbs green light and emits a longer wavelength (Stoke's shift), which can be removed with bandpass filters on the camera lenses. The rhodamine mixture was applied with an airbrush. The gloss clear coat was applied on top of the rhodamine and behaved like a mirror, reflecting light away from the camera instead of scattering light toward the camera the way a matte

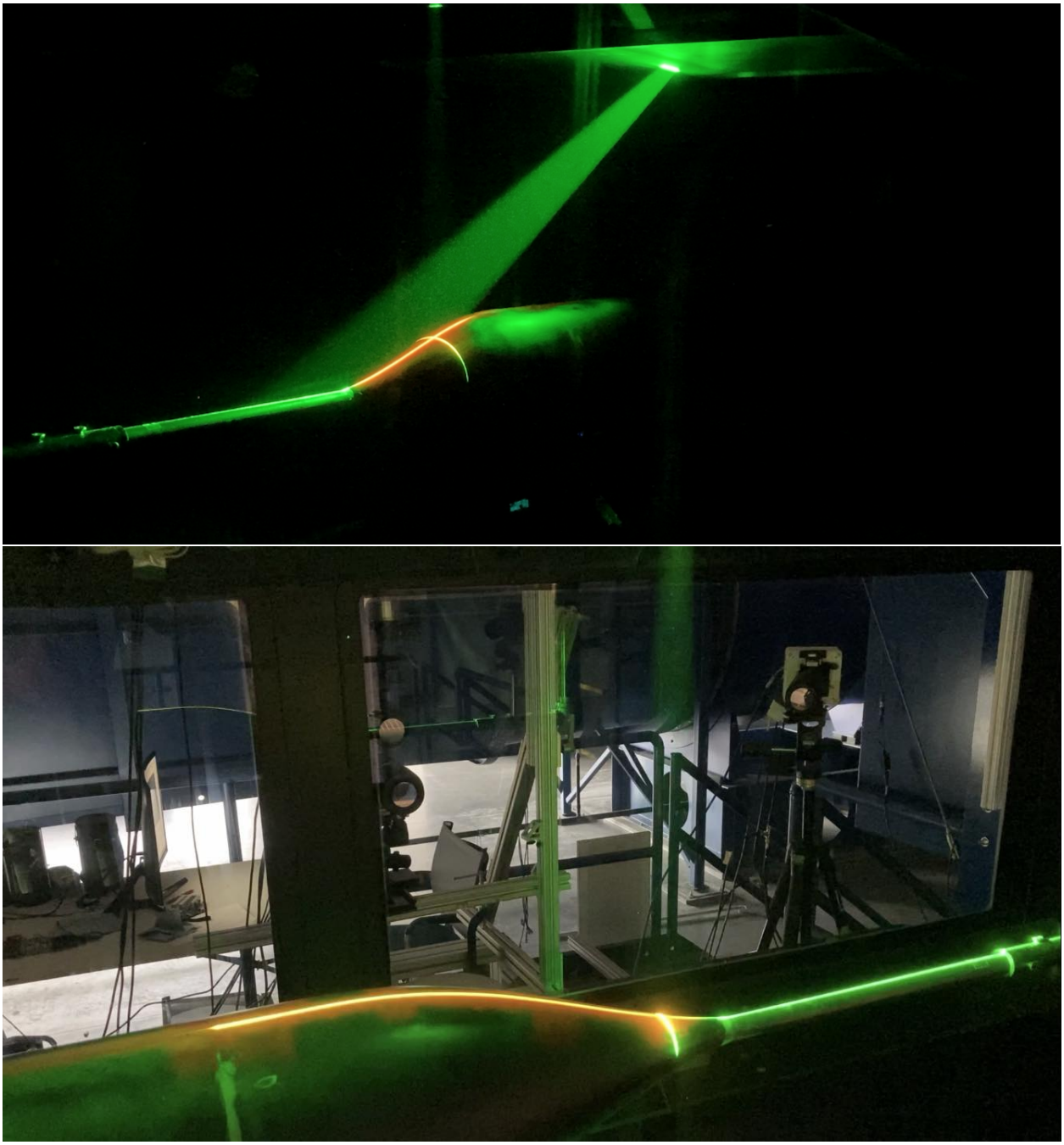

Figure 2.28 The model surface glowed orange when illuminated by green Nd:YAG (532 nm) and Nd:YLF (527 nm) lasers as a result of the rhodamine Stoke's shift.

finish would function. Even fingerprints degraded the gloss finish, so the model surface was cleaned before each run. Also, the laser orientation is crucial. Introducing the laser sheet at a shallow angle relative to the surface showed significant improvement relative to positioning the laser directly above the measurement domain [195]. The combination of these three methods significantly attenuated the laser reflection.

An image of the model surface treated with the rhodamine solution and the ceramic clear coat is shown in Fig. 2.27. Figure 2.28 shows the dual-plane PIV in operation, where the streamwise laser was introduced at a shallow angle to reduce laser scatter toward the camera. The surface glowed orange because the green (532 nm and 527 nm) lasers were red-shifted by the rhodamine. Notice that the lasers appeared simultaneous because the image was acquired with a relatively long exposure.

The effectiveness of this approach can be observed in Fig. 3.15. These figures scaled with viscous units show that the lowest data point measured with reasonable confidence was roughly 0.5 mm above the wall for the large-FOV configuration (described in Section 2.4.1).

2.4.6 Data Post-Processing

After the flow vectors were computed in DaVis, post-processing of the data was necessary. First, the wall location was determined by performing vibration correction and fitting a polynomial through the estimated wall positions. Then, image stitching was performed to ensure smooth transitions between adjacent fields of view. The wall locations were subsequently used to transform the stitched vector fields from a cylindrical into a wall-normal–wall-parallel coordinate system. This transformation was done to facilitate comparisons with existing flat plate boundary layers, so that the combined effect of pressure gradient and surface curvature could be better assessed.

2.4.6.1 Wall Location and Vibration Correction

Estimating the wall location is necessary for computing the boundary layer thickness, momentum thickness, and other information about the flow. The significant departure from equilibrium implied that the commonly used composite fits were unsuitable. The challenge in

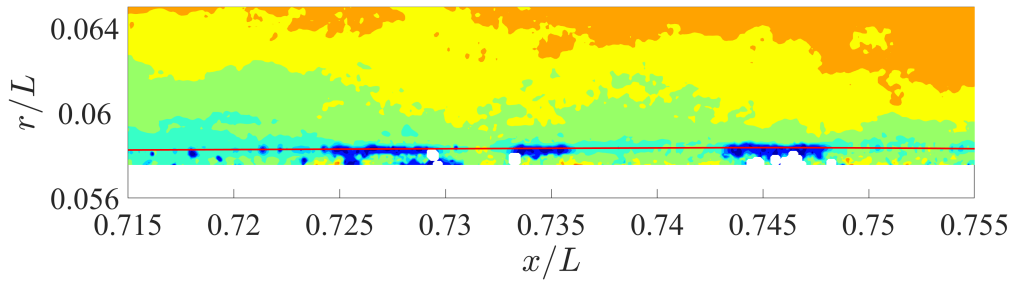

(a) Position 1

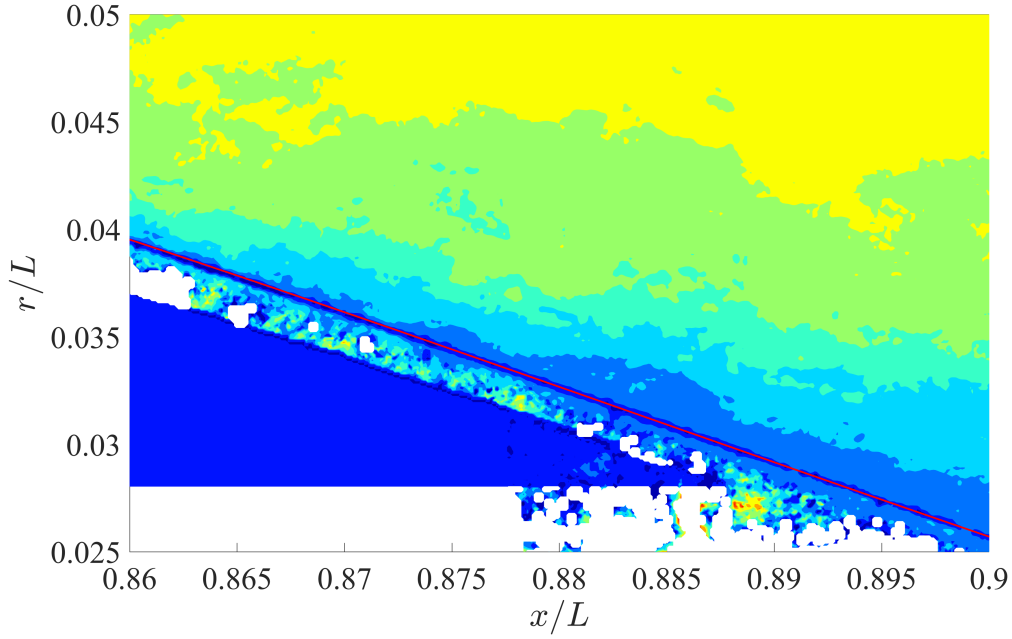

(b) Position 2

Figure 2.29 Zoomed-in views at two x/L regions showing that the fitted wall was a reasonable estimate.

determining the wall position directly from PIV images is that the laser reflection saturates the near-wall pixels, obscuring the precise location of the wall. To expound on this point, suppose 20 pixels were saturated and the camera resolution used for the large-FOV setup in Section 2.4.1 was 22 $\mu m\,px^{-1}$, there would be a 0.4 mm or 18 wall unit (at 50 $ft\,s^{-1}$) band where the wall could be located. A more precise method of determining the wall location was necessary. To this end, the wall reflection was used in the current work following De Silva et al. [118], which was possible as a result of the glossy, mirror-like finish of the model surface. The accuracy of the wall location was described by De Silva et al. [118] as one wall unit.

For the large-FOV PIV outlined in Section 2.4.1, the wall was determined as follows.

First, given the vector fields, the MatLab "fminsearch" optimization function [196] was used to minimize the difference between the upstream and downstream FOVs in each overlap region by applying relative translations. Then, a few vectors above and below the wall were identified at each streamwise position, assuming that the wall-parallel velocities should nearly mirror one another. A parabola was then fit to these identified vectors, and the minimum of this parabola was used as the estimated wall location. If the symmetry condition was not met, then the wall was not calculated at this streamwise location. The estimated wall positions across all FOVs were collectively shifted to best match the prescribed geometry of the Suboff. This process was repeated for each snapshot of the flow field.

Ten snapshots were then used to fit a polynomial through the estimated wall positions. The fitted wall position is shown using a red line in Fig. 2.29 overlaying a representative axial velocity u_x snapshot. Two zoomed-in perspectives are provided, showing that above and below the wall, there was visible symmetry in the axial velocity u_x. Notice that these were not final snapshots used in the subsequent data analysis. Data below the wall were discarded, along with those above the wall that were above an uncertainty threshold. This fitted polynomial line agreed with the Suboff geometry to the previously quoted tolerance of 0.015 in.

This approach also accounted for individual camera vibrations, which became noticeable at the higher flow speed of 200 $\mathrm{ft\,s^{-1}}$. The reason for not using the vibration correction in DaVis 10.2, which relies on recurring patterns (e.g., laser reflection, screws) in the raw images, was the occurrence of non-physical results, e.g., much larger than expected free-stream velocities. This outcome may have resulted from a lack of clear patterns for the DaVis routine to latch onto.

The above process of shifting the four FOVs was repeated for the $U_\infty = 50$ $\mathrm{ft\,s^{-1}}$ measurements. The relative shift between adjacent cameras was, on average, less than 10 µm, corresponding to $0.5l_\nu$ in the FPG region and $0.2l_\nu$ in the APG region. The minute shift in the low-speed data confirmed the small vibration levels and validated the procedure's

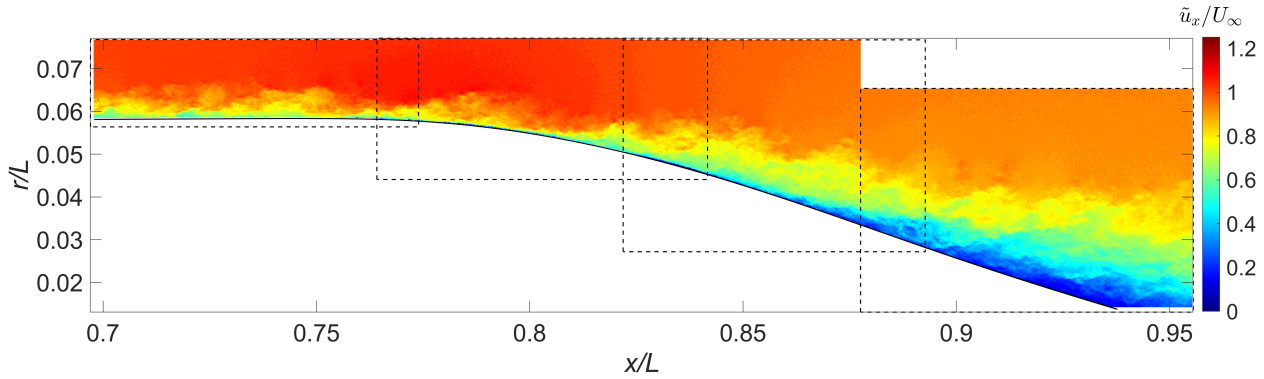

(a) Axial velocity $\tilde{u}_x/U_\infty$

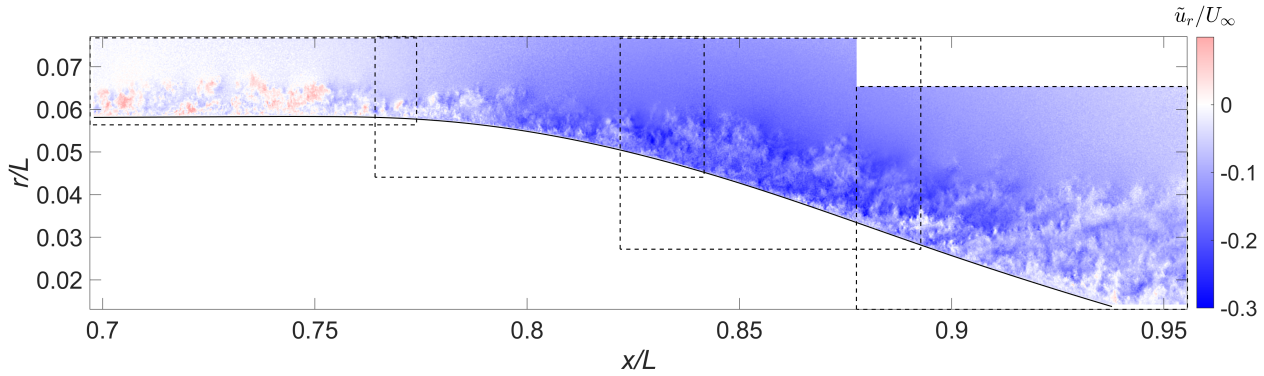

(b) Radial velocity $\tilde{u}_r/U_\infty$

Figure 2.30 Instantaneous snapshot of the velocity field normalized by the free stream shows smooth transitions between adjacent FOVs.

accuracy.

The wall was estimated similarly for the spanwise plane. The wall location was calculated in each column by fitting a quadratic function to the points about which the axial velocity u_x was symmetric. The wall estimates across all columns were then fit to a circle whose radius was determined by the axial location of the spanwise plane. The wall was identified in the high-frequency dataset using particle reflections.

2.4.6.2 Image Stitching

For the large-FOV PIV setup, a unique velocity was computed for each spatial position in the overlap regions of adjacent FOVs. A linear weighting function was implemented to ensure a smooth transition between the adjacent FOVs. In other words, locations closer to the upstream FOV in the overlapping region weighted the upstream camera measurement

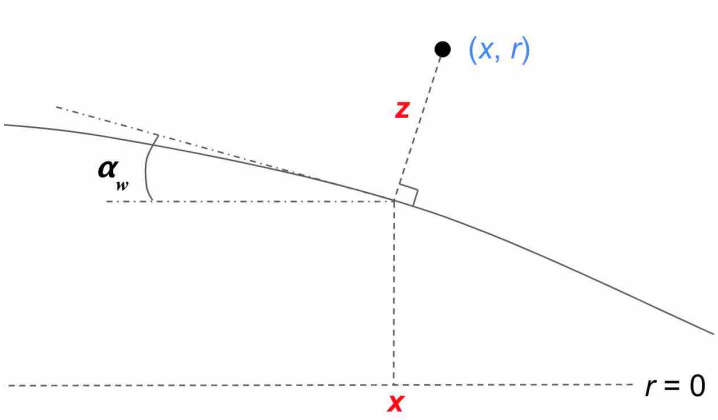

Figure 2.31 Explanation of the coordinate transformation. Not to scale.

more heavily than the downstream camera measurement, and vice versa. The outcome of this approach is shown in Fig. 2.30, where the representative snapshot shows both axial and radial flow velocities transitioned smoothly between adjacent FOVs. The solid black line is the estimated wall position. The boxes drawn with the dashed line indicate the original FOVs, highlighting the camera overlaps.

2.4.6.3 Coordinate Transformation

Many types of boundary layers experience pressure gradients because of surface curvature, such as along the hull of a ship or the fuselage of an aircraft. This motivates the current effort to study the combined effects of pressure gradient and surface curvature. A coordinate transformation was used to reshape the cylindrical coordinates into a flat-plate equivalent to facilitate comparisons between the Suboff boundary layer and the numerous existing results for boundary layers developing on flat plates. Also, the wall-tangent–wall-normal frame was considered a natural coordinate for analyzing the boundary layer.

For the streamwise plane, the coordinate was transformed from a cylindrical x–r frame into a wall-normal–wall-parallel x–z frame. Figure 2.31 overviews this mapping. Each x–r location (shown in blue) was transformed based on where it was perpendicular to the estimated wall. This x location of the nearest point on the wall, and the length z of the perpendicular line were used to define the new coordinate system. This approach was identical to the one

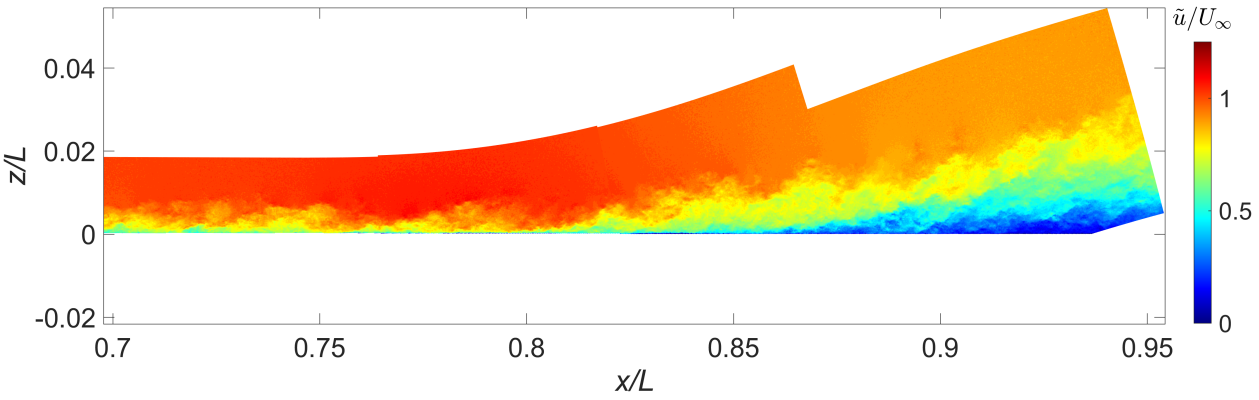

(a) Wall-parallel velocity $\tilde{u}/U_\infty$

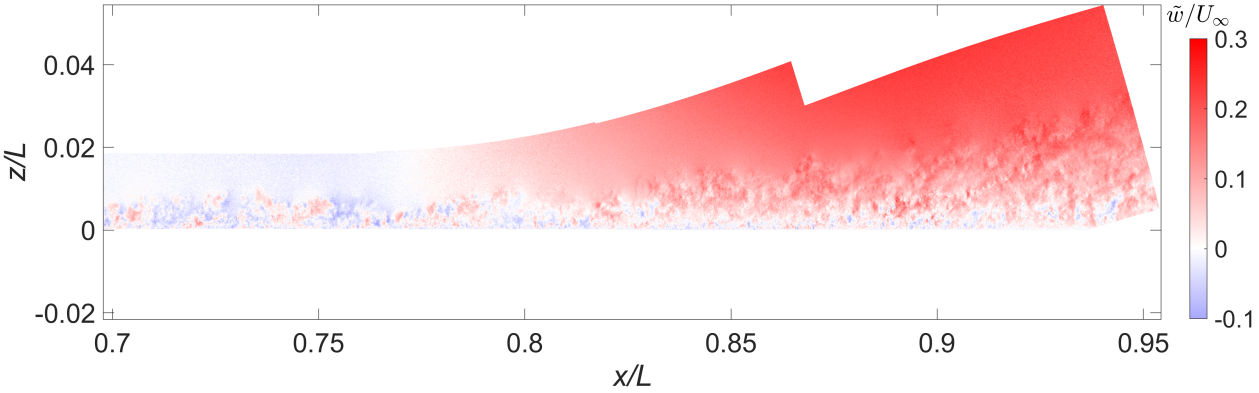

(b) Wall-normal velocity $\tilde{w}/U_\infty$

Figure 2.32 Instantaneous snapshot of the velocity field normalized by the free-stream in the transformed wall-parallel–wall-normal coordinate.

used by Patel et al. [109].

The outcome of this transformation is shown in Fig. 2.32 for both components of velocity, which have been rotated at each grid point based on the corresponding wall angle α_w,

$$\begin{aligned} \tilde{u} &= \tilde{u}_x \cos(\alpha_w) - \tilde{u}_r \sin(\alpha_w) \\ \tilde{w} &= \tilde{u}_x \sin(\alpha_w) + \tilde{u}_r \cos(\alpha_w) \end{aligned} \tag{2.1}$$

In this equation, $\tilde{u}$ and $\tilde{w}$ represent the wall-parallel and wall-normal velocities. Observing the potential flow region in Fig. 2.32(a), the wall-parallel flow accelerates through the favorable pressure gradient (FPG), and decelerates through the adverse pressure gradient (APG). Correspondingly, the wall-normal velocity $\tilde{w}$ in Fig. 2.32(b) was nearly zero at the inlet, slightly negative in the FPG region, and increased significantly to 25% of the free-stream

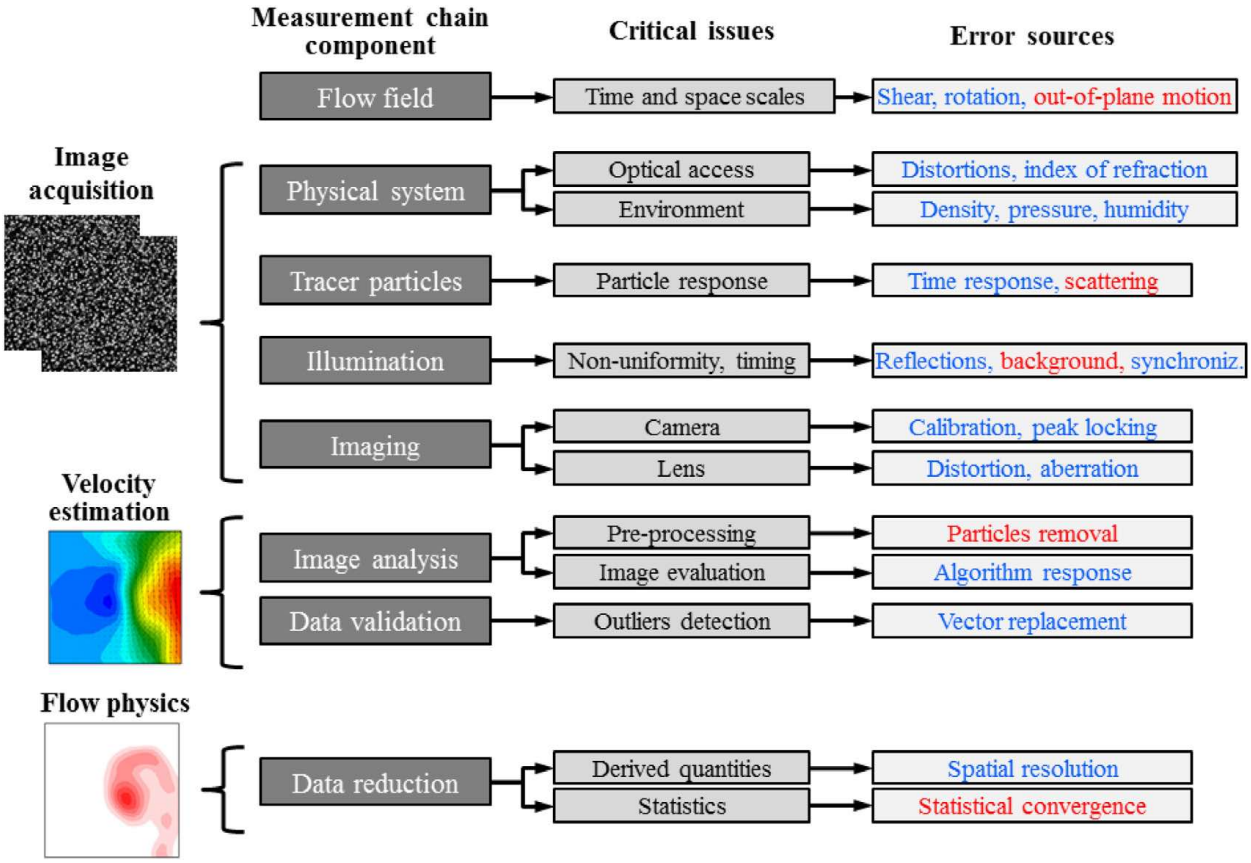

Figure 2.33 Overview of error sources in PIV from Sciacchitano [38] and Wieneke [39]

velocity in the APG region. These trends were similar, at least qualitatively, to flat-plate pressure-gradient boundary layers. This coordinate transformation did not indicate that longitudinal streamline curvatures were unimportant—it has been the topic of many detailed investigations [197–200]—rather, it provides a rational basis for comparisons with planar boundary layers.

2.4.7 Uncertainty

Numerous factors affect PIV measurement uncertainty, which is essential to know because it helps the analyst determine whether trends in the data are related to the physics of the flow. The figure commonly quoted for PIV uncertainty is 0.1 px, based on the accuracy of the sub-pixel Gaussian or polynomial fit [201]. However, this is a very ambitious, perhaps unachievable goal, and in actual experiments, the uncertainty is typically higher depending on several factors. Figure 2.33 from Sciacchitano [38] and Wieneke [39] overviews the prominent

factors that affect measurement uncertainty. The discussion below elucidates relevant error sources and measures to mitigate these errors. Lastly, uncertainty levels for the PIV are reported.

During image acquisition, straddling time compromises between dynamic velocity range (DVR) and appropriately resolving spatial gradients and out-of-plane motion. Small pixel displacements decrease the DVR; large displacements increase the number of unmatched particles when correlating the two frames. In this work, the free-stream particle displacement was roughly 15 px.

The tracer or seed particles used in this work were 0.2–0.3 µm in diameter according to the calibration provided by the manufacturer. The Stokes number, the ratio of the particle response time to the flow's characteristic time scale, is commonly used to determine whether the tracer will faithfully follow the flow [201]. The particle response time is $\tau_p = (\rho_p d^2)/(18\nu\rho_f)$, derived by Stokes for a sphere in a creeping flow. In this equation, ρ_p is the particle density, d is the tracer diameter, and ρ_f is the ambient fluid density. The time scale of the large eddies is $\tau_c \sim \delta/U_c$, where U_c is the convection speed, and the viscous time scale is $\tau_c \sim \nu/u_\tau^2$. The Stokes numbers were then calculated to be $\tau_p/\tau_c \sim \mathcal{O}(10^{-7})$ for the large scales and $\mathcal{O}(10^{-4})$ for the small scales. Also, the flow velocity in this work was well above 1 $\mathrm{mm\,s^{-1}}$ where Brownian motion [202] occurs.

Care was taken to minimize laser reflection off of the wall, as discussed in Appendix B, but the residual reflection remained significant enough to raise the near wall measurement uncertainty. Points where the average uncertainty, obtained by the method of Wieneke [203], was higher than $0.05U_\infty$ were omitted. Further, any near-wall points showing anomalous statistics were also removed.

Synchronization of the cameras and lasers can also introduce some uncertainty. Electronic signals are generated with a high accuracy of roughly 1 ns [39] and are not a concern. However, according to Bardet et al. [204], the time delay between the trigger and the laser output can be up to 50 ns and 1.5 µs for the Nd:YAG and dual-cavity Nd:YLF lasers in this work

[38]. The YLF laser introduces a potentially significant bias error that could be corrected by measuring the laser output with a photo-diode. However, this correction was not made in the current measurements.

Calibration plates were either manufactured by LaVision or were made in-house. The plate was positioned to bisect the laser sheet, ensuring good calibration. Further, self-calibration was performed in stereoscopic PIV to improve the alignment. Regarding the two-component PIV, good calibration was evident in the smooth transitions between adjacent fields of view.

Peak locking introduces a bias in pixel displacements toward integer values [180, 205, 206]. This bias occurs when the particle image diameter is less than or around 1 px. Michaelis et al. [206] studied the effects of particle image diameter, interrogation window size and deformation, interpolation techniques, etc., using a synthetic flow field. These works recommended a particle image size of at least 2 px for good results. Therefore, a 3-by-3 smoothing was applied to increase the particle image diameter to 2 px without significantly affecting spatial resolution [180]; additional smoothing would elevate the random error [38]. The sub-pixel displacement histogram showed no bias.

Regarding image analysis, the background subtraction approach used the average of all images. The cross-correlation was performed using the multi-pass scheme in DaVis 10.2 with window deformation. The universal outlier detection [181] was applied after each pass, removing vectors with residuals greater than 2. Vectors computed with peak ratios of less than 1.5 were also deleted.

Much of the analysis in this work relied on first and second-order statistics. Random and bias errors are respectively associated with a finite number of snapshots and unresolved scales. Sciacchitano and Wieneke [207] explained the random error associated with the mean and RMS scale with $N^{-1/2}$, where N is the number of uncorrelated snapshots. Therefore, a 2% random error was expected for 3,000 snapshots. It is well known that a finite-sized sensor cannot resolve the smallest scales and attenuates the RMS values [184, 208]. The

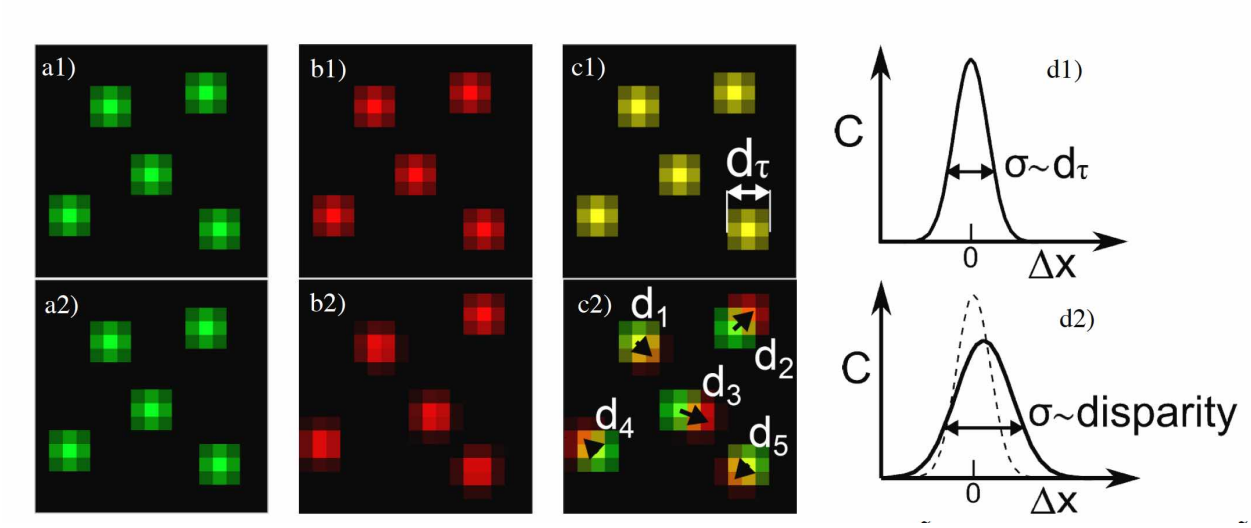

Figure 2.34 The particle disparity method works by displacing the particles based on the computed velocity, and comparing the two frames. The top row shows how an ideal matching, where there is a direct correspondence between the *(a)* green and *(b)* red particles, as shown in *(c)* and *(d)*. The bottom row shows a more realistic scenario where disparities between the two frames lead to *(d)* uncertainty in correlation peak location. Figure from Sciacchitano et al. [40].

sensor resolution in wall units for each setup was detailed in their dedicated sections. Finally, spectra were computed based on data with at least 10,000 eddy turnovers ($TU_\infty/\delta > 10{,}000$) for good convergence [184]. The sampling rate was essentially too slow to resolve the flow temporally, according to the criteria of Hutchins et al. [184] that requires a Nyquist frequency of $f_c > u_\tau^2/(3\nu)$. The large scales, however, should be well resolved.

As explained by Sciacchitano [38], the uncertainty can be quantified *a priori* or *a posteriori*, i.e., before or after the experiments. The former assesses the measurement chain to guide the experiment setup, whereas the latter computes uncertainty bounds based on the acquired data. Uncertainties in the PIV measurements were computed in DaVis 10.2, which uses the particle disparity method of Wieneke [203] and Sciacchitano et al. [40] explained in Fig. 2.34. Using this method, the average uncertainty of the large-FOV PIV setup was $0.01U_\infty$. The high-frequency strips at both magnifications had uncertainties of 0.02–$0.03U_\infty$. The spanwise plane uncertainty was also $0.03U_\infty$. The uncertainty levels for quantities involving gradients in space or time were expected to be higher [207].

2.4.8 Data Summary

The current work investigated two flow speeds of $U_\infty = 50$ ft s^{-1} and 200 ft s^{-1}. The corresponding numbers were $Re_\tau = u_\tau \delta/\nu \approx 700$ and $Re_\tau \approx 2800$, respectively. Here, u_τ is the friction velocity, δ is the boundary layer thickness, and ν is the kinematic viscosity from the recorded temperature. The momentum thickness θ increased rapidly with the APG, and the momentum-based Reynolds numbers were $Re_\theta \approx$ 1560–7700 and $Re_\theta \approx$ 5000–24000, respectively. Tables 2.1, 2.2, 2.3, and 2.4 summarize the measurements performed.

Table 2.1 reports the extensive FOV data acquired using four side-by-side cameras as described in Section 2.1. The symbol l^+ is the final interrogation window in wall units. Table 2.2 enumerates the measurements made with high-frequency cameras and lasers in Section 2.4.2, In this table, three datasets were acquired with a sampling rate of $f_s =$ 16 kHz over $T_s = 10$ s for each test condition. The temporal and spatial resolutions of the measurements, $t^+ = t_c u_\tau^2/\nu$ and l^+, were also computed; the time $t_c = 2/f_s$ is the inverse of the Nyquist frequency [184]. The total eddy turnover time TU_∞/δ was greater than 10,000 for good statistical convergence. Columns with two entries separated by commas indicate cameras with different magnifications.

The results from the dual-plane PIV setup are shown in Tables 2.3 and 2.4. Table 2.3 includes the high- and normal-magnification streamwise cameras, while the spanwise camera results were omitted because of calibration issues. The high-magnification camera was processed with a PIV/PTV algorithm in DaVis, although these results have not been analyzed. Four spanwise planes along the afterbody were measured as summarized in Table 2.4. Further details can be found in their respective dedicated sections.

U_∞ $\mathrm{m\,s^{-1}}$	x/L	Image Pairs	Window/Overlap $\mathrm{px^2}$	Pixel Resolution $\mathrm{\mu m\,s^{-1}}$	l^+	Uncertainty $\mathrm{m\,s^{-1}}$
15.24	0.70–0.95	2,373	16×16/50%	22.5	6–17	$0.01U_\infty$
60.96		2,914			17–56	

Table 2.1 Data summary for the large-FOV PIV. Details found in Section 2.4.1.

U_∞ $\mathrm{m\,s^{-1}}$	x/L	f_s kHz	T_s s	Window/Overlap $\mathrm{px^2}$	Pixel Res. $\mathrm{\mu m\,px^{-1}}$	t^+	l^+	TU_∞/δ	Uncertainty $\mathrm{m\,s^{-1}}$
15.24	0.65	16	10	32×32/50%	13.7, 40	4.2	20.6, 60.0	>10,000	$0.02U_\infty$
15.24	0.78					4.9	22.3, 65.1		
15.24	0.85					2.0	14.1 41.1		
15.24	0.92					0.6	7.6, 22.2		
60.96	0.65					46.0	68.5, 200.0		
60.96	0.78					56.8	76.1, 222.2		
60.96	0.85					23.1	48.5, 141.5		
60.96	0.92					6.1	24.9, 72.7		

Table 2.2 Data summary for the time-dependent PIV. Details found in Section 2.4.2.

U_∞ $\mathrm{m\,s^{-1}}$	x/L	Image Pairs	Window/Overlap $\mathrm{px^2}$	Pixel Res. $\mu\mathrm{m\,px^{-1}}$	l^+	Uncertainty $\mathrm{m\,s^{-1}}$
15.24	0.65	3,000			8.6, 16.9	
15.24	0.78	3,000			9.3, 18.3	
15.24	0.85	3,000			5.9, 11.6	
15.24	0.92	3,000	32×32/50%,	5.7, 22.5	3.2, 6.2	$0.01U_\infty$
60.96	0.65	1,500	16×16/50%		28.5 56.3	
60.96	0.78	1,500			31.7, 62.5	
60.96	0.85	1,500			20.2, 39.8	
60.96	0.92	1,500			10.4, 20.4	

Table 2.3 Data summary for the streamwise planes acquired with the dual-plane PIV. The spanwise plane data is omitted because it was reacquired separately as described in Table 2.4. Details found in Section 2.4.3.

U_∞ $\mathrm{m\,s^{-1}}$	x/L	Image Pairs	Window/Overlap $\mathrm{px^2}$	Pixel Res. $\mu\mathrm{m\,px^{-1}}$	l^+	Uncertainty $\mathrm{m\,s^{-1}}$
15.24	0.65		16×16/50%		49.5	
15.24	0.78		16×16/50%		53.7	
15.24	0.85		16×16/50%		33.9	
15.24	0.92	3000	24×24/50%	66	27.5	$0.03U_\infty$
60.96	0.65		16×16/50%		165.0	
60.96	0.78		16×16/50%		183.3	
60.96	0.85		16×16/50%		116.7	
60.96	0.92		24×24/50%		90.0	

Table 2.4 Data summary for the spanwise plane stereoscopic PIV. Details found in Section 2.4.3.

3 Results and Discussion

This chapter presents the results of this research effort. First, the measured static pressure agreed with other published measurements. The relevant dimensionless pressure gradient parameters are established. Integral quantities and relevant lateral and longitudinal curvature parameters are presented to characterize the boundary layer. The mean and standard deviation of the turbulence are reported, followed by two-point statistics that give insight into the boundary layer structure. Lastly, the turbulent/non-turbulent interface is considered by studying the conditional fields and the small and large scales comprising the interface geometry.

3.1 Pressure Gradient

The static pressure was measured, as outlined in Section 2.3. The results of these measurements are reported in Fig. 3.1. This figure shows the pressure coefficient, $C_p = 2(p - p_\infty)/(\rho U_\infty^2)$, distribution along the model length, with the blue line denoting the 3D source-sink potential flow, the red markers the published measurements, and the triangles the measurements at two flow speeds. The agreement overall was found to be good, with minor differences in the favorable pressure gradient region near $x/L = 0.8$.

The circumferential distribution of static pressure measurements is shown in Fig. 3.2(a) and (b) for free streams of $U_\infty = 50\ \mathrm{ft\,s^{-1}}$ and $200\ \mathrm{ft\,s^{-1}}$, respectively. Notice that the gauge pressures (relative to the test section static) in the figure have Pa (Pascal) units and were intentionally dimensional to convey the minute differences at various circumferential stations. These measurements provided confidence in the axisymmetry of the boundary layer, which was further verified by the spanwise planes as discussed in Appendix A.

A few pressure gradient parameters [6, 53, 58, 67, 87] have been proposed in the literature, the most notable ones being β_c and p_x^+ used to describe pressure gradient effects in the outer and inner layers [200], respectively.

$$\beta_c = \frac{\delta^*}{\tau_w}\frac{dp}{dx} = \frac{\delta^*}{\rho u_\tau^2}\frac{dp}{dx}, \tag{3.1}$$

and

$$p_x^+ = \frac{l_\nu}{\tau_w}\frac{dp}{dx} = \frac{\nu}{\rho u_\tau^3}\frac{dp}{dx}. \tag{3.2}$$

In the preceding expressions, δ^* is the displacement thickness, τ_w is the wall shear stress, ν is the kinematic viscosity, ρ is the density, $u_\tau = \sqrt{\tau_w/\rho}$ is the friction velocity, $l_\nu = \nu/u_\tau$ is the viscous length scale, and dp/dx is the longitudinal pressure gradient. These quantities that constitute β_c and p^+ will be discussed in the next section and are used here to describe the strength of the pressure gradient. The pressure gradient parameters β_c and p^+ are plotted against the streamwise position in Fig. 3.3(a) and (b), respectively.

By either of these metrics, the beginning of the PIV region ($x/L \approx 0.70$) was nearly zero pressure gradient, followed by a mildly favorable pressure gradient up to $x/L \approx 0.8$, beyond which the boundary layer was strongly decelerated. The mild favorable pressure gradient resulted from the flow accelerating around the convex region. This type of initially favorable and then adverse pressure gradient scenario is relevant to engineering boundary layers, and has been investigated by several workers such as Parthasarathy and Saxton-Fox [209], Knopp et al. [89], and Balantrapu et al. [5].

The acceleration parameter K is displayed in Fig. 3.3(c). The parameter is quantified as,

$$K = \frac{\nu}{U_e^2}\frac{dU_e}{dx}, \tag{3.3}$$

where U_e is the wall-parallel edge velocity. Some workers [3, 6] have also used this parameter to describe the pressure gradient. The importance of this pressure gradient parameter relative to others is unclear [6]. This parameter K had a similar trend to the pressure gradient dp/dx, shown in (d). However, the zero-crossing of K was shifted upstream relative to the other parameters. Therefore, where the FPG ended and the APG began based on K was unclear.

The static pressure was measured with the mirror fixture installed in the tunnel for the time-dependent measurements described in Fig. 2.17(b). The resulting static pressure distribution is shown in Fig. 3.4. The top and bottom figures correspond to the two flow speeds,

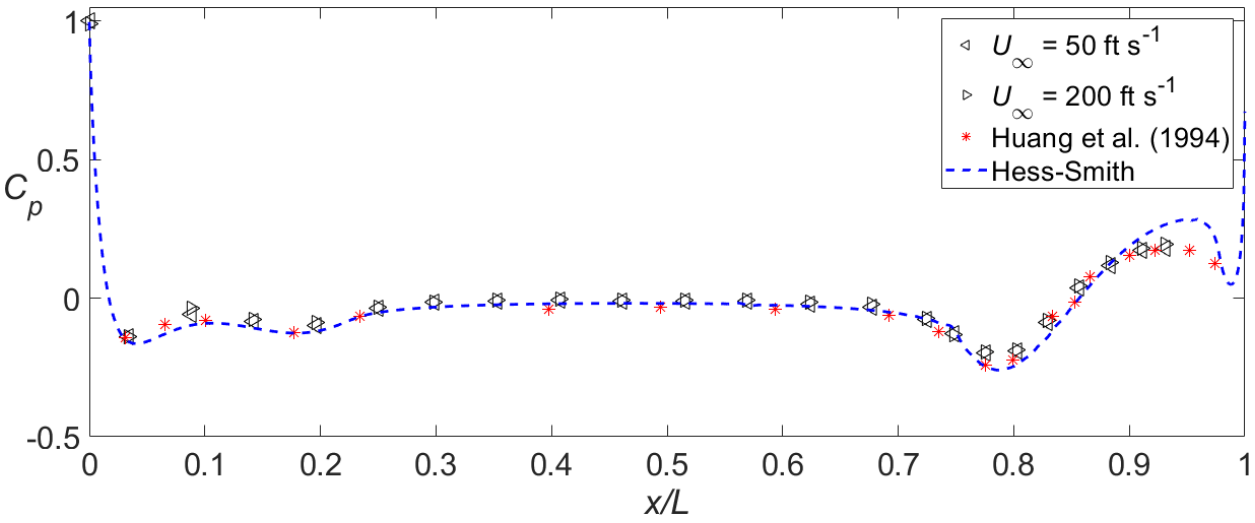

Figure 3.1 Distribution of pressure coefficient C_p along the SUBOFF for two flow speeds of 50 ft s^{-1} and 200 ft s^{-1}

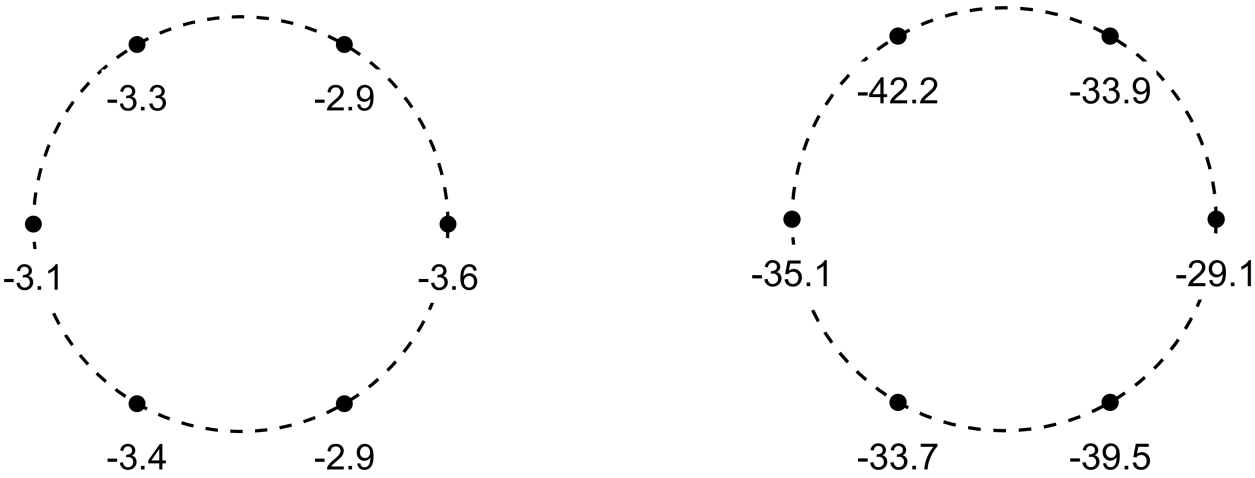

(a) $U_\infty = 50$ ft s^{-1} *(b)* $U_\infty = 200$ ft s^{-1}

Figure 3.2 Circumferential distribution of six static pressure ports have good agreement at both flow speeds, indicating an axisymmetric flow. Gauge pressures shown have units of Pascal.

and the measurements obtained with the fixture installed are denoted by the magenta triangles (△). The agreement was good, but some minor deviations were observed downstream.

The differences between the pressure coefficients with and without the mirror fixture in the tunnel were calculated as shown in Figure 3.5. The blue curve is a second-order polynomial fit to the last ten data points, highlighting the growing differences in C_p resulting from the mirror fixture. Here, the positive values indicated the static pressure was higher with

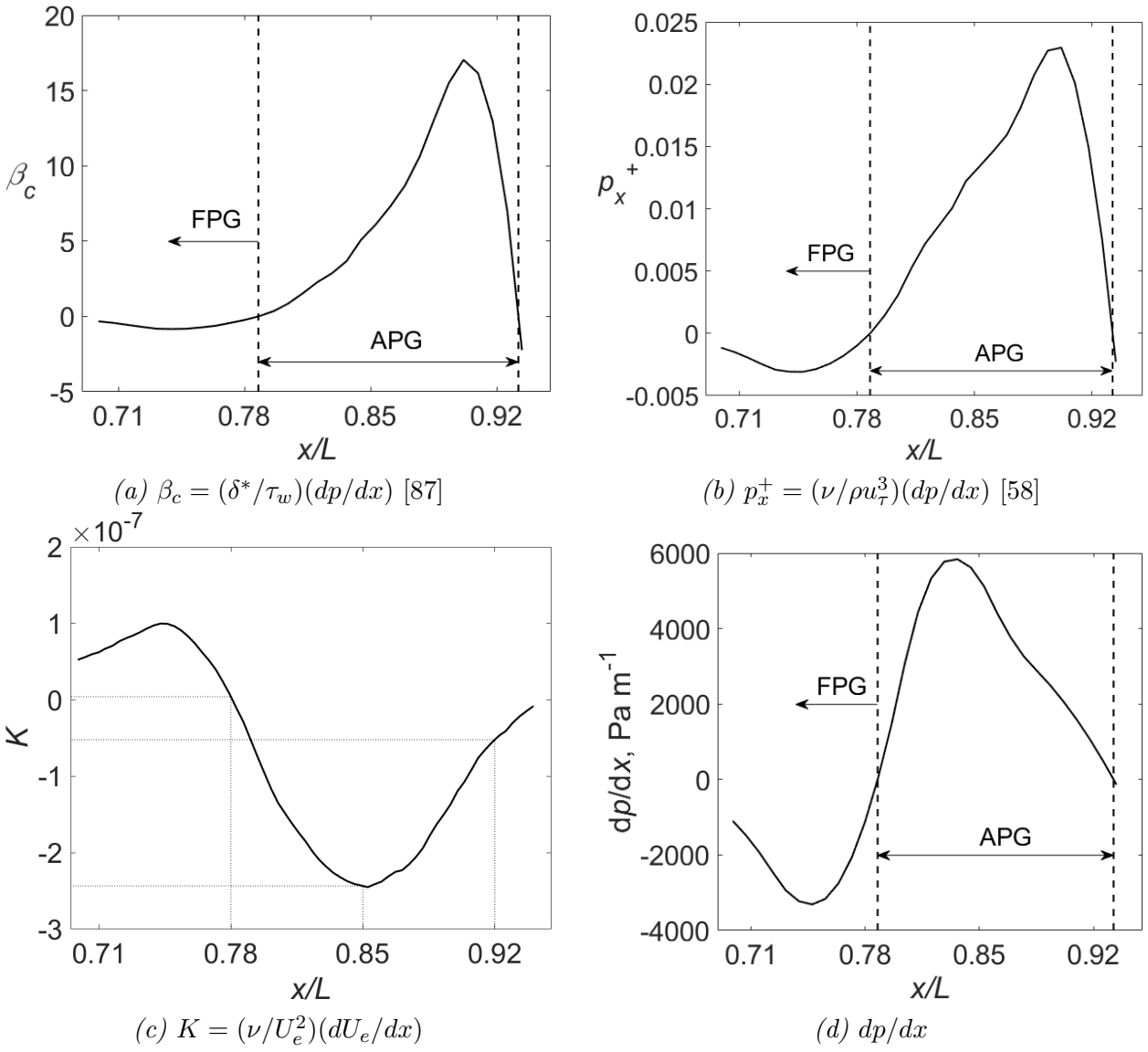

(a) $\beta_c = (\delta^*/\tau_w)(dp/dx)$ [87]

(b) $p_x^+ = (\nu/\rho u_\tau^3)(dp/dx)$ [58]

(c) $K = (\nu/U_e^2)(dU_e/dx)$

(d) dp/dx

Figure 3.3 Pressure gradient parameters commonly used to describe the flow. $U_\infty = 200$ ft s^{-1}.

the additional downstream blockage. The dashed line shows where the deviations exceeded $\Delta C_p = 0.01$, which was $x/L > 0.8$ at both flow speeds. Therefore, the mirror fixture did not significantly impact the measurements at $x/L = 0.65$ and 0.78. Notice that measurements at $x/L = 0.85$ and 0.92 were acquired without the mirror assembly in the tunnel.

3.2 Single-Point Statistics

This section overviews the boundary layer characteristics and analyzes the mean and variance of the boundary layer velocities. These results follow the Reynolds decomposition

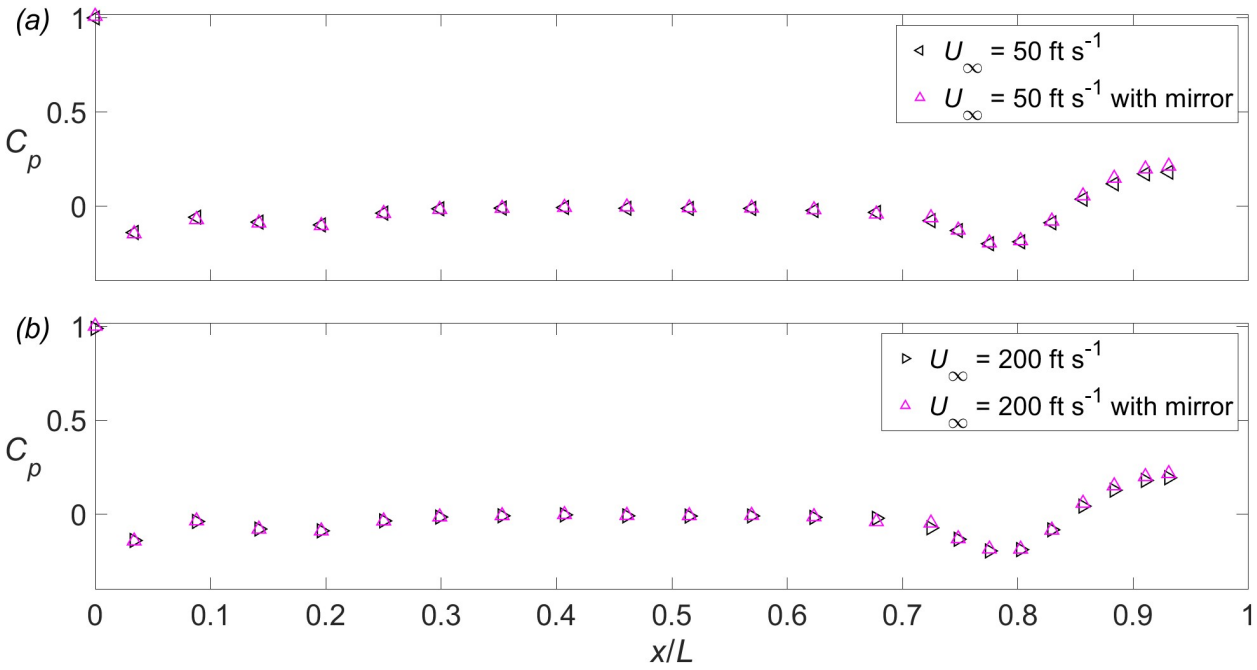

Figure 3.4 Comparison of pressure coefficient C_p distribution at two flow speeds of *(a)* 50 ft s^{-1} and *(b)* 200 ft s^{-1} with (magenta △) and without the mirror fixture.

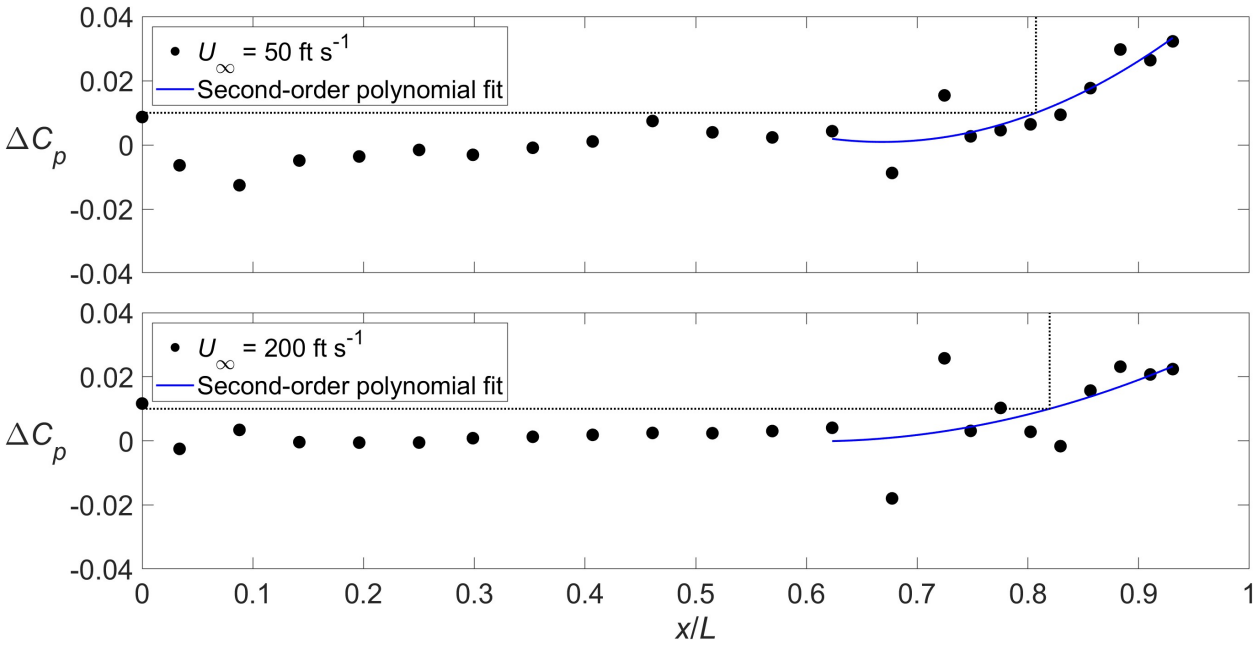

Figure 3.5 Difference between pressure coefficient C_p distribution with and without the mirror fixture in the tunnel at two flow speeds of *(a)* 50 ft s^{-1} and *(b)* 200 ft s^{-1}. The blue lines are second-order polynomial fits to convey increasing deviation with downstream distance. The dotted lines show where the deviation magnitudes exceeded 0.01 in the fitted curve.

of the flow into mean and fluctuating components, $\tilde{u}_i = U_i + u_i$, where the subscript implies different velocity components. The results in this section were computed from the higher Reynolds number ($Re_\tau \approx 2700$), large FOV data set based on wall-normal profiles extracted at 30 equally-spaced streamwise stations.

First, the velocity root-mean-squared (RMS) profile was used to estimate the boundary layer thickness δ, as discussed in Section 3.2.1. The inner scales were then determined through the Clauser chart method as overviewed in Section 3.2.3. The most upstream part of the FOV was shown in Section 3.2.2 to be nearly canonical. Lastly, seven streamwise stations were then chosen to inspect the variations in time-averaged velocity and RMS profiles in Sections 3.2.3 and 3.2.4.

Contour plots are first presented to showcase the Suboff boundary layer. Colored contours of the time-averaged wall-parallel U and wall-normal W velocities are shown in Fig. 3.6. In these figures, the dashed line shows the boundary layer edge determined based on a turbulent kinetic energy (TKE) criterion [5]. Inspecting U in Fig. 3.6(a), the outer potential flow accelerated through the favorable pressure gradient (FPG) and then relaxed through the adverse pressure gradient (APG) region, where the boundary layer became significantly thicker.

In Fig. 3.6(b), the time-averaged wall-normal velocity W was initially nearly zero, became negative through the FPG, and eventually grew to a significant positive $0.25U_\infty$. This concurrent variation in wall-parallel and wall-normal mean velocities was necessary because for an incompressible flow, for which $\mathrm{d}U/\mathrm{d}x = -\mathrm{d}W/\mathrm{d}z$. Figure 3.7 shows the in-plane TKE, $k = (\overline{u^2} + \overline{w^2})/2$. Much of the energy resided in the near-wall region, as expected for a boundary layer. Interestingly, the near-wall turbulence intensity noticeably decayed beyond $x/L \approx 0.85$, and the most intense k region gradually shifted away from the wall.

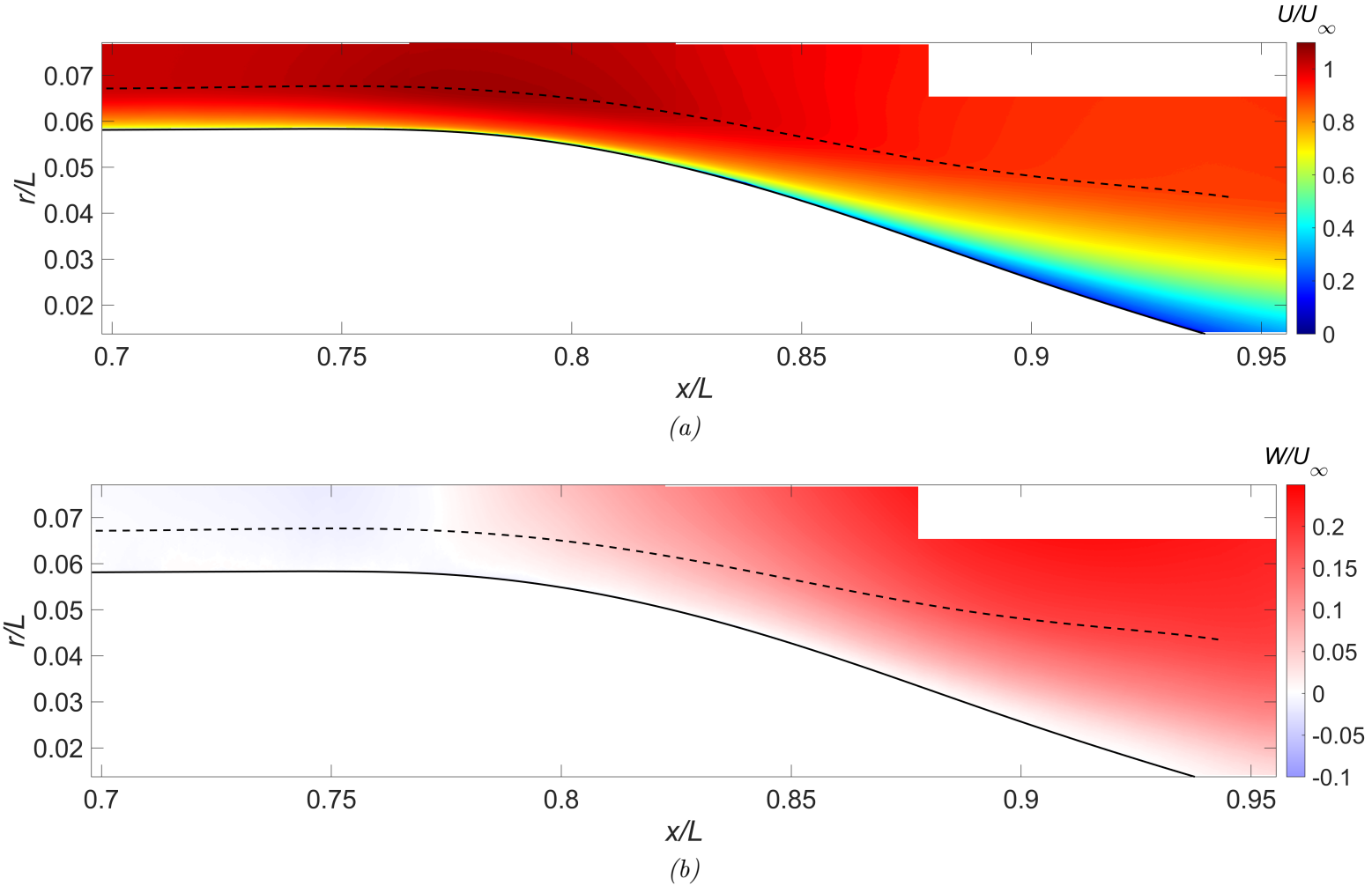

Figure 3.6 Time-averaged velocities *(a)* parallel and *(b)* normal to the wall at $U_\infty = 200$ ft s^{-1}. Dashed line shows boundary layer edge.

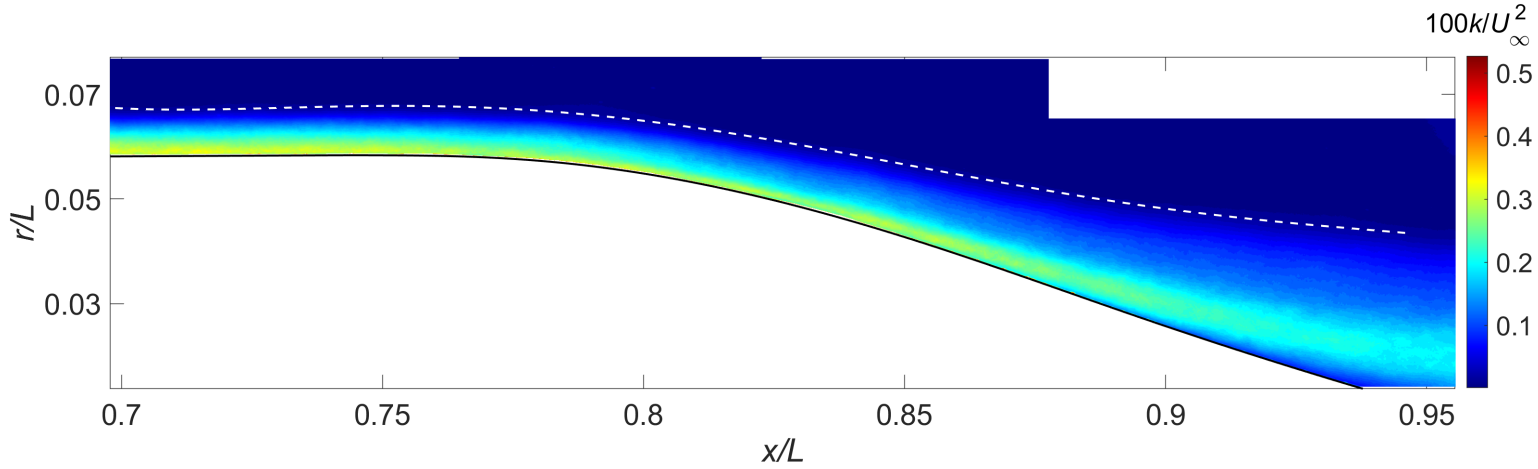

Figure 3.7 Turbulent kinetic energy (TKE) k distribution for $U_\infty = 200$ ft s^{-1}. $k = (\overline{u^2} + \overline{w^2})/2$. Dashed line shows boundary layer edge.

3.2.1 Boundary Layer Characteristics

This section overviews the boundary layer characteristics. The boundary layer thickness, along with the displacement and momentum thickness, is discussed. The Reynolds number variations with axial position are shown. Lastly, the lateral and longitudinal curvature are quantified and evaluated. The results presented are based on the higher Reynolds number measurements.

A non-trivial question in analyzing this type of boundary layer is how to compute the boundary layer thickness δ, which was used to nondimensionalize the results and was the upper integration limit for other integral quantities. An integration limit is necessary because, unlike a canonical boundary layer, displacement and momentum thickness, δ^* and θ, do not approach constant values at the boundary layer edge as a result of the streamline curvatures in the potential flow. Inconsistent definitions of these fundamental quantities may lead to difficulties in comparing different axisymmetric boundary layers, such as with the ones studied by Balantrapu et al. [5] and Manovski et al. [146], and ultimately inaccurate understanding of the effects of pressure gradient $\beta = \delta^*/\tau_w(dp/dx)$ and surface curvature δ/a (a is the local geometry radius).

There are numerous ways to define the boundary layer thickness δ for planar boundary layers. Many works have defined δ based on where the time-averaged streamwise velocity gradient dU/dy, the vorticity $\omega = dv/dx - du/dy$, the Reynolds stress [89], etc., fell below a threshold [210]. Chauhan et al. [32] proposed a composite law to describe well-behaved ZPG boundary layers, from which δ can be obtained through a least-squares fit to the measurement. Similarly, Nickels [58] formulated a composite form that better suits equilibrium pressure gradient flows.

Alfredsson and Örlü [211] devised a method of identifying well-behaving canonical boundary layers based on the collapse of the wake region in the plot of $u_{\mathrm{rms}}/U(z)$ against $U(z)/U_e$ which they coined the diagnostic-plot method. Then, Dróżdż et al. [41] and Vinuesa et al. [42] extended the diagnostic plot method to pressure gradient cases by showing that, for

up to (and perhaps beyond) $\beta_c = 85$, the outer region showed similarity when weighted by $\sqrt{H}$ ($H = \delta^*/\theta$ is the shape factor). The thickness, δ_{99}, where $U = 0.99\,U_\infty = U_e$, was then defined as where $u_{\rm rms}/(U\sqrt{H}) = 0.02$. This diagnostic plot method was argued to provide the most consistent definition of δ_{99} in large defect boundary layers ($\beta_c > 7$) [42] and has been endorsed by recent workers such as Parthasarathy and Saxton-Fox [209]. Therefore, the diagnostic plot method was used as the starting point.

The diagnostic plot method in Fig. 3.8(a) shows that the boundary layers at different stations did not collapse in the outer region. This figure shows the most upstream station in blue and the furthest downstream in red. The solid black line is a ZPG direct numerical simulation (DNS) [176] showing roughly the expected distribution of $u_{\rm rms}/U$. While the upstream stations (blue curves) followed the canonical boundary layer (solid black line), the red curves that correspond to strongly decelerated boundary layers, deviated significantly. Figure 3.8(b) is a zoomed-in view of Fig. 3.8(a) that better shows the deviation. Because the consistent definition of δ_{99} rests upon the invariance of the outer region with pressure gradient and Reynolds number, the diagnostic plot method was deemed ineffective for the current boundary layer.

The diagnostic plots did not collapse on each other because of the increasing transverse curvature δ/a, a factor that becomes significant when $\delta/a \sim \mathcal{O}(1)$ according to Schlichting [212]. The variable a is the geometric radius and δ is described in the next paragraph. Figure 3.8(b) indicates significant deviation occurring at $x/L = 0.81$–0.85, where $\delta/a = 0.199$–0.336; see Table 3.2 or Fig. 3.12(b). If an order of magnitude is defined roughly as $(\delta/a)/\sqrt{10} < \delta/a < \sqrt{10}(\delta/a)$, then the value of $\delta/a = 0.336$ at $x/L = 0.85$ is $\mathcal{O}(1)$ because $1/\sqrt{10} = 0.316$.

Because pressure gradient strengths up to $\beta_c = 85$ did not affect the diagnostic plot collapse [42], it must be the transverse and/or longitudinal [199] surface curvature that led to the deviation. This observation agreed with those of Kumar and Mahesh [45], who also highlighted that at as early as $\delta/a = 0.3$, there was a decreased RMS for the Suboff relative

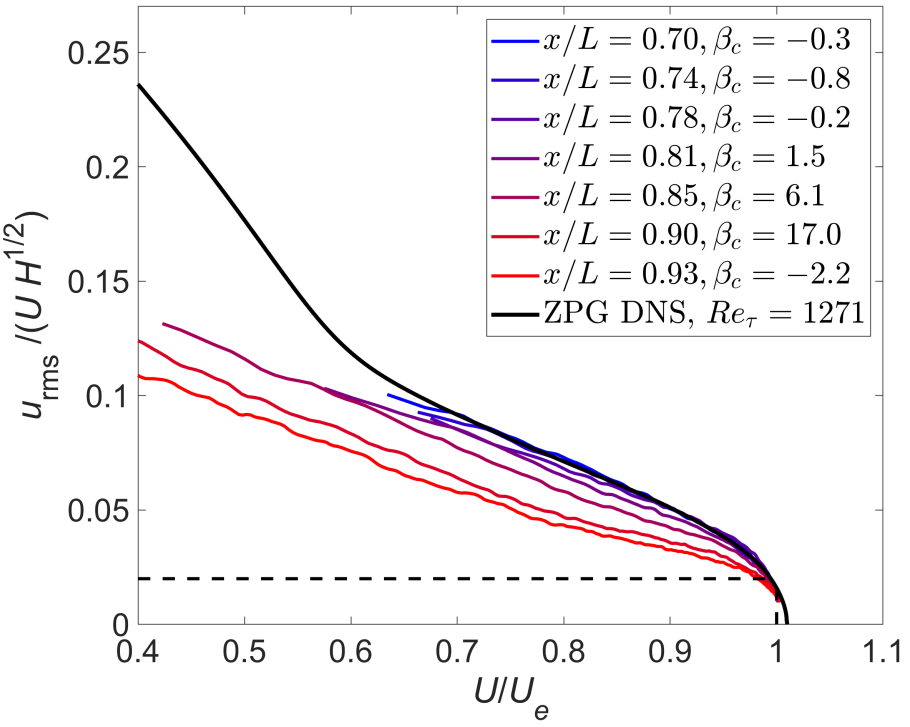

(a)

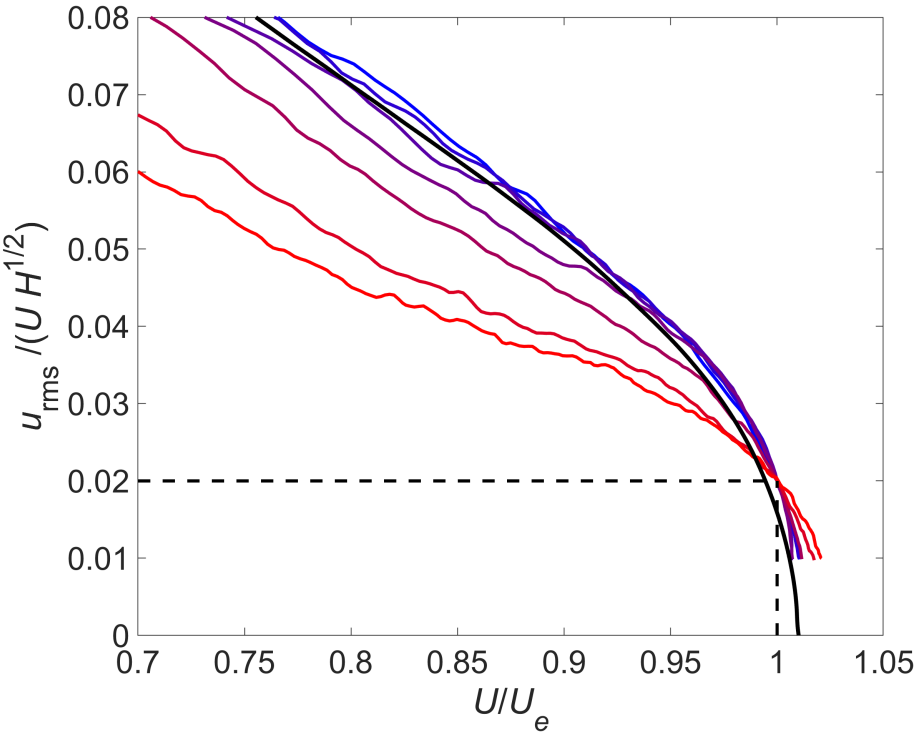

(b)

Figure 3.8 Diagnostic plot method for determining δ_{99} following the works of Dróżdż et al. [41] and Vinuesa et al. [42].

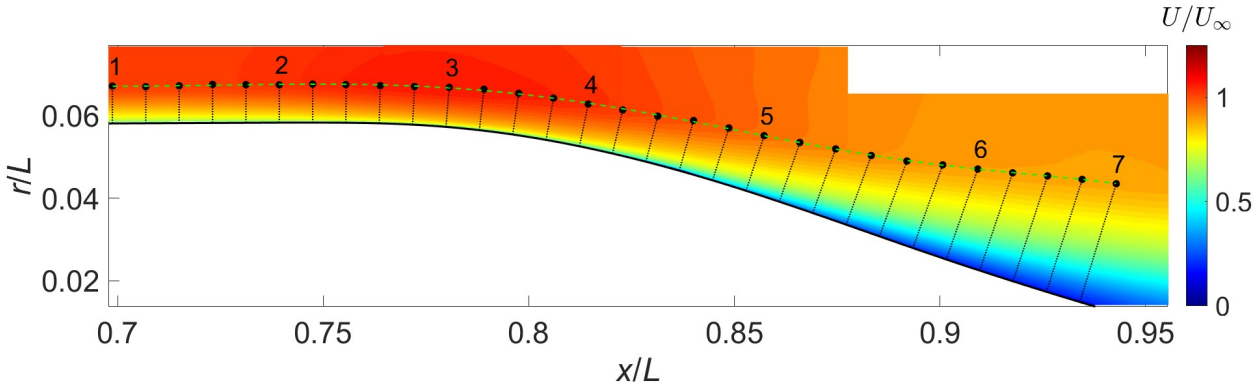

Figure 3.9 Boundary layer thickness δ was estimated at 30 axial locations from the wall-normal dotted lines as denoted by the circles, and a 5th order polynomial was used to fit the points as shown by the green dashed line. Velocity profiles from seven stations will be examined. Contour shows normalized wall-tangent velocity U/U_∞.

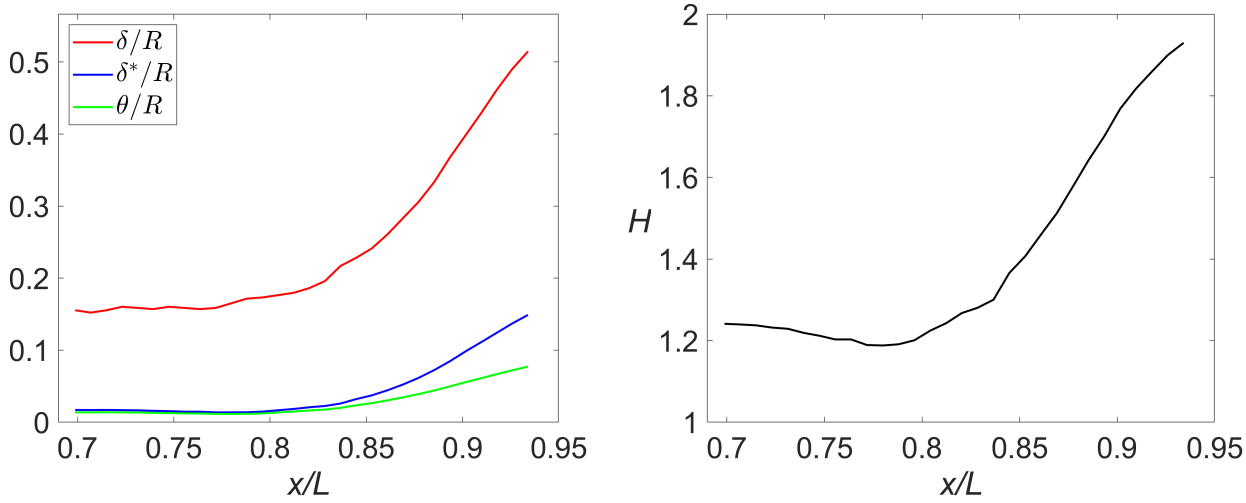

Figure 3.10 (a) Boundary layer thickness δ, displacement thickness δ^*, and momentum thickness θ, and **(b)** shape factor H. R is the maximum hull radius.

to a flat plate. Although the diagnostic plot was not used to compute δ_{99}, it provided a sense of where the curvature effects became noticeable.

The present work defines the boundary layer thickness based on the turbulent kinetic energy [5]. Specifically, δ was defined as where $\sqrt{\overline{u^2} + \overline{w^2}} = 0.02U_\infty$, equal to the statistical uncertainty (see Section 2.4.7). Using this definition, the boundary layer thickness δ was computed for 30 wall-normal mean velocity profiles as shown using the circles in Fig. 3.9. The green line is a sixth-order polynomial fit. Subsequently, the displacement and momentum

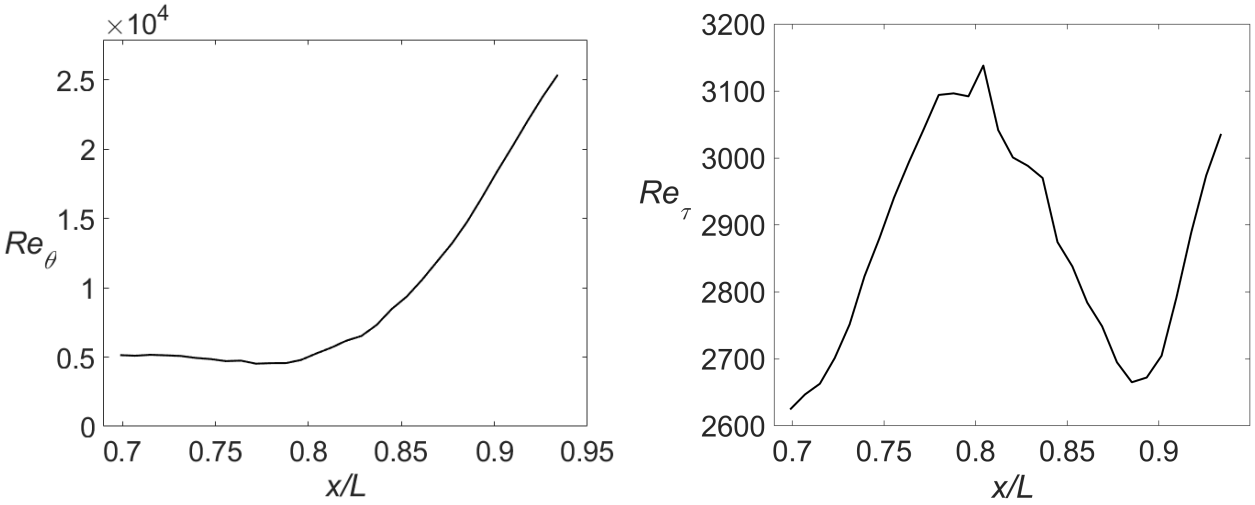

Figure 3.11 Reynolds number *(a)* $Re_\theta = U_e\theta/\nu$ and *(b)* $Re_\tau = \delta u_\tau/\nu$ along the afterbody.

thicknesses δ^* and θ followed the planar boundary layer approach, defined as

$$\delta^* = \int_0^\delta \left(1 - \frac{U}{U_e}\right) dz, \tag{3.4}$$

and

$$\theta = \int_0^\delta \frac{U}{U_e}\left(1 - \frac{U}{U_e}\right) dz. \tag{3.5}$$

These quantities are shown in Fig. 3.10(a). The displacement and momentum thickness were extrapolated to the wall using a third-order polynomial with appropriate boundary conditions. Figure 3.10(b) shows the shape factor $H = \delta^*/\theta$, which was initially 1.25, decreasing through the FPG before increasing up to 1.93. Note that Patel et al. [109] also derived axisymmetric and physical definitions of the integral parameters, which can have very different values and trends.

Reynolds numbers based on momentum thickness and friction velocity are shown in Fig. 3.11(a). The friction velocity was computed using the Clauser chart method as discussed in Section 3.2.3. Figure 3.11(a) shows $Re_\theta = U_e\theta/\nu$ increasing rapidly because of the APG. Figure 3.11(b) shows $Re_\tau = \delta u_\tau/\nu = \delta/l_\nu = \delta^+$. The initial increase in Re_τ was driven by increasing u_τ and δ. The ensuing decrease was because of the diminishing wall shear stress

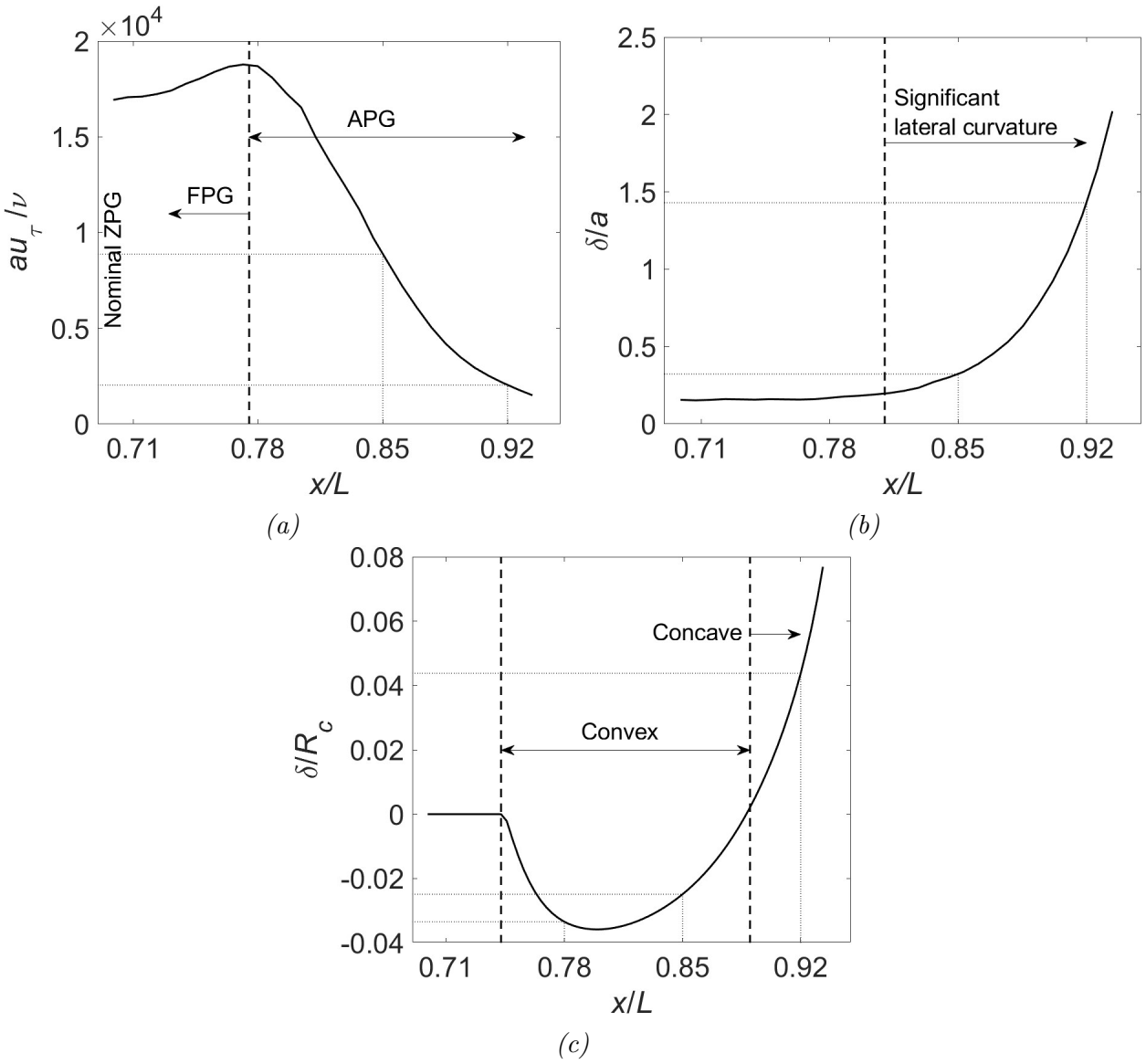

Figure 3.12 Parameters quantifying the *(a,b)* lateral and *(c)* longitudinal curvature. *(a)* Geometric radius a in wall units. *(b)* Ratio of boundary layer thickness δ to geometric radius a. *(c)* Ratio of δ to longitudinal radius of curvature R_c.

and, therefore, u_τ. The final upward trend can be explained by the continued growth of δ and relatively steady u_τ. These trends were similar to those observed by Knopp et al. [89].

Surface curvature can significantly modify the boundary layer [129, 200]. As such, the Suboff wall curvatures are reported in Fig. 3.12. The lateral curvature was described by $a^+ = au_\tau/\nu$ and δ/a in Figs. 3.12(a) and (b), respectively. Notice that the four abscissa tick marks denote the nominal ZPG, end of FPG, increasing APG, and decreasing APG regions

referenced in the remainder of this writing. The horizontal dotted lines are visual aids. The ratio between the geometric radius a and the viscous length scale l_ν was large, as shown in Fig. 3.12(a). Figure 3.12(b) reports the boundary layer thickness δ as a multiple of a. As previously noted, $\delta/a \sim 1$ at $x/L > 0.81$ was considered significant [212].

The longitudinal curvature was documented as the ratio between δ and the longitudinal radius of curvature R_c in Figure 3.12(c). According to Patel and Sotiropoulos [200], $\delta/R_c < 0.01$ is insignificant, $\delta/R_c \sim 0.1$ is moderate, and $\delta/R_c \sim 1$ is significant. Figure 3.12(c) shows the convex (negative second derivative) and concave (positive second derivative) curvatures to be insignificant or, at best, moderate. In addition, longitudinal curvatures affect the flow in manners similar to pressure gradient [200], and a dedicated experiment with, e.g., curved top and bottom walls [213] to alleviate the pressure gradient, is required to isolate and understand its effect. Nonetheless, the present work will highlight longitudinal curvature effects.

3.2.2 Zero-Pressure Gradient Inflow

The axisymmetric boundary layer was characterized at the most upstream station ($x/L = 0.699$) before significant pressure gradient and surface curvature effects. The details of this boundary layer are documented in Table 3.1. Although this writing focuses on the data set with $Re_\tau = 2700$, the inflow from $Re_\tau = 689$ is provided here for comparison. Because this approaching boundary layer was nearly canonical, the Chauhan fit [82] was used to estimate the actual boundary layer thickness δ_0, δ_{99} where $U = 0.99U_e = 0.99U(z = \delta_0)$, and Π, the wake strength parameter. As shown in Table 3.1, the value of δ estimated based on TKE resided between the two δ's obtained from Chauhan's fit. This δ was used to compute other quantities in this table, such as the shape factor $H = \delta^*/\theta$ and the Kármán number Re_τ.

The wake strength parameter Π was lower than that of a canonical boundary layer at a matched $Re_{\delta^*} = \delta^* U_e/\nu$ (see Chauhan et al. [82]), which could be attributed to the axisymmetry and the slight favorable pressure gradient, also evident in the lower shape factor H of 1.25. The pressure gradient was quantified following the work of Clauser [87] as

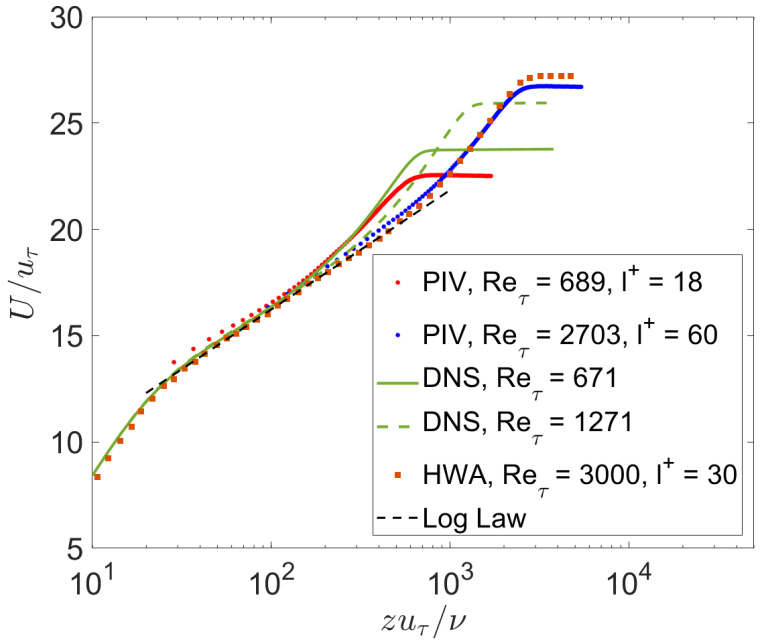
30
25
20
15
10
5
U/u_τ
10^1
10^2
10^3
10^4
zu_τ/ν
PIV, Re$_\tau$ = 689, l$^+$ = 18
PIV, Re$_\tau$ = 2703, l$^+$ = 60
DNS, Re$_\tau$ = 671
DNS, Re$_\tau$ = 1271
HWA, Re$_\tau$ = 3000, l$^+$ = 30
Log Law

(a)

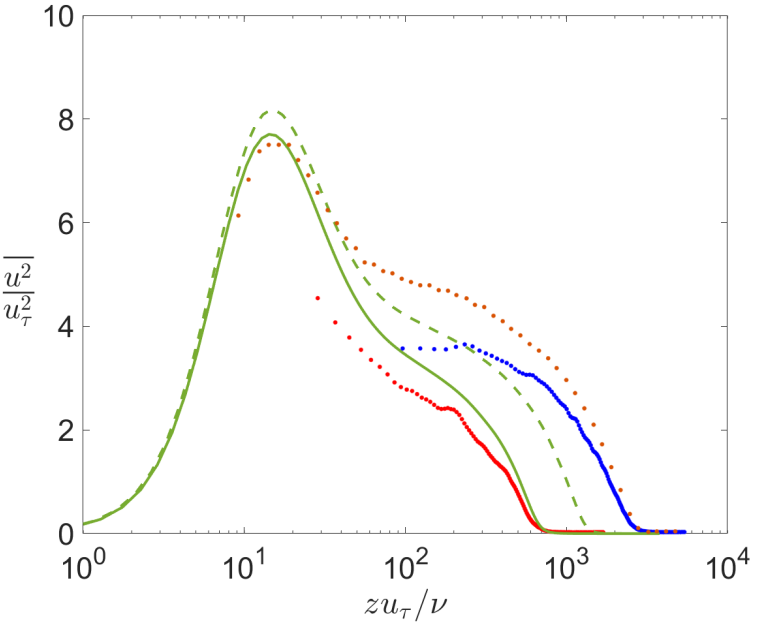
10
8
6
4
2
0
$\overline{u_\tau^2}|\overline{u_\tau^2}|$
10^0
10^1
10^2
10^3
10^4
zu_τ/ν

(b)

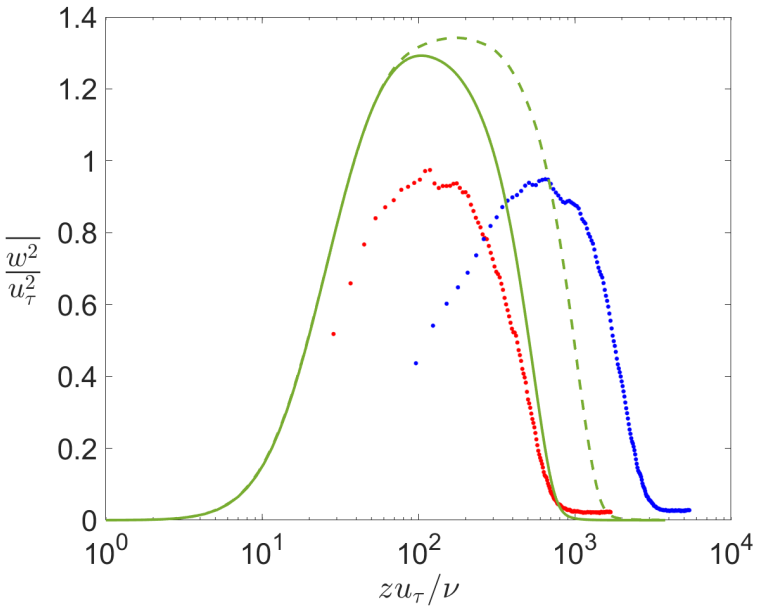

(c)

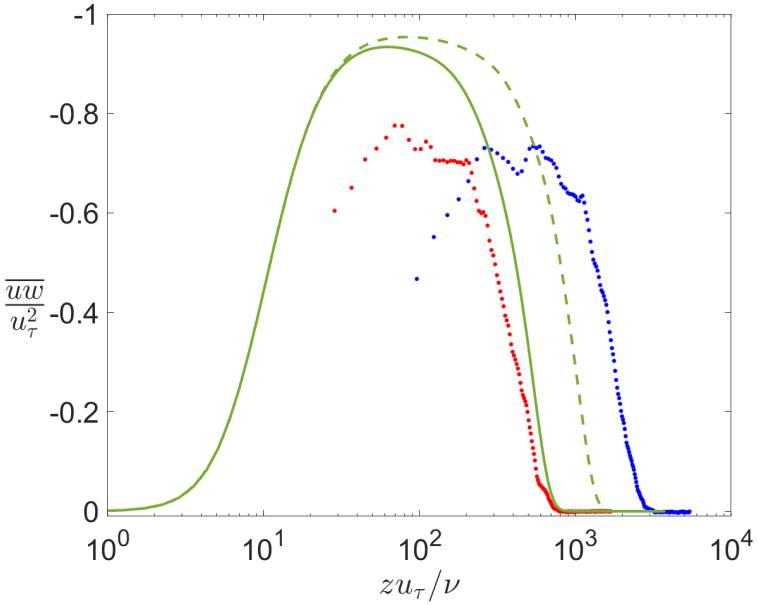

(d)

Figure 3.13 (a) Mean velocity U, *(b)* variance of velocity fluctuation $\overline{u^2}$, *(c)* variance of wall-normal fluctuation $\overline{w^2}$, and *(d)* Reynolds shear stress $\overline{uw}$ compared with direct numerical simulation [43] and hot-wire anemometry [9]

$\beta_c = (\delta^*/\tau_w)(dp/dx)$. Negative values of β_c imply favorable pressure gradients (FPG), and positive values indicate adverse pressure gradients (APG). The transverse curvature effect was quantified by the boundary layer thickness relative to the geometry radius, which at the local value of 0.15 was insignificant [45].

Figure 3.13 shows the average velocity U and the variance of the velocity fluctuation $\overline{u^2}$ using inner scaling. The viscous quantities used to normalize the wall-normal z and the velocity are from Table 3.1. Red and blue markers represent the low and high Reynolds number cases. The solid and dashed green lines correspond to the DNS results from Schlatter and Örlü [214] at $Re_\tau = u_\tau \delta_{99}/\nu = 671$ and $Re_\tau = 1271$. The orange square was a planar, ZPG, smooth-wall boundary layer measured with $Re_\tau = 3{,}000$ digitized from Harun [9].

Comparisons of the time-averaged wall-parallel velocity U in Fig. 3.13(a) showed good collapse with the log law (dashed line). The wake region of the PIV measurement was lower than the ZPG data [9, 214], in line with the slightly favorable pressure gradient measured. The variance of u measured at $Re_\tau = 689$ showed reasonable agreement with the DNS results in Fig. 3.13(b), given the current measurement resolution of $l^+ = 18$. At the higher $Re_\tau = 2700$, agreement with Harun [9] was good, with some expected attenuation in the small scales close to the wall as a consequence of the lower resolution of $l^+ = 60$ and the slight favorable pressure gradient. Comparisons of the wall-normal variance $\overline{w^2}$ and Reynolds stress $\overline{uw}$ were also favorable as shown in Figs. 3.13(c) and 3.13(d) with some expected attenuation. The trends of the time-mean U and the second-order statistics, including Reynolds number effects, were comparable to previous works [184, 214].

U_∞	x/L	U_e/U_∞	u_τ/U_∞	δ_0	δ_{99}	δ	Π	H	Re_θ	ν/u_τ	Re_τ	β_c	δ/a
$\mathrm{m\,s^{-1}}$				mm	mm	mm				µm			
15.24	0.699	1.035	0.046	17.88	13.00	15.24	0.168	1.248	1097	21.40	670	-0.161	0.139
60.96	0.699	1.020	0.038	20.71	15.5	17.02	0.299	1.241	5140	6.45	2620	-0.327	0.155

Table 3.1 Characteristics of the boundary layer at the most upstream station ($x/L = 0.699$) indicate a near canonical state.

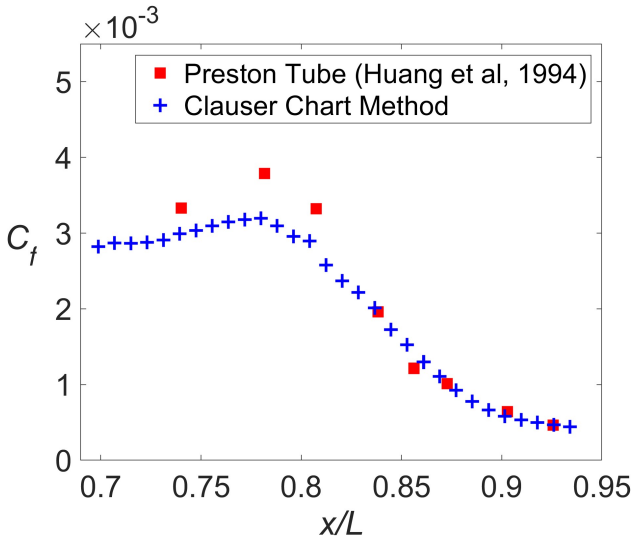

Figure 3.14 The friction coefficient C_f obtained through the Clauser chart method is shown in blue "+," and the red squares were digitized from Huang and Liu [44] and scaled following $C_f \sim Re_L^{-0.2}$ [45].

3.2.3 Time-Averaged Velocity

Velocity profiles were extracted at seven stations as labeled in Fig. 3.9 for analysis. The flow characteristics at these stations are summarized in Table 3.2, providing a sense of the spatially evolving boundary layer. Station 1 was immediately downstream of the ZPG region. Station 2 coincided with the strongest FPG. However, station 3 had the lowest shape factor because of the FPG history, despite the local β_c being nearly zero. Mild, moderate, and strong APGs were observed at stations 4, 5, and 6. The APG rapidly thickened the boundary layer, and when combined with the eroding Suboff body, led to large values of δ/a and therefore notable transverse curvature effects [129, 212]. Finally, station 7 was the most downstream location in the measurement domain. Although the concave curvature created a local FPG, the history of APG dictates the flow characteristics. A discussion is now provided on how the viscous scaling was obtained.

The Clauser chart method (CCM) was used to estimate the wall shear stress. The major assumption of this method is that the constants of the logarithmic law are invariant with pressure gradients. This assumption could introduce significant error as shown by several workers, including Harun [9] and Knopp et al. [89], who used independent oil-film inter-

Station	x/L	U_e/U_∞	u_τ/U_∞	δ	H	Re_θ	l_ν	Re_τ	β_c	δ/a
				mm			µm			
1	0.699	1.020	0.038	17.02	1.241	5140	6.45	2640	-0.32	0.155
2	0.739	1.036	0.040	17.20	1.218	4940	6.17	2790	-0.84	0.157
3	0.779	1.074	0.043	18.08	1.188	4560	5.76	3140	-0.24	0.168
4	0.811	1.045	0.038	19.68	1.242	5680	6.59	2990	1.55	0.199
5	0.851	0.963	0.027	26.42	1.407	9360	9.30	2840	6.11	0.336
6	0.899	0.903	0.015	43.62	1.768	18400	16.06	2720	17.03	0.924
7	0.931	0.896	0.013	56.38	1.930	25350	18.55	3040	-2.23	2.046

Table 3.2 Summary of the seven streamwise stations chosen for analysis at $U_\infty = 200$ ft s^{-1}.

ferometry measurements to show the changing Kármán constant κ with pressure gradient. Knopp et al. [89] estimated the error in u_τ obtained from the CCM to be 5%.

Nonetheless, using values of $\kappa = 0.384$ and $C = 0.41$, the CCM was sufficient for qualitative discussion of the trends. After obtaining the value of u_τ, the wall shear stress $\tau_w = \rho u_\tau^2$, the friction coefficient $C_f = 2\tau_w/(\rho U_e^2)$, and viscous length scale $l_\nu = \nu/u_\tau$ were also calculated. The variable U_e is the local streamwise edge velocity. The resulting C_f is shown in Fig. 3.14 with the blue "+", and the red squares represent Preston tube measurements from Huang and Liu [44] scaled by $C_f \sim Re_L^{-0.2}$ [45]. The general trend of the C_f increasing with FPG and decreasing with APG was observed in the current measurements, although the extent of the increase in the FPG was not as large compared to the Preston tube data. The agreement was good in the APG region.

The time-mean wall-parallel velocity was scaled by the computed inner quantities, as presented in Fig. 3.15. The line color transitions from blue to red with increasing streamwise location. In agreement with previous studies, the extent of the log region grew with the FPG and eroded with the APG. Conversely, the wake region was reduced by the FPG and enhanced by the APG. The variations in the log and wake regions suggested changes to the intermittency and perhaps entrainment [85]. The turbulent/non-turbulent interface is detailed in Section 3.4.

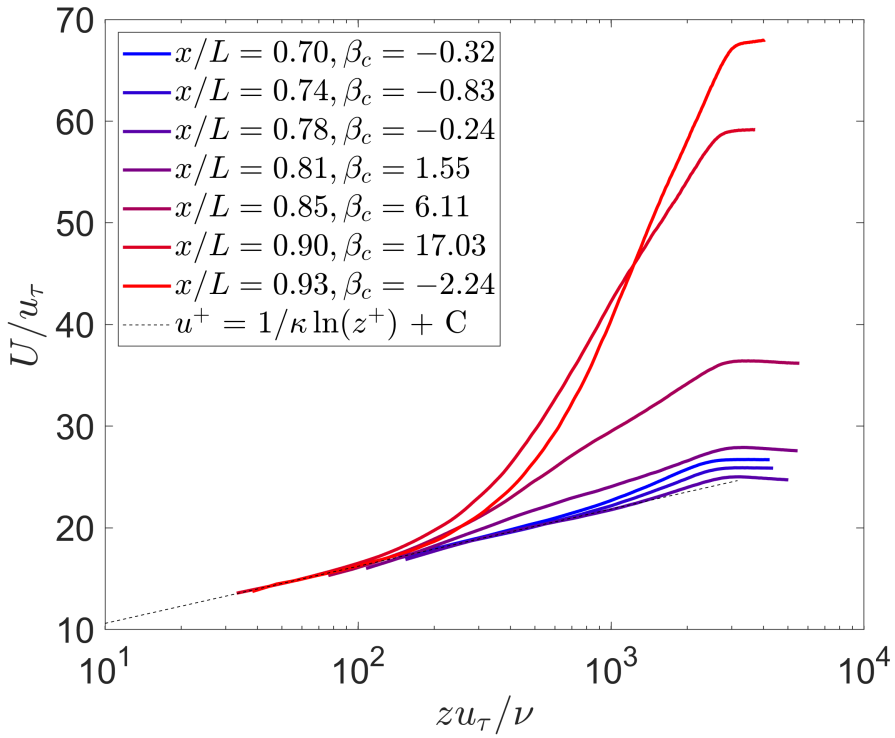

Figure 3.15 The time-averaged wall parallel u velocity computed at the streamwise stations shown in Table 3.2. The color changes from blue to red with increasing streamwise position. The logarithmic law used $\kappa = 0.41$ and $C = 5$.

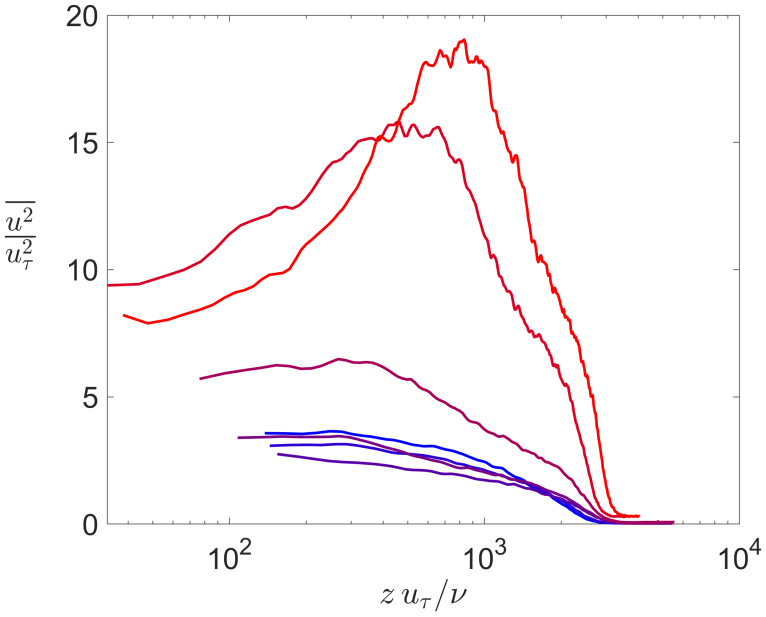
20
15
10
5
0
$\frac{\overline{u^2}}{u_\tau^2}$
10^2
10^3
10^4
$z\,u_\tau/\nu$

(a)

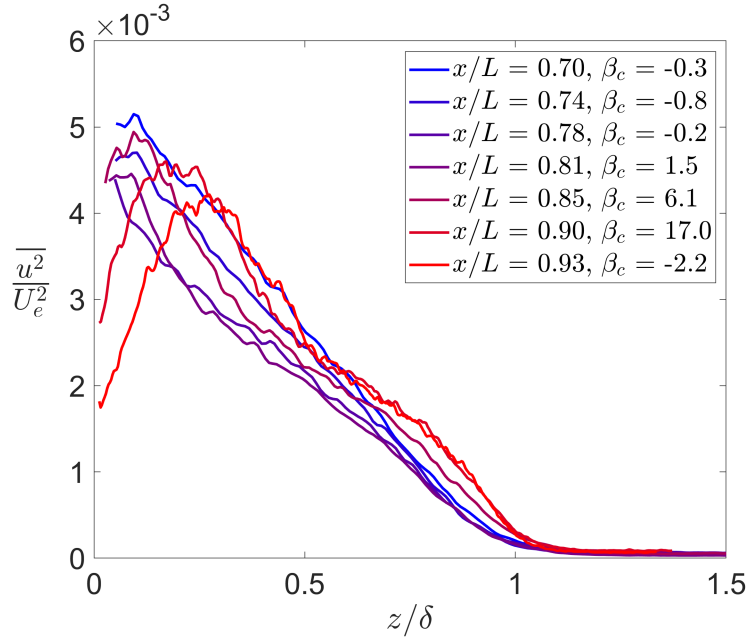
$\times 10^{-3}$
6
5
4
3
2
1
0
$\frac{\overline{u^2}}{U_e^2}$
0
0.5
1
1.5
z/δ
$x/L = 0.70,\ \beta_c = -0.3$
$x/L = 0.74,\ \beta_c = -0.8$
$x/L = 0.78,\ \beta_c = -0.2$
$x/L = 0.81,\ \beta_c = 1.5$
$x/L = 0.85,\ \beta_c = 6.1$
$x/L = 0.90,\ \beta_c = 17.0$
$x/L = 0.93,\ \beta_c = -2.2$

(b)

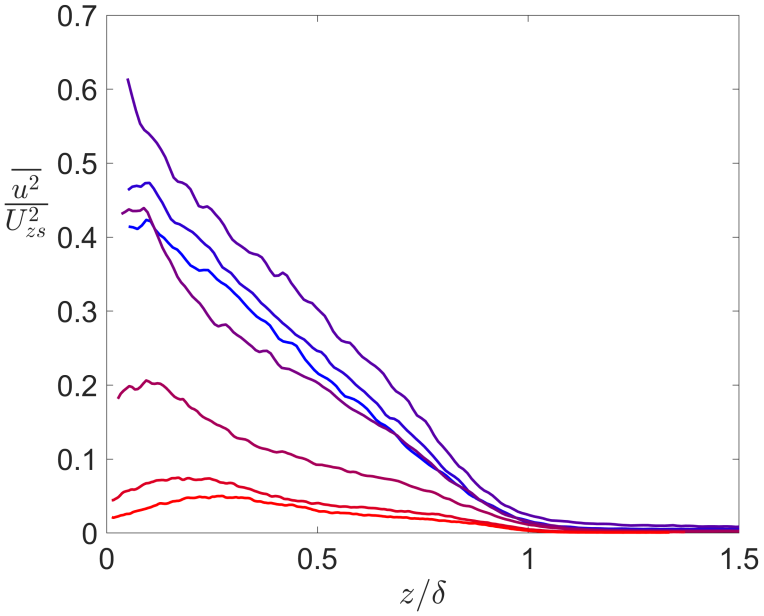

(c)

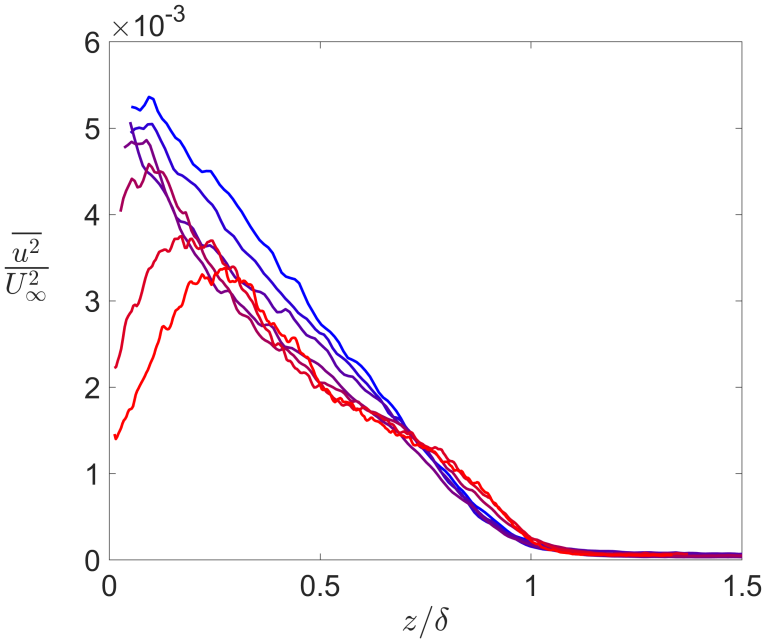

(d)

Figure 3.16 Wall-parallel velocity fluctuation $\overline{u^2}$ normalized by *(a)* friction velocity u_τ *(b)* edge velocity U_e, *(c)* Zagarola-Smits velocity $U_{zs} = U_e\delta^*/\delta$, and *(d)* free-stream velocity U_∞.

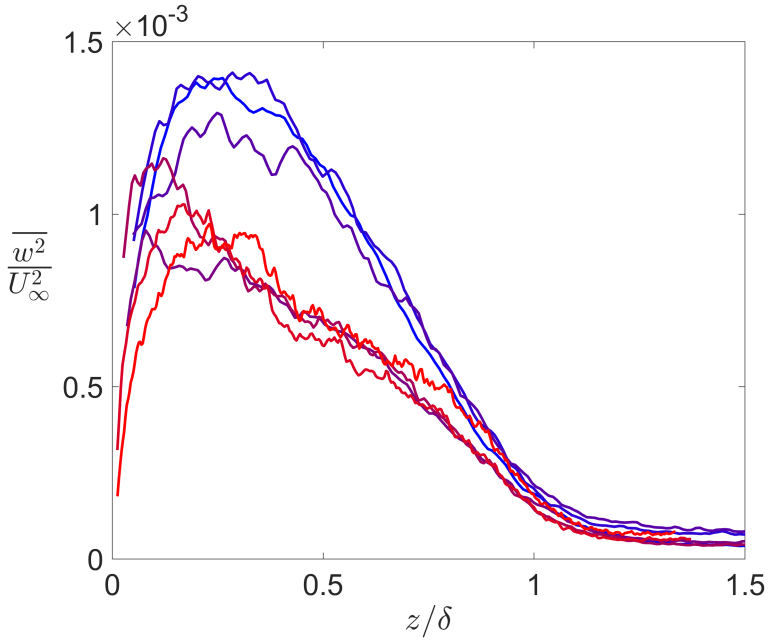

Figure 3.17 Variance of wall-normal fluctuation $\overline{w^2}$ at seven streamwise stations from Table 3.2. See Fig. 3.16b for legend.

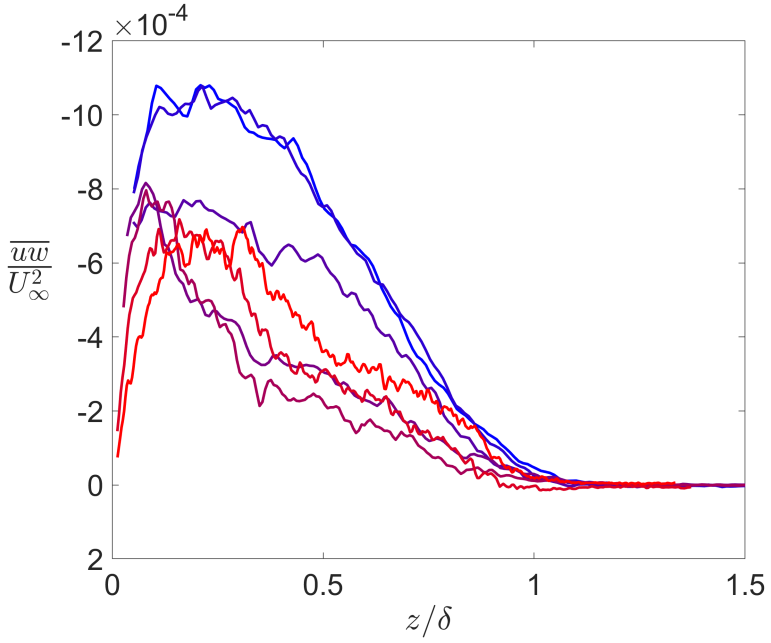

Figure 3.18 Reynolds shear stress $\overline{uw}$ at seven streamwise stations from Table 3.2. See Fig. 3.16b for legend.

3.2.4 Reynolds Stresses

The streamwise turbulence intensity is displayed in Fig. 3.16. The four subfigures show $\overline{u^2}$ normalized by *(a)* the friction velocity u_τ, *(b)* the edge velocity U_e, *(c)* the Zagarola-Smits velocity $U_{zs} = U_e\delta^*/\delta$ [68], and *(d)* the free-stream velocity U_∞. Seven streamwise stations are shown in each plot, with blue again denoting the upstream location and red indicating the downstream location.

Figure 3.16(a) uses a viscous scaling for the wall-parallel turbulence intensity. The inner scaled variance $\overline{u^2}/u_\tau^2$ develops an "outer peak" that shifted outward with downstream distance. The current outer peak was, to an extent, an artifact of the diminishing wall shear stress that inflated the u variance. This inner scaling was not particularly meaningful in the outer region because, for a non-equilibrium boundary layer, the wall shear stress has little correspondence to the outer region directly above, as the turbulence produced at the wall requires time to traverse the boundary layer thickness [51, 215].

In Figs. 3.16(b) and 3.16(d), the local wall-parallel edge velocity U_e and free-stream velocity U_∞ were used. Neither of these scalings provided a satisfactory collapse of the streamwise variance. However, they highlight the decreasing energy near the wall at downstream positions, as previous workers have demonstrated for APG boundary layers [4, 5].

The Zagarola-Smits scaling $U_{zs} = U_e\delta^*/\delta$ [216] was also examined as shown in Fig. 3.16(c), showing little success. The quantity u_{rms}/U_{zs} was also inspected with a similar conclusion. Balantrapu et al. [5] showed that the embedded shear layer scaling based on the vorticity thickness and the edge velocity was superior to the ZS scaling in their decelerating axisymmetric boundary layer. The ESL would likely be successful for the current boundary layer too. Recently, Silva and Wolf [73] found roller structures that support the inflectional instability as the mechanism responsible for this outer peak.

The trends of $\overline{u^2}$ were analyzed by inspecting Fig. 3.16(d), which used a constant U_∞ for scaling. There were two distinct trends. First, $\overline{u^2}$ in the outer region was nearly "frozen" as the streamwise energy decayed near the wall, forming a "peak" that continuously shifted

outward [4, 5]. Second, there was a subtle but noticeable decrease in $\overline{u^2}$ from $x/L = 0.70$–0.78 across nearly the entire boundary layer thickness.

The first trend was similar to the planar APG boundary layer shown in Fig. 1.5 [4], except for the region $z/\delta < 0.1$, where the current $\overline{u^2}$ continued to decrease whereas the planar case inflected upward. This difference could be explained by the higher Reynolds number shifting the inner peak closer to the wall. The second trend of decreasing $\overline{u^2}$ between $x/L = 0.70$–0.78 resulted from the FPG because neither longitudinal nor lateral curvature was present. This trend was consistent with those observed in Fig. 3 of Harun et al. [3]. Overall, the streamwise turbulence intensity seemed more sensitive to the pressure gradients than the wall curvature.

The diagnostic plot in Fig. 3.8 showed wall-parallel turbulence intensity to decrease continuously downstream because of the lateral curvature. However, $\overline{u^2}$ in Fig. 3.16(d) was relatively constant in the outer region. This apparent contradiction is resolved by understanding that the diagnostic plot indicated a difference from planar boundary layers under a specific scaling, whereas Fig. 3.16(d) shows that $\overline{u^2}$ was comparable to itself across different stations.

Figure 3.17 shows the wall-normal velocity variance relative to the free-stream velocity. The blue and red lines denote the most up and downstream stations. Relative to $\overline{w^2}$ at the inlet, the wall-normal fluctuation intensity was suddenly and significantly attenuated in the outer region at $x/L = 0.81$. This attenuation was likely unrelated to the pressure gradient because Nagano et al. [4] showed in Fig. 1.5 that $\overline{w^2}$ was entirely insensitive to the adverse pressure gradients. Lateral curvature effects were nascent at these axial stations, as discussed in Section 3.2.3. Therefore, the longitudinal curvature could be responsible for this rapid decrease in $\overline{w^2}$.

The spatial variations in $\overline{w^2}$ and longitudinal curvature parallel one another. Muck et al. [213] described convex curvature as stabilizing, attenuating the turbulence intensity without modifying the average eddy shape. In Fig. 3.17, the suppressed $\overline{w^2}$ was initially observed at $x/L = 0.78$ and was pushed closest to the wall at $x/L = 0.85$. The values in the outer

region $z/\delta > 0.3$ were largely invariant further downstream, as expected for an APG flow [4]. In comparison, Fig. 3.12(c) shows the longitudinal convex curvature spanning $x/L \approx 0.75$–0.87, with δ/R_c being most significant at $x/L \approx 0.8$. This concurrence perhaps indicated the longitudinal convex curvature attenuated $\overline{w^2}$, knowing that convex curvature effects manifest much more rapidly than concave curvature effects [213].

For positions beyond $x/L = 0.85$, the wall-normal fluctuation intensity was progressively reduced in the near-wall region, leading to a small plateau at $z/\delta = 0.3$. This near-wall reduction was unrelated to the pressure gradient, which Nagano et al. [4] showed did not affect $\overline{w^2}$. Because this trend persisted through the convex and concave regions, the longitudinal curvature was unlikely to be the cause. Concave and convex curvatures have drastically different effects, and Muck et al. [213] expected an almost discontinuous change in flow characteristics when transitioning from one to the other. Therefore, the lateral curvature should be responsible for this trend. The initial decrease at $x/L = 0.85$ and the continued decrease downstream align with the δ/a trends shown in Fig. 3.12(b).

Figure 3.18 shows the wall-tangent–wall-normal Reynolds shear stress $\overline{uw}$ in this boundary layer. In the outer region, $\overline{uw}$ decreased from $x/L = 0.78$–0.85, likely because the convex curvature attenuated the wall-normal activity, suppressing the exchange of high and low momentum fluids. The near-wall ($z/\delta < 0.2$) reduction was a result of both the pressure gradient and the transverse curvature, as previously explained for $\overline{u^2}$ and $\overline{w^2}$.

Because turbulence is a multi-scale phenomenon, the flow was decomposed into large and small scales. The two scales can be examined individually [97] to understand better how the pressure gradient and wall curvature affected flow statistics. The large scales are particularly important as ingestion leads to distinct peaks in the noise spectra [28].

Most previous works chose a Fourier cutoff wavelength of $\lambda_x = \delta$, above which is the large scale and the remainder is the small scale. However, the proper orthogonal decomposition (POD) would be better suited to the current boundary because of the longitudinal inhomogeneity. The procedure for computing the POD and the mode truncation is discussed

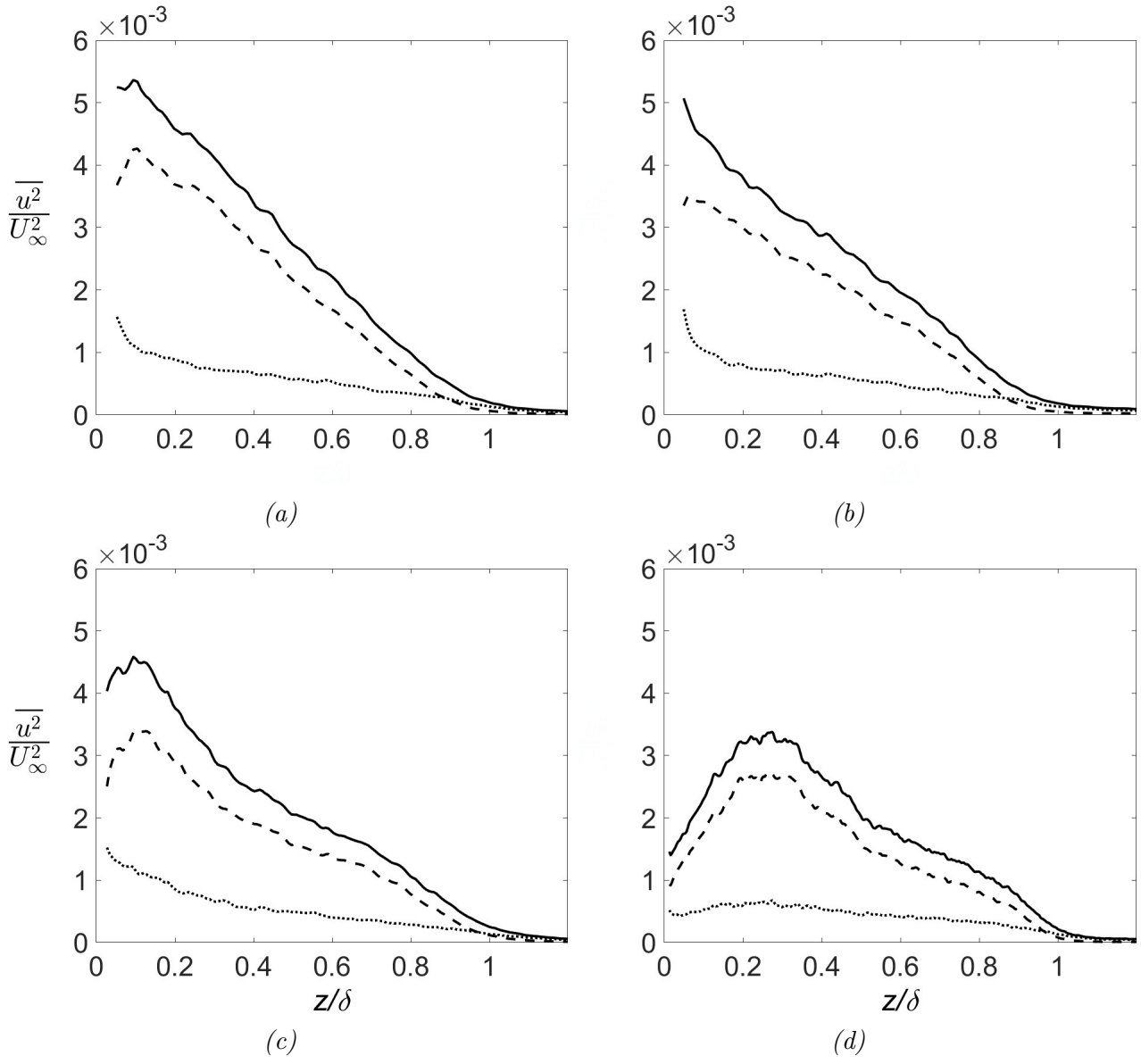

Figure 3.19 Wall-parallel velocity variance $\overline{u^2}$. The solid lines are u, dashed lines are u_L, and dotted lines are u_S. *(a)* $x/L = 0.70$ with nearly ZPG; *(b)* $x/L = 0.78$ at the end of FPG; *(c)* $x/L = 0.85$ with increasing APG; *(d)* $x/L = 0.93$ with decreasing APG.

in Appendix C.

It suffices to explain here that all four FOVs were used simultaneously in the POD, and a low-rank flow field representing the energetic large scales was created as

$$U_L = \Phi_r \Sigma_r \Psi_r^T \tag{3.6}$$

using the leading 200 modes that resolved 50% of the measured turbulent kinetic energy (TKE), following the threshold choice of Wu and Christensen [217]. In the preceding equation, $U_L \in \mathbb{R}^{n_s \times n_t}$ contains all velocity components at various spatial locations. The matrices $\Phi_r \in \mathbb{R}^{n_s \times n_m}$ and $\Psi \in \mathbb{R}^{n_t \times n_m}$ are the leading $n_m = 200$ spatial and temporal modes, respectively. The number of spatial locations multiplied by the number of velocity components is n_s, the number of snapshots is n_t, and number of modes used in the low-rank flow was n_m. Large (subscript "L") and small (subscript "S") scales sum to the original flow field.

$$\begin{aligned} u &= u_L + u_S, \\ w &= w_L + w_S. \end{aligned} \tag{3.7}$$

Following this definition, $\overline{u^2} = \overline{(u_L + u_S)^2} = \overline{u_L^2} + \overline{u_S^2} + 2\overline{u_L u_S}$. However, the cross term $\overline{u_L u_S}$ was omitted from the analysis because it was virtually zero.

The wall-parallel profile of $\overline{u^2}$ was divided into large- and small-scale contributions in Fig. 3.19 at four different streamwise locations of $x/L = 0.70$, 0.78, 0.85, and 0.93. These stations correspond to regions of nominally ZPG, end of FPG, increasing APG, and end of APG. In each figure, the solid line denotes u, the dashed line u_L, and the dotted line u_S. Note the abscissa is not in logarithmic scale.

At the most upstream position in Fig. 3.19(a), the energy peak of the large scale appeared in the log region at $z/\delta = 0.1$. The small-scale energy peak was closer to the wall in a region inaccessible to the current PIV setup. These large and small scale distributions were

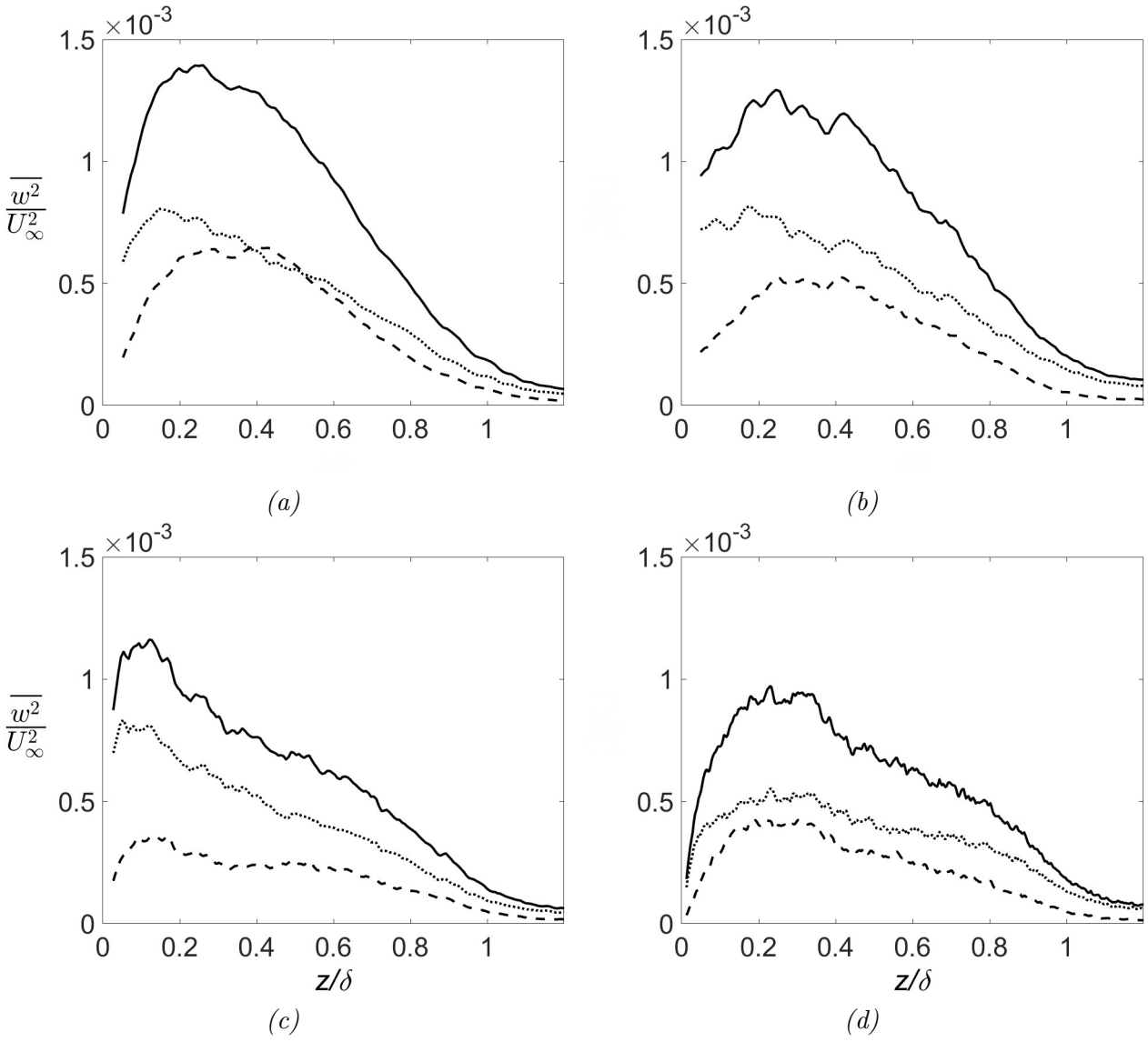

Figure 3.20 Wall-parallel velocity variance $\overline{w^2}$. The solid lines are u, dashed lines are w_L, and dotted lines are w_S. *(a)* $x/L = 0.70$; *(c)* $x/L = 0.78$; *(c)* $x/L = 0.85$; *(d)* $x/L = 0.93$.

consistent with the work of Monty et al. [6]. Similar trends were observed at streamwise locations of $x/L = 0.78$ and 0.85, although the peak energy of the large scales gradually shifted outward with the APG. This outward shift was most pronounced at $x/L = 0.93$ and aligned with the energy peak of $\overline{u^2}$ at the same z/δ. This coincidence confirms that the outer peak in $\overline{u^2}$ can be attributed to large-scale activity.

The wall-parallel velocity from the POD is shown in Fig. 3.20. The figure follows the same format as Fig. 3.19. Across all the axial stations, the small scale was more energetic than

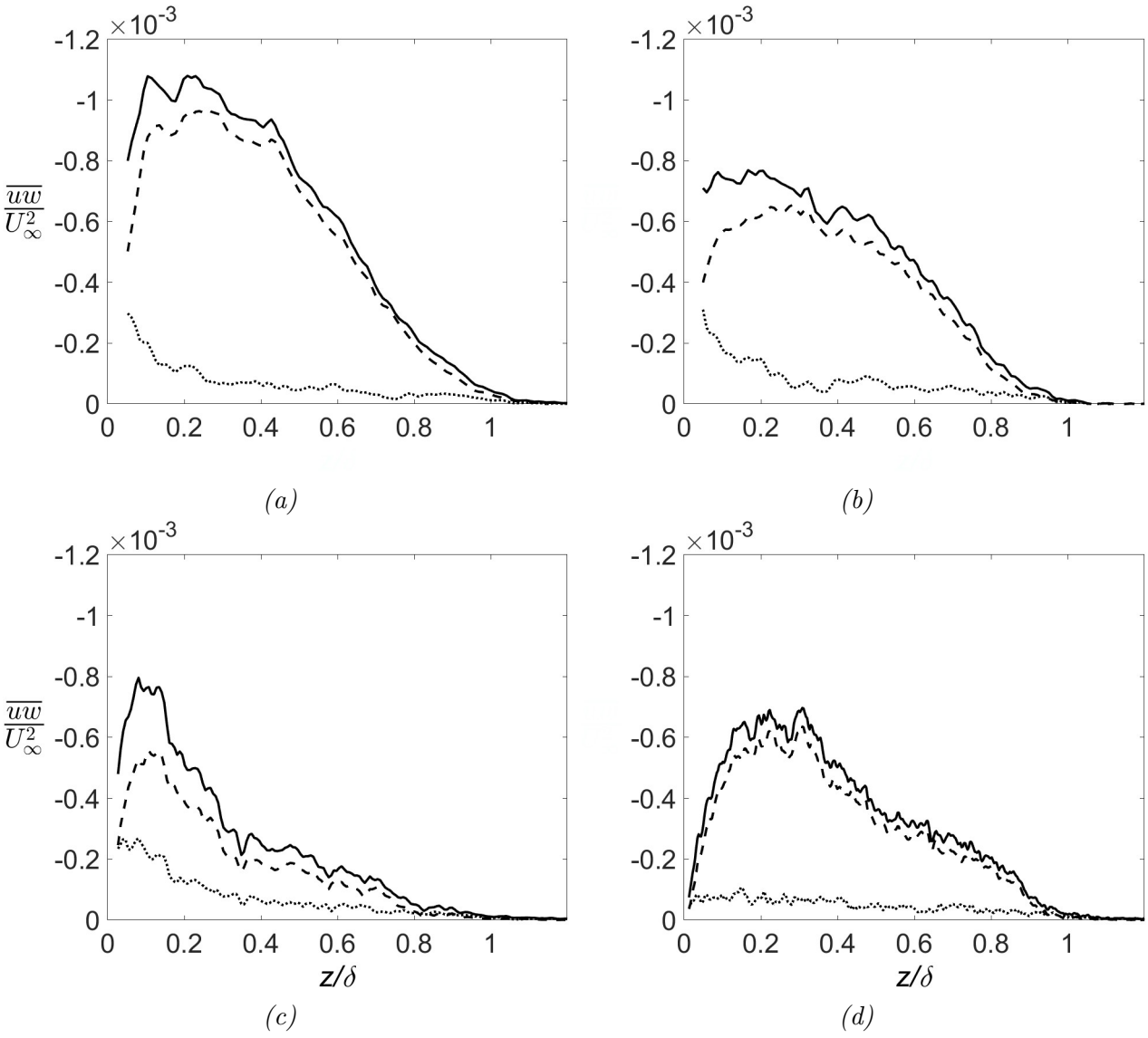

Figure 3.21 Reynolds shear stress $\overline{uw}$. The solid lines are $\overline{uw}$, dashed lines are $\overline{u_L w_L}$, and dotted lines are $\overline{u_S w_S}$. *(a)* $x/L = 0.70$; *(c)* $x/L = 0.78$; *(c)* $x/L = 0.85$; *(d)* $x/L = 0.93$.

the large, likely because the wall-normal fluctuations were not as intense and well-organized as the streamwise velocity, which dominated the reconstructed low-rank flow. The spectral analysis in the subsequent chapter shows the wall-normal fluctuation to be significantly higher in frequency content.

The Reynolds shear stress was also decomposed using the POD as shown in Fig. 3.21, following the same format. Across all streamwise stations, $\overline{uw}$ was determined almost entirely by large-scale structures. These figures highlight the persisting role that large eddies have in

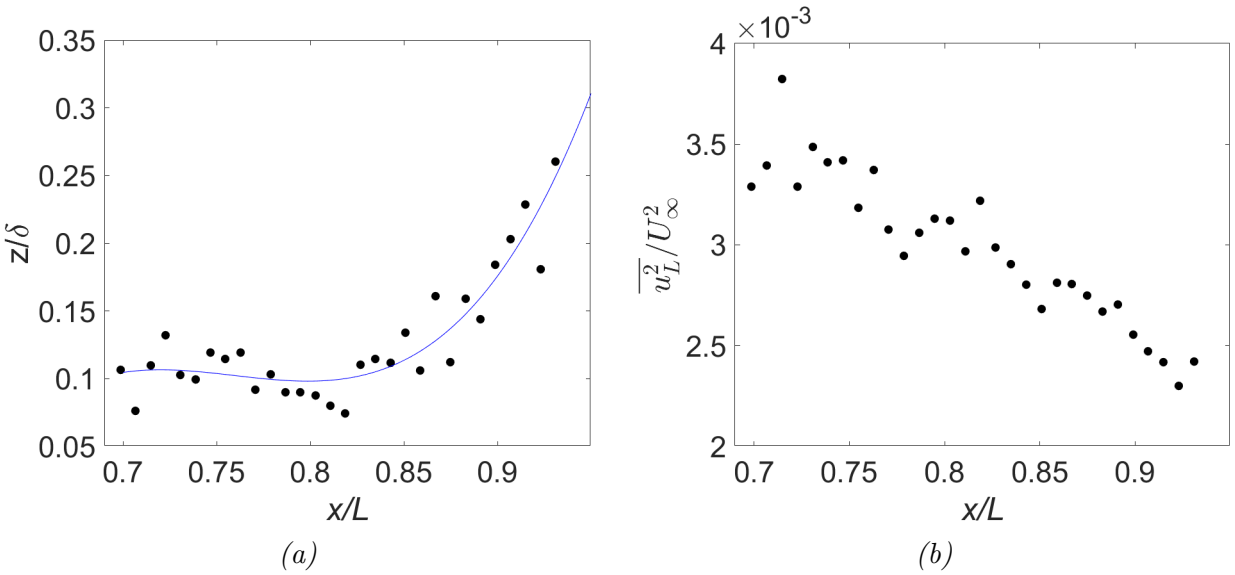

Figure 3.22 (a) Location and *(b)* value of maximum variance for the large scales $\overline{u_L^2}$.

turbulent mixing, irrespective of pressure gradient and wall curvature.

The effects of wall curvature and pressure gradient on the large and small scales are shown in Fig. 3.23. The first, second, and third rows show $\overline{u^2}$, $\overline{w^2}$, and $\overline{uw}$. The left and right columns correspond to large and small scales. Line colors transition from blue to red with increasing axial position. The nominal ZPG condition is shown using solid lines, the FPG region using dashed lines, and the APG region using dotted lines.

Figure 3.23(a) shows that the small scales associated with the wall-tangent velocity were minimally impacted in the outer region. In contrast, (b) demonstrates that the pressure gradient significantly modified the large scales and likely the surface curvature. In Fig. 3.23(c) and (d) of $\overline{w^2}$, the large and small-scale energy levels were comparable. However, one distinction was that the $\overline{w^2}$ decrease from the blue to the red curves was more pronounced in the large scales. Another was the small-scale near-wall energy was attenuated with streamwise distance. The Reynolds shear stress $\overline{uw}$ shown in Fig. 3.23(e) and (f) highlight the critical role of the large scales. Again, these large-scale sweeps and ejections followed the trends of u_L and w_L. Overall, it was evident that the non-equilibrium conditions predominantly affected the large scales.

Figure 3.23(a) shows that large-scale wall-tangent fluctuations dominated the Reynolds stress by an order of magnitude. The location and value of the maximum wall-parallel variance $\overline{u_L^2}$ were recorded at 30 stations to understand the large-scale dynamics. Figure 3.22(a) shows the large-scale energy peak shifting closer to the wall with FPG and outward with the APG, as highlighted by the blue line, a best-fit polynomial. Figure 3.22(b) shows the maximum variance decreasing downstream nearly linearly. These variations were challenging to interpret. To this end, the next chapter will elaborate on how the pressure gradient and wall curvature modified the large-scale flow structures.

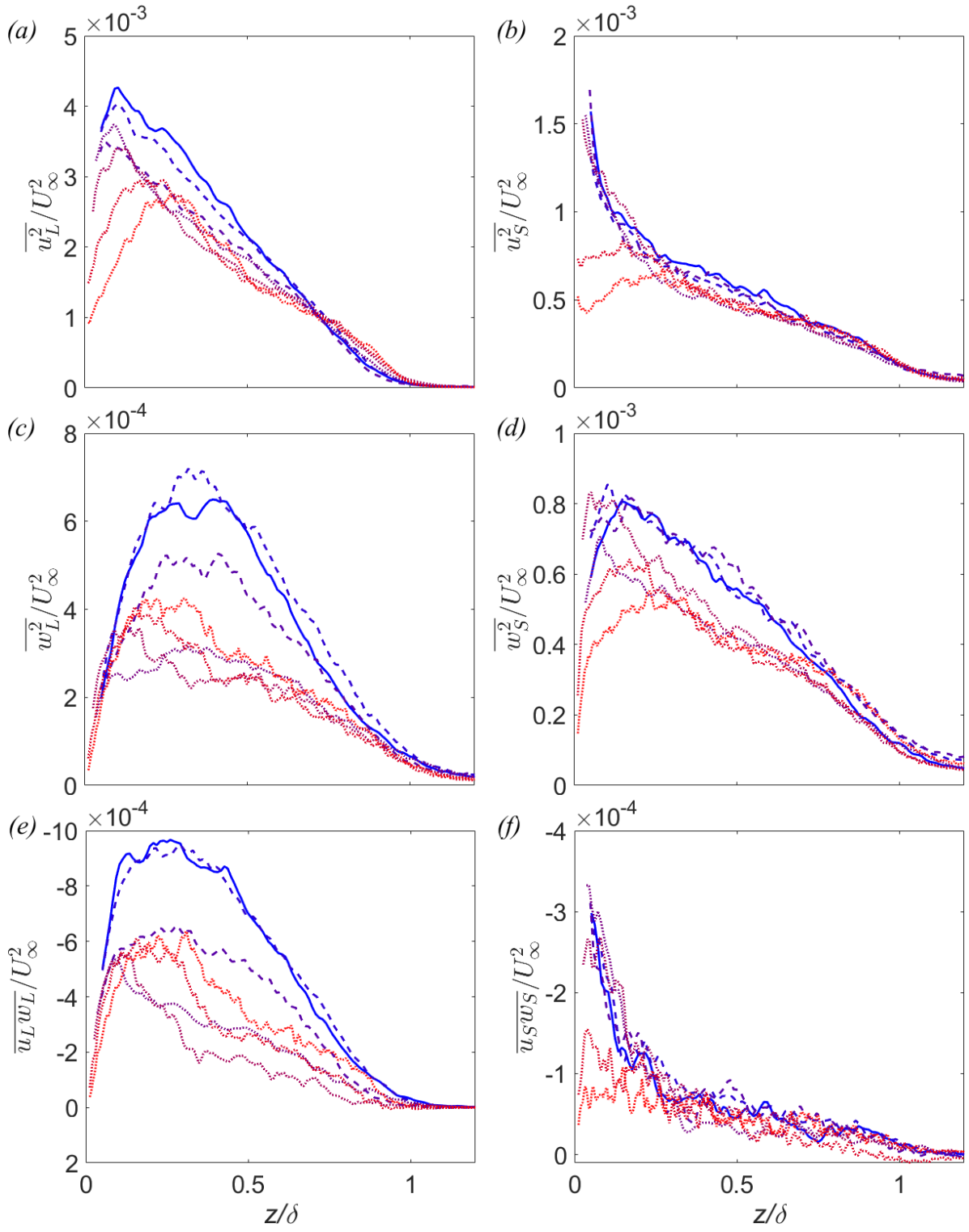

Figure 3.23 Decomposition of Reynolds stresses *(a,b)* $\overline{u^2}$, *(c,d)* $\overline{w^2}$, and *(e,f)* $\overline{uw}$ using the POD into *(a,c,e)* large and *(b,d,f)* small scales. Blue to red indicates increasing axial position. Solid lines indicate ZPG, dashed lines indicate FPG, and dotted lines denote APG. See Fig. 3.16b for color legend.

3.2.5 Summary of Single-Point Statistics

The boundary layer, formed along the constant diameter midbody, exhibited nearly canonical characteristics at the onset of the afterbody. However, the pressure gradient and the wall curvatures quickly modified the canonical state of the boundary layer. To comprehend these modifications, the pressure gradient was assessed as discussed in Section 3.1. Also, the longitudinal [200] and lateral [129] convex curvatures were quantified, and their relative significance was evaluated. Several inferences were made comparing the spatial variations in flow statistics and the known effects of these various factors. Contrary to prior works [109] that explained pressure gradient and wall curvature to affect the inner and outer regions, respectively, the statistical trends showed that their effects may extend the boundary layer thickness.

1. The diagnostic plot (Figure 3.8) revealed lower wall-parallel fluctuation intensity $\overline{u^2}$ relative to a canonical flow for $x/L > 0.81$, likely resulting from the growing lateral wall curvature shown in Fig. 3.12(b).

2. The wall-parallel fluctuation intensity $\overline{u^2}$ initially decreased in the outer region because of the FPG [3]. Subsequently, the APG attenuated the inner region fluctuation intensity in a manner comparable to a planar APG boundary layer [4]. Therefore, the pressure gradient appeared to have a more significant impact than the wall curvature on the wall-parallel flow statistics.

3. The wall-normal $\overline{w^2}$ was rapidly attenuated in the outer region as shown in Fig. 3.17 from $x/L = 0.74$–0.85, paralleling the longitudinal convex curvature [213].

4. The wall-normal $\overline{w^2}$ in Figs. 3.17 and 3.23(d) gradually diminished in the inner region ($z/\delta < 0.2$) beyond $x/L = 0.81$, following the trend of the lateral wall curvature δ/a in Fig. 3.12(b).

5. A proper orthogonal decomposition into large and small scales revealed that large scales

were more susceptible to the effects of pressure gradient and wall curvatures than small scales.

3.3 Two-Point Statistics

Two-point correlations are used to deduce the average eddy and how it correlates with flow quantities at different points in space. Understanding and modeling these correlations underpin much of turbulence research and is crucial for engineering applications. Therefore, this chapter gives insight into the boundary layer structural response to pressure gradient and wall-curvature effects. First, the energy spectra were investigated in Section 3.3.1. Next, Section 3.3.2 examines the spatial two-point correlations. Subsequently, the hairpin vortex organization was elicited through linear stochastic estimation [25] in Section 3.3.3. Lastly, high and low-speed regions were studied in Section 3.3.4 to better understand the flow kinematics at the boundary layer edge.

3.3.1 Energy Spectra

Whereas the velocity variance discussed in Section 3.2.4 is the energy integrated across all the (resolved) scales, this section decomposes the turbulence into its harmonic components for a deeper understanding. Spectra are commonly presented in the wavenumber k or wavelength λ space, perhaps because thinking of turbulence structures as having a certain length is more intuitive. However, the present results were interpreted in the frequency domain without invoking Taylor's frozen field hypothesis. The longitudinal inhomogeneity suggested that the convection velocity may not equal the mean [5, 116].

As described in Section 2.4.2, the boundary layer was sampled at four streamwise stations of $x/L = 0.65$, 0.78, 0.85, and 0.92. The spectral analysis used data from the lower Reynolds number with $U_\infty = 50\ \mathrm{ft\,s^{-1}}$, as the measurements with $U_\infty = 200\ \mathrm{ft\,s^{-1}}$ were still being processed. The lower Reynolds number does imply a limited separation between the large and small scales. Nonetheless, interesting trends were observed, highlighting the effects of pressure gradient and wall curvature on the flow structures.

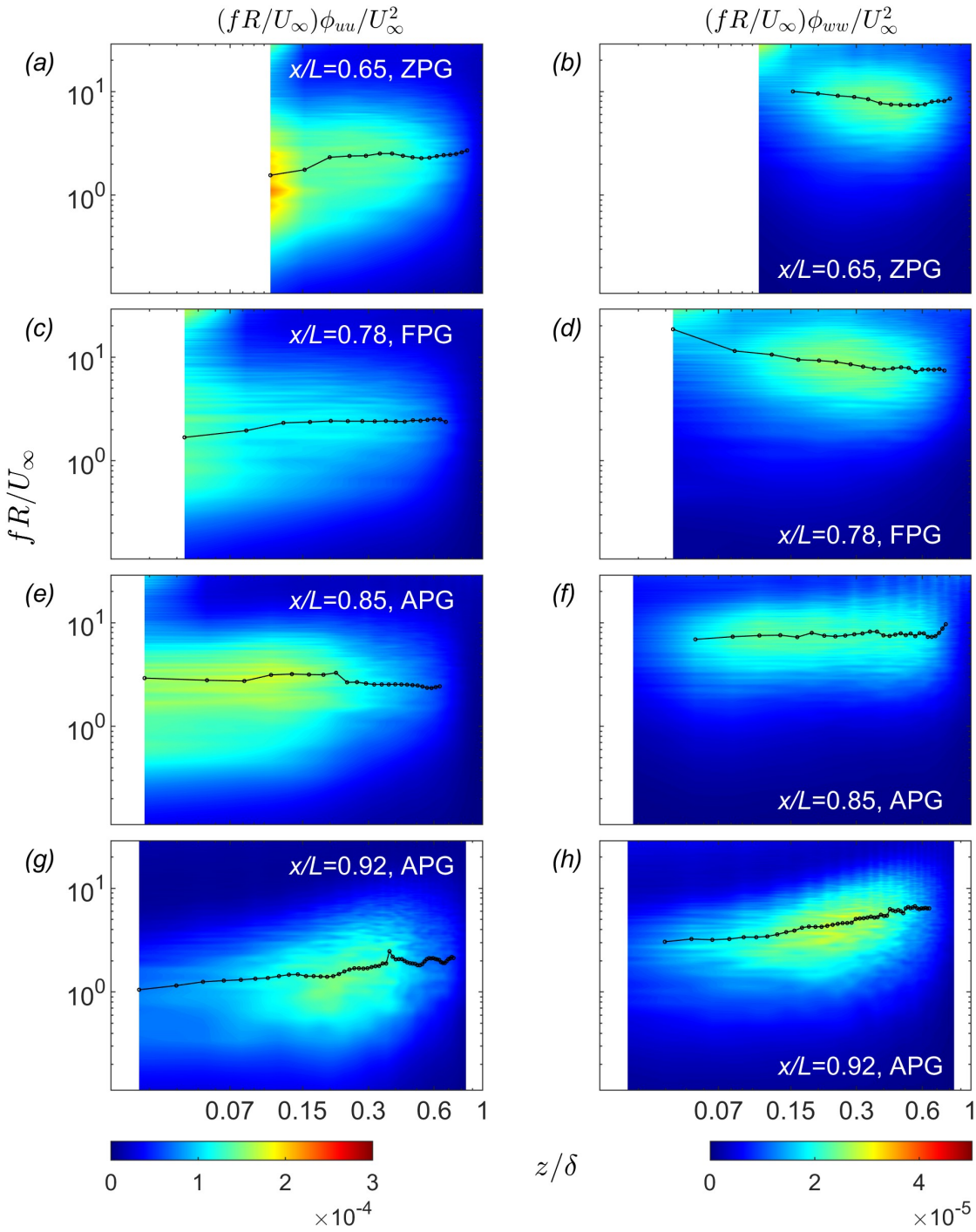

Figure 3.24 Premultiplied power spectra of *(a,c,e,g)* wall-parallel ϕ_{uu} and *(b,d,f,h)* wall-normal ϕ_{ww} across the four streamwise locations of *(a,b)* $x/L = 0.65$, *(c,d)* $x/L = 0.78$, *(e,f)* $x/L = 0.85$, and *(g,h)* $x/L = 0.92$. The abscissa is the wall-normal z made dimensionless by the local boundary layer thickness δ, and the ordinate is the frequency f multiplied by the hull radius R and divided by the free stream U_∞. The black dotted lines indicate the frequency of the peak energy. The color scales are below the figures.

The discrete Fourier transform was performed by dividing the 160,000 vector fields sampled contiguously over 10 s into overlapping (50%) intervals of 2^{10} elements. Hann windows were used to reduce spectral leakage. Up to three of these datasets were sometimes used to achieve better statistical convergence. Results from the low-magnification camera were used because they were sufficient for analyzing the outer region's large-scale structures.

The premultiplied spectra of the wall-parallel and wall-normal velocities are shown in Fig. 3.24 for all measurement locations based on the low-magnification camera. The left column (a, c, e, g) shows the premultiplied, nondimensional wall-parallel velocity spectra of $(fR/U_\infty)\phi_{uu}/U_\infty^2$, and the right column (b, d, f, h) shows the wall-normal counterpart.

The abscissa in this figure is the wall-normal z made dimensionless by the local boundary layer thickness δ, and the ordinate is the frequency f multiplied by the hull radius R and divided by the free stream U_∞. These scaling variables were chosen to understand the ϕ behavior. The black dotted lines indicate the (premultiplied) peak energy frequency at each wall-normal location, similar to Romero et al. [74]; peak frequencies are not shown at heights where the spectra were below an energy threshold. Finally, the color scales below the figures show an order of magnitude difference between the wall-parallel u and wall-normal w.

The premultiplied ϕ_{uu} is shown in the left column of Fig. 3.24. Figure 3.24(a) shows where the boundary layer was nearly ZPG. The tick marks on the horizontal axis correspond to where line plots of the spectra will be studied. The inner peak, typically reported around $z^+ = 12$–15, was not visible as the lowest point in this figure is $z^+ \approx 70$ or $z/\delta \approx 0.1$. However, the energy was concentrated in the near wall region as expected [218].

As for the outer peak in the log region, Hutchins and Marusic [79] reasoned that it would be located between $z^+ > 100\nu/u_\tau$ and $z/\delta < 0.15$, and Mathis et al. [76] refined the peak location to $z^+ = \sqrt{15Re_\tau}$, the geometric center of the log region. At the current $Re_\tau = 822$, the outer peak would be located at $z^+ = \sqrt{15Re_\tau} = 110$ or $z/\delta = 0.135$ and is expected to be weak. Examining the line plot for $z/\delta = 0.15$ in Fig. 3.27(a), the spectrum shows a brief plateau with the lower end at $f \approx 0.6U_\infty/R$. Using Taylor's hypothesis of $\lambda_x = U_c/f$ and

$U_c = 0.7U_e$ yielded $\lambda_x \approx 120$ mm $\approx 6\delta$ [219]. Overall, the trends reaffirmed the near canonical state at $x/L = 0.65$, establishing a baseline for the subsequent analysis of non-equilibrium effects.

The effects of pressure gradient and surface curvature on the wall-parallel velocity spectra are shown in Figs. 3.24(c), (e), and (g). Figure 3.24(c) shows the spectra measured at $x/L = 0.78$, the end of the FPG region. Here, the contour shape was quite similar to that in Fig. 3.24(a), while the intensity of the fluctuations was attenuated across all frequencies and wall-normal positions. This outcome was in accord with how the FPG reduced the variance across the outer region, as previously discussed in Fig. 3.16(d).

Entering the APG region at $x/L = 0.85$ shown in Fig. 3.24(e), the frequency contours remained qualitatively unchanged. However, the most intense fluctuation shifted away from the wall, consistent with the trends observed in Fig. 3.7. Lastly, Fig. 3.24(g) shows $x/L = 0.92$, where the APG decreased in strength. The contour appeared quite different from the previous ones. There was a low-frequency (large-scale) signature near the wall, but the energy peak was located around $z/\delta = 0.3$ centered about a premultiplied frequency of $f = 2U_\infty/R$.

The wall-normal velocity spectra are shown in the right column of Fig. 3.24. In the ZPG region ($x/L = 0.65$), the energy was concentrated in an oval region spanning $0.15 < z/\delta < 1$ with (premultiplied) frequency peaks located around $f = 10U_\infty/R$. By the end of the FPG ($x/L = 0.78$), the oval region appeared more elongated with more intense peak values.

The ϕ_{ww} spectra extended even deeper into the boundary layer in the increasingly APG region ($x/L = 0.85$). A different pattern emerged at $x/L = 0.92$ as shown in Fig. 3.24(h). The near-wall ($z/\delta < 0.15$) energy shifted toward lower frequencies. In contrast to ϕ_{uu} in Fig. 3.24(g), ϕ_{ww} in Fig. 3.24(h) showed an increased energy level relative to upstream measurement stations.

The black markers in Fig. 3.24 denote the frequencies of the maximum (premultiplied) energy. These frequencies are summarized in Fig. 3.25 for the wall-tangent (left) and wall-normal (right) velocities. Examining Fig. 3.25(a), the curves had two values in the outer

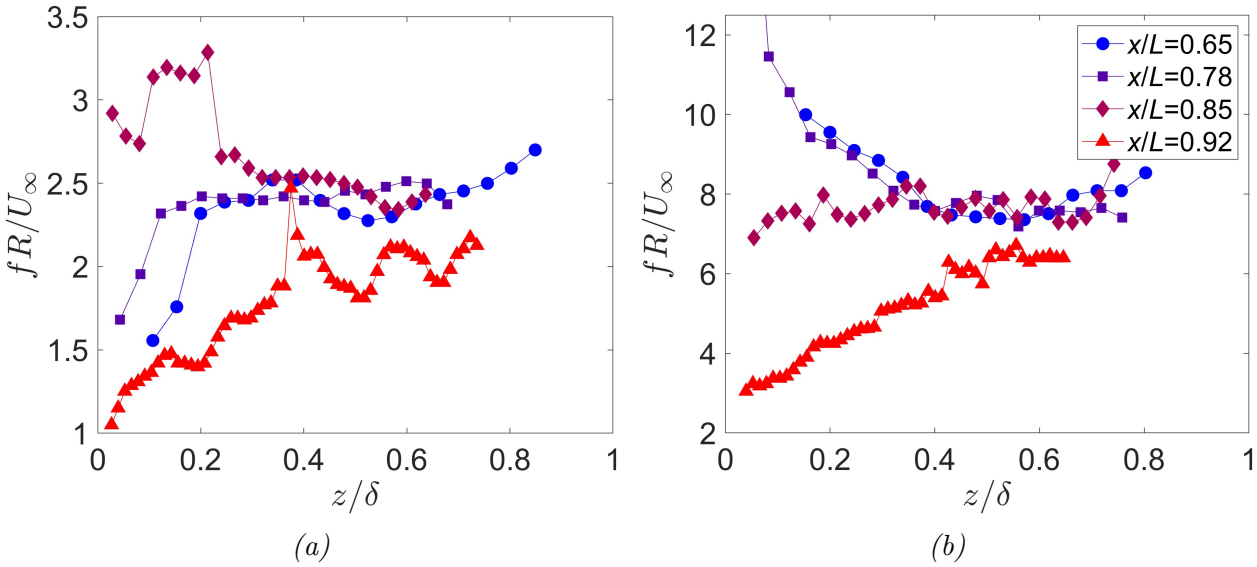

Figure 3.25 Summary across different heights of the frequencies where *(a)* wall-parallel u and *(b)* wall-normal w were most energetic. Frequencies were normalized by the hull radius R and free-stream velocity U_∞.

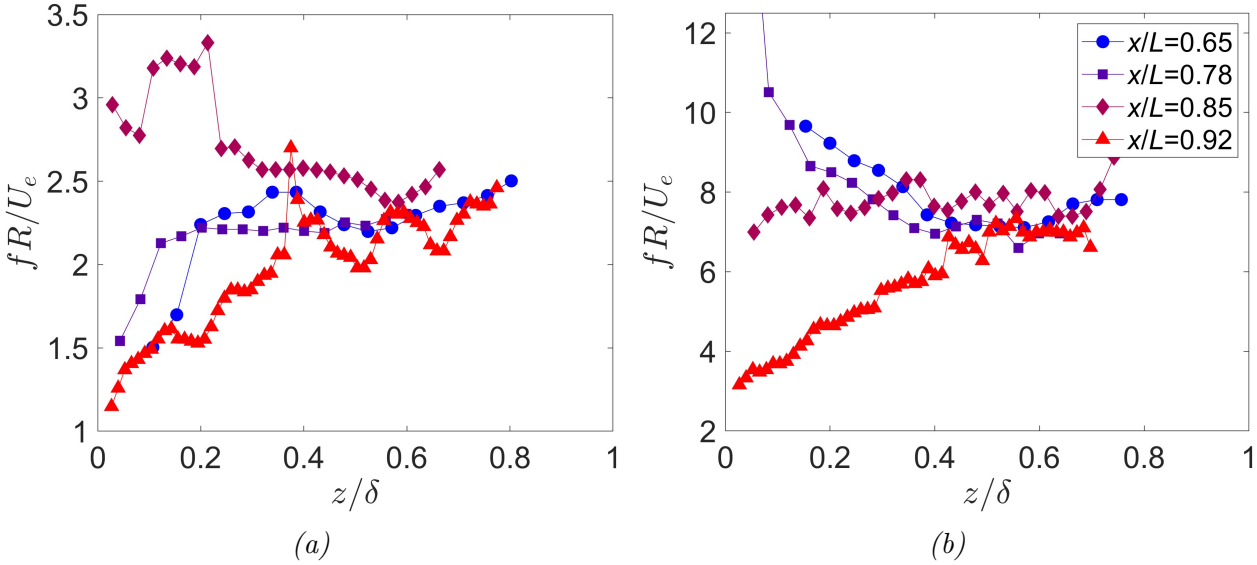

Figure 3.26 Summary across different heights of the frequencies where *(a)* wall-parallel u and *(b)* wall-normal w were most energetic. Frequencies were normalized by the hull radius R and the edge velocity U_e.

region ($z/\delta > 0.3$). The first included the results from $x/L = 0.65$, 0.78, and 0.85, which collapsed onto $f \approx 2.5U_\infty/R$ (to within some experimental scatter). The second group included only $x/L = 0.92$ (triangle), showing lower frequencies across the entire boundary layer thickness relative to the three upstream stations. Inspection of the wall-normal velocity

in Fig. 3.25(b) revealed a trend similar to the wall-parallel velocity—virtually no effect was observed in the outer region ($z/\delta > 0.3$) in the first three stations, and the peak frequencies at $x/L = 0.92$ were relatively lower across all heights.

This deviation in the outer region could be attributed to convection velocity. To this end, Fig. 3.26 shows the frequencies normalized by the edge velocity U_e. The outer region showed an improved agreement in non-dimensional frequency, indicating that the previously noted discrepancy was mainly attributable to the differences in convection speed. Therefore, subsequent figures will be scaled with U_e to help interpret the results.

The second trend noted in Figs. 3.25 and 3.26 was the significant premultiplied peak variations in the inner region. The wall-parallel u variations could be explained as an effect of the pressure gradient. Prior works have noted the u flow structure to contract in response to APG, suggesting that the corresponding frequency at $x/L = 0.85$ would be higher. Interestingly, the near-wall ($z/\delta < 0.2$) premultiplied peaks in Fig. 3.26(a) had similar values at $x/L = 0.65$ and 0.92, suggesting a recovery in the streamwise length scale as the APG was removed. The wall-tangent u length scales were examined using two-point correlation and will be discussed in Section 3.3.2.1.

The boundary layer state, however, was not entirely the same at $x/L = 0.65$ and 0.92. The wall-normal premultiplied peak frequencies in Fig. 3.26(b) decreased with increasing streamwise distance, distinct from its wall-tangent counterpart in (a). Consider u and w at $x/L = 0.65$. While eddies carry both wall-tangent and -normal fluctuations, different eddies were likely responsible for the dominant premultiplied frequencies at $x/L = 0.65$, which were separated by an order of magnitude. This reasoning was supported by examining spatial two-point correlations R_{uu} and R_{ww} for a ZPG boundary layer (Fig. 1.14), which have different spatial footprints.

In contrast, Figs. 3.26(a) and (b) show that the peak frequencies of ϕ_{uu} and ϕ_{ww} at $x/L = 0.92$ were proportional by a factor of 2.5. These two spectra also have similar contour shapes in Fig. 3.24(g) and (h). This similarity suggested that the same eddies were responsible for

the $f\phi_{uu}$ and $f\phi_{ww}$ peak frequencies at $x/L = 0.92$, because a hairpin packet induces a single low-speed u region but creates upwash and downwash (see LSE in Fig. 1.25 [20]), leading to w frequencies twice that of u. The trends in $f\phi_{ww}$ peak frequencies were not compatible with the pressure gradient trends, suggesting that the wall curvatures were responsible for this change.

Prior analysis in Section 3.2.4 showed that the wall-normal variances $\overline{w^2}$ in Fig. 3.17 were significantly attenuated, likely by the longitudinal curvatures. The current spectral analysis further showed that the w frequencies were reduced considerably in the near wall. Section 3.3.2.1 will provide a structural perspective for a more complete understanding.

An analysis was conducted to understand how the spectra changed with wall-normal and axial locations. Figure 3.27 presents the premultiplied spectra $f\phi_{uu}$ at four axial stations of $x/L = 0.65$, 0.78, 0.85, and 0.92. Each figure shows results across four different heights, with the lowest and highest denoted by the thin blue and thick red lines. The hull radius R and the edge velocity U_e were the reference length and velocity, respectively.

At $x/L = 0.65$ in Fig. 3.27(a), the spectra were most energetic near the wall and gradually shifted their peaks toward higher frequencies with wall distance. ($z/\delta = 0.07$ was inaccessible at this location with the low magnification camera.) This shift toward higher frequencies with wall-normal distance was consistent with fewer coherent hairpin packets in the outer region [9, 106]. A similar trend was noted at $x/L = 0.78$ in Fig. 3.27(b) except that energy levels were lower, likely an artifact of the FPG as discussed in Section 3.2.4. At these two upstream locations, results at $z/\delta = 0.07$ and 0.15 showed a plateau, pointing to a balance between the large and small scales.

In the increasingly APG region at $x/L = 0.85$, there was a brief plateau at $z/\delta = 0.07$, but the higher frequencies prevailed further from the wall, reminiscent of Harun [9]'s finding shown in Fig. 1.12(c). At the last streamwise location of $x/L = 0.92$, two trends were noted. First, the energy level increased with height until $z/\delta = 0.30$ and decreased after that, consistent with the maximum variance around $z/\delta = 0.3$ shown in Fig. 3.16(d). Second,

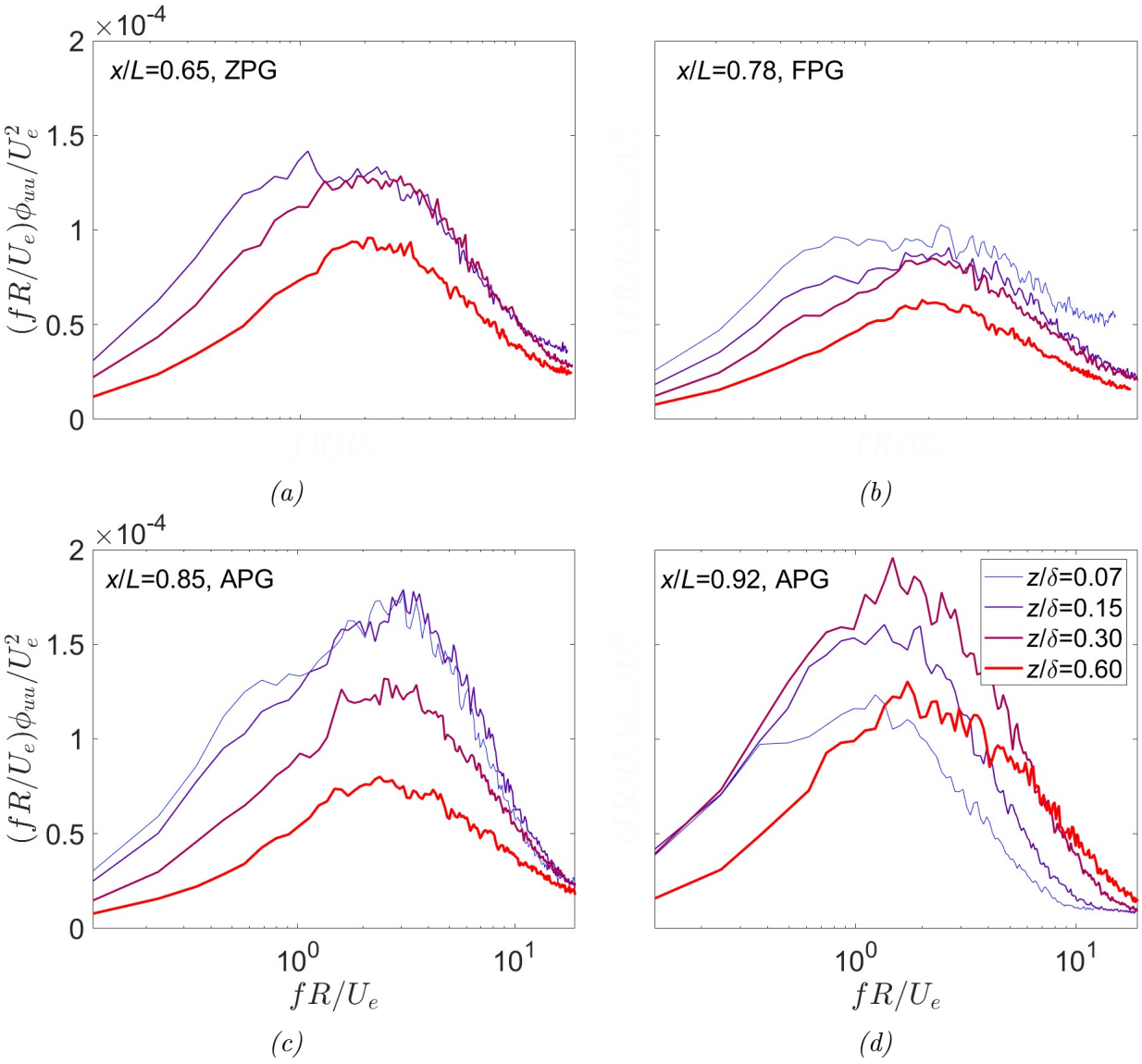

Figure 3.27 Premultiplied u spectra from four axial stations of *(a)* $x/L = 0.65$, *(b)* $x/L = 0.78$, *(c)* $x/L = 0.85$, and *(d)* $x/L = 0.92$. Each figure contains five spectra from different heights. As explained in the legend, the thin blue and thick red lines represent the lowest and highest wall-normal positions.

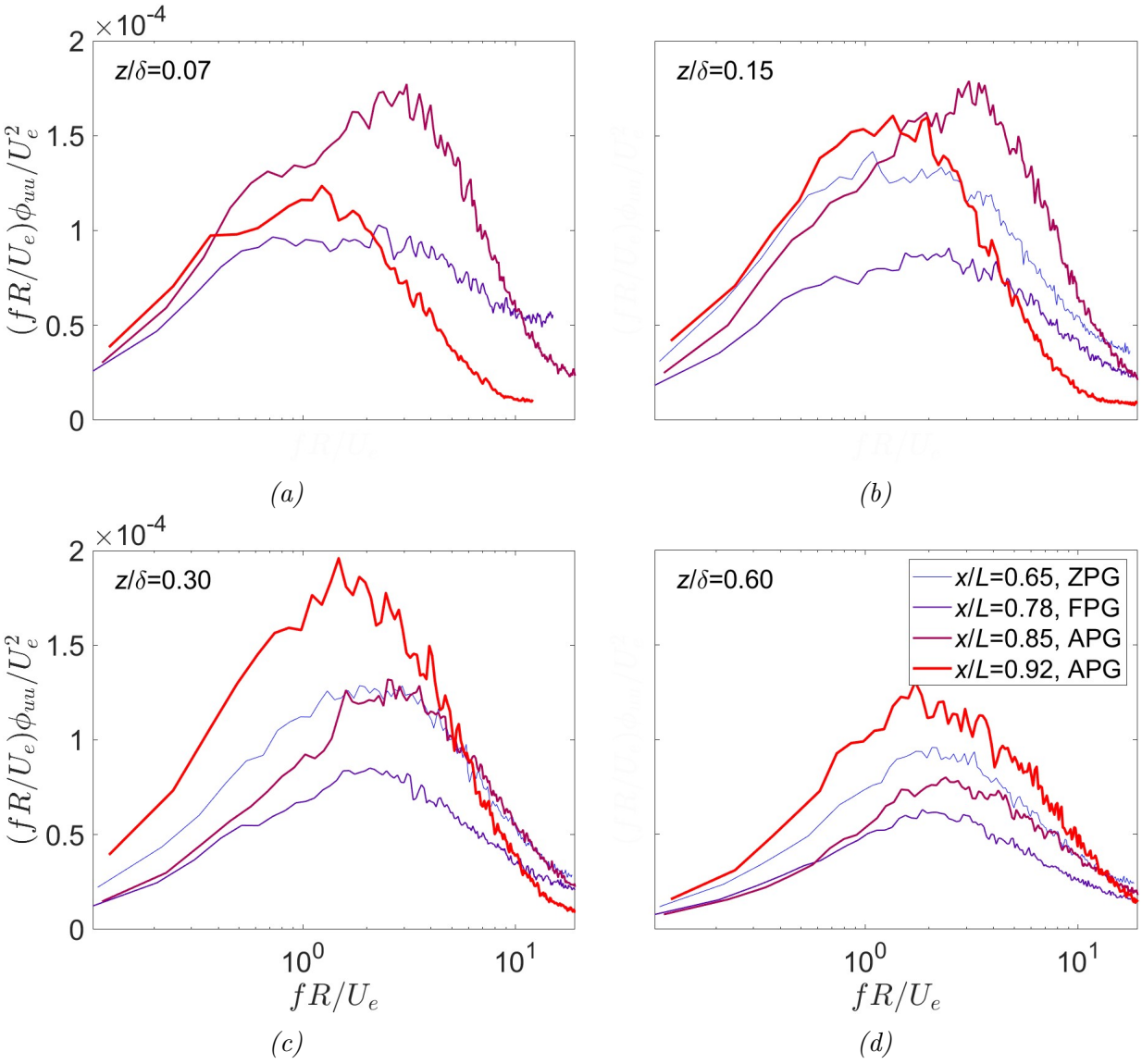

Figure 3.28 Premultiplied u spectra at four different heights of *(a)* $z/\delta = 0.07$, *(b)* $z/\delta = 0.15$, *(c)* $z/\delta = 0.3$, and *(d)* $z/\delta = 0.6$. Each figure contains four spectra from the different streamwise stations. As explained in the legend, the thin blue and thick red lines represent the most upstream and downstream stations.

there was a shift toward higher (premultiplied) peak frequencies with height, which could be related to higher convection velocities further from the wall.

An additional analysis focused on how the pressure gradient and curvature affected the spectra at a given height z/δ, as shown in Fig. 3.28. Each subfigure corresponds to a different height, and in each subfigure, there are four lines representing different streamwise locations. The reference length and velocity were again the hull radius R and the edge velocity U_e. The

thin blue and thick red lines represent the most upstream and downstream locations. The measurement at $x/L = 0.65$ did not reach $z/\delta = 0.07$ and was excluded from (a).

Examining Fig. 3.28(a), there was initially a plateau in the spectra at $x/L = 0.78$. Moving downstream to $x/L = 0.85$, the higher frequencies were energized, and a peak emerged at $fR/U_e \approx 3$. Lastly, the spectral peak was reduced to $fR/U_e = 1$ at $x/L = 0.92$. The increasing and decreasing spectral peaks likely indicated that the streamwise length scales were elongated and compressed in the log region. This trend was also apparent at the log layer edge ($z/\delta = 0.15$) in Fig. 3.28(b).

The results at $z/\delta = 0.3$ are shown in Fig. 3.28(c). Here, the peak frequencies were comparable across all four stations. This trend was also observed at $z/\delta = 0.6$ in (d) with lower energy levels. The trends in magnitude were an artifact of edge velocity variations, as determined based on inspection of line plots (figures not shown) normalized by the free stream U_∞.

Premultiplied spectra are shown in Fig. 3.29 for the wall-normal velocity fluctuation w. Each subfigure shows the wall-normal variation at an axial location. The thin blue and thick red lines correspond to points near and far from the wall. The w fluctuations were most intense at $z/\delta \approx 0.3$ across all the sampled locations but were roughly one-fifth the magnitude of their wall-parallel counterpart.

The upstream locations ($x/L = 0.65$ and 0.78) had similar trends, where the frequency peaks decreased with height. At $x/L = 0.85$, the energy level and peak location were comparable across all heights. The spectra at $x/L = 0.92$ showed the premultiplied peak frequency increasing with distance from the wall, contrary to the first two locations. This trend of increasing peak frequency with wall distance may highlight changes in the flow physics of w, as previously noted when inspecting Fig. 3.26(b).

Figure 3.30 shows the premultiplied spectra for the wall-normal w fluctuations but reorganized to convey variations with axial position, following a format identical to Fig. 3.28. In the log region at $z/\delta = 0.07$ and 0.15 shown in (a) and (b), the premultiplied peak decreased

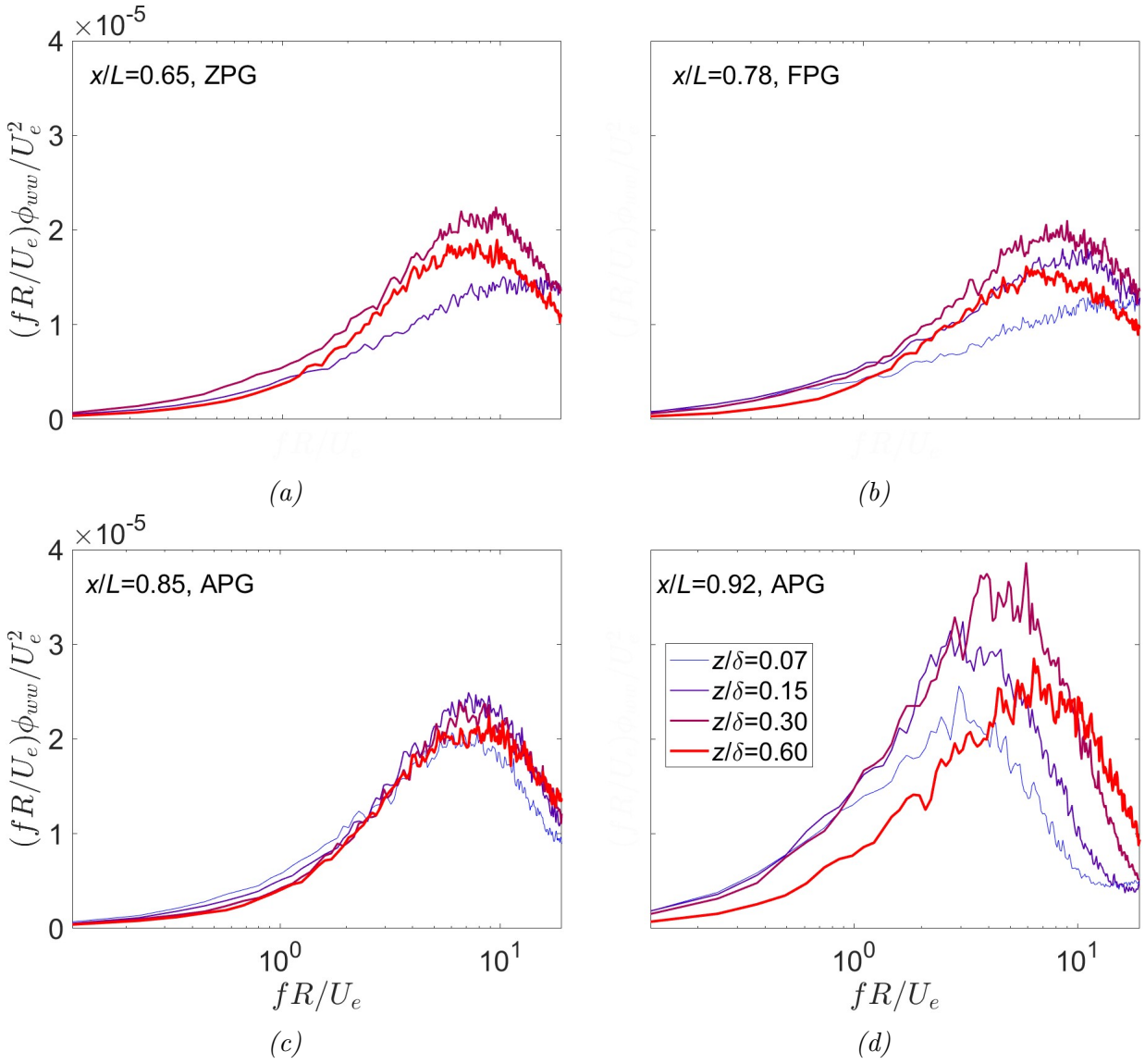

Figure 3.29 Premultiplied w spectra from four axial stations of *(a)* $x/L = 0.65$, *(b)* $x/L = 0.78$, *(c)* $x/L = 0.85$, and *(d)* $x/L = 0.92$. Each figure contains five spectra from different heights. As explained in the legend, the thin blue and thick red lines represent the lowest and highest wall-normal positions.

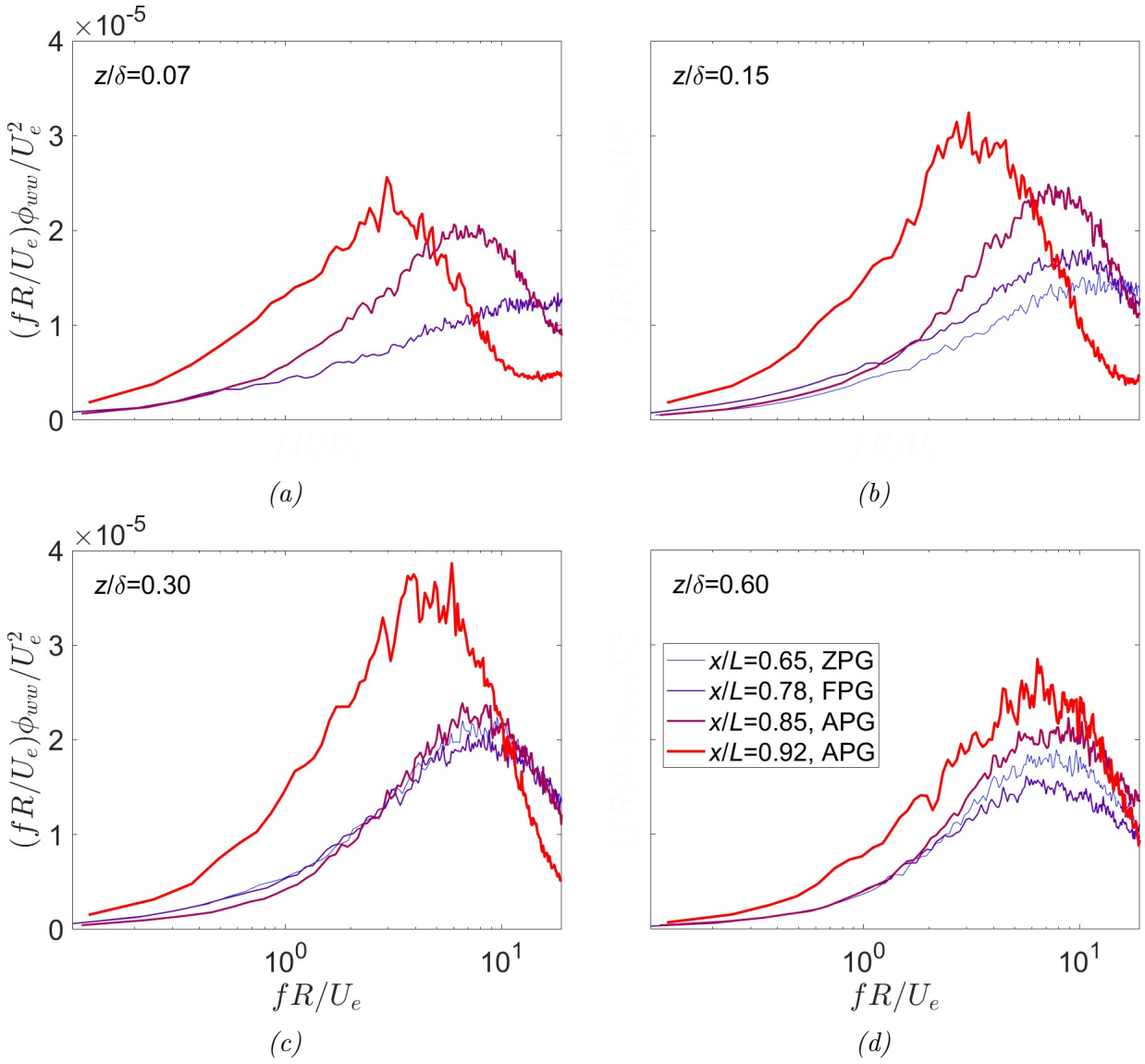

Figure 3.30 Premultiplied w spectra at four different heights of *(a)* $z/\delta = 0.07$, *(b)* $z/\delta = 0.15$, *(c)* $z/\delta = 0.3$, and *(d)* $z/\delta = 0.6$. Each figure contains four spectra from the different streamwise stations. As explained in the legend, the thin blue and thick red lines represent the most upstream and downstream stations.

with the streamwise position, identical to the trend highlighted in Fig. 3.26. At $z/\delta = 0.3$ shown in (c), the premultiplied peaks were comparable except for at $x/L = 0.92$, which had a lower frequency and a greater magnitude. Lastly, at $z/\delta = 0.6$, the premultiplied peak frequencies were similar across all sample locations. The variations in peak magnitude at $z/\delta = 0.60$ resulted from different edge velocities, based on inspection of figures (not shown) normalized by U_∞. These line plots highlighted the trends observed in the spectrograms in

Fig. 3.24 and the peak frequency analysis in Fig. 3.26.

The following conclusions could be drawn from the frequency spectra ($Re_\tau \approx 700$).

1. Neither the pressure gradient nor the wall curvature appreciably affected the u and w spectral peaks in the outer region [109], suggesting consistent u and w structures above $z/\delta = 0.4$ along the Suboff afterbody. See Fig. 3.25.

2. The increasing APG at $x/L = 0.85$ shifted the premultiplied energy peak of ϕ_{uu} to higher frequencies in the near wall region ($z/\delta < 0.3$). Then, the weak APG at $x/L = 0.92$ reduced the premultiplied peak frequencies near the wall to values comparable to the ZPG region at $x/L = 0.65$. This near-wall variation in ϕ_{uu} peak frequency likely indicated flow structure compression and elongation.

3. The ϕ_{ww} peak (premultiplied) frequency increased with wall-normal distance at $x/L = 0.65$ and 0.78. The trend was reversed at $x/L = 0.92$, where the peak frequency decreased with wall-normal distance. This reversal suggested that the surface curvature modified the physics governing the wall-normal velocity spectra.

4. At $x/L = 0.92$, hairpin packets were hypothesized to underlie the wall-normal fluctuation. This hypothesis was based on similar spectrograms, and that $f\phi_{ww}$ peaked at roughly twice the frequency of $f\phi_{ww}$. The latter is consistent with how a hairpin packet low-speed region induces upwash and downwash.

5. The wall-tangent ϕ_{uu} energy was roughly five times the wall-normal ϕ_{ww} energy, and the premultiplied frequency peak was roughly one-fifth to one-half that of ϕ_{ww}. See Fig. 3.24.

These findings should be reassessed in the future with higher Reynolds number data. Nonetheless, complementing the spectral analysis, the subsequent section presents spatial two-point correlations to understand better how the pressure gradient and wall curvature modified the large scales.

3.3.2 Two-Point Correlation

The two-point correlation provides a sense of the average eddy. In this section, two-point correlations of the wall-parallel velocity were first performed along streamlines. These results were similar to what would be obtained using hot-wire anemometry. Then, two-point correlations in the streamwise-wall–normal plane showed the average shape and inclination of the turbulent structures. Correlations were subsequently computed for all three velocity components in the four spanwise planes. Finally, this section provides a 3D perspective of the conditional structures. The results were based on data with $Re_\tau \approx 2{,}700$.

The two-point correlation was computed as,

$$R_{u_i u_j}(\boldsymbol{x}, \Delta\boldsymbol{x}) = \frac{\langle u_i(\boldsymbol{x}) u_j(\boldsymbol{x} + \Delta\boldsymbol{x}) \rangle}{\sqrt{u_i^2(\boldsymbol{x})}\sqrt{u_j^2(\boldsymbol{x} + \Delta\boldsymbol{x})}}. \tag{3.8}$$

In the above equation, u_i and u_j are placeholders for variables such as velocity, vorticity, etc. The reference quantity position is the vector $\boldsymbol{x}$, and the quantity to be correlated with the reference is displaced by $\Delta\boldsymbol{x}$ relative to the reference. The inner product of the two quantities is normalized by the product of their standard deviations.

3.3.2.1 Streamwise Plane

The length scale of the flow field was first examined using data from the large-FOV PIV setup described in Section 2.4.1. Two-point correlations were computed along streamlines based on the wall-tangent velocity u. Figure 3.31(a) shows three u correlations at $x/L = 0.726$ along streamlines from three wall-normal locations $z/\delta = 0.1$, 0.3, and 0.9. The tails of the blue curve in Fig. 3.31(a) indicate that the largest eddies were on average 6δ in the log layer ($z/\delta = 0.1$), reaffirming the near canonical boundary layer state [97]. Spanwise meandering of the large scales was not captured in this current setup [135, 219].

A length scale L_s was computed as the distance between where the two sides of R_{uu} first intersect 0.15. This threshold was chosen to reduce the noise level and best highlight variations in length scale. The length scale L_s reported in Fig. 3.31(b) shows a decreasing

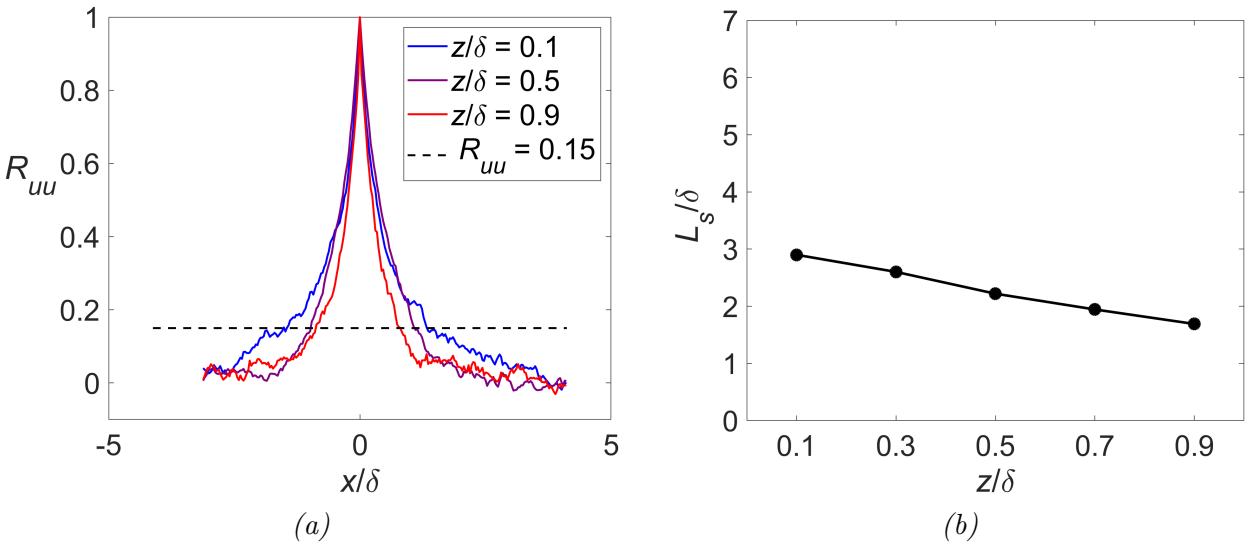

Figure 3.31 (a) Two-point correlation of u along streamlines for various wall-normal positions at $x/L = 0.726$. *(b)* Length scale L_s is defined as distance between where $R_{uu} = 0.15$.

trend with wall-normal distance z/δ, where δ is the local boundary layer thickness. This decreasing trend is consistent with the behavior of a canonical boundary layer measured by Hutchins and Marusic [97]. This decrease was also consistent with the growing $f\phi_{uu}$ peak frequencies with wall-normal distance in Figure 3.27(a).

The length scale was computed for other streamwise x and wall-normal z positions denoted by the red markers in Fig. 3.32. The results are summarized in Figs. 3.33, 3.34 and 3.35. Figure 3.33(a) shows a contour of the length scale L_s normalized by the local boundary layer thickness δ, whereas Fig. 3.33(b) shows the same length scale L_s now normalized by the maximum hull radius R. Figure 3.34 shows the same results but uses a logarithmic ordinate normalized by δ. Line plots of the same information are shown in Fig. 3.35(a) and Fig. 3.35(b) to highlight the trends better; certain reference points in Fig. 3.32 were omitted to reduce clutter. There are a few notable trends in these figures,

1. The quantity L_s/δ increased with FPG and decreased with APG. The variations in L_s/δ were greatest in the log layer (e.g., $z/\delta = 0.1$) and least near the boundary layer edge. However, the behavior of L_s itself was somewhat masked by the spatially evolving

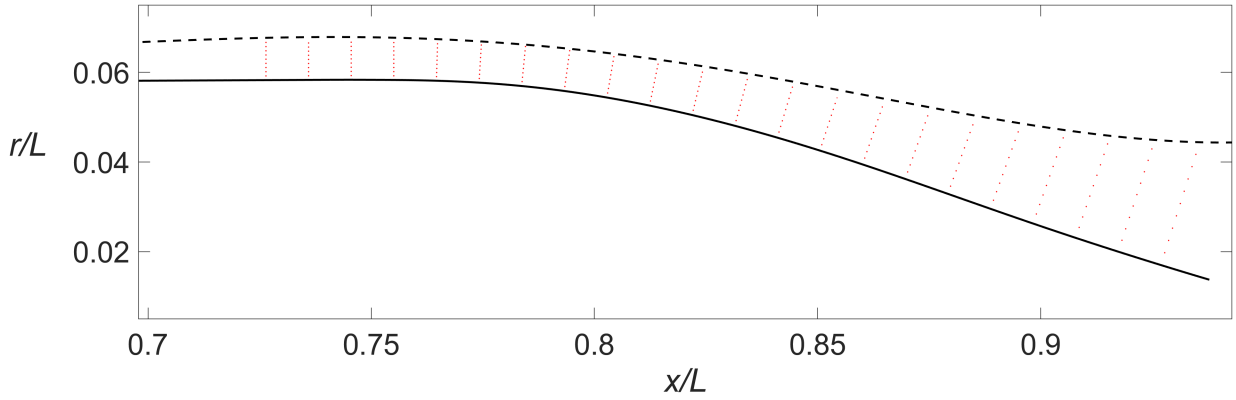

Figure 3.32 Red markers denote the nine wall-normal ($z/\delta = 0.1$ to 0.9) and 22 axial positions at which the 1D two-point correlation analysis was conducted. The dashed line is the boundary layer edge.

boundary layer thickness δ.

2. The quantity L_s/R revealed a different set of trends in Fig. 3.35(b). R is the maximum hull radius. This figure shows that the near-wall length scales were most affected, whereas L_s was largely invariant near the boundary layer edge. The length L_s at $z/\delta = 0.1$ in Fig. 3.35(b) form a sine-wave pattern reminiscent of dp/dx in Fig. 3.3(c), and were nearly equal at $x/L = 0.72$ and 0.95.

3. There was a decrease in L_s with increasing wall-normal distance in Fig. 3.35(b), consistent with a canonical boundary layer [97]. This decrease was more pronounced in the FPG and less noticeable in the APG. The reason was that while L_s in the outer region was insensitive to pressure gradients, L_s near the wall were stretched and compressed, thus increasing and decreasing the change in L_s across wall-normal z.

Some consideration was given to whether these were pressure gradient or wall curvature effects. The longitudinal curvature was an unlikely candidate because prior work has reported little effect on structure [213]. The lateral curvature [109] was insignificant until $x/L = 0.81$, which would not explain the increase in the FPG region. Consequently, the major changes observed below $z/\delta = 0.5$ likely resulted from the pressure gradient. This outcome was substantiated by how L_s/δ and L_s/R closely followed the trends of β_c and

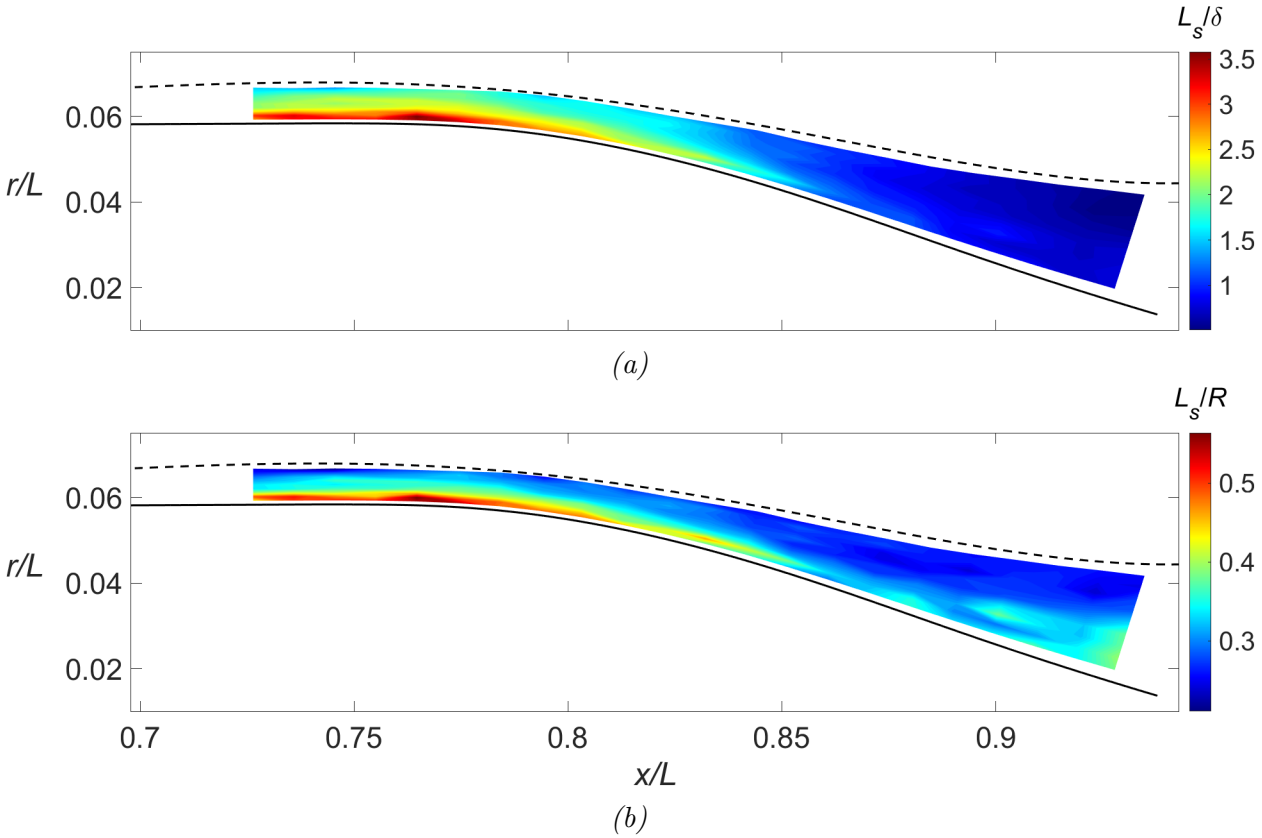

Figure 3.33 Variation in streamwise length scale L_s computed based on the wall-parallel velocity u normalized by *(a)* the local boundary layer thickness and *(b)* the hull radius $R = 109.54$ mm. Threshold was $R_{uu} = 0.15$.

dp/dx (or K) in Fig. 3.3. The observed trends resonated with those observed in the wall-tangent velocity spectra in Fig. 3.26(a), where the inner region frequency peaks were shifted to higher frequencies by the intense APG at $x/L = 0.85$.

For a more holistic understanding of how pressure gradient and surface curvature affect the boundary layer structure, two-point correlations were simultaneously performed in the wall-parallel and wall-tangent directions for selected reference points in Fig. 3.32. Figure 3.36 shows examples of the two-point correlation contours R_{uu} based on the wall-parallel velocity u at three wall-normal locations of $z_{\text{ref}}/\delta = 0.1$, 0.5, and 0.9. The contour levels increase from 0.2 to 0.8 in increments of 0.2. As discussed later, the red contour $R_{uu} = 0.2$ was used to compute the inclination angle denoted using the bisecting red dashed line.

As observed in Fig. 3.36a, the contours in the log region ($z/\delta = 0.1$) were elongated and

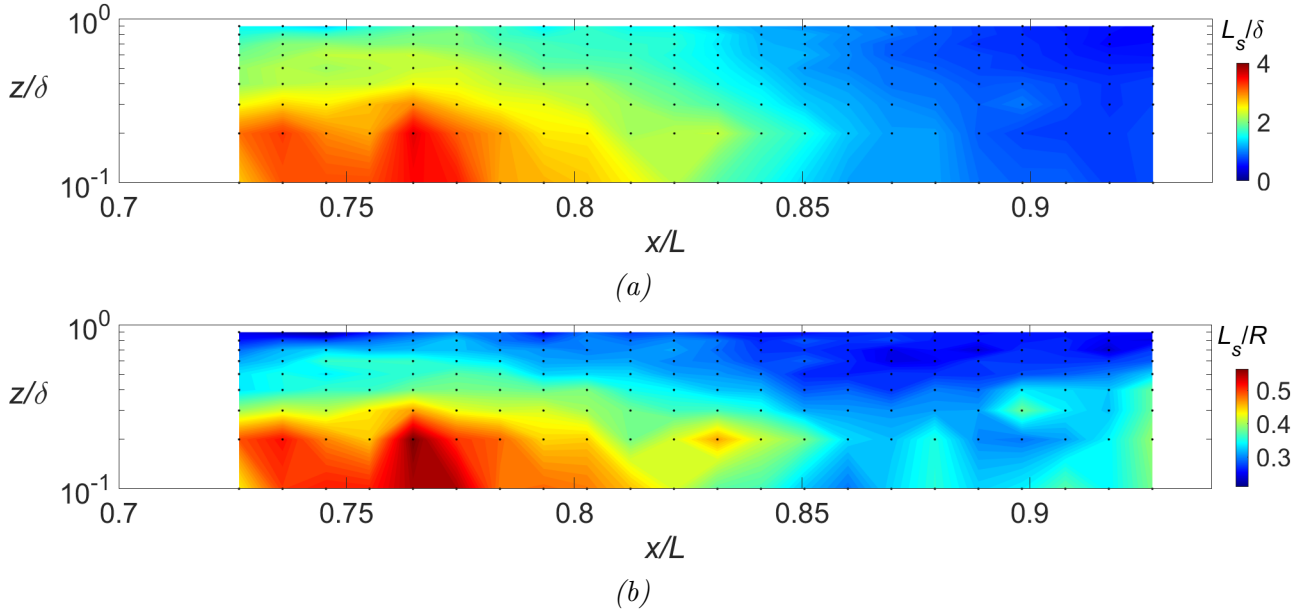

Figure 3.34 Variation in streamwise length scale L_s computed based on the wall-parallel velocity u normalized by *(a)* the local boundary layer thickness and *(b)* the hull radius $R = 109.54$ mm. Threshold was $R_{uu} = 0.15$. The logarithmic ordinate is normalized by local boundary layer thickness. The block dots show the reference points.

forward-leaning. This contour shape has been interpreted as hairpin packets that cooperatively induce significant regions of uniform low-speed flow [19–21]. In contrast, near the intermittent boundary layer edge ($z/\delta = 0.9$), the average eddy was more rounded. This difference in the correlated region, under the hairpin paradigm, suggested fewer or perhaps yawed [135] hairpin packets in the wake region [19]. Comparing these trends with those shown in Fig. 1.33 obtained from LES with a lightly loaded rotor (advance ratio $J = 1.44$), the Suboff structures did not grow as much. This difference could be traced to the Stratford body [5, 28, 143] having a more extensive APG region.

The changes in the two-point correlation contour were assessed by computing the inclination angles and spatial dimensions. The inclination angles were based on the singular value decomposition (SVD) of all the x–r coordinates bounded by $R_{uu} = 0.2$. The dominant singular vector relative to the local wall was defined as the inclination angle α. In Fig. 3.37(a), the inclination α increased across z/δ but decreased at the edge. Across all wall-normal z positions, the inclination angle decreased through the FPG and increased with the APG

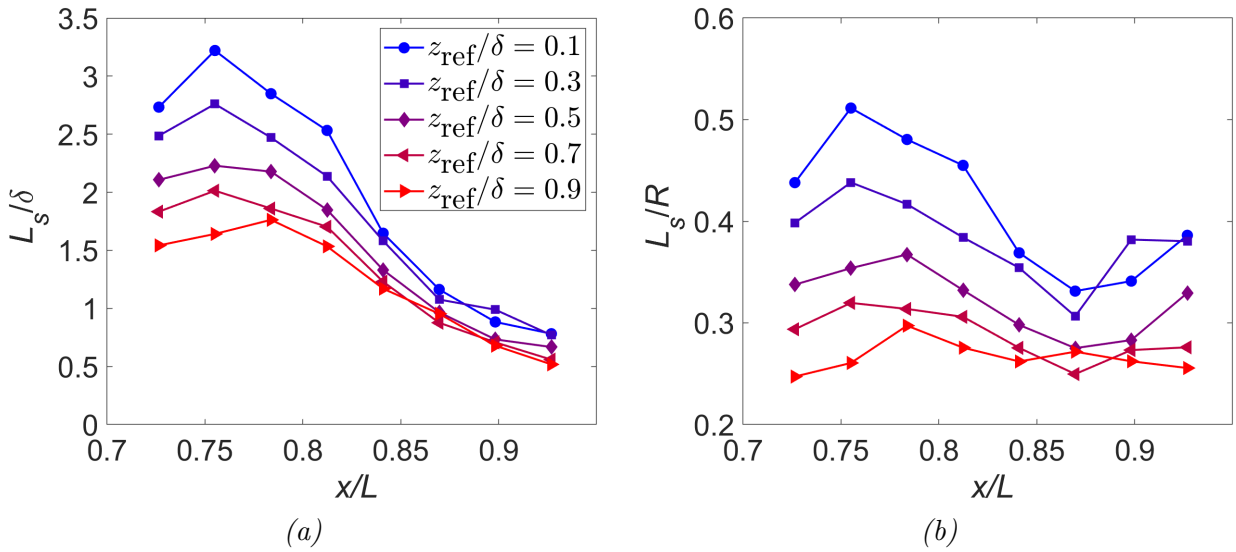

Figure 3.35 Variation in streamwise length scale L_s computed based on the wall-parallel velocity u normalized by *(a)* the local boundary layer thickness δ and *(b)* the hull radius $R = 109.53$ mm. Threshold was $R_{uu} = 0.15$.

consistent with the work of Krogstad and Skåre [115]. However, the outer region structures rotated more drastically than the inner region.

These trends in the inclination angle helped explain the variations in L_s along a streamline. When a structure became more inclined (or tilted upward) relative to the wall, the streamline intersected a shorter part of the two-point correlation contour and vice versa. The local angle was referenced to the local wall, whereas the global angle was referenced to the longitudinal symmetry axis. The global angles of the correlation contours computed relative to the longitudinal symmetry axis are shown in Fig. 3.37(b), where a more complex trend emerged. Line plots at two heights were extracted to understand the trends better.

Figure 3.38 examines the inclination trends by plotting the local and global angles at two wall-normal locations of $z_{\mathrm{ref}}/\delta = 0.1$ and 0.7. In Fig. 3.38(a), the black lines report the changing inclination angle with x/L. The blue diamond markers (and blue ordinate on the right) show the Clauser parameter β_c.

There were two noticeable trends in Fig. 3.38(a). First, the inclination angle at the two wall-normal locations decreased and increased simultaneously, i.e., there was little relative phase lead/lag in the structure response at different heights, perhaps indicating uniform

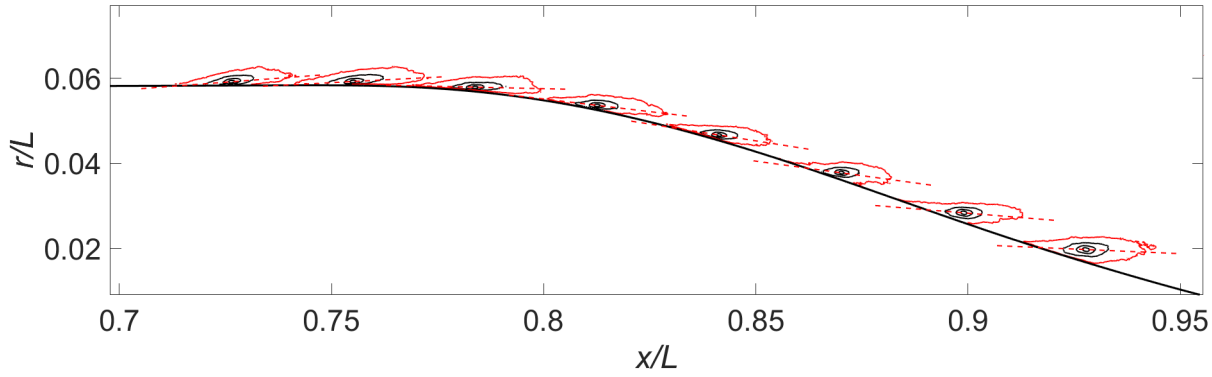

(a) $z_{\text{ref}}/\delta = 0.1$.

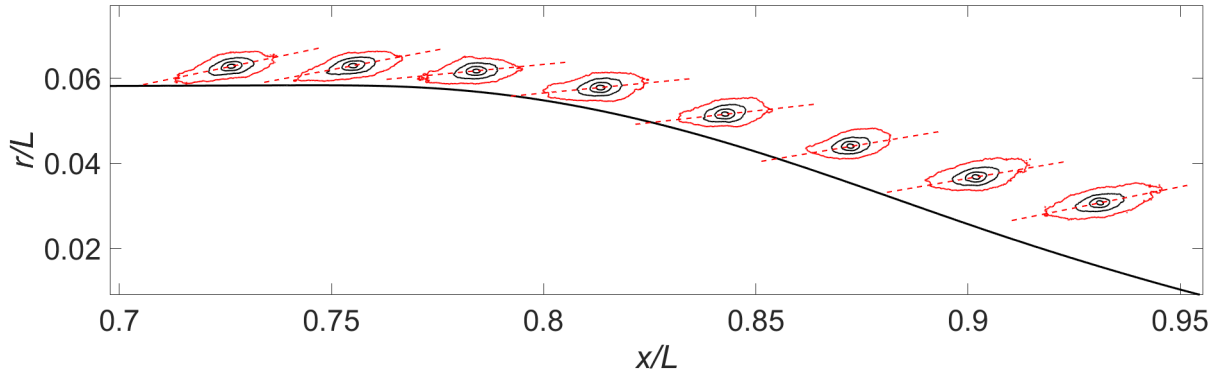

(b) $z_{\text{ref}}/\delta = 0.5$.

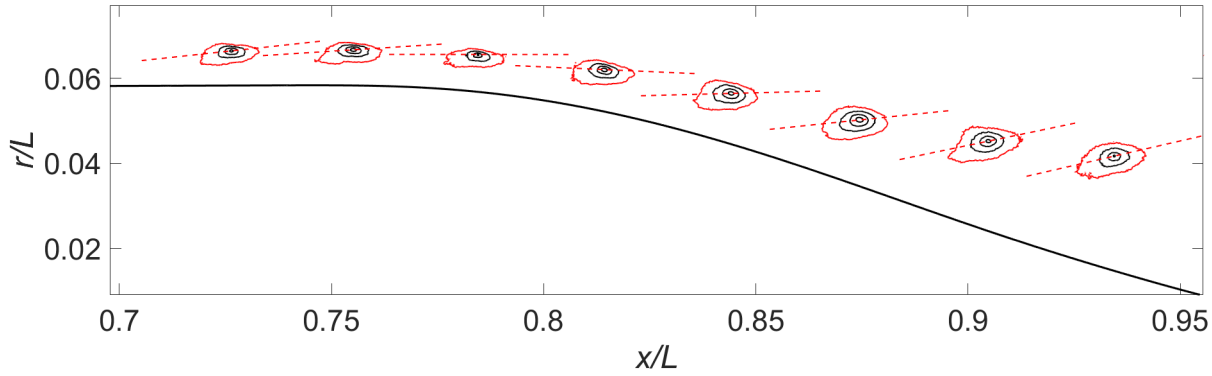

(c) $z_{\text{ref}}/\delta = 0.9$.

Figure 3.36 Two-correlation contours R_{uu} computed with respect to reference u velocity at eight streamwise x/L and three wall normal z/δ positions. Contour levels: 0.2:0.2:1. Red contour is $R_{uu} = 0.2$ used to compute the direction of maximum variance denoted by the red dashed line.

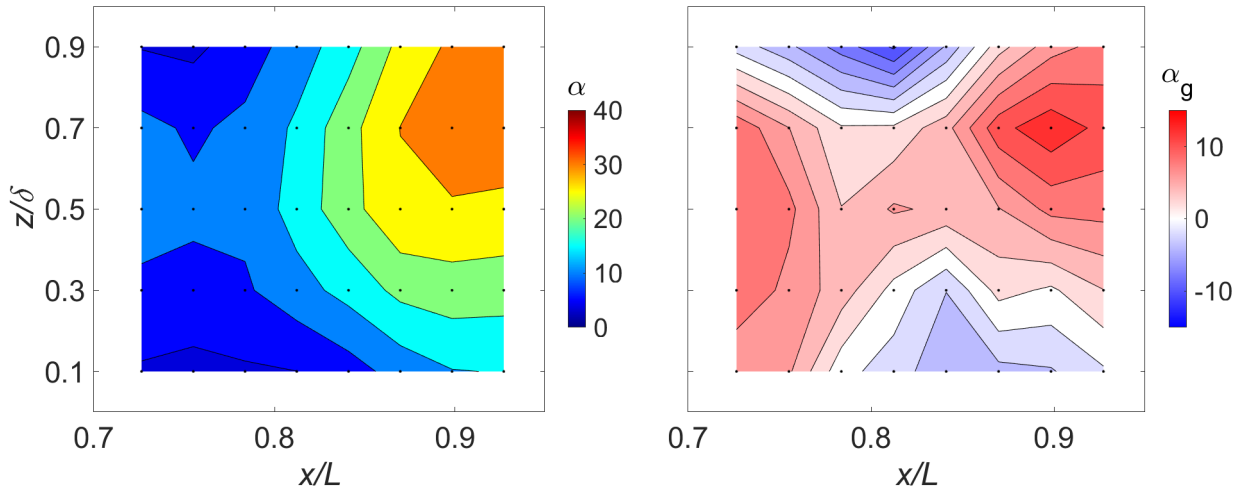

Figure 3.37 (a) Local and *(b)* global angles across five z/δ heights and eight axial locations.

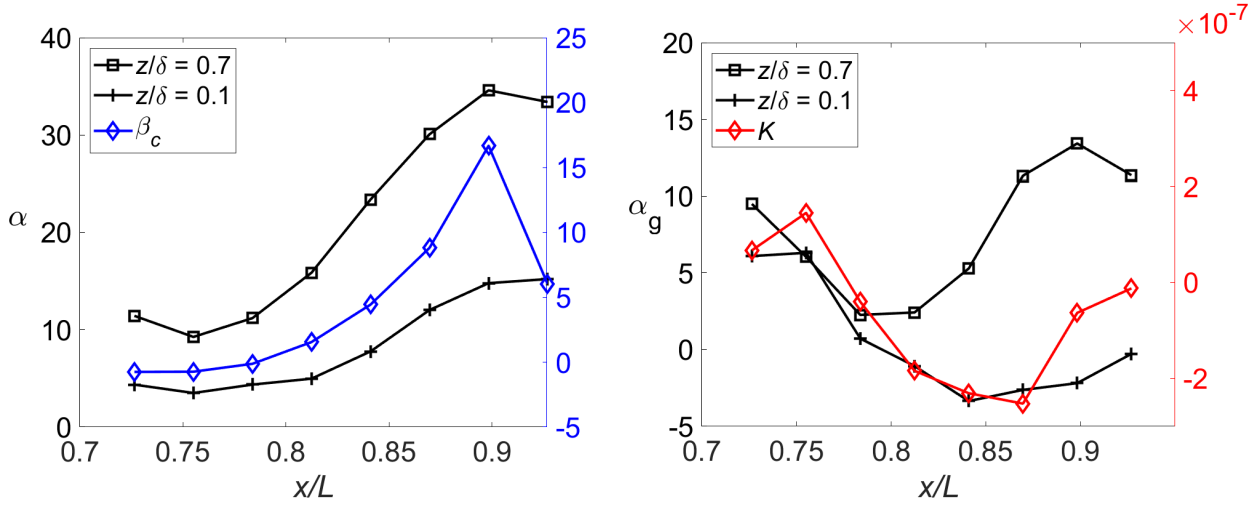

Figure 3.38 (a) Local and *(b)* global angles at two heights taken from Fig. 3.37. *(a)* The blue line shows the Clauser parameter β_c, and *(b)* the red line shows the acceleration parameter $K = (\nu/U_e^2)dU_e/dx$.

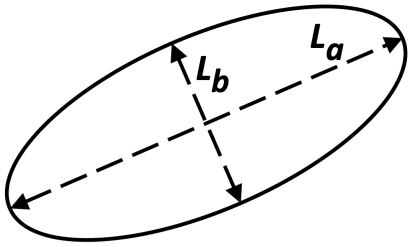

Figure 3.39 Idealized eddy with major axis L_a and minor axis L_b.

pressure gradients throughout the layer. Second, the inclination angle α at both wall-normal locations had a similar trend as the pressure gradient parameter β_c, decreasing through the FPG region and increasing more drastically with the APG.

Figure 3.38(b) studies the global angle α_g trends. The black lines correspond to α_g; the red line is the acceleration parameter $K = (\nu/U_e^2)dU_e/dx$. The near-wall ($z/\delta = 0.1$) global angle α_g trends were comparable to the acceleration parameter K. However, the global angle near the boundary layer appeared unrelated to K. Section 3.3.2.4 explores these trends in more detail.

While the length scales L_s varied as the streamline intersected shorter or longer parts of the rotated correlation contours, it remained unclear whether these contours were also distorted. To this end, each correlation contour of $R_{uu} = 0.2$ in Fig. 3.36 was idealized as an ellipse with major axis L_a and minor axis L_b as illustrated in Fig. 3.39. These lengths were computed as the furthest distance between any two points in the directions of the major and minor axes determined from the SVD.

The variation in L_a across the entire measurement domain is shown using colored contour plots in Fig. 3.40, and the quantitative trends at selected heights are more clearly shown in the line plots of Fig. 3.41. When normalized by the local boundary layer thickness, L_a/δ in Figs. 3.40(a) and 3.41(a) showed a slight increase in the FPG region followed by a decrease through the APG. These trends were more pronounced near the wall, in agreement with prior calculations of length scale along a streamline L_s/δ shown in Fig. 3.34(a). Additionally, the structures at the boundary layer edge had a more delayed response relative to the near-wall

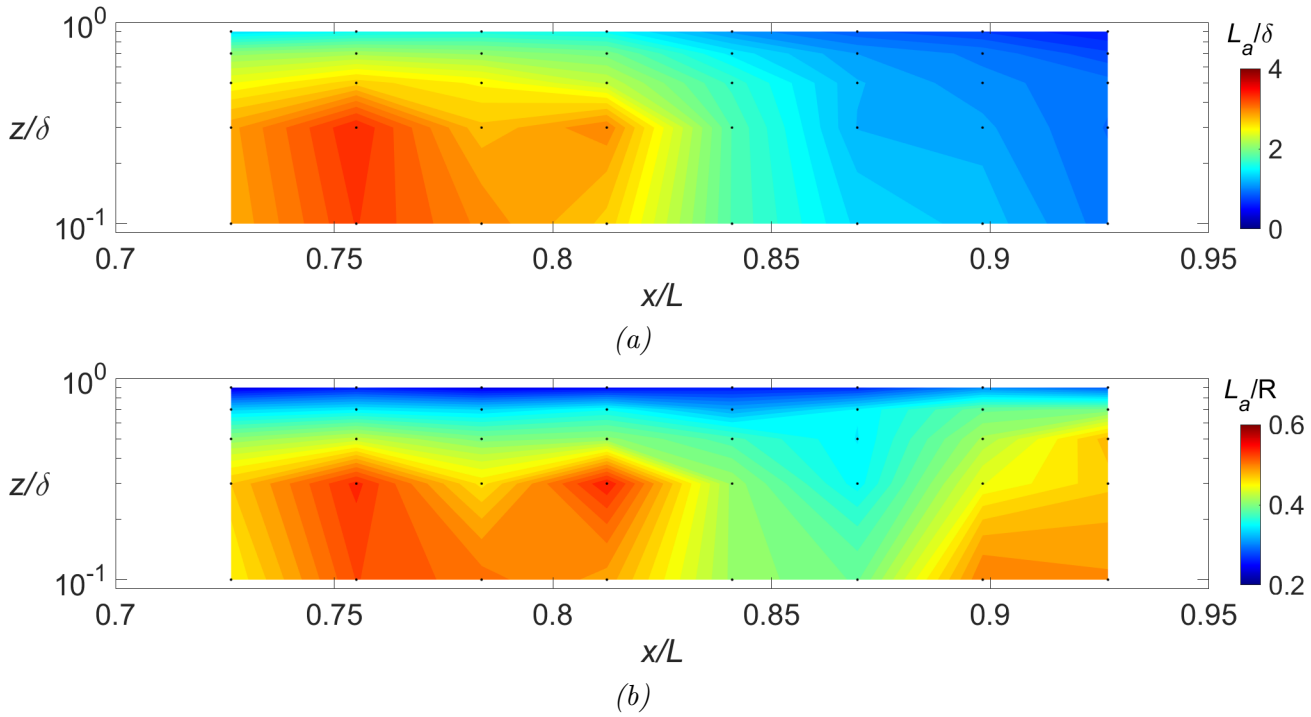

Figure 3.40 Surface plot of the major axes based on structures defined by $R_{uu} = 0.2$ normalized by the *(a)* local boundary layer thickness and *(b)* the hull radius R.

structures.

Different trends emerged when inspecting L_a/R in Figs. 3.40(b) and 3.41(b), where R is the hull radius. The variations in L_a with x were sinusoidal, similar to the acceleration parameter K or the pressure gradient dp/dx in Fig. 3.3(c) and (d). The magnitude of the elongation and compression was most intense near the wall ($z_{\text{ref}} = 0.1$ and 0.3), and least significant near the boundary layer edge ($z_{\text{ref}} = 0.7$ and 0.9). The outer region peak L_a lagged the near-wall peak, pointing to different response times of the structures. These distortions resulted from the pressure gradient. Further, there was a gradual increase in L_a/R near the boundary layer edge.

These trends in L_a were roughly in agreement with the length scale L_s/R computed along streamlines. Also, these results reaffirmed the peak frequency analysis in Fig. 3.26, highlighting how the near-wall structures were more sensitive to pressure gradients than the outer region structures. Crucially, this analysis demonstrated the variations in the length

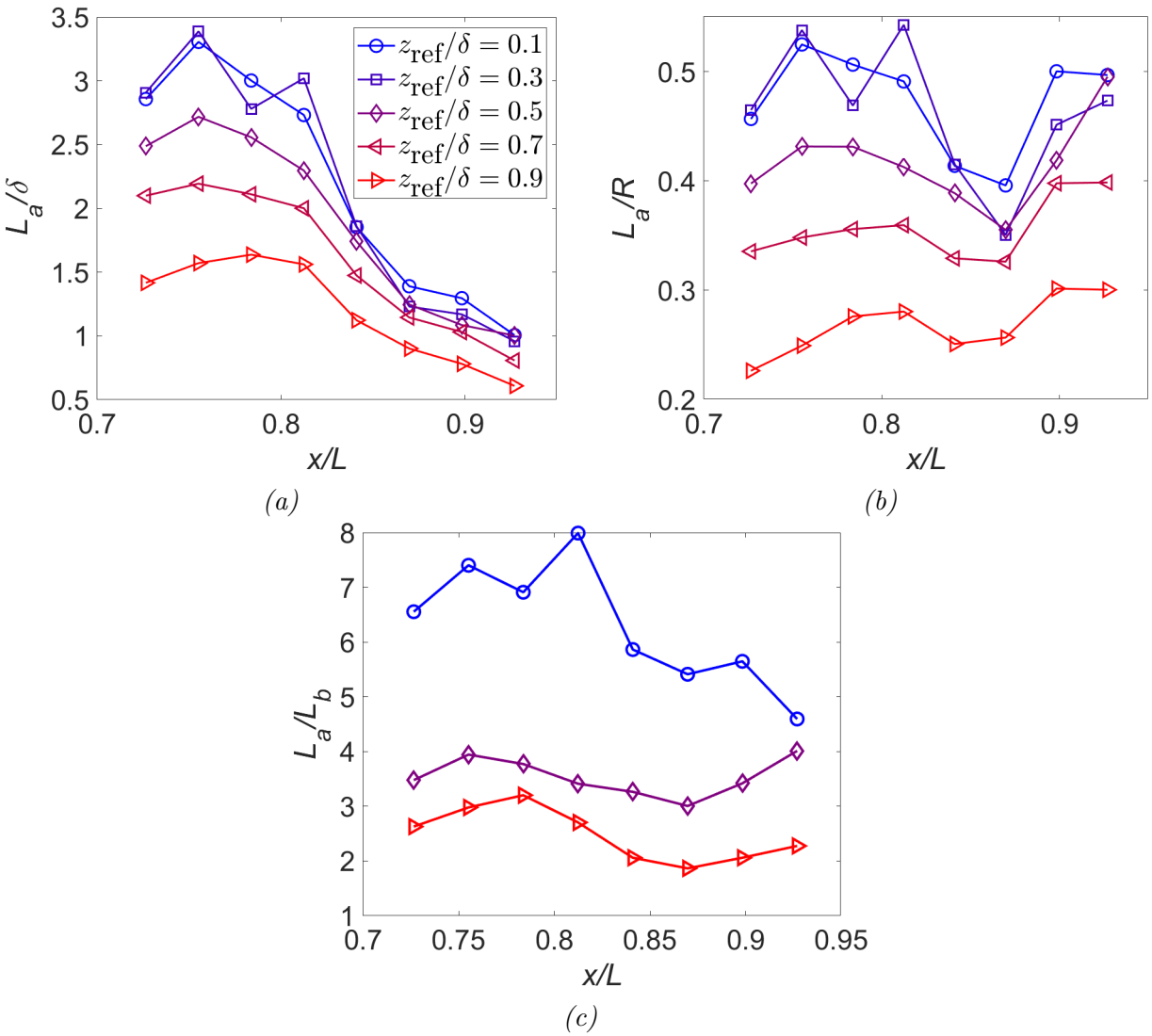

Figure 3.41 The major axis of a structure defined by $R_{uu} = 0.2$ normalized by the *(a)* local boundary layer thickness and *(b)* the hull radius R. *(c)* Aspect ratio of major and minor axis L_a/L_b.

scale along a streamline in Fig. 3.35(b) were products of structure rotation and elongation/compression.

Lastly, the structures' aspect ratios (AR) were computed as L_a/L_b as displayed in Fig. 3.41(c). The log region ($z/\delta = 0.1$) AR experienced an initial increase through the FPG, followed by a decrease as the minor axis L_b increased. The aspect ratio of the structures centered about $z/\delta = 0.5$ and 0.9 increased and decreased with the FPG and APG, respectively. The AR at $z/\delta = 0.9$ was 2–3, consistent with the observations of Kovasznay et al. [110] that turbulent bulges were elongated in the streamwise direction with a roughly 2 to 1 AR. The gradual increases in L_a and L_b visible at $x/L \approx 0.5$ and 0.7 supported the growing two-point correlation observed in the LES of [28].

The key observations of this two-dimensional R_{uu} analysis were that

1. The structure of R_{uu} in the log region ($z/\delta = 0.1$) was stretched and compressed by the FPG and APG by up to 25% of the initial length (at $x/L = 0.70$), and experienced no more than 10° of rotation.

2. In the outer region, the structures were rotated by up to 25° by the pressure gradient and wall curvature. However, the dimensions of the eddies, i.e., major and minor axes, experienced less distortion from the pressure gradient.

3. The structures' major axis increased gradually in the outer region.

4. The variations in R_{uu} length scale along a streamline can be attributed to structure distortion and rotation.

5. The inclination angle of R_{uu} closely followed the pressure gradient; the major axis length of R_{uu} followed the pressure gradient and the acceleration parameter.

Following the wall-tangent velocity, the correlation contours R_{ww} based on the wall-normal velocity are shown in Fig. 3.42 at $z_{\text{ref}}/\delta = 0.1, 0.5$, and 0.9. The contour levels shown are 0.1, 0.5, and 0.9. Examining the trends at $z_{\text{ref}}/\delta = 0.1$ in Fig. 3.42(a), the contour shape

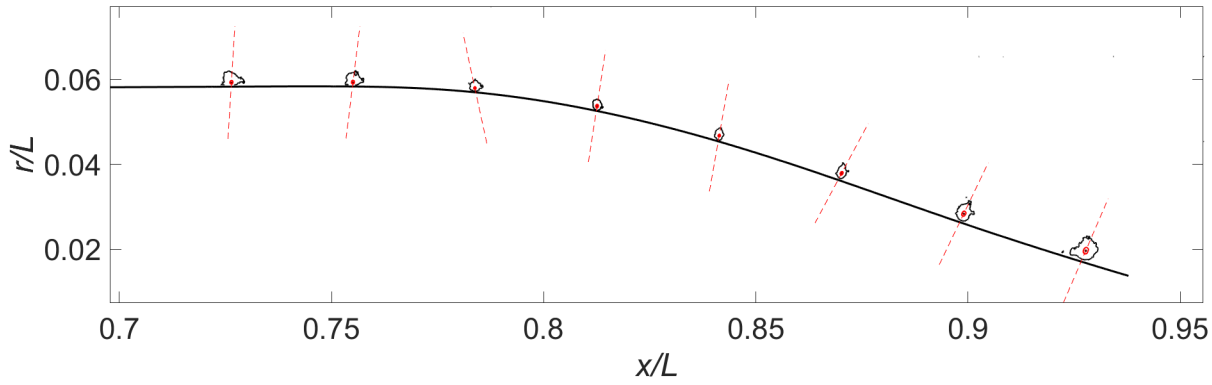

(a) $z_{\text{ref}}/\delta = 0.1$.

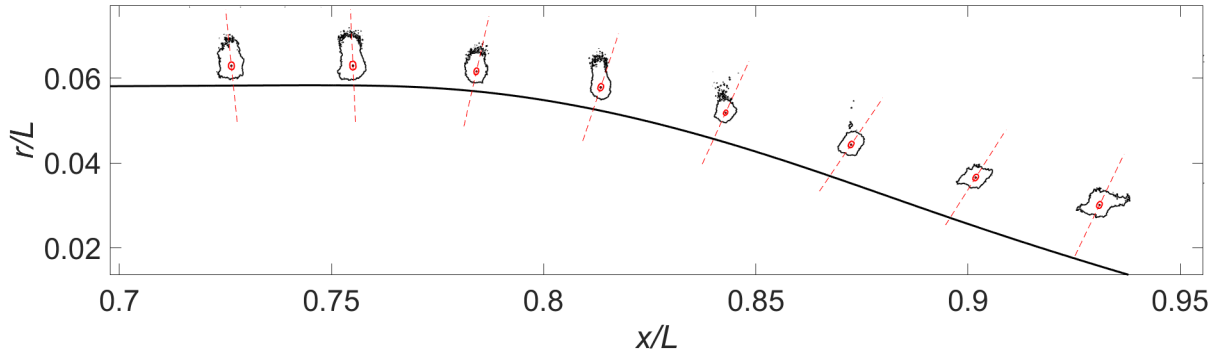

(b) $z_{\text{ref}}/\delta = 0.5$.

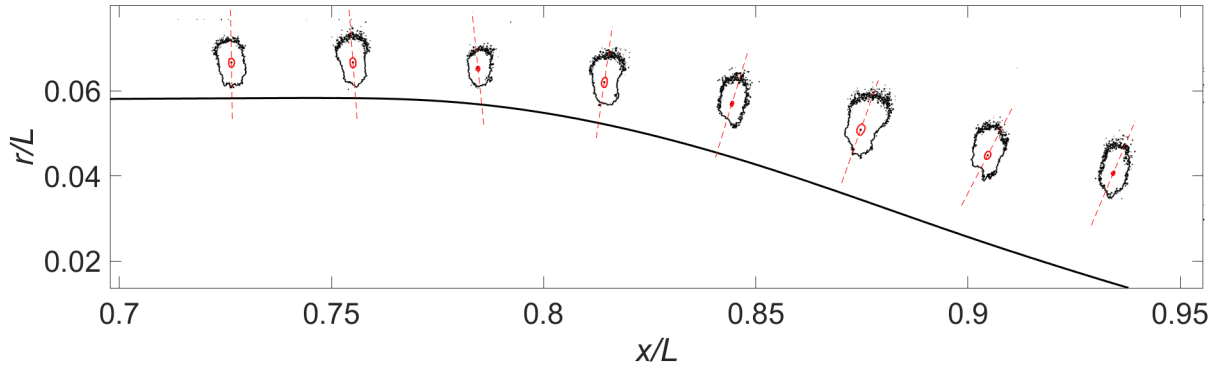

(c) $z_{\text{ref}}/\delta = 0.9$.

Figure 3.42 Two-correlation contours R_{ww} computed with respect to reference w velocity at eight streamwise x/L and three wall normal z/δ positions. Contour levels: 0.1, 0.5, and 0.9. The red contour is $R_{ww} = 0.5$ used to compute the direction of maximum variance denoted by the red dashed line.

of $R_{ww} = 0.1$ varied appreciably, in agreement with the spectral analysis in Fig. 3.26(b) showing that for $z/\delta < 0.4$ the wall-normal w flow frequencies were significantly modified.

Further, R_{ww} developed a forward lean at $x/L \approx 0.93$, suggesting that the w coherence was at least partially determined by the hairpin packets. This observation supported the hairpin packet hypothesis in Section 3.3.1, where the w frequencies were observed to be twice those of u, perhaps because each hairpin packet's low-momentum zone had both upwash and downwash. The change from vertical columns to forward-leaning structures was more apparent at $z_{\text{ref}}/\delta = 0.5$ in (b), occurring as early as $x/L = 0.87$. Examining the results at $z/\delta = 0.9$ in (c), the R_{ww} contours were column structures, similar to the ZPG case in Sillero et al. [10]. This invariance of R_{ww} was in accord with the spectral analysis in Section 3.3.1 that suggested little change in R_{ww} in the outer region.

The effects of pressure gradient and curvature on the R_{ww} inclination were assessed. The direction of the maximum variance was defined as the leading right singular vector of the x-r pairs enclosed by $R_{ww} = 0.5$ highlighted using the red contour in Fig. 3.42. This threshold was chosen to elucidate the wall-normal bias of the correlated region. Examining Fig. 3.42, the direction of maximum variance shown using the red dashed line was roughly normal to the wall at all streamwise and wall-normal stations.

The direction of maximum variance was described in terms of two separate angles, one relative to the local wall and the other to the longitudinal x axis of symmetry. Figure 3.43(a) shows the angle α relative to the wall as roughly constant around 90° throughout the measurement domain. This observation perhaps supported the wall-normal–wall-parallel frame as the correct orientation for interpreting the boundary layer. The decreased angle downstream ($x/L > 0.85$) resulted from the structures developing a slight forward lean. In contrast, the angle relative to the symmetry axis α_g in Fig. 3.43(b) decreased more significantly with streamwise distance. Interestingly, the local angle α showed that the R_{ww} structure near the boundary layer edge ($z_{\text{ref}}/\delta = 0.9$) in Fig. 3.42(c) leaned backward and forward in response to the favorable and adverse pressure gradients (Fig. 3.3).

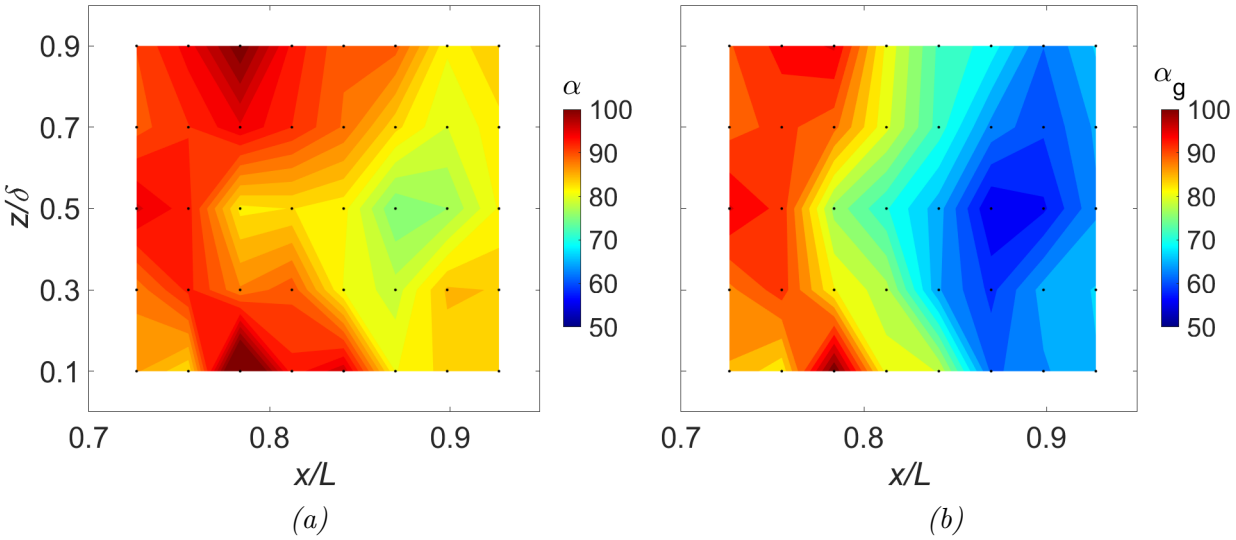

Figure 3.43 (a) Local and *(b)* global inclination angles (in degrees) computed with respect to the wall and to the x axis based on the x-r pairs enclosed by the $R_{ww} = 0.5$ contour line. Black dots indicate measurement location.

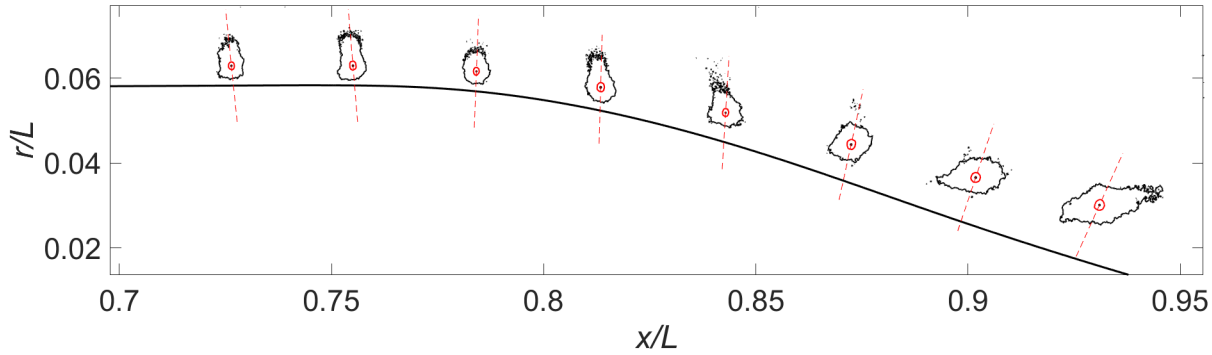

Figure 3.44 Two-correlation contours $R_{u_r u_r}$ computed with respect to reference radial velocity u_r at eight streamwise x/L and $z/\delta = 0.5$. Contour levels: 0.1, 0.5, and 0.9. Red contour is $R_{u_r u_r} = 0.5$ used to compute the direction of maximum variance denoted by red dashed line.

Additionally, contours of $R_{u_r u_r}$ based on the radial velocity fluctuations are displayed in Fig. 3.44 to assess the effect of a cylindrical coordinate. This figure follows Fig. 3.42 in terms of contour levels and structural inclination calculation. Compared with Fig. 3.42(b), the contours and inclinations were identical at upstream locations ($x/L < 0.75$), because without longitudinal curvature, $u_r = w$.

Moving downstream, the contours of $R_{u_r u_r} = 0.1$ developed a forward-leaning structure at $x/L = 0.87$, similar to R_{ww}. The difference, however, was that the forward lean was

more significant at $x/L = 0.93$ for $R_{u_r u_r}$. When examining the inclination, the contours $R_{u_r u_r} = 0.5$ used to compute the inclination angle were more rounded than those of R_{ww}. Further, $R_{u_r u_r}$ did not adjust its fore-aft lean as quickly as R_{ww} did to remain roughly wall-normal. Based on this comparison of $R_{u_r u_r}$ and R_{ww}, the wall-parallel–wall-normal frame was arguably better for interpreting this boundary layer.

The sweep and ejection motions were studied by examining the cross-correlation R_{uw}. The correlation between $u(x)$ and $w(x + \Delta x)$ is shown in Fig. 3.45 with the same reference points as before. In this figure, The blue contour is $R_{uw} = -0.15$, the black contour is $R_{uw} = -0.3$, and the red contour is $R_{uw} = +0.1$; the reference is the green "+." In the nearly canonical region ($x/L = 0.7$–0.75), the negative values of R_{uw} were consistent with the idea that Q2 ($u < 0, w > 0$) and Q4 ($u > 0, w < 0$) motions were more dominant over the other two quadrants. The backward-leaning organization at $z_{\text{ref}}/\delta = 0.5$ was consistent with previous findings of Volino [13].

The correlated region of R_{uw} at $z_{\text{ref}}/\delta = 0.1$ was biased in the streamwise direction as shown in Fig. 3.45(a). This correlated region was stretched and compressed, suggesting an influence of the FPG and APG. At $z_{\text{ref}}/\delta = 0.5$ in Fig. 3.45(b), although the structure was initially similar to that shown in Volino [13], the negatively correlated region virtually disappeared around $x/L = 0.85$. A slight positive region ($R_{uw} = 0.1$) emerged downstream of the reference point. This observation implied that the second and fourth quadrant motions were no longer dominant and that a high streamwise momentum event was associated with an upwash immediately downstream, or vice versa. This upwash pattern became more significant near the boundary layer edge at $z_{\text{ref}}/\delta = 0.9$.

The appearance of a positive correlation region required further consideration. First, the positive region expanded with increasing wall distance, suggesting that this R_{uw} pattern in the wake region was related to the turbulent entrainment process, which dictates the flow dynamics at the boundary edge. Second, was this positively correlated region a consequence of the pressure gradient or the surface curvature?

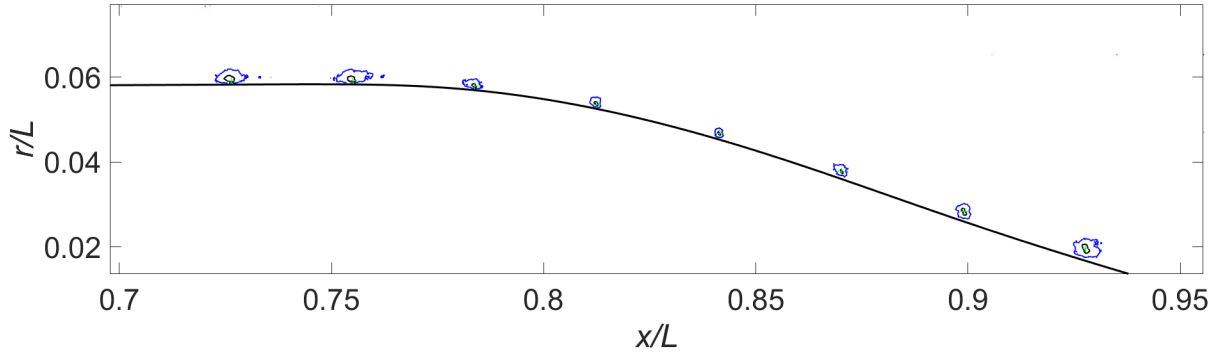

(a) $z_{\text{ref}}/\delta = 0.1$.

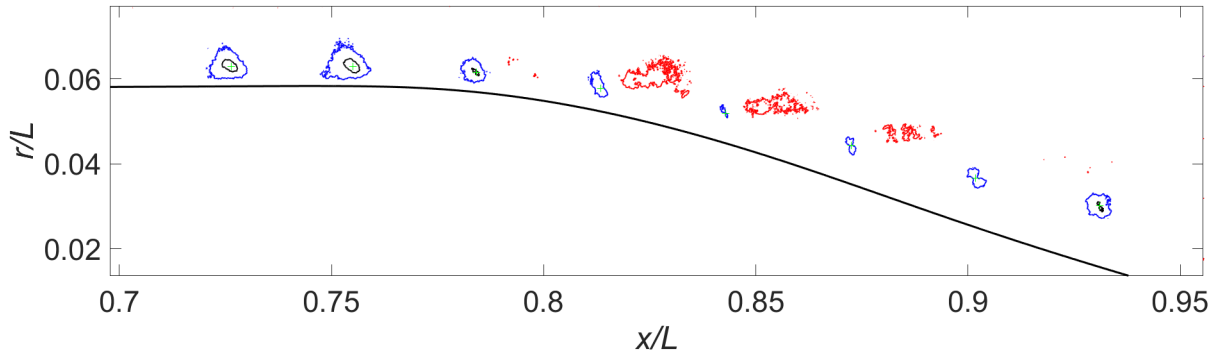

(b) $z_{\text{ref}}/\delta = 0.5$.

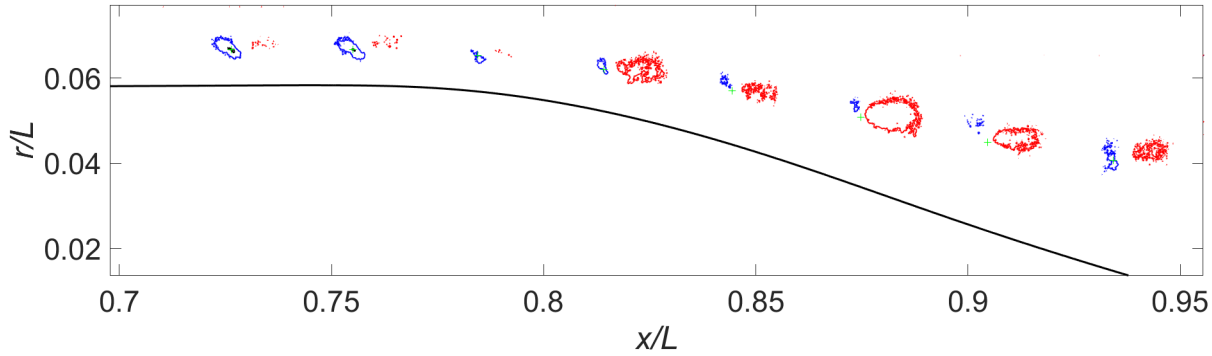

(c) $z_{\text{ref}}/\delta = 0.9$.

Figure 3.45 Two-correlation contours R_{uw} computed with respect to reference w velocity at eight streamwise x/L and three wall normal z/δ positions. The blue contour is $R_{uw} = -0.15$, the black contour is $R_{uw} = -0.3$, and the red contour is $R_{uw} = 0.1$. The green "+" is the reference point.

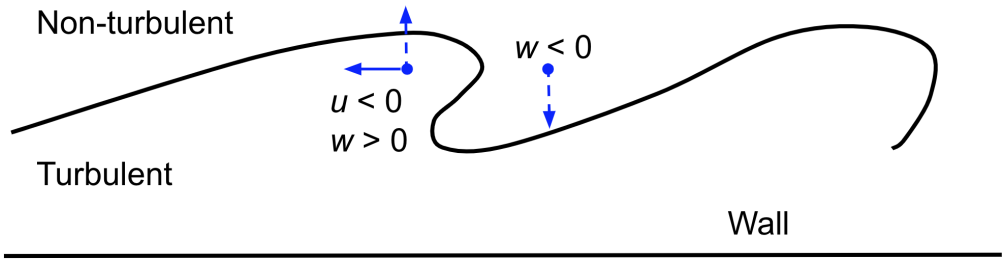

(a) Low-speed event.

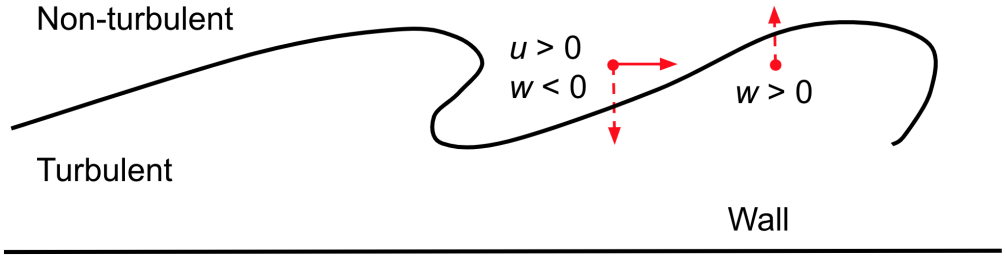

(b) High-speed event.

Figure 3.46 Idealization of turbulent/non-turbulent interface to explain the positively correlated region downstream of the reference points in Figs. 3.45(b) and 3.45(c).

Although the pressure gradient may appear as a good candidate because R_{uw} was most pronounced in the APG region in Figs. 3.45(b) and (c), the pressure gradients alone cannot explain the trends. The main counterpoint was that the maximum positive correlation in R_{uw} appeared at $x/L = 0.82$ for $z/\delta = 0.5$ and further downstream at $x/L = 0.88$ for $z/\delta = 0.9$. This lead-lag relationship may indicate a wall-normal pressure gradient.

Such a gradient was possible [109] but unlikely because Patel et al. [109] found essentially constant pressure up to $x/L = 0.90$ ($\delta/a = 0.62$) on a comparable model. Instead, it was more plausible that the longitudinal convex curvature modified R_{uw} in the outer region. Different streamline curvatures could explain the difference between the two heights. Fluid elements at $z/\delta = 0.5$ may have rounded the corner earlier than those at $z/\delta = 0.9$ and experienced curvature effects sooner. Nonetheless, this hypothesis should be verified by a study that isolates the convex curvature.

This pattern of locally negative and subsequently positive correlation regions could perhaps be understood as turbulent bulges and valleys. As illustrated in Fig. 3.46, turbulent bulges separate the rotational and the irrotational flows, and two scenarios of high and low

u momentum are considered:

1. In Fig. 3.46(a), a low-momentum u event (solid blue arrow) resides in the turbulent bulge with a locally positive wall-normal w (dashed blue arrow). Then, the positive correlation downstream implies $w < 0$ (dashed blue arrow). This scenario could correspond to a turbulent bulge rising to help entrain the irrotational fluid [35].

2. In Fig. 3.46(b), the solid red arrow denotes a high-speed u event in the irrotational region. Then, this irrotational region had a downward motion ($w < 0$), and the fluid downstream was uplifted ($w > 0$). This scenario could correspond to turbulent entrainment of irrotational flow in the valley and a rising downstream turbulent bulge [35].

A more complete picture of the high and low-speed events can be obtained through analysis of cross-stream planes [11, 72] as the following Section 3.3.2.2 will discuss. Ultimately, a three-dimensional perspective provided in Section 3.3.2.3 would be most insightful.

3.3.2.2 Spanwise Planes

Analysis of cross-stream planes perpendicular to the free stream provides additional insights into the boundary layer structure. In a canonical boundary layer, the legs of hairpin-type structures manifest in the spanwise plane as pairs of vortices [11, 117]. To this end, this section uses two-point correlations to document pressure gradient and wall curvature effects on the spanwise footprint of the eddies. This analysis of the four spanwise planes provided results that complemented those from the streamwise plane in Section 3.3.2. Note that because stereoscopic PIV is known to have higher uncertainty relative to two-component PIV, the spanwise planes were validated against the large-FOV PIV in Appendix A, where the axisymmetry of the flow is also demonstrated.

The coordinate system employed in this analysis requires discussion. Consistent with the approach in the streamwise plane, the preferred coordinate system was wall-parallel–wall-normal. Under this coordinate system, the spanwise planes perpendicular to the body

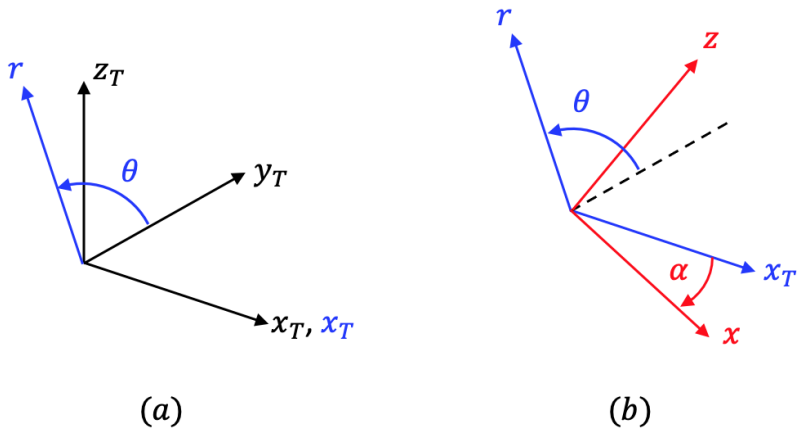

Figure 3.47 Coordinate transformation for the spanwise plane. *(a)* Transformation from the wind tunnel frame (black) to a cylindrical frame (blue); x_T remains invariant. *(b)* Transformation from the cylindrical frame (blue) into a wall-parallel–wall-tangent frame (red) by rotating about the dashes reference line, where α is the angle of the wall relative to the wind tunnel frame x_T.

symmetry axis would be reclined, similar to the measurement planes in Hutchins et al. [11]. However, the maximum inclination relative to the local wall was roughly 17°, minor compared to the 45° in Hutchins et al. [11].

The velocity vectors were transformed into the appropriate coordinate system to facilitate comparisons with canonical boundary layers. In the spanwise plane, the DaVis cross-correlation resulted in vectors defined on a Cartesian x_T-y_T-z_T aligned with the wind tunnel frame, denoted by the black axis system in Fig. 3.47(a). The grid was then transformed into a cylindrical frame with x_T-r-θ shown in blue. Next, each x-r value pair was converted into a wall-parallel–wall-normal frame (red) following the approach used for the streamwise plane, as shown in Fig. 3.47(b).

The velocities were also transformed into a cylindrical coordinate system u_x, u_r, u_θ. Finally, u_x and u_r were transformed into the wall-normal–wall-parallel u and w. This transformation did imply that velocity vectors with greater radii had smaller x/L values, i.e., were located more upstream. However, it was assumed that differences in streamwise x/L were small enough for the boundary layer characteristics to be virtually identical.

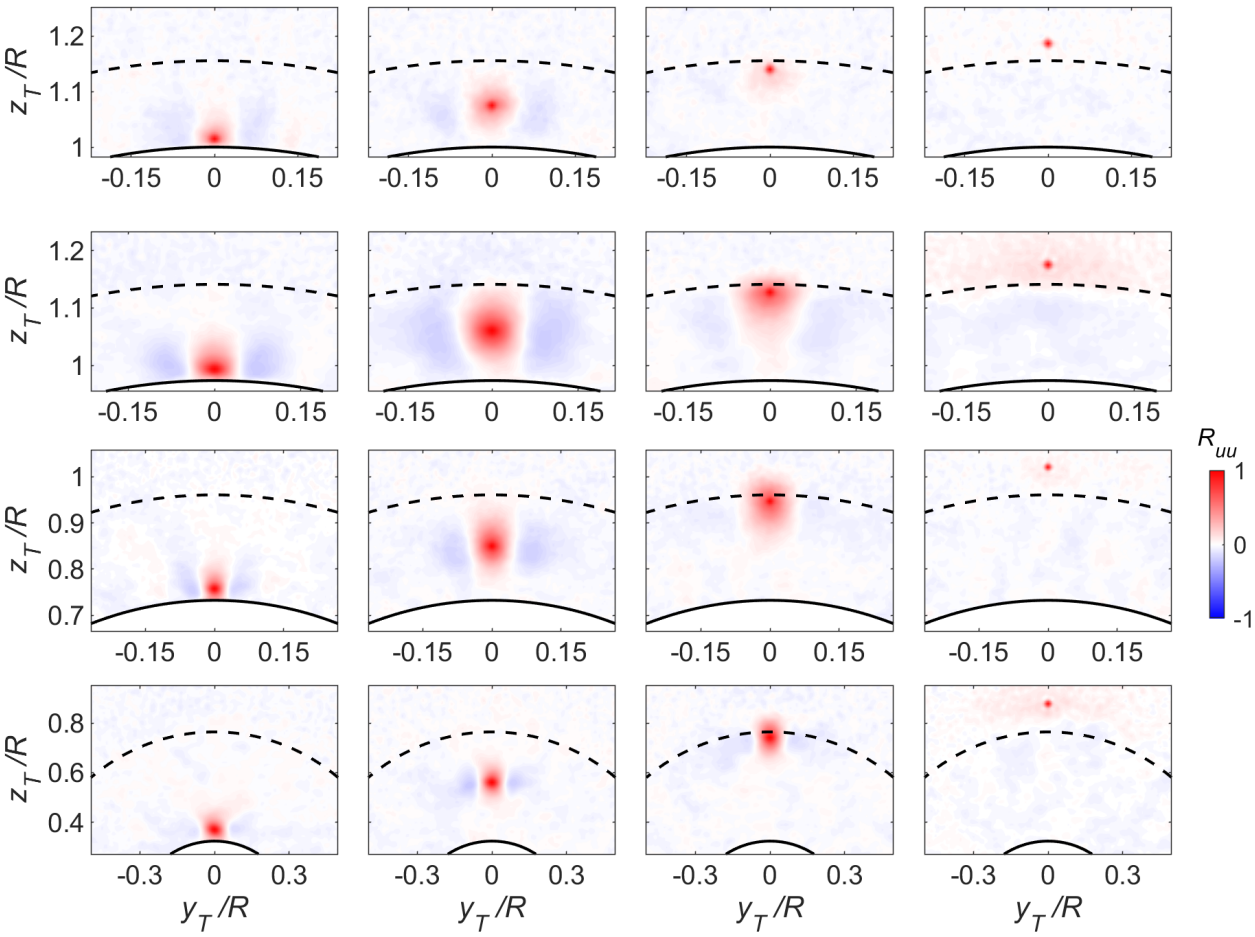

Figure 3.48 Each column shows R_{uu} computed at four radial positions of roughly $z_{\text{ref}}/\delta = 0.1, 0.5, 0.9, 1.2$. The four rows correspond to spanwise planes measured at $x/L = 0.71, 0.785, 0.85, 0.92$.

The two-point correlations were computed with reference velocities at various wall-normal z positions, similar to the approach by Hutchins et al. [11]. The analysis below begins with studying the two-dimensional two-point correlation, followed by an inspection of the one-dimensional correlation. Then, a circumferential length scale was defined to quantify the footprint of the eddies. Deviations from the canonical boundary layer were observed.

The two-point correlation contours of streamwise velocity u, R_{uu}, were computed at four streamwise locations as shown in Fig. 3.48. In this figure, the four columns correspond to reference velocities located at $z_{\text{ref}}/\delta = 0.1, 0.5, 0.9, 1.2$; each row represents a different spanwise plane measured at $x/L = 0.71, 0.785, 0.85,\ 0.92$. The solid line at the bottom of

each figure is the wall, and the dashed line above is the boundary layer edge. The abscissa and ordinate are the wind tunnel frame (subscript "T") with the symmetry axis as the origin. Note the different FOVs for each spanwise plane.

Inspecting the results in Fig. 3.48, there was a recurring pattern of a positively correlated region flanked by negative lobes, qualitatively similar to R_{uu} observed in canonical boundary layers [11, 21]. These patterns were spanwise cuts of the elongated, forward-leaning structures whose streamwise extent was showcased in Fig. 3.36. For this reason, the contours were maximum at $z_{\text{ref}}/\delta = 0.5$ and showed structures attached or detached from the wall [11] depending on the wall-normal position of the reference point z_{ref}/δ. The variations in spanwise footprint were quantified as follows.

A circumferential length scale was computed for the wall-parallel velocity R_{uu} and compared with a canonical boundary layer. Figure 3.49(a) shows an R_{uu} sample, where the solid and dashed lines represent the wall and the boundary layer edge. The dotted-dashed line in the middle is the arc length along which the R_{uu} correlations were extracted, as displayed in Fig. 3.49(b). The characteristic negative peaks surrounding the center peak were visible. A circumferential length scale was defined as the product of the angle $\Delta\theta_c$ between where the legs intersect $R_{uu} = 0.1$ and the arc radius. This threshold was slightly higher than the $R_{uu} = 0.05$ chosen by Hutchins et al. [11].

The circumferential length scale $L_\theta(R_{uu})$ was calculated at various wall-normal locations in all four spanwise planes. Figure 3.49(c) shows L_θ normalized by the local boundary layer thickness. The $L_\theta(R_{uu})$ of a canonical boundary layer digitized from Hutchins et al. [11] is denoted by the right-pointing triangle. Here, spanwise Plane 1 (SP1) showed good agreement with results from the canonical boundary layer, providing additional evidence for the flow being near canonical at the most upstream part of the FOV. Traversing the afterbody, the spanwise length scale relative to the local boundary layer thickness increased through the FPG and decreased through the APG. Interestingly, while SP1, 2, and 3 all exhibited a growing trend with wall-normal distance, L_θ/δ in SP4 remained relatively invariant across

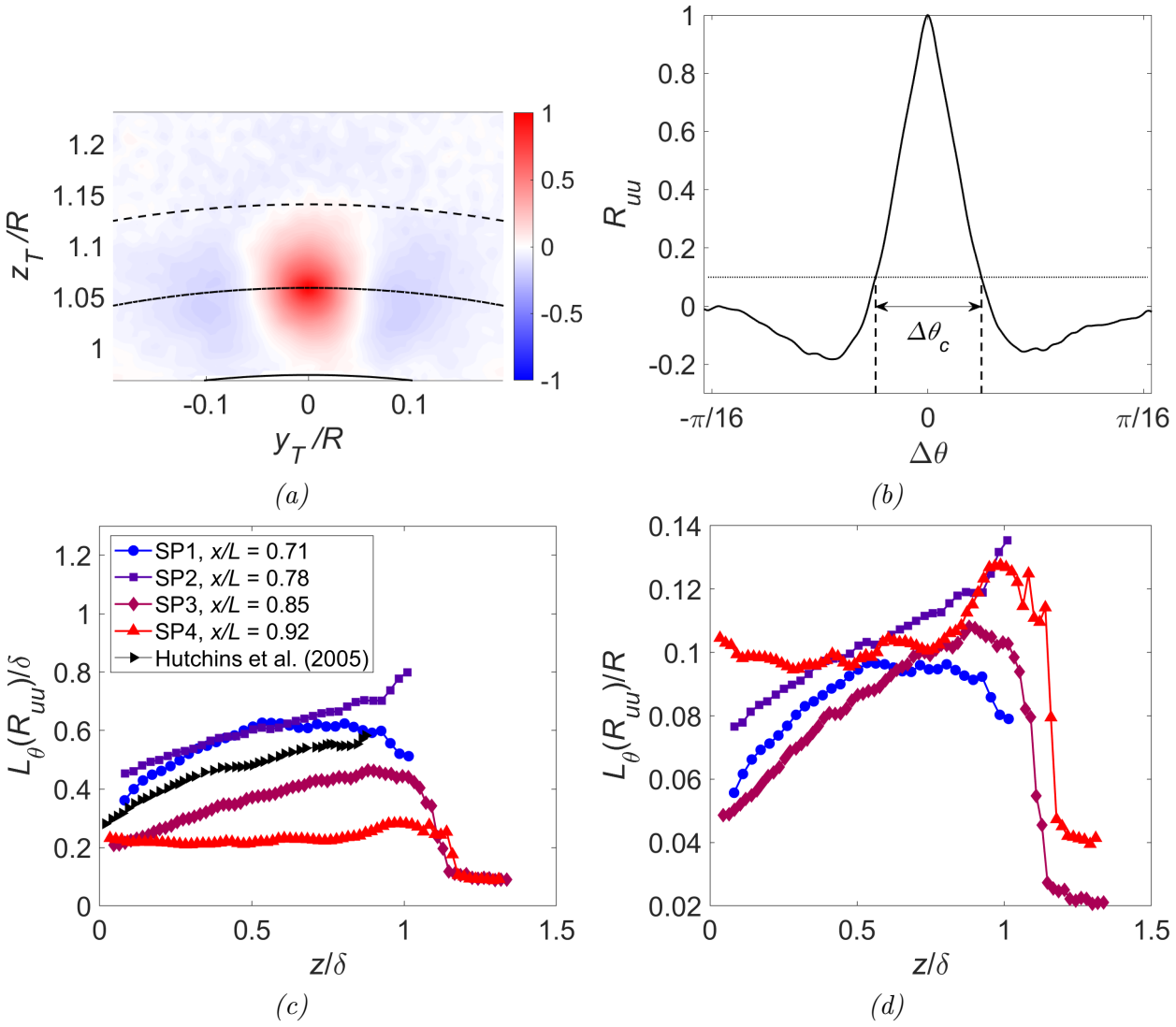

Figure 3.49 (a) R_{uu} contour; circumferential correlation was computed along arc lengths such as the dotted-dashed line. *(b)* Correlation values along circumferential θ, with length scale defined as the angle between where the two legs intersect $R_{uu} = 0.1$ multiplied by the radius. Length scale along θ associated with R_{uu} normalized by *(c)* boundary layer thickness δ and *(d)* hull radius R.

the layer.

The length scale L_θ was also reported as a fraction of the hull radius R in Fig. 3.49(d). The spanwise correlation increased (shown in SP2) and decreased (SP3) uniformly across the boundary layer thickness through the FPG and the APG. In other words, the three curves had comparable (roughly) linear growth rates with wall distance but with different vertical offsets. However, SP4 deviated from this trend, showing a roughly constant length scale across the boundary layer. This difference in trend requires some consideration.

The vertical shifts of the three curves (SP1–3) coincided with the pressure gradient trends. The different trend observed in SP4 could also be a pressure gradient effect; Lee and Sung [122] showed increasing spanwise length scale in the inner region in response to APG. However, lateral curvature effects on L_θ in SP4 could not be excluded. Axisymmetric boundary layer studies of Wietrzak and Lueptow [128] and Neves et al. [26] (Fig. 1.31) suggested that large δ/a enables structures to traverse the cylinder and interact with structures on the other side. Wietrzak and Lueptow [128] also reported yawed structures based on spanwise two-point correlation. The detailed growth mechanism, e.g., vortex packet merging [117], still requires clarification.

Figure 3.50 shows two-point correlation contours $R_{\theta\theta}$ based on the circumferential velocity u_θ. Each column represents a different wall-normal position, and each row is a new spanwise plane, identical to the layout in Fig. 3.48. In Plane 1, the positive regions were still flanked by negative ones. However, in Planes 2 and 3, a rounded square positive region with four negative lobes emerged at $z/\delta = 0.5$, similar to the pattern in a canonical boundary layer [10]. In SP4, however, the structures appeared circular. As described below, an azimuthal length scale was also computed for $R_{\theta\theta}$.

A spanwise length scale L_θ was computed based on $R_{\theta\theta}$ in the same manner as $L_\theta(R_{uu})$, with a cutoff of $R_{\theta\theta} = 0.1$. Figures 3.51(a) and (b) show an example of the correlation $R_{\theta\theta}$ from Plane 2, with mildly negative lobes surrounding the center peak. Figures 3.51(c) and (d) show $L_\theta(R_{\theta\theta})$ profiles with maximum values in the middle of the boundary layer. In

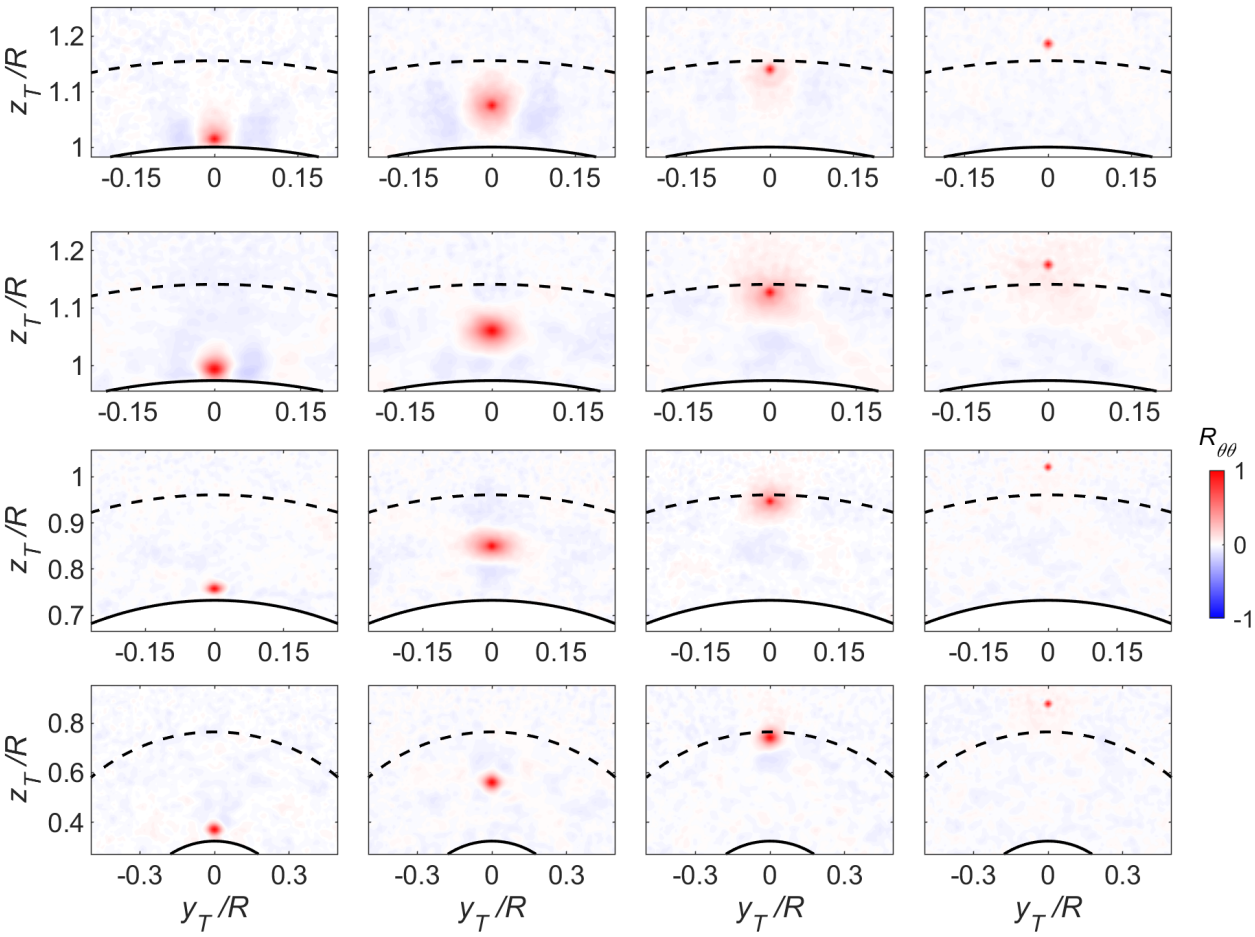

Figure 3.50 Each column shows $R_{\theta\theta}$ computed at four radial positions of roughly $z_{\text{ref}}/\delta = 0.1, 0.5, 0.9, 1.2$. The four rows correspond to spanwise planes measured at $x/L = 0.71, 0.785, 0.85, 0.92$.

Fig. 3.51(c), Plane 1, denoted using the blue circles, showed good agreement with measurements from a canonical boundary layer [11] denoted by black, right-pointing triangles. (Note that Hutchins et al. [11] used a threshold of $R_{vv} = 0.05$).

Figure 3.51(c) shows the circumferential length scale as a fraction of the boundary layer thickness increased with the FPG and decreased through the APG region. The length scale $L_\theta(R_{\theta\theta})$ was normalized by the hull radius R in Fig. 3.51(d). The quantity L_θ/R was invariant in the inner region $z/\delta < 0.3$ across all the planes except for the increase observed in SP4. In the outer region, L_θ increased until SP3 located at $x/L = 0.85$ and remained constant after that. This spatial variation did not align with any of the three factors shown in Fig. 3.12.

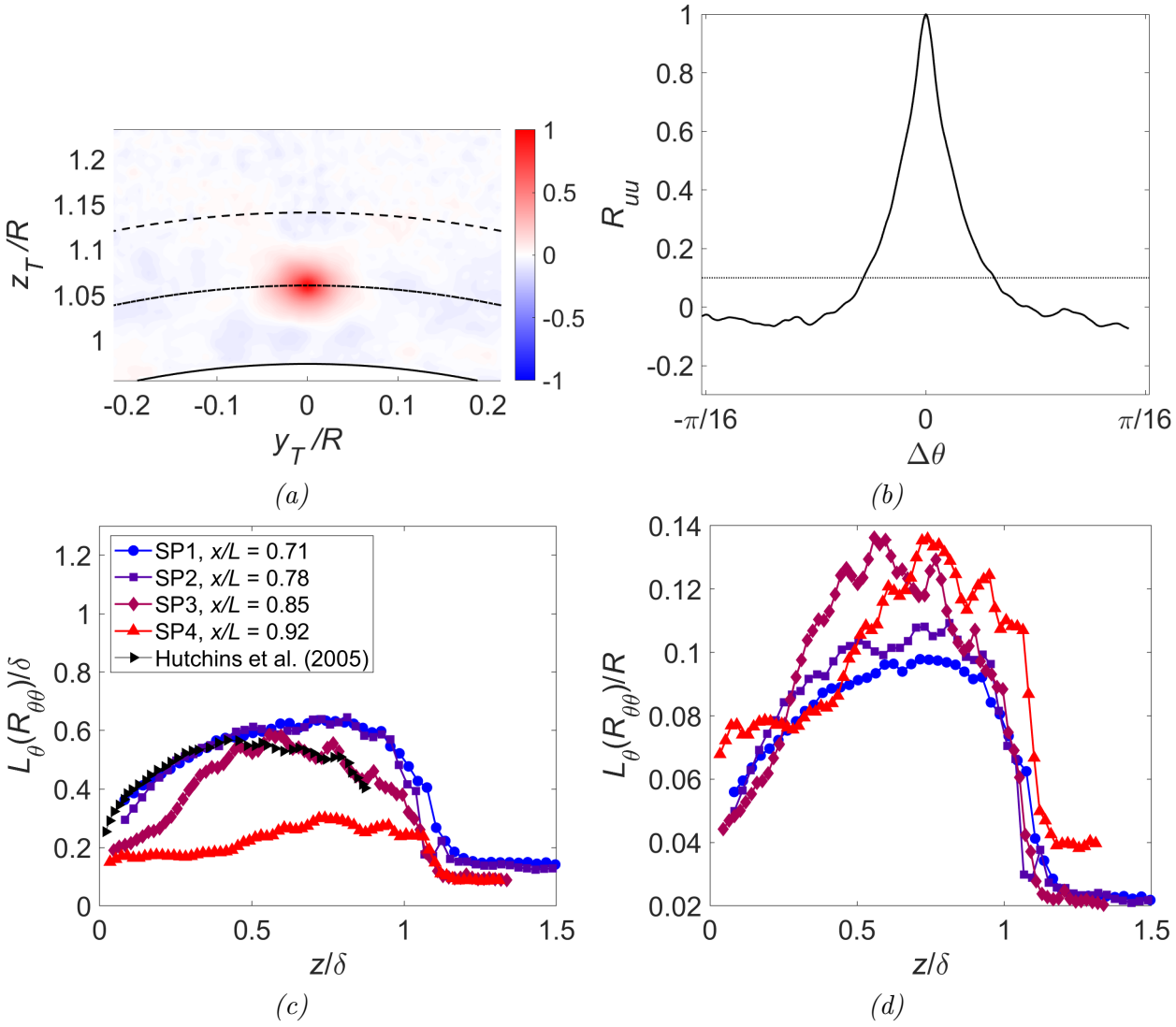

Figure 3.51 (a) $R_{\theta\theta}$ contour; circumferential correlation was computed along arc lengths such as the dotted-dashed line. *(b)* Correlation values along circumferential θ, with length scale defined as the angle between where the two legs intersect $R_{\theta\theta} = 0.1$ multiplied by the radius. Length scale along θ associated with $R_{\theta\theta}$ normalized by *(c)* boundary layer thickness δ and *(d)* hull radius R.

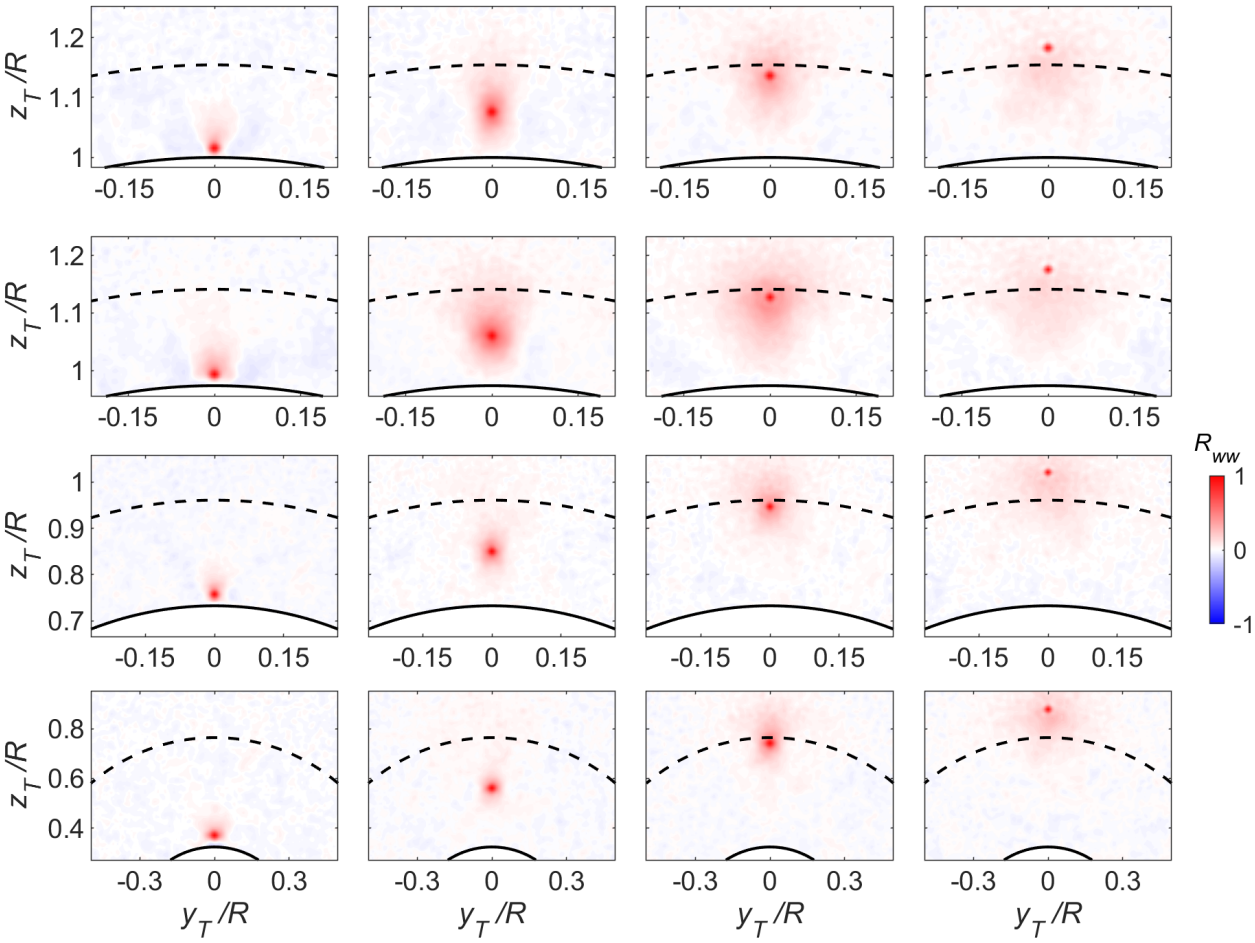

Figure 3.52 Each column shows R_{ww} computed at four radial positions of roughly $z/\delta = 0.1, 0.5, 0.9, 1.2$. The four rows correspond to spanwise planes measured at $x/L = 0.71, 0.785, 0.85, 0.92$.

Perhaps a combination of factors was responsible for the trends in $L_\theta(R_{\theta\theta})$.

It was curious that R_{uu} and $R_{\theta\theta}$ exhibited different trends. There were two possibilities. First, the correlations resulted from entirely different sets of coherent structures. Second, the velocity components were affected by pressure gradient and curvature differently. Limited azimuthal velocity measurements in the current research prohibited a deeper investigation. Future studies should explore u_θ in greater detail.

Contours for R_{ww} are shown in Fig. 3.52 in the same format as Fig. 3.48. Whereas the correlated region was biased in the circumferential direction for $R_{\theta\theta}$, the correlations for R_{ww} in the outer region were biased in the vertical direction, consistent with DNS [10] and the

streamwise plane results in Fig. 3.42(b).

Azimuthal length scales based on R_{ww} are shown in Figs. 3.53(c) and (d). In Fig. 3.53(c), the most upstream plane shown using the blue marker agreed with the results from Hutchins et al. [11]. The length scale $L_\theta(R_{ww})/\delta$ increased with the FPG and decreased with the APG relative to the local boundary layer thickness, although this was likely an artifact of the changing δ. In Fig. 3.53(d), L_θ/R for SP1 through SP3 grew linearly with wall-normal z. The magnitude of $L_\theta(R_{ww})$ in SP4 was significant at the boundary layer edge. The variation of L_θ/R in (d) with the streamwise position was challenging to decipher. As previously stated, studying how different velocity components respond to pressure gradient and/or curvature is worthwhile.

Further insight into the structure of the boundary layer can be obtained by cross-correlating the velocities. To this end, R_{uw} and $R_{u\theta}$ were also computed. Figure 3.54 shows the wall-tangent u denoted by the black circles correlated with the wall-normal w at other spatial locations. The three columns correspond to $z_{\text{ref}}/\delta = 0.1$, 0.5, and 0.9; each row represents a different spanwise plane. The dashed and solid lines indicate the boundary layer edge and the wall, respectively. The color scale is now -0.3 to 0.3.

The first row of Fig. 3.54 shows R_{uw} in SP1 (with near ZPG conditions) having a negative peak with positive regions on the sides. This pattern was most pronounced at $z_{\text{ref}}/\delta = 0.5$ and least noticeable at the boundary layer edge $z_{\text{ref}}/\delta = 0.9$. This pattern implied that high- and low-speed u regions were associated with spanwise alternating regions of up and downwash [11]. Examining the center column representing $z_{\text{ref}}/\delta = 0.5$, a subtle but interesting observation was that the correlated region was shifted up and down relative to the reference marker in the FPG (SP2) and the APG (SP3 and SP4).

Figure 3.55 correlates u at the reference circles to u_θ at various other locations. The format follows that of Fig. 3.54. In Fig. 3.55, SP1 in the first row showed the expected pattern when correlating the streamwise and spanwise velocities in a canonical boundary layer, with negative and positive regions arranged in a diagonal pattern. One outstanding

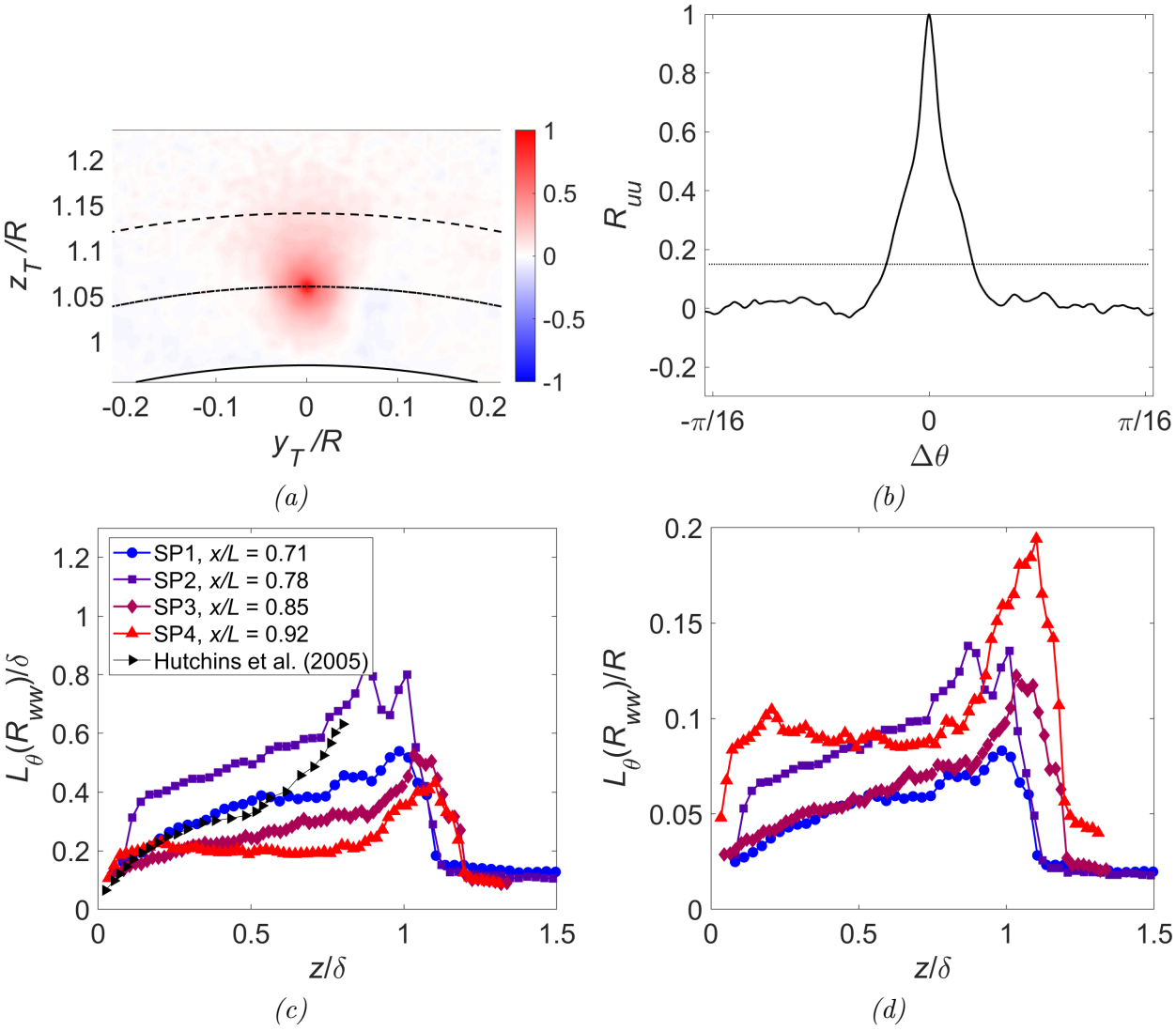

Figure 3.53 (a) R_{ww} contour; circumferential correlation was computed along arc lengths such as the dotted-dashed line. *(b)* Correlation values along circumferential θ, with length scale defined as the angle between where the two legs intersect $R_{ww} = 0.15$ multiplied by the radius. Length scale along θ associated with R_{ww} normalized by *(c)* boundary layer thickness δ and *(d)* hull radius R.

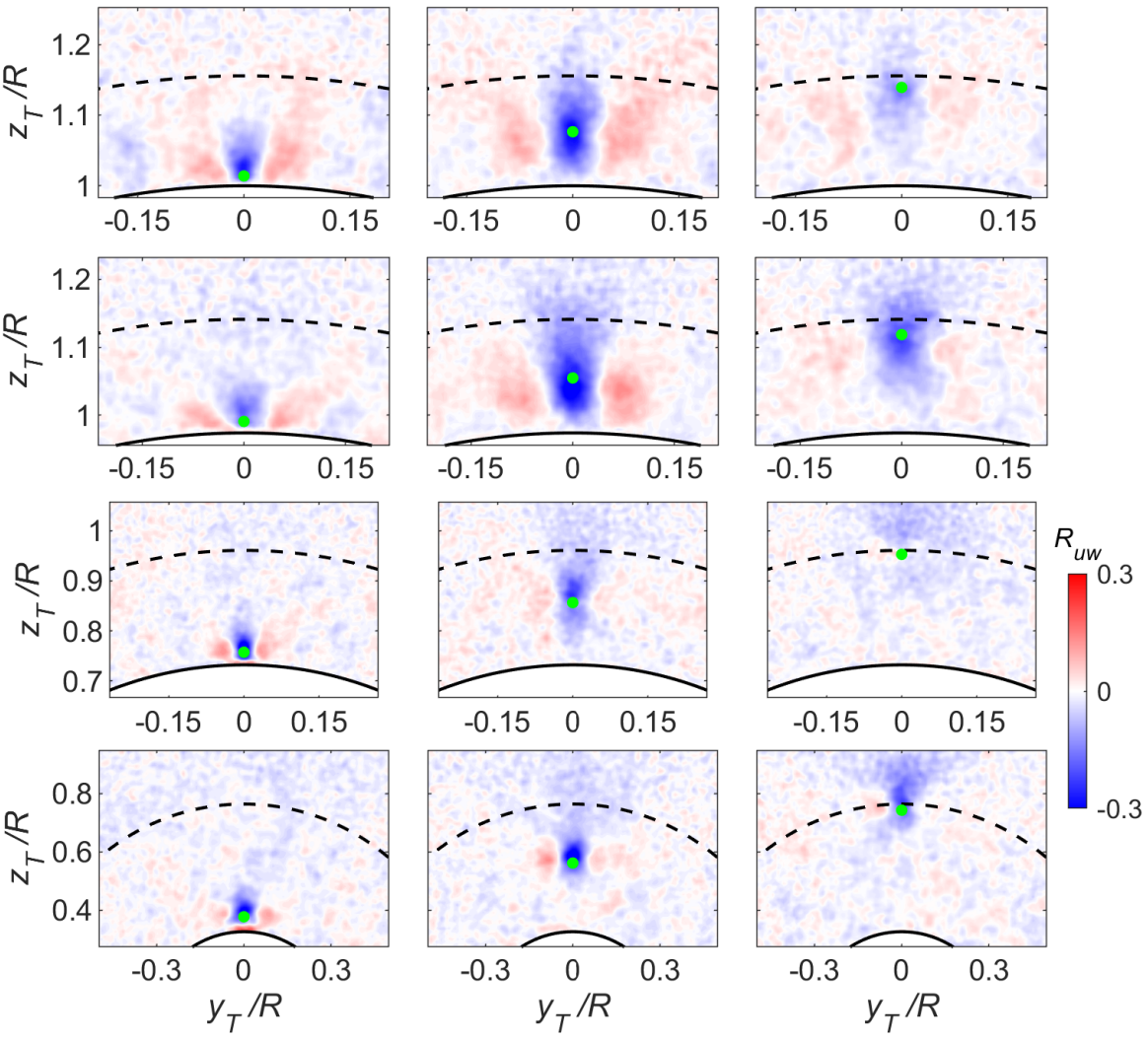

Figure 3.54 Correlation of wall-tangent u with wall-normal w. The three columns correspond to reference u located at $z/\delta = 0.1$, 0.5, and 0.9 denoted by the green circle, and the rows from top to bottom represent spanwise Planes 1 to 4. The dashed line is the boundary layer edge, and the solid line is the wall.

feature of these plots was the varying vertical bias in the correlation. The pattern in SP2 was biased toward the wall and vice versa in SP3 and SP4.

The correlations R_{uw} and $R_{u\theta}$ were combined into quiver plots in Fig. 3.56 to help visualize the flow structure. This approach was possible because w and u_θ were computed by referencing the same time history of u at $z_{\text{ref}}/\delta = 0.5$. These two-point correlations were the same as the linear stochastic estimation, which approximates the conditional average [25]. Note that the quivers in Fig. 3.56 were drawn using $-R_{u\theta}$, as the azimuthal θ was roughly

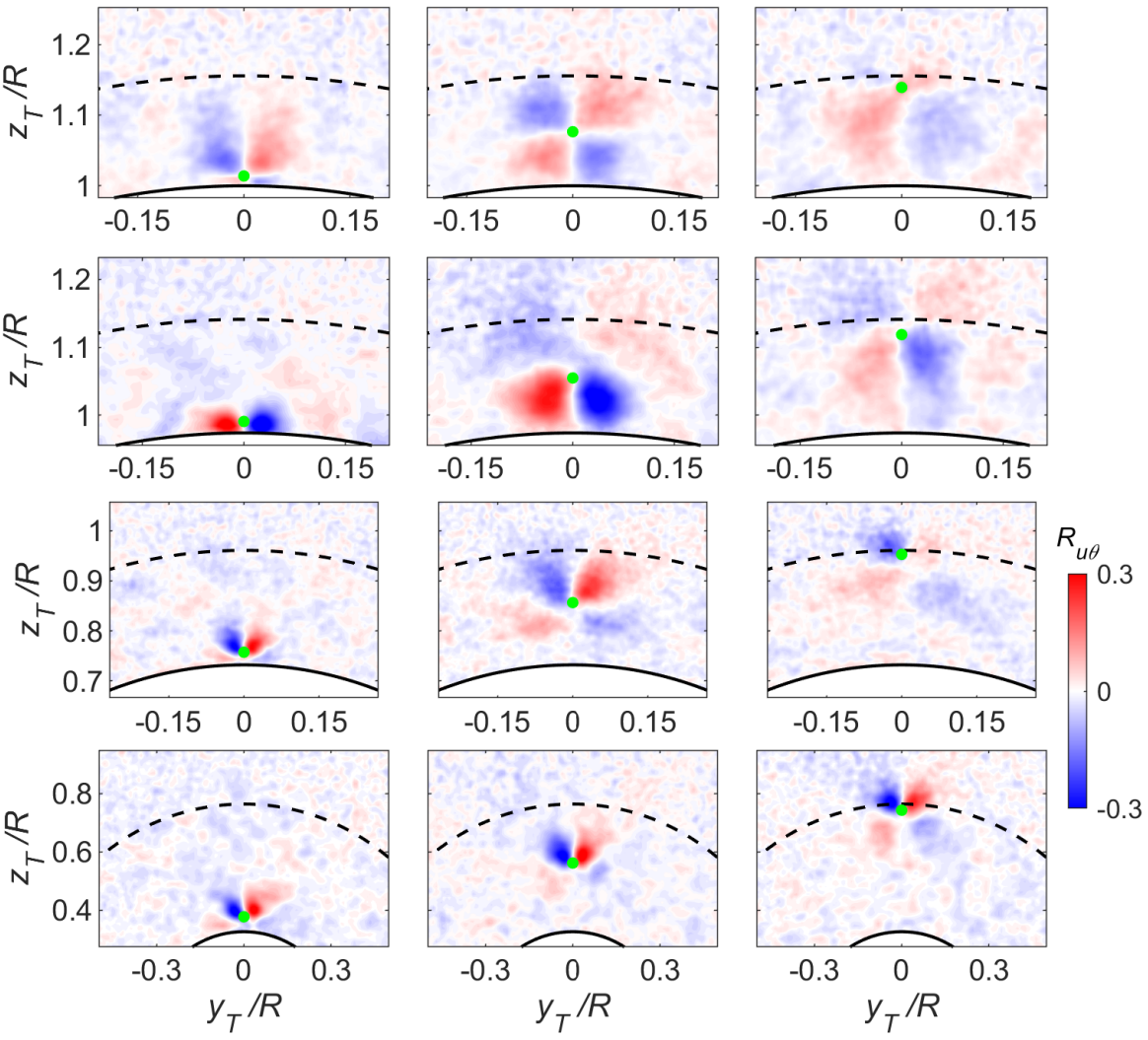

Figure 3.55 Correlation of wall-tangent u with circumferential u_θ. The three columns correspond to reference u located at $z/\delta = 0.1$, 0.5, and 0.9 denoted by the green circle, and the rows from top to bottom represent spanwise Planes 1 to 4. The dashed line is the boundary layer edge, and the solid line is the wall.

opposite of the spanwise y in these measurement domains. This sign change helped visualize the roller structures and had a similar effect as the coordinate choice in Baltzer et al. [72].

Figure 3.56(a) shows the average structure conditioned on a low-speed u event at $z/\delta = 0.5$ in SP1, located in a nearly ZPG zone. Flanking this low-momentum region were counter-rotating rollers similar to a ZPG flow [11]. Entering the pressure gradient region, SP2 in Fig. 3.56(b) showed significant azimuthal velocity drawn toward the reference point from below, whereas in SP3 and SP4, the azimuthal velocity above the reference point pushed

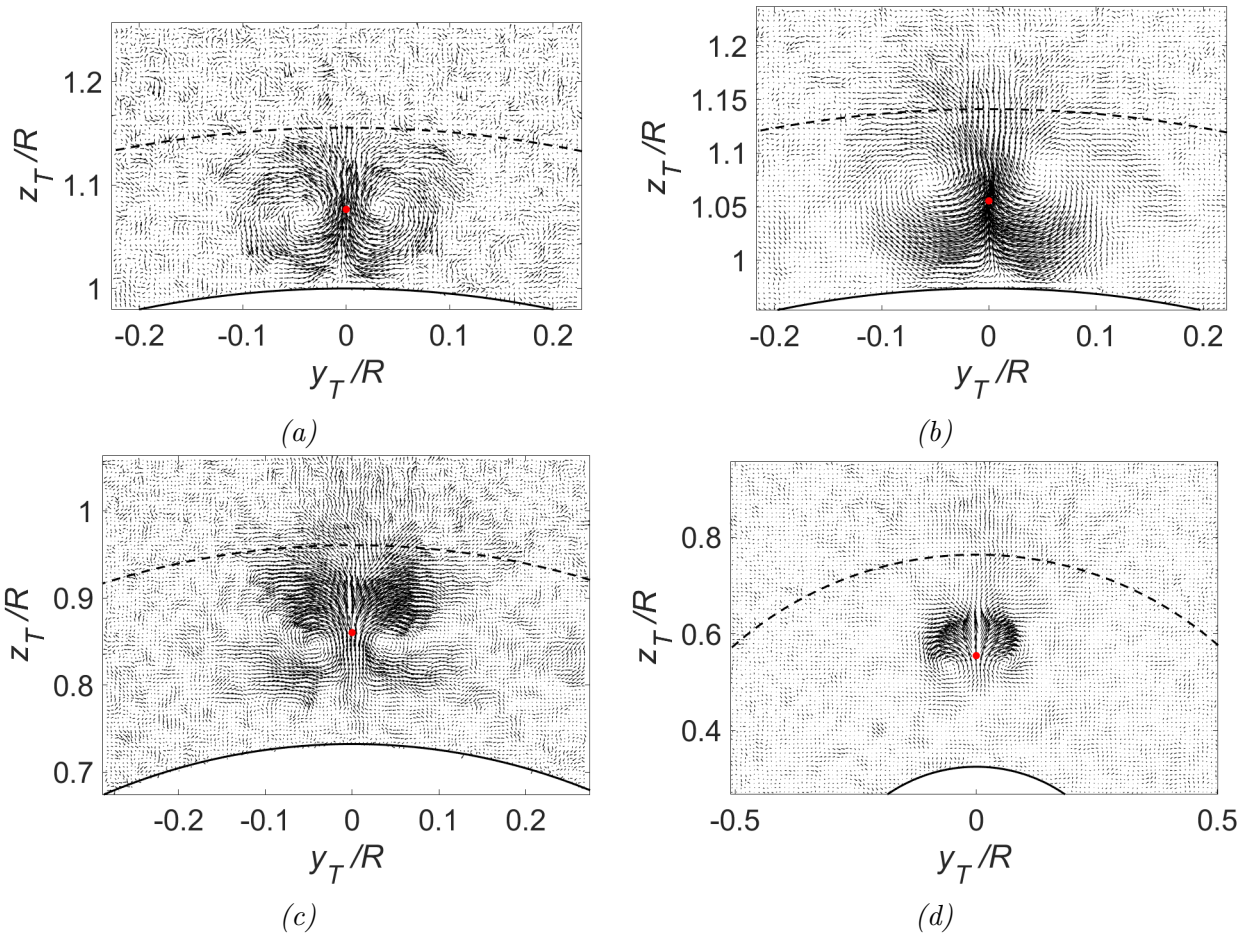

Figure 3.56 R_{uw} and $R_{u\theta}$ shown in Figs. 3.55 and 3.54 are plotted simultaneously to show quivers of the average flow field conditioned upon a low-speed u event. *(a)* SP1, $x/L = 0.71$; *(b)* SP2, $x/L = 0.78$; *(c)* SP3, $x/L = 0.85$; *(d)* SP4, $x/L = 0.92$. The red circles show reference points at $z_{\text{ref}}/\delta = 0.5$.

fluid away.

The location of the flanking rollers relative to the reference was also modified. In SP1 shown in Fig. 3.56(a), the centers of the rollers were roughly in line with the reference velocity at the red circle. However, the rollers in SP2 were shifted upward relative to the reference, and those in SP3 and SP4 were shifted downward.

These deviations in the spanwise rollers from the ZPG case were not because of the inclined measurement planes, which were at most 18° relative to the free stream. The pressure gradient could explain these changes, where the FPG biased the rollers toward the wall and the APG biased them toward the boundary layer edge. However, Lee [14]'s simulations

of a planar APG boundary layer did not demonstrate such trends in the spanwise roller. Therefore, these variations in the conditional structure were likely related to the longitudinal curvature effects. As noted previously in the streamwise plane in Fig. 3.63, R_{uw} could be sensitive to the wall curvature.

A two-point correlation analysis was conducted for four spanwise planes perpendicular to the free stream at $x/L = 0.71$, 0.785, 0.85, and 0.92. These results were used to compute circumferential length scales and visualize the transverse boundary layer structure. The following observations were made:

1. The azimuthal length scale based on R_{uu} increased linearly from the wall except for spanwise Plane 4 ($x/L = 0.92$), where it equaled $0.1R$ across nearly the whole boundary layer thickness, as shown in Fig. 3.49(d).

2. Variations in the spanwise footprint of R_{uu} were driven by the pressure gradient (Fig. 3.49(d)), although the influence of lateral curvature δ/a was not excluded.

3. The azimuthal length scale based on $R_{\theta\theta}$ was significant in the outer region ($z/\delta > 0.3$). The length scale grew with streamwise distance, although the reason for the growth remained unclear. Results are shown in Fig. 3.51(d).

4. The azimuthal length scale based on R_{ww} grew roughly linearly with wall distance except for Plane 4, where it equaled $0.1R$ at $z/\delta = 0.8$ and $0.2R$ at $z/\delta \approx 1$. See Fig. 3.53(d).

5. Linear stochastic estimation revealed counter-rotating vortex pairs. These vortices were translated upward or downward (Fig. 3.56) relative to the reference, likely because of the longitudinal wall curvature.

It was challenging to pinpoint the reasons that underlay these changes in flow structure, partially because the spanwise planes were spaced far away. Future studies should isolate pressure gradient and curvature effects for better comprehension.

3.3.2.3 Three-Dimensional Structures

The three-dimensional structures of the eddies were elucidated by simultaneously performing the two-point correlation in the streamwise and spanwise planes. The reference velocities of this analysis were located along the radial lines where the streamwise and four spanwise planes intersected. Following the approach in previous sections, the distances along the radial lines were converted into the local wall-normal–wall-parallel frame, and three reference heights of $z_{\text{ref}}/\delta = 0.1, 0.5$, and 0.9 were chosen for analysis. The spatial two-point correlation of wall-tangent u and wall-normal w, as well as their cross-correlation were considered in the following paragraphs.

Figures 3.57, 3.58, and 3.59 show R_{uu} based on the wall-parallel velocity referenced to three different wall-normal positions, $z_{\text{ref}}/\delta = 0.1, 0.5$, and 0.9. In these figures, the contours in the streamwise and spanwise planes used cutoff values of 0.1 and 0.05, and are transparent to visualize the structures better. While (a) provides the global perspective, subfigures (b–e) zoom into each spanwise plane location.

In the log region ($z_{\text{ref}}/\delta = 0.1$), the elongated, forward-leaning structures were flanked by negative lobes [10]. At $z_{\text{ref}}/\delta = 0.5$, the structures were more inclined relative to the wall, spanning much of the boundary layer thickness. Near the boundary layer edge at $z/\delta = 0.9$, the structures were more rounded. Negative lobes were not apparent in all the spanwise planes, perhaps because the spanwise-alternating high and low momentum regions were not as dominant. Based on prior analyses in Sections 3.3.2.1 and 3.3.2.2, these results were expected.

Figure 3.60 gives a sense of the three-dimensional R_{ww} based on the wall-normal velocity. Observing the streamwise and spanwise planes, the correlated regions of w were predominantly vertical, wall-normal columns in the outer region, which are better shown in Fig. 3.52. In contrast, a forward-leaning organization was noticed near the wall at the most downstream location, likely pointing to the influence of hairpin packets, as previously discussed in Section 3.3.2.1.

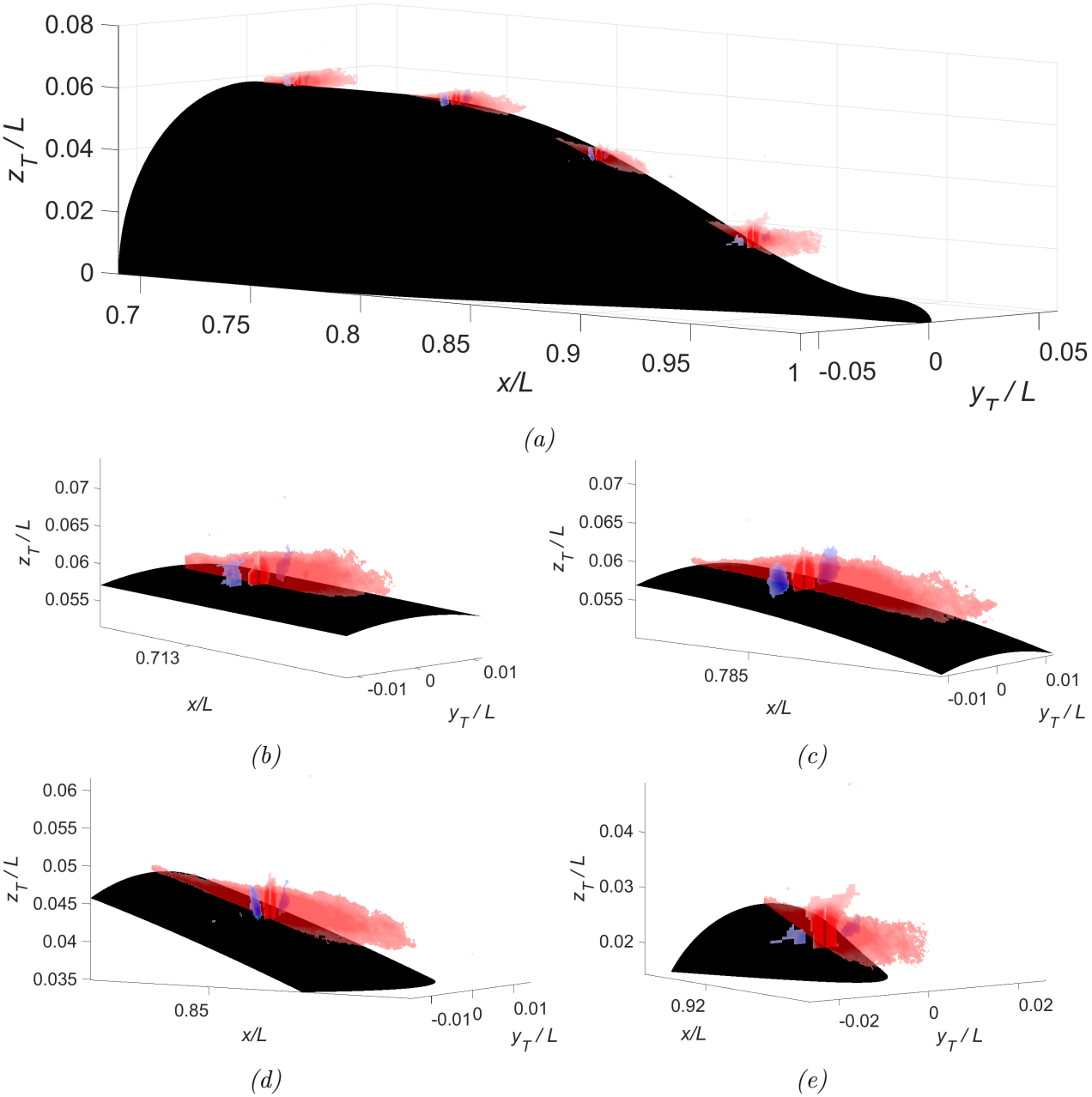

Figure 3.57 R_{uu} correlation contours computed with reference to the wall-parallel u velocity at *(a)* $z_{\text{ref}}/\delta = 0.1$ along the radial line of where the streamwise and spanwise planes intersect. *(b–d)* Zoom in to each streamwise-spanwise intersection to closely examine the flow structure.

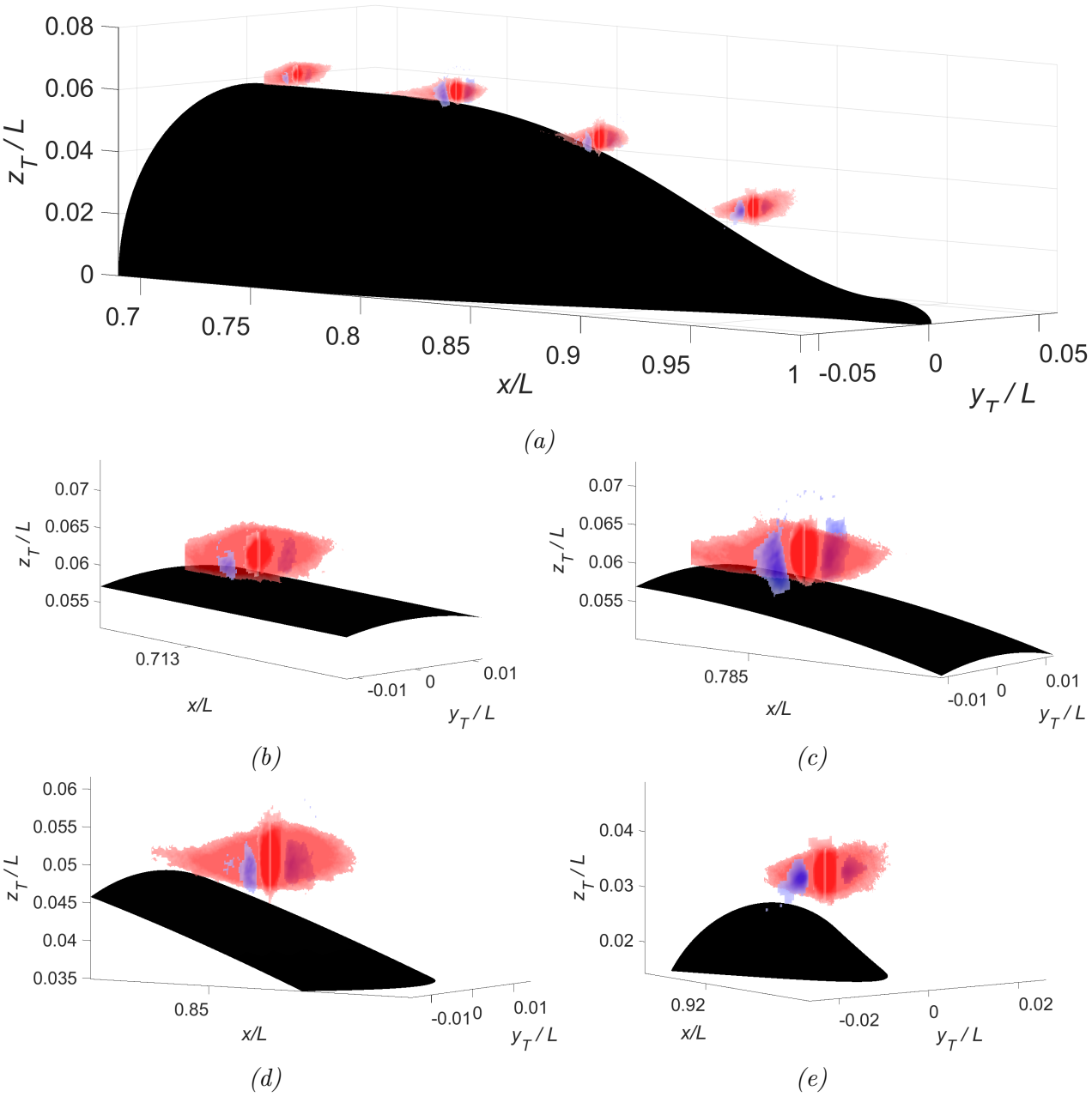

Figure 3.58 R_{uu} correlation contours computed with reference to the wall-parallel u velocity at *(a)* $z_{\text{ref}}/\delta = 0.5$ along the radial line of where the streamwise and spanwise planes intersect. *(b–d)* Zoom in to each streamwise-spanwise intersection to closely examine the flow structure.

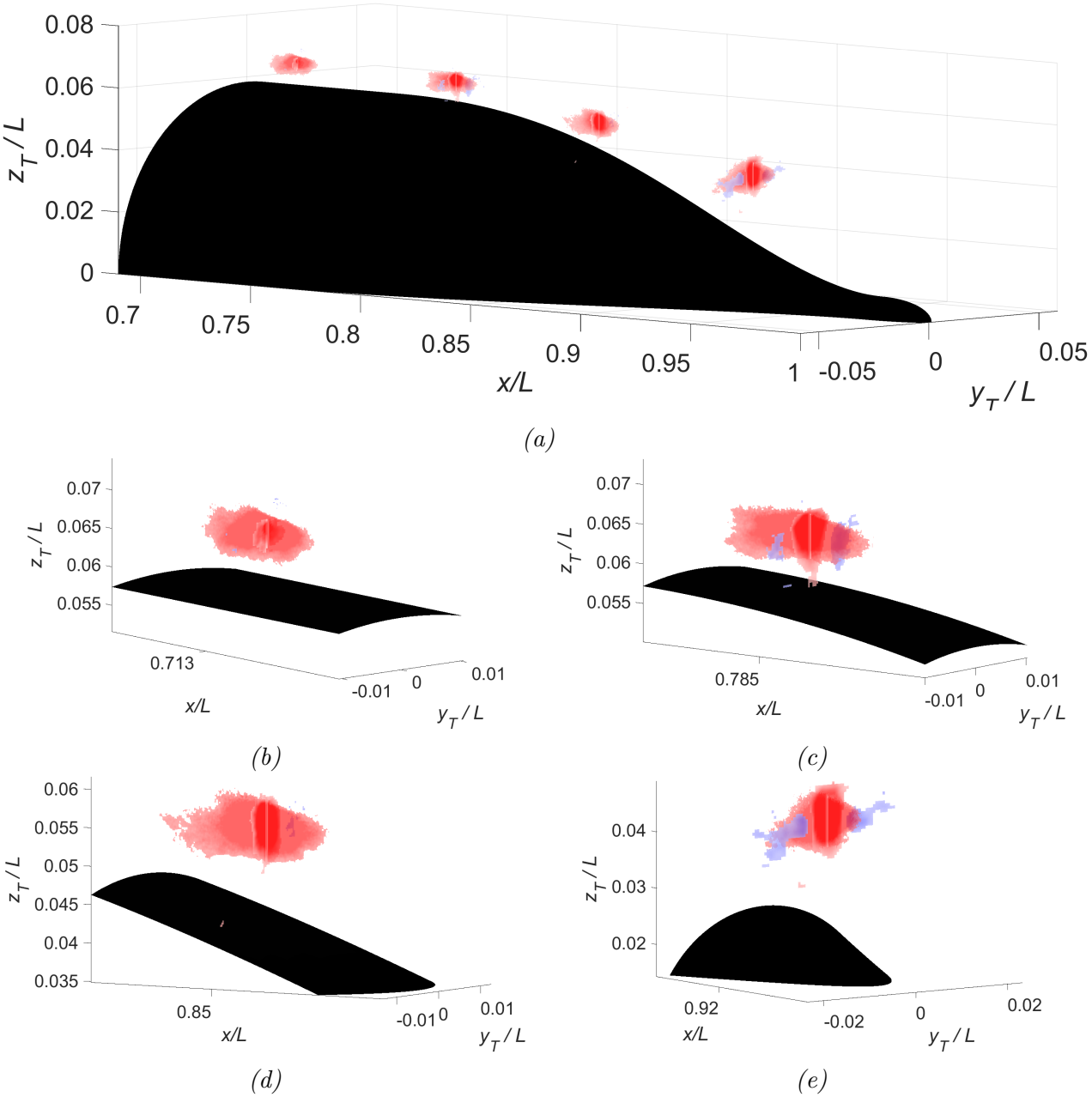

Figure 3.59 R_{uu} correlation contours computed with reference to the wall-parallel u velocity at *(a)* $z_{\text{ref}}/\delta = 0.9$ along the radial line of where the streamwise and spanwise planes intersect. *(b–d)* Zoom in to each streamwise-spanwise intersection to closely examine the flow structure.

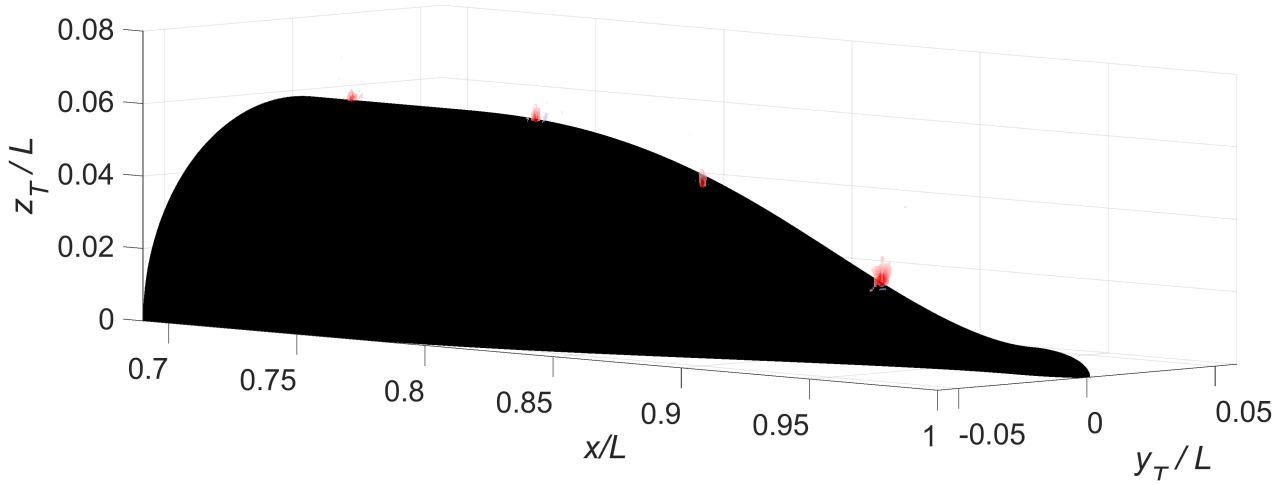

(a)

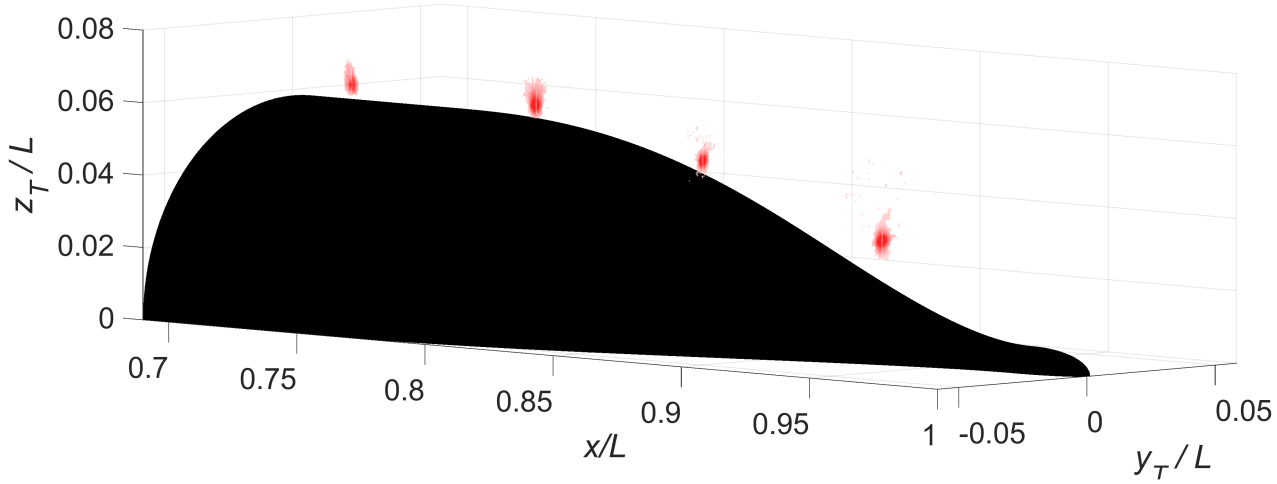

(b)

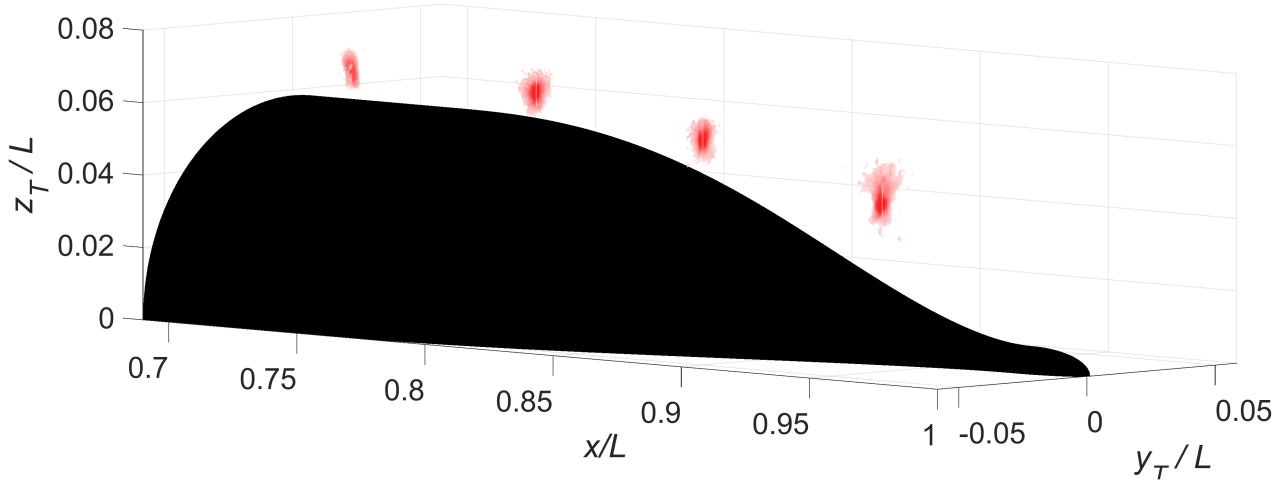

(c)

Figure 3.60 R_{ww} correlation contours computed with reference to the wall-normal w velocity at *(a)* $z_{\text{ref}}/\delta = 0.1$, *(b)* $z/\delta = 0.5$, and *(c)* $z/\delta = 0.9$ along the radial line of where the streamwise and spanwise planes intersect.

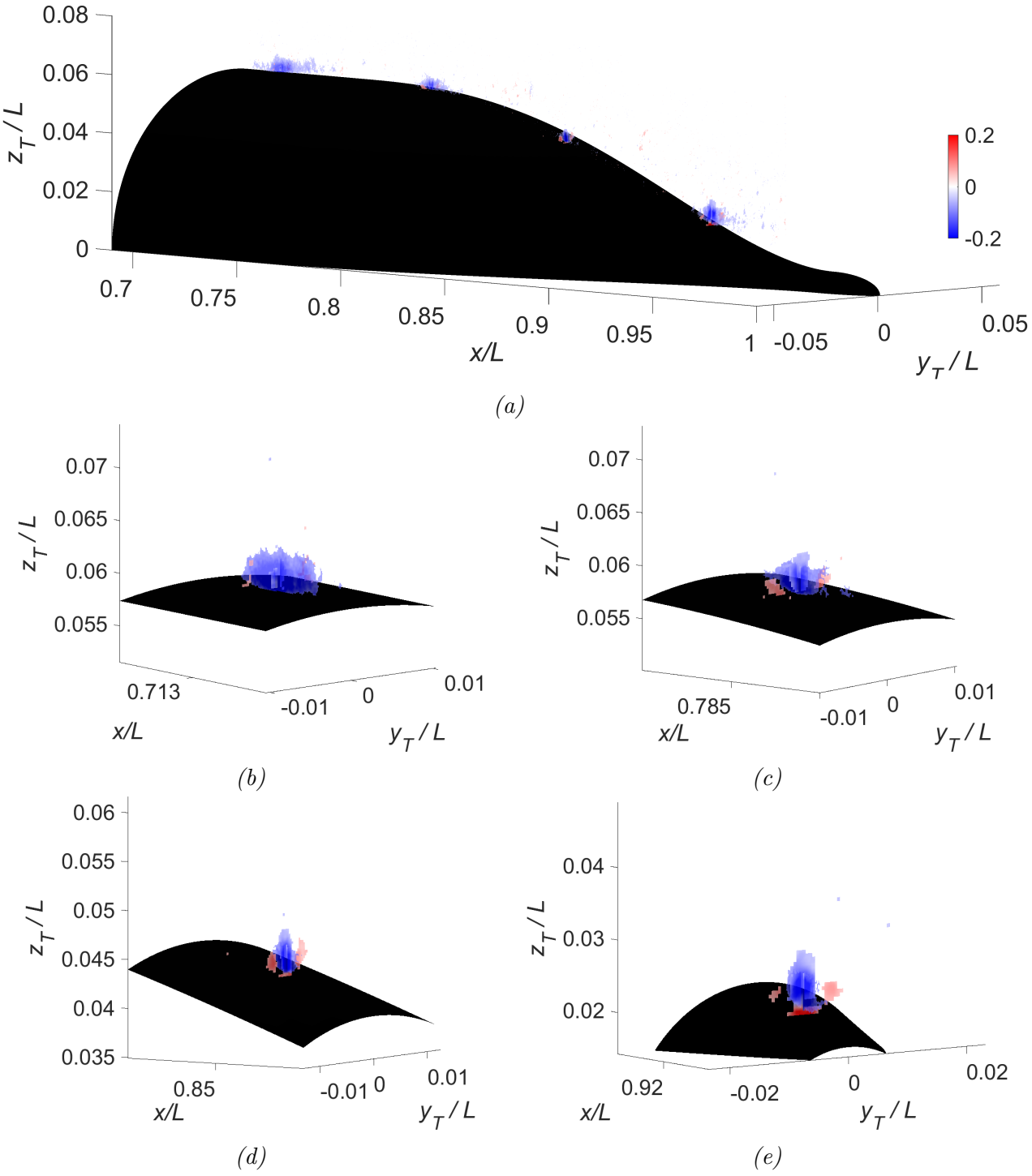

Figure 3.61 R_{uw} correlation contours computed with reference to the wall-parallel u velocity at *(a)* $z_{\text{ref}}/\delta = 0.1$ along the radial line of where the streamwise and spanwise planes intersect. *(b–d)* zooms in to each SP1–4 to closely examine the flow structure.

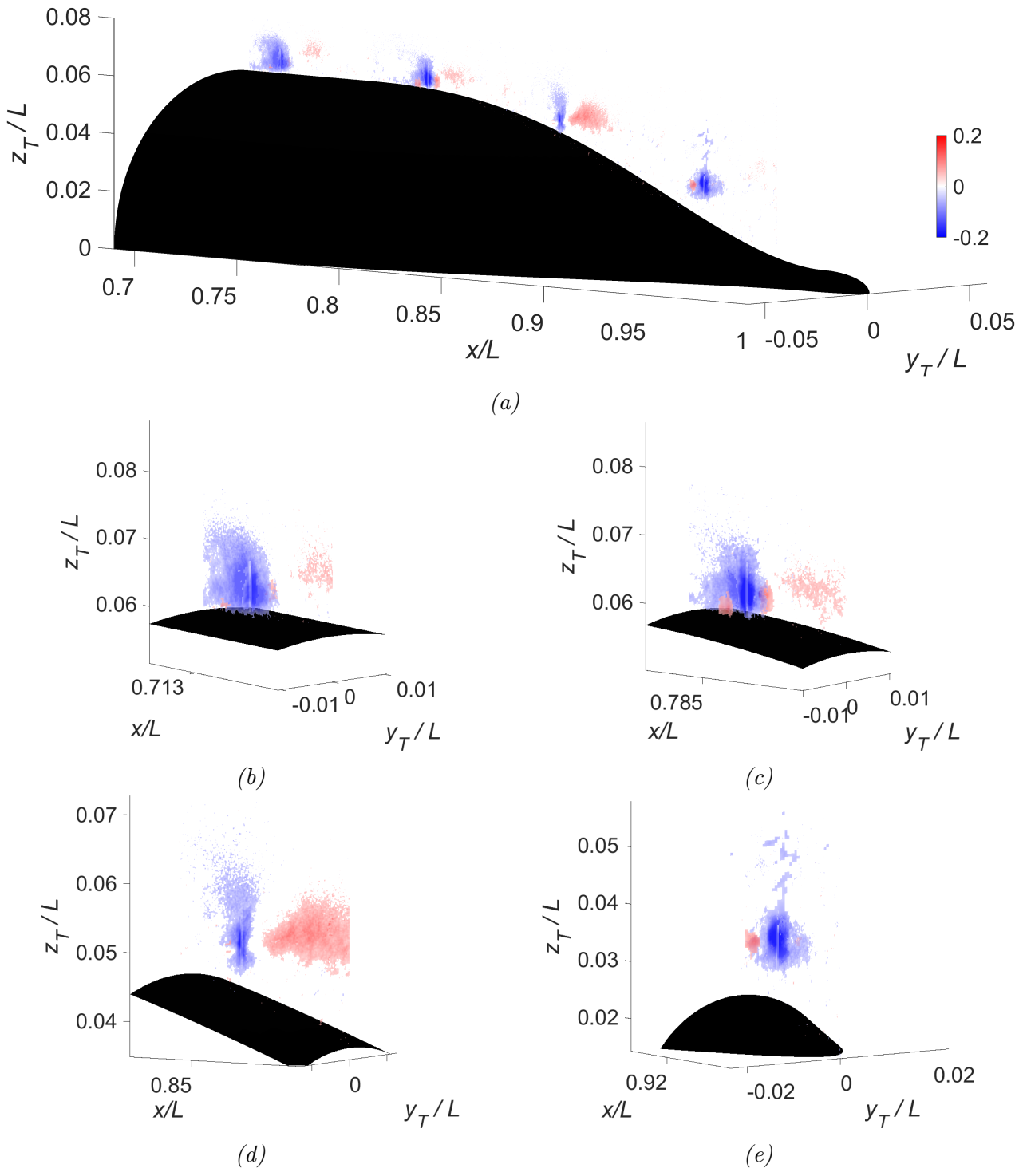

Figure 3.62 R_{uw} correlation contours computed with reference to the wall-parallel u velocity at *(a)* $z_{\text{ref}}/\delta = 0.5$. *(b–e)* Zoom into spanwise planes.

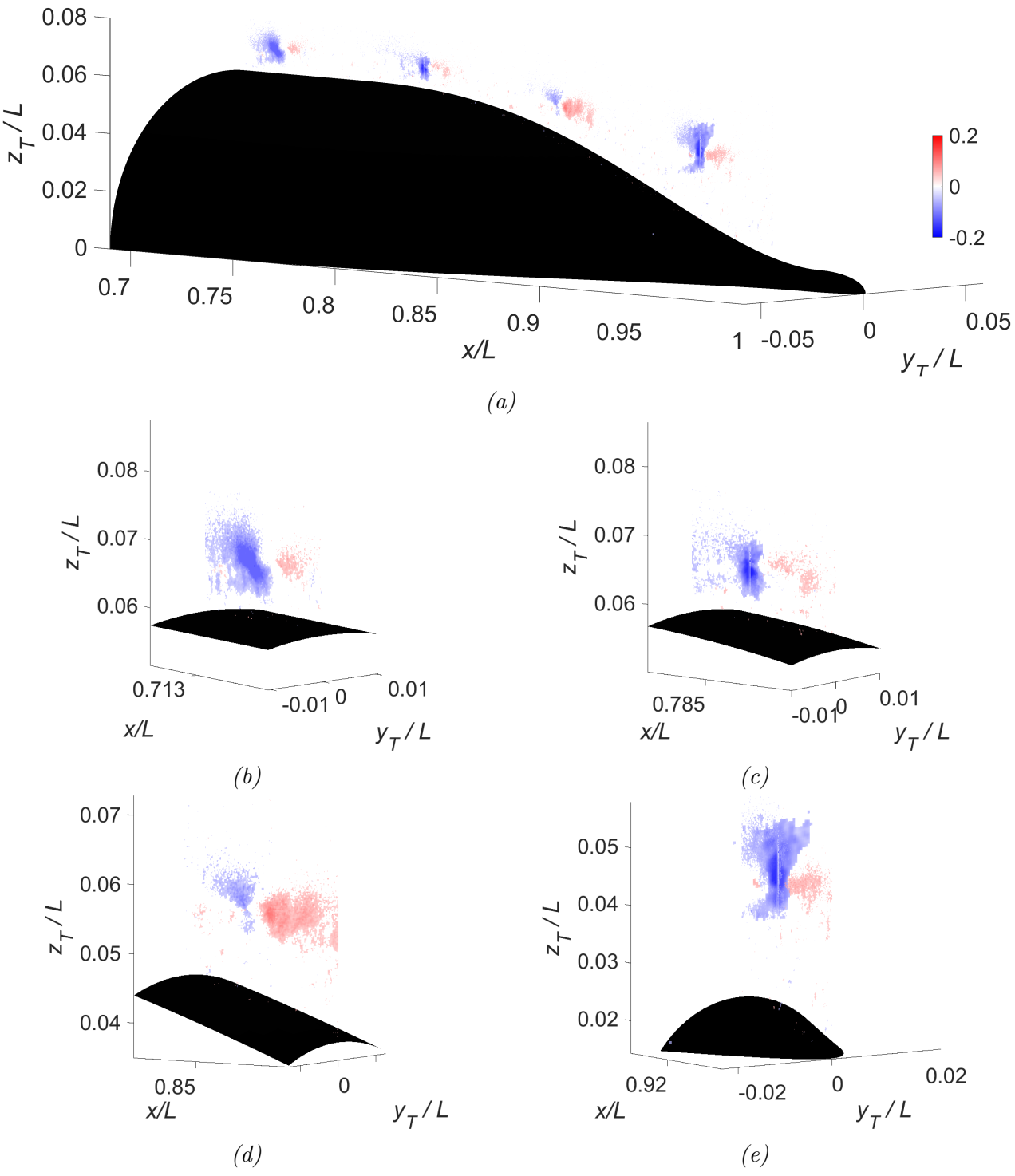

Figure 3.63 R_{uw} correlation contours computed with reference to the wall-parallel u velocity at *(a)* $z_{\text{ref}}/\delta = 0.9$. *(b–e)* Zoom into spanwise planes.

Figures 3.61, 3.62, and 3.63 show the correlation between u at one point and w elsewhere. The reference u was located at $z_{\mathrm{ref}}/\delta = 0.1, 0.5$, and 0.9. The layout of these figures follows those before in Fig. 3.57, with (a) providing a global view, and (b–e) zooming into each of the spanwise planes. The structures shown in the streamwise and the spanwise planes used a cutoff of $R_{uw} = 0.05$.

Figure 3.61 shows the three-dimensional structure of R_{uw} in the log region ($z_{\mathrm{ref}}/\delta = 0.1$). Here, R_{uw} had a spanwise alternating pattern with limited streamwise extent. The spanwise structures were reminiscent of the legs of hairpin-like structures in Lee and Sung [122] and Dennis and Nickels [24]. In the streamwise plane, the correlated regions were compressed and elongated, which likely indicated a more inclined arrangement of hairpins relative to the wall, as expected based on prior analysis of R_{uu}. These contours suggested persistent hairpin activity near the wall.

The structure of R_{uw} referenced to u at $z_{\mathrm{ref}}/\delta = 0.5$ is presented in Fig. 3.62. When the boundary layer was under a nearly canonical state in Fig. 3.62(b), R_{uw} comprised a negative region surrounded by positive lobes on its sides and downstream [13], pointing to the signature of hairpin packets. In the subsequent spanwise planes, the flanking negative lobes were apparent in SP2 (c), nonexistent in SP3 (d), and reappeared in SP4 (e), suggesting that the hairpin packets did not always dictate the correlation.

Contrarily, the positive region in the streamwise plane immediately downstream of the reference velocity was mild in SP1 (ZPG) and SP2, strongest in SP3, and disappeared again in SP4. This positive correlation in the streamwise plane was hypothesized in Fig. 3.46 to result from the activity of turbulent bulges. Then, there appeared to be a trade-off between the spanwise and streamwise regions of positive correlation. This trade-off perhaps suggested an interplay between the hairpin packets and the turbulent bulges, but this requires further investigation.

Lastly, the structure of R_{uw} was examined at $z/\delta = 0.9$ as shown in Fig. 3.63. Following the same format, (a) provides the global view, whereas (b–e) focuses more on the spanwise

planes. In contrast to R_{uw} at $z/\delta = 0.5$ in Fig. 3.62, Fig. 3.63 shows that, at $z/\delta = 0.9$, the spanwise planes no longer possessed the flanking positive lobes. The streamwise plane consistently showed a structure in which the negative region was followed immediately downstream by a positive region, most pronounced in Fig. 3.63(d) around SP3 ($x/L = 0.85$). This streamwise plane structure was similar to those observed at $z/\delta = 0.5$, and likely represented the same flow phenomenon. This streamwise plane upwash/downwash pattern, being more apparent near the boundary layer edge, suggested a relation to the turbulent bulges and valleys.

A three-dimensional understanding of the boundary layer structure was obtained by simultaneously calculating the two-point correlation in the streamwise and spanwise planes. The following key observations were made,

1. The wall-tangent R_{uu} showed elongated, forward-leaning correlation regions with spanwise alternating regions of high and low momentum. As expected, the favorable/adverse pressure gradients reduced/increased the inclination of the R_{uu} contour with respect to the wall, consistent with numerous prior works. The spanwise signature in R_{uu} also appeared to vary.

2. The wall-normal R_{ww} showed, in the outer region, column structures roughly perpendicular to the local wall, a structure that was relatively insensitive to the pressure gradient [13, 115]. Near the wall, the R_{ww} shape varied along the afterbody. In particular, a forward lean in the R_{ww} appeared at the downstream stations, likely resulting from hairpin vortex packets as previously discussed in Sections 3.3.2.1.

3. The cross-correlation R_{uw} revealed unexpected trends. Near the wall, R_{uw} suggested hairpin-like structures akin to those in Dennis and Nickels [24], because of the up and downwash in the spanwise planes. In contrast, R_{uw} was dominated by up and downwash in the streamwise plane at the boundary layer edge, likely related to the activity of the turbulent bulges. Interestingly, in the middle of the boundary layer at

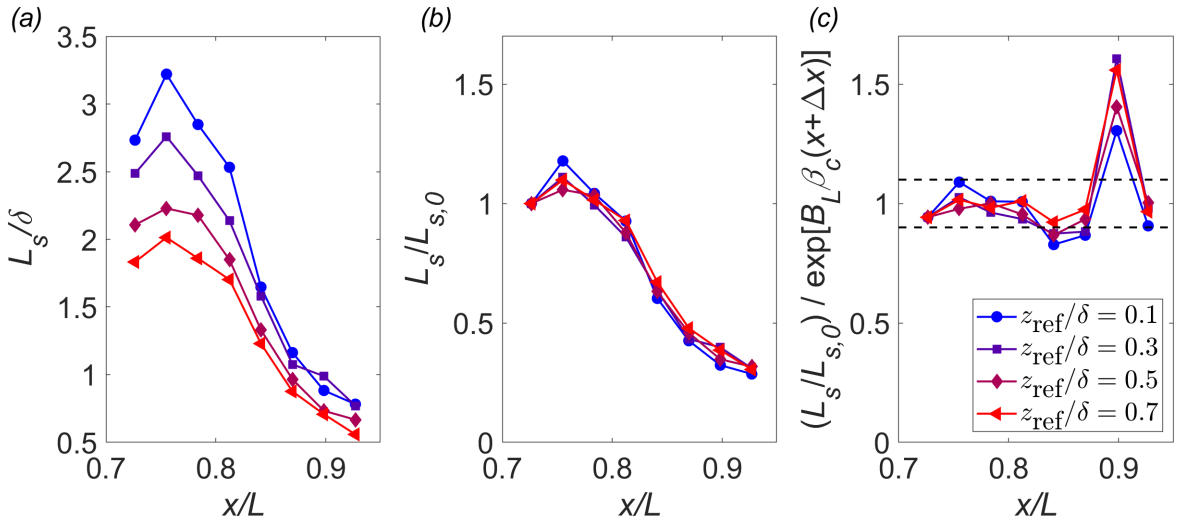

Figure 3.64 (a) Variation in length scale L_s/δ at different heights computed from R_{uu} along streamlines, as discussed in Section 3.3.2.1. *(b)* Length scale L_s relative to the length scale at the most the upstream location $L_{s,0}$. *(c)* The relative length scale scaled by a function of the Clauser parameter β_c, with empirical constants $\Delta x = 0.0079$ m and $B_L = -0.096$.

$z_{ref}/\delta = 0.5$, whether the streamwise or spanwise plane pattern was more apparent depended on the streamwise location, likely pointing to the influence of longitudinal streamline curvature.

Inspection of streamwise and spanwise conditional averages provided insights into the three-dimensional structure of the boundary layer. The near-wall region behaved as expected, with hairpin packets modulated by the pressure gradient. There could also be curvature effects near the wall, but they were challenging to pinpoint concretely. The interesting phenomenon was the interplay between the hairpin vortex and the turbulent bulges in the outer region revealed by R_{uw}. To this end, Section 3.3.4 further investigates R_{uw} near the boundary layer edge using conditional averaging to isolate the positive and negative contributions.

3.3.2.4 Flow History and Modeling

The analyses in prior sections have highlighted the variations in flow structures. This section focuses on the flow history effect by relating the observed flow structure changes to the pressure gradient trends in the large-FOV streamwise plane. Here, an equation is proposed to describe the streamwise variation in length scale across different heights and axial

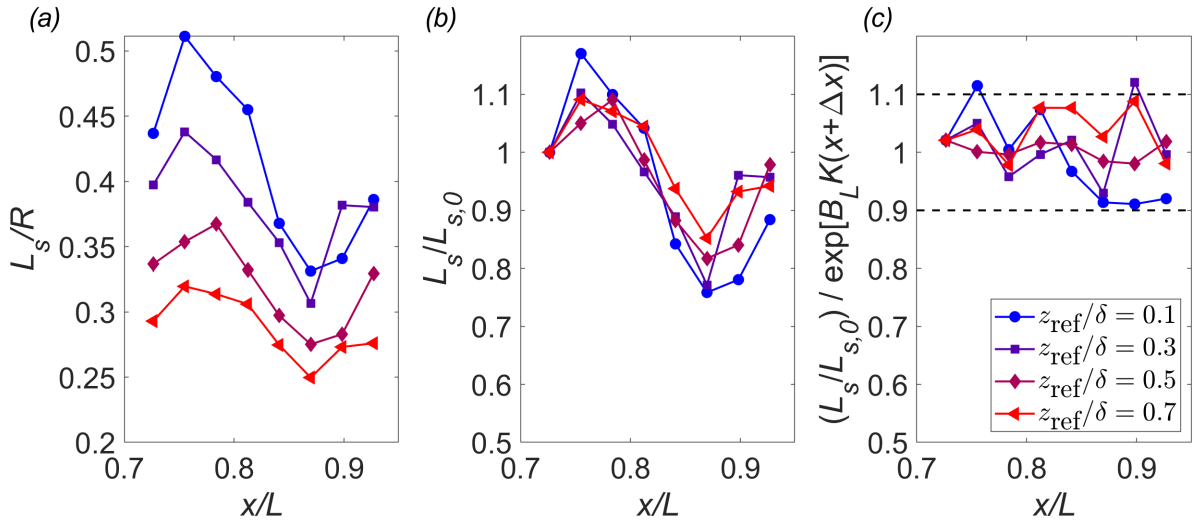

Figure 3.65 (a) Variation in length scale L_s/R at different heights computed from R_{uu} along streamlines, as discussed in Section 3.3.2.1. *(b)* Length scale L_s relative to the length scale at the most the upstream location $L_{s,0}$. *(c)* The relative length scale scaled by some function of the acceleration parameter K, with empirical constants $\Delta x = 0.0264$ m and $B_L = 6.54 \times 10^6$.

locations. This equation uses a pressure gradient parameter, either the Clauser parameter or the acceleration parameter, and two constants, one accounting for the time delay of response and the other adjusting for magnitude. These constants were obtained through an error minimization process.

The modeling approach is best understood by examining a specific example. To this end, the R_{uu} length scale L_s computed along streamlines in Section 3.3.2.1 was analyzed. These length scales L_s/δ are shown again in Fig. 3.64(a), nearly identical to the results in Fig. 3.35; the difference is $z_{ref}/\delta = 0.9$ was omitted because the length scale at the boundary layer edge exhibited different trends.

The wall-normal variations in length scale were removed by recognizing that the percentage change relative to the initial length scale $L_{s,0}$ was relatively consistent across different heights, as illustrated in (b). Further, the pressure gradient β_c (see Fig. 3.3(a)) had a similar trend as L_s. Consequently, the Clauser parameter was used to collapse the streamwise variations in L_s/δ as shown in (c).

The function used to remove the longitudinal length scale variation had the form

$$f = \exp[B_L P(x + \Delta x)]. \tag{3.9}$$

In this equation, P is a pressure gradient parameter such as the Clauser parameter β_c. The constants B_L and Δx were determined to minimize the difference between f and $L_s/L_{s,0}$. The constant B_L is an empirical constant that governs the magnitude of the pressure gradient parameter. The quantity Δx is a response distance, which is necessary because the system does not respond instantaneously to pressure gradient effects. The results in Fig. 3.64(c) used $B_L = -0.096$ and $\Delta x = 0.0079$. The resulting streamwise collapse was $\pm 10\%$ except at $x/L = 0.9$.

An identical analysis was conducted for the length scale L_s normalized by the max hull radius R, as shown in Fig. 3.65. As expected based on the previous analysis, good collapse across different wall-normal distances was achieved in the percentage change relative to the initial length scale $L_{s,0}$, as shown in (b). To further collapse the results across axial locations, the acceleration parameter $K = (\nu/U_e^2)dU_e/dx$ was employed as the pressure gradient function in Eq. 3.9. Figure 3.65(c) shows good collapse to within $\pm 10\%$ with constants of $B_L = 6.54 \times 10^6$ and $\Delta x = 0.0264$.

The response distance Δx was the distance between the maximum (pressure gradient) input and the maximum system response (L_s). For L_s/δ and L_s/R, Δx was on the order of one boundary layer thickness (at $x/L \approx 0.70$). In contrast to the 50δ required to remake a boundary layer after a step change in flow condition previously deduced on a dimensional basis [220], the results in this analysis gave insights into the transient response of the boundary layer structures.

The current section studied and modeled two-point correlation contours, representing composite footprints of all turbulent eddies. However, a deeper understanding could be obtained by examining the form of the coherent structure that constitutes the boundary layer.

Toward this aim, the subsequent section shows the hairpin packet organization by performing linear stochastic estimation (LSE) conditioned on the swirling strength [25].

3.3.3 Hairpin Vortices

Hairpin vortices are foundational to boundary layer structure [15, 16, 19, 49, 69, 70]. Hairpins, also called horseshoe or omega vortices, are populous coherent structures found from the near wall region up to the wake region [19]. As such, visualizing hairpin organization is essential to understanding the boundary layer structure.

Identifying a vortex requires the strain rate tensor to have a stronger rotational component than a shear component because a rotational flow (i.e., $\nabla \times u \neq 0$) is not a sufficient criterion for a closed vortex. Understanding that the boundary layer cannot "see" the mean flow from the Reynolds decomposition, the hairpin heads are better visualized by performing a Galileon decomposition [102], which subtracts a constant vortex convection velocity from the flow. Different aged hairpin packets are located at different wall-normal locations, so the choice of convection velocity may elucidate some hairpins better than others. Indeed, choosing a convection velocity is an iterative process.

The average hairpin organization can be elicited through linear stochastic estimation (LSE) [20, 217]. Christensen and Adrian [20] showed that the hairpins, on average, appear in inclined packets that collectively induce between their legs region of low-speed flow [22]. A similar analysis was conducted using the streamwise plane data to show how the hairpin arrangement was affected by pressure gradients and surface curvature. To this end, a proper orthogonal decomposition (POD) reduced-order flow focusing on the large scales was used to showcase the hairpin vortices, similar to the work of Wu and Christensen [217]. This low-rank flow helped de-noise the PIV measurement to clearly showcase the hairpin arrangement and the induced large-scale motions.

Many references describe the POD in detail [221]. As discussed in Section 3.2.4, the leading modes that resolved 50% of the TKE were used to reconstruct a low-rank flow field [217]. The goal was not to preserve all of the energy but to highlight the trends of how the

large scales respond to pressure gradients. This low-rank flow field is shown in the subsequent paragraphs to have retained the hairpin organization.

Figure 3.66(a) shows the LSE of the velocity fields u and w based on the swirling strength [18] at $x/L = 0.71$ and $z_{\text{ref}}/\delta = 0.15$ denoted by the red marker. Notice the quivers all have unit lengths to better illustrate the vortical structures further from the reference point. The hairpins were arranged on an inclined slope at roughly 6°, lower than that of a canonical flow's 13°. The slight FPG or the axisymmetry could explain this lower angle.

The LSE was repeated at three other downstream locations of $x/L = 0.78$, 0.85, and 0.91 to understand pressure gradient and wall curvature effects. While the inclined hairpins at $x/L = 0.78$ in (b) were at a modest 8°, the inclination angle relative to the surface increased to 14.7° at $x/L = 0.91$ shown in (d). These inclination angles were comparable to those from the two-point correlation of R_{uu} shown in Fig. 3.37(a) and 3.38(a). These computed angles were lower than those reported for planar APG boundary layers in Lee and Sung [121].

These LSE flow fields provided compelling evidence for the crucial role that hairpins continued to play in the near-wall region of boundary layers with intense pressure gradients and wall curvatures. Lastly, zooming out from the reference point, Fig. 3.67 shows an extended field of view for the LSE in Fig. 3.66(d). This figure highlights zones of roughly uniform momentum collectively induced by the hairpin packets and how older packets seemed to overlay the younger ones [19]. Any roller structures associated with an embedded shear layer [5, 73] were not apparent in the LSE.

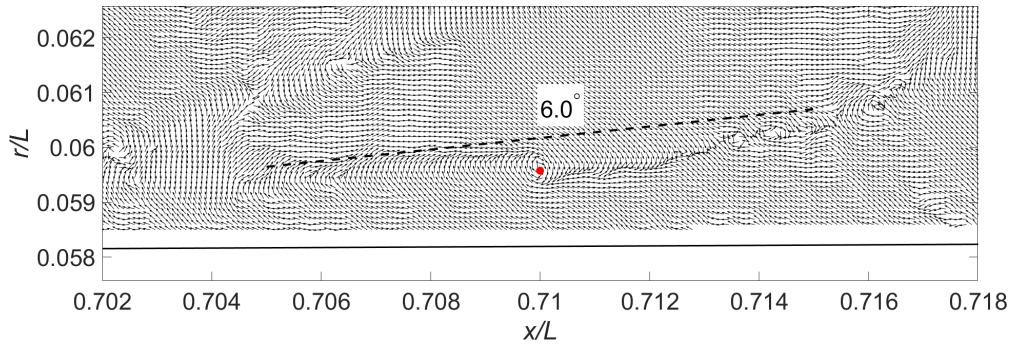

(a) $x/L = 0.71$

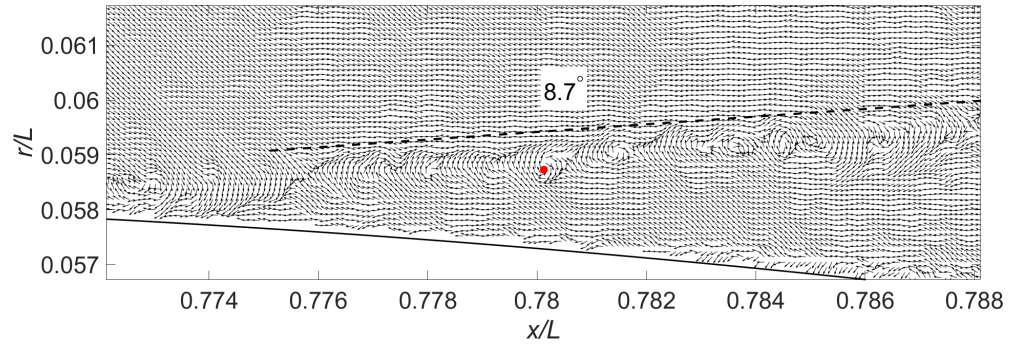

(b) $x/L = 0.78$

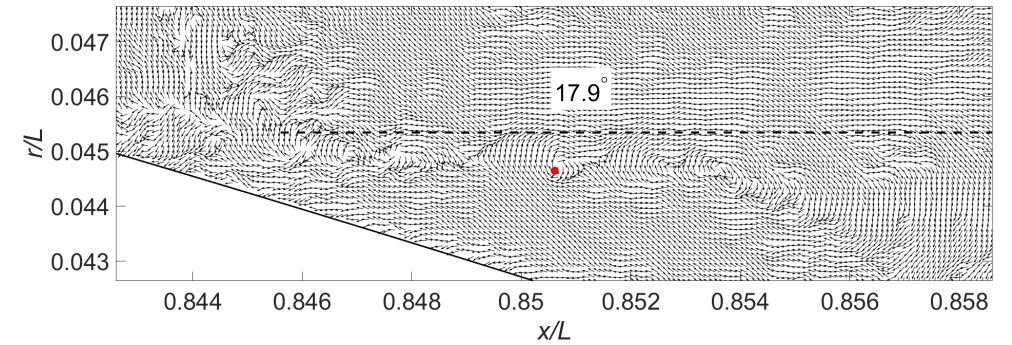

(c) $x/L = 0.85$

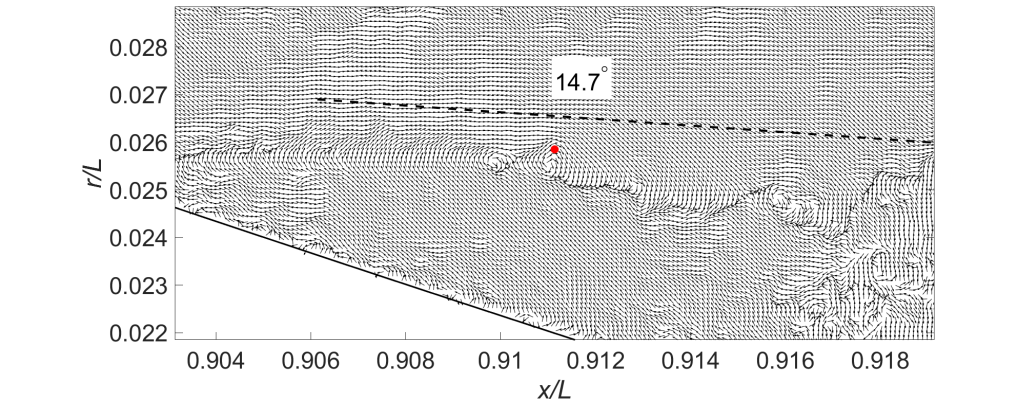

(d) $x/L = 0.91$

Figure 3.66 Linear stochastic estimation of velocities u_L and w_L based on swirling strength λ_L [18] from a POD-based low-rank flow field.

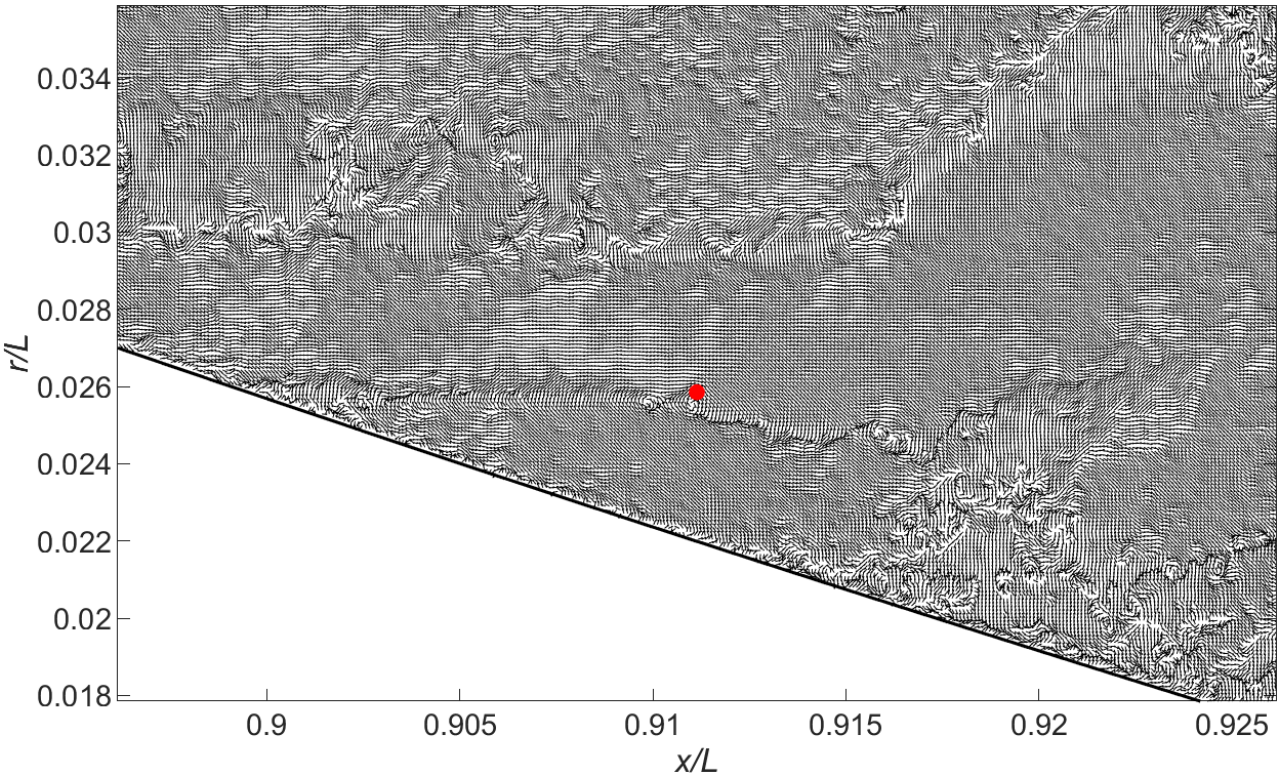

Figure 3.67 Zoomed-out view of Fig. 3.66(d) shows overlaying regions of roughly uniform momentum zones [16] in a POD low-rank flow field.

3.3.4 Low and High-Speed Events

The objective of this section is to investigate the R_{uw} correlation contours shown in Figs. 3.45 and 3.62. These contours exhibited unusual trends that were not encountered in the literature survey. To this end, conditional averaging was used to understand the flow structure when the instantaneous velocity was below a set threshold. The emphasis in the section is placed on the outer region because the inner region, as shown through LSE, continued to be dominated by hairpin packets.

As noted previously in Sections 3.3.2.1 and 3.3.2.3, the R_{uw} structure differed in the log and wake regions. In the log region ($z/\delta = 0.1$), R_{uw} showed hairpin signatures, as indicated by the spanwise alternating regions of up and downwash; see Fig. 3.61. However, as the hairpin coherence decreased with wall distance in the outer region ($z/\delta = 0.5$) [19, 24], an unusual pattern of alternating up/downwash in R_{uw} appeared in the streamwise plane, in place of the spanwise alternating pattern. This streamwise pattern was dominant at the boundary layer edge ($z/\delta = 0.9$), and has not been documented in prior literature (to this author's knowledge).

To this end, conditional averages were calculated based on low-momentum and downwash events at the boundary layer edge, where the interesting patterns of R_{uw} appeared. Each conditional average was computed at the intersection of the streamwise and spanwise planes to obtain a three-dimensional perspective of the spatial development. Conditional averages are first presented for low-momentum events and subsequently for instances of intense downwash.

The condition for calculating an average low-speed event was $u < -u_{\text{rms}}$ at $z_{\text{ref}}/\delta = 0.9$. Using this condition, Figs. 3.68 and 3.69 respectively show the conditionally averaged wall-tangent u and wall-normal w flow fields. Each subfigure zooms into a region near the corresponding spanwise plane, respectively located at $x/L = 0.71$, 0.785, 0.85, and 0.92. The green circle denotes the reference velocity location. The contour lines in Fig. 3.68 represent constant velocity, and these lines form a local "bump" representing a turbulent bulge

with lower velocity than the surrounding irrotational flow. These conditional averages were consistent with those shown in the DNS results of Lee et al. [34] in Fig. 1.41.

Examining the wall-normal velocity fluctuation in Fig. 3.69 based on the same low-speed criterion, the recurring pattern was an upwash followed immediately by a downwash. The red and blue indicate the positive and negative averaged wall-normal fluctuation normalized by the free stream. These up and downwash patterns varied with streamwise distance, where SP3 ($x/L = 0.85$) showed the most compact positive region and the most coherent, extensive downwash, consistent with the prior R_{uw} correlations in Fig. 3.45(c). This similarity indicated that R_{uw} corresponded to the turbulent bulges displayed in Fig. 3.68 revealed by the same low-speed criterion. Additional conditional averaging was performed based on downwash events at the boundary edge to comprehend the flow dynamics better.

Conditional averages were computed based on when the wall-normal fluctuation $w < -w_{\text{rms}}$. Figures 3.70(a) and (b) show the streamwise plane, while (c) and (d) present the spanwise plane results. Subfigures (b) and (d) zoom into the boxed regions surrounding the conditional point $z_{\text{ref}}/\delta = 0.9$ denoted by the green circle. The solid green line is where the planes intersect; the dotted-dashed cyan line is the boundary layer edge (Section 3.2.3). The colored contours are $\langle u \rangle / U_\infty$, the conditionally-averaged wall-tangent velocity fluctuation. The quivers in (b) show the conditionally-averaged $\langle u \rangle$ and $\langle w \rangle$; quivers in (d) show the conditional $\langle w \rangle$ and $-\langle u_\theta \rangle$. These quivers were normalized to indicate the in-plane flow directions.

A significant wall-tangent velocity deficit was observed upstream of the green reference location in Figs. 3.70(a) and (b). The structure extended to the wall and was reminiscent of a turbulent bulge. In the streamwise plane, surrounding the green circle, were regions of high and low streamwise momentum arranged in a diagonal pattern. This pattern was the product of two vortex structures, one upstream and the other downstream of the spanwise plane, indicating a downward motion toward the wall. According to the flow model of Reuther and Kähler [35], this conditional field suggested high-speed fluid traveling around a turbulent

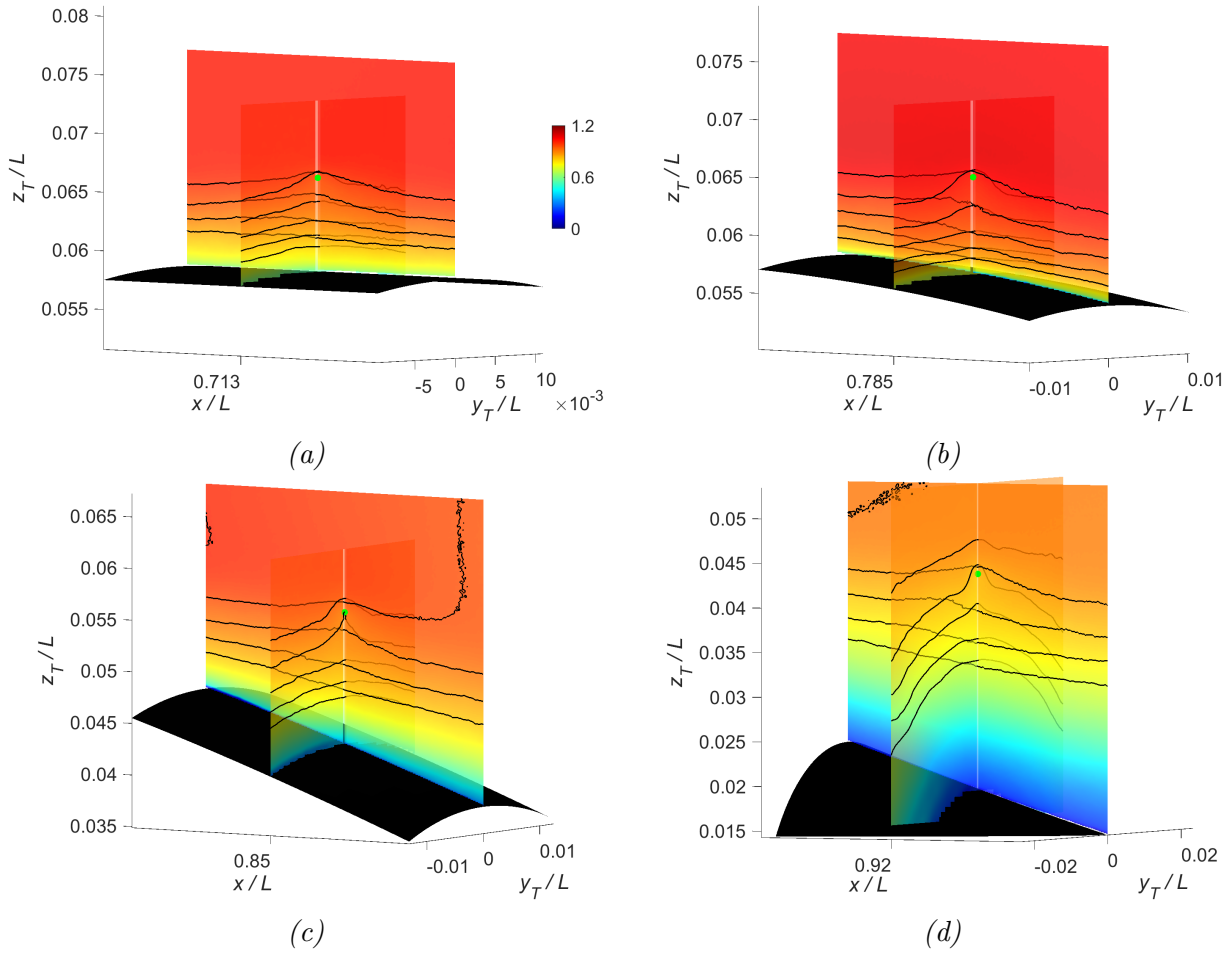

Figure 3.68 Conditionally averaged U/U_∞ based on $u < -u_{\text{rms}}$ at $z_{\text{ref}}/\delta = 0.9$ where the streamwise plane intersects *(a)* SP1, *(b)* SP2, *(c)* SP3, and *(d)* SP4

bulge into a valley where entrainment occurred.

The corresponding SP1 is shown in Figs. 3.70(c) and (d). The contour in (c) showed a positive region flanked by negative correlations. This pattern suggested that the spanwise extent of the high-speed fluid, or the width of the turbulent valley, was roughly δ. The quivers in (d) indicated the flow was funneled from the top down toward the green centerline, consistent with the idea that high-speed fluid accelerates around the turbulent bulge into valleys [35].

The results for SP2 are shown in Fig 3.71, following the same format as Fig. 3.70. The conditional velocity contour in (a) appeared detached from the wall. Zooming into the conditional point, the streamwise plane vortex pair was not as apparent as SP1 in Fig. 3.70(b).

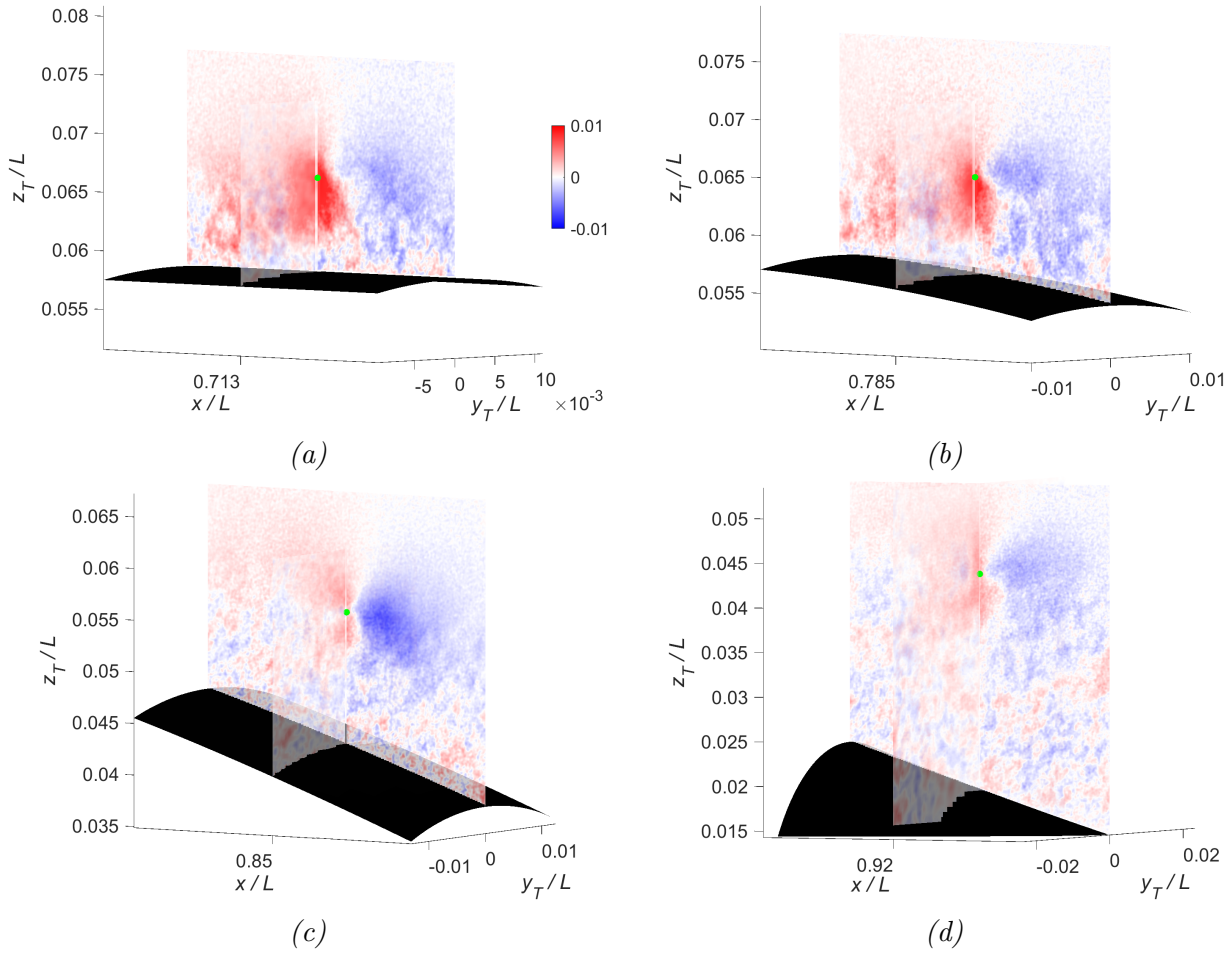

Figure 3.69 Conditionally averaged $\langle u \rangle / U_\infty$ based on $u < -u_{\text{rms}}$ at $z_{\text{ref}}/\delta = 0.9$ in *(a)* SP1, *(b)* SP2, *(b)* SP3, and *(b)* SP4.

However, the quivers suggested irrotational flow traveling around a turbulent bulge into a valley. The spanwise plane shown in (c) revealed alternating high and low streamwise momentum patterns spanning much of the boundary layer thickness. The quivers in (d) indicated that fluid merged toward the centerline and was pushed closer to the wall.

The conditional velocity fields surrounding SP3 are shown in Fig. 3.72. In (a), a familiar diagonal pattern of high and low-speed wall-tangent velocity emerged. The blue turbulent bulge was more inclined relative to the wall than the upstream spanwise plane locations. The structure remained detached from the wall, perhaps indicating that the wall did not immediately affect the outer region. SP3 shown in (c) bisected the turbulent bulge apex, which was surrounded in SP3 by high-momentum fluid. Despite the difference in the $\langle u \rangle$

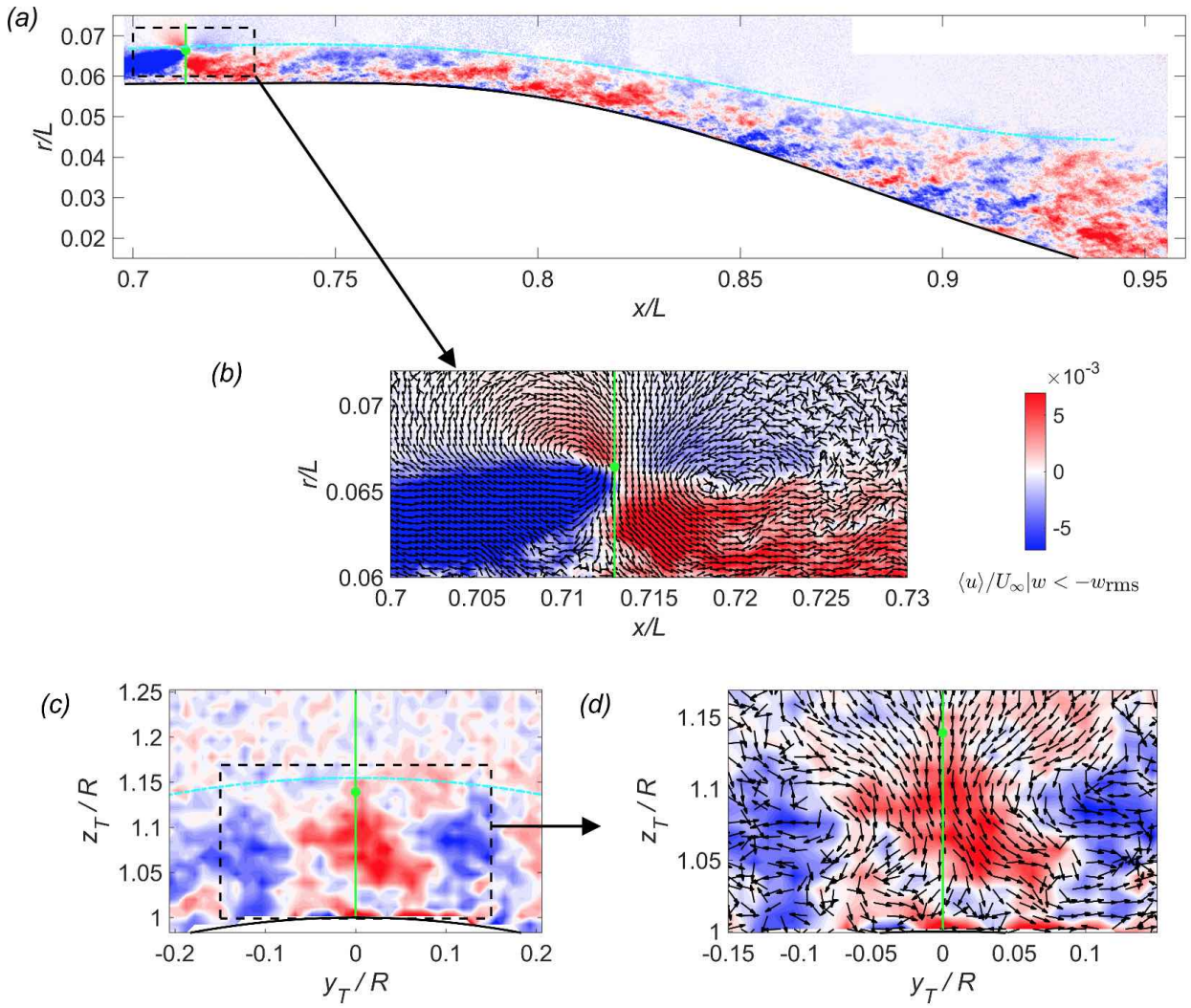

Figure 3.70 Average *(a,b)* streamwise and *(c,d)* spanwise plane flow fields conditioned on the wall-normal velocity fluctuation $w < -w_{\text{rms}}$ at $z/\delta = 0.9$ along the green line, where the orthogonal planes intersect. The colored contour represents the average wall-tangent fluctuation $\langle u \rangle | w < -w_{\text{rms}}$, normalized by the free stream U_∞. *(b,c)* Zoomed-in view of the streamwise and spanwise planes, where the quivers represent the in-plane $\langle w \rangle$ and $-\langle u_\theta \rangle$ conditioned on $w < -w_{\text{rms}}$.

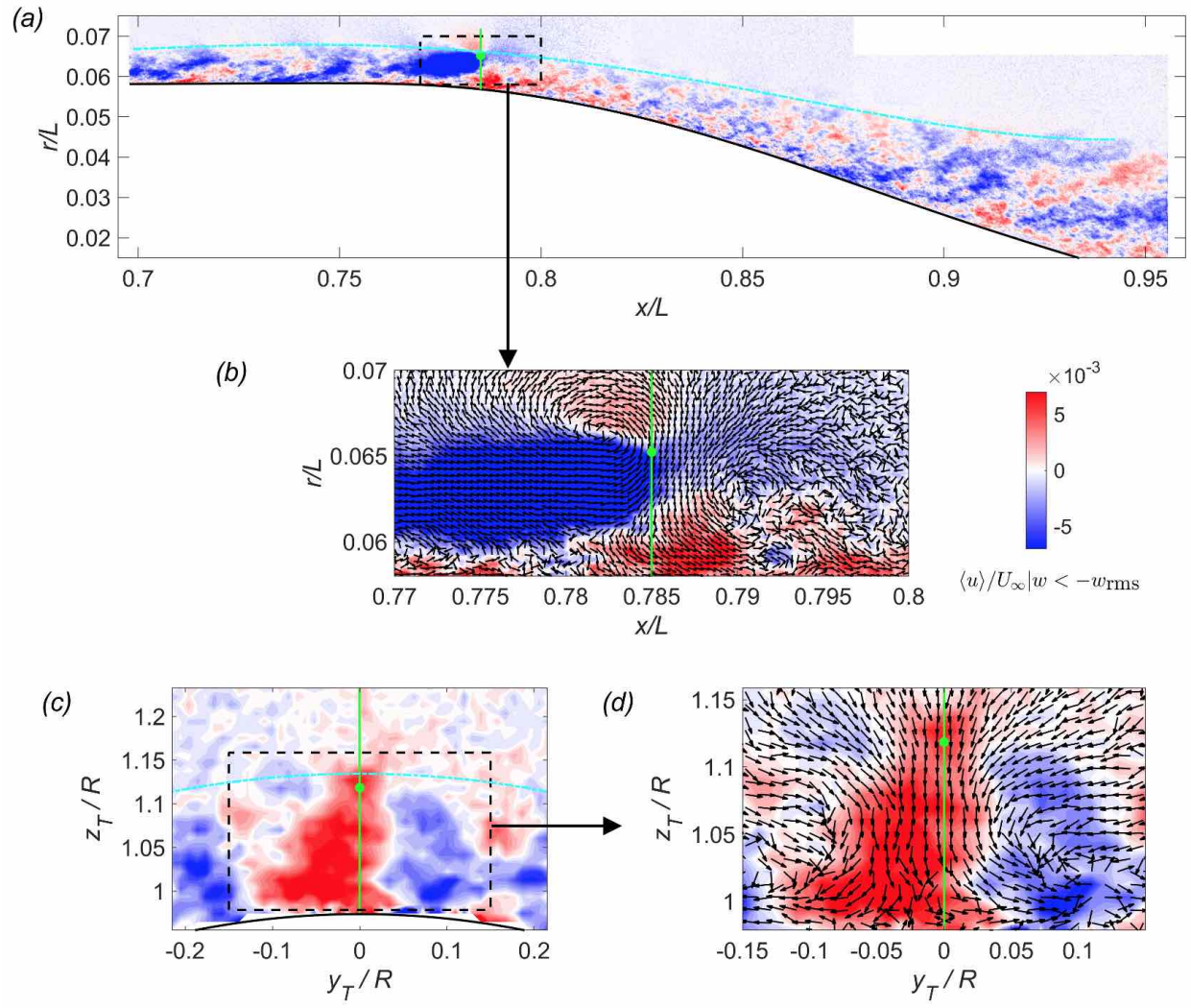

Figure 3.71 Conditional average results for spanwise Plane 2. See Fig. 3.70 for discussion of figure layout.

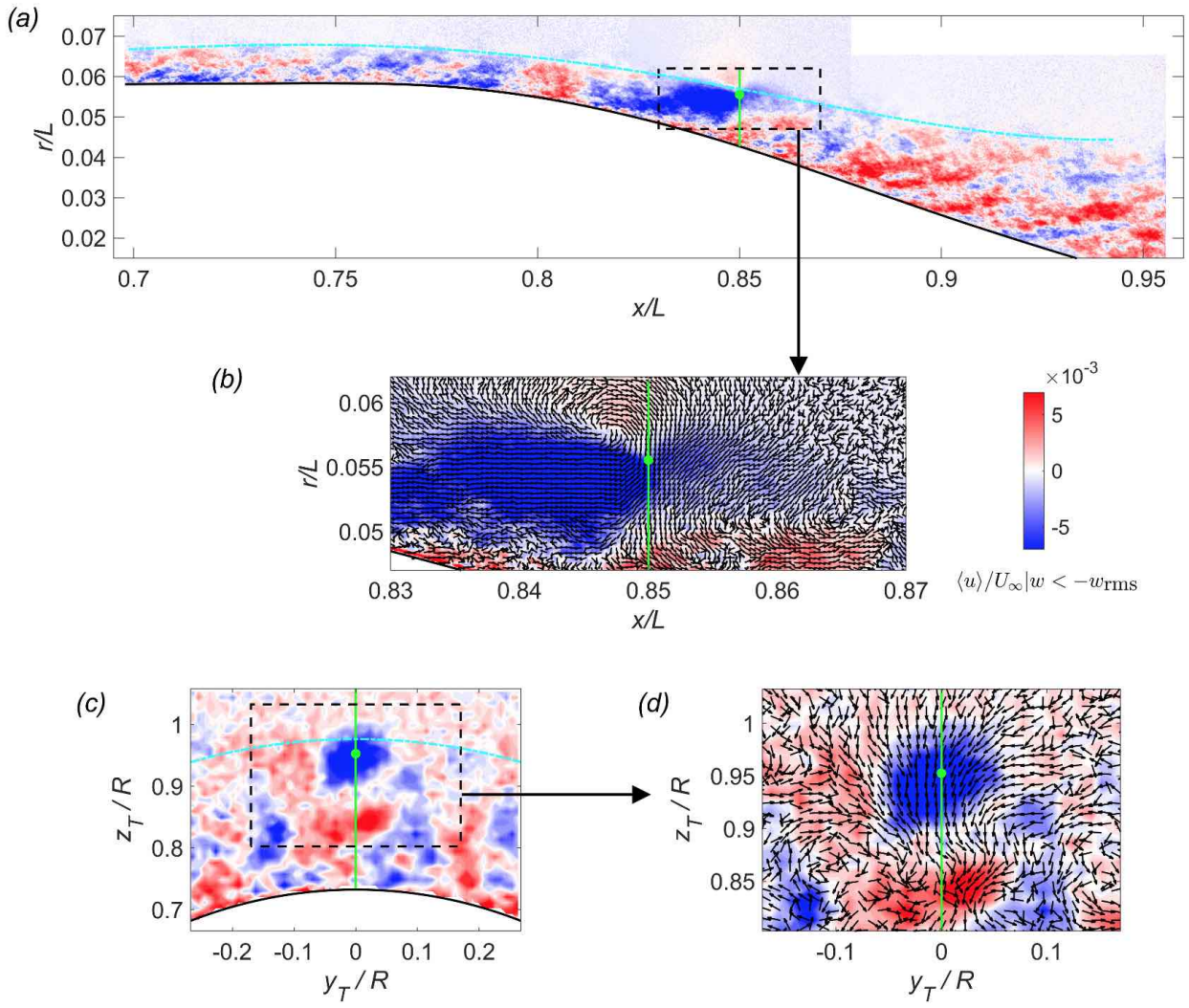

Figure 3.72 Conditional average results for spanwise Plane 3. See Fig. 3.70 for discussion of figure layout.

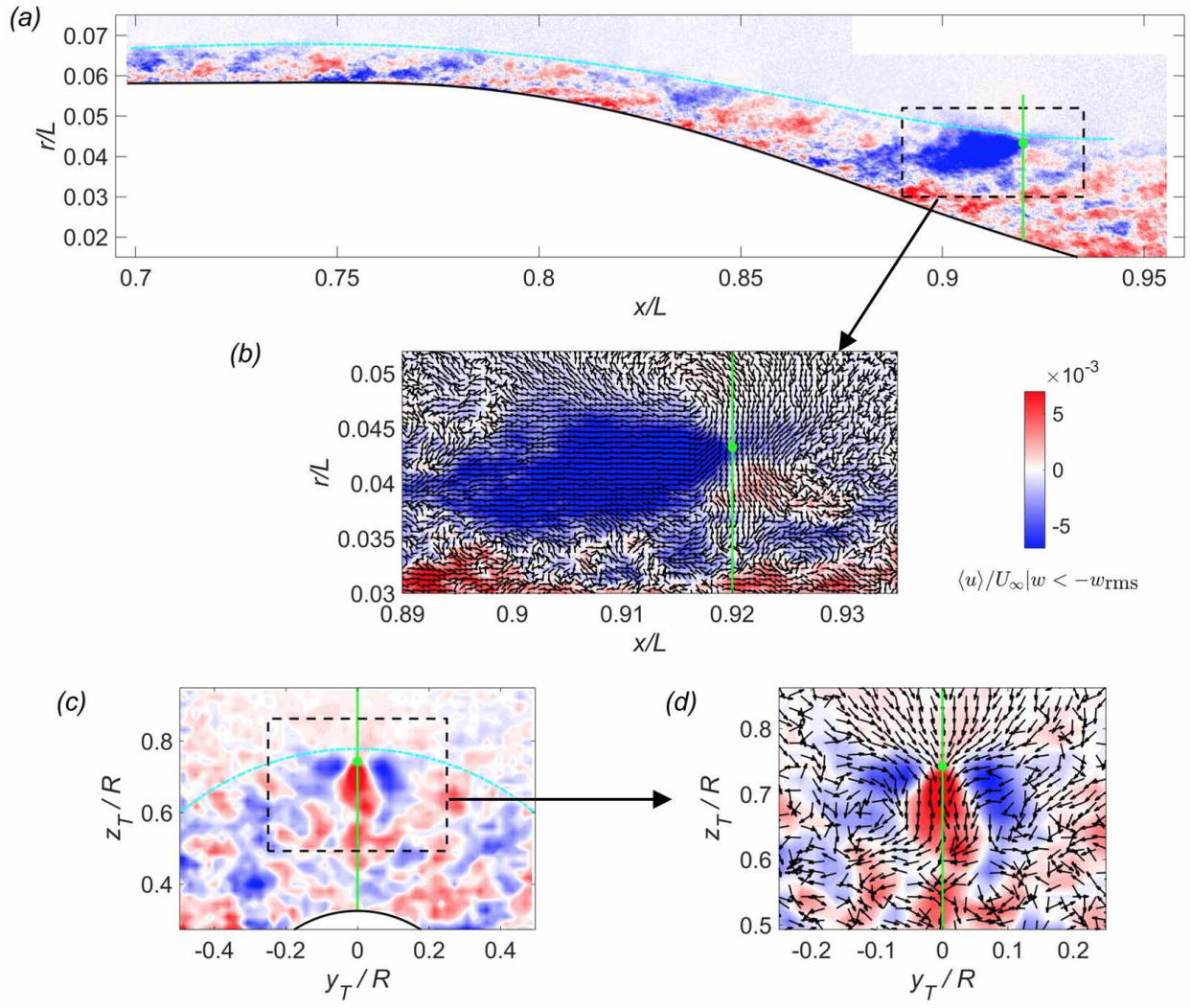

Figure 3.73 Conditional average results for spanwise Plane 4. See Fig. 3.70 for discussion of figure layout.

contour relative to the upstream locations, the quivers indicated that the spanwise flow directions remained comparable.

Figure 3.73 shows the conditional velocity fields surrounding SP4. The streamwise plane in (a) showed that the wall did not influence the turbulent bulge, which is consistent with upstream planes. However, the streamwise plane double roller structure found in SP1 and SP2 in Figs. 3.70(a) and 3.71(a) was not visible. The spanwise organization is shown in (c), and a similar pattern as SP3 shows the spanwise plane intersecting the turbulent bulge apex. This coincidence perhaps indicated that the most intense downwash w occurred when the

fluid traveled downward around the turbulent bulge into the valley. Again, the quivers in (d) show the fluid entrained by the centerline downwash.

This conditional average analysis suggested that the unique R_{uw} pattern in Fig. 3.63 was related to the large-scale motions that underlie the turbulent bulges and valleys. Further, the conditional fields revealed patterns similar to the description in Reuther and Kähler [35] and in Fig. 3.46, where the fluid appeared to speed up around the turbulent bulge and travel downward into the subsequent valley. This understanding of R_{uw} indicated variations in the large scales that govern the entrainment. To this end, the following chapter continues to study the boundary layer edge, focusing on the interface that segregates the turbulent and potential flows.

3.3.5 Summary of Two-Point Statistics

The two-point statistics provided detailed insights into the boundary layer structure. The frequency contents of u and w were modified near the wall. Further insight into the flow structure was obtained from spatial two-point correlation performed in the streamwise and the spanwise planes. Unique patterns of R_{uw} were visible in the streamwise and the spanwise planes. To understand these patterns, conditional averages of u and w based on low-speed events near the boundary layer edge revealed turbulent bulges, suggesting that the turbulent entrainment process may have been modified.

1. Studying the premultiplied spectra revealed that,

   (a) The premultiplied peak frequencies of u and w were invariant in the outer region when scaled by the edge velocity and the hull radius. Therefore, the outer region flow structures were expected to be largely insensitive to pressure gradient and wall curvature effects.

   (b) Near the wall ($z/\delta < 0.3$), the APG increased the wall-tangent velocity (premultiplied) peak frequency, whereas the subsequent weak APG reduced the premultiplied peak frequency. This increase and decrease suggested variations in the

streamwise length scale of u resulting from the pressure gradient.

(c) The near-wall premultiplied peak frequency of wall-normal w continuously decreased along the afterbody, suggesting changes in the underlying physics. Hairpin packets were hypothesized to have induced the low-frequency peak at downstream locations.

2. In the streamwise-wall–normal plane:

(a) The near-wall ($z_{\text{ref}}/\delta \approx 0.1$) two-point correlation contours R_{uu} based on the wall-parallel velocity, were a result of hairpin packets, as demonstrated through linear stochastic estimation. These structures were stretched and compressed by the FPG and APG by up to 25% while experiencing at most 10° of rotation. These findings were consistent with the prior spectral analysis.

(b) The two-point correlation contours at $z_{\text{ref}}/\delta = 0.9$ were more rounded. They were primarily rotated while experiencing a gradual elongation with streamwise distance.

(c) The near wall length scale computed based on the two-point correlation R_{uu} roughly followed the acceleration parameter K and pressure gradient dp/dx. In contrast, this length scale normalized by the boundary layer thickness roughly followed the Clauser pressure gradient parameter β_c.

(d) The inclination angle of R_{uu} contours relative to the local wall followed the Clauser parameter β_c across the boundary layer thickness. The inclination angle relative to the longitudinal symmetry axis better followed the acceleration parameter K and pressure gradient dp/dx.

(e) An equation was proposed to collapse the length scale variations of R_{uu} across the wall-tangent and -normal directions. The equation comprised one pressure gradient parameter, β_c or K, and two empirical constants to account for the delay in response and the differences in magnitude.

(f) The R_{uu} length scale variations lagged the pressure gradient by roughly one boundary layer thickness.

(g) The two-point correlation of wall-normal velocity w, R_{ww}, was invariant near the boundary layer edge. However, for wall-normal locations up to $z/\delta = 0.5$, R_{ww} varied noticeably along the afterbody, eventually developing a slight forward lean at $x/L > 0.9$. This forward lean suggested the role of hairpin packets, supporting the hypothesis from the spectral analysis.

(h) R_{uw} was modified significantly in the outer region. Contrary to negative correlations in a canonical flow indicative of sweep and ejection events, R_{uw} developed a positive correlation downstream of the reference velocity. This unique behavior has not been recorded in the literature.

3. In the spanwise-radial plane:

   (a) The FPG increased the azimuthal length scale of R_{uu}, and the APG had the opposite effect. At $x/L = 0.92$, the APG also elevated the near-wall length scale, creating a uniform distribution across the boundary layer thickness roughly 10% of the hull radius.

   (b) The $R_{\theta\theta}$ azimuthal length scale was significant in the outer region with values up to 14% of the hull radius. The R_{ww} length scale grew roughly linearly with wall distance up to 20% of the hull radius. These length scales varied with streamwise location but were challenging to attribute to pressure gradient or wall curvature.

   (c) The spanwise plane rollers of hairpin-like structures were shifted up and down by the FPG and the APG relative to the ZPG case.

4. The three-dimensional cross-correlation R_{uw} near the boundary layer edge suggested an interplay between the hairpin packets and the turbulent bulges hypothesized to vary with longitudinal streamline curvature.

5. Conditional averaging near the boundary layer edge at $z/\delta = 0.9$ showed that R_{uw} was associated with the turbulent bulges. Further, this analysis demonstrated that the flow accelerated around the turbulent bulges into the valleys, similar to the model proposed by Reuther and Kähler [35]. These turbulent bulges were not attached, suggesting little direct wall influence. Additionally, variations in the turbulent bulges were observed with streamwise distance, suggesting changes to the underlying large-scale motions that require a deeper analysis in the future.

Detailed conclusions and supporting evidence can be found by navigating the sections. The varying R_{uw} structure was a curious outcome of the analyses near the boundary layer edge. Analysis of the conditional fields near the boundary layer edge suggested variations in the large-scale motions that underlie the turbulent entrainment process. To this end, the turbulent/non-turbulent interface was investigated as discussed in the following section.

3.4 Turbulent/Non-Turbulent Interface

The turbulent/non-turbulent interface (TNTI) segregates the rotational boundary layer and the outer potential flow. This interface is closely tied to turbulent entrainment and, therefore, the growth rate of boundary layers, wakes, and jets alike. Further, because propeller loading and noise are generated near the blade tips, which are in the intermittent region, abrupt velocity changes across the TNTI could lead to significant unsteady loading.

In this chapter, Section 3.4.1 describes the method used to define the TNTI. Then, the intermittency statistics in Section 3.4.2 and conditional averages in Section 3.4.3 help to understand the TNTI structure and how it differed from a canonical flow. Lastly, the geometry of the interface is discussed in Section 3.4.4. The analysis in this chapter uses the higher Reynolds number dataset with $Re_\tau \approx 2{,}700$.

3.4.1 Interface Detection Method

There are a few methods for deciding whether the flow at a point is turbulent. The most common approach uses a vorticity threshold [154, 156, 173]. However, the local kinetic energy method described by Chauhan et al. [30] was used in the current work with some modifications. The method of Chauhan et al. [30] computes a local kinetic energy, i.e.,

$$k_i = 100 \times \frac{1}{9U_\infty^2} \sum_{m,n=-1}^{1} [(\tilde{u}_{m,n} - U_e)^2 + \tilde{w}_{m,n}^2]. \tag{3.10}$$

The preceding equation sums the deviation of the instantaneous velocities $\tilde{u}$ and $\tilde{w}$ from the edge velocity U_e across a 3-by-3 grid region traversed by the indices m and n. The values of k_i are prominent in the boundary layer and nearly zero in the free stream, except for PIV measurement noise and the tunnel's free-stream turbulence.

This method was modified to suit the current flow for two reasons. First, the boundary layer edge wall-normal velocity W_e was no longer nearly zero because of the APG. Second, k_i had significant values well above the boundary layer edge as $U(x, r)$ and $W(x, r)$ differed from U_e and W_e because of the streamline curvature. The remedy to these challenges was a

piece-wise version of the original implementation:

$$k_i = \begin{cases} 100 \times \dfrac{1}{9U_\infty^2} \displaystyle\sum_{m,n=-1}^{1} [(\tilde{u}_{m,n} - U_e)^2 + (\tilde{w}_{m,n} - W_e)^2], & z \leq \delta, \\ 100 \times \dfrac{1}{9U_\infty^2} \displaystyle\sum_{m,n=-1}^{1} [(\tilde{u}_{m,n} - U(x,r))^2 + (\tilde{w}_{m,n} - W(x,r))^2], & z > \delta. \end{cases} \tag{3.11}$$

In this equation, W_e is the wall-normal edge velocity; $U(x,r)$ and $W(x,r)$ are the time-mean velocities. This piece-wise version of the criterion includes the wall-normal edge velocity, and any point above the boundary layer edge δ uses the mean velocity instead of the edge velocity, to minimize artificial local kinetic energy. The boundary layer edge δ was determined using a TKE criterion described in Section 3.2.1.

As outlined in Chauhan et al. [30], a threshold value for k_i must be chosen to demarcate the boundary between the turbulent and non-turbulent regions. To this aim, a streamwise domain of 0.25δ in length centered about $x/L = 0.7$ was isolated to calibrate the threshold value for k_i. The value of k_i was varied at increments of 0.05 until $\delta_0 \approx Z_i + 3\sigma_i$. The actual boundary layer thickness δ_0, above which there is no turbulence, was obtained from Chauhan's fit at the most upstream location where the boundary layer was near canonical; Z_i is the mean interface location; and σ_i is the standard deviation of the interface position. The final threshold value was $k_i = 0.075$. This approach led, expectedly, to a mean interface position of $Z_i = 0.66$ and a standard deviation of $\sigma_i = 0.11$.

This threshold value was used to calculate the interface that distinguished the turbulent and non-turbulent regions in all four fields of view and all 2914 snapshots. One such interface is shown in Fig. 3.74. The corrugated blue line segregates the turbulent and potential regions, overlaying the velocity magnitude in Fig. 3.74(a) and the local kinetic energy in Fig. 3.74(b). The analyses in this section were based on these interfaces. Small pockets of lighter color immediately below the interface in Fig. 3.74(b) may be irrotational pockets recently engulfed by the boundary layer [161, 222].

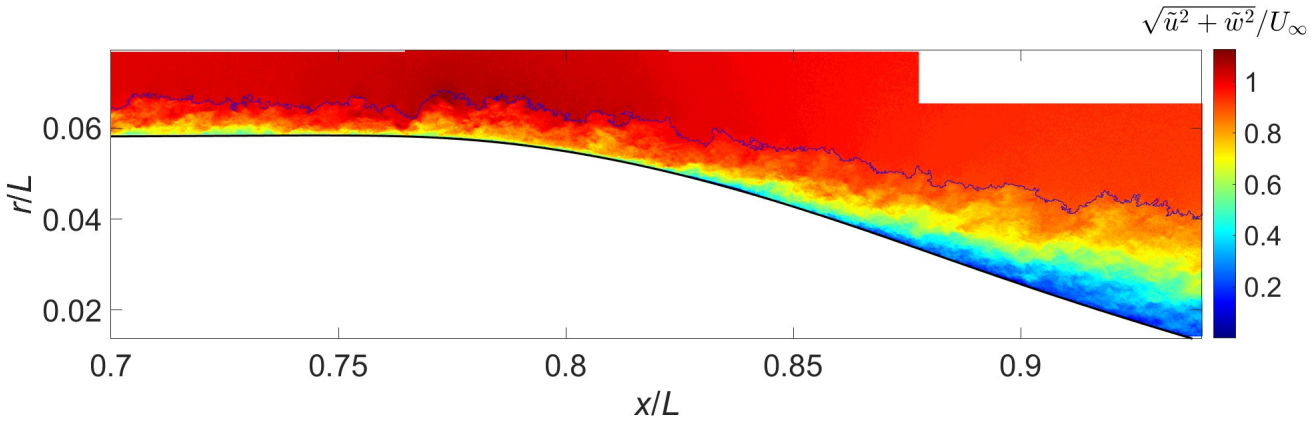

(a)

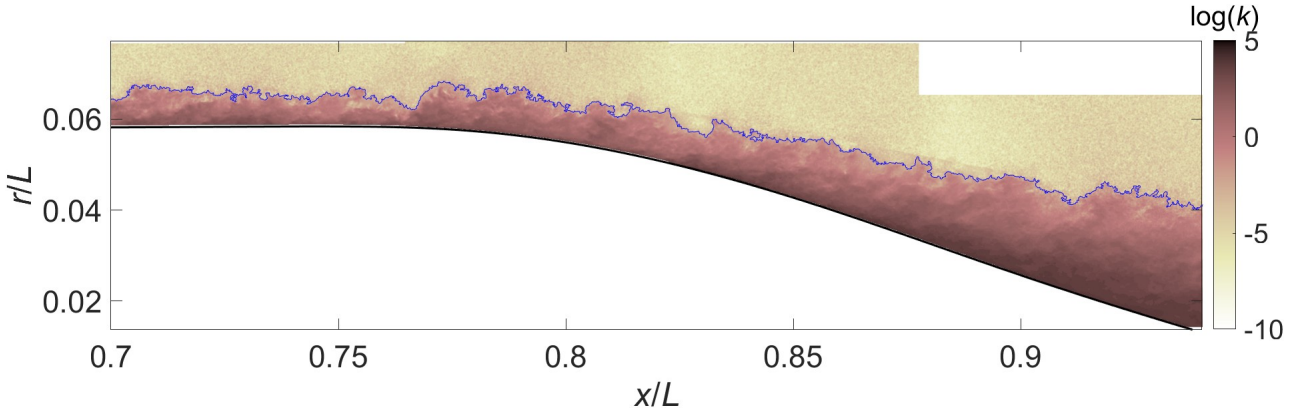

(b)

Figure 3.74 The corrugated blue line shows an instantaneous turbulent/non-turbulent interface overlaying *(a)* normalized velocity magnitude $\sqrt{\tilde{u}^2+\tilde{w}^2}/U_\infty$ and *(b)* local kinetic energy k_i from Eq. 3.11 modified based on work of Chauhan et al. [30].

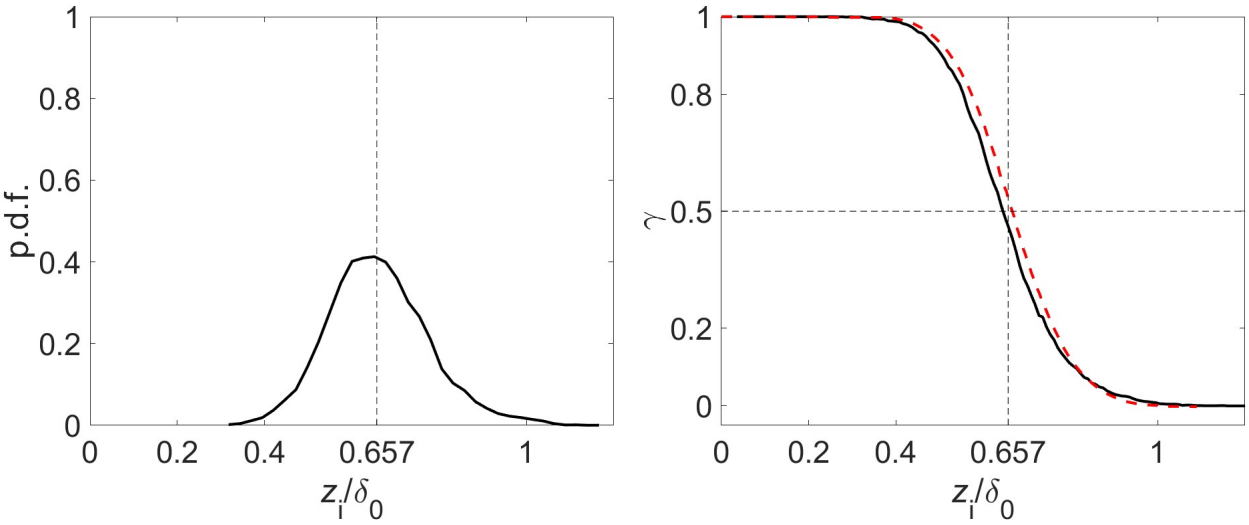

Figure 3.75 (a) Probability density function (p.d.f.) of interface location. *(b)* Intermittency distribution γ; the solid line represents current measurements, and the dashed red line is from Chauhan et al. [30] at $Re_\tau = 14{,}500$. The vertical dashed line shows the average interface position Z_i.

3.4.2 Intermittency Statistics

A statistical description of the TNTI is provided here. The intermittency distribution [155] and the probability density function (p.d.f.) of the wall-normal interface position are discussed, shedding light on the effects of pressure gradient and wall curvature.

The statistics at the near canonical part of the FOV were computed to establish a comparison basis. Figure 3.75 shows the probability density function (p.d.f.) and the intermittency distribution γ of the TNTI. The p.d.f. shows a roughly Gaussian distribution with a mean interface position of $Z_i/\delta_0 = 0.66$ denoted by the black dashed line. The skewness was 0.35, and the flatness was 3.21.

The intermittency shown in Fig. 3.75(b) equaled one at heights up to $z/\delta_0 \approx 0.4$ and decreased to zero at $z/\delta_0 = 1$ following the error function. The red dashed line shows the results from Chauhan et al. [30] measured with $Re_\tau = 14{,}500$. The minor differences between the solid and dashed lines could be related to the order of magnitude difference in Reynolds number. Overall, the current measurements agreed with prior canonical boundary layers [30].

Pressure gradient and wall curvature effects on the canonical state were investigated.

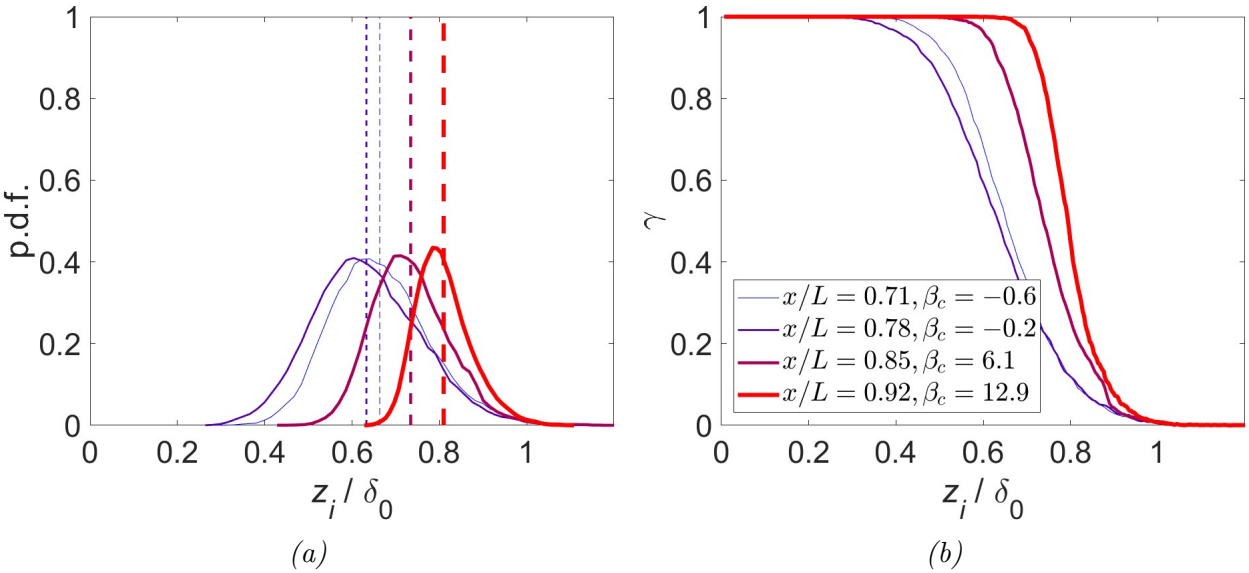

Figure 3.76 (a) Probability density function (p.d.f.) and *(b)* the intermittency distribution γ at different streamwise locations highlight the effects of pressure gradient. The vertical dashed lines show the mean interface locations. Thicker lines correspond to locations further downstream.

Figure 3.76 overviews the intermittency statistics at four streamwise stations of $x/L = 0.71, 0.78, 0.85$, and 0.92, denoted using progressively thicker lines. A streamwise domain of 0.25δ (δ is based on the in-plane kinetic energy) was isolated for each station. The mean Z_i and the variance σ_i of the interface were recorded. The true δ_0, above which there is no boundary layer turbulence, was estimated as $\delta_0 = Z_i + 3\sigma_i$, assuming that the interface characteristics were not significantly modified over the streamwise domain. This domain was considerably smaller than the $\sim$50 boundary layer thickness required for a boundary layer to remake itself as predicted by Devenport and Lowe [51], and an order of magnitude smaller than the response distance discussed in Section 3.3.2.4. The threshold value of $k_i = 0.075$ was used, as discussed previously.

In Fig. 3.76(a), the vertical dashed line shows the average interface position Z_i/δ_0, which decreased with the FPG and increased in the APG region to nearly $Z_i/\delta_0 \approx 0.8$. Although the first station at $x/L = 0.71$ had a greater FPG than the second station at $x/L = 0.78$ (i.e., a more negative β_c), the effects of the FPG were more pronounced at $x/L = 0.78$ than at $x/L = 0.71$ because of hysteresis [51, 53].

The intermittency γ in Fig. 3.76(b) showed similar trends, because γ is a cumulative distribution function of the p.d.f. in Fig. 3.76(a). In the APG, at any given z/δ, the flow was more frequently turbulent than in the FPG or ZPG cases, and the extent of the intermittent region (as a fraction of δ) shrank. These trends were consistent with those of Fiedler and Head [31] and disagreed with the results from the simulation of Yang et al. [173]. Comparing the intermittency distributions at $x/L = 0.71$ and 0.78, the profiles were similar above $z/\delta_0 \approx 0.7$ but $\gamma < 1$ was found deeper (i.e., at lower z/δ_0 values) in the boundary layer at $x/L = 0.78$. This observation perhaps supported the hypothesis of Fiedler and Head [31] that a flow undergoing relaminarization may experience intermittency that spans the entire boundary layer thickness.

The mean and standard deviation of the TNTI were computed at nine streamwise stations to examine the effect of pressure gradient and wall curvature, following a procedure identical to the one in Fig. 3.76. Figures 3.77(a) and (b) report changes in the mean interface location when normalized by the estimated local boundary layer thickness $\delta_0 = Z_i + 3\sigma_i$ and the constant hull radius R, respectively. The value of Z_i/δ_0 decreased through the FPG region and increased in the APG region, and Z_i/R followed a similar trend. The interface standard deviation σ_i is reported in Figs. 3.77(c) and (d). The variance σ_i/δ_0 increased with the FPG and, conversely, reduced through the APG. In contrast, σ_i/R increased through the FPG, plateaued between $x/L = 0.78$–0.82, and increased again beyond $x/L = 0.85$.

It is worthwhile to consider whether these changes were driven by pressure gradient or wall curvature. In Fig. 3.77(a), Z_i/δ showed an initial ($x/L <= 0.76$) decrease but increased thereafter. Figure 3.77(b) of Z_i normalized by the hull radius R followed a similar trend, where the minimum at $x/L = 0.76$ was more subtle. Because the lateral and longitudinal curvature were unimportant until after the initial decrease in Z_i, the interface location was likely significantly influenced by the pressure gradients.

The trends in the standard deviation σ_i in Fig. 3.77(d) could be understood as follows. The initial increase from $x/L = 0.7$–0.78 was because of the favorable pressure gradient.

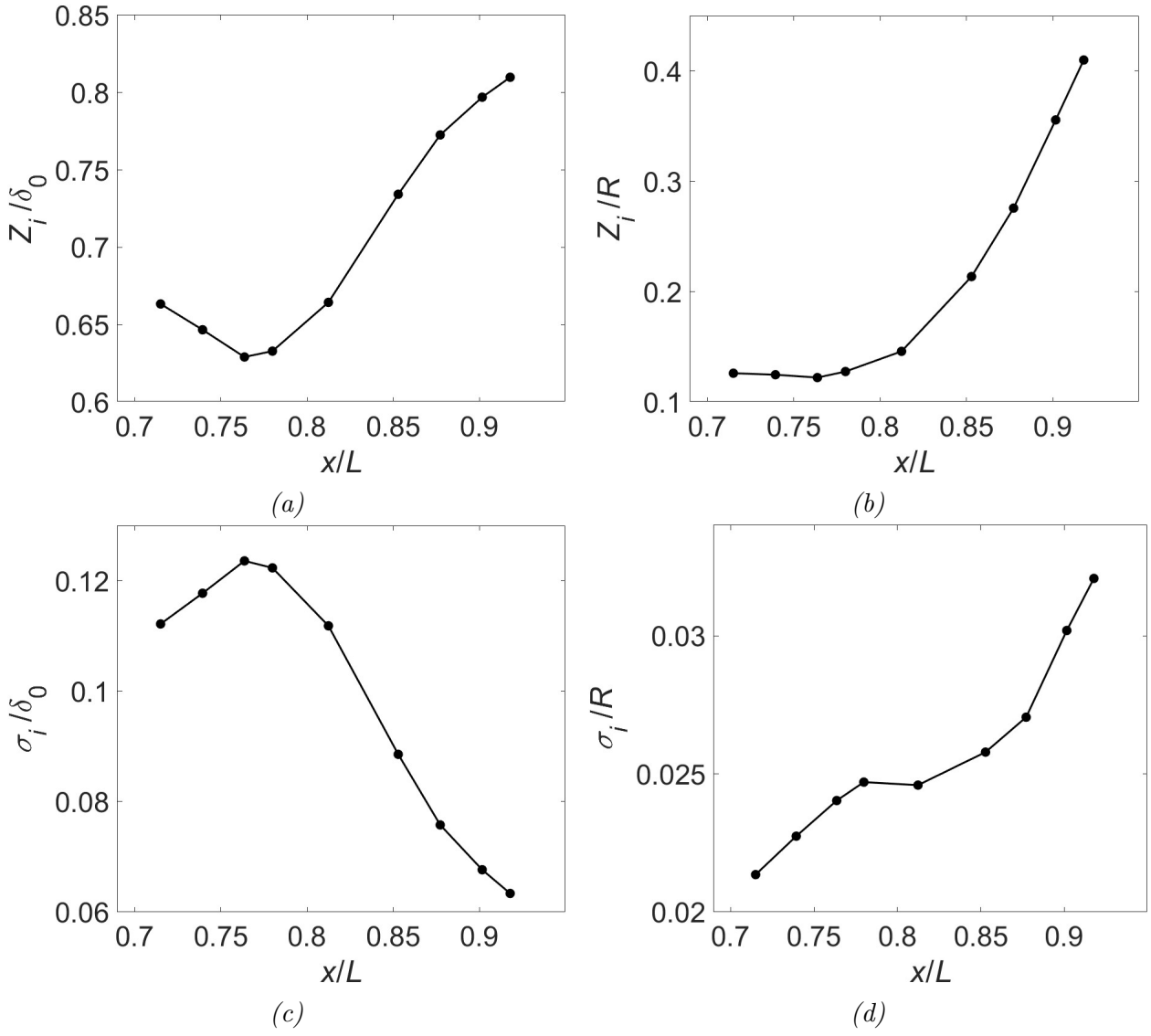

Figure 3.77 Variation of the interface location *(a,b)* mean Z_i and *(c,d)* standard deviation σ_i with streamwise location and pressure gradient normalized by *(a,c)* the local boundary layer thickness δ_0 and *(b,d)* the hull radius R.

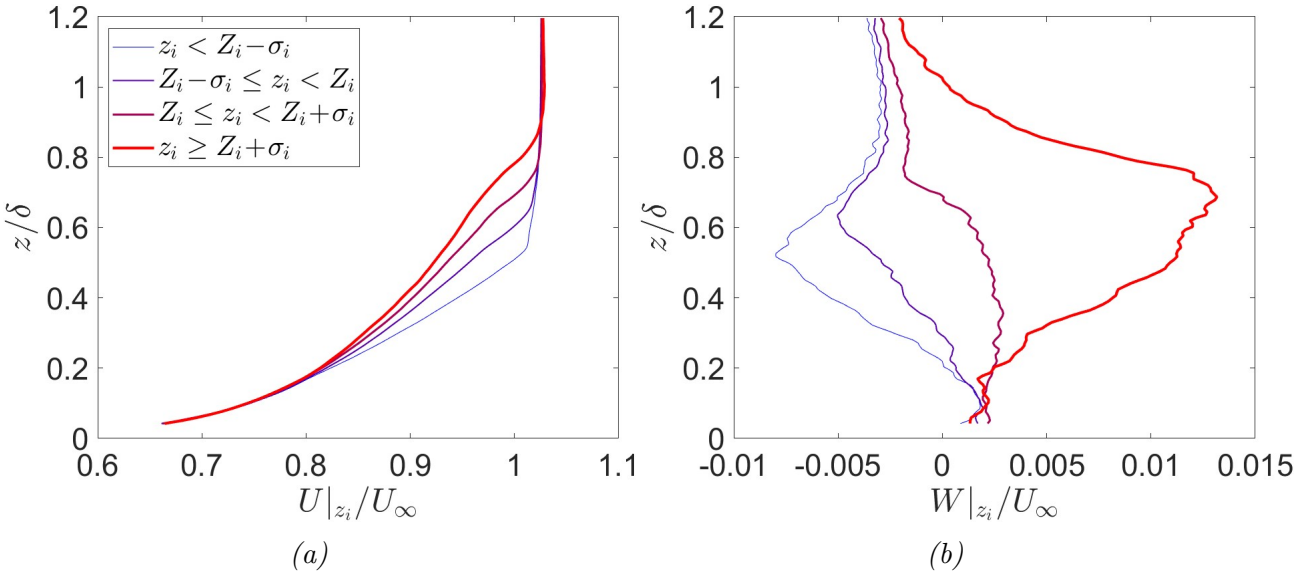

Figure 3.78 Conditional *(a)* U and *(b)* W velocity profiles normalized by the free stream U_∞ based on interface position z_i.

The subsequent plateau from $x/L = 0.78$–0.85 could be explained by the onset of APG. The ensuing growth beyond $x/L = 0.85$ was perhaps a product of the growing boundary layer thickness resulting from the decelerating boundary layer. This increase in variance σ_i with downstream distance perhaps indicated enhanced large-scale motion, as will be discussed in Section 3.4.4.

3.4.3 Interface Conditional Fields

The flow field surrounding the TNTI was examined through conditional averaging. First, the average wall-parallel velocity jump was assessed in the near-canonical region of the flow. Subsequently, the combined effects of pressure gradient and wall curvature on the conditional fields were demonstrated. Lastly, the additional interface height criterion was used to comprehend the TNTI further.

Conditional averaging was performed based on the location and orientation of the inter-

face. In particular, four separate profiles were computed based on when

$$\begin{aligned} &\text{Condition 1}: z_i < Z_i - \sigma_i, \\ &\text{Condition 2}: Z_i - \sigma_i \leq z_i < Z_i, \\ &\text{Condition 3}: Z_i \leq z_i < Z_i + \sigma_i, \\ &\text{Condition 4}: z_i \geq Z_i + \sigma_i. \end{aligned} \tag{3.12}$$

Here, z_i is the instantaneous interface location, Z_i is the mean interface location, and σ_i is the standard deviation of the interface location. An additional constraint was that the surface orientation was required to be $\pm 20^\circ$ relative to the local wall. The surface orientation was computed with a polynomial fit through three neighboring points.

Figures 3.78(a) and (b) show the conditional profiles $U|_{z_i}$ and $W|_{z_i}$ based on the interface location criterion described above. The thin blue line corresponds to condition 1 in 3.12, and the thickest red line represents condition 4. These profiles differed from the unconditional mean, namely that they had steep velocity gradients when transitioning from the turbulent to the non-turbulent region. For the wall-normal velocity, those with an interface position of $z_i < Z_i$ had $W|_{z_i} < 0$, and, conversely, $z_i > Z_i$ was correlated with $W|_{z_i} > 0$. These results agreed with the conditional profiles in Chauhan et al. [30] and Reuther and Kähler [35].

Conditional averages centered on the interface were also computed. In other words, each wall-normal velocity profile was shifted relative to one another so that their interface positions coincided. Locations where the interface was multi-valued, i.e., when it folded over itself, were omitted from the average. Interfaces that deviated by more than 20° from the local wall were also disregarded. The data was sampled from a streamwise domain of 0.25δ centered about the axial position to minimize the spatial variations effects. Figure 3.79(a) shows the conditional profile in the near canonical region [30]. This figure is centered on the interface z_i. The vertical and horizontal axes are scaled by the actual boundary layer thickness δ_0 and the corresponding edge velocity U_e.

Across the TNTI, Fig. 3.79(a) reveals a jump in wall-tangent velocity [29, 223]. Further,

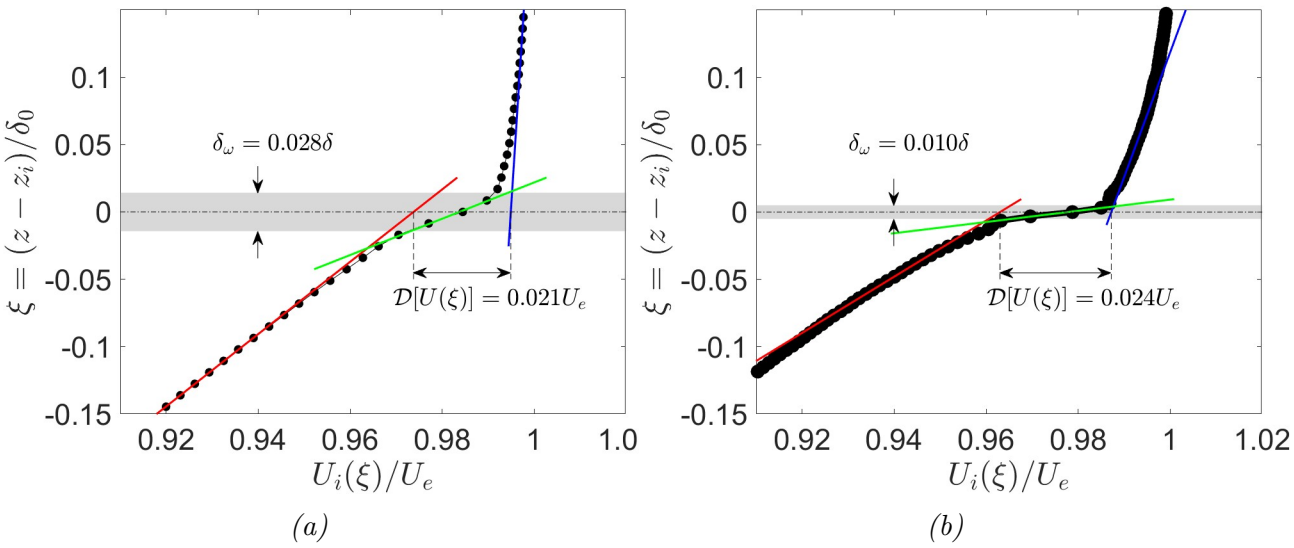

Figure 3.79 Conditionally averaged wall-tangent velocity profile at *(a)* $x/L = 0.71$ and *(b)* $x/L = 0.92$. The shaded band represents the TNTI which roughly has a width equal to the vorticity thickness δ_ω, and the velocity jump across the TNTI is $\mathcal{D}[U]$.

above and below the interface were regions where the velocity varied roughly linearly, as represented by the red and blue lines. A "jump" in velocity across the interface was defined based on the difference in the linearly extrapolated values equal to $0.021U_e$. The vorticity thickness $\delta_\omega = 0.028\delta$ was based on this velocity jump and the maximum velocity gradient dU/dz [165], determined from the green line fit.

This vorticity thickness δ_ω was smaller than the one in Chauhan et al. [30] and can be partially explained by Reynolds number effects [33]. Increasing Reynolds number has the effect of increasing the velocity jump $\mathcal{D}[U]$ (without u_τ scaling) and the max slope of dU/dz. However, Figs. 5(b) and 6(b) in Chauhan et al. [33] indicate values of $\delta_\omega/\delta = 0.035$–$0.04$ and $\delta_\omega^+ \approx 125$ for the present Reynolds number, still greater than the computed values of $\delta_\omega/\delta_0 = 0.028$ and $\delta_\omega^+ = 90$. These deviations could be lateral curvature effects.

Conditional averaging was performed for other quantities. The wall-tangent and wall-normal velocities were decomposed as $\tilde{u}_i = U_i + u_i$ and $\tilde{w}_i = W_i + w_i$ into mean and fluctuating parts. Similarly, the vorticity $\tilde{\omega}_i = \Omega_i + \omega_i$. Figure 3.80 shows U_i, W_i, and Ω_i nondimensionalized by the hull radius R and the free stream U_∞. The ordinate is the distance from the interface normalized by the radius. Figure 3.80(a) shows the average velocity

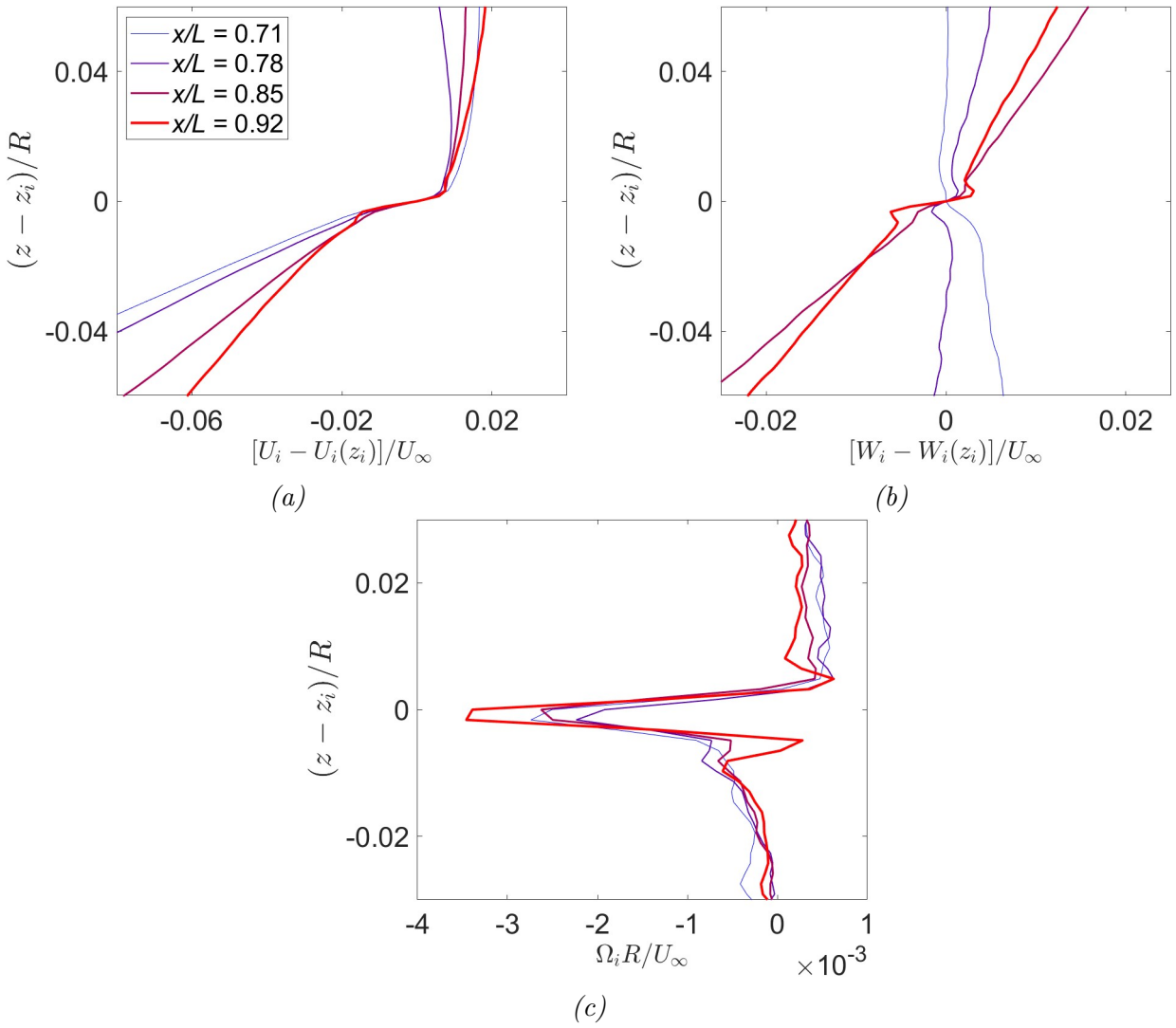

Figure 3.80 Quantities conditionally averaged about the interface compared across different streamwise stations. The thin blue and thick red lines are the upstream and downstream locations. *(a)* Wall-tangent and *(b)* normal velocities subtracted by the velocity at the interface. *(c)* Vorticity discontinuity at the interface.

U_i shifted by the interface velocity to facilitate comparisons between different streamwise stations. The thin blue and thick red lines correspond to the upstream and downstream positions. Despite the significantly different pressure gradient and wall curvature conditions, the wall-tangent velocity "jump" appeared similar at all positions.

Figure 3.80(b) displays the corresponding wall-normal velocity W_i, where the thin blue line representing $x/L = 0.71$ was comparable to the canonical boundary layer of Chauhan et al. [30]. The profiles at the downstream positions of $x/L = 0.85$ and $x/L = 0.92$ were both

forward-leaning and developed velocity jumps. It is well-known that the TNTI contains a vorticity spike [154, 160], which usually equals dU/dy. However, dW/dx was also included in the vorticity calculated in Fig. 3.80(c). This figure shows the vorticity discontinuity decreased at $x/L = 0.78$ and increased at $x/L = 0.85$ and 0.92, suggesting the influence of pressure gradients.

Figure 3.81 presents the same data as Fig. 3.80 but makes the additional distinction of interface height according to the criteria in Eq. 3.12, which are respectively denoted using blue, orange, yellow, and purple. Each column in Fig. 3.81 shows a different streamwise location, and each row represents a different variable. The abscissa scales are equal in each row so that visual inspections can be made.

In the first row, U_i is the mean wall-tangent velocity at the interface. The trends were similar across the four stations, with the interfaces further from the wall showing a lesser velocity jump. The second row shows the conditional wall-normal velocity W_i. For upstream locations in the left columns, the negative jump was pronounced in the interface furthest from the wall (purple line). In contrast, the positive jump in W_i at the downstream location (rightmost column) was most prominent when the interface was close to the wall.

The mean interface vorticity is given in the third row of Fig. 3.81. The vorticity Ω_i was generally smaller for interfaces further away from the wall, similar to the trends of dU/dy. However, the peak vorticity location varied with the streamwise stations. The vorticity jump at $x/L = 0.78$ was most intense when the interface was closest to the wall. In contrast, the jump at $x/L = 0.85$ was more intense when the interface was further away. Interestingly, the vorticity values at $x/L = 0.92$ were comparable to $x/L = 0.71$.

Figure 3.82 shows various fluctuation intensities conditionally averaged about the interface. The four subfigures represent the wall parallel and wall-normal fluctuation intensity, the Reynolds stress, and the enstrophy. The thin blue and thick red lines correspond to the most upstream and downstream stations. The variance $\overline{u_i^2}$ at $x/L = 0.71$ shown using the thin blue line in Fig. 3.82(a) was comparable to the results from a canonical flow in Chauhan

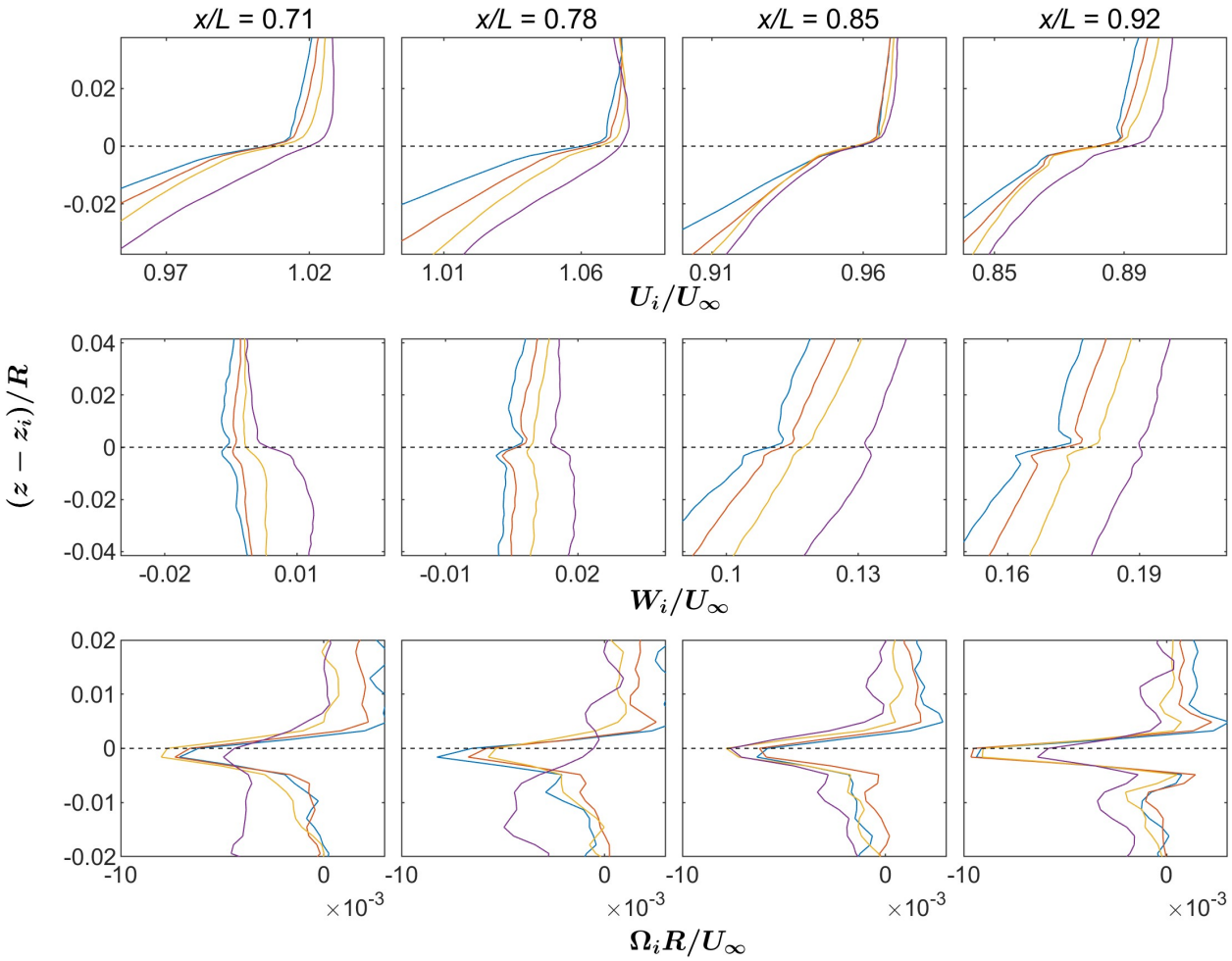

Figure 3.81 Conditional averages about the interface. Each row corresponds to a different variable labeled below. Each column represents a different axial station as labeled at the top. Blue, orange, yellow, and purple lines correspond to the four conditions in 3.12.

et al. [30].

The FPG and the APG appeared to make the u fluctuations parallel to the interface more and less intense, respectively, as observed in Fig. 3.82(a). The trends of the wall-normal velocity variance $\overline{w_i^2}$ were similar in (b). The reduced variance in both u_i and w_i led to smaller magnitudes of $\overline{u_i w_i}$ at the downstream stations $x/L = 0.85$ and 0.92 as shown in Figure 3.82(c). Interestingly, while the mean vorticity Ω_i was lowest at $x/L = 0.78$, the vorticity fluctuations ω_i (purple) were most intense at this location. A more detailed understanding of these statistics could be obtained by imposing the additional constraint of interface height.

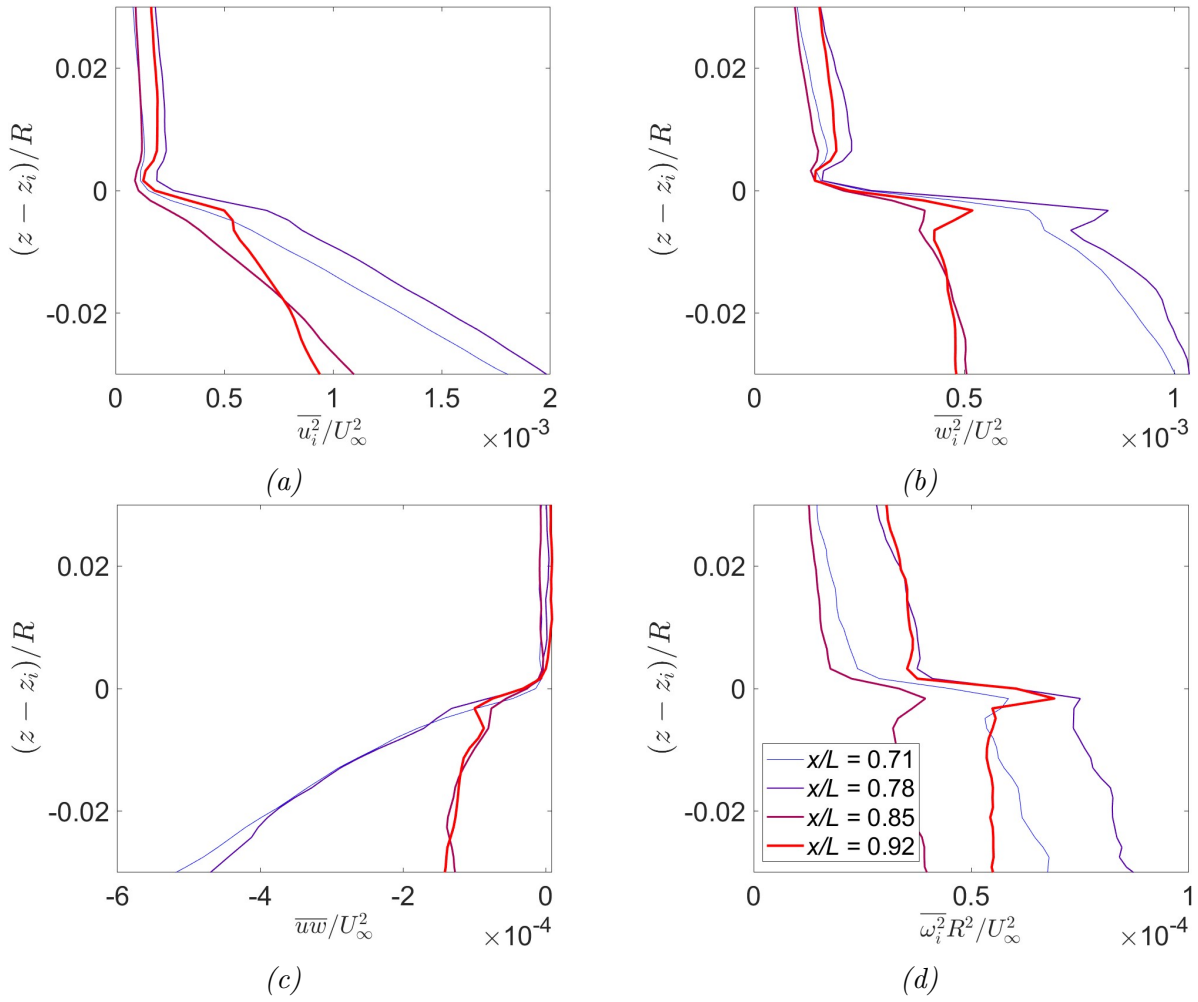

Figure 3.82 Quantities conditionally averaged about the interface compared across different streamwise stations. The thin blue and thick red lines are the upstream and downstream locations. *(a)* Wall-tangent fluctuation $\overline{u_i^2}$. *(b)* Wall-normal fluctuation $\overline{w_i^2}$. *(a)* Cross correlation $\overline{u_i w_i}$. *(a)* Variance of vorticity $\overline{\omega_i^2}$.

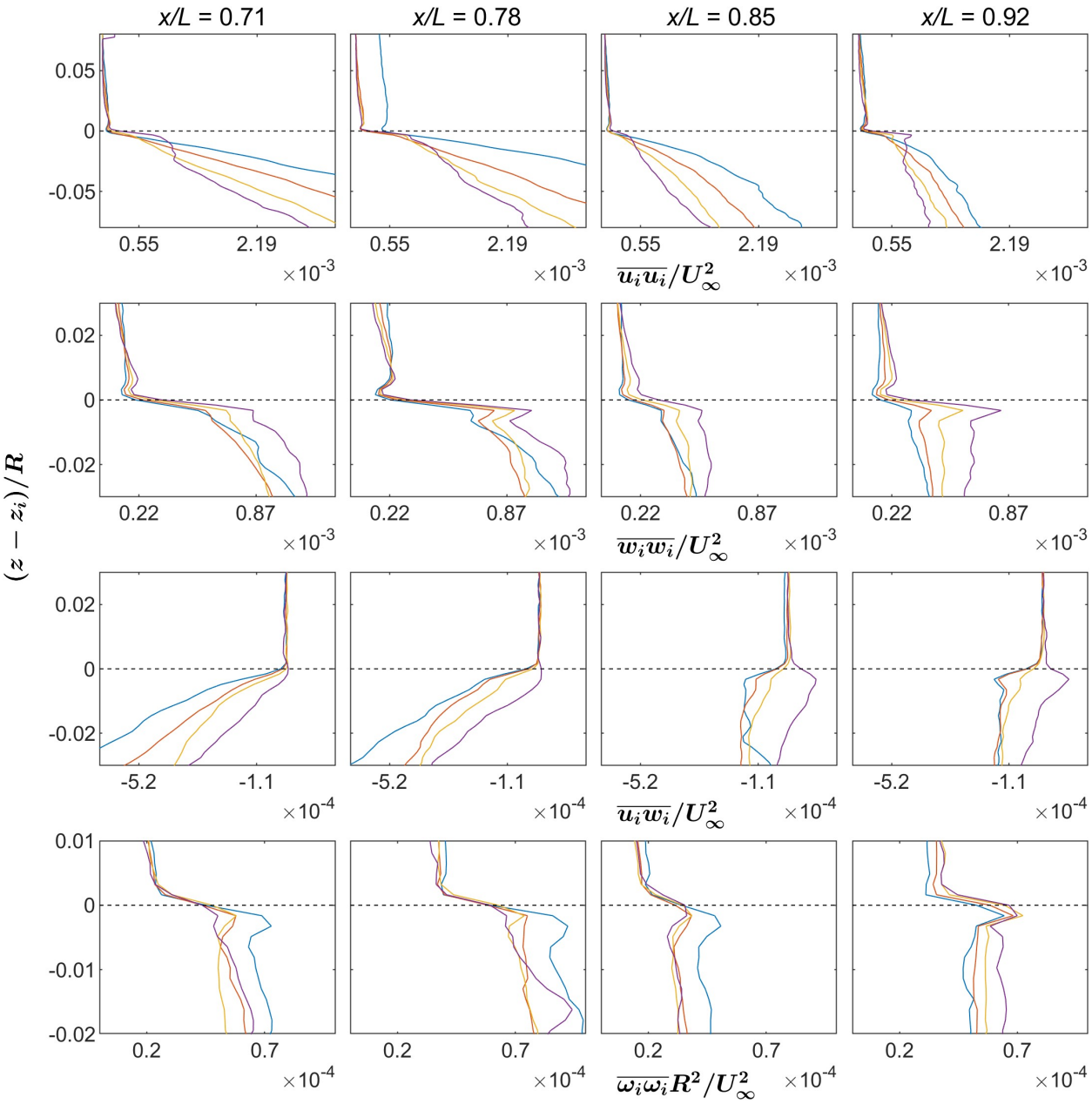

Figure 3.83 Conditional averages about the interface. Each row corresponds to a different variable labeled below. Each column represents a different axial station as labeled at the top. Blue, orange, yellow, and purple lines correspond to the four conditions in 3.12.

Figure 3.83 shows detailed conditional averages by additionally imposing the interface height criteria. The columns from left to right correspond to the four axial locations of $x/L = 0.71$, 0.78, 0.85, and 0.92. The blue, orange, yellow, and purple lines in each figure denote the lowest to highest interface positions outlined in Eq. 3.12. The horizontal axes in

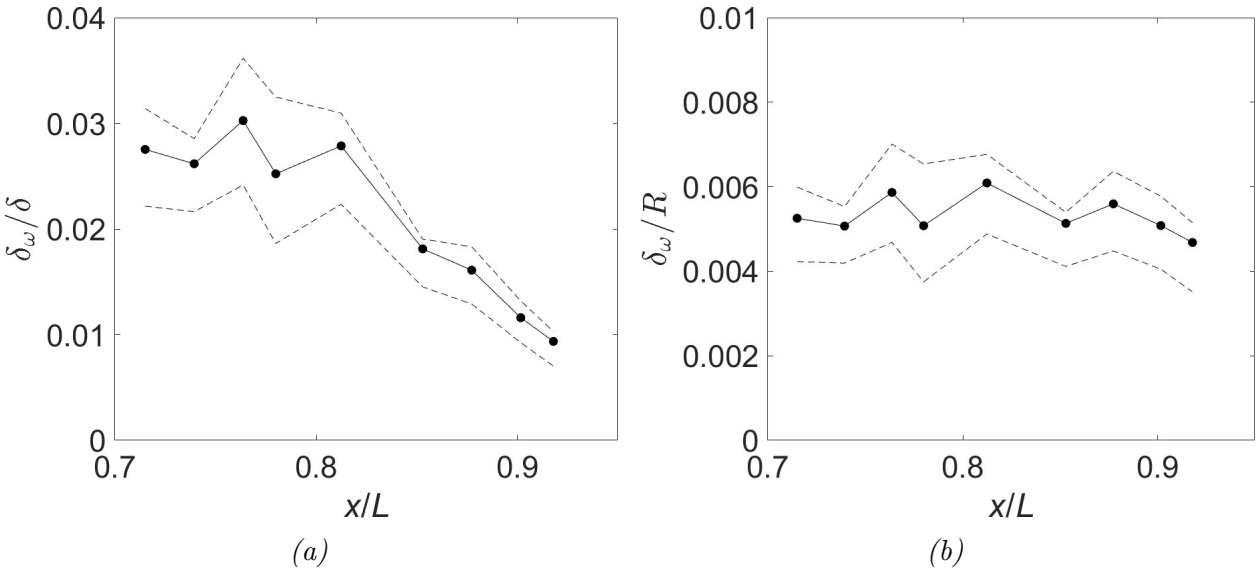

Figure 3.84 Variation of vorticity thickness δ_ω with axial position x/L normalized by *(a)* the local boundary layer thickness δ and *(b)* the hull radius R.

each row have equal scales for visual comparison.

The first row of Fig. 3.83 shows $\overline{u_i^2}$. The trend common to all figures was that $\overline{u_i^2}$ was most intense when the interface was low. Reuther and Kähler [35] suggested valleys, i.e., low interfaces, are where entrainment occurs. Perhaps there was a correlation between intense interface-tangent velocity and enhanced entrainment [36]. The wall-normal intensity $\overline{w_i^2}$ is presented in the second row, and was most intense when the interface was far from the wall.

For $\overline{u_i w_i}$ in the third row, the upstream stations $x/L = 0.71$ and 0.85 were comparable. In contrast, the downstream stations showed less correlation between the two flow velocities, perhaps pointing to less intense large-scale, which, as observed in Fig. 3.21, carries most of the Reynolds shear stress. The fourth row showcases the enstrophy, i.e., vorticity fluctuation intensity. The lowest interface height (thin blue line) showed the greatest vorticity fluctuation, except at $x/L = 0.92$. The vorticity variance increased at $x/L = 0.78$, decreased at $x/L = 0.85$, and returned to similar levels at $x/L = 0.92$, perhaps an outcome of the pressure gradient.

The vorticity thickness was computed at nine different streamwise stations across the FOV to understand the effect of pressure gradient and curvature on the length scales in

the TNTI. The vorticity thickness and velocity jump were visually inspected, such as in Fig. 3.79(b), ensuring the fitted lines were reasonable. Figures 3.84(a) and (b) respectively show the varying vorticity thickness relative to the local boundary layer thickness δ and the constant hull radius R.

First examining Fig. 3.84(a), δ_ω/δ_0 denoted by the solid line decreased with streamwise distance, although this trend was a consequence of the growing δ_0. Instead, Fig. 3.84(b) shows that δ_ω/R denoted by the solid line was invariant with streamwise distance. The dashed lines above and below the solid one show the outcome of using points slightly closer or further from the interface to fit the linear lines, which modified the velocity jump. These dashed lines could be interpreted as uncertainty bounds for the computed vorticity thickness.

There was no appreciable change in vorticity thickness with streamwise distance, as shown in Fig. 3.84(b), irrespective of the linear fits. The pressure gradient and wall curvature appeared not to affect the vorticity thickness. It was also possible that the spatial resolution was insufficient to resolve the maximum velocity gradient, and the current estimate of vorticity thickness was an upper bound [30].

3.4.4 Interface Geometry

Turbulent entrainment is a multi-scale phenomenon [222], comprising structures on the order of the boundary layer thickness down to the Kolmogorov scales, where vorticity diffusion occurs [170]. The large scales are responsible for the bulges, valleys, and folds, whereas the small scales form the wrinkled interface. To quantify the entrainment associated with the contorted geometry, time-resolved measurements are required to divide the measured velocity into the interface and entrainment velocities [36]. Nonetheless, the present analysis relied on the interface geometry to deduce the length scales involved in the entrainment process following the approach of Westerweel et al. [171] and Chauhan et al. [30].

The small scale of the entrainment was determined through the auto-correlation of the interface-normal velocity $\tilde{u}_n$. The interface normal at any location was calculated based on the neighboring points. Figure 3.85(a) shows a collection of unit normal vectors along a

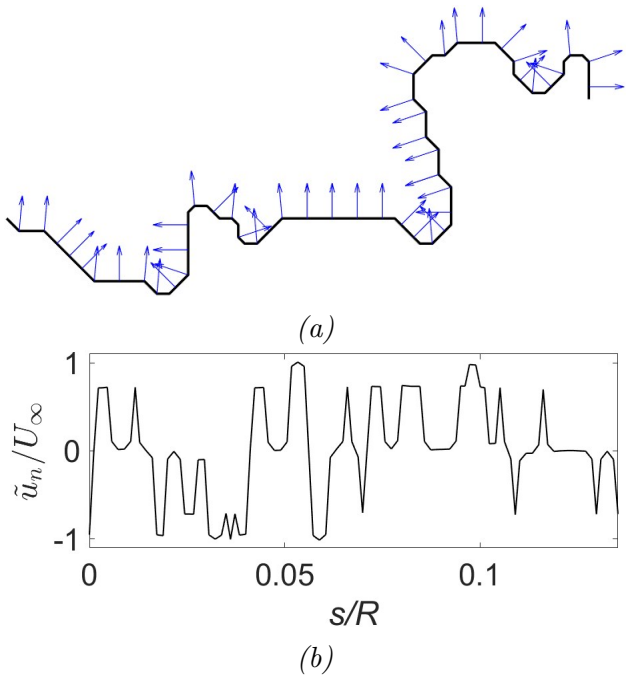

Figure 3.85 (a) TNTI with unit normals pointing outward. (b) Spatial variation of the interface normal velocity $\tilde{u}_n$ along the curvilinear coordinate s.

corrugated interface. The dot products of the measured velocity $\tilde{u}$ at the interface and the unit normal were then used as the instantaneous $\tilde{u}_n$.

A sample of the spatial variation in interface-normal velocity is shown in Fig. 3.85(b), where the abscissa is the curvilinear coordinate s along the interface. The abrupt variations in velocity resulted from the directional changes of the wrinkled interfaces [30]. Velocity segments such as this were used to compute the auto-correlation averaged over 2914 snapshots. This process was repeated for different segments along the afterbody, where each segment was confined to 0.25δ in the axial direction to minimize the effect of spatial variation.

Figure 3.86(a) shows sample auto-correlation curves of the interface-normal velocity from four axial stations with significantly different pressure gradients and wall curvatures. These curves suggest little variation in the small scales of the entrainment process. This observation is corroborated in Fig. 3.86(b), which demonstrates the small scale λ_S was invariant across 30 axial positions. Here, λ_S is the integral scale [171] from the $\tilde{u}_n$ auto-correlation curve. The dotted-dash, dash, and solid lines represent λ_S computed with threshold values of $R_{u_n u_n} = 0$,

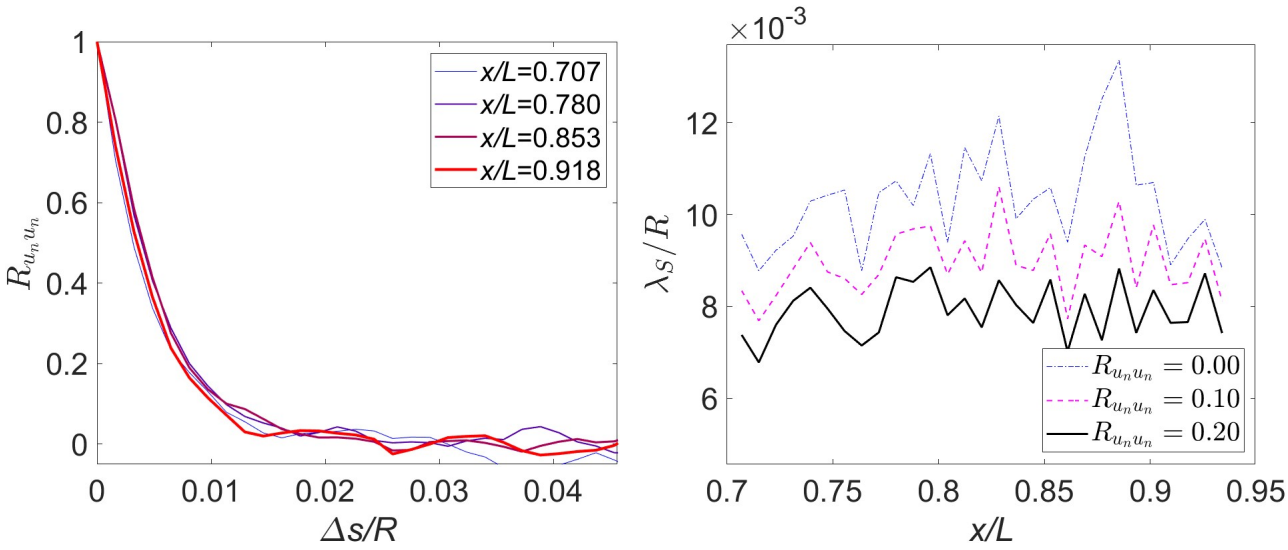

Figure 3.86 (a) Sample correlation curves of the interface-normal velocity. *(b)* summary of the length scale computed by integrating the two-point correlation curve. Different lines represent thresholds of 0, 0.1, and 0.2

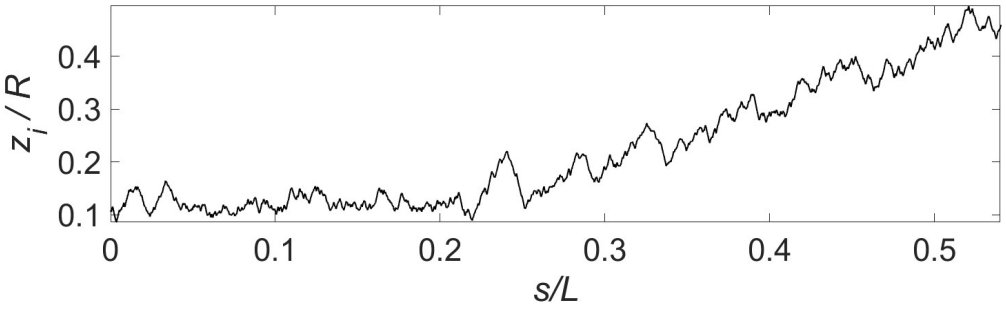

Figure 3.87 Position of the interface unraveled with curvilinear coordinate s shows large contortions $\mathcal{O}(\delta)$.

0.05, and 0.1. In terms of viscous units, the small scales in the TNTI were roughly $\lambda_S^+ = 150$. This value was comparable to the vorticity thickness [224] $\delta_\omega^+ = 90$ obtained from the conditional wall-tangent velocity profile, in agreement with results from Chauhan et al. [33].

Although entrainment occurs at the Taylor microscale, large-scale contortions increase the interface surface area over which nibbling occurs. Therefore, the large scales in the interface should also be examined. Figure 3.87 shows a sample of the interface wall distance across the entire Suboff afterbody. The interface height z_i grew to significant values at the end of the domain following the increased boundary layer thickness. However, a visual inspection

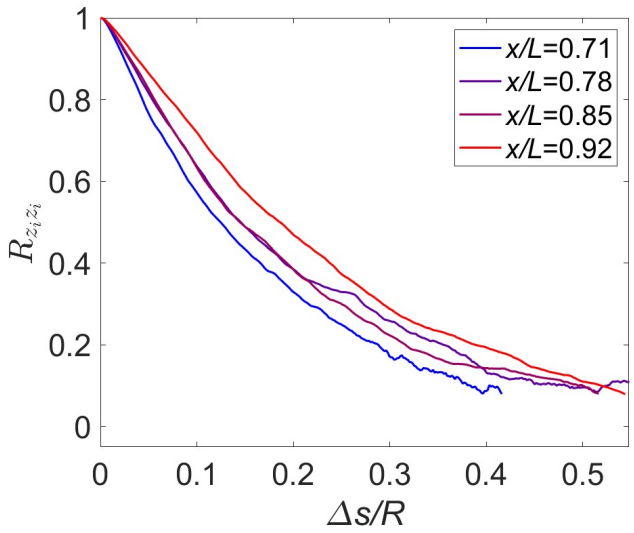

Figure 3.88 Sample two-point correlation curves for the interface position z_i.

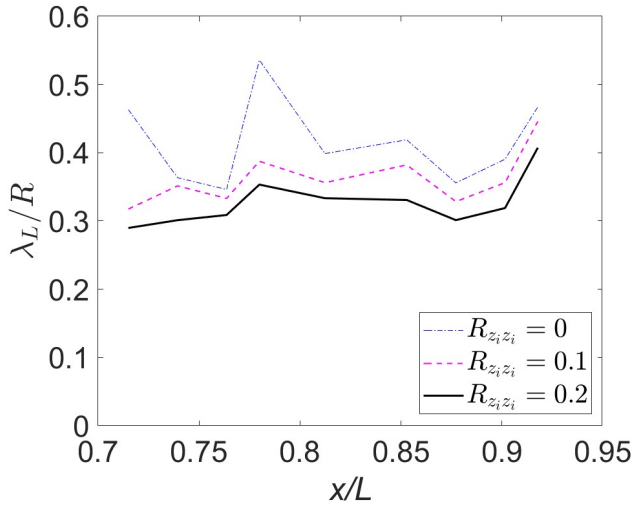

Figure 3.89 Summary of integral scale computed based on two-point correlation curves similar to the ones in Figure 3.88. Different lines represent varying threshold levels to assess sensitivity.

of the fluctuations does not indicate growing contortions.

A quantitative investigation of the contortion was performed following the work of Westerweel et al. [171] and Chauhan et al. [30]. The two-point correlation was performed using the interface deviation from its time-mean value. Figure 3.88 shows sample two-point correlations from four streamwise stations. The blue and red lines represent up and downstream locations. The figure indicates that downstream locations had more surface area per unit axial distance.

Lastly, a length scale for the bulges and valleys was defined by integrating the two-point correlation curves in Figure 3.88. Note that the two-point correlation was mirrored about $\Delta s = 0$ before the integration. The analysis outcome is shown in Figure 3.89, where the three lines correspond to different threshold levels for computing λ_L. At the most upstream station of $x/L = 0.715$, $\lambda_L \approx 0.3R = 1.6\delta_0$, where δ_0 is the actual local boundary layer thickness. This result agreed with Chauhan et al. [82] who found $\lambda_L = 1.7\delta_0$ in a canonical boundary layer.

The combined effect of pressure gradient and wall curvature was evident in the black line, where the slight upward trend indicated that the eddies responsible for the interface contortions grew gradually with streamwise distance. While the small-scale nibbling appeared relatively invariant, the growing area available for nibbling suggested that entrainment increased with downstream distance. This gradual increase in length scale also agreed with the two-point correlation analysis in Section 3.3.2.1, having an almost identical trend to the length scale in Figure 3.41(b) at $z_{\text{ref}}/\delta = 0.9$.

3.4.5 Summary of the TNTI

Contrary to how a time-averaged boundary layer transitions smoothly into the free stream, the instantaneous boundary layer is intermittent, characterized by irregular periods of quiescence and turbulence. At any moment, the boundary layer is segregated from the potential flow by a ragged barrier known as the turbulent/non-turbulent interface (TNTI), as shown in Fig. 3.74. The corrugated TNTI is a thin layer of concentrated vorticity that converts the potential outer flow into turbulence (or vice versa). Examination of this interface revealed significant "jumps" in flow properties on the order of the flow's turbulence intensity calculated in Section 3.2.4. The analysis in this section, in particular, contributed to an understanding of pressure gradient and wall curvature effects on the TNTI.

1. The interface detection criterion of Chauhan et al. [82] was modified to account for the growing wall-normal velocity (because of the APG) and the streamline curvature in the potential flow.

2. The average interface shifted closer to and further from the wall with FPG and APG, respectively. The lateral curvature was unlikely the reason for these shifts [154].

3. The standard deviation of the interface location, when normalized by the local boundary layer thickness, increased with favorable pressure gradient and decreased in the adverse pressure gradient region.

4. Variations were noted in conditional statistics averaged about the interface

   (a) The velocity "jump" across the interface was most pronounced when the interface was near the wall

   (b) The peak vorticity in the TNTI followed the trend of the pressure gradient

5. The "nibbling" length scale in the TNTI was roughly 150 wall units. The length scale of bulges and valleys was on the order of the boundary layer thickness. The small scales responsible for nibbling were constant (to within the experimental uncertainty), but the large-scale motions were gradually enlarged across the afterbody.

4 Conclusions

The boundary layer of a representative submarine model called the Suboff was investigated in the Embry-Riddle Low-Speed Wind Tunnel. The appendages and sail were removed to focus on the axisymmetric boundary layer. Three particle image velocimetry (PIV) configurations were used to interrogate the boundary layer with high spatial and temporal resolution. Particular attention was given to reducing the laser wall reflections, the outcome of which permitted measurements deeper into the boundary layer than previously possible (Appendix B). Measurements were acquired at considerable Reynolds numbers of up to $Re_\tau \approx 2{,}700$, $Re_\theta = 5{,}000$–$25{,}000$, or $Re_L \approx 8 \times 10^6$ based on model length.

The principal objective was to understand how the initially near-canonical (i.e., zero-pressure gradient, smooth-wall, nearly planar) Suboff boundary layer was modified along the afterbody by the simultaneous presence of pressure gradient and wall curvature, which are commonplace in engineering applications. To this end, significant changes were observed in the mean and variance of the turbulence. Additionally, two-point correlation analyses revealed how the boundary layer structures were distorted and rotated in the streamwise and spanwise directions. Unique two-point correlation contours near the boundary layer edge motivated an investigation of the turbulent/non-turbulent interface. This investigation detailed average flow fields conditioned on the interface and the behaviors of the large and small scales that constituted the wrinkled surface.

The variations in flow characteristics were attributed to three factors: 1. The pressure gradient; 2. The lateral wall curvature; 3. The longitudinal wall curvature. The factor responsible for the observed change in a flow characteristic was inferred by comparing their relative spatial patterns. However, because these factors had overlapping regions of influence, inferences were also guided by prior studies examining isolated effects. Ascribing an observed trend to one of these three factors was not always possible because multiple factors may produce similar or opposite effects.

Three guiding research questions were outlined in Section 1.2. The conclusions drawn

from the results will concurrently address the first two questions of how and why the boundary layer was altered. A separate discussion considers the flow history. These findings were primarily based on the higher Reynolds number case, i.e., $Re_\tau \approx 2{,}700$.

4.1 Pressure Gradient and Curvature Effects

The axisymmetric boundary layer along the constant diameter section of the Suboff was comparable to a zero-pressure gradient (ZPG), planar boundary layer. The mean velocity and Reynolds stress compared well with previous studies [9, 82, 176]. The streamwise length scale in the logarithmic region was roughly six times the local boundary layer thickness [97], as evident in the two-point correlation and the frequency spectra. This near-canonical boundary layer experienced strong pressure gradients and wall curvatures along the Suboff afterbody.

The pressure gradient and wall curvature continuously changed along the afterbody. A non-dimensional pressure gradient was computed following the work of Clauser [87]. The pressure gradient was favorable up to 79% of the body length, most adverse at 90%, and quickly returned to zero after that. The lateral curvature was quantified as the ratio between the boundary layer thickness and the geometry radius. This variable became increasingly significant beyond 80% of the body length [129]. The longitudinal curvature was described as the ratio of the boundary layer thickness to the local radius of curvature. The longitudinal curvature was convex from 75% to 88% of the length, and concave further downstream [200]. These factors significantly modified the flow statistics and structure in the inner and outer regions of the turbulent boundary layer.

4.1.1 Single-Point Statistics

1. Using an inner scaling, the semi-logarithmic plot of wall-tangent velocity followed the law of the wall even at 92% of the body length, the most downstream station in the measurement. However, the wake region grew significantly while the logarithmic region eroded. This outcome was predominantly a consequence of the pressure gradient, although the lateral curvature likely had an effect.

2. The wall-parallel velocity variance appeared more affected by the pressure gradient than the other two factors. The observed trends were comparable to a planar adverse pressure gradient flow, implying that wall curvature had a limited effect.

3. The wall-normal velocity variance was rapidly attenuated in the outer region from 75–85% of the body length, paralleling the longitudinal convex curvature. Convex curvature is known [213] to reduce the turbulence intensity. The pressure gradient and lateral curvature were eliminated because their trends seemed inconsistent with the wall-normal velocity variance.

4. The diagnostic plot [211] did not collapse the profiles across different axial locations. This outcome indicated smaller wall-tangent fluctuation intensity relative to a canonical flow beyond 80% of the body length, resulting from the growing lateral curvature. The lateral curvature could have reduced the intensity level, but the mean profile is also known to become "fuller" for axisymmetric flows, which could have also explained this trend.

5. A proper orthogonal decomposition of the flow field suggested that the large scales, particularly in the outer region, were more affected by the pressure gradient and wall curvature compared to the small scales [51].

4.1.2 Two-Point Statistics

1. Inspection of the premultiplied spectra offered insights into the flow structure, which were complemented by spatial two-point correlation analysis:

   (a) The premultiplied peak frequencies in the outer region were not noticeably affected by pressure gradient or wall curvature when scaled by the edge velocity and hull radius. Frequency peaks in the inner region, however, varied significantly in the wall-tangent and wall-normal velocities.

   (b) The premultiplied peak frequency of the wall-tangent velocity increased with the adverse pressure gradient near the wall. However, the peak frequency quickly

became similar to the ZPG results as the adverse pressure gradient was removed. These variations were attributed to pressure gradient effects.

(c) The premultiplied peak frequency of wall-normal velocity fluctuations continuously decreased along the afterbody in the near-wall region, suggesting changes in the underlying physics. In particular, it was hypothesized that the low-frequency wall-normal fluctuations at downstream locations were dictated by hairpin packets, because

i. The wall-normal and wall-parallel velocity spectrograms had comparable contour shapes, and the wall-parallel velocity near the wall was governed by hairpin packets as shown by linear stochastic estimation.

ii. The wall-normal velocity peak (premultiplied) frequency was roughly twice that of the wall-tangent velocity, consistent with the idea that each low-speed region induced by a hairpin packet contains up and downwash.

2. In the streamwise–wall-normal plane, the spatial two-point correlation demonstrated that:

(a) The near-wall two-point correlation contours based on the wall-parallel velocity were stretched and compressed by the favorable and adverse pressure gradients by up to 25% while experiencing at most 10° of rotation. These structures resulted from hairpin vortex packets, as demonstrated through linear stochastic estimation [25]. These length scale variations explained the changes in the frequency content.

(b) The two-point correlations near the boundary layer edge were more rounded. They were primarily rotated by the pressure gradient (or streamline curvature), and experienced a gradual elongation with downstream distance. This observation was consistent with the (premultiplied) frequency peaks being largely invariant in the outer region.

(c) The inclination angle of the wall-tangent velocity correlation contour was com-

puted using the singular value decomposition. The local inclination angle, i.e., calculated relative to the wall, followed Clauser's pressure gradient parameter. In contrast, relative to the longitudinal symmetry axis, the global inclination angle followed the acceleration parameter better.

(d) The length scale of the wall-tangent velocity normalized by the local boundary layer thickness followed Clauser's parameter. In contrast, the length of the structure without normalization followed the acceleration parameter, which had a similar trend to the pressure gradient. A gradual increase in length scale was observed near the boundary layer edge and hypothesized to result from the lateral curvature.

(e) An equation composed of a pressure gradient parameter and two free variables was successfully fit to the wall-tangent velocity length scale. Further, the results suggested that the boundary layer response lagged the pressure gradient by roughly one boundary layer thickness.

(f) The two-point correlation contours of the wall-normal velocity were invariant near the boundary layer edge. However, up to 50% of the boundary layer thickness, the contours changed appreciably across the afterbody. In particular, a forward lean was observed beyond 80% of the body length, supporting the hypothesis that hairpin packets strongly influenced the wall-normal fluctuations.

(g) The two-point cross correlation between the wall-parallel and the wall-normal velocities exhibited an unusual pattern. This correlation contour is negative for a canonical flow and indicates a preference for sweep and ejection. However, a region of positive correlation downstream of the reference point appeared in the outer region after 80% of the body length, likely resulting from the longitudinal curvature.

3. In the spanwise-radial plane, the spatial two-point correlation showed that:

(a) The favorable pressure gradient resulted in a uniform increase in the azimuthal length scale across the entire boundary layer thickness for the wall-tangent velocity. Conversely, an adverse pressure gradient consistently reduced this length scale throughout the boundary layer.

(b) The adverse pressure gradient increased the near-wall azimuthal length scale [121] of the wall-tangent velocity after 85% of the body length. This increase resulted in a nearly uniform length scale, approximately 10% of the maximum hull radius, across the boundary layer in the most downstream spanwise plane at 92% of the body length.

(c) The azimuthal length scales based on the circumferential and wall-normal velocities also increased near the wall after 85% of the body length. These azimuthal length scales in the most downstream measurement plane were roughly 15% of the hull radius.

(d) The spanwise plane hairpin-type roller structures were modified. These rollers were biased toward the wall in the favorable pressure gradient but toward the boundary layer edge in the adverse pressure gradient. This result was likely related to the modified correlation between the wall-parallel and wall-normal velocities.

4. Three-dimensional insights were obtained by simultaneously analyzing the streamwise and spanwise planes,

   (a) The cross-correlation between the wall-parallel and wall-normal velocities exhibited unique trends:

      i. Near the wall in the log region, the alternating up and downwash patterns in the spanwise plane were the footprint of hairpin vortex packets.

      ii. Near the boundary layer edge, a pattern of up and downwash was visible in the streamwise plane. This pattern was related to the turbulent bulges through a conditional average analysis.

iii. Interestingly, the spanwise plane and streamwise plane up/downwash pattern did not coexist at 50% of the boundary layer thickness. Whether one pattern prevailed over the other depended on the axial location, suggesting an interplay between the hairpin packets and the turbulent bulges likely modulated by the longitudinal streamline curvature.

(b) Conditional averaging near the boundary layer edge showed that the variations in the wall-parallel–wall-tangent velocity correlations were associated with turbulent bulges. In particular, the flow accelerated around the low-speed turbulent bulges into the valleys [35]. Variations in flow patterns around the turbulent bulges were observed across the afterbody, suggesting changes to the underlying large-scale motions that require a deeper analysis in the future.

4.1.3 Turbulent/Non-Turbulent Interface

1. The interface detection method of Chauhan et al. [30] was modified to address wall-normal velocity and streamline curvature present in the Suboff boundary layer. The proposed piece-wise implementation used the mean velocities instead of the edge velocity beyond the boundary layer thickness.

2. The average interface shifted closer to and further from the wall with favorable and adverse pressure gradients. The standard deviation of the interface location normalized by the local boundary layer thickness had the opposite trend. The initial decrease and subsequent increase in mean interface location suggested that the pressured gradient was primarily responsible, although wall curvature effects were not excluded. These variations suggested that pressure gradients can also impact the outer region.

3. Sudden increases in velocity, or "jumps," were observed at the interface, in accord with prior works. This jump in wall-parallel velocity was more significant when the interface was closer to the wall, equal to roughly 2% of the edge velocity. A jump in wall-normal velocity also appeared after 85% of the body length. The interface

peak vorticity magnitude increased and decreased with favorable and adverse pressure gradients, respectively.

4. The integral scale of nibbling was insensitive to pressure gradient and wall curvature effects. However, the integral length of the large-scale motions that underlie the hills, valleys, and folds was roughly 30% of the hull radius and grew gradually in size with downstream distance, similar to the spatial two-point correlation contours. More than one factor may have caused this growth.

Although it was interesting to assess the altered flow characteristics, the spatial variations in pressure gradient and wall curvature are equally important considerations when studying non-equilibrium boundary layer flows.

4.2 Flow History Effects

Flow history effects were visible in the boundary layer. For example, the lowest shape factor was located at the end of the favorable pressure gradient region instead of coinciding with the maximum favorable pressure gradient. Devenport and Lowe [51] reasoned through a comparison of scales that a boundary layer, when subjected to step changes in the wall shear stress or even mild pressure gradients, requires an adjustment distance of roughly 50 boundary layer thicknesses. The Suboff afterbody was roughly 20 times the initial boundary layer thickness, so the flow did not settle into a new equilibrium, especially considering the spatially varying pressure gradient and wall curvature. Indeed, in engineering applications such as the Suboff, the boundary layer constantly adjusts to the environment. Equilibrium is the exception, not the norm, so it is essential to consider how varying conditions should be handled.

An interesting and useful outcome of this work was the collapse of the wall-tangent velocity length scale across all wall-normal (up to 80% of the boundary layer thickness) and wall-tangent locations. Two observations enabled this collapse:

1. The percentage change relative to the initial length scale was comparable across all wall-normal positions.

2. The streamwise variations in length scale closely mimicked the trends in the pressure gradient.

From a flow physics perspective, the first point indicated that pressure gradient effects on the turbulent structures were felt throughout the boundary layer. The second trend demonstrated that turbulent structures responded rapidly to the imposed pressure gradient—the maximum length scale lagged the maximum favorable pressure gradient by merely one boundary layer thickness.

Nonetheless, the structural response was more nuanced upon closer inspection. The forward-leaning structures near the wall were primarily elongated and compressed by the pressure gradient, whereas the more rounded structures further from the wall were rotated without much distortion. Therefore, the length scale variations across different heights resulted from two distinct mechanisms—rotation and distortion. The rotation and distortion of the structures also roughly followed the pressure gradient.

Although turbulence is generally nonlinear because of the quadratic Navier-Stokes equations, certain aspects of the boundary layer could behave linearly. For example, the distortion and rotation of the large scales were similar to an elastic deformation, where the structures returned to their original state after the "volume strain" from the increased pressure was alleviated. While this proportionality is almost undoubtedly untrue in general, specific boundary layer characteristics may exhibit linearity with respect to external forcing, a potentially helpful observation depending on the engineering objective. Ultimately, a deeper comprehension of the transient effects induced by non-equilibrium conditions would help engineers make better-informed decisions.

4.3 Suggested Future Work

There are several future research possibilities using the Suboff body shape:

1. The large field of view PIV can be used to study the uniform momentum zones in the flow. Contrary to the smooth time-mean velocity profile, the instantaneous profile is more step-like, comprising regions of approximately uniform momentum.

2. The high magnification results are currently being processed using particle tracking velocimetry. Measurements in the viscous sublayer could be used to infer the friction velocity and the viscous length scale more accurately than the Clauser chart method.

3. Time-resolved measurements targeting the turbulent/non-turbulent interface would help understand the entrainment kinematics. It is impossible to distinguish between the interface and entrainment velocities from flow field snapshots.

4. Alternate afterbody geometries can be fabricated to investigate different pressure gradient and wall curvature histories.

5. The appendages and the sail could be inserted to investigate vortical structures. Junction flows create horseshoe/necklace vortices that are a significant noise source if ingested by the propeller.

6. A fan or propeller can be added to investigate how propeller thrust induces pressure gradient and swirl. Transient conditions such as propulsor "crashback" or retrograde flow could be interesting.

7. Time-resolved measurements of cross-stream (propeller rotation) planes could give invaluable insights into the length and time scales ingested by the propeller.

There are three general suggestions for future pressure gradient and curvature studies:

1. It is crucial to separate the effects of pressure gradient, lateral curvature, and longitudinal curvature to obtain a more definitive understanding of each factor. These factors often appear in conjunction and may affect similar aspects of the flow, leading to ambiguities about their relative importance. A clear understanding of each factor will lead

to more informed engineering decisions. Much of the work on lateral and longitudinal curvature was before the advent of particle image velocimetry and detailed numerical simulations, which would offer a wealth of information on wall curvature effects.

2. History effects of pressure gradient and wall curvature should be studied more systematically. Much research has indicated that the upstream conditions significantly affect the flow. Still, little effort has been devoted to quantifying the extent of the effect, which appears to be a secondary concern. Vinuesa et al. [66] used an integrated Clauser parameter to account for the flow history, which gave good predictions of the skin friction. However, history effects could be studied more systematically by investigating how boundary layers respond to harmonic variations in pressure gradient. This approach will help understand how different wavenumbers impact the cascade of length scales and enable more comprehensive modeling. For example, a high-frequency variation in pressure gradient will unlikely affect large scales with significant inertia. As another example, are isotropic small scales affected by pressure gradient [51]? What are the scales relevant to the engineering objective? The key is to break down the flow history into building blocks, which can then be reassembled in other ways to generalize the findings.

3. With an intuition of how the turbulence responds to external perturbation, such as variations in wall shear stress or pressure gradient, dynamical models could be formulated to inform flow control efforts. However, achieving this goal is a more distant prospect.

REFERENCES

[1] Squire, D. T., "The Structure and Scaling of Rough-Wall Turbulent Boundary Layers," Ph.D. thesis, Univesity of Melbourne, Dec 2016.

[2] Pope, S., *Turbulent Flows*, Cambridge University Press, 2000.

[3] Harun, Z., Monty, J. P., Mathis, R., and Marusic, I., "Pressure Gradient Effects on the Large-Scale Structure of Turbulent Boundary Layers," *Journal of Fluid Mechanics*, Vol. 715, 2013, pp. 477–498. https://doi.org/10.1017/jfm.2012.531.

[4] Nagano, Y., Tsuji, T., and Houra, T., "Structure of Turbulent Boundary Layer Subjected to Adverse Pressure Gradient," *International Journal of Heat and Fluid Flow*, Vol. 19, No. 5, 1998, pp. 563–572. https://doi.org/10.1016/S0142-727X(98)10013-9.

[5] Balantrapu, N. A., Hickling, C., Alexander, W. N., and Devenport, W., "The Structure of a Highly Decelerated Axisymmetric Turbulent Boundary Layer," *Journal of Fluid Mechanics*, Vol. 929, 2021. https://doi.org/10.1017/jfm.2021.845.

[6] Monty, J. P., Harun, Z., and Marusic, I., "A Parametric Study of Adverse Pressure Gradient Turbulent Boundary Layers," *International Journal of Heat and Fluid Flow*, Vol. 32, No. 3, 2011, pp. 575–585. https://doi.org/10.1016/j.ijheatfluidflow.2011.03.004.

[7] Baars, W. J., and Marusic, I., "Data-Driven Decomposition of the Streamwise Turbulence Kinetic Energy in Boundary Layers. Part 1. Energy Spectra," *Journal of Fluid Mechanics*, Vol. 882, 2020, p. A25. https://doi.org/10.1017/jfm.2019.834.

[8] Kim, K. C., and Adrian, R. J., "Very Large-Scale Motion in the Outer Layer," *Physics of Fluids*, Vol. 11, No. 2, 1999, pp. 417–422. https://doi.org/10.1063/1.869889.

[9] Harun, Z., "The Structure of Adverse and Favourable Pressure Gradient Turbulent Boundary Layers," Ph.D. thesis, University of Melbourne, 2012.

[10] Sillero, J. A., Jiménez, J., and Moser, R. D., "Two-Point Statistics for Turbulent Boundary Layers and Channels at Reynolds Numbers up to $\delta^+ \approx 2000$," *Physics of Fluids*, Vol. 26, No. 10, 2014. https://doi.org/10.1063/1.4899259.

[11] Hutchins, N., Hambleton, W. T., and Marusic, I., "Inclined Cross-Stream Stereo Particle Image Velocimetry Measurements in Turbulent Boundary Layers," *Journal of Fluid Mechanics*, Vol. 541, 2005, pp. 21 – 54. https://doi.org/10.1017/S0022112005005872.

[12] Kitsios, V., Sekimoto, A., Atkinson, C., Sillero, J. A., Borrell, G., Gungor, A. G., Jiménez, J., and Soria, J., "Direct Numerical Simulation of a Self-Similar Adverse Pressure Gradient Turbulent Boundary Layer at the Verge of Separation," *Journal of Fluid Mechanics*, Vol. 829, 2017, pp. 392–419. https://doi.org/10.1017/jfm.2017.549.

[13] Volino, R. J., "Non-Equilibrium Development in Turbulent Boundary Layers with Changing Pressure Gradients," *Journal of Fluid Mechanics*, Vol. 897, 2020. https://doi.org/10.1017/jfm.2020.319.

[14] Lee, J. H., "Large-Scale Motions in Turbulent Boundary Layers Subjected to Adverse Pressure Gradients," *Journal of Fluid Mechanics*, Vol. 810, 2017, pp. 323–361. https://doi.org/10.1017/jfm.2016.715.

[15] Head, M., and Bandyopadhyay, P., "New Aspects of Turbulent Boundary-Layer Structure," *Journal of Fluid Mechanics*, Vol. 107, 1981, pp. 297–338. https://doi.org/10.1017/S0022112081001791.

[16] Meinhart, C. D., and Adrian, R. J., "On the Existence of Uniform Momentum Zones in a Turbulent Boundary Layer," *Physics of Fluids*, Vol. 7, No. 4, 1995, pp. 694–696. https://doi.org/10.1063/1.868594.

[17] Kim, J., Moin, P., and Moser, R., "Turbulence Statistics in Fully Developed Channel Flow at Low Reynolds Number," *Journal of Fluid Mechanics*, Vol. 177, 1987, pp. 133–166. https://doi.org/10.1017/S0022112087000892.

[18] Zhou, J., Adrian, R. J., Balachandar, S., and Kendall, T. M., "Mechanisms for Generating Coherent Packets of Hairpin Vortices in Channel Flow," *Journal of Fluid Mechanics*, Vol. 387, 1999, pp. 353–396. https://doi.org/10.1017/S002211209900467X.

[19] Adrian, R. J., Meinhart, C. D., and Tomkins, C. D., "Vortex Organization in the Outer Region of the Turbulent Boundary Layer," *Journal of Fluid Mechanics*, Vol. 422, 2000, pp. 1 – 54. https://doi.org/10.1017/S0022112000001580.

[20] Christensen, K. T., and Adrian, R. J., "Statistical Evidence of Hairpin Vortex Packets in Wall Turbulence," *Journal of Fluid Mechanics*, Vol. 431, 2001, pp. 433 – 43. https://doi.org/10.1017/S0022112001003512.

[21] Ganapathisubramani, B., Hutchins, N., Hambleton, W., Longmire, E., and Marusic, I., "Investigation of Large-Scale Coherence in a Turbulent Boundary Layer Using Two-Point Correlations," *Journal of Fluid Mechanics*, Vol. 524, 2005, pp. 57–80. https://doi.org/10.1017/S0022112004002277.

[22] Ganapathisubramani, B., Longmire, E. K., and Marusic, I., "Characteristics of Vortex Packets in Turbulent Boundary Layers," *Journal of Fluid Mechanics*, Vol. 478, 2003, pp. 35–46. https://doi.org//10.1017/S0022112002003270.

[23] Del Alamo, J. C., Jiménez, J., Zandonade, P., and Moser, R. D., "Self-Similar Vortex Clusters in the Turbulent Logarithmic Region," *Journal of Fluid Mechanics*, Vol. 561, 2006, pp. 329–358. https://doi.org/10.1017/S0022112006000814.

[24] Dennis, D. J., and Nickels, T. B., "Experimental Measurement of Large-Scale Three-Dimensional Structures in a Turbulent Boundary Layer. Part 1. Vortex Packets," *Journal of Fluid Mechanics*, Vol. 673, 2011, pp. 180–217. https://doi.org/10.1017/S0022112010006324.

[25] Adrian, R. J., and Moin, P., "Stochastic Estimation of Organized Turbulent Structure:

Homogeneous Shear Flow," *Journal of Fluid Mechanics*, Vol. 190, 1988, pp. 531–559. https://doi.org/10.1017/S0022112088001442.

[26] Neves, J. C., Parviz, M., and Moser, R. D., "Effects of Convex Transverse Curvature on Wall-Bounded Turbulence. Part 1. The Velocity and Vorticity," *Journal of Fluid Mechanics*, Vol. 272, 1994, pp. 349–382. https://doi.org/10.1017/S0022112094004490.

[27] Hammache, M., Browand, F. K., and Blackwelder, R. F., "Whole-Field Velocity Measurements Around an Axisymmetric Body with a Stratford–Smith Pressure Recovery," *Journal of Fluid Mechanics*, Vol. 461, 2002, pp. 1–24. https://doi.org/10.1017/S0022112002008479.

[28] Zhou, D., Wang, K., and Wang, M., "Rotor Aeroacoustic Response to an Axisymmetric Turbulent Boundary Layer," *Journal of Fluid Mechanics*, Vol. 981, 2024, p. A25. https://doi.org/10.1017/jfm.2024.29.

[29] Corrsin, S., and Kistler, A. L., "Free-stream Boundaries of Turbulent Flows," Tech. rep., 1955. NACA-TR-1244.

[30] Chauhan, K., Philip, J., De Silva, C. M., Hutchins, N., and Marusic, I., "The Turbulent/Non-Turbulent Interface and Entrainment in a Boundary Layer," *Journal of Fluid Mechanics*, Vol. 742, 2014, pp. 119–151. https://doi.org/10.1017/jfm.2013.641.

[31] Fiedler, H., and Head, M., "Intermittency Measurements in the Turbulent Boundary Layer," *Journal of Fluid Mechanics*, Vol. 25, No. 4, 1966, pp. 719–735. https://doi.org/10.1017/S0022112066000363.

[32] Chauhan, K., Philip, J., De Silva, C. M., Hutchins, N., and Marusic, I., "The Turbulent/Non-turbulent Interface and Entrainment in a Boundary Layer," *Journal of Fluid Mechanics*, Vol. 742, 2014, pp. 119–151. https://doi.org/10.1017/jfm.2013.641.

[33] Chauhan, K., Philip, J., and Marusic, I., "Scaling of the Turbulent/Non-Turbulent Interface in Boundary Layers," *Journal of Fluid Mechanics*, Vol. 751, 2014, pp. 298–328. https://doi.org/10.1017/jfm.2013.255.

[34] Lee, J., Sung, H. J., and Zaki, T. A., "Signature of Large-Scale Motions on Turbulent/Non-Turbulent Interface in Boundary Layers," *Journal of Fluid Mechanics*, Vol. 819, 2017, pp. 165–187. https://doi.org/10.1017/jfm.2017.170.

[35] Reuther, N., and Kähler, C. J., "Effect of the Intermittency Dynamics on Single and Multipoint Statistics of Turbulent Boundary Layers," *Journal of Fluid Mechanics*, Vol. 897, 2020, p. A11. https://doi.org/10.1017/jfm.2020.384.

[36] Mistry, D., Philip, J., and Dawson, J. R., "Kinematics of Local Entrainment and Detrainment in a Turbulent Jet," *Journal of Fluid Mechanics*, Vol. 871, 2019, pp. 896–924. https://doi.org/10.1017/jfm.2019.327.

[37] Zhou, Z., Li, Z., Yang, X., Wang, S., and Xu, D., "Investigation of the Wake Characteristics of an Underwater Vehicle With and Without a Propeller," *Ocean Engineering*, Vol. 266, 2022, p. 113107. https://doi.org/10.1016/j.oceaneng.2022.113107.

[38] Sciacchitano, A., "Uncertainty Quantification in Particle Image Velocimetry," *Measurement Science and Technology*, Vol. 30, No. 9, 2019, p. 092001. https://doi.org/10.1088/1361-6501/ab1db8.

[39] Wieneke, B., "PIV Uncertainty Quantification and Beyond," Ph.D. thesis, Delft University of Technology, 2017.

[40] Sciacchitano, A., Wieneke, B., and Scarano, F., "PIV Uncertainty Quantification by Image Matching," *Measurement Science and Technology*, Vol. 24, No. 4, 2013, p. 045302. https://doi.org/10.1088/0957-0233/24/4/045302.

[41] Dróżdż, A., Elsner, W., and Drobniak, S., "Scaling of Streamwise Reynolds Stress for Turbulent Boundary Layers With Pressure Gradient," *European Journal of Mechanics-B/Fluids*, Vol. 49, 2015, pp. 137–145. https://doi.org/10.1016/j.euromechflu.2014.08.002.

[42] Vinuesa, R., Bobke, A., Örlü, R., and Schlatter, P., "On Determining Characteristic Length Scales in Pressure-Gradient Turbulent Boundary Layers," *Physics of fluids*, Vol. 28, No. 5, 2016. https://doi.org/10.1063/1.4947532.

[43] Schlatter, P., and Orlu, R., "Quantifying the Interaction Between Large and Small Scales in Wall-Bounded Turbulent Flows: A Note of Caution," *Physics of Fluids*, Vol. 22, No. 5, 2010, pp. 1 – 4. https://doi.org/10.1063/1.3432488.

[44] Huang, T., and Liu, H., "Measurements of flows over an axisymmetric body with various appendages in a wind tunnel: the DARPA SUBOFF experimental program," 1994.

[45] Kumar, P., and Mahesh, K., "Large-Eddy Simulation of Flow over an Axisymmetric Body of Revolution," *Journal of Fluid Mechanics*, Vol. 853, 2018, pp. 537–563. https://doi.org/10.1017/jfm.2018.585.

[46] Minniti, R. J., Blake, W. K., and Mueller, T. J., "Inferring Propeller Inflow and Radiation from Near-Field Response, Part 1: Analytic Development," *AIAA Journal*, Vol. 39, No. 6, 2001, pp. 1030–1036. https://doi.org/10.2514/2.1443.

[47] Anderson, J. M., Kaler, Z., Manar, F., Joiner, J., Worden, T., and Catlett, M. R., "Close-Proximity Sound Pressure Measurements to Characterize Rotor Turbulence Ingestion Sound," *AIAA AVIATION 2020 FORUM*, American Institute of Aeronautics and Astronautics, 2020. https://doi.org/10.2514/6.2020-2592.

[48] Robinson, S. K., "Coherent Motions in the Turbulent Boundary Layer," *Annual Re-*

view of Fluid Mechanics, Vol. 23, No. 1, 1991, pp. 601–639. https://doi.org/10.1146/annurev.fl.23.010191.003125.

[49] Adrian, R. J., "Hairpin Vortex Organization in Wall Turbulence," *Physics of Fluids*, Vol. 19, No. 4, 2007. https://doi.org/10.1063/1.2717527.

[50] Marusic, I., Mathis, R., and Hutchins, N., "Predictive Model for Wall-Bounded Turbulent Flow," *Science*, Vol. 329, No. 5988, 2010, pp. 193–196. https://doi.org/10.1126/science.1188765.

[51] Devenport, W. J., and Lowe, K. T., "Equilibrium and Non-equilibrium Turbulent Boundary Layers," *Progress in Aerospace Sciences*, Vol. 131, 2022, p. 100807. https://doi.org/j.paerosci.2022.100807.

[52] Vila, C. S., Örlü, R., Vinuesa, R., Schlatter, P., Ianiro, A., and Discetti, S., "Adverse-Pressure-Gradient Effects on Turbulent Boundary Layers: Statistics and Flow-Field Organization," *Flow Turbulence and Combustion*, Vol. 99, No. 3–4, 2017, pp. 589–612. https://doi.org/s10494-017-9869-z.

[53] Bobke, A., Vinuesa, R., Örlü, R., and Schlatter, P., "History Effects and Near Equilibrium in Adverse-Pressure-Gradient Turbulent Boundary Layers," *Journal of Fluid Mechanics*, Vol. 820, 2017, pp. 667–692. https://doi.org/10.1017/jfm.2017.236.

[54] Balantrapu, N. A., Alexander, W. N., and Devenport, W., "Wall-Pressure Fluctuations in an Axisymmetric Boundary Layer Under Strong Adverse Pressure Gradient," *Journal of Fluid Mechanics*, Vol. 960, 2023. https://doi.org/10.1017/jfm.2023.225.

[55] Pozuelo, R., Li, Q., Schlatter, P., and Vinuesa, R., "Spectra of Near-Equilibrium Adverse-Pressure-Gradient Turbulent Boundary Layers," *Physical Review Fluids*, Vol. 8, No. 2, 2023, p. L022602. https://doi.org/10.1103/PhysRevFluids.8.L022602.

[56] Marusic, I., McKeon, B. J., Monkewitz, P. A., Nagib, H. M., Smits, A. J., and Sreenivasan, K. R., "Wall-Bounded Turbulent Flows at High Reynolds Numbers: Recent Advances and Key Issues," *Physics of Fluids*, Vol. 22, 2010, p. 065103. https://doi.org/10.1063/1.3453711.

[57] Prandtl, L., "Report on Investigation of Developed Turbulence," *Zeitschrift fuer Angewandte Matematik und Mechanik*, Vol. 5, No. NACA-TM-1231, 1949.

[58] Nickels, T., "Inner Scaling for Wall-Bounded Flows Subject to Large Pressure Gradients," *Journal of Fluid Mechanics*, Vol. 521, 2004, pp. 217–239. https://doi.org/10.1017/S0022112004001788.

[59] Meneveau, C., and Marusic, I., "Generalized Logarithmic Law for High-Order Moments in Turbulent Boundary Layers," *Journal of Fluid Mechanics*, Vol. 719, 2013, p. R1. https://doi.org/10.1017/jfm.2013.61.

[60] Townsend, A., *The Structure of Turbulent Shear Flow*, Cambridge University Press, 1976.

[61] Marušić, I., and Perry, A. E., "A Wall-Wake Model for the Turbulence Structure of Boundary Layers. Part 2. Further Experimental Support," *Journal of Fluid Mechanics*, Vol. 298, 1995, pp. 389–407. https://doi.org/10.1017/S0022112095003363.

[62] McKeon, B. J., and Sharma, A. S., "A Critical-Layer Framework for Turbulent Pipe Flow," *Journal of Fluid Mechanics*, Vol. 658, 2010, pp. 336–382. https://doi.org/10.1017/S002211201000176X.

[63] Baars, W. J., Talluru, K. M., Hutchins, N., and Marusic, I., "Wavelet Analysis of Wall Turbulence To Study Large-Scale Modulation of Small Scales," *Experiments in Fluids*, Vol. 56, No. 10, 2015. https://doi.org/10.1007/s00348-015-2058-8.

[64] Marusic, I., and Monty, J. P., "Attached Eddy Model of Wall Turbulence," *Annual Review of Fluid Mechanics*, Vol. 51, 2019, pp. 49–74. https://doi.org/10.1146/annurev-fluid-010518-040427.

[65] Monty, J. P., Hutchins, N., Ng, H. C. H., Marusic, I., and Chong, M. S., "A Comparison of Turbulent pipe, Channel and Boundary Layer flows," *Journal of Fluid Mechanics*, Vol. 632, 2009, pp. 431–442. https://doi.org/10.1017/S0022112009007423.

[66] Vinuesa, R., Örlü, R., Sanmiguel Vila, C., Ianiro, A., Discetti, S., and Schlatter, P., "Revisiting History Effects in Adverse-Pressure-Gradient Turbulent Boundary Layers," *Flow, turbulence and combustion*, Vol. 99, 2017, pp. 565–587. https://doi.org/10.1007/s10494-017-9845-7.

[67] Castillo, L., and George, W. K., "Similarity Analysis for Turbulent Boundary Layer with Pressure Gradient: Outer Flow," *AIAA journal*, Vol. 39, No. 1, 2001, pp. 41–47. https://doi.org/10.2514/2.1300.

[68] Maciel, Y., Wei, T., Gungor, A. G., and Simens, M. P., "Outer Scales and Parameters of Adverse-Pressure-Gradient Turbulent Boundary Layers," *Journal of Fluid Mechanics*, Vol. 844, 2018, pp. 5–35. https://doi.org/10.1017/jfm.2018.193.

[69] Theodorsen, T., "Mechanism of Turbulence," *Proceedings of the 2nd Midwestern Conference on Fluid Mechanics*, 1952, pp. 1–19.

[70] Zhou, J., Adrian, R. J., and Balachandar, S., "Autogeneration of Near-Wall Vortical Structures in Channel Flow," *Physics of Fluids*, Vol. 8, No. 1, 1996, pp. 288–290. https://doi.org/10.1063/1.868838.

[71] Del Alamo, J. C., Jiménez, J., Zandonade, P., and Moser, R. D., "Scaling of the Energy Spectra of Turbulent Channels," *Journal of Fluid Mechanics*, Vol. 500, 2004, pp. 135–144. https://doi.org/10.1017/S002211200300733X.

[72] Baltzer, J., Adrian, R., and Wu, X., "Structural Organization of Large and Very Large Scales in Turbulent Pipe Flow Simulation," *Journal of Fluid Mechanics*, Vol. 720, 2013, pp. 236–279. https://doi.org/10.1017/jfm.2012.642.

[73] Silva, L. J., and Wolf, W. R., "Embedded Shear Layers in Turbulent Boundary Layers of a NACA0012 Airfoil at High Angles of Attack," *International Journal of Heat and Fluid Flow*, 2024, p. 109353. https://doi.org/10.1016/j.ijheatfluidflow.2024.109353.

[74] Romero, S., Zimmerman, S., Philip, J., and Klewicki, J., "Velocity Spectra and Scale Decomposition of Adverse Pressure Gradient Turbulent Boundary Layers Considering History Effects," *International Journal of Heat and Fluid Flow*, Vol. 102, 2023, p. 109143. https://doi.org/10.1016/j.ijheatfluidflow.2023.109143.

[75] Hoyas, S., and Jiménez, J., "Scaling of the Velocity Fluctuations in Turbulent Channels up to $\mathrm{Re}_\tau = 2003$," *Physics of Fluids*, Vol. 18, No. 1, 2006. https://doi.org/10.1063/1.2162185.

[76] Mathis, R., Hutchins, N., and Marusic, I., "Large-Scale Amplitude Modulation of the Small-Scale Structures in Turbulent Boundary Layers," *Journal of Fluid Mechanics*, Vol. 628, 2009, pp. 311–337. https://doi.org/10.1017/S0022112009006946.

[77] Mckeon, B. J., Li, J.-d., Jiang, W., Morrison, J. F., and Smits, A. J., "Further Observations on the Mean Velocity Distribution in Fully Developed Pipe Flow," *Journal of Fluid Mechanics*, Vol. 501, 2004, pp. 135–147. https://doi.org/10.1017/S0022112003007304.

[78] Klewicki, J. C., "Reynolds Number Dependence, Scaling, and Dynamics of Turbulent Boundary Layers," *Journal of Fluids Engineering*, Vol. 132, No. 9, 2010, p. 094001. https://doi.org/10.1115/1.4002167.

[79] Hutchins, N., and Marusic, I., "Large-Scale Influences in Near-Wall Turbulence," *Philosophical Transactions of the Royal Society A: Mathematical, Physical and Engineering*

Sciences, Vol. 365, No. 1852, 2007, pp. 647–664. https://doi.org/10.1098/rsta.2006.1942.

[80] Millikan, C. B., "A Critical Discussion of Turbulent Flows in Channels and Circular Tubes," *Proc. Fifth Intern. Congr. Appl. Mech., Cambridge*, 1938, pp. 386–392.

[81] Coles, D., "The Law of the Wake in the Turbulent Boundary Layer," *Journal of Fluid Mechanics*, Vol. 1, No. 2, 1956, pp. 191–226. https://doi.org/10.1017/S0022112056000135.

[82] Chauhan, K. A., Monkewitz, P. A., and Nagib, H. M., "Criteria for Assessing Experiments in Zero Pressure Gradient Boundary Layers," *Fluid Dynamics Research*, Vol. 41, No. 2, 2009, p. 021404. https://doi.org/10.1088/0169-5983/41/2/021404.

[83] Zimmerman, S., "Experimental Investigation of Velocity and Vorticity in Turbulent Wall Flows," Ph.D. thesis, University of Melbourne, 2019.

[84] Schubauer, G. B., "Turbulent Processes as Observed in Boundary Layer and Pipe," *Journal of Applied Physics*, Vol. 25, No. 2, 1954, pp. 188–196. https://doi.org/10.1063/1.1721601.

[85] Krug, D., Philip, J., and Marusic, I., "Revisiting the Law of the Wake in Wall Turbulence," *Journal of Fluid Mechanics*, Vol. 811, 2017, pp. 421–435. https://doi.org/10.1017/jfm.2016.788.

[86] Kwon, Y., Philip, J., De Silva, C., Hutchins, N., and Monty, J., "The Quiescent Core of Turbulent Channel Flow," *Journal of Fluid Mechanics*, Vol. 751, 2014, pp. 228–254. https://doi.org/10.1017/jfm.2014.295.

[87] Clauser, F. H., "Turbulent Boundary Layers in Adverse Pressure Gradients," *Journal of the Aeronautical Sciences*, Vol. 21, No. 2, 1954, pp. 91–108.

[88] Dixit, S. A., and Ramesh, O., "Determination of Skin Friction in Strong Pressure-Gradient Equilibrium and Near-Equilibrium Turbulent Boundary Layers," *Experiments in Fluids*, Vol. 47, No. 6, 2009, pp. 1045–1058. https://doi.org/10.1007/s00348-009-0698-2.

[89] Knopp, T., Reuther, N., Novara, M., Schanz, D., Schülein, E., Schröder, A., and Kähler, C., "Experimental Analysis of the Log Law at Adverse Pressure Gradient," *Journal of Fluid Mechanics*, Vol. 918, 2021, p. A17. https://doi.org/10.1017/jfm.2021.331.

[90] Novara, M., Schanz, D., Reuther, N., Kähler, C. J., and Schröder, A., "Lagrangian 3D Particle Tracking in High-Speed Flows: Shake-the-Box for Multi-Pulse Systems," *Experiments in Fluids*, Vol. 57, 2016, pp. 1–20. https://doi.org/10.1007/s00348-016-2216-7.

[91] Kumar, P., and Mahesh, K., "A Method To Determine Wall Shear Stress From Mean Profiles in Turbulent Boundary Layers," *Experiments in Fluids*, Vol. 63, No. 1, 2022, p. 6. https://doi.org/10.1007/s00348-021-03352-y.

[92] Volino, R. J., and Schultz, M. P., "Determination of Wall Shear Stress From Mean Velocity and Reynolds Shear Stress Profiles," *Physical Review Fluids*, Vol. 3, No. 3, 2018, p. 034606. https://doi.org/10.1103/PhysRevFluids.3.034606.

[93] Kumar, P., and Mahesh, K., "Simple Model for Mean Stress in Turbulent Boundary Layers," *Physical Review Fluids*, Vol. 6, No. 2, 2021, p. 024603. https://doi.org/10.1103/PhysRevFluids.6.024603.

[94] Perry, A., "Turbulent Boundary Layers in Decreasing Adverse Pressure Gradients," *Journal of Fluid Mechanics*, Vol. 26, No. 3, 1966, pp. 481–506. https://doi.org/10.1017/S0022112066001344.

[95] Samuel, A., and Joubert, P., "A Boundary Layer Developing in an Increasingly Adverse

Pressure Gradient," *Journal of Fluid Mechanics*, Vol. 66, No. 3, 1974, pp. 481–505. https://doi.org/10.1017/S0022112074000322.

[96] Kline, S. J., Reynolds, W. C., Schraub, F. A., and Runstadler, P. W., "The Structure of Turbulent Boundary Layers," *Journal of Fluid Mechanics*, Vol. 30, No. 4, 1967, pp. 741–773. https://doi.org/10.1017/S0022112067001740.

[97] Hutchins, N., and Marusic, I., "Evidence of Very Long Meandering Features in the Logarithmic Region of Turbulent Boundary Layers," *Journal of Fluid Mechanics*, Vol. 579, 2007, pp. 1–28. https://doi.org/10.1017/S0022112006003946.

[98] Marusic, I., Monty, J. P., Hultmark, M., and Smits, A. J., "On the Logarithmic Region in Wall Turbulence," *Journal of Fluid Mechanics*, Vol. 716, 2013, p. R3. https://doi.org/10.1017/jfm.2012.511.

[99] Schatzman, D., and Thomas, F., "An Experimental Investigation of an Unsteady Adverse Pressure Gradient Turbulent Boundary Layer: Embedded Shear Layer Scaling," *Journal of Fluid Mechanics*, Vol. 815, 2017, pp. 592–642. https://doi.org/10.1017/jfm.2017.65.

[100] Sieber, M., Paschereit, C. O., and Oberleithner, K., "Spectral Proper Orthogonal Decomposition," *Journal of Fluid Mechanics*, Vol. 792, 2016, pp. 798–828. https://doi.org/10.1017/jfm.2016.103.

[101] Maciel, Y., Rossignol, K.-S., and Lemay, J., "Self-Similarity in the Outer Region of Adverse-Pressure-Gradient Turbulent Boundary Layers," *AIAA Journal*, Vol. 44, No. 11, 2006, pp. 2450–2464. https://doi.org/10.2514/1.19234.

[102] Adrian, R., Christensen, K., and Liu, Z.-C., "Analysis and Interpretation of Instantaneous Turbulent Velocity Fields," *Experiments in Fluids*, Vol. 29, No. 3, 2000, pp. 275–290. https://doi.org/10.1007/s003489900087.

[103] Richardson, L. F., *Weather Prediction by Numerical Process*, 1922.

[104] Perry, A., and Abell, C., "Asymptotic Similarity of Turbulence Structures in Smooth–and Rough-Walled Pipes," *Journal of Fluid Mechanics*, Vol. 79, No. 4, 1977, pp. 785–799. https://doi.org/10.1017/S0022112077000457.

[105] Perry, A., Henbest, S., and Chong, M., "A Theoretical and Experimental Study of Wall Turbulence," *Journal of Fluid Mechanics*, Vol. 165, 1986, pp. 163–199. https://doi.org/10.1017/S002211208600304X.

[106] Nickels, T., Marusic, I., Hafez, S., and Chong, M., "Evidence of the k_1^{-1} law in a high-Reynolds-number turbulent boundary layer," *Physical Review Letters*, Vol. 95, No. 7, 2005, p. 074501. https://doi.org/10.1103/PhysRevLett.95.074501.

[107] Nikora, V., "Origin of the "-1" Spectral Law in Wall-Bounded Turbulence," *Physical Review Letters*, Vol. 83, No. 4, 1999, p. 734. https://doi.org/10.1103/PhysRevLett.83.734.

[108] Perry, A., and Chong, M., "On the Mechanism of Wall Turbulence," *Journal of Fluid Mechanics*, Vol. 119, 1982, pp. 173–217. https://doi.org/10.1017/S0022112082001311.

[109] Patel, V. C., Nakayama, A., and Damian, R., "Measurements in the Thick Axisymmetric Turbulent Boundary Layer near the Tail of a Body of Revolution," *Journal of Fluid Mechanics*, Vol. 63, 1974, pp. 345–367. https://doi.org/10.1017/S0022112074001170.

[110] Kovasznay, L. S., Kibens, V., and Blackwelder, R. F., "Large-Scale Motion in the Intermittent Region of a Turbulent Boundary Layer," *Journal of Fluid Mechanics*, Vol. 41, No. 2, 1970, pp. 283–325. https://doi.org/10.1017/S0022112070000629.

[111] Nakagawa, H., and Nezu, I., "Structure of Space-Time Correlations of Bursting Phenomena in an Open-Channel Flow," *Journal of Fluid mechanics*, Vol. 104, 1981, pp. 1–43. https://doi.org/10.1017/S0022112081002796.

[112] Townsend, A., "The Turbulent Boundary Layer," *Grenzschichtforschung/Boundary Layer Research: Symposium Freiburg/Br. 26. Bis 29. August 1957/Symposium Freiburg/Br. August 26–29, 1957*, Springer, 1958, pp. 1–15.

[113] Grant, H., "The Large Eddies of Turbulent Motion," *Journal of Fluid Mechanics*, Vol. 4, No. 2, 1958, pp. 149–190. https://doi.org/10.1017/S0022112058000379.

[114] Taylor, G. I., "Correlation Measurements in a Turbulent Flow Through a Pipe," *Proceedings of the Royal Society of London. Series A-Mathematical and Physical Sciences*, Vol. 157, No. 892, 1936, pp. 537–546. https://doi.org/10.1098/rspa.1936.0214.

[115] Krogstad, P.-Å., and Skåre, P. E., "Influence Of a Strong Adverse Pressure Gradient on the Turbulent Structure in a Boundary Layer," *Physics of Fluids*, Vol. 7, No. 8, 1995, pp. 2014–2024. https://doi.org/10.1063/1.868513.

[116] Dróżdż, A., Niegodajew, P., Romańczyk, M., and Elsner, W., "Convection Velocity in Turbulent Boundary Layers Under Adverse Pressure Gradient," *Experimental Thermal and Fluid Science*, Vol. 145, 2023, p. 110900. https://doi.org/10.1016/j.expthermflusci.2023.110900.

[117] Tomkins, C., and Adrian, R., "Spanwise Structure and Scale Growth in Turbulent Boundary Layers," *Journal of Fluid Mechanics*, Vol. 490, 2003, pp. 37–74. https://doi.org/10.1017/S0022112003005251.

[118] De Silva, C. M., Gnanamanickam, E. P., Atkinson, C., Buchmann, N. A., Hutchins, N., Soria, J., and Marusic, I., "High Spatial Range Velocity Measurements in a High Reynolds Number Turbulent Boundary Layer," *Physics of Fluids*, Vol. 26, No. 2, 2014, p. 025117. https://doi.org/10.1063/1.4866458.

[119] Monty, J., Stewart, J., Williams, R., and Chong, M., "Large-Scale Features in Turbulent Pipe and Channel flows," *Journal of Fluid Mechanics*, Vol. 589, 2007, pp. 147–156. https://doi.org/10.1017/S002211200700777X.

[120] Hambleton, W., Hutchins, N., and Marusic, I., "Simultaneous Orthogonal-plane Particle Image Velocimetry Measurements in a Turbulent Boundary Layer," *Journal of Fluid Mechanics*, Vol. 560, 2006, pp. 53–64. https://doi.org/10.1017/S0022112006000292.

[121] Lee, J. H., and Sung, H. J., "Very-Large-Scale Motions in a Turbulent Boundary Layer," *Journal of Fluid Mechanics*, Vol. 673, 2011, pp. 80–120. https://doi.org/10.1017/S002211201000621X.

[122] Lee, J.-H., and Sung, H. J., "Structures in Turbulent Boundary Layers Subjected to Adverse Pressure Gradients," *Journal of Fluid Mechanics*, Vol. 639, 2009, pp. 101–131. https://doi.org/10.1017/S0022112009990814.

[123] Bradshaw, P., "The Turbulence Structure of Equilibrium Boundary Layers," *Journal of Fluid Mechanics*, Vol. 29, No. 4, 1967, pp. 625–645. https://doi.org/10.1017/S0022112067001089.

[124] Chesnakas, C. J., and Simpson, R. L., "Detailed investigation of the three-dimensional separation about a 6:1 prolate spheroid," *AIAA Journal*, Vol. 35, No. 6, 1997, pp. 990–999. https://doi.org/10.2514/2.208.

[125] Peters, N. J., Wissink, A., and Ekaterinaris, J., "On the Construction of a Mode Based Reduced Order Model for a Moving Store," *Aerospace Science and Technology*, Vol. 123, 2022, p. 107484. https://doi.org/10.1016/j.ast.2022.107484.

[126] Peters, N., Wissink, A., and Ekaterinaris, J., "Machine Learning-Based Surrogate Modeling Approaches for Fixed-Wing Store Separation," *Aerospace Science and Technology*, Vol. 133, 2023, p. 108150. https://doi.org/10.1016/j.ast.2023.108150.

[127] Luxton, R., Bull, M., and Rajagopalan, S., "The Thick Turbulent Boundary Layer on a Long Fine Cylinder in Axial Flow," *The Aeronautical Journal*, Vol. 88, No. 875, 1984, pp. 186–199. https://doi.org/10.1017/S0001924000020480.

[128] Wietrzak, A., and Lueptow, R. M., "Wall Shear Stress and Velocity in a Turbulent Axisymmetric Boundary Layer," *Journal of Fluid Mechanics*, Vol. 259, 1994, pp. 191–218. https://doi.org/10.1017/S0022112094000091.

[129] Piquet, J., and Patel, V., "Transverse Curvature Effects in Turbulent Boundary Layer," *Progress in Aerospace Sciences*, Vol. 35, No. 7, 1999, pp. 661–672. https://doi.org/10.1016/S0376-0421(99)00007-X.

[130] Willmarth, W. W., Winkel, R. E., Sharma, L., and Bogar, T., "Axially Symmetric Turbulent Boundary Layers on Cylinders: Mean Velocity Profiles and Wall Pressure Fluctuations," *Journal of Fluid Mechanics*, Vol. 76, No. 1, 1976, pp. 35–64. https://doi.org/10.1017/S002211207600311X.

[131] Afzal, N., and Narasimha, R., "Axisymmetric Turbulent Boundary Layer Along a Circular Cylinder at Constant Pressure," *Journal of Fluid Mechanics*, Vol. 74, No. 1, 1976, pp. 113–128. https://doi.org/10.1017/S002211207600171.

[132] Lueptow, R. M., Leehey, P., and Stellinger, T., "The Thick, Turbulent Boundary Layer on a Cylinder: Mean and Fluctuating Velocities," *The Physics of fluids*, Vol. 28, No. 12, 1985, pp. 3495–3505. https://doi.org/10.1063/1.865417.

[133] Lueptow, R. M., and Haritonidis, J. H., "The Structure of the Turbulent Boundary Layer on a Cylinder in Axial Flow," *The Physics of fluids*, Vol. 30, No. 10, 1987, pp. 2993–3005. https://doi.org/10.1063/1.866078.

[134] de Silva, C. M., Kevin, K., Baidya, R., Hutchins, N., and Marusic, I., "Large Coherence of Spanwise Velocity in Turbulent Boundary Layers," *Journal of Fluid Mechanics*, Vol. 847, 2018, pp. 161–185. https://doi.org/10.1017/jfm.2018.320.

[135] Kevin, K., Monty, J., and Hutchins, N., "The Meandering Behaviour of Large-Scale Structures in Turbulent Boundary Layers," *Journal of Fluid Mechanics*, Vol. 865, 2019, p. R1. https://doi.org/10.1017/jfm.2019.131.

[136] Willmarth, W., and Yang, C., "Wall-Pressure Fluctuations Beneath Turbulent Boundary Layers on a Flat Plate and a Cylinder," *Journal of Fluid Mechanics*, Vol. 41, No. 1, 1970, pp. 47–80. https://doi.org/10.1017/S0022112070000526.

[137] Snarski, S. R., "Relation Between the Flucutating Wall Pressure and the Turbulent Structure of a Boundary Layer on a Cylinder in Axial Flow," Ph.D. thesis, Northwestern University, Dec 1992.

[138] Huang, T. T., Groves, N. C., and Belt, G., "Boundary-Layer Flow on an Axisymmetric Body with Inflected Stern," DTNSRDC-80/064, Naval Surface Warfare Center Carderock Division, Bethesda, MD, Aug. 1980.

[139] Groves, N. C., Huang, T. T., Chang, M. S., et al., "Geometric characteristics of DARPA (Defense Advanced Research Projects Agency) SUBOFF models (DTRC model numbers 5470 and 5471)," *David Taylor Research Center Bethesda MD Ship Hydromechanics Dept*, 1989.

[140] Jiménez, J. M., Reynolds, R., and Smits, A. J., "The Effects of Fins on the Intermediate Wake of a Submarine Model," *Journal of Fluids Engineering*, Vol. 132, No. 3, 2010. https://doi.org/10.1115/1.4001010.

[141] Banks, J. T., Huang, S.-F., Palanganda, S. T., Chen, D., Alexander, W. N., and Devenport, W. J., "Ingestion of Transient Disturbances into an Open Rotor Immersed in a Boundary Layer," *AIAA AVIATION 2023 Forum*, 2023. https://doi.org/10.2514/6.2023-3653.

[142] Hickling, C., Balantrapu, N. A., Millican, A., Alexander, W. N., Devenport, W. J., and Glegg, S. A., "Turbulence Ingestion into a Rotor at the Rear of an Axisymmetric Body," *25th AIAA/CEAS Aeroacoustics Conference*, 2019. https://doi.org/10.2514/6.2019-2571.

[143] Hickling, C., Alexander, W. N., Molinaro, N. J., Devenport, W. J., and Glegg, S. A., "Efficient Beamforming Techniques for Investigating Turbulence Ingestion Noise with an Inhomogeneous Inflow," American Institute of Aeronautics and Astronautics, 2017. https://doi.org/10.2514/6.2017-4179.

[144] Joubert, P., "Some Aspects of Submarine Design. Part 1. Hydrodynamics," *Australian Department of Defence*, 2004.

[145] Joubert, P., "Some Aspects of Submarine Design. Part 2. Shape of a Submarine," Tech. rep., 2006.

[146] Manovski, P., Jones, M. B., Henbest, S. M., Xue, Y., Giacobello, M., and de Silva, C., "Boundary Layer Measurements over a Body of Revolution using Long-Distance Particle Image Velocimetry," *International Journal of Heat and Fluid Flow*, Vol. 83, 2020, p. 108591. https://doi.org/10.1016/j.ijheatfluidflow.2020.108591.

[147] Novara, M., Schanz, D., Geisler, R., Gesemann, S., Voss, C., and Schröder, A., "Multi-Exposed Recordings for 3D Lagrangian Particle Tracking with Multi-Pulse Shake-The-Box," *Experiments in Fluids*, Vol. 60, 2019, pp. 1–19. https://doi.org/10.1007/s00348-019-2692-7.

[148] Manovski, P., Loveday, D., Ng, H., Giacobello, M., de Silva, C., Hutchins, N., and Marusic, I., "Turbulent Boundary Layer Measurements in the Presence of Pressure Gradients and Curvature," 15th International Symposium on Particle Image Velocimetry, San Diego, CA, 2023.

[149] Huang, T. T., and Liu, H. L., "Measurements of Flows Over an Axisymmetric Body with Various Appendages in a Wind Tunnel: the DARPA SUBOFF Experimental Program," *19th Symposium on Naval Hydrodynamics*, 1994, pp. 321–346.

[150] Smits, A. J., McKeon, B. J., and Marusic, I., "High-Reynolds Number Wall Tur-

bulence," *Annual Review of Fluid Mechanics*, Vol. 43, 2011, pp. 353 – 75. https://doi.org/10.1146/annurev-fluid-122109-160753.

[151] Morse, N., and Mahesh, K., "Large-Eddy Simulation and Streamline Coordinate Analysis of Flow over an Axisymmetric Hull," *Journal of Fluid Mechanics*, Vol. 926, 2021. https://doi.org/10.1017/jfm.2021.714.

[152] Posa, A., and Balaras, E., "A Numerical Investigation of the Wake of an Axisymmetric Body with Appendages," *Journal of Fluid Mechanics*, Vol. 792, 2016, pp. 470–498. https://doi.org/10.1017/jfm.2016.47.

[153] Posa, A., and Balaras, E., "A Numerical Investigation about the Effects of Reynolds Number on the Flow Around an Appended Axisymmetric Body of Revolution," *Journal of Fluid Mechanics*, Vol. 884, 2020, p. A41. https://doi.org/10.1017/jfm.2019.961.

[154] Bisset, D. K., Hunt, J. C., and Rogers, M. M., "The turbulent/non-turbulent interface bounding a far wake," *Journal of Fluid Mechanics*, Vol. 451, 2002, pp. 383–410. https://doi.org/10.1017/S0022112001006759.

[155] Townsend, A., "Local Isotropy in the Turbulent Wake of a Cylinder," *Australian Journal of Chemistry*, Vol. 1, No. 2, 1948, pp. 161–174.

[156] Taveira, R. R., and da Silva, C. B., "Kinetic Energy Budgets Near the Turbulent/Nonturbulent Interface in Jets," *Physics of Fluids*, Vol. 25, No. 1, 2013. https://doi.org/10.1063/1.4776780.

[157] Holzner, M., and Lüthi, B., "Laminar Superlayer at the Turbulence Boundary," *Physical Review Letters*, Vol. 106, No. 13, 2011, p. 134503. https://doi.org/10.1103/PhysRevLett.106.134503.

[158] Holzner, M., Liberzon, A., Nikitin, N., Kinzelbach, W., and Tsinober, A., "Small-Scale

Aspects of Flows in Proximity of the Turbulent/Nonturbulent Interface," *Physics of Fluids*, Vol. 19, No. 7, 2007. https://doi.org/10.1063/1.2746037.

[159] Holzner, M., Liberzon, A., Nikitin, N., Lüthi, B., Kinzelbach, W., and Tsinober, A., "A Lagrangian Investigation of the Small-Scale Features of Turbulent Entrainment Through Particle Tracking and Direct Numerical Simulation," *Journal of Fluid Mechanics*, Vol. 598, 2008, pp. 465–475. https://doi.org/10.1017/S0022112008000141.

[160] Westerweel, J., Fukushima, C., Pedersen, J. M., and Hunt, J. C., "Momentum and Scalar Transport at the Turbulent/Non-Turbulent Interface of a Jet," *Journal of Fluid Mechanics*, Vol. 631, 2009, pp. 199–230. https://doi.org/10.1017/S0022112009006600.

[161] Mathew, J., and Basu, A. J., "Some Characteristics of Entrainment at a Cylindrical Turbulence Boundary," *Physics of Fluids*, Vol. 14, No. 7, 2002, pp. 2065–2072. https://doi.org/10.1063/1.1480831.

[162] Philip, J., Meneveau, C., de Silva, C. M., and Marusic, I., "Multiscale Analysis of Fluxes at the Turbulent/Non-Turbulent Interface in High Reynolds Number Boundary Layers," *Physics of Fluids*, Vol. 26, No. 1, 2014. https://doi.org/10.1063/1.4861066.

[163] da Silva, C. B., and Taveira, R. R., "The thickness of the turbulent/nonturbulent interface is equal to the radius of the large vorticity structures near the edge of the shear layer," *Physics of Fluids*, Vol. 22, No. 12, 2010. https://doi.org/10.1063/1.3527548.

[164] Borrell, G., and Jiménez, J., "Properties of the Turbulent/Non-Turbulent Interface in Boundary Layers," *Journal of Fluid Mechanics*, Vol. 801, 2016, pp. 554–596. https://doi.org/10.1017/jfm.2016.430.

[165] Brown, G. L., and Roshko, A., "On Density Effects and Large Structure in Turbulent Mixing Layers," *Journal of Fluid Mechanics*, Vol. 64, No. 4, 1974, pp. 775–816. https://doi.org/10.1017/S002211207400190X.

[166] Sreenivasan, K., Prasad, R., Meneveau, C., and Ramshankar, R., "The Fractal Geometry of Interfaces and the Multifractal Distribution of Dissipation in Fully Turbulent Flows," *Fractals in Geophysics*, 1989, pp. 43–60.

[167] Sreenivasan, K., Ramshankar, R., and Meneveau, C., "Mixing, Entrainment and Fractal Dimensions of Surfaces in Turbulent Flows," *Proceedings of the Royal Society of London. A. Mathematical and Physical Sciences*, Vol. 421, No. 1860, 1989, pp. 79–108. https://doi.org/10.1098/rspa.1989.0004.

[168] de Silva, C. M., Philip, J., Chauhan, K., Meneveau, C., and Marusic, I., "Multiscale Geometry and Scaling of the Turbulent-Nonturbulent Interface in High Reynolds Number Boundary Layers," *Physical Review Letters*, Vol. 111, No. 4, 2013, p. 044501. https://doi.org/10.1103/PhysRevLett.111.044501.

[169] Kovasznay, L. S., "Structure of the Turbulent Boundary Layer," *The Physics of Fluids*, Vol. 10, No. 9, 1967, pp. S25–S30. https://doi.org/10.1063/1.1762462.

[170] Da Silva, C. B., Taveira, R. R., and Borrell, G., "Characteristics of the Turbulent/Nonturbulent Interface in Boundary Layers, Jets and Shear-Free Turbulence," *Journal of Physics: Conference Series*, Vol. 506, IOP Publishing, 2014, p. 012015. https://doi.org/10.1088/1742-6596/506/1/012015.

[171] Westerweel, J., Fukushima, C., Pedersen, J., and Hunt, J. C., "Mechanics of the Turbulent-Nonturbulent Interface of a Jet," *Physical Review Letters*, Vol. 95, No. 17, 2005, p. 174501. https://doi.org/10.1103/PhysRevLett.95.174501.

[172] Kwon, Y., Hutchins, N., and Monty, J., "On the Use of the Reynolds Decomposition in the Intermittent Region of Turbulent Boundary Layers," *Journal of Fluid Mechanics*, Vol. 794, 2016, pp. 5–16. https://doi.org/10.1017/jfm.2016.161.

[173] Yang, J., Yoon, M., and Sung, H. J., "The Turbulent/Non-Turbulent Interface in an Adverse Pressure Gradient Turbulent Boundary Layer," *International Journal of Heat*

and Fluid Flow, Vol. 86, 2020, p. 108704. https://doi.org/10.1016/j.ijheatfluidflow.2020.108704.

[174] Seth, D., "Contributions to the Understanding of Ship Airwake Using Advanced Flow Diagnostic Techniques," Ph.D. thesis, Embry-Riddle Aeronautical University, 2020.

[175] Erm, L., Jones, M., and Henbest, S., "Boundary Layer Trip Size Selection on Streamlined Bodies of Revolution," *18th Australian Fluids Mechanics Conference*, 2012.

[176] Schlatter, P., and Örlü, R., "Turbulent Boundary Layers at Moderate Reynolds Numbers: Inflow Length and Tripping Effects," *Journal of Fluid Mechanics*, Vol. 710, 2012, pp. 5–34. https://doi.org/0.1017/jfm.2012.324.

[177] Marusic, I., Chauhan, K., Kulandaivelu, V., and Hutchins, N., "Evolution of Zero-Pressure-Gradient Boundary Layers From Different Tripping Conditions," *Journal of Fluid Mechanics*, Vol. 783, 2015, pp. 379–411. https://doi.org/10.1017/jfm.2015.556.

[178] Schetz, J. A., and Bowersox, R. D. W., *Boundary Layer Analysis*, 2nd ed., AIAA, 2011.

[179] Leishman, J. G., *Introduction to Aerospace Flight Vehicles*, Embry-Riddle Aeronautical University, 2023. https://doi.org/10.15394/eaglepub.2022.1066.9.

[180] Hearst, R. J., and Ganapathisubramani, B., "Quantification and Adjustment of Pixel-Locking in Particle Image Velocimetry," *Experiments in Fluids*, Vol. 56, 2015, pp. 1–5. https://doi.org/10.1007/s00348-015-2062-z.

[181] Westerweel, J., and Scarano, F., "Universal Outlier Detection for PIV Data," *Experiments in Fluids*, Vol. 39, 2005, pp. 1096–1100. https://doi.org/10.1007/s00348-005-0016-6.

[182] Wieneke, B., and Pfeiffer, K., "Adaptive PIV with Variable Interrogation Window Size and Shape," 2010. URL https://api.semanticscholar.org/CorpusID:174777310.

[183] Ligrani, P., and Bradshaw, P., "Spatial Resolution and Measurement of Turbulence in the Viscous Sublayer Using Subminiature Hot-Wire Probes," *Experiments in Fluids*, Vol. 5, No. 6, 1987, pp. 407–417. https://doi.org/10.1007/BF00264405.

[184] Hutchins, N., Nickels, T. B., Marusic, I., and Chong, M. S., "Hot-Wire Spatial Resolution Issues in Wall-Bounded Turbulence," *Journal of Fluid Mechanics*, Vol. 635, 2009, pp. 103 – 136. https://doi.org/10.1017/S0022112009007721.

[185] Dróżdż, A., Örlü, R., Sokolenko, V., Schlatter, P., Elsner, W., and Niegodajew, P., "Hot-Wire Spatial Resolution Issues in Adverse Pressure Gradient Turbulent Boundary Layers," *Measurement*, 2024, p. 115229. https://doi.org/10.1016/j.measurement.2024.115229.

[186] Zhu, N., Mazzilli, G., Palm, K., Zhang, Z., Gnanamanickam, E. P., and Leishman, J. G., "Dual-Plane PIV for Three-Dimensional, Low-Order Turbulence Reconstruction," *15th International Symposium on Particle Image Velocimetry*, 2023.

[187] Ramasamy, M., Johnson, B., and Leishman, J. G., "Turbulent Tip Vortex Measurements Using Dual-Plane Stereoscopic Particle Image Velocimetry," *AIAA journal*, Vol. 47, No. 8, 2009, pp. 1826–1840. https://doi.org/10.2514/1.39202.

[188] Hu, H., Saga, T., Kobayashi, T., Taniguchi, N., and Yasuki, M., "Dual-Plane Stereoscopic Particle Image Velocimetry: System Set-up and its Application on a Lobed Jet Mixing Flow," *Experiments in Fluids*, Vol. 31, No. 3, 2001, pp. 277–293. https://doi.org/10.1007/s003480100283.

[189] Ganapathisubramani, B., Longmire, E. K., Marusic, I., and Pothos, S., "Dual-Plane PIV Technique to Determine the Complete Velocity Gradient Tensor in a Turbulent Boundary Layer," *Experiments in Fluids*, Vol. 39, No. 2, 2005, pp. 222–231. https://doi.org/10.1007/s00348-005-1019-z.

[190] Kim, K. C., Yoon, S. Y., Kim, S. M., Chun, H. H., and Lee, I., "An Orthogonal-Plane PIV Technique for the Investigations of Three-Dimensional Vortical Structures in a Turbulent Boundary Layer Flow," *Experiments in Fluids*, Vol. 40, No. 6, 2006, pp. 876–883. https://doi.org/10.1007/s00348-006-0125-x.

[191] Regunath, G. S., Zimmerman, W. B., Tesař, V., and Hewakandamby, B. N., "Experimental Investigation of Helicity in Turbulent Swirling Jet Using Dual-Plane Dye Laser PIV Technique," *Experiments in Fluids*, Vol. 45, No. 6, 2008, pp. 973–986. https://doi.org/10.1007/s00348-008-0515-3.

[192] Tanahashi, M., Hirayama, T., Taka, S., and Miyauchi, T., "Measurement of Fine Scale Structure in Turbulence by Time-Resolved Dual-Plane Stereoscopic PIV," *International Journal of Heat and Fluid Flow*, Vol. 29, No. 3, 2008, pp. 792–802. https://doi.org/10.1016/j.ijheatfluidflow.2008.02.009.

[193] Mullin, J., and Dahm, W., "Highly-Resolved Three-Dimensional Velocity Measurements via Dual-Plane Stereo Particle Image Velocimetry (DSPIV) in Turbulent Flows," *40th AIAA Aerospace Sciences Meeting & Exhibit*, 2002. https://doi.org/10.2514/6.2002-290.

[194] Zhu, N., Zhang, Z., Gnanamanickam, E. P., and Leishman, J. G., "Estimation of 3D Ship Airwakes Using Dual-Plane PIV," *Experiments in Fluids*, Vol. 65, No. 1, 2024, p. 11. https://doi.org/10.1007/s00348-023-03727-3.

[195] Kähler, C. J., Scholz, U., and Ortmanns, J., "Wall-Shear-Stress and Near-Wall Turbulence Measurements up to Single Pixel Resolution by Means of Long-Distance Micro-PIV," *Experiments in Fluids*, Vol. 41, 2006, pp. 327–341. https://doi.org/10.1007/s00348-006-0167-0.

[196] Lagarias, J. C., Reeds, J. A., Wright, M. H., and Wright, P. E., "Convergence Properties

of the Nelder–Mead Simplex Method in Low Dimensions," *SIAM Journal on Optimization*, Vol. 9, No. 1, 1998, pp. 112–147. https://doi.org/10.1137/S1052623496303470.

[197] Thompson, B., "A New Two-Parameter Family of Mean Velocity Profiles for Incompressible Turbulent Boundary Layers on Smooth Walls," 1965.

[198] Meroney, R., and Bradshaw, P., "Turbulent Boundary-Layer Growth Over a Longitudinally Curved Surface," *AIAA Journal*, Vol. 13, No. 11, 1975, pp. 1448–1453. https://doi.org/10.2514/3.7014.

[199] Bradshaw, P., "The Analogy Between Streamline Curvature and Buoyancy in Turbulent Shear Flow," *Journal of Fluid Mechanics*, Vol. 36, No. 1, 1969, pp. 177–191. https://doi.org/10.1017/S0022112069001583.

[200] Patel, V., and Sotiropoulos, F., "Longitudinal Curvature Effects in Turbulent Boundary Layers," *Progress in Aerospace Sciences*, Vol. 33, No. 1-2, 1997, pp. 1–70. https://doi.org/10.1016/S0376-0421(96)00001-2.

[201] Adrian, R., and Westerweel, J., *Particle Image Velocimetry*, Cambridge University Press, 2011.

[202] Olsen, M. G., and Adrian, R. J., "Brownian Motion and Correlation in Particle Image Velocimetry," *Optics & Laser Technology*, Vol. 32, No. 7-8, 2000, pp. 621–627. https://doi.org/10.1016/S0030-3992(00)00119-5.

[203] Wieneke, B., "PIV Uncertainty Quantification from Correlation Statistics," *Measurement Science and Technology*, Vol. 26, No. 7, 2015, p. 074002. https://doi.org/10.1088/0957-0233/26/7/074002.

[204] Bardet, P. M., André, and Neal, D., "Systematic Timing Errors in Laser-Based Transit-Time Velocimetry," *10th Int Symp on Particle Image Velocimetry*, 2013.

[205] Christensen, K., "The Influence of Peak-Locking Errors on Turbulence Statistics Computed From PIV Ensembles," *Experiments in Fluids*, Vol. 36, 2004, pp. 484–497. https://doi.org/10.1007/s00348-003-0754-2.

[206] Michaelis, D., Neal, D. R., and Wieneke, B., "Peak-Locking Reduction for Particle Image Velocimetry," *Measurement Science and Technology*, Vol. 27, No. 10, 2016, p. 104005. https://doi.org/10.1088/0957-0233/27/10/104005.

[207] Sciacchitano, A., and Wieneke, B., "PIV Uncertainty Propagation," *Measurement Science and Technology*, Vol. 27, No. 8, 2016, p. 084006. https://doi.org/10.1088/0957-0233/27/8/084006.

[208] Bradshaw, P., "The Response of a Constant-Pressure Turbulent Boundary Layer to the Sudden Application of an Adverse Pressure Gradient," Tech. rep., 1967.

[209] Parthasarathy, A., and Saxton-Fox, T., "A Family of Adverse Pressure Gradient Turbulent Boundary Layers With Upstream Favourable Pressure Gradients," *Journal of Fluid Mechanics*, Vol. 966, 2023, p. A11. https://doi.org/10.1017/jfm.2023.429.

[210] Spalart, P. R., and Watmuff, J. H., "Experimental and Numerical Study of a Turbulent Boundary Layer With Pressure Gradients," *Journal of Fluid Mechanics*, Vol. 249, 1993, pp. 337–371. https://doi.org/10.1017/S002211209300120X.

[211] Alfredsson, P. H., and Örlü, R., "The Diagnostic Plot—A Litmus Test for Wall Bounded Turbulence Data," *European Journal of Mechanics-B/Fluids*, Vol. 29, No. 6, 2010, pp. 403–406. https://doi.org/10.1016/j.euromechflu.2010.07.006.

[212] Schlichting, H., *Boundary-layer theory*, McGraw-Hill, 1968.

[213] Muck, K., Hoffmann, P., and Bradshaw, P., "The Effect of Convex Surface Curvature on Turbulent Boundary Layers," *Journal of Fluid Mechanics*, Vol. 161, 1985, pp. 347–369. https://doi.org/10.1017/S002211208500297X.

[214] Schlatter, P., and Örlü, R., "Assessment of Direct Numerical Simulation Data of Turbulent Boundary Layers," *Journal of Fluid Mechanics*, Vol. 659, 2010, pp. 116–126. https://doi.org/10.1017/S0022112010003113.

[215] Han, M., Ma, M., and Yan, C., "Consistent Outer Scaling and Analysis of Adverse Pressure Gradient Turbulent Boundary Layers," *Journal of Fluid Mechanics*, Vol. 982, 2024, p. A17. https://doi.org/10.1017/jfm.2024.97.

[216] Zagarola, M. V., and Smits, A. J., "Mean-Flow Scaling of Turbulent Pipe Flow," *Journal of Fluid Mechanics*, Vol. 373, 1998, pp. 33–79. https://doi.org/10.1017/S0022112098002419.

[217] Wu, Y., and Christensen, K. T., "Spatial Structure of a Turbulent Boundary Layer With Irregular Surface Roughness," *Journal of Fluid Mechanics*, Vol. 655, 2010, pp. 380–418. https://doi.org/10.1017/S0022112010000960.

[218] Kulandaivelu, V., "Evolution and Structure of Zero Pressure Gradient Turbulent Boundary Layer," Ph.D. thesis, University of Melbourne, 2011.

[219] Hutchins, N., and Marusic, I., "Evidence of Very Long Meandering Features in the Logarithmic Region of Turbulent Boundary Layers," *Journal of Fluid Mechanics*, Vol. 579, 2007, pp. 1 – 28. https://doi.org/10.1017/S0022112006003946.

[220] Balantrapu, N. A., Hickling, C., Millican, A. J., Vishwanathan, V., Garguilo, A., Alexander, W. N., Lowe, K. T., Devenport, W. J., and Glegg, S., "Turbulent Boundary Layer in a Strong Adverse Pressure Gradient over a Body of Revolution," *11th International Symposium on Turbulence and Shear Flow Phenomena*, Southampton, UK, 2019.

[221] Taira, K., Brunton, S. L., Dawson, S. T. M., Rowley, C. W., Colonius, T., McKeon, B. J., Schmidt, O. T., Gordeyev, S., Theofilis, V., and Ukeiley, L. S., "Modal Analysis

of Fluid Flows: An Overview," *AIAA Journal*, Vol. 55, No. 12, 2017. https://doi.org/10.2514/1.J056060.

[222] Philip, J., and Marusic, I., "Large-Scale Eddies and Their Role in Entrainment in Turbulent Jets and Wakes," *Physics of Fluids*, Vol. 24, No. 5, 2012. https://doi.org/10.1063/1.4719156.

[223] Semin, N., Golub, V., Elsinga, G., and Westerweel, J., "Laminar Superlayer in a Turbulent Boundary Layer," *Technical Physics Letters*, Vol. 37, 2011, pp. 1154–1157. https://doi.org/10.1134/S1063785011120285.

[224] Phillips, O. M., "The Entrainment Interface," *Journal of Fluid Mechanics*, Vol. 51, No. 1, 1972, pp. 97–118. https://doi.org/10.1017/S0022112072001090.

[225] Paterna, E., Moonen, P., Dorer, V., and Carmeliet, J., "Mitigation of Surface Reflection in PIV Measurements," *Measurement Science and Technology*, Vol. 24, No. 5, 2013, p. 057003. https://doi.org/10.1088/0957-0233/24/5/057003.

[226] Sydney, A. J., "Contributions Towards the Understanding of Rotor-Induced Dust Particle Mobilization and Transport," Ph.D. thesis, University of Maryland, College Park, 2014.

[227] Lumley, J. L., "The Structure of Inhomogeneous Turbulent Flows," *Atmospheric Turbulence and Radio Wave Propagation*, 1967, pp. 221–227.

[228] Baars, W. J., and Tinney, C. E., "Proper Orthogonal Decomposition-Based Spectral Higher-Order Stochastic Estimation," *Physics of Fluids*, Vol. 26, No. 5, 2014, p. 055112. https://doi.org/10.1063/1.4879255.

[229] Ukeiley, L., and Murray, N., "Velocity and surface Pressure Measurements in an Open Cavity," *Experiments in Fluids*, Vol. 38, No. 5, 2005, pp. 656–671. https://doi.org/10.1007/s00348-005-0948-x.

[230] Berkooz, G., Holmes, P., and Lumley, J. L., "The Proper Orthogonal Decomposition in the Analysis of Turbulent Flows," *Annual Review of Fluid Mechanics*, Vol. 25, No. 1, 1993, pp. 539–575. https://doi.org/10.1146/annurev.fl.25.010193.002543.

[231] Weiss, J., "A Tutorial on the Proper Orthogonal Decomposition," *AIAA Aviation Forum*, 2019, p. 3333. https://doi.org/10.2514/6.2019-3333.

[232] Sirovich, L., "Turbulence and the Dynamics of Coherent Structures. I–Coherent Structures," *Quarterly of Applied Mathematics*, Vol. 45, No. 3, 1987, pp. 561–571. https://doi.org/10.1090/qam/910463.

PUBLICATIONS

Journal

1. **Zhu, N.**, Zhang, Z., Gnanamanickam, E. P., and Leishman, J. G., "Space-Time Characterization of Ship Airwakes," *AIAA Journal*, Vol. 61, No. 2, 2023, pp. 681–697.

2. **Zhu, N.**, Zhang, Z., Gnanamanickam, E. P., and Leishman, J. G., "Estimation of 3D Ship Airwakes Using Dual-Plane PIV," *Experiments in Fluids*, Vol. 65, No. 1, 2024, p. 11.

Conference

1. **Zhu, N.**, Zhang, Z., Gnanamanickam, E., and Leishman, J. G., "Dynamics of Large-Scale Flow Structures Within Ship Airwakes," AIAA SciTech Forum, 2022.

2. **Zhu, N.**, Zhang, Z., Gnanamanickam, E., and Leishman, J. G., "Flow Field Estimation based on Dual-Plane PIV Measurements," 1st Florida Fluids Symposium, 2022.

3. **Zhu, N.**, Zhang, Z., Gnanamanickam, E. P., and Leishman, J. G., "Effects of a Simulated Atmospheric Boundary Layer on Ship Airwakes," AIAA SciTech Forum, 2023.

4. Mazzilli, G. A., **Zhu, N.**, Gnanamanickam, E. P., Leishman, J. G., and Zhang, Z., "A Study of Extreme Vertical Flow Fluctuations of the Ship Airwake," AIAA SciTech Forum, 2023.

5. Mazzilli, G., **Zhu, N.**, Zhang, Z., Gnanamanickam, E. P., and Leishman, J. G., "Experimental Investigation of the Recirculation Region Within Ship Airwakes," 2nd Florida Fluids Symposium, 2023.

6. **Zhu, N.**, Mazzilli, G., Palm, K., Zhang, Z., Gnanamanickam, E. P., and Leishman, J. G., "Dual-Plane PIV for Three-Dimensional, Low-Order Turbulence Reconstruction," 15th International Symposium on Particle Image Velocimetry, 2023.

7. **Zhu, N.**, Zhang, Z., Minniti, R., Gnanamanickam, E., and Leishman, J., "Structure of an Axisymmetric Turbulent Boundary Layer with Pressure Gradients," Bulletin of the American Physical Society, 2023.

8. Mazzilli, G. A., **Zhu, N.**, Zhang, Z., Gnanamanickam, E. P., and Leishman, J. G., "Investigation of the Ship Airwake Bistable Recirculation Region," AIAA SciTech Forum, 2024.

9. Palm, K. H., **Zhu, N.**, Zhang, Z., Gnanamanickam, E. P., and Leishman, J. G., "Behavior of Ship Airwakes Under Quartering Wind Conditions," AIAA SciTech Forum, 2024.

A Spanwise Plane Accuracy and Axisymmetry

The axisymmetry of the boundary layer was assessed through spanwise planes measured using stereoscopic PIV. The velocity vectors computed from DaVis 10.2 were in a Cartesian grid x_T, y_T, and z_T aligned with the test section. This coordinate system was transformed into a cylindrical frame with velocities $\tilde{u}_x$, $\tilde{u}_r$, and $\tilde{u}_\theta$. Then, radial profiles of the mean velocities and the fluctuation intensities were compared at different azimuthal stations. Although the limited PIV FOVs could not verify the axisymmetry around the entire circumference, this appendix verifies the axisymmetry in the analysis domain relevant to this writing. Further, the spanwise plane measurements are shown to agree with the streamwise plane.

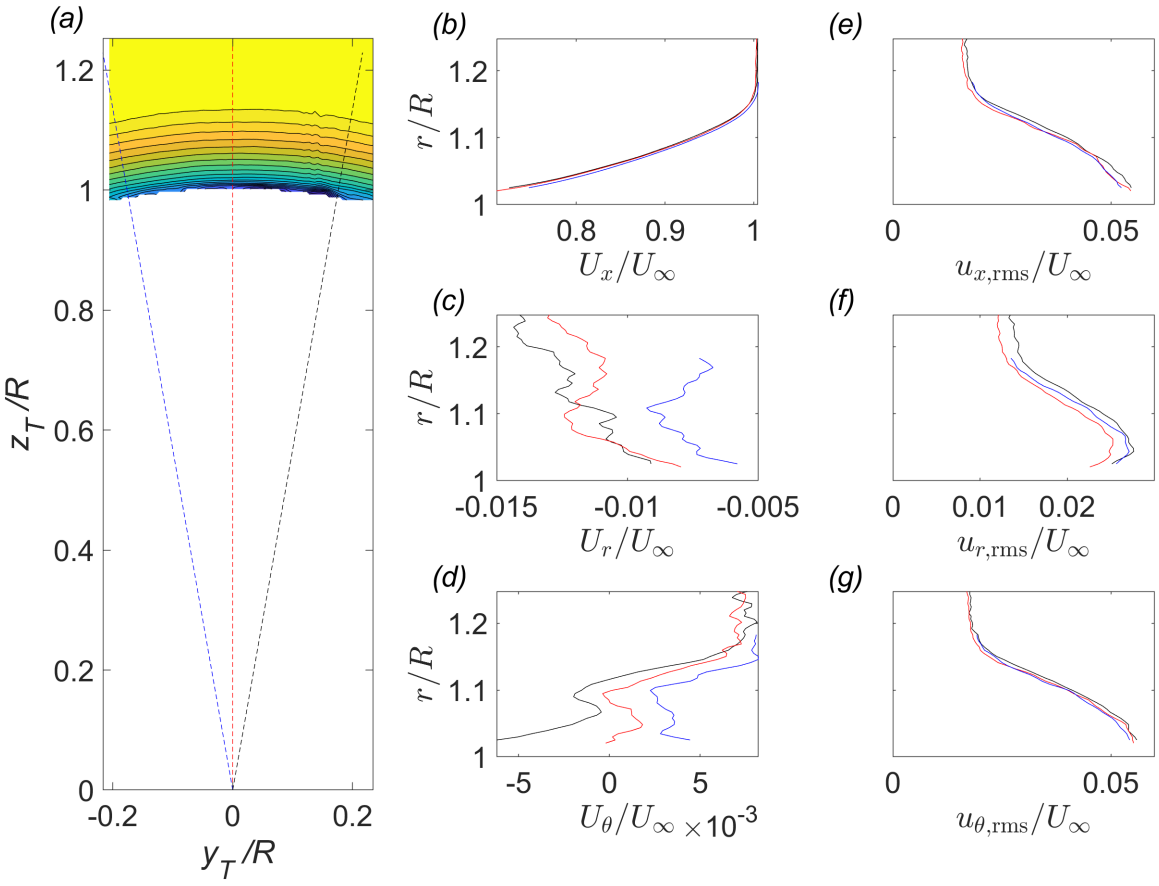

Figure A.1 Spanwise Plane 1 axisymmetry assessment. *(a)* Comparisons were made along radial lines emanating from the longitudinal x axis. The remaining figures show *(b)* mean axial velocity U_x, *(c)* mean radial velocity U_r, *(d)* mean azimuthal velocity U_θ, *(e)* axial velocity rms, $u_{x,\mathrm{rms}}$, *(f)* radial velocity rms, $u_{r,\mathrm{rms}}$, and *(g)* azimuthal velocity rms, $u_{\theta,\mathrm{rms}}$.

The axisymmetry of spanwise Plane 1 (SP1) was assessed as shown in Fig. A.1. Velocity

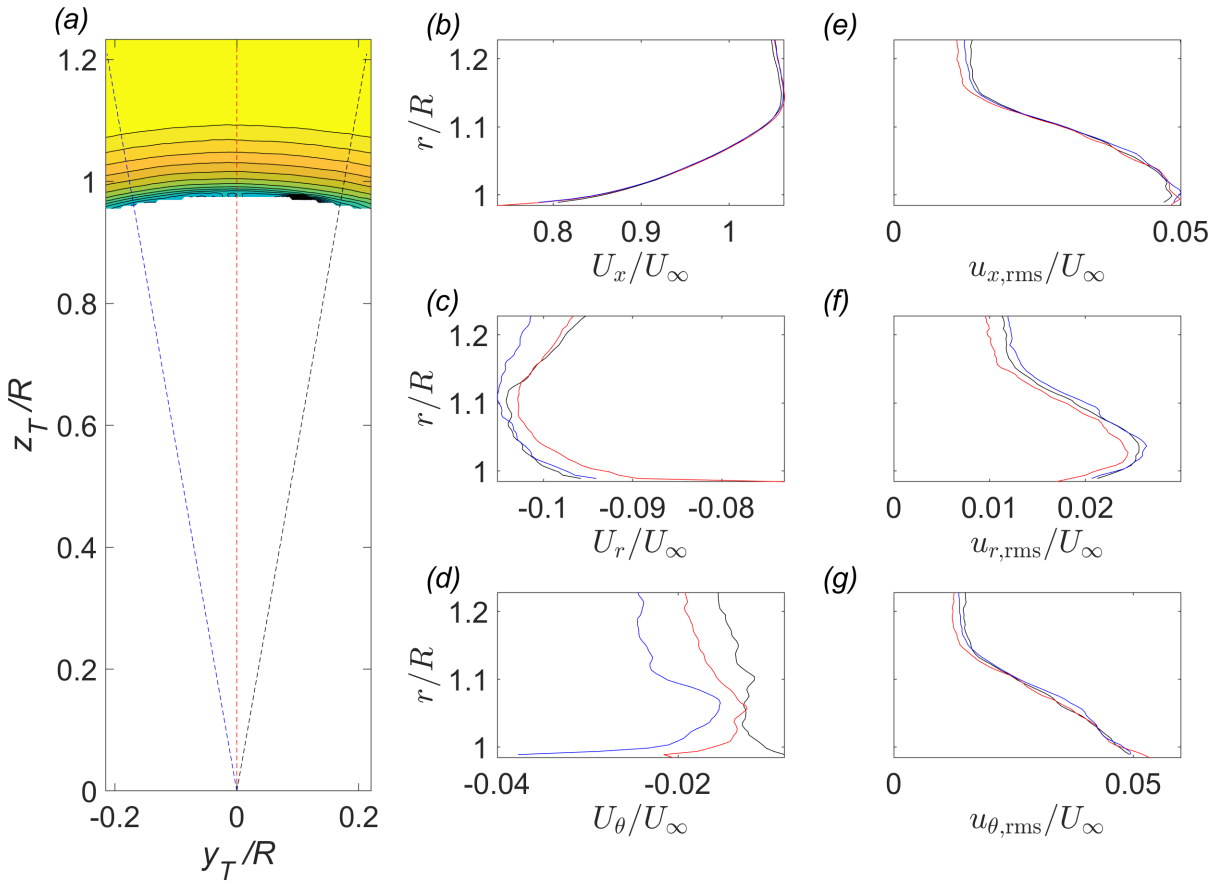

Figure A.2 Spanwise Plane 2 axisymmetry assessment. See Figure A.1 for description of layout.

profiles were extracted along the radial dashed lines in Fig. A.1(a), where the mean axial velocity U_x is the background contour. The remaining figures show radial profiles of (b) mean axial velocity U_x, (c) mean radial velocity U_r, (d) mean azimuthal velocity U_θ, (e) axial velocity root-mean-square (RMS) $u_{x,\mathrm{rms}}$, (f) radial velocity RMS $u_{r,\mathrm{rms}}$, and (g) azimuthal velocity RMS $u_{\theta,\mathrm{rms}}$. These figures show that the measurements at various circumferential stations agreed. Good axisymmetry was also found for other spanwise planes in Figs. A.2, A.3, and A.4.

The spanwise plane velocities $\tilde{u}_x$ and $\tilde{u}_r$ were validated against streamwise plane measurements. The mean and the RMS of these velocities are respectively shown in Figs. A.5 and A.6, with red circles and blue squares denoting the streamwise and spanwise planes. The left and right columns in these figures correspond to the axial and radial velocities. Each

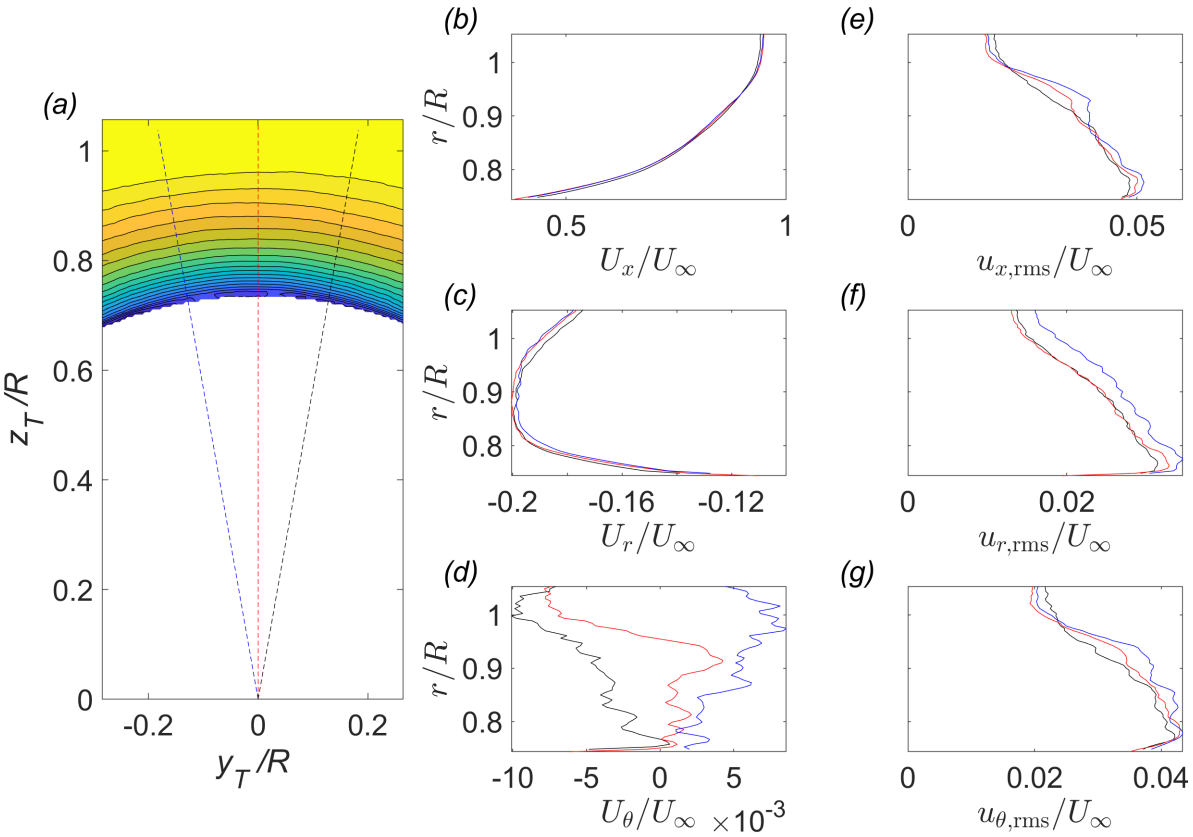

Figure A.3 Spanwise Plane 3 axisymmetry assessment. See Figure A.1 for description of layout.

row corresponds to a different spanwise plane, i.e, *(a,b)* SP1, *(c,d)* SP2, *(e,f)* SP3, and *(g,h)* SP4.

When inspecting the mean velocities in Fig. A.5, the deviation was at most a few percent of the free stream. Figure A.6 shows good agreement in the RMS profiles. The trends were similar, but the energy levels were lower in the spanwise plane because of the lower spatial resolution [184].

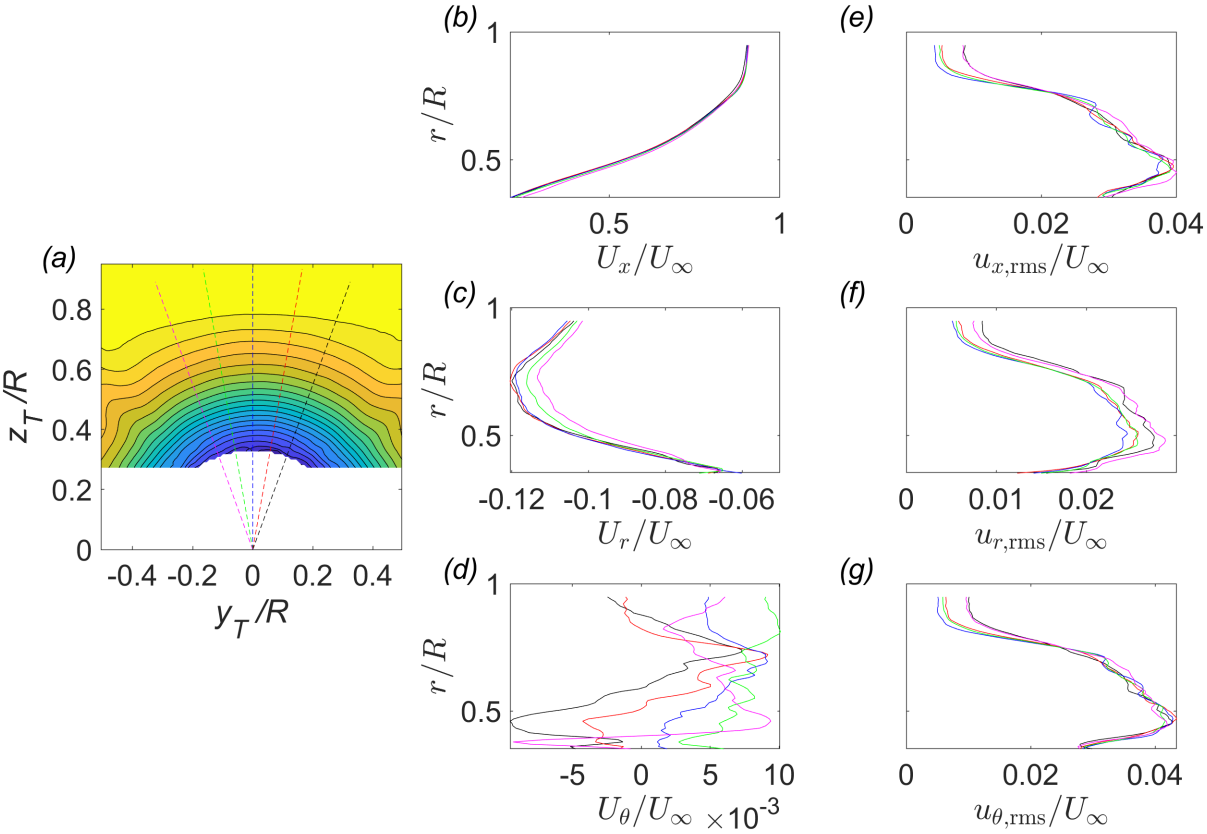

Figure A.4 Spanwise Plane 4 axisymmetry assessment. See Figure A.1 for description of layout.

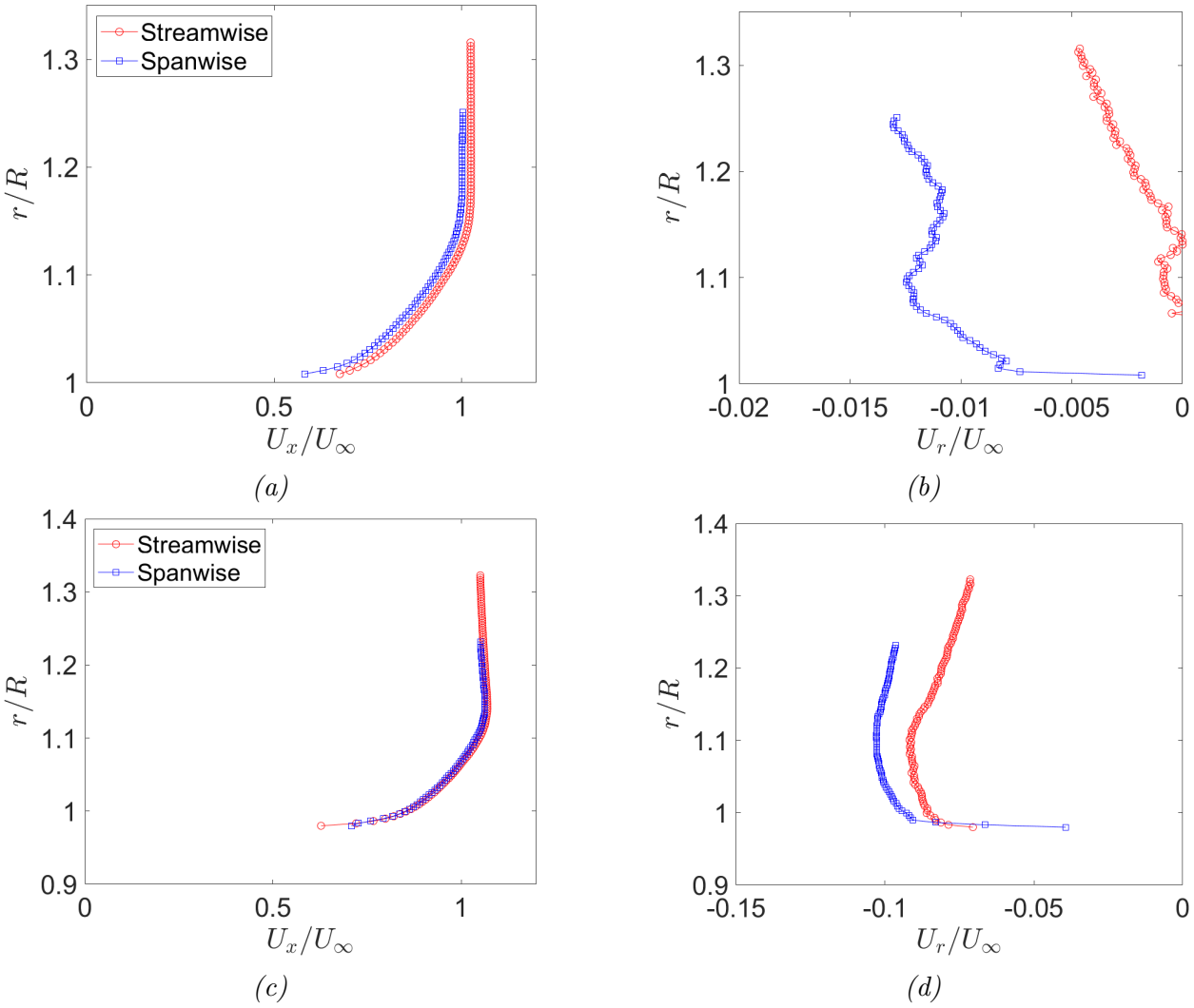

Figure A.5 Continued on next page.

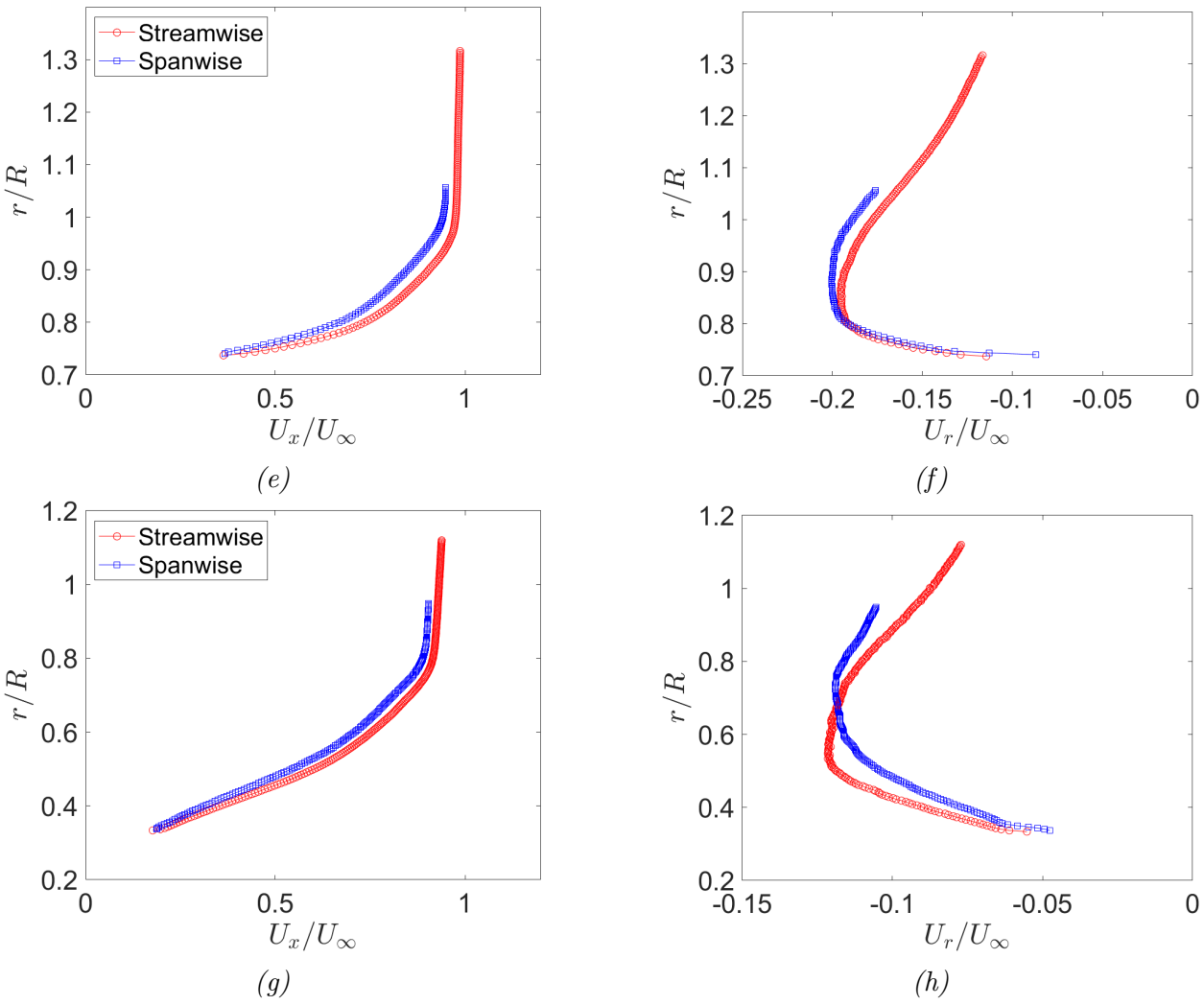

Figure A.5 The mean of axial (left) and radial (right) velocities taken from where the spanwise and streamwise planes intersect. *(a,b)* SP1 *(c,d)* SP2 *(e,f)* SP3 *(g,h)* SP4.

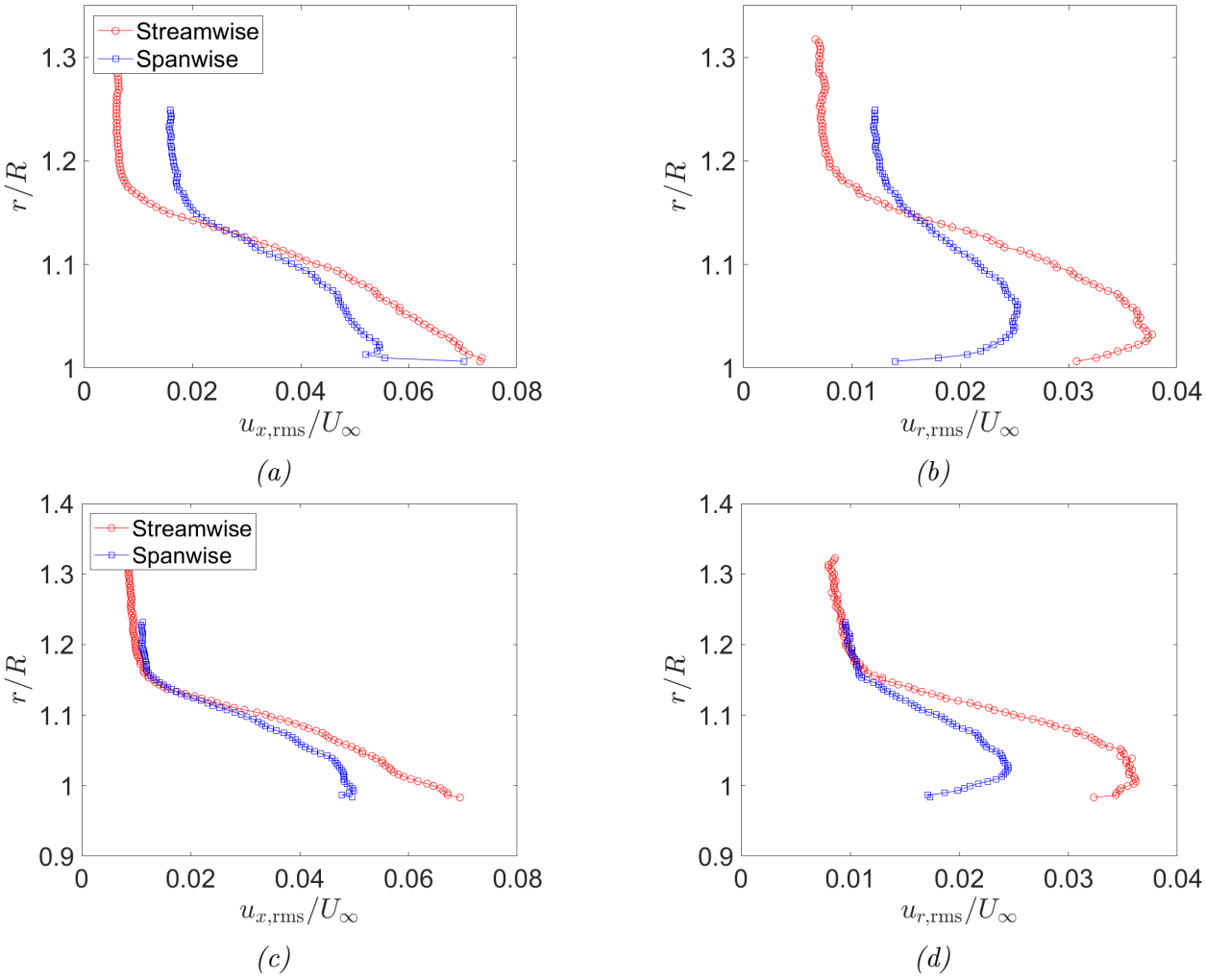

Figure A.6 Continued on next page.

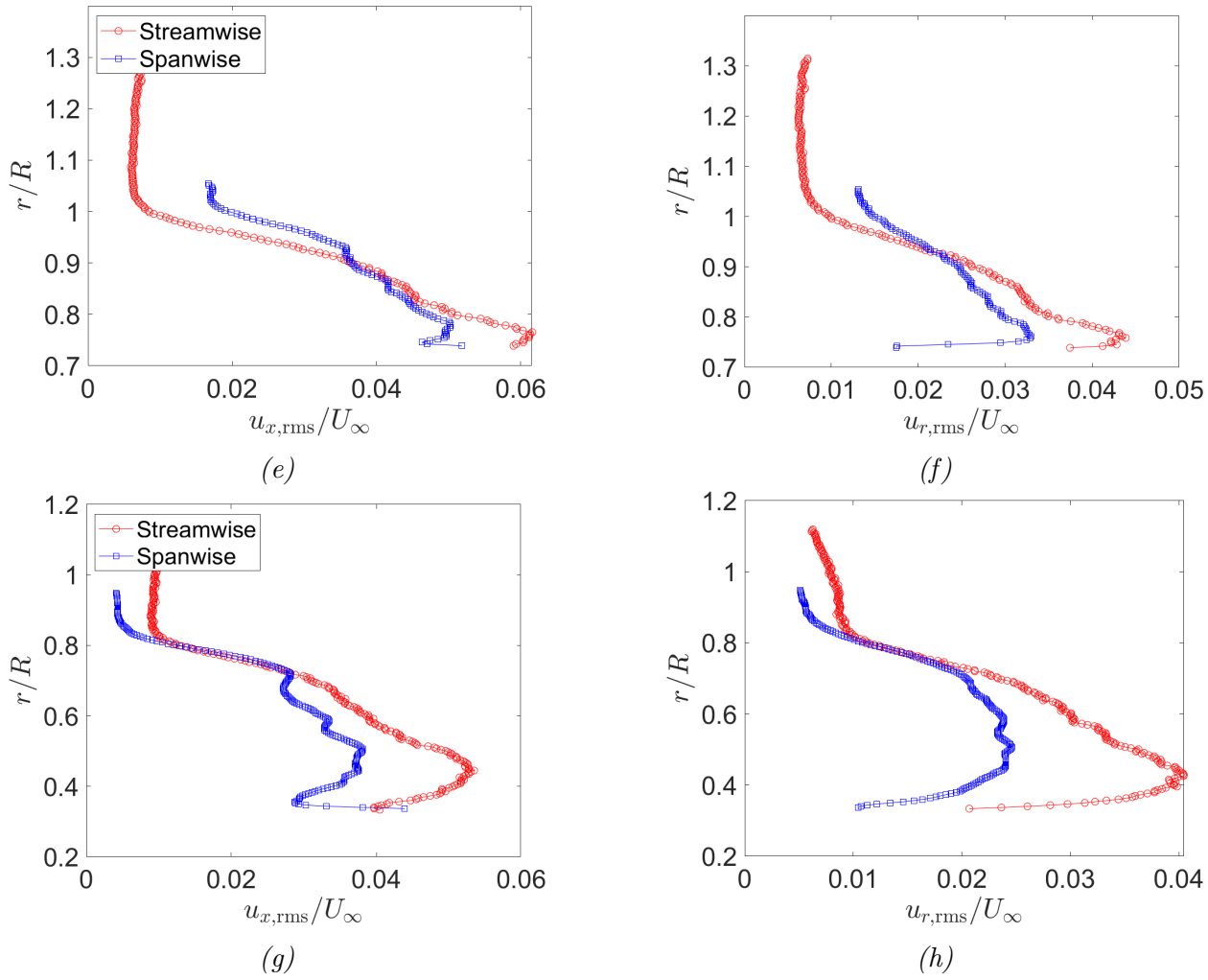

Figure A.6 The RMS of axial (left) and radial (right) velocity fluctuations taken from where the spanwise and streamwise planes intersect. *(a,b)* SP1 *(c,d)* SP2 *(e,f)* SP3 *(g,h)* SP4.

B Near-Wall PIV

For wall-bounded flows, many energetic and interesting activities occur near the wall. From a PIV measurement standpoint, the principal challenge is that the laser surface reflection is significantly brighter than the particles. As a result, the camera pixels targeting the near-wall region become saturated by the laser reflection, unable to distinguish particle patterns needed to compute velocity vectors.

The laser reflection does not need to be removed entirely. Instead, the reflection should be sufficiently low for the experimentalist to measure close enough to the wall. While this is easily attainable over flat glass plates, near-wall measurements can be challenging on opaque surfaces. To this end, this appendix describes a series of techniques that helped attenuate the wall reflection intensity without compromising the particle illumination intensity.

There are several well-known methods to attenuate the laser surface reflection [225]:

1. Use a transparent floor and illuminate the field of view with a laser from below.

2. Polish the surface to a smooth finish so that the light is predominantly reflected, instead of being scattered by surface roughness toward the camera sensor [195].

3. Use a fluorescent coating. A fluorescent absorbs a range of wavelengths but emits them at longer wavelengths (Stokes shift) that can be removed with a filter.

Because the current model has curved surfaces, using glass was not an option because manufacturing curved glass with the precise geometry of the model was impractical. Therefore, the second and third methods were used as described below.

Benchtop experiments were performed, and a combination of techniques was used to minimize the laser reflection intensity on an opaque wall. In order of their importance, methods used to reduce laser reflection include:

1. Reducing the incident angle of the laser sheet relative to the wall [226].

2. Creating a polished/glossy surface finish.

3. Applying a fluorescent coating.

4. Avoiding excess laser brightness.

Depending on the measurement goal, employing all of the techniques may be unnecessary. Therefore, understanding the required effort and the expected outcome of each method can help tailor the measurement setup based on the constraints of time and resources.

Measuring closer to the wall requires judicious orientation of the laser sheet. Therefore, consideration of laser placement during the experiment design phase is highly recommended. Introducing the laser path parallel to the surface resulted in drastic reductions in light scattered toward the camera relative to if the laser path was perpendicular to the surface. For the Suboff, the optical apparatus was placed well upstream of the region of interest, and a rectangular mirror directed the laser sheet downstream, as shown in Fig. 2.17, illuminating the surface at a shallow angle to decrease laser reflection.

The drawback of introducing the laser sheet at a shallow angle was the increased distance between the laser source and the measurement domain. Increased distance reduced the particle image intensity because of the laser sheet divergence with distance, the mirrors needed to steer the light, and the light scattered by particles in a globally seeded tunnel. These challenges could be mitigated with a seeding rake or a large focal-length cylindrical lens.

The second point of using a polished or glossy surface was also important. Minute imperfections on the surface acted as roughness that scattered light toward the camera. Even fingerprints significantly increased the surface reflection intensity. To achieve a polished finish on a surface, the model was roughly 1,000-grit before applying a few thin layers of clear coat. A ceramic clear coat was used in this work as it had the added benefit of improved temperature resistance. The result was a mirror-like finish that reflected light away from the camera instead of scattering light toward it. This technique was simple yet effective and is therefore always recommended.

The third approach of applying a fluorescent coating was more intricate than the previous

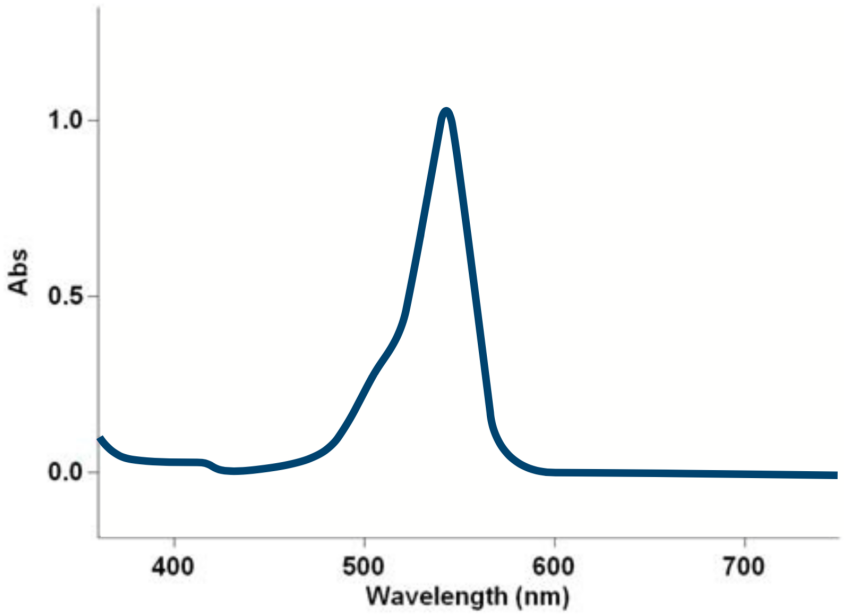

Figure B.1 Absorbance spectrum of Keyacid Rhodamine WT

two. The fluorescent coating can significantly attenuate the laser reflection and is crucial to measuring velocities, for example, in the viscous sublayer. There are, however, various challenges in utilizing a fluorescent coat:

1. Fluorescent solutions such as the Rhodamine WT used in this work experience self-quenching.

2. Rhodamine WT is known to dry to a "bumpy" finish. This additional surface roughness may modify the boundary layer and scatter light toward the cameras.

3. Rhodamine WT decays with light exposure, a rarely discussed but important point.

The paragraphs below elaborate on how these challenges were addressed or alleviated.

A benchtop experiment illustrated in Fig. B.2 was performed to study and overcome these challenges of using rhodamine. Tracer particles were enclosed in a box with plexiglass windows. The sample surface was illuminated by a 200 mJ/pulse, Nd: YAG laser (2 Hz) spread into a 1 mm sheet by a 20 mm cylindrical lens. The laser sheet was angled to be representative of the actual experimental setup. The CCD camera had a magnification of

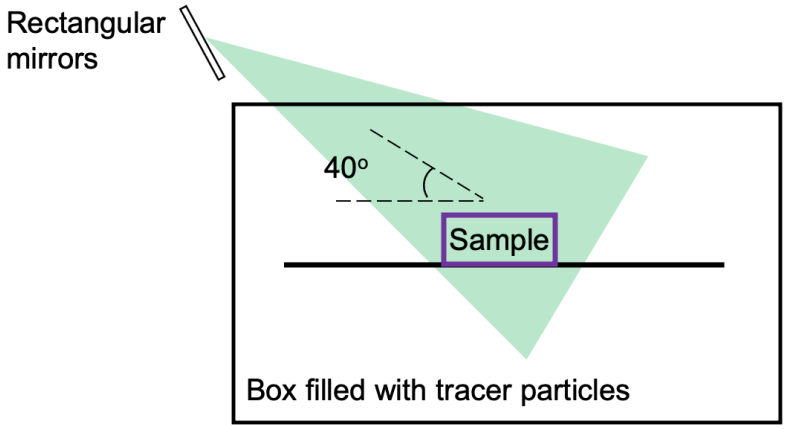

Figure B.2 Benchtop setup for testing various rhodamine samples. The camera perspective is into the page.

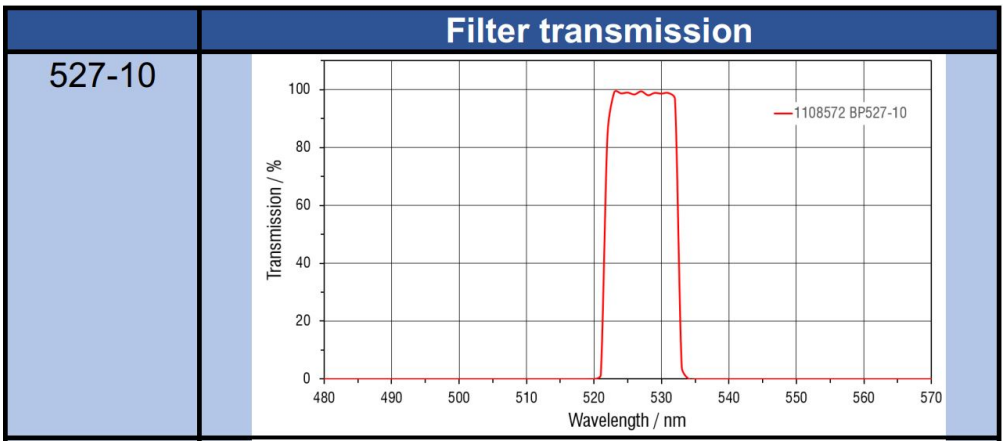

(a)

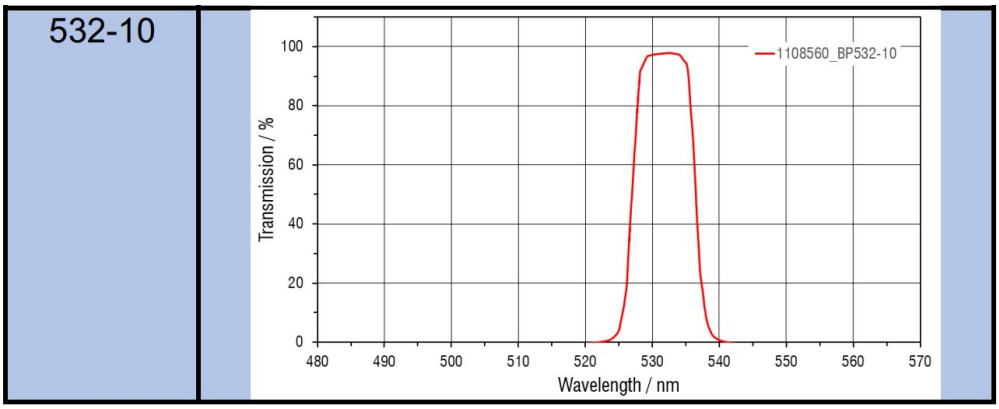

(b)

Figure B.2 Transmission of bandpass filters used. *(a)* 527±5 nm; *(b)* 532±5 nm. Filters courtesy of LaVision.

$M = 1$ and a pixel resolution of roughly 5.5 µm px^{-1}. The pass bands of the filters are shown in Fig. B.2.

he fluorescent used in this work was the Keyacid Rhodamine WT from Milliken. The absorbance spectrum of this rhodamine is shown in Figure B.1. Although the peak absorbance did not align with the laser wavelength (527 nm and 532 nm), it nonetheless helped significantly reduce the surface reflection.

The challenge of self-quenching was addressed by suspending the rhodamine in a sealer, as Callum Gray from LaVision recommended. Various concentrations were studied. A ratio of one part Rhodamine and 300 parts Varathane (water-based) by mass was used. Distilled water was added to adjust the solution viscosity for ease of application.

Another well-known challenge of using rhodamine is the rough surface finish after drying. Applying the rhodamine/sealer mixture in thin layers using an airbrush created a smooth finish such that no roughness elements were apparent to the naked eye or the touch. Then, self-leveling clear coats eliminated any remaining roughness. The clear coats transmitted the light while protecting the rhodamine coating.

The rhodamine decay was studied with repeated light exposure. The medium-density fiber (MDF) sample in this study was first sealed with polyurethane, then coated with black paint, three to four thin coats of the rhodamine solution, and two layers of clear coat. The black paint was used because as the rhodamine decayed, it appeared to take on the color of the substrate, and black is the least reflective color.

The raw images from this setup were analyzed by averaging the laser sheet surface reflection across each image, as shown in Fig. B.3(a). The minimal peak reflection was merely 70 counts, which can be removed entirely with background subtraction. The width and brightness of the laser reflection increased with the number of images. The baseline configuration without rhodamine, i.e., black paint and clear coats, is denoted by the highest curve with orange triangles, where the peak reflection was roughly 270 counts.

The peak brightness in Fig. B.3(b) showed a linear increase with image pairs. This linear

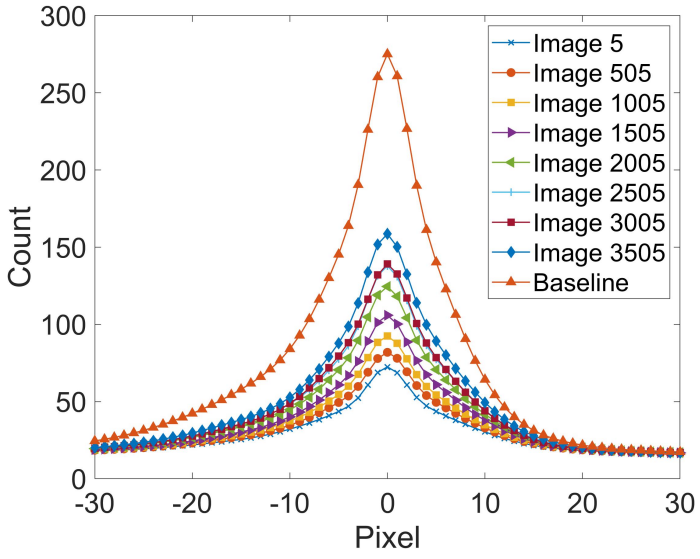

(a) Intensity distribution.

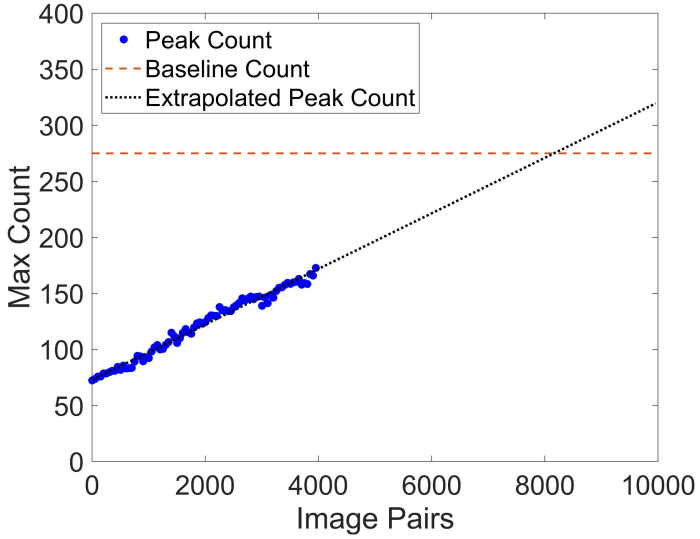

(b) Peak intensity.

Figure B.3 Surface reflection increased with images sampled, both in terms of width and peak intensity.

trend was extrapolated and intersected the baseline case at 8,000 image pairs, although an asymptote toward the baseline case was expected. This slope would likely vary with the experimental setup. Ultimately, the acceptable amount of laser reflection and whether the rhodamine should be reapplied depends on the experimentalist's judgment of acceptable uncertainty levels.

Rhodamine decay is inevitable with light exposure but can be alleviated. In particular,

high surface temperatures were noted to accelerate the decay. Therefore, two methods to reduce the surface temperature are:

1. Orienting the laser at a shallow angle relative to the surface, as shown in Figs. 2.21, 2.14, and 2.17. These setups show that while the light intensity above the surface was preserved, the light per unit length on the surface was reduced.

2. Using a substrate with good thermal conductivity to distribute the energy deposited by the laser. An aluminum substrate was superior to carbon fiber and wood in this regard. Alternatively, a clear ceramic coat appeared to help protect the rhodamine when cured over a few days. Allowing the ceramic paint to harden with time was an alternative to a heat cure, which harmed the epoxy matrix and potentially the rhodamine.

The fourth and final recommendation is to increase the laser brightness only as necessary. Through trial and error, the experimentalist must decide on the point of diminishing returns, where additional laser brightness only increases the surface reflection intensity without improving the measurement quality.

C POD for Scale Decomposition

Lumley [227] introduced the proper orthogonal decomposition (POD) to the fluids community to quantify turbulence in terms of deterministic structures. In recent years, given the enormous amount of data produced by simulations and experiments, the method has become a popular way to extract energetic coherent motions in turbulent flow fields, either for a deeper physical understanding or for modeling/prediction in flow control [194, 228, 229].

The POD was used to investigate how the large and small scales respond to pressure gradient and wall curvature. The reason for using the POD instead of the traditional Fourier scale separation was the inhomogeneous longitudinal direction, which resulted from the pressure gradient and wall curvature. Nevertheless, a brief outline of the POD is provided here, and the interested reader is directed to Refs. [221, 230, 231] for more in-depth discussions.

The snapshot POD by Sirovich [232] was used to reduce the random access memory usage. The first step was computing the spatial covariance matrix Q,

$$Q = U^T U. \tag{C.1}$$

In this equation, $U \in \mathbb{R}^{n_s \times n_t}$ was a matrix with a spatial dimension n_s and a temporal dimension n_t containing the mean-subtracted velocities (u and w). The covariance matrix dimensions were $Q \in \mathbb{R}^{n_t \times n_t}$. Then, an eigendecomposition of this symmetric correlation matrix provided the temporal modes Ψ and the corresponding energy levels Λ,

$$Q\Psi = \Psi\Lambda. \tag{C.2}$$

The POD spatial modes were then obtained by rearranging the singular value decomposition,

$$U = \Phi\Sigma\Psi^T \tag{C.3}$$

and using the relation $\Sigma^2 = \Lambda$ (which can be shown by substituting C.3 into C.1 and

comparing with C.2),

$$\Phi = U\Psi\Lambda^{-1/2}. \tag{C.4}$$

Note that Λ or Σ^2 was interpreted as the turbulent kinetic energy embedded within each mode.

A reduced-order or low-rank representation U_r of the original flow U was created by retaining the most energetic n_m modes,

$$U_r = \Phi_r \Sigma_r \Psi_r^T. \tag{C.5}$$

The low-rank U_r permitted analysis of the coherent large scales and how they were affected by surface curvature and pressure gradient. In the present work, the leading 200 modes, which resolved 50% of the measured turbulent kinetic energy, were used in the low-rank flow U_r to represent the large scales. The remainder was the small scale. This energy criterion was selected based on the prior work of Wu and Christensen [217].